Doctoral Dissertation
Doctoral Program in Mechanical Enginering (33.th cycle)

Mixing the Power of Water and Oil

The Hydraulic PTO for Wave Energy Conversion

Mauro Bonfanti

* * * * *

Supervisors
Prof.ssa Giuliana Mattiazzo

Doctoral Examination Committee:
Prof. Antonio Carcaterra, Referee, Università degli Studi di Roma "La Sapienza" (Italy)
Prof. Francesco Braghin, Referee, Politecnico di Milano (Italy)
Prof. Benedetto Allotta, Università degli Studi di Firenze (Italy)
Prof. Stefano Mauro, Politecnico di Torino (Italy)
Prof. Massimo Sorli, Politecnico di Torino (Italy)

Politecnico di Torino
September 03, 2021

I hereby declare that, the contents and organisation of this dissertation constitute my own original work and does not compromise in any way the rights of third parties, including those relating to the security of personal data.

. . . . . .

Mauro Bonfanti

Torino, September 03, 2021

Summary

Power Take-Off (PTO) systems are the heart of a Wave Energy Converter (WEC) and many academic researchers and developer companies are actively working to design and improve the PTO. It is known that the economic viability, efficiency and complexity of a wave energy device depends on its PTO system. This thesis pursues the development of a hydraulic PTO for WECs with the intention of encouraging new research activities in this energy field. The ISWEC (Inertial Sea Wave Energy Converter), developed by the Marine Offshore Renewable Energy Lab (MOREnergy Lab) of Politecnico di Torino (Italy), represents the reference device. The work consists in the derivation of a novel spectral-domain model including both mechanical and hydraulic PTO technologies, the creation of a techno-economic design tool and the application of an optimal control technique to the ISWEC. The hydraulic PTO technology aims to drive the ISWEC system, originally designed for the Mediterranean Sea, toward an oceanic implementation. The research activities started with the implementation of a spectral-domain model, able to reduce the computational burden associated to the ISWEC simulation and to give, at the same time, the accuracy of the expected results. The new spectral-domain framework is implemented in a multi-stage design tool. Such a design tool exploits the potential of an in-house MATLAB-based Genetic Algorithm to effectively design the ISWEC system with respect to different deployment sites, PTO technologies, and the desired techno-economic metrics. The comparison between the optimal mechanical and hydraulic PTO devices in four chosen installation sites demonstrates that the hydraulic transmission reduces the cost of energy up to 20% decreasing the initial investment almost of 25%. The economic efficiency together with the high power density of the hydraulic technology is advantageous for the future industrialization, resulting in a more efficient and higher wave energy harvesting. A Model Predictive Control (MPC) is finally proposed for further optimization of the hydraulic PTO performances. The extracted power of the ISWEC is evaluated in irregular wave conditions with promising results. The major outcomes of this dissertation are the detailed overview of the hydraulic PTO advantages together with some guidelines for the modelling, design and control improvement of this technology.

Acknowledgements

Vorrei ringraziare la mia relatrice, Giuliana, che in questi splendidi 5 anni mi ha accompagnato con la sua inesauribile carica dentro e fuori dal progetto. Per la sua capacità di valorizzare le persone e per avermi dato fiducia facendomi esprimere al meglio del mio potenziale. Per avermi dato l'opportunità di essere parte di questo fantastico gruppo. Un grazie a Giovanni, con il quale ho lavorato a stretto contatto per realizzare quel banco prova che ci ha dato e continuerà a dare tanti problemi. Grazie per avermi insegnato la virtù della calma e della tranquillità.

Grazie a tutti i colleghi del Politecnico e di Wave for Energy per avermi fatto crescere tecnicamente e professionalmente. Ho apprezzato ogni singolo lavoro svolto con voi, ogni viaggio, ogni successo e ogni errore. Ho imparato qualcosa da ognuno di voi, da coloro con cui ho lavorato per 5 anni, a coloro che sono rimasti anche solo per pochi mesi. L'aver incontrato degli amici, oltre a dei colleghi, ha un valore per me inestimabile. Un grazie particolare ad Antonello, il collega e compagno di viaggio migliore che potessi mai desiderare.

Il ringraziamento più grande va alla mia famiglia, Mamma, Papà, Andrea, Nonni e Monica per essere stati il sostegno più importante fin dall'inizio. Grazie alla loro pazienza e al loro affetto, fondamentale nei momenti più duri. Un grazie particolare a Monica, per avermi dato la possibilità di inseguire i miei sogni e i miei progetti. Grazie agli amici di una vita, quelli che conosci dalle elementari, quelli che sai che potrai stare via 10 giorni o 10 anni ma che non se ne andranno mai.

E un grazie a Me, per aver sempre anteposto il divertimento, la famiglia e le amicizie al lavoro, per mettere sempre al primo posto il viaggio e mai la destinazione.

Computational resources were provided by the Eni High Performance Computing – layer 4 (HPC4).

Abbiamo sempre così
poco tempo per fare così
tanto.

Contents

List of Tables

List of Figures

Chapter 1

Introduction

Nowadays, renewable energy is considered fundamental by the European Union (EU) to achieve the clean energy consumption objectives [1, 2]. The target include a renewable energy utilization up to 32% for 2030 [3]. The Earth's natural resources, like sunlight, wind, marine and biomass energies are abundantly available within the EU, and are becoming increasingly cost-competitive with fossil fuels. As such, they play a crucial role to make the energy system independent on imported coal and oil resources. Moreover, the potential to create a broad range of new jobs and industrial opportunities must not go unnoticed.

The International Energy Agency (IEA) Global Energy Review of 2020 highlights that renewable energies were the only source that faced a growth in demand, despite the COVID-19 pandemic induced a global macroeconomic shock. In particular, solar and wind energies experienced a significant growth in the last year due to their technological maturity, giving cost-effective solutions to handle the climate objectives of the EU [4]. As reported in [5], in the first Quarter (Q1) of 2020, the global use of renewable energy was 1.5% higher than in Q1 2019. The increase was driven by a rise of about 3% in renewable electricity generation with solar panel and wind power installations.

Over the last decade, the growth in the renewable sector was due to a number of factors including political support, financial incentives and reduction in the costs of technologies, making the renewable energy cost competitive. However, a considerable Research and Development (R&D) effort has to be continued and extended to other renewable sources. Among them, one of the most promising alternative is the Marine Renewable Energy (MRE), including the resource of tidal and ocean currents, tidal rise and fall, salinity gradients, ocean thermal energy and wave energy. The wave energy sector could potentially equal and even exceed the offshore wind sector, if we take into account that waves are a concentrated form of wind energy capable of travelling large distances with minimal losses. Promising resource assessments declares a virtually untapped 151300 TWh/year of clean energy in the oceans, which is comparable with the world primary energy demand

[6]. In particular, the potential related to the wave energy power, alone, ranges from 1 to 10 TW [7], leading an annual expected energy roughly between 8000 and 90000 TWh/year, up to 93000 TWh/year according to Melikoglu [8]. The world wide distribution of the wave power density, that expresses the power carried by a wave 1 meter wide front, is depicted in Figure 1.1. The ocean waves can generate over 100 kW/m of power density, which is far higher than solar and wind intensity. Moreover, the wave power, as against most of the other alternative energy sources, is easily predictable and consistent proving much better than other sources that are dependent on wind or sun exposure.

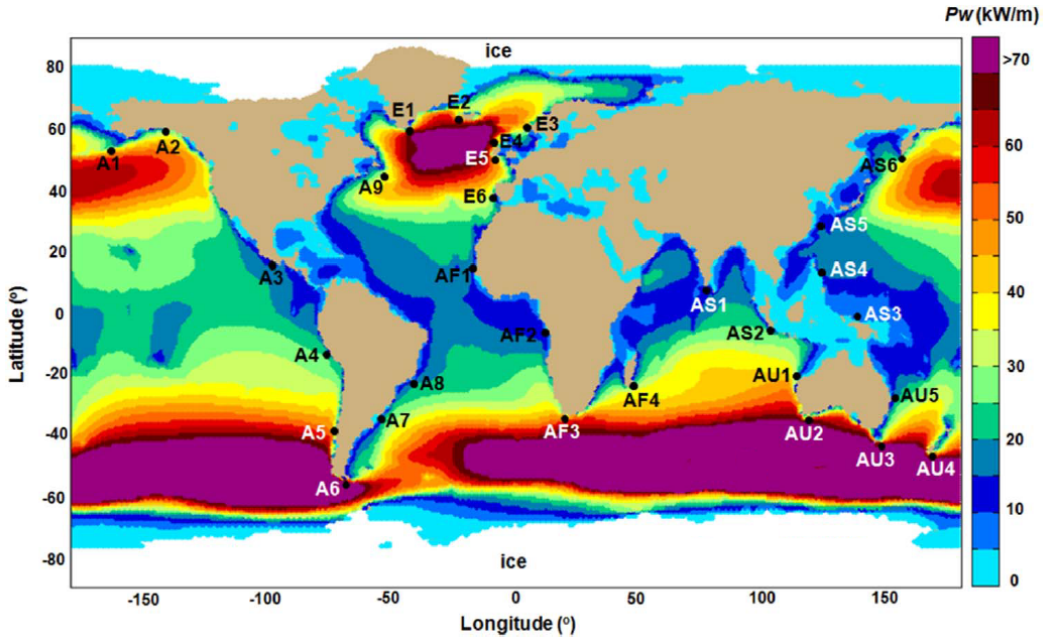

Figure 1.1: Map of the mean wave power density corresponding to the 15-year interval from January 2000 to December 2014 [9].

1.1 Wave energy devices and technologies

Over the last decade, the ocean energy industry has made significant progresses. However, despite the potential of the wave power, the WEC concepts are far from being reliable, robust and cost-effective [10]. In addition, storing the converted energy, its regulation and the transfer to mainland electricity grid is not trivial. In [11], the principal obstacles to the development and competitiveness of wave energy devices are detailed as the lack of technological maturity and high develop costs, resulting in a high Levelized Cost of Energy (LCoE) of the solutions proposed. In

sum, the risk underlying the development of a WEC discourages the investors, particularly at a high TRL. On the other hand, strong research sources are employed to fill the gap between more mature technologies, e.g. solar panels and wind turbines. Research ambitions lies on designing a WEC with maximum efficiency, reliability, survivability, reduced costs and minimum environmental impacts. To harness the wave power it is important to design a structure that can efficiently capture and harvest the energy transmitted by the waves. A further key factor is that the structure must be able to survive the marine environment, in particular, storm events wherein the wave power significantly increases. Then, a WEC should be conceived to protect the relative motion of its mechanical parts from the corrosive marine environment, limiting also the sea pollution.

1.1.1 Wave energy converter classification

The development of a WEC is characterized by different concepts for how to utilize the wave energy resource. There are a variety of ways to gather the wave power and, from the first concepts proposed by Yoshio Masuda in the 40s and by Salter in the 70s [12], a wide range of technologies have been studied, tested and (some of them) installed in real sea locations (for an exhaustive review of the WEC concepts see e.g. [13, 14, 15]). The categorization used by the IEA - Ocean Energy Systems [16] is reported in Figure 1.2.

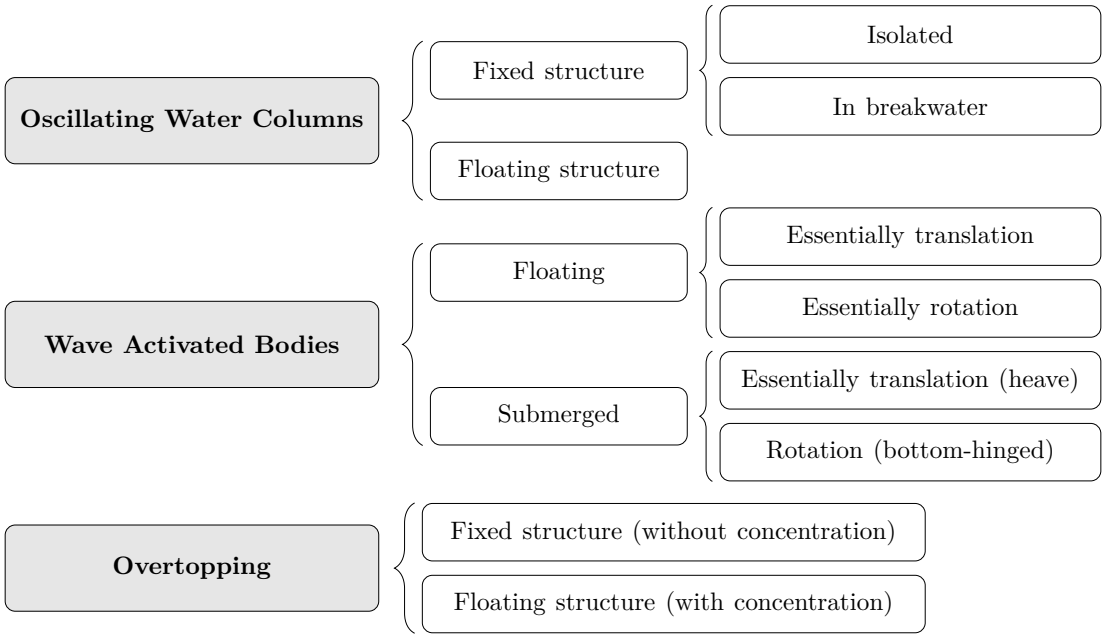

Figure 1.2: Categorization of wave energy technologies according to the IEA – Ocean Energy Systems. Adapted from [16].

A comprehensive picture of existing wave technologies being used for wave energy extraction is reviewed in [17]. The review explained their potential and also the challenges that wave technologies face. Figure 1.3 illustrates the main types of WECs whether they are installed onshore, nearshore or offshore. In the onshore area the most common systems are based on oscillating water columns (a), where the air is trapped in a semi-submerged chamber and it is compressed and decompressed to rotate a turbine that generate electricity. In a nearshore environment, which is defined by shallow water areas, two types of WEC system solution are the oscillating wave surge converter (b), that acts as a pendulum under the wave action, and the point absorber (c), that harnesses the heave motion of a heaving floater. Lastly, in offshore regions, the most promising results comes from the attenuator (d), point absorber (slack-moored to the sea bed) and rotating/oscillating mass converter (e).

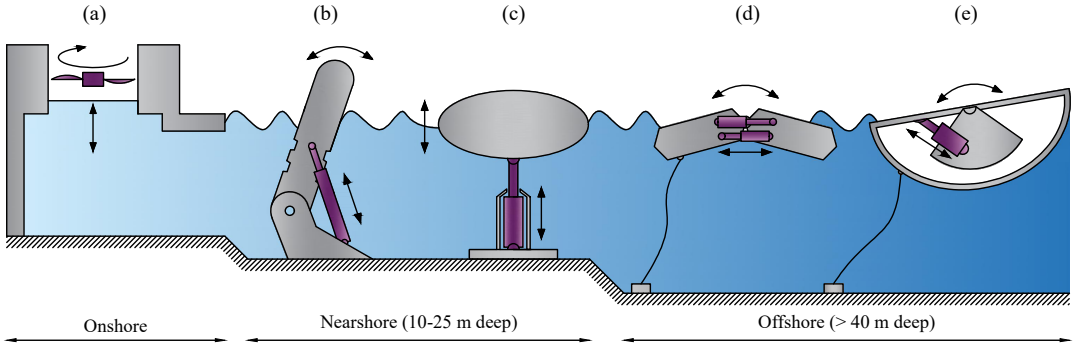

Figure 1.3: Wave converter devices: (a) oscillating water column, (b) oscillating surge converter, (c) point absorber, (d) attenuator, (e) rotating/oscillating mass.

Here, all WECs consisting of oscillating bodies are put into one category named Wave Activated Bodies (WABs), which the device studied in this thesis belongs. WABs can be classified according to their working principles in three categories:

- **Point Absorbers**: a Point Absorber (PA) is characterized by small dimensions compared to the incident wavelength. PAs are floating or submerged structures moored at the sea-bed. Incident waves (typically) induce a heave motion of the structure that is damped to extract energy. Examples of PAs are the floating device Powerbuoy, developed by Ocean Power Technology [18] and the fully-submerged buoy CETO ,developed by Carnegie [19], shown in Figure 1.4a. The Seabased AB [20] is a WEC equipped with a linear generator coupled with PA buoy systems. Wavebob [21] represents a self-reacting PA where the energy is extracted through the differential vertical motion between a submerged mass and a buoyant float structure;

- **Attenuators**: Attenuators are constituted by multi-body parts slack-moored at the sea-bed with a total length longer than the incident wavelength. These devices are composed of several floating sections linked together by hinged joints including the energy extraction systems that harvests the wave energy. During normal operation the multi-body structure is aligned with the direction of the dominant wave. The Pelamis represents one of the most famous Attenuator developed in full scale (750 kW of rated power), being the first offshore WEC connected to the electrical grid [22]. Another famous Attenuator-like device is the Wavestar [23], developed by the Danish company Wave Star A/S in collaboration with the Aalborg University. As shown in Figure 1.4b, it consists of a multiple absorber concept composed by hemisphere shaped floats attached to a single fixed platform;

- **Terminators**: in Terminator WECs the main dimension is faced perpendicular to the incoming wave direction. The wave motion induces an oscillation of the WEC absorber and the energy is captured (usually) damping the alternating WEC motion. WECs that exploit the oscillating motion of a flapper hinged to the sea-bed are the most common and the best known is the Oyster WEC [24], reported in Figure 1.4c. Another example of Terminator WEC is the Wave Dragon [25], that is constituted by a floating structure with two wave reflectors that drives the incoming waves towards a reservoir with set of low-head hydraulic turbines.

(a) (b) (c)

Figure 1.4: Examples of WEC devices: (a) CETO [26], (b) Wavestar [27] and (c) Oyster [28].

Technically speaking, one of the main challenges faced by the wave energy technologies is the harsh conditions of the marine environment: high corrosion due to salt water and high loads due to extreme events. One means to convert the wave energy into mechanical energy is by using a generator that is fixed on the sea bottom with mechanical and structural parts in contact with the corrosive marine environment, inevitably reducing the reliability of the whole system. Some WEC

concepts have been developed to better address these challenges, namely by mitigating issues related to maintenance and accessibility procedures. This is achieved by sheltering the sensitive electro-mechanical equipment from the surrounding sea environment by placing them inside the WEC. Moreover, the reaction needed to obtain relative motion between the power extraction parts and the floater has to be fully-enclosed in a protected environment. Different technology solutions seek to address this issue transmitting the motion of the floater to an internal translating or rotating mass, generating a Self-Reacting WEC (SRWEC). The main ideas, schematic in Figure 1.5, are to harvest wave energy damping the floater motion by controlling an inertial damper fully enclosed inside the hull. Within this category, successful architectures are proposed in literature and these concepts can serve as a reference for the development of a new generation of more capable and robust devices.

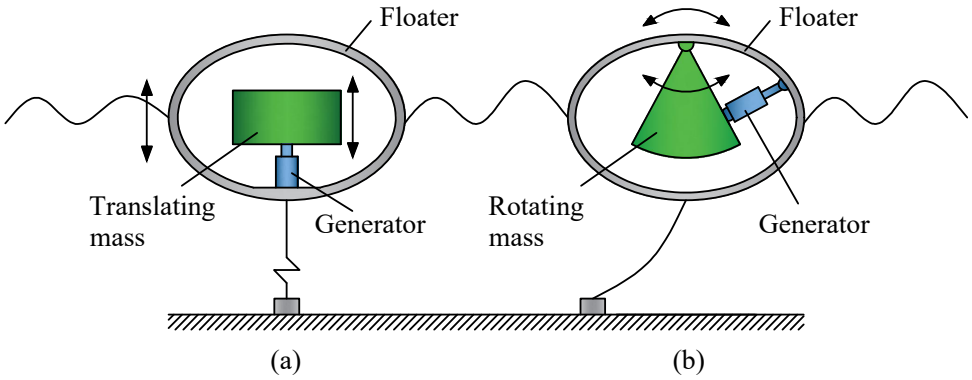

Figure 1.5: Concepts of SRWEC: (a) translating mass solution, (b) rotating mass solution.

The device PS FROG MK 5 developed by the University of Lancaster [29] consists of a large floater containing a sliding mass connected to a linear Power Take-Off. The wave force induces a pitching motion of the hull damped by the translating mass, placed at the top of the device to maximize its oscillation. A rendering of the PS FROG MK 5 concept is shown in Figure 1.6a. Rotating mass concepts are the PeWEC (Figure 1.6b), developed by Politecnico di Torino in collaboration with ENEA [30], and the SEAREV device (Figure 1.6c), developed by Ecole Centrale de Nantes [31]. Such concepts are based on pendulum working principle exploiting the wave power damping the pitching motion of the floater. They need a slack mooring system allowing the device to align with the dominant sea-state. Penguin Wello (Figure 1.6d) represents another valid SRWEC solution [32]. The device working principle is based on a rotational mass with vertical axis installed inside a sealed hull, shaped to exploit all the DoFs of motion. Another pendulum-based device is WITT, developed by WITT Limited, that can harvest the wave energy through two

translational and two rotational motions along surge, sway, pitch and roll Degree of Freedom (DoF) [33].

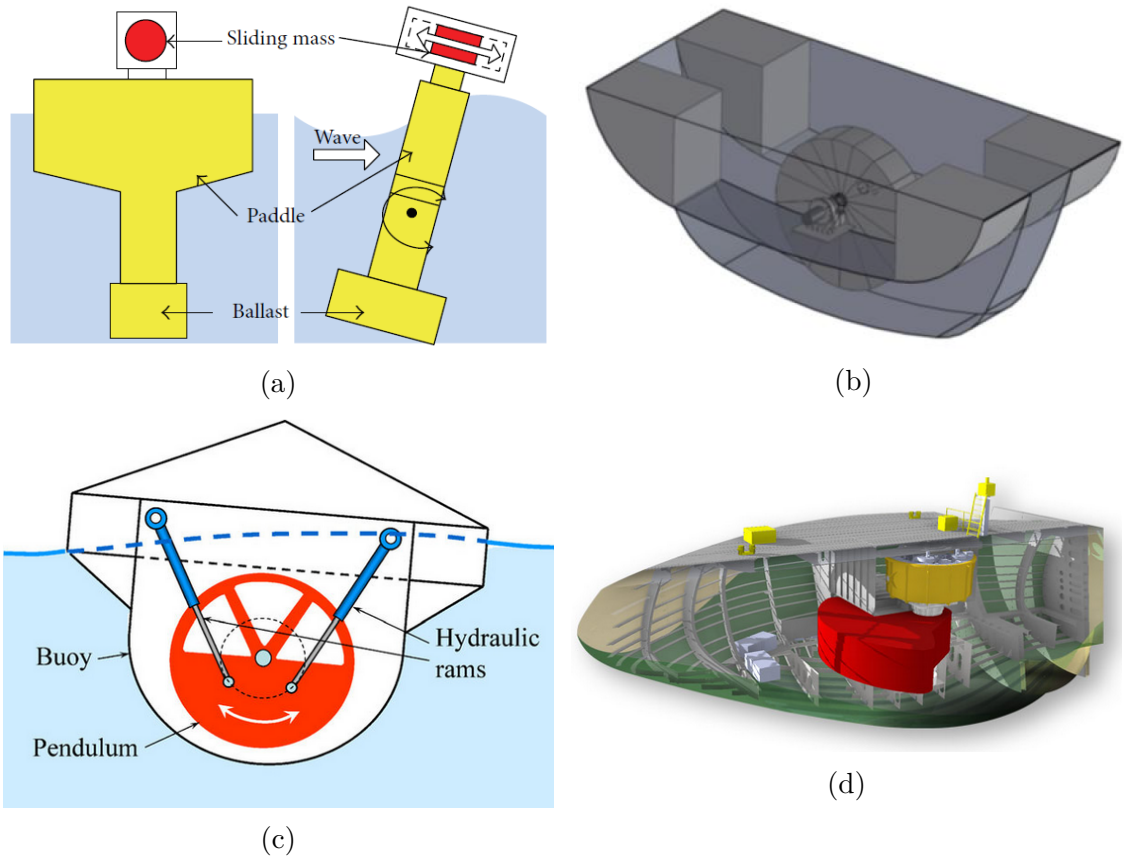

Figure 1.6: Examples of SRWEC devices: (a) PS FROG MK 5 [14], (b) SEAREV [14], (c) PeWEC [30], and (d) Penguin Wello [32].

A particular category of rotating mass concepts are the gyroscope based systems. OCEANTEC device [34] is an example of how the motion of a gyroscope installed inside a pitching floater can be exploited for wave energy conversion, as represented in Figure 1.7a. The inertial Sea Wave Energy Converter (ISWEC), argument of this thesis, is a well known gyroscope based WEC developed at the Politecnico di Torino. It is composed of a sealed hull carrying inside two or more gyroscopic units, as shown in Figure 1.7b. The wave energy is captured by damping the rocking motion of the floater by controlling the oscillation of the gyroscopic units. The ISWEC state of the art is introduced in Section 1.4 and its numerical model accurately described in Chapter **??**. This device possesses an extra degree of controllability compared to the previous described SRWEC solutions, represented by the flywheel speed. This feature gives the ability to modify the inertial characteristics in respect to the incoming wave to maximize the power extraction for a broad range of sea-states.

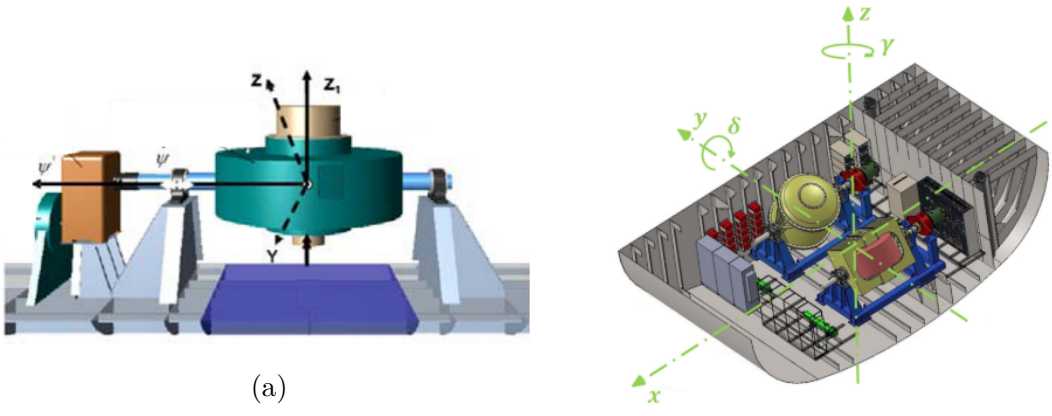

(a) (b)

Figure 1.7: gyroscope based devices: (a) OCEANTEC device [34] and (b) ISWEC device [35].

These solutions could be the most promising technologies along with the fixed structure ones (e.g. Wavestar) since the relative motion with the harsh marine environment is completely avoided except for the installation structure and/or the mooring system.

1.1.2 Wave energy converter subsystems

Most of the WEC concepts consist of the same primary sub-systems, which is due to their common environment and goal. Each sub-system has a direct impact on the reliability, survivability, and cost of the device. It also contributes to the mass, size and structural dynamics of the WEC. The main sub-systems, that are represented in Figure 1.8, consist of:

- **Wave absorption subsystem**: it is the primary wave absorption part that exploits the wave power converting it into kinetic energy. Simply called hull, floater or WEC body, it can be shaped depending on the technology and connected to both the reaction and power extraction subsystems against which forces and motions are transferred;
- **Power extraction subsystem**: it converts the captured wave energy into electricity transferring the kinetic motion to its moving part and reacting on the WEC body. Usually, it is designed and controlled to enhance the WEC motion making it resonant with the incoming wave in order to maximize the power extraction;
- **Control and instrumentation subsystem**: control and instrumentation represents the brain of the WEC as it take care of the WEC's control and its

measurements. They made up hardware and software for the automation and control processes, the sensors and their data acquisition, the communication and data transfer, and the human interface.

In the end, the reaction subsystem has to be mentioned: it maintains the WEC into position relative to the seabed or to a fixed structure providing a reaction point for the power extraction subsystem and/or for the WEC body. This thesis focuses on the power extraction and control-instrumentation subsystem, filled in gray in Figure 1.8.

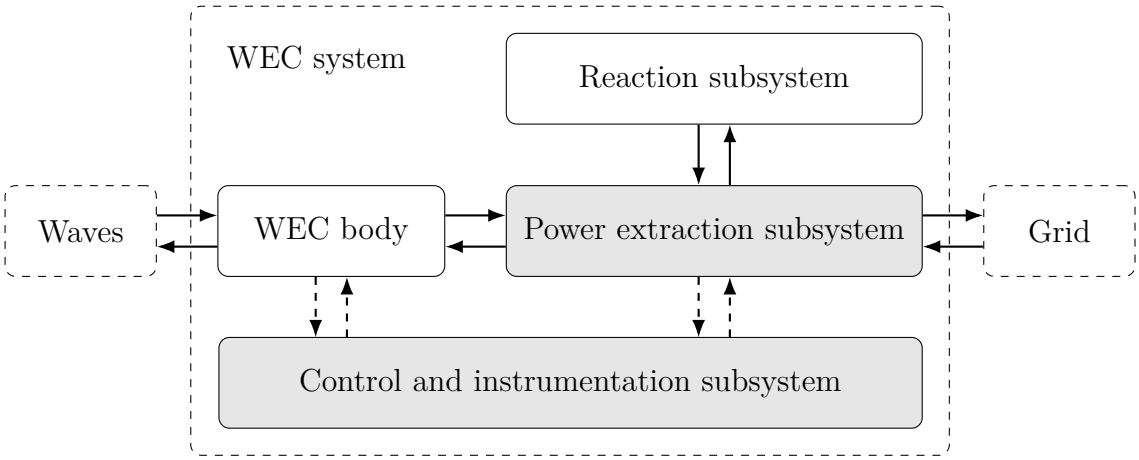

Figure 1.8: WEC subsystems. Continuous lines represent the loads exchanged between WEC parts; dashed lines are the acquisitions and control signals. The grey-filled blocks are the focus of this thesis.

In the following section, the most used power extraction subsystems are presented and briefly described, highlighting their pros and cons in respect to their main components and working principles.

1.2 Power take-off mechanisms for WECs

The power extraction subsystem, know in literature as Power Take-Off (PTO), concerns the power conversion stage of a WEC. The PTO has a direct impact on the annual energy production along with the reliability and, thus, the cost-effectiveness of the WEC. The PTO affects directly the capital cost by accounting for typically 20÷30% of the total capital cost [36]. As opposed to the wind energy sector, there is no an established standard for the wave energy conversion and many different types of PTO systems have been investigated in literature so far. In this section, a general overview of the main PTO mechanism for WECs is provided along with the challenges faced in the PTO design process.

1.2.1 Challenges in power take-off design

Develop a efficient, reliable and cost-effective PTO constitutes one of the main challenges in WEC industry. The movement or oscillations of bodies caused by sea waves are very slow, bidirectional and irregular, and the torque density requirements for wave power is immense. Moreover, the wave power is characterized by having more than a factor of 10 between mean and peak power, determining irregular torque and velocity profiles of the PTO, as seen in Figure 1.9. The peaks contributes heavily to the overall production [37] and may not simply be discarded (e.g. saturating the electrical generator of the PTO). Figure 1.9 also shows that the energy is grouped and its flux through the WEC subsystem is not uniform over time. Resultantly, energy storage is required to store the energy overcome maintaining a stable power production. Moreover, to extract adequate amounts of energy from waves, the PTO load force, or torque, should be controlled as a function of incident wave and body movement. Finally, to fully maximize the energy extraction, the PTO should be able to operate in four quadrant mode. Four quadrant mode means that all four combination of force and velocity direction should be managed, as the PTO sometimes is required to aid the float motion (reactive control strategies). The controllability and four quadrant behaviour is required to compensate for the inherit off-resonance behaviour of WEC devices, characterized by being narrow-banded with an under-damped resonance. To correct this deficiency, the force applied by the PTO to the absorber is controlled to adjust the absorber's resonance frequency to match the incoming wave frequency [12, 38]. Then, another difficult is testing and validating at small scale as the friction constitutes a critical issue for the PTO mechanism.

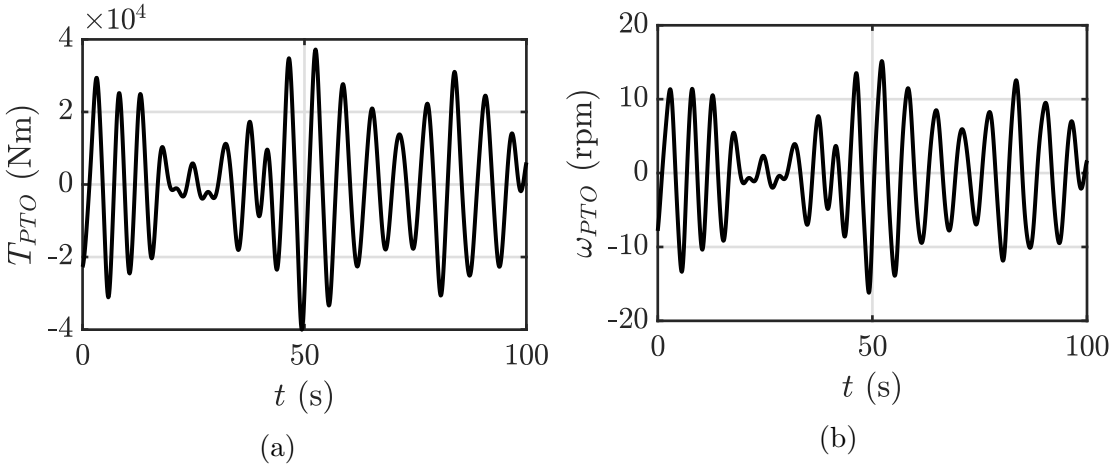

Figure 1.9: Example of torque (a) and angular velocity (b) profiles of the PTO system in a 500 kW rated power ISWEC device. The ISWEC is simulated under irregular wave profile that matches the device resonance conditions.

To sum up, several problems are faced in designing WECs and their PTO systems. The main challenges regards [37, 39]:

- The high variability of the wave resource in the short-term period having more than a factor of 10 between peak and mean extracted power;
- The broadness and variability of the wave spectrum increase the challenges of produce effective control algorithms;
- Slow, bi-directional and irregular kinematic behaviour of bodies forced by waves;
- High torque densities required compared with wind turbines;
- Harsh and corrosive marine environment heavily impacts on the life-cycle of the WEC, increasing its maintenance cost;
- High costs for prototyping and testing.

1.2.2 Power take-off classification

A large variety of PTO systems has been suggested throughout the years with fundamental different characteristics, ranging from using direct drive solutions to using various transmissions based on hydraulics, mechanical gears or magnetic gears. Their properties like efficiency, overload capabilities and force control make a direct comparison nearly impossible. Several reviews offer a precise description of the main PTO technologies and their working principles. The PhD thesis of Hansen [40] compared numerous PTO solutions for the Wavestar WEC basing on the expected power-production, PTO size, durability and storage capability. In the author's opinion the review proposed by Hansen remains one of the most detailed and precise PTO-based research for a WECs.

According to one of the most recent review [41], the types of PTO can be categorized into five main categories: air turbines, hydro turbines, direct mechanical drive system, direct electrical drive system and hydraulic transmission. Since the hydraulic PTO is the main subject of this work, it is treated in a separate section in more depth.

Air turbines

Pneumatic air turbines represent a very well-known type of PTO for WECs. The idea, schematic in Figure 1.10, is to drive a turbine with the oscillating air pressure in an enclosed chamber as a consequence of oscillating water level induced by the ocean waves. The compressed air runs directly the turbine that is rigidly connected to an electrical generator to produce usable energy. Air turbines as mean

for converting wave power are mostly used in Oscillating Water Column (OWC) and breakwater integrated OWCs. The reviews of Setoguchi and Takao [42, 43] presented different types of air turbines which can be used in wave converters. An exhaustive list regarding the pneumatic air turbine transfer system is reported in [41]. For example, plants such us Pico [44], Limpet [45], Leacon [46], etc. install air turbine as PTO system. In particular, Limpet is the most well-known and its first commercial 500 kW prototype was installed in 2000 on the shoreline of the Island of Islay (Scotland) [47].

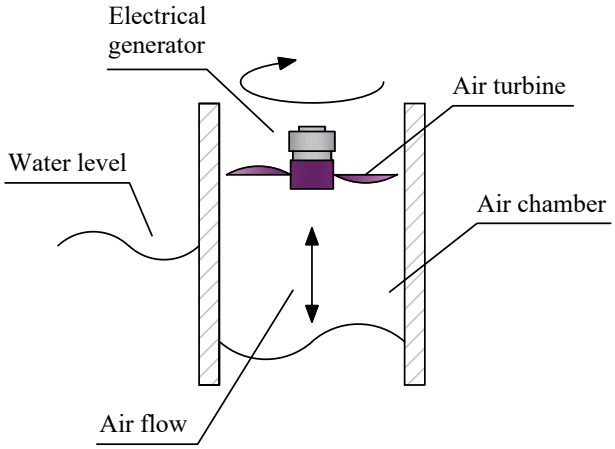

Figure 1.10: Example of a air turbine system.

Advantages of pneumatic air turbine concern their ability to increase the wave slow velocities into high air flow rates using the air as the working fluid. Moreover, the pneumatic air turbine does not have environmental impact like the oil transmission systems. The harsh marine environment is not a problem for the air turbines, as they can be located away from the potentially corrosive salt water and destructive high waves, requiring low maintenance [13]. However, the main challenge for the air turbine-based PTOs comes from the bidirectional nature of the flow. Non-return check-valves coupled with a traditional turbines are a suitable solution to this problem, but the non-return rectification systems require complicated maintenance. In this regards, the Wells, Impulse and Dennis-Auld turbines are the most popular pneumatic air turbines due to their ability to rotate in the same direction, regardless of airflow direction. The major disadvantage is the low conversion efficiency, usually around 60÷65% [15]. Moreover, they generate high noise resulting in a noteworthy acoustic pollution.

Hydro turbines

A schematic example of a hydro turbine system is shown in Figure 1.11. The system exploits a compressed water flow running through a rotating turbine that

directly drive an electrical generator. For this system, several types of turbine can be used, such as Kaplan, Francis and Pelton. Hydro turbines are normally employed in overtopping devices or hydraulic pump systems using seawater as working fluid. Modern overtopping devices like Wave Dragon [25], Aquabuoy [48], Tapchan [49], etc. install hydro turbine as a PTO. In particular, the Wave Dragon design is suitable to accommodate an hydro turbine PTO: the device consists of two arms that assist the water to flow in the reservoir, whose level is higher than the surface level of the ocean. The stored water returns to the sea via channels that run the turbine to generate energy. Moreover, the CETO WEC [19] uses buoys to induce a pressure difference inside a hydraulic cylinder to push the water through underwater pipes that drive a hydroelectric turbine to generate electricity. A complete overview of the hydro turbine installed in real plants is reported in [41].

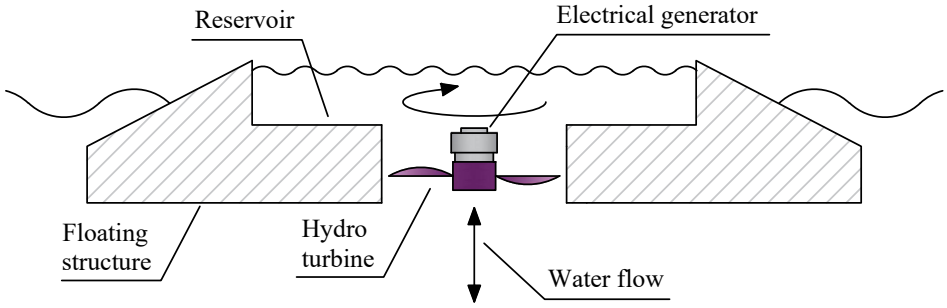

Figure 1.11: Example of a hydro turbine system.

The main benefit of hydro turbine-based PTO systems is the technological maturity, where the designs of the Kaplan turbine have been applied for power generation for many decades. Strong points are the conversion efficiency (up to 90%) and low maintenance. However, the bottleneck resides in the energy extraction from waves [36] that cannot provide enough head and flow to be economical for the Kaplan turbine generator unit. No environmental problems are caused by fluid leakages but, due to the harsh marine environment, the components can be damaged [15].

Direct mechanical drive system

Direct mechanical drive systems generate energy directly damping the wave converter motion. Usually, direct mechanical drive system consists on translating the mechanical energy of an oscillating body subjected to waves into electricity by means mechanical interface. Such an interface can be a gear boxes, pulleys, cables, sprockets and rand geared shafts/racks. An example of the direct mechanical drive-based PTO system is shown in Figure 1.12. There are various WEC devices based on the direct mechanical PTOs: Penguin [32], which used an electric generator directly connected to a rotating mass to generate energy, the Smart Power Buoy

[50], CECO [51], which implements a gear-rack system and electric generator, etc. The complete list of WECs which have used the direct mechanical drive system is reported in [41].

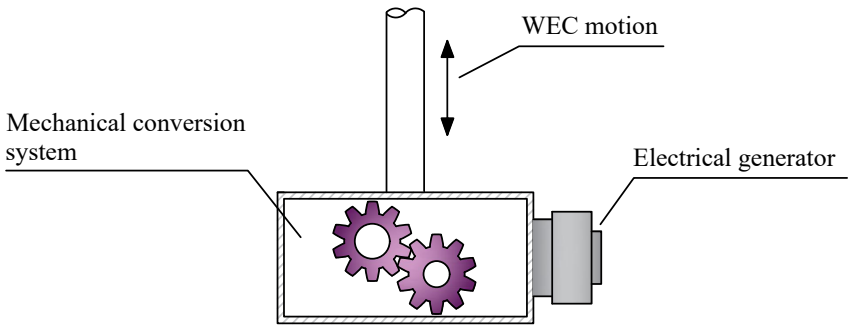

Figure 1.12: Example of a direct mechanical drive system.

A direct mechanical drive implies that the power conversion occurs by means a linear-to-rotary conversion systems without any pneumatics or hydraulic transmission. In this regards, only up to three energy conversions are necessary, resulting in high efficiency of such a PTO [41], up to 97% according to [52]. One disadvantage is the frequent maintenance and short lifetime since a direct mechanical drive undergoes higher load cycles. Costs and feasibility are another big challenge of the direct system since large size of gearboxes are required to reduce the high loads exerted on the PTO [53].

Direct electrical drive system

Direct electrical drive refer to systems for which the primary converter is directly coupled to the moving part of a linear electrical generator. The translator is composed of permanent magnets and the stator is equipped with coil windings. The ocean waves induce a motion to this subsystem with respect to a stationary stator, inducing electrical current and then creating electric power. The direct-electrical drive PTO system is much simple compared to the other types of PTOs, as it has no mechanical interface between the WEC and the PTO mover. In this regards, the mechanical interfaces are unnecessary and the friction energy loss are greatly reduced. Figure 1.13 shows the schematic of the direct electrical PTO system. In this context, Uppsala University developed 14 WEC prototypes implementing a rectangular shaped translator that consisted of a number of permanent magnets with the stator containing the wound coils [54]. Another very popular linear generator-based WEC was the SINN which consisted of a variable number of buoys that are attached to a fixed steel frame lifting a rod which runs a linear generator unit [55]. Other examples of linear generator-based WEC are Wavebob [21] and L10 buoy

[56]. The complete list is reported in [41].

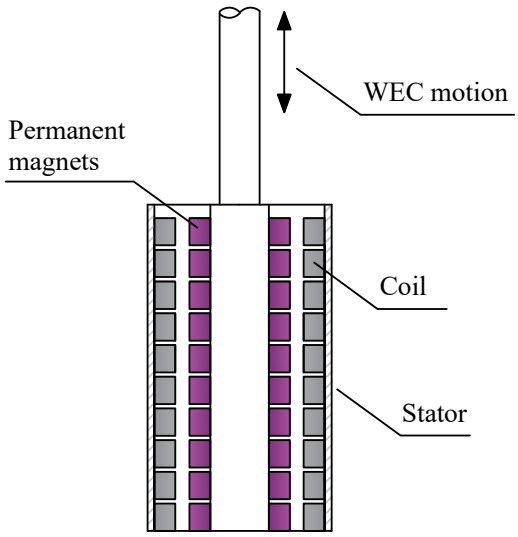

Figure 1.13: Example of a direct electrical drive system.

There are several types of conventional linear generators that can be used. The permanent magnet synchronous generator has been the most selected option for wave energy conversion applications. In general, this type of PTO system is well-suited for small-scale (<10 kW) WEC devices. This system has the advantage of not requiring an intermediate mechanical interface (for example a gear-rack transmission) and thus reducing losses and maintenance costs compared to other PTO systems [57]. Moreover, the possibility of continuous force control constitutes a great advantages in respect to other types of PTOs such as hydraulic PTOs [58]. Disadvantages are the limited admissible linear velocity of the translator and the commercial size, giving low power-to-weight ratio available (very large machines with low power density) [52]. Moreover, since there is a direct coupling with the floater the and no smoothing system are installed, the power transmission is very complicated due to the irregular generated voltage [59].

1.3 State-of-the-art of the hydraulic PTO

Since the hydraulic PTO is the main focus of this thesis, the state-of-the-art of the hydrauic transmissions used in the wave energy context is expanded to explore the most common solutions presented in literature. First concepts of electro-hydraulic PTO or, simply, Hydraulic PTO (HPTO) applied to a WEC are dated back to the 70s, when Budal and Falnes [60] proposed an all-enclosed hydraulic transmission connected with three gas accumulator in a PA of “type E”. The phase

control was performed in a latching-unlatching fashion, without providing reactive power to the floater [61]. In 1979, Professor Salter (University of Edinburgh) proposed the Salter duck WEC [62] equipped with a hydraulic transmission. Then, in 1982, Professor David Evans (University of Bristol) designed a power conversion system based on a double-acting reciprocating pump implemented in a cylinder-shaped WEC [63]. The pumps fed sea water to a common manifold shared by other cylinders and a large Pelton wheel which ran at synchronous speed. The spring-effect was provided by oil/nitrogen accumulators activated by single-acting hydraulic pumps. In [64], a piston pump, feeding a hydraulic swash-plate motor with power generator is proposed for the concept of a bipartite PA. Moreover, the simultaneous horizontal motions of the whole system was damped by the mooring lines attached provided with spring restored piston pumps, producing additional power. In [65], the combination of wave powered single working piston pumps, submerged turbines and generators has been tested on a multiple absorber configuration. In [66], a PA-like device, damped by a single-acting hydraulic cylinder, has been tested in the laboratory. The PTO was equipped with a rectifier bridge to rectify the pressurized flow which irregularities was filtered by hydraulic accumulators. Moreover, the large ratio of the piston area enables the system to amplify the wave-induced dynamic pressure up to 700-800 psi (48.3-55.1 bar), required for the reverse osmosis desalination process. In 1993, Salter studied a novel digital hydraulic pump/motor [67], originally intended for a wave energy application, capable of offering a continuously variable transmission of hydraulic power at much higher efficiencies than conventional hydrostatic transmissions. In 1995, Salter and Lin [68] applied the HPTO to the Sloped IPS WEC [69], a vertical heaving buoy with a PTO mechanism that carries its own internal reaction mass in the form of a body of water contained within a large vertical tube. In 1996, Eidsmoen [70, 71] proposed the same architecture shown in [60] (an all-enclosed hydraulic transmission connected with three gas accumulator in a PA of "type E") adding a fourth gas accumulator used to smooth the pressure in the system pipes. Both works described the implementation of a phase control applied to a tight and slack-moored heaving WEC through a single-stroke hydraulic cylinder coupled with an extra accumulator. In 1998, model tests have been performed on the P.S.FROG system [72], a reaction-less ocean WEC [73]. The WEC has been conceived with a PTO equipped with a variable displacement oil-hydraulic pump. This allowed to vary the damping acting on the floater continuously and rapidly, conferring great flexibility and scope for the sophisticated control strategies to maximise the energy captured in irregular waves.

Going back to most recent applications, an exhaustive review of hydraulic technologies applied to the wave energy field has been collected in [74]. The scope of this review is to explain the various concepts of hydraulic PTO for WEC, their configurations and characteristics along with the effectiveness of specific components. Finally, advantages and disadvantages of the most popular architectures

are discussed. In the work of Lin [75], the most popular hydraulic PTO architectures coupled with various kinds of WEC (e.g. raft type [76], point absorber [77], duck type [12] and pendulum type [78]) systems are presented. In particular, a new water/oil transmission concept it proposed to reduce the pollution caused by oil leakage along with a digital cylinder group to regulate the circuit pressure in array configurations. Another interesting review has been published by Hansen [40], where a comparison between different hydraulic technologies is carried out on the Wavestar WEC [23]. Another overview of the hydraulic PTO application is collected in [79] by Zhang.

1.3.1 The hydraulic PTO concept

Hydraulic systems are the most used PTOs in the literature which can be used in WECs to convert the low-speed oscillating motion into usable electrical energy [15]. This transmission is able to handle the high-torque and low-speed requirements providing large power density solutions having reliable, standardized and scalable technology [80]. Generally, the WEC motion is used to pressurize a hydraulic circuit which feeds a hydraulic motor, that in turn translates the energy to an electrical generator. A conventional hydraulic transmission for wave energy is seen in Figure 1.14, where a cylinder operates as a pump, producing a bi-directional flow which drives a hydraulic motor that is rigidly connected to an electrical generator. Moreover, a controlled manifold and accumulators are used to improve the controllability of the PTO and smooth the irregular flow generated by the hydraulic cylinder, respectively. The transmission suits for both translation and rotational types of wave energy conversion systems [74]. The most famous WEC systems which implement the hydraulic PTO are reported in Table 1.1.

To date, there is no industrial standard of a hydraulic power take-off unit applicable to WECs, but most of the investigations are carried out with very similar configurations. According to Jusoh [74], there are different topologies of hydraulic PTO that can be grouped into two main categories in relation of the pressure with which the hydraulic motor operates: constant-pressure and variable-pressure configurations.

Variable-pressure configurations

Variable-pressure hydraulic PTOs concern the simplest and most economical hydraulic transmission for WECs. Generally, the most common solutions consist of double-acting hydraulic cylinder, directly connected to the WEC prime mover, that drives flow to a bi-directional hydraulic motor which is coupled with an electric generator [100]. A simple concept of such a configuration is depicted in Figure 1.15. The hydraulic cylinder operates as a bi-directional flow generator, driving flow

Device	Company	Deploy	Power (kW)	Ref.
Pendulor	Muroran Institute of Technology (https://www.muroran-it.ac.jp/en/)	Japan (1983)	5	[81]
Kaiyo	Japan Institute for Shipbuilding Advancement	Japan (1984)	10	[82]
McCabe Wave Pump	Hydam Technology Limited	Ireland (1996)	400	[83]
EB Frond	Lancaster University (www.lancaster.ac.uk/)	UK (2003)	263	[84]
PS Frog	Lancaster University (www.lancaster.ac.uk/)	UK (2005)	2000	[29]
SEAREV	Ecole Centrale de Nantes (www.ec-nantes.fr/)	France (2006)	500	[31]
OBB	Guangzhou Institute of Energy Conversion (GIEC) (www.english.giec.cas.cn/)	China (2006)	50	[85]
WEC (FO3)	Fred Olsen Company (www.fredolsen.no/) ABB (https://new.abb.com/)	Norway (2006)	2520	[86]
Wavebob	Wavebob Ltd (www.vimeo.com/wavebob)	Ireland (2007)	1000	[75]
Pelamis	Ocean Power Delivery Ltd (www.oceanpd.com)	UK (2009)	750	[75]
Wavestar	Wave star A/S (http://wavestarenergy.com/)	Denmark (2009)	600	[87]
SDE	SDE Energy Ltd (www.sde-energy.com/)	Israel (2010)	40	[88]
Langlee Wave Power	Langlee Wave Power (www.langleewp.com/)	Denmark (2011)	132	[89]
SyncWave Power Resonator	SyncWave (www.naturefirstusa.org/Special%20Reports/Ocean%20Energy/SyncWave%20Systems.htm)	Canada (2011)	25	[90]
WaveNET	Albatern (www.albatern.co.uk/)	Scotland (2012)	7.5	[91]
Wave Roller	AW-Energy (www.aw-energy.com/)	Portugal (2012)	300	[75]
Duck	Guangzhou Institute of Energy Conversion (www.english.giec.cas.cn/)	China (2013)	100	[75]
OHS	Atmocean Inc (www.atmocean.com/)	UK (2014)	249	[92]
CCell	Zyba Renewables (www.ccell.co.uk/)	UK (2015)	20	[93]
Sharp Eagle	Guangzhou Institute of Energy Conversion (http://english.giec.cas.cn/)	China (2015)	100	[94]
BioWave	BioPower Systems Pty Ltd (https://bps.energy/)	Australia (2015)	250	[95]
Triton	Oscilla Power (www.oscillapower.com/triton-wec/)	US (2016)	600	[96]
Sharp Eagle	Guangzhou Institute of Energy Conversion (www.english.giec.cas.cn/)	China (2018)	120	[97]
Azura	Northwest energy innovations (NWEL) (http://azurawave.com/)	USA (2018)	20	[98]
DEXA WEC	DEXA Wave ApS (www.dexawave.com/)	Denmark (–)	160	[99]
FLOW	Martifer Energy (www.martifer.pt/)	Portugal (–)	2000	[92]

Table 1.1: Hydraulic PTO based WECs. Adapted from [41].

directly through a variable or constant displacement hydraulic motor. The downstream hydro-electrical components are required to provide at least two-quadrant operation since their motion is bi-directional. Moreover, if required, four-quadrant operation will enable to deliver power from the grid to the WEC to make it resonant with the incoming wave, for example as required by the reactive-control [101]. In addition, an overrating pump coupled with a low pressure accumulator

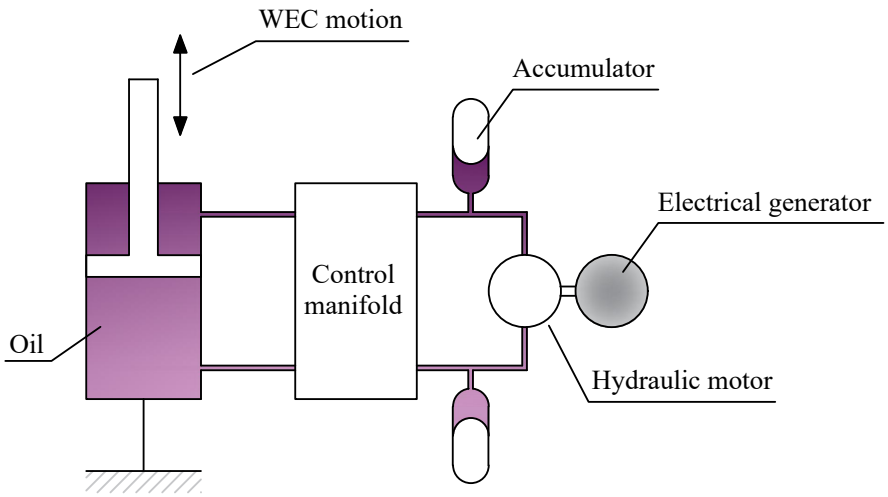

Figure 1.14: Example of a hydraulic PTO system.

are provided to prevent the cavitation of the hydraulic pump and motor. A relief valve can be used to avoid over-pressure and protect the hydraulic components. A variable-pressure configuration can be interpreted as an equivalent gearbox with, theoretically, unlimited gear ratio, that is able to convert the high-torque/low-speed wave power into a more manageable low-torque/high-speed power. Despite the simplicity and the small number of components required, the variable pressure architecture has the drawback of unable to provide an energy storage system since no hydraulic accumulators are provided, apart the one used for charging the low pressure ram of the circuit.

Examples of variable-pressure concepts can be found in [100], where the investigated PTO system is composed of a symmetrical cylinder, which is operated in closed circuit with a variable displacement swash-plate pump/motor. Here, the control is performed through the swash-plate motor in order to control the torque applied to the float. Hansen [87] also proposed different fluid power based PTO systems applied to the Wavestar, including a simple variable pressure architecture. Penalba [102, 103] modelled and validated a variable-pressure PTO similar to the one schematic in Figure 1.15, where the hydraulic cylinder is directly connected to a variable-displacement hydraulic motor and only the low-pressure accumulator is included with a boost pump. Recently, Calvario [104] studied a configuration similar to the one proposed in [100, 105] that is based on two single-rod cylinders, attached on both sides of an oscillating wave surge converter. The WEC oscillates around a "fulcrum" and two cylinders move in opposite directions in order to extract power from the plate forward and backward oscillations. The circuit is equipped with a variable four quadrant mode hydraulic motor, which is connected to an electrical generator.

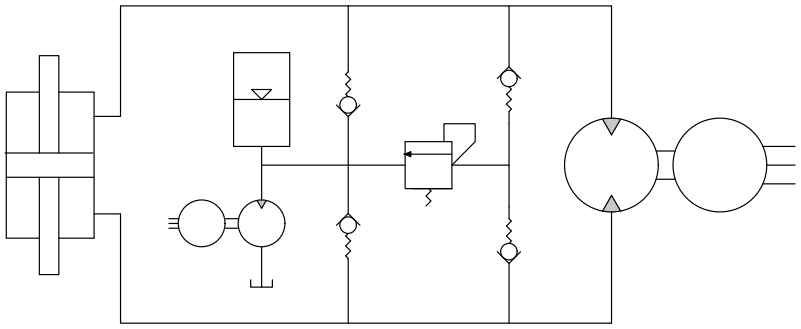

Figure 1.15: Scheme of typical variable pressure configuration. Adapted from [102].

Constant-pressure configurations

Constant-pressure configurations are by far the most widespread solutions for WECs. Generally, it consists of a primary hydraulic actuation (e.g. hydraulic cylinder or pump), a rectification module, some accumulators, a leakage ram and a generation module. A constant-pressure system provides significant advantages in terms of efficiency, flexibility and control, compared with a variable-pressure solution. In particular, the claimed efficiency is up to 90% [87]. Moreover, the presence of the rectification and accumulation systems allow to rectify the bi-directional motion obtained from the WEC into a smooth regular uni-directional motion of the generation stage, increasing the efficiency of the electrical generation and allowing a downsize of the electrical components. In short, the accumulator has the effect of peak clipping and valley the flow peaks generated from the prime mover cushioning the impact of irregular wave energy, as well as guarantee the stability of hydraulic transmission. However, the complexity of such systems could negatively affect the reliability of the PTO and increase its cost.

Starting from the simplest constant-pressure configuration, Figure 1.16 shows a basic scheme of such a kind of hydraulic PTO. The transmission is composed of four-check-valves that rectify the flow of a double-acting actuator. The fluid flows in the hydraulic motor in unidirectional mode forcing the generation stage to spin in the same direction. Two accumulators are used to smooth the irregular hydraulic power generated from the primary stage while a relief valve discharges the pressure peaks. The third accumulator is necessary to fill up the leakage of the hydraulic motor. Since only one pressure level is provided (e.g. only one high-pressure accumulator with a constant displacement primary hydraulic unit) an on-off modulation know as declutching control [106] can be performed to digitally regulate the pressure acting on the primary unit. This kind of hydraulic transmission is proposed with some modifications depending on the intended use in several works.

Falcão [107] proposed a simple constant-pressure configuration with a single-rod cylinder while So [108] replaced the primary system with a double-rod cylinder

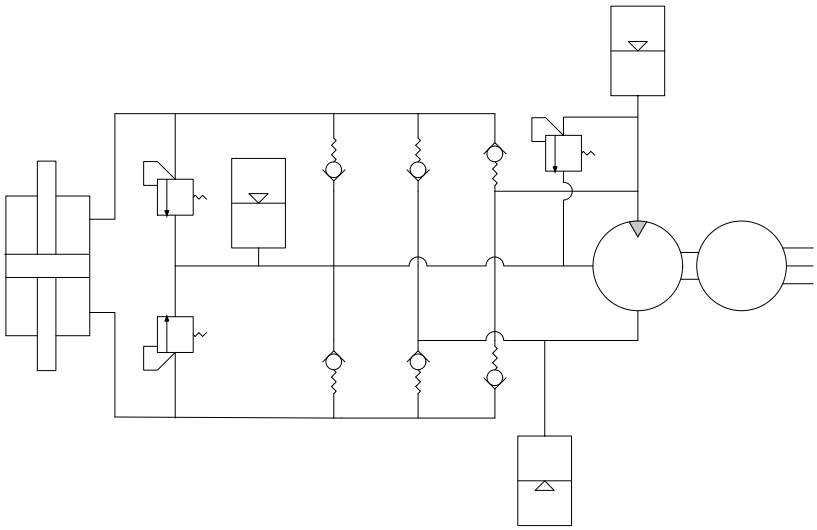

Figure 1.16: Scheme of a constant pressure configuration with rectifier bridge. Adapted from [102].

in order to avoid asymmetrical behaviour of the floater. In [109], Beirão used an oil-tank instead of a low pressure accumulator, resulting in a less efficient hydraulic PTO due to the use of an external pressure source to charge the low pressure ram. A booster pump is implemented in [102] to overcome the disadvantages of the architecture proposed by Beirão. Moreover, in order to make a closed circuit, a charge accumulator could be a valid solution instead of a booster pump as reported in Figure 1.16 and in [110]. Another modification of the four-check-valves configuration aims to add two extra accumulators near the hydraulic cylinder to ensure the WEC moves in phase with the waves, performing the well-known phase control [111, 112]. The modularity of the hydraulic transmission enables the possibility to connect multiple hydraulic cylinder that drive flow toward a unique generation stage [113] or a multiple-generators with different capacities assembled in parallel and controlled to ensure high efficiency operations [114]. It is worth to specify that also simpler two-check-valves concepts are proposed in literature that uses a single-acting cylinder as prime hydraulic unit. However, simulations demonstrated that this type of transmission is inefficient due to the single-acting cylinder that waste part of the extracted power during the backward motion, harvesting the wave energy only during the upward motion [74]. Two-check valves concepts are treated in [115, 116].

Another category of constant-pressure hydraulic PTO concerns directional control valves. An example of such a topology is represented in Figure 1.17. A multi-chamber hydraulic cylinder is connected to a digital manifold equipped with eight two-way valves. In constant-pressure systems the control of the primary pump

or cylinder can be achieved by valve transitions [40, 87] that select between discrete effort levels determined by the fluid pressure and alternative cylinder areas. Through the arrangement of valves, 16 different combinations of the active cylinder area can be achieved allowing a pseudo-continuous force control of the PTO. The resulting force is generated as the sum of forces produced by the different cylinder chambers. If the opening and closing time of the valves was kept less than 15 ms the efficiency reaches 90% [87]. The generation stage implements two accumulators with the same purposes of the four-check-valve concept. This configuration has been proposed also in [117, 118].

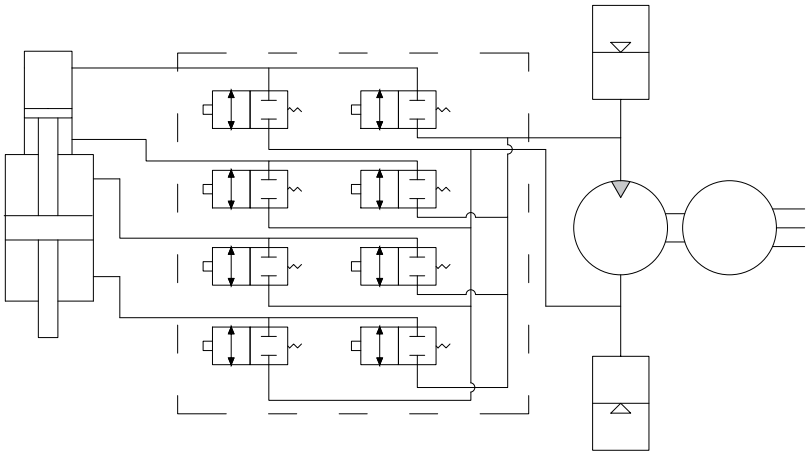

Figure 1.17: Scheme of a constant pressure configuration with directional control valves. Adapted from [87].

The last category of constant-pressure PTO relies on the hydraulic transformer: it consists of two variable displacement pump with four operation modes that are coupled to regulate the pressure over the primary hydraulic unit and rectify its generated motion [80]. A possible scheme is shown in Figure 1.18, which however presents other precautions. A symmetrical hydraulic cylinder catches the mechanical energy from WEC device and, through different modules, the energy is moved, and it is sent to the generation stage. The core of this transmission is the hydraulic transformer that converts the bi-directional motion of the cylinder into a unidirectional high-speed rotation for driving the generator. Pressure modulation is achieved by regulating the swash-plate angle of the downstream hydraulic transformer. Then, the force discharged on the hydraulic cylinder can be regulated with the first hydraulic transformer. Overflow lines are used to recover the excess of flow that cannot be disposed by the downstream hydraulic motor. In this scheme a reactive control can be used since the hydraulic unit connected to the cylinder is able to operate in a four-quadrant mode, delivering power to the cylinder. Overall, the hydraulic transformer improves the PTO controllability also performing the

rectification stage; however, the continuous back-to-back operation of the two variable displacement pump/motor could reduce the PTO efficiency and its lifespan. A simple concept of hydraulic transformer is proposed by Hansen [87], a modified solution is studied in [40] and the configuration depicted in Figure 1.18 is proposed by Gaspar in [80]. Gaspar introduced two piloted vales close the bypass line to deliver reactive power to the hydraulic actuator. In [119, 120], Gaspar proposed a modified concept including a secondary hydraulic PTO in parallel to the one presented in Figure 1.18 for control purposes. The secondary hydraulic PTO is used only during the reactive mode to adjust the phase between the WEC velocity and the wave force. The author assessed that the introduction of a secondary PTO unit allows to reduce the size of the primary PTO components and at the same time minimize the consumption of the booster pump stage.

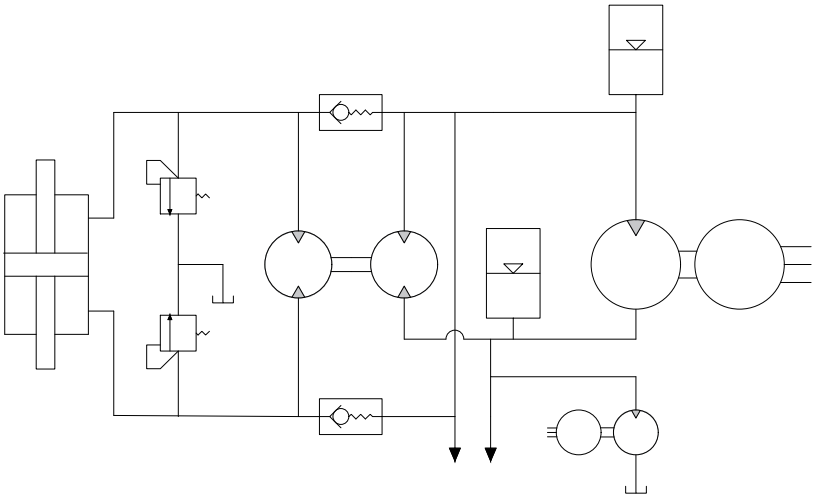

Figure 1.18: Scheme of a constant pressure configuration with hydraulic transformer. Adapted from [80].

Other examples and variants of constant-pressure configurations can be found in [121, 122, 123, 124, 125, 126, 127].

1.3.2 Reasume of advantages and disadvantages of hydraulic PTOs

The hydraulic solutions offer, in general, higher power/weight ratio compared with other PTO architectures. In fact, hydraulic components can handle large amounts of power and they can effectively extract energy from the continuous variation of the wave energy converter movement. Moreover, the possibility to install various accumulator units, the irregular power can be smoothed with a cost-effective solution compared to super-capacitor modules [40]. Another advantage is

represented by the possibility to convey the hydraulic power of a multiple-absorber WEC in a single high speed hydraulic motor downstream to the transmission, allowing a cheaper and more stable electric conversion compared to a direct-drive solution.

Despite the advantages just outlined, hydraulic PTO has an overall claimed efficiency ranging from 69% to 80% but in the real-world it would be lower [87]. The fluid leakage represents another issue for the hydraulic PTO, which can harm the marine environment [117, 128]. Compared to a variable pressure configuration, the advantage of constant pressure configuration is the higher efficiency. With same control technology, constant-pressure PTO efficiency is 10 percentage points higher than variable pressure PTO. The problem of ocean pollution caused by leakage can be solved if water is used instead of hydraulic oil, but the price of water is higher. A water hydraulic system can cost between 30% and 200% more than an oil-based system [129]. Furthermore, the hydraulic PTO system consists of a lot of mechanical moving parts and its complex configuration needs regular maintenance that is, specially in ocean environment, costly, risky and time consuming [15].

1.4 ISWEC: a gyroscope based WEC

The major disadvantage of PA-like devices is that they harness wave energy damping directly the motion of an oscillating buoy, exploiting the relative motion of mechanical parts in contact with the harsh marine environment. The ISWEC device, the WEC of interest of this thesis, is a gyroscope based device that harness the effect of a gyroscope system enclosed in a rocking floater to extract energy from waves. The system schematic is shows in Figure 1.19. ISWEC is a directional WEC since, in normal working conditions, it is able to align itself with the wave direction. Notwithstanding the energy required to keep the flywheel in rotation, the possibility to regulate its speed along with the tuning of the PTO torque allows the adaptation of the natural resonant frequency of the system to the incoming wave. The full-scale system is composed of a steel-built hull containing two (or more) independent gyroscopic units. Each unit is constituted by a flywheel driven by an electric motor, mounted on a support frame that is directly connected to an electrical generator. The power absorption is based on the gyroscopic effect induced through the pitch motion of a cradle shaped hull housing a spinning flywheel [35]. The dynamic coupling between the pitch motion and the flywheel induces a precession motion of the gyroscope. This mechanical energy can be converted into electrical energy through different PTO technologies. The ISWEC device extracts this mechanical energy through a mechanical gearbox and an electrical generator, but in the case of an oceanic device, where the entities of the mechanical torques increase, the adoption of hydraulic-electrical PTO may be a more suitable solution. Two radial roller bearings and two spherical roller thrust bearings are used to

support both axial and radial loads of the gyroscope. Bearings have an oil cooling and lubrication system. The system is highly scalable and modulable since the hull can be designed to accommodate more than two gyroscopic units and adapted to the sea site of interest. The PTO components are mainly enclosed within the main structure; only the hull is in contact with the aggressive marine environment. For all components inside the structure, an extra level of protection is provided, such that if the hydraulic PTO is implemented the fluid leakage is contained inside the WEC. The only part that has continuity from the inside out is the electric cable, following the idea of a "deploy and plug" device [35]. Another advantage of ISWEC is the degree of controllability provided by the flywheel: the flywheel speed changes the dynamics response of the whole system allowing a precise tuning of its resonance condition in respect to the incoming sea state. Moreover, the resonance-matching of the device dynamics can be achieved with a proper control logic of PTO system. An accurate description of the internal components and their working principle can be found in the works of [130, 131, 35].

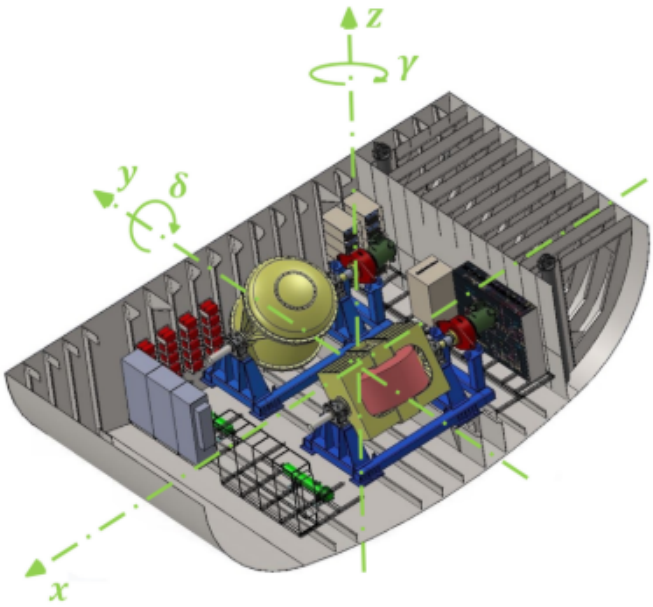

Figure 1.19: Scheme of the ISWEC device internal structure.

The ISWEC prototype was conceived by the renewable group of the Department of Mechanical and Aerospace Engineering of the Politecnico di Torino (Italy) in 2005. The first wave tank tests were carried out in 2012 at the INSEAN in Rome, where a 1:8 prototype was realized and tested to draw the main guidelines for a full-scale ISWEC design. In 2012, the design of a 60 kW rated power ISWEC prototype (shown in Figure 1.20) started and, in Summer 2015, the device has been installed in Pantelleria island (Sicily, Italy). The project addressed the energy production

capabilities and efficiency providing the experimental data to validate the ISWEC numerical models. In 2018, a new collaboration with the Italian company Eni S.p.a. led to the construction of a new full-scale prototype, installed in the Adriatic Sea (Italy). The development of more accurate numerical models together with ad hoc optimization algorithms validated by the experimental data of the Pantelleria device enabled some efficiency and reliability improvements to the overall device.

(a) (b)

Figure 1.20: ISWEC device installed in Pantelleria island (Sicily, Italy): hull (a) and gyroscope (b).

This thesis aims to improve the ISWEC device studying a HPTO system designed for increase the WEC performances, opening up to the possibility of an oceanic version of the device. The ability of such type of PTO to handle larger power densities in respect to the actual mechanical system seeks to give an alternative solution: the main scope is to expand the sea-domain for which the ISWEC device was originally conceived (Mediterranean Sea) toward an oceanic implementation reducing the system cost and increasing its reliability. The hydraulic PTO is studied with respect to the modelling, design and control point of view in order to asses its overall performances and provide a fair comparison with the mechanical PTO.

Chapter 2

Modelling the ISWEC WEC

In literature, a variety of WEC models are presented for both frequency and time domain simulation, with various benefits depending on the intended use and on the specific device considered. Multitudes of WEC models are proposed with different levels of confidence and uncertainties [132, 133] making difficult to find a general formulation for WEC models. The work of Folley [134] collets the state-of-the-art of numerical modelling approaches presented in a simple and effective manner. A WEC mathematical model aims to describe the full dynamics of different conversion stages, from ocean waves to the electricity grid. Generally, several moving components are activated by the interaction with the fluid, gravity forces and the WEC floater. Interacting with each other, the internal mechanical components transform the wave power into usable electrical energy. The basis of WEC modelling is the *Newton's Second Law*, which relates the motion of moving parts to the forces exerted onto the WEC system. The forces can be split into external, due to the hydrodynamic interaction between the WEC floater and the fluid pressure, and reaction, which are due to the internal coupling between moving parts (e.g. mooring system, gyroscope and PTO). The dynamic equation of a WEC reads:

$$\mathbf{M}\ddot{\mathbf{X}} = \mathbf{f}(t) \tag{2.1}$$

where $\mathbf{X}$ represents the generalised coordinates describing the motion of WEC moving parts, $\mathbf{M}$ indicates the inertia matrix of the WEC and $\mathbf{f}$ the internal, external, and reaction forces acting on the system. In particular, the vector $\mathbf{f}$ can be split into several components that are schematically represented in Figure 2.1 and discussed in the next sections. Referring again to Figure 2.1, the ISWEC mathematical model is obtained by coupling the hull hydrodynamics, the gyroscope and PTO dynamics. Moreover, specifically for the time domain models, the effect of the mooring along with the data acquisition system are considered. As described afterwards, $\mathbf{f}_f$ are the gravity and fluid forces acting on the WEC floater, $\mathbf{f}_m$ the mooring reactions, T_ε and $\mathbf{f}_{gf}$ the gyroscopic effects exchanged between the floater and the gyroscope units, T_{PTO} the PTO reaction acting on the gyroscope shaft, $\mathbf{X}_f$,

$\mathbf{X}_\varepsilon$ and $\mathbf{X}_{PTO}$ the signals acquired by the data acquisition system describing the motion of the floater, gyroscope and PTO physical quantities, respectively, $\mathbf{C}_{PTO}$ the control signals elaborated by the control system of the ISWEC and $\mathbf{w}_d$ the disturbances affecting on the acquisition system.

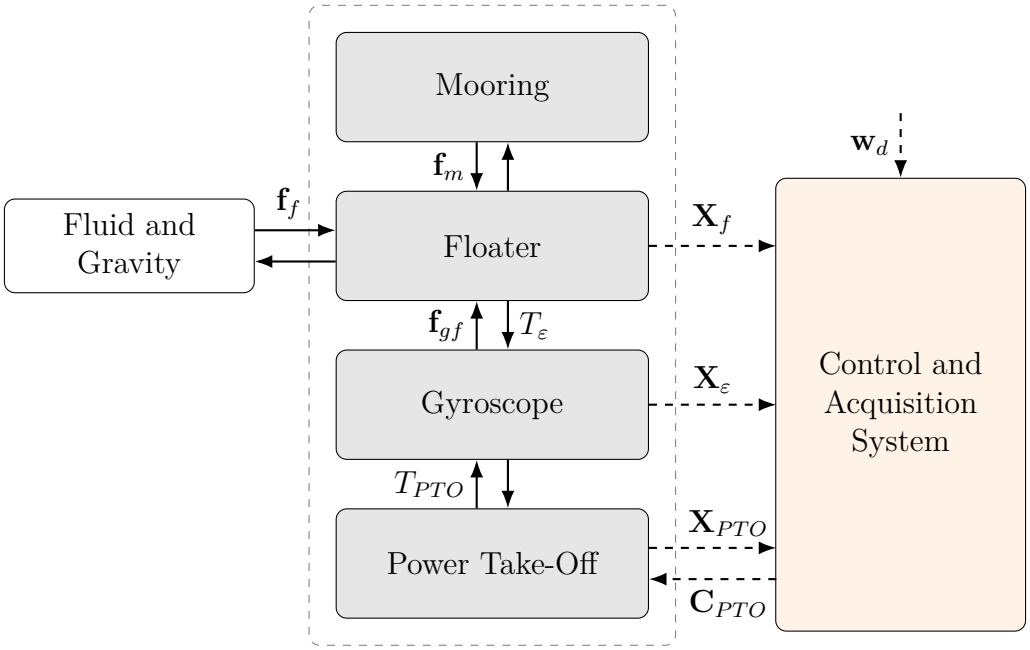

Figure 2.1: ISWEC device block diagram. Forces and reactions acting on WEC parts in solid lines. Acquisition, control signals and disturbances in dashed lines.

The integro-differential equations have been implemented in the MATLAB® / Simulink® environment. The experimental validation of the model equations is not within the scope of this work and details can be found in the studies of [130, 135, 136, 137]. In particular, the hydraulic PTO model validation will be object of future works.

This chapter describes the mathematical framework modelling the parts in Figure 2.1, including the main non-linear dynamics and losses. The following sections are articulated in:

- Hydrodynamic model: the linear model of the wave-floater interaction in both frequency and time domain is derived following the linear potential flow theory;
- Ocean waves model: a consistent stochastic description of wave fields in the form of a Gaussian process is presented along with the statistical properties associated to compute the performances of the WEC under study;
- Gyro-pendulum model: a simple non-linear gyroscope-pendulum model of the ISWEC is treated in the third section of this chapter;

- Power Take-Off models: the electro-mechanical and electro-hydraulic PTO models presented in a time-domain framework along with their control logic;
- Power loss models: a detailed power losses model of the ISWEC is crucial for a precise and reliable analysis of the system performances.

In each section, the characteristic equations for modelling each ISWEC element are reported.

2.1 Hydrodynamic model

Generally, there is no analytical solution for the description of motion of a floating body and the system is described numerically solving the Navier-Stokes equations. However, for the description of a WEC motion induced by ocean waves, the *Potential Flow Theory* offers a well-known, simple and effective mathematical framework for modelling a lumped parameter numerical model of the device. This branch of models requires limited computational efforts and so particularly suitable for the model-based design methodology of a WEC [138]. In this section both frequency and time domain hydrodynamic models of the ISWEC are presented and derived through the *Potential Flow Theory* and *Linear Wave Theory* by Airy, which are the simplest available model to account for elementary gravity waves on water and their effect on the body motion.

2.1.1 Potential flow theory

The fluid motion and its interaction with the rigid body are generally described by two fundamentals equations: the *Continuity Equation* and the *Navier-Stokes Equations*. In this work, the assumption of incompressible, homogeneous, and irrotational and Newtonian fluid is valid. Moreover, the body motion is considered to have zero time-averaged speed and small amplitudes. Then, since the hydrodynamic pressure is non-linear, in order to consider valid the linear wave theory small wave steepness of the incident waves is required (this assumption results to be valid in most wave-induced body motions but may be not for extreme sea states). Under these assumptions, the equation of the velocity field $\mathbf{v}_f = [v_x \quad v_y \quad v_z]^T$ follows, expressed in terms of the velocity potential field Φ, such that:

$$\mathbf{v}_f = \begin{bmatrix} \dfrac{\partial \Phi}{\partial x} & \dfrac{\partial \Phi}{\partial y} & \dfrac{\partial \Phi}{\partial z} \end{bmatrix}^T \tag{2.2}$$

where $[x \quad y \quad z]$ is a Cartesian coordinate system with the z-axis assumed vertical and pointing upward. Then the fluid velocity field $\mathbf{v}_f$ will satisfy the equation of continuity:

$$\nabla\Phi = \frac{\partial v_x}{\partial x} + \frac{\partial v_y}{\partial y} + \frac{\partial v_z}{\partial z} = 0 \tag{2.3}$$

Introducing the fluid velocity field $\mathbf{v}_f$ in the equation 2.3, the *Laplace Equation* is obtained:

$$\frac{\partial^2\Phi}{\partial x^2} + \frac{\partial^2\Phi}{\partial y^2} + \frac{\partial^2\Phi}{\partial z^2} = 0 \tag{2.4}$$

As well as the boundary conditions:

- **Sea bed boundary condition**: it involves the not permeability of the sea bed. The vertical velocity v_z must be equal to zero at every instant of time t at $z = -H$:

$$v_z = \frac{\partial\Phi}{\partial z} = 0 \tag{2.5}$$

- **Free surface dynamic boundary condition**: it is derived assuming that the pressure at the water free surface is given by the *Bernoulli Equation*, defining the continuity of the pressure field at the interface between air and water. However, in view of the assumption of small wave steepness, the quadratic terms can be neglected and the boundary condition can be written as (at $z = 0$):

$$\frac{\partial\Phi}{\partial t} + g\eta = 0 \tag{2.6}$$

  where η is the free surface elevation and g indicates the gravity acceleration.

- **Free surface kinematic boundary condition**: so-called no-leak condition, states that the fluid velocity component normal to the free-surface must be equal to the surface velocity at $z = 0$:

$$\frac{\partial\eta}{\partial t} = \frac{\partial\Phi}{\partial z} \tag{2.7}$$

Solutions to the Laplace Equation 2.4 imply the boundary conditions 2.5, 2.6 and 2.7 in the form:

$$\eta(\mathbf{x}, t) = \hat{\eta}\mathrm{e}^{\mathrm{i}(\mathbf{k}.\mathbf{x}-\omega t)} \tag{2.8a}$$

$$\Phi(x, y, z, t) = \frac{g}{\omega}\frac{\cosh(|\mathbf{k}|(z+H))}{\cosh(|\mathbf{k}|H)}\hat{\eta}\mathrm{e}^{\mathrm{i}(\mathbf{k}.\mathbf{x}-\omega t)} \tag{2.8b}$$

where:

- $\mathbf{x} = [x \quad y]^T$ denotes the horizontal coordinates of the wave elevation;
- $\mathbf{k} = [k_1 \quad k_2]^T$ is the wave number in bi-dimensional form;
- $\hat{\eta} = |\eta_0| e^{i\phi}$ is the complex amplitude of the wave elevation;
- ω is the wave frequency;
- i is the imaginary unit.

In this context, $\mathbf{k}$ and ω are related by the dispersion relation:

$$\omega^2 = g|\mathbf{k}| \tanh(|\mathbf{k}|H) \tag{2.9}$$

The detailed mathematical framework behind the *Seakeeping Theory* and *Potential Flow Theory* can be appreciated in the book of Chakrabarti [139] and Falnes [138].

2.1.2 Wave-Body interaction

In Figure 2.2 is shown the (X_o, Y_o, Z_o) be the Cartesian global coordinate system with the Z_o-axis assumed vertical and pointing upward and the X_o-axis coincident with the mean free surface, which origin is fixed to $Z_o = 0$.

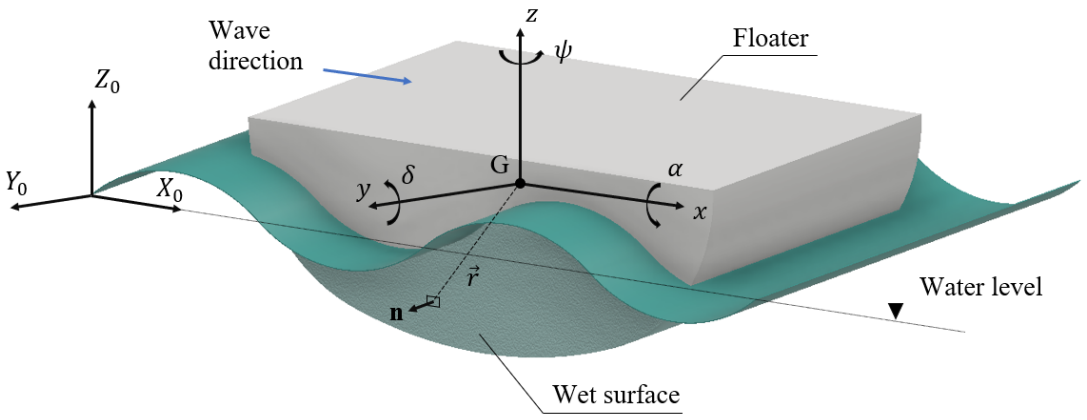

Figure 2.2: Geometrical and inertial reference system of the ISWEC device.

The motion of a floating rigid body $\mathbf{X}_f \in \mathbb{R}^{n_D}$ can be described in a six Degree of Freedom (DoF) framework with the following local coordinates:

$$\mathbf{X}_f = \begin{bmatrix} x \\ y \\ z \\ \alpha \\ \delta \\ \psi \end{bmatrix} = \begin{bmatrix} surge \\ sway \\ heave \\ roll \\ pitch \\ yaw \end{bmatrix} \tag{2.10}$$

where n_D is the number of DoFs, equal to six. Assuming that the only external forces $\mathbf{f} \in \mathbb{R}^{n_D}$ acting on the body are the gravity forces $\mathbf{F_g}$, pressure forces $\mathbf{F_p}$ and pressure torques $\mathbf{T_p}$ from the fluid, the *Newton's Second Law* can be written as follows:

$$\mathbf{M}_f \ddot{\mathbf{X}}_f = \mathbf{f}_f(t) = \begin{bmatrix} \mathbf{F_p}(t) + \mathbf{F_g}(t) \\ \mathbf{T_p}(t) \end{bmatrix} \tag{2.11}$$

where $\mathbf{M} \in \mathbb{R}^{n_D \times n_D}$ is the inertia matrix of the body:

$$\mathbf{M}_f = \begin{bmatrix} m & 0 & 0 & 0 & 0 & 0 \\ 0 & m & 0 & 0 & 0 & 0 \\ 0 & 0 & m & 0 & 0 & 0 \\ 0 & 0 & 0 & I_{44} & 0 & 0 \\ 0 & 0 & 0 & 0 & I_{55} & 0 \\ 0 & 0 & 0 & 0 & 0 & I_{66} \end{bmatrix} \tag{2.12}$$

where m is the floater mass and the terms I are the moments of inertia. Following the *Linear Wave Theory* developed by Airy [140], for a monochromatic wave with amplitude η_0 propagating along the direction θ, and defining $\hat{\eta}(\omega, \theta) = \eta_0 \mathrm{e}^{-\mathrm{i}\phi}$, the wave elevation given as follows:

$$\eta(t) = \Re\left\{\hat{\eta}(\omega, \theta)\mathrm{e}^{\mathrm{i}k(\omega)(x\cos(\theta)+y\sin(\theta))}\mathrm{e}^{-\mathrm{i}\omega t}\right\} \tag{2.13}$$

If $\theta = 0$ the wave travels along the x-direction. Therefore, since the linear assumption holds and assuming that all phenomena involved are harmonic in time, both the fluid and body motions are expressed by a complex quantity:

$$\begin{aligned} \Phi(x, y, z, t) &= \Re\left\{\hat{\Phi}(x, y, z)\mathrm{e}^{-\mathrm{i}\omega t}\right\} \\ \mathbf{X}_f(t) &= \Re\left\{\hat{\mathbf{X}}_f \mathrm{e}^{-\mathrm{i}\omega t}\right\} \end{aligned} \tag{2.14}$$

The *Linear Superposition Theorem* can be applied to describe the wave field interacting with a floating body as the sum of three different contributions [141]: incident, diffracted and radiated wave field. Then wave potential can be written as:

$$\hat{\Phi}(x, y, z) = \hat{\Phi}_I + \hat{\Phi}_D + \hat{\Phi}_R \tag{2.15}$$

where:

- **Incident potential** Φ_I is the potential of the undisturbed incident wave propagating in the absence of the body. The complex amplitude of the potential of the undisturbed wave field is given by:

$$\hat{\Phi}_I = -\eta_0 \frac{\mathrm{i}g}{\omega} \frac{\cosh(k(\omega)|(z+H))}{\cosh(k(\omega)H)} \mathrm{e}^{\mathrm{i}k(\omega)(x\cos(\theta)+y\sin(\theta))-\mathrm{i}\phi} \tag{2.16}$$

  where ω and the wave number k satisfy the dispersion relation 2.9.

- **Diffracted potential** Φ_D: it is the potential of the diffracted or scattered wave with motionless floater. Here, the sum of the incident and diffracted potential must satisfy the body boundary condition on the floater wet surface S_w with normal n:

$$\frac{\partial \hat{\Phi}_I}{\partial n} = -\frac{\partial \hat{\Phi}_D}{\partial n} \tag{2.17}$$

- **Radiated potential** Φ_R: it is the potential of the radiated wave which is generated by the body motions in the absence of the incident wave field. The complex amplitude of the potential is expressed as a function of the $d-th$ DoF motion amplitude $\hat{X}_{fd}$ and its associated radiated potential $\hat{\Phi}_{Rd}$:

$$\hat{\Phi}_R = \sum_{d=1}^{6} -\mathrm{i}\omega \hat{X}_{fd} \hat{\Phi}_{Rd} \tag{2.18}$$

  The radiation boundary conditions for the radiation problem are similar to the previous case, except for the absence of waves. Here, the $d-th$ radiation term $\hat{\Phi}_{Rd}$ is split into a spatial dependent component and an oscillatory velocity of the body. The boundary condition on the wet surface wet surface S_w with normal n can be written as:

$$\frac{\partial \hat{\Phi}_R}{\partial n} = \sum_{d=1}^{6} \frac{\partial \hat{\Phi}_{Rd}(x,y,z)}{\partial n} v_d(t) \tag{2.19}$$

  where v_n is the normal velocity at a point of the hull surface, v_d is the oscillatory velocity of the body and $\frac{\partial \hat{\Phi}_{Rd}}{\partial n}$ can be interpreted as the generalized direction cosine for the associated DoF d. Moreover, the radiation boundary condition has to be satisfied: the potential must decay as the distance from the body R_b increases. This physically means that the wave field will coincide to the undisturbed wave field far from the body:

$$\lim_{R_b \to \infty} \hat{\Phi}_R = 0 \tag{2.20}$$

First order hydrodynamic loads

The pressure forces are the external forces acting on a floating WEC interacting with ocean waves, and can be divided in hydrostatic and hydrodynamic action, obtained integrating the hydrostatic and hydrodynamic pressure on the wet surface of the body. The pressure acting on the wet body can be expressed through the *Linearised Bernoulli Equation* [141]:

$$p = \rho \frac{\partial \Phi}{\partial t} - \rho g z \tag{2.21}$$

where ρ is the water density. The forces $\mathbf{F}_p$ and torques $\mathbf{T}_p$ acting on the floater can be calculated integrating the pressure from Equation 2.21 acting on the wet surface of the floater S_w discretized in points with normal $\mathbf{n}$ and distance from the centre of gravity $\overrightarrow{r}$:

$$\begin{aligned} \mathbf{F}_p &= \mathbf{F}_{hs} + \mathbf{F}_{hd} = \\ &= -\iint_{S_w} p\mathbf{n}\, dS_w = -\iint_{S_w} \rho \left(\frac{\partial \Phi}{\partial t} - gz \right) \mathbf{n}\, dS_w \end{aligned} \tag{2.22}$$

and:

$$\begin{aligned} \mathbf{T}_p &= \mathbf{T}_{hs} + \mathbf{T}_{hd} = \\ &= -\iint_{S_w} p\,(\overrightarrow{r} \times \mathbf{n})\; dS_w = -\iint_{S_w} \rho \left(\frac{\partial \Phi}{\partial t} - gz \right) (\overrightarrow{r} \times \mathbf{n})\; dS_w \end{aligned} \tag{2.23}$$

where $\mathbf{n}$ and $\overrightarrow{r} \times \mathbf{n}$ can be grouped as $\mathbf{N} \in \mathbb{R}^{n_D}$:

$$\mathbf{N} = \begin{bmatrix} \mathbf{n} \\ \overrightarrow{r} \times \mathbf{n} \end{bmatrix} \tag{2.24}$$

Assuming small displacements, the surface S_w is approximated with the wet surface at rest S_{w0}. The pressure forces need to be calculated by solving the potential flow boundary value problem presented in the previous sections in order to compute the force vectors. Panel methods are generally used to solve the boundary integral equation using the Green function [[141, 134]. Different commercial codes are available to tackle the integration problem and, in this thesis, all the hydrodynamic linear parameters are computed via the Boundary Element Method (BEM) software NEMOH [142, 143], an open-source routine developed at the LHEEA Centrale Nantes [144].

Hydrostatic forces

First, the hydrostatic forces are calculated integrating the fluid static pressure over the wet surface, obtaining the linearised hydrostatic forces:

$$\mathbf{F}_{hs} = \iint_{S_{w0}} \rho g z \mathbf{n} \, dS_w \tag{2.25}$$

and torques:

$$\mathbf{T}_{hs} = \iint_{S_{w0}} \rho g z \, (\overrightarrow{r} \times \mathbf{n}) \, dS_w \tag{2.26}$$

When the floating body is in hydrostatic equilibrium the force $\mathbf{F}_{hs}$ cancels gravity $\mathbf{F}_g$ and the the torque $\mathbf{T}_{hs}$ is zero. Then, if a generic displacement of the floater happens, the geometry of the submerged volume is modified resulting in a non-zero vertical force $\mathbf{F}_{hs} + \mathbf{F}_g$, and a non-zero torque $\mathbf{T}_{hs}$. Defining $\mathbf{F}_s = \mathbf{F}_{hs} + \mathbf{F}_g$ and $\mathbf{T}_s = \mathbf{T}_{hs}$. Assuming small body displacements, the hydrostatic component $\mathbf{f}_s \in \mathbb{R}^{n_D}$ can be combined with the gravity one in a linear expression, function of the displacement $\mathbf{X}_f$, as follows:

$$\mathbf{f}_s(t) = \begin{bmatrix} \mathbf{F}_s(t) \\ \mathbf{T}_s(t) \end{bmatrix} = -\mathbf{K}_f \mathbf{X}_f \tag{2.27}$$

Solving the boundary element problem the stiffness matrix $\mathbf{K}_f \in \mathbb{R}^{n_D \times n_D}$ can be obtained:

$$\mathbf{K}_f = \begin{bmatrix} 0 & 0 & 0 & 0 & 0 & 0 \\ 0 & 0 & 0 & 0 & 0 & 0 \\ 0 & 0 & K_{33} & 0 & 0 & 0 \\ 0 & 0 & 0 & K_{44} & 0 & 0 \\ 0 & 0 & 0 & 0 & K_{55} & 0 \\ 0 & 0 & 0 & 0 & 0 & 0 \end{bmatrix} \tag{2.28}$$

The only non-zero terms refer to the vertical motion z, the roll α and pitch δ oscillations.

Hydrodynamic forces

The hydrodynamic pressure effect on the floating body is addressed via boundary value problem along with the Airy's linear theory which defines the wave potential. The hydrodynamic forces and torques $\mathbf{f}_{hd} \in \mathbb{R}^{n_D}$ due to the interaction of the incident wave with the diffraction wave and the radiation wave generated by the body motions are composed of three effects:

$$\begin{aligned}\mathbf{f}_{hd} &= \mathbf{f}_E + \mathbf{f}_R = \mathbf{f}_I + \mathbf{f}_D + \mathbf{f}_R = \\ &= -\iint_{S_{w0}} \rho \frac{\partial \Phi_I}{\partial t} \mathbf{N}\, dS_w - \iint_{S_{w0}} \rho \frac{\partial \Phi_D}{\partial t} \mathbf{N}\, dS_w - \iint_{S_{w0}} \rho \frac{\partial \Phi_R}{\partial t} \mathbf{N}\, dS_w\end{aligned} \tag{2.29}$$

where:

- **Wave excitation force**, $\mathbf{f}_E \in \mathbb{R}^{n_D}$: the excitation force considers the effect of the pressure forces acting on a fixed body in regular wave and represents the active component of the total dynamic force. It can be divided into:
  - **Froude-Krylov force**, $\mathbf{f}_I \in \mathbb{R}^{n_D}$: it takes into account the undisturbed incident wave velocity potential on the mean wet surface of the motionless body;
  - **Diffraction force**, $\mathbf{f}_D \in \mathbb{R}^{n_D}$: it results from the integration of the scattered wave potential over the mean wet surface of the motionless body. It represents a correction to the Froude-Krylov term that considers the effective disturbance of the wave field due to the presence of the body.
- **Radiation force**, $\mathbf{f}_R \in \mathbb{R}^{n_D}$: the radiation force represents the reactive component and it is due to the displacement of water induced by the forced motion of the body in absence of an incident wave field.

Integrating the pressure due to the incident and diffracted potentials yields:

$$\begin{aligned}\mathbf{f}_E = \mathbf{f}_I + \mathbf{f}_D &= -\iint_{S_{w0}} \rho \left(\frac{\partial \Phi_I}{\partial t} + \frac{\partial \Phi_D}{\partial t} \right) \mathbf{N}\, dS_w = \\ &= \Re \left\{ \left[\mathrm{i}\omega \iint_{S_{w0}} \rho \left(\hat{\Phi}_I + \hat{\Phi}_D \right) \right] \eta_0 \mathrm{e}^{-\mathrm{i}(\omega t + \phi)} \right\}\end{aligned} \tag{2.30}$$

From equation 2.30 it is possible to compute the Froude-Krylov and diffraction complex coefficients for each DoF, wave frequency and direction. These coefficients represent the external wave excitation forces acting on the floater. The output of the integration is the transfer function $\mathbf{H}_{\eta E} \in \mathbb{C}^{n_D}$ that relates the wave incident on the floater and the resultant excitation forces:

$$\hat{\mathbf{f}}_E(\omega, \theta) = \mathbf{H}_{\eta E}(\omega, \theta) \hat{\eta}(\omega, \theta) \tag{2.31}$$

The effects of incident and diffracted waves can be examined individually expressing the force due to the incident potential - called the dynamic Froude-Krylov force, with its transfer function $\mathbf{H}_{\eta FK} \in \mathbb{C}^{n_D}$ - and the force due to the diffracted waves, with its transfer function $\mathbf{H}_{\eta D} \in \mathbb{C}^{n_D}$:

$$\hat{\mathbf{f}}_I(\omega, \theta) = \mathbf{H}_{\eta FK}(\omega, \theta) \hat{\eta}(\omega, \theta) \tag{2.32a}$$

$$\hat{\mathbf{f}}_D(\omega,\theta) = \mathbf{H}_{\eta D}(\omega,\theta)\hat{\eta}(\omega,\theta) \tag{2.32b}$$

Then, the expressions of $\mathbf{f}_E(t)$, $\mathbf{f}_I(t)$ and $\mathbf{f}_D(t)$ follow:

$$\mathbf{f}_E(t) = \sum_{\omega}\sum_{\theta} \Re\left\{\hat{\mathbf{f}}_E(\omega,\theta)\mathrm{e}^{-\mathrm{i}\omega t}\right\} \tag{2.33a}$$

$$\mathbf{f}_I(t) = \sum_{\omega}\sum_{\theta} \Re\left\{\hat{\mathbf{f}}_I(\omega,\theta)\mathrm{e}^{-\mathrm{i}\omega t}\right\} \tag{2.33b}$$

$$\mathbf{f}_D(t) = \sum_{\omega}\sum_{\theta} \Re\left\{\hat{\mathbf{f}}_D(\omega,\theta)\mathrm{e}^{-\mathrm{i}\omega t}\right\} \tag{2.33c}$$

Equations 2.33 implies an incident wave field composed by superposition of wave trains at different amplitudes and frequencies hitting the floater from different directions.

The radiation force is obtained from the third integral of equation 2.29. Introducing 2.18 in 2.29, the $d-th$ component of the radiation force reads:

$$\begin{aligned}\mathbf{f}_{Rd} &= -\iint_{S_{w0}} \rho\frac{\partial\Phi_R}{\partial t}\mathbf{N}\,dS_w = \\ &= \Re\left\{\left[\iint_{S_{w0}} \omega^2\rho\hat{\Phi}_{Rd}\mathbf{N}\,dS_w\right]\hat{X}_{fd}\mathrm{e}^{-\mathrm{i}\omega t}\right\}\end{aligned} \tag{2.34}$$

Then, the $d-th$ radiation force component can be split into two terms: one in phase with the acceleration and the other component in phase with the velocity:

$$\mathbf{f}_{Rd} = \Re\left\{\left[-\omega^2\mathbf{A}_{Rd} - \mathrm{i}\omega\mathbf{B}_{Rd}\right]\hat{X}_{fd}\mathrm{e}^{-\mathrm{i}\omega t}\right\} \tag{2.35}$$

The frequency dependent hydrodynamic added mass $\mathbf{A}_{Rd} \in \mathbb{R}^{n_D}$ and the radiation damping $\mathbf{B}_{Rd} \in \mathbb{R}^{n_D}$ matrices can be defined for the generic $d-th$ component:

$$\mathbf{A}_{Rd} = -\Re\left\{\iint_{S_{w0}} \rho\hat{\Phi}_{Rd}\mathbf{N}\,dS_w\right\} \tag{2.36a}$$

$$\mathbf{B}_{Rd} = -\omega\Im\left\{\iint_{S_{w0}} \rho\hat{\Phi}_{Rd}\mathbf{N}\,dS_w\right\} \tag{2.36b}$$

Considering all the six modes simultaneously and different wave frequencies, the radiation term $\mathbf{f}_R \in \mathbb{R}^{n_D}$ becomes:

$$\mathbf{f}_R(t) = \Re\left\{\sum_{\omega}\left[-\omega^2\mathbf{A}_R(\omega) - \mathrm{i}\omega\mathbf{B}_R(\omega)\right]\hat{\mathbf{X}}_f(\omega)\mathrm{e}^{-\mathrm{i}\omega t}\right\} \tag{2.37}$$

The symmetry properties of the ISWEC floater with respect to its longitudinal and transversal plane lead some $\mathbf{A}_R \in \mathbb{R}^{n_D \times n_D}$ and $\mathbf{B}_R \in \mathbb{R}^{n_D \times n_D}$ coefficients equal to zero:

$$\mathbf{A}_R(\omega) = \begin{bmatrix} A_{11} & 0 & 0 & 0 & A_{15} & 0 \\ 0 & A_{22} & 0 & A_{24} & 0 & 0 \\ 0 & 0 & A_{33} & 0 & 0 & 0 \\ 0 & A_{42} & 0 & A_{44} & 0 & 0 \\ A_{51} & 0 & 0 & 0 & A_{55} & 0 \\ 0 & 0 & 0 & 0 & 0 & A_{66} \end{bmatrix} \tag{2.38a}$$

$$\mathbf{B}_R(\omega) = \begin{bmatrix} B_{11} & 0 & 0 & 0 & B_{15} & 0 \\ 0 & B_{22} & 0 & B_{24} & 0 & 0 \\ 0 & 0 & B_{33} & 0 & 0 & 0 \\ 0 & B_{42} & 0 & B_{44} & 0 & 0 \\ B_{51} & 0 & 0 & 0 & B_{55} & 0 \\ 0 & 0 & 0 & 0 & 0 & B_{66} \end{bmatrix} \tag{2.38b}$$

2.1.3 Frequency domain hydrodynamic model

Under the assumption of harmonic motions and incident monochromatic wave of frequency ω, it is possible to write the sea-keeping equation to formulate the frequency domain model, combining the hydrostatic and hydrodynamic forces defined in 2.27, 2.33 and 2.37 in the *Second Newton's Law* 2.11:

$$\left[-\omega^2(\mathbf{M}_f + \mathbf{A}_R(\omega)) + \mathrm{i}\omega\mathbf{B}_R(\omega) + \mathbf{K}_f\right] \hat{\mathbf{X}}_f = \mathbf{H}_{\eta E}(\omega)\hat{\eta}(\omega) \tag{2.39}$$

where $\hat{\eta}$ and $\hat{\mathbf{X}}_f$ are the wave elevation and body motion complex amplitude, respectively. The equation 2.39 is written assuming a wave elevation directed along the x-direction. Then, the transfer function of the body motions $\mathbf{H}_{\eta X_f}(\omega) \in \mathbb{C}^{n_D}$ is defined as:

$$\mathbf{H}_{\eta X_f}(\omega) = \frac{\mathbf{H}_{\eta E}(\omega)}{-\omega^2(\mathbf{M}_f + \mathbf{A}_R(\omega)) + \mathrm{i}\omega\mathbf{B}_R(\omega) + \mathbf{K}_f} \tag{2.40}$$

The relation above is known as Response Amplitude Operator (RAO) and it represents the complex frequency-domain transfer function which relates the wave elevation to the floater motion amplitudes at the frequency ω:

$$\mathbf{X}_{f0} = |\mathbf{H}_{\eta X_f}(\omega)|\eta_0 \tag{2.41}$$

2.1.4 Time domain hydrodynamic model

The fluid-structure interaction model is based on linear potential flow theory under the assumptions of irrotational flow, inviscid and incompressible fluid, harmonic oscillations of the hull for each DoF and zero-forward-speed conditions [141]. Moreover, the incoming wave is considered directed along the x-direction leading the incident angle θ equal to zero. Then, according to the well-known *Cummins' Equation* [145], the dynamic behaviour of a floating body can be derived in the time domain:

$$[\mathbf{M}_f + \mathbf{A}_R(\infty)]\,\ddot{\mathbf{X}}_f + \int_0^\infty \mathbf{K}_R(\tau)\dot{\mathbf{X}}_f(t-\tau)\,d\tau + \mathbf{K}_f\mathbf{X}_f + \mathbf{f}_m = \mathbf{f}_E(t) + \mathbf{f}_{Dr}(t) \quad (2.42)$$

where $\mathbf{A}_R(\infty) \in \mathbb{R}^{n_D \times n_D}$ is the added mass contribution evaluated for infinite oscillation frequency, $\mathbf{K}_R \in \mathbb{R}^{n_D \times n_D}$ is the radiation impulse response kernel, $\mathbf{f}_m \in \mathbb{R}^{n_D}$ the mooring recall and $\mathbf{f}_{Dr} \in \mathbb{R}^{n_D}$ the drift forces. The mathematical framework behind the generation of $\mathbf{f}_E(t)$ and $\mathbf{f}_{Dr}(t)$ is treated in Section 2.2.5.

Radiation forces approximation

The radiation forces $\mathbf{f}_R \in \mathbb{R}^{n_D}$ arise from the motion of the hull through the water that results in inertia and friction components. These contributions can be obtained by solving the convolution integral of the impulse response kernel $\mathbf{K}_R$ [146]:

$$\mathbf{f}_R(t) = \int_0^t \mathbf{K}_R(\tau)\dot{\mathbf{X}}_f(t-\tau)\,d\tau \quad (2.43)$$

As the computation of the convolution integral can be very time consuming, it is convenient to express this term with a state-space representation:

$$\begin{aligned} \dot{\boldsymbol{\zeta}} &= \mathbf{A}_r\boldsymbol{\zeta} + \mathbf{B}_r\dot{\mathbf{X}}_f \\ \mathbf{f}_R &= \mathbf{C}_r\boldsymbol{\zeta} + \mathbf{D}_r\dot{\mathbf{X}}_f \end{aligned} \quad (2.44)$$

The vector $\boldsymbol{\zeta} \in \mathbb{R}^{n_R}$ represents the state vector that approximates the radiation force contributions and n_R is the approximation order. The state space matrices $\mathbf{A}_r \in \mathbb{R}^{n_R \times n_R}$, $\mathbf{B}_r \in \mathbb{R}^{n_R \times n_D}$, $\mathbf{C}_r \in \mathbb{R}^{n_D \times n_R}$ and $\mathbf{D}_r \in \mathbb{R}^{n_D \times n_D}$ can be identified following the well-known Perez and Fossen and approach [146, 147], leading a satisfactory approximation of the transfer function $\mathbf{H}_{\dot{X}_f R}(\omega) = \omega^2\mathbf{A}_R(\omega) + \mathrm{i}\omega\mathbf{B}_R(\omega)$ which relates the body velocity to the resulting radiation force.

Mooring forces

The mooring system is modelled via quasi-static approach according to the formulation proposed by Pozzi [30]. The mooring forces are derived by varying the $\mathbf{X}_f$ coordinates of the connection point of the hull. Computing the equilibrium condition of the mooring line for all the different possible positions of the device, the mooring tensions are identified. In the numerical model, different MATLAB® look-up tables map the mooring forces in respect to the hull motion. As shown in Figure 2.3, the ISWEC mooring system consists in slack catenaries equipped with jumpers and clump-weights to avoid snatches. Two bridles connect the hull to a central joint to prevent the roll motion of the device. To guarantee the weather-vaning of the device in respect to the wave direction, the mooring connection points are placed towards the bow with respect to the centre of gravity of the device [148].

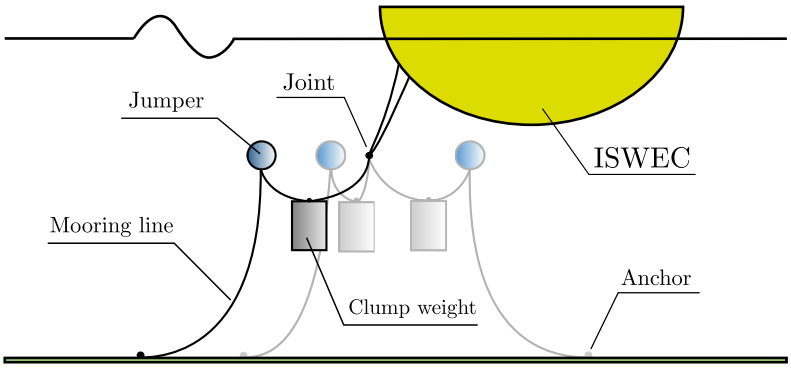

Figure 2.3: ISWEC mooring system [149].

2.2 A Gaussian model for ocean waves

Before introducing the gyroscope and the PTO models, the first step is building the wave generation framework based on the assumption that the ocean waves follows a Gaussian random phenomenon. This work aims to collect the most important relations describing the mathematical tools behind the Gaussian wave description. More detailed developments may be found in the important articles by Pierson [150], in the books by Whitham [151] and Ochi [152].

The equation 2.8 gives a simple time dependent solution for the wave elevation. In particular, considering the wave elevation at a single point measurement, the time history of the free surface $\eta(t)$ should be a simple sinusoidal function. However, oceans waves derives from countless number of natural events, which atmospheric conditions (mean wind speed and direction, temperature, tidal rises, currents, storms, earthquakes etc.) that are impossible to anticipate and, even more, replicate [153]. This randomness of the wave elevation calls for a more sophisticated

description to account for the ocean surface behaviour. Therefore, when observed locally (e.g. fixing the location $\mathbf{x}$), the resulting waves cannot be accounted with a deterministic description.

From the linearity of the problem stated in Section 2.1.1, a free-surface elevation solution is composed with various frequencies, phases and propagation directions. This superposition principle was first introduced in hydrodynamics in [154]. In this work, the wave field is modelled at a fixed location in space and the wave spectrum is studied unidirectional. From here on, the dependence on location $\mathbf{x}$ and wave direction θ can be removed without loss of generality. Then, the wave elevation is supposed to be recorded for a finite duration and it is approximated locally by:

$$\eta(t) = \sum_{k=1}^{M} \eta_{0k} \cos(\omega_k t + \phi_k) \tag{2.45}$$

where M is the number of frequencies, η_{0k} and ϕ_k are the $k-th$ amplitude and phase associated to $\eta(t)$, respectively. However, equation 2.45 does not properly predict the wave elevation since, as stated above, the actual wave elevation cannot be described by any finite-order Fourier approximation of the form 2.45. Clearly, equation 2.45 is not yet a satisfactory model for an actual sea state, generated from the result of uncountable, infinitesimal elementary random contributions. Therefore, a more rigorous model which incorporates the randomness of ocean waves is required. In 1952, Pierson proposed a wave elevation model based on the *Random Noise Theory* [155], giving a mathematical expression of the wave elevation at a fixed point in space as follows [156, 157]:

$$\eta(t) = \int_0^\infty \cos(\omega t + \phi(\omega)) \sqrt{2 S_{\eta\eta}(\omega)\, d\omega} \tag{2.46}$$

where:

- $\phi(\omega)$ is a random function of ω, uniformly distributed in [0,2π], resulting that $\phi(\omega)$ at all frequencies are statistically independent from each other;
- $S_{\eta\eta}(\omega)$ is the Spectral Density Function (SDF) or Power Spectral Density (PSD) or the energy spectrum. It represents the mean squared amplitude of the waves with frequency ω.

Equation 2.46 gives a stochastic representation of the wave elevation $\eta(t)$. In particular, the stochastic integral 2.46 should be solved of for any arbitrary realisation of the random function $\phi(\omega)$, resulting in a realisation $\tilde{\eta}(t)$ of the random process $\eta(t)$ underlying spectrum $S_{\eta\eta}(\omega)$. Thus, the SDF is not the spectrum of the single wave $\tilde{\eta}(t)$ captured in a finite time interval at a fixed location but instead the mean of infinite spectra resulted from infinite single realisations of the process $\eta(t)$. $\eta(t)$ is now described as a random function, indexed by time t and position $\mathbf{x} = \mathbf{0}$, and generated through the random integral 2.46. The basic properties of

this random function are now presented in Section 2.2.2, while more details about random functions in general may be found in [158].

From here on, the wave model is considered Gaussian, following the mathematical framework proposed in the PhD thesis of Mérigaud [159]. In [159], the relatively simple mathematical tools for the Gaussian description of a random sea are given, along with the most important properties and calculations for the Gaussian representation of random waves. In this section, mathematical expressions to generate a statistically correct Gaussian sea along with the statistical parameters of interest for the performance analysis of a WEC are described. However, precise details about the performance indexes employed for the design and performance evaluation of the ISWEC device will be detailed further in Sections 3.6.1 and 4.5. A comprehensive treatment of the stochastic approach for ocean waves can be found in the book by Ochi [152].

2.2.1 Spectral density function model

In literature, different analytical SDF are proposed to model the real measured wave spectra. In the offshore industry two wave spectra functions are widely used [141]: the JONSWAP and Bretshneider functions [160]. In this work the JONSWAP (Joint North Sea Wave Project, [161]) parametric form is considered. Different examples highlighting the influence of three different JONSWAP parameters are pictured in Figure 2.4. The SDF of a JONSWAP spectrum can be written as:

$$S_{\eta\eta}(\omega) = A_J \omega^{-5} \mathrm{e}^{-B_J \omega^{-4}} \gamma^{\alpha_J} \tag{2.47}$$

where γ is the peak enhancement factor, which value, if increased, determines more sharply concentrated spectra. The other coefficients in equation 2.47 are defined as follows:

- $A_J = \frac{4\pi H_s^2}{T_p^4}$
- $B_J = \frac{23\pi^3}{T_p^4}$
- $\alpha_J = \mathrm{e}^{\frac{0.2049 T_p \omega - 1}{\sqrt{2}\sigma_J}}$
- $\sigma_J = \begin{cases} 0.07 & \text{if } \omega \leq \dfrac{4.88}{T_p} \\ 0.09 & \text{if } \omega > \dfrac{4.88}{T_p} \end{cases}$

where, among others, H_s is the significant wave height and T_p the peak period.

Many parameters of interest can be derived from the wave SDF, along to those which can be directly estimated from the time Coulombs realisations [162, 163]. The most common parameters are:

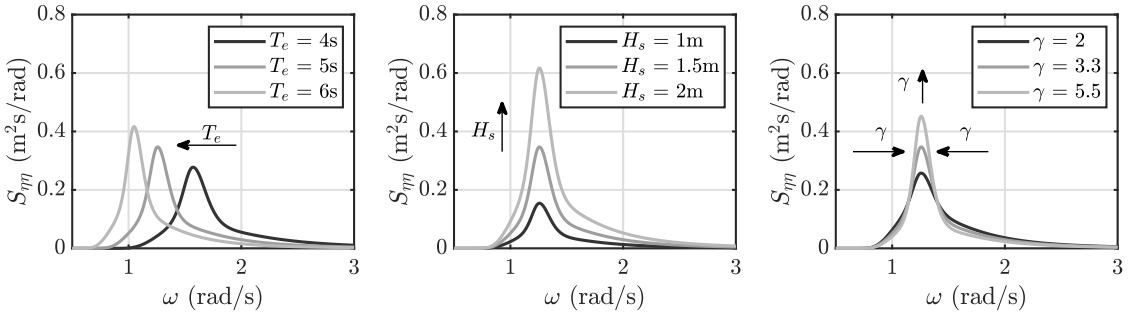

(a) (b) (c)

Figure 2.4: JONSWAP spectra examples: (a) JONSWAP spectra with increasing wave energy period, (b) JONSWAP spectra with increasing significant wave height and (c) JONSWAP spectra with increasing peak enhancement factor.

- m_i: moment of order i:

$$m_i = \int_0^\infty \omega^i S_{\eta\eta}(\omega)\, d\omega \tag{2.48}$$

- m_0: the moment of order 0 represents the area under the wave spectrum and measures the average energy of the random process, equals to the variance of the process itself [164]:

$$m_0 = \sigma_\eta^2 = \int_0^\infty S_{\eta\eta}(\omega)\, d\omega \tag{2.49}$$

- H_s: the significant wave height, defined as the average peak-to-trough height of the one third largest waves. Assuming a narrow-band spectrum, which means that the free surface elevation does not have any positive minima or negative maxima, the distribution of wave amplitudes follows a Rayleigh distribution, and H_s can be estimated directly from the wave spectrum [152]:

$$H_s \approx H_{m0} = 4.01\sqrt{m_0} \tag{2.50}$$

- T_p: the peak wave period corresponds to the inverse of the frequency which has the highest energy in the wave SDF. It is linked to the wave energy period, T_e, calculated from the spectrum as:

$$T_e = \frac{m_{-1}}{m_0} \tag{2.51}$$

The combination of the significant wave height and the energy period of a sea state defines the Wave Power Density of an irregular wave:

$$P_w = \frac{\rho g^2}{64\pi} H_s^2 T_e \tag{2.52}$$

2.2.2 Stationary Gaussian processes in a nutshell

Lets define a Gaussian random function $\mathcal{X}(t)$ of time t described by the SDF $\mathcal{S}_{\mathcal{X}\mathcal{X}}(\omega)$. Formally, for any discrete set of points $\{t_1, ..., t_n\}$, the set $\{\mathcal{X}(t_1), ..., \mathcal{X}(t_n)\}$ follows a Gaussian distribution. In particular, the probability law followed by $\mathcal{X}(t)$, is a normal random variable with the following probability density function (pdf) defined as:

$$f_{\mathcal{X}}(\mathcal{X}) = \frac{1}{\sqrt{2\pi}\sigma_{\mathcal{X}}} \mathrm{e}^{-\frac{(\mathcal{X}-\mu_{\mathcal{X}})^2}{2\sigma_{\mathcal{X}}^2}} \tag{2.53}$$

where $\mu_{\mathcal{X}}$ and $\sigma_{\mathcal{X}}^2$ are the mean and the variance of the Gaussian process defined as follows:

$$\mu_{\mathcal{X}} = \langle \mathcal{X} \rangle = \int_{-\infty}^{\infty} \mathcal{X} f_{\mathcal{X}}(\mathcal{X})\, d\mathcal{X} \tag{2.54a}$$

$$\sigma_{\mathcal{X}}^2 = \langle (\mathcal{X} - \langle \mathcal{X} \rangle)^2 \rangle = \langle \mathcal{X}^2 \rangle - \langle \mathcal{X} \rangle^2 \tag{2.54b}$$

For the bi-variate case, considering two normal random variables $\mathcal{X}$ and $\mathcal{Y}$, the following relation holds:

$$f_{\mathcal{X}\mathcal{Y}}(\mathcal{X}, \mathcal{Y}) = \frac{1}{2\pi |\mathbf{\Sigma}_{\mathcal{X}\mathcal{Y}}|^{\frac{1}{2}}} e^{-\frac{1}{2}(\boldsymbol{\chi}-\boldsymbol{\mu}_{\mathcal{X}\mathcal{Y}})^T \mathbf{\Sigma}_{\mathcal{X}\mathcal{Y}}^{-1} (\boldsymbol{\chi}-\boldsymbol{\mu}_{\mathcal{X}\mathcal{Y}})} \tag{2.55}$$

where:

- $\boldsymbol{\chi} = [\mathcal{X} \quad \mathcal{Y}]^T$ is the vector of random variables;
- $\boldsymbol{\mu}_{\mathcal{X}\mathcal{Y}} = [\mu_{\mathcal{X}} \quad \mu_{\mathcal{Y}}]^T$ is the vector of mean values;
- $\mathbf{\Sigma}_{\mathcal{X}\mathcal{Y}} = \begin{bmatrix} \sigma_{\mathcal{X}}^2 & \sigma_{\mathcal{X}\mathcal{Y}} \\ \sigma_{\mathcal{X}\mathcal{Y}} & \sigma_{\mathcal{Y}}^2 \end{bmatrix}$ is the covariance matrix.

The Gaussian process under study implies the following properties:

- **Stationarity**: if the statistical properties of the random function $\mathcal{X}(t)$ do not vary over time, then $\mathcal{X}(t)$ is stationary. Since $\mathcal{X}(t)$ is Gaussian, stationariness reduces to the fact that the covariance between $\mathcal{X}$, measured at any two instants t_1 and t_2, only depends on the relative time $\tau = t_2 - t_1$, which is called weak stationariness [164]. Thus, a process $\mathcal{X}(t)$ is said to be Weak-Sense Stationary or Wide-Sense stationary (WSS) if the mean is a constant and the covariance function depends only on the difference between the time indices:

$$\langle \mathcal{X}(t_1) \rangle = \langle \mathcal{X}(t_2) \rangle = \mu_{\mathcal{X}} \tag{2.56a}$$
$$\langle \mathcal{X}(t_1)\mathcal{X}(t_2) \rangle = \mathcal{R}_{\mathcal{X}\mathcal{X}}(t_2 - t_1) = \mathcal{R}_{\mathcal{X}\mathcal{X}}(\tau) \tag{2.56b}$$

In particular, the variance, defined also as $\mathcal{R}_{\mathcal{X}\mathcal{X}}(0)$, does not depend on the time. In short, stationary processes exhibit statistical properties that are invariant to shift in the time index. Since $\mathcal{X}(t)$ is a stationary Gaussian random process, it is entirely characterised by its mean and its Auto-Correlation Function $\mathcal{R}_{\mathcal{X}\mathcal{X}}$ [164], defined as:

$$\mathcal{R}_{\mathcal{X}\mathcal{X}}(\tau) = \langle \mathcal{X}(t)\mathcal{X}(t+\tau) \rangle \tag{2.57}$$

Since the mean of the process will be supposed to be zero, the Auto-Correlation Function (ACF) equals, by definition, the Auto-Covariance Function (ACF). Furthermore, the ACF and the SDF constitute a Fourier transform pair, which is a fundamental property of the *Wiener-Khinchine Theorem* [158, 164]. The Wiener-Khinchine relation states that the ACF of a WSS random process has a spectral decomposition given by the power spectrum of that process:

$$\mathcal{S}_{\mathcal{X}\mathcal{X}}(\omega) = 2 \int_{-\infty}^{\infty} \mathcal{R}_{\mathcal{X}\mathcal{X}}(\tau) \mathrm{e}^{-\mathrm{i}\omega\tau} \, d\tau \tag{2.58a}$$

$$\mathcal{R}_{\mathcal{X}\mathcal{X}}(\tau) = \frac{1}{2} \int_{-\infty}^{\infty} \mathcal{S}_{\mathcal{X}\mathcal{X}}(\omega) \mathrm{e}^{\mathrm{i}\omega\tau} \, d\omega \tag{2.58b}$$

It is straightforward to reformulate the equation 2.58b in:

$$\mathcal{R}_{\eta\eta}(\tau) = \int_{0}^{\infty} \mathcal{S}_{\mathcal{X}\mathcal{X}}(\omega) \cos(\omega\tau) \, d\omega \tag{2.59}$$

- **Ergodicity**: Another important property is the ergodicity [150], which means that statistics results obtained on time averages equals to those based on ensemble averages. For example, the mean and the variance, which are mathematically defined as the ensemble average of $\langle \mathcal{X}(t) \rangle$ and $\langle \mathcal{X}(t)^2 \rangle$, can also be obtained by computing the time average of $\mathcal{X}(t)$ and $\mathcal{X}(t)^2$, respectively, for any specific realisation of $\mathcal{X}(t)$:

$$\mu_{\mathcal{X}} = \lim_{T \to \infty} \frac{1}{T} \int_0^T \tilde{\mathcal{X}}(t)\, dt \tag{2.60a}$$

$$\sigma^2_{\mathcal{X}} = \lim_{T \to \infty} \frac{1}{T} \int_0^T \tilde{\mathcal{X}}(t)^2\, dt \tag{2.60b}$$

  where $\tilde{\mathcal{X}}(t)$ denotes a finite-length realisation of the process $\mathcal{X}(t)$.

Before transferring the relations obtained for a Gaussian representation of ocean waves, it useful to define the mathematical framework to analyse a series of conceptual experiments where $\mathcal{X}$ is repeated R times and recorded over a finite duration T. As illustrated in Figure 2.5, it would be observed that the sequence $\mathcal{X}(t)$, for $t \in [0; T]$, is never the same for any two experiments. More precisely, $\mathcal{X}(t)$ is a stationary Gaussian random function of a discrete or continuous set $t \in [0; T]$ [158]. Furthermore, the covariance between measures at different instants separated by τ follows equation 2.59. The statistical properties characterizing the numerical (or real) experiments could be calculated by considering the ensemble statistics obtained through averages over the set of experiments. Moreover, the same statistical results could be obtained with the time domain averaging if the ergodicity property is guaranteed (infinite-length signal). In short, when generating a realisation $\tilde{\mathcal{X}}(t)$, underlying a given spectrum $\mathcal{S}_{\mathcal{X}\mathcal{X}}(\omega)$, the aim should be to reproduce the above experiment, consisting of sampling $\mathcal{X}(t)$ from the target spectrum. As stated in [159], two criteria are necessary and sufficient for the generated signal to be an accurate representation of the target Gaussian sea:

- Criterion 1 (C1): The generated signal $\mathcal{X}(t)$ should be a zero-mean Gaussian random function of $t \in [0, T]$;
- Criterion 2 (C2): The covariance function of the generated signal should satisfy the equation 2.59 for all $t \in [0, T]$.

The randomness of the generated signal and its statistical properties can only be appreciated by generating: (I) a large number of finite-length signals, whereby ensemble statistics can be characterised or (II) an infinitely-long time horizon realisation, where the time statistic can be obtained. A concise but effective analysis

of the influence of finite-length wave profiles on the ISWEC performances is carried out for different durations and number of realisation in Section 3.6.2 of Chapter 3 for different time length and realisation number.

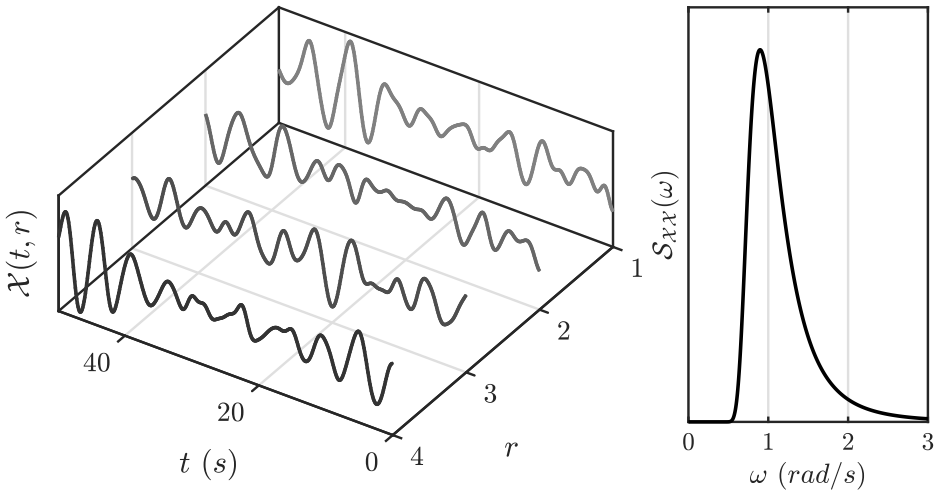

Figure 2.5: Illustrative example of four $\mathcal{X}(t)$ realizations being repeatedly sampled in the same experiment conditions undelying the same SDF $\mathcal{S}(\omega)$.

2.2.3 Finite-length Gaussian waves statistics

As anticipated at the beginning of Section 2.2, the wave elevation $\eta(t)$ can be assimilated as Gaussian random function of time t. The Gaussian model implies, among others, that the probability law followed by the free surface elevation, sampled at one location $\mathbf{x}$, is a normal random variable. Moreover, in this work the wave elevation $\eta(t)$ is considered a zero-mean signal without any loss of generality. Now, assuming a stationary and ergodic Gaussian wave representation of equation 2.46, the random function $\eta(t)$, is entirely characterised by its SDF $S_{\eta\eta}(\omega)$ and its ACF $R_{\eta\eta}(t)$ and formulae from 2.53 to 2.60 can be transferred for the calculation of the Gaussian waves properties.

Given a zero-mean signal $\tilde{\eta}(t)$ of duration T, the mean-square value of the signal is estimated as:

$$\tilde{m}_0 = \frac{1}{T}\int_0^T \tilde{\eta}(t)^2\, dt \tag{2.61}$$

The zero-order spectral moment $\tilde{m}_0$ of the wave elevation, computed with equation 2.61, is merely an estimate, which differs from the theoretical m_0. In particular, because the free-surface elevation η is a random variable, quantities which depend on η (e.g. the WEC extracted power) are also random, and hence their variance

differs from the theoretical one. However, repeating many[1] instances of $\tilde{\eta}(t)$ would provide a more accurate estimate of m_0 and thus of the WEC performances in a statistical sense. The degree to which $\tilde{m}_0$ fluctuates around m_0 determines the level of uncertainty associated to the repeated process. The variance of $\tilde{m}_0$ can be computed as:

$$\begin{aligned}\sigma^2_{\tilde{m}_0} &= \langle \tilde{m}_0^2 \rangle - \langle \tilde{m}_0 \rangle^2 = \\ &= \left\langle \frac{1}{T} \int_0^T \tilde{\eta}(t)^2 \, dt \right\rangle - m_0^2 \\ &= \left\langle \frac{1}{T^2} \int_0^T \int_0^T \tilde{\eta}(t_1)^2 \tilde{\eta}(t_2)^2 \, dt_2 dt_1 \right\rangle - m_0^2 \\ &= \frac{1}{T^2} \int_0^T \int_0^T \left(\langle \tilde{\eta}(t_1)^2 \tilde{\eta}(t_2)^2 \rangle - m_0^2 \right) \, dt_2 dt_1\end{aligned} \tag{2.62}$$

In the expression above, since for any t_1 and t_2, the random variables $\eta(t_1)$ and $\eta(t_2)$ are jointly Gaussian, *Isserlis's Theorem* [165] may be applied to obtain:

$$\begin{aligned}\langle \tilde{\eta}(t_1)^2 \tilde{\eta}(t_2)^2 \rangle &= \langle \tilde{\eta}(t_1)^2 \rangle \langle \tilde{\eta}(t_2)^2 \rangle + 2 \langle \tilde{\eta}(t_1) \tilde{\eta}(t_2) \rangle^2 = \\ &= m_0^2 + 2 R_{\eta\eta}(t_2 - t_1)^2\end{aligned} \tag{2.63}$$

Substituting equation 2.63 in 2.62, exploiting the properties of integrals and the fact that $R_{\eta\eta}$ is even yields to:

$$\sigma^2_{\tilde{m}_0} = \frac{2}{T} \int_{-T}^{T} \left(1 - \frac{|t|}{T} \right) R_{\eta\eta}(t)^2 \, dt \tag{2.64}$$

The detailed derivation of equation 2.64 can be found in [159]. When T grows and becomes significantly larger than the autocorrelation length of the process, the equation 2.64 can be approximated as:

$$\sigma^2_{\tilde{m}_0} \approx \frac{2}{T} \int_{-\infty}^{\infty} R_{\eta\eta}(t)^2 \, dt = \frac{1}{T} \int_0^{\infty} S_{\eta\eta}(f)^2 \, df \tag{2.65}$$

For large values of T, the variance of the m_0 estimator follows an asymptotic law in $1/T$ [164]. Unsurprisingly, approaching the ergodicity limit with a infinite-length wave profile $\tilde{\eta}$, the estimated $\tilde{m}_0$ almost equals the theoretical m_0, and hence the estimator variance tends to zero. In contrast, when considered over a shorter time

[1] The number of realisations required to obtain a reliable statistical estimation of the WEC behaviour will be treated in Section 3.6.2.

period, individual $\tilde{m}_0$ estimates can differ significantly from m_0, fluctuating around the theoretical value with variance $\sigma^2_{\tilde{m}_0}$.

In [159] an exhaustive experimental validation using real wave data has been carried out on formula derived above. In particular, the variability of $\tilde{m}0$ with respect to m_0 have been evidenced by means of real sea wave records, choosing a specific time period in which the wave elevation can be reasonably considered stationary. The author shown how the estimate $\tilde{m}_0$ varies more when considered over shorter wave durations. Moreover, consistently with Equation 2.65, $\sigma^2_{\tilde{m}0}$ exhibits larger values in more energetic sea states which underlines larger wave spectra. In practice, the wave conditions (characterised by the wave spectrum $S\eta\eta$) are never perfectly stationary leading to consider a small duration of the wave properties compared to the rate at which meteorological conditions evolve. As stated in [159], real sea observations validates, at least qualitatively, the key points behind the Gaussian model of ocean waves.

2.2.4 Harmonic random amplitude wave generation

In literature, several methods are proposed for Gaussian process generation, relying on (I) superposition of harmonic functions with different amplitudes and phases randomly determined from the wave spectrum or based on the (II) filtering of white noise through an AR, MA, or ARMA model. This work focuses on a Wave Superposition (WS) method known as Harmonic Random Amplitude (HRA) to generate the so-called realisation $\tilde{\eta}$ of the Gaussian process η.

The rationale behind HRA

WS methods count on the frequency discretization of the target spectrum and on a random generation of wave elevation amplitudes and phase between its frequency components. Different modes are offered to discretize the spectrum and consequently generates the random amplitudes, which are critically discussed and compared in [159]. Briefly, the advantage of WS methods consist in being fast and simple and, in particular, no filter are needed to be desgined to generate the wave profile time-series $\tilde{\eta}(t)$. Moreover, they can reproduce, with arbitrary accuracy, the Gaussian wave model of an infinite set of wave components since each realisation may represent a single elementary wave. Then, since the $\tilde{\eta}(t)$ is described through a linear superposition of single frequency components, it allows computing the steady-state response of a linear or non-linear WEC system very efficiently in frequency and spectral domain (see Section 3.2 and 3.3).

Among the different WS methods, the wave amplitudes may be chosen either randomly or deterministically and the frequency discretization may be either harmonic or non-harmonic. For what concern the wave amplitudes, Random Amplitude (RA) generations statistically represent the Gaussian property of ocean waves

[166], while a Deterministic Amplitude (DA) times-series is statistically accurate only when the frequency discretization approaches to infinity [167]. Despite the attention given to the DA approach [168, 169] due to the possibility to reduce the simulation time compared to RA [170], the related mistake that is committed and its effect on wave group statistics has been argued by Tucker [168] and, recently, the Det Norske Veritas (DNV) guidelines promoted the use of the theoretically correct method (RA) [171]. Mérigaud [172] shows that HRA realistically produces the variability associated to the spectral moments at each realization. One drawback of harmonic methods, compared with filtering methods, is to produce a periodic signal with period $T_{per} = 1/\Delta f$, where Δf represents the frequency discretization step. This limit can be tackled by non-harmonic methods producing a long non-periodic time-series avoiding its self-repetition [166, 173, 174, 175]. However, since non-harmonic methods cause statistical distortion [173, 176], the HRA is chosen as the generation method. In order to avoid periodicity with HRA, it is suggested to simply discard the initial samples (say, $5 \div 10$ % of the total samples) of the signals generated obtaining a null autocorrelation of the target spectrum.

The description of the filtering methods is out of the scope of this thesis an the interested reader is referred to the works of Spanos et al. [177, 178].

Harmonic random amplitude method

First, a generic JONSWAP spectrum $S_{\eta\eta}$, depicted in Figure 2.6, is discretized with the frequency step Δf. The choice of the cut frequency f_c is related to the frequency content of $S_{\eta\eta}$ along with the WEC frequency response that is, generally, assimilated to a low-pass filter, cutting the high frequencies of the incident wave. From Δf, it is possible to divide the interval $[0, f_c]$ into $M+1$ frequencies $f_k = k\Delta f$, $\forall k \in \{0, ..., M\}$. Furthermore, lets define:

$$\nu_k = S_{\eta\eta}(f_k)\Delta f \tag{2.66}$$

where ν_k the area under of the $k-th$ spectrum interval, as shown in Figure 2.6. Then, the wave signal $\tilde{\eta}(t)$ is generated as:

$$\tilde{\eta}(t) = \frac{1}{2} \sum_{k=-M}^{M} \upsilon_k \mathrm{e}^{-2i\pi f_k t} \tag{2.67}$$

where $\forall k \geq 0$, $\upsilon_k = a_k + ib_k$, a_k and b_k are chosen as independent, normally distributed random variables with zero-mean and variance ν_k [169]. Another equivalent formulation of the HRA realisation $\tilde{\eta}(t)$ is defined with the same notation of Equiation 2.45:

$$\tilde{\eta}(t) = \sum_{k=0}^{M} \tilde{\eta}_{0k} \cos(2\pi f_k t + \phi_k) \tag{2.68}$$

where ϕ_k are randomly chosen, following a uniform distribution in [0,2π], and $\tilde{\eta}_{0k}$ follows a Rayleigh distribution with variance $2\nu_k$. The two formulations 2.67 and 2.68, are equivalent since $\tilde{\eta}_{0k}^2 = a_k^2 + b_k^2$. This method produces a periodic realisation with period $T_{per} = 1/\Delta f$, and therefore the frequency step has to be picked in respect to the required duration of a time domain simulation. Reducing Δf, the accuracy of the approximation can be made arbitrarily good leading an increase of the simulation time.

Let us consider a discrete time collection of N samples of $\tilde{\eta}$ such that $\tilde{\eta} = \{\tilde{\eta}(t_1), ..., \tilde{\eta}(t_N)\}$. The covariance between $\tilde{\eta}(t)$ and $\tilde{\eta}(t+\tau)$ can be calculated as the discrete version of equation 2.59:

$$R_{\tilde{\eta}\tilde{\eta}}(\tau) = \sum_{k=0}^{N} S_{\eta\eta}(k\Delta f)\cos(2\pi f_k \tau)\Delta f \tag{2.69}$$

From the expressions derived above, Δf should be chosen small enough to accurate reproduce the target spectrum. Moreover, periodicity play an important role to find the appropriate simulation time T. Choosing a simulation time $T = 1/\Delta f$ results in a correlation between the first and last generated samples. However, in general, the first part of the simulation is cut away to account for the transient period of the WEC dynamics.

Lastly, the expression of the expectation of $\tilde{m}_0$, defined as $\langle\tilde{m}_0\rangle$, and its variance $\sigma^2_{\tilde{m}_0}$ follows. Assuming a single discrete-time $\tilde{\eta}$ realisation of N time steps, the discrete-time version of equation 2.61 can be used to compute the single $\tilde{m}_0$:

$$\tilde{m}_0 = \frac{1}{T}\sum_{n=1}^{N} \tilde{\eta}(n)^2 \tag{2.70}$$

It is straightforward to obtain the following relations for the generated process $\tilde{\eta}$ for $T = 1/\Delta f$:

$$\langle\tilde{m}_0\rangle = \sum_{k=0}^{M} S_{\eta\eta}(f_k)\Delta f \tag{2.71a}$$

$$\sigma^2_{\tilde{m}_0} = \sum_{k=1}^{M} S_{\eta\eta}(f_k)^2\Delta f \tag{2.71b}$$

Equations 2.71 demonstrates that the HRA method produces an accurate approximation of the m_0 value of the target spectrum, provided that the frequency discretization step Δf is small enough ($\Delta f \approx f_c/100$ from [159]) and for a simulation time $T = 1/\Delta f$. Then, for a given choice of f_c and T, there are $M = f_c/\Delta f = f_c T$ frequency components.

In short, if the finite-length simulated wave signal are employed under the assumptions of a random sea, then $\tilde{m}_0$ evaluated from the single $\tilde{\eta}(t)$ should not be equal to its statistical average $\langle\tilde{m}_0\rangle$, but should instead exhibit some fluctuation

around it given by the variance $\sigma^2_{\tilde{m}_0}$. Then, the statistical properties of a generic output $\tilde{\mathcal{X}}$ of a WEC (e.g. mean value $\mu_{\tilde{\mathcal{X}}}$) subjected to several $\tilde{\eta}(t)$ inputs, should exhibits a fluctuation around the mean value between all the realizations $\langle \mu_{\tilde{\mathcal{X}}} \rangle$ with magnitude $\sigma^2_{\mu_{\tilde{\mathcal{X}}}}$. For our concrete system, for example, the mean extracted power under a specific wave spectrum $S_{\eta\eta}$ is computed as the mean of several mean extracted power values obtained with several time domain simulations underlying the same wave spectrum.

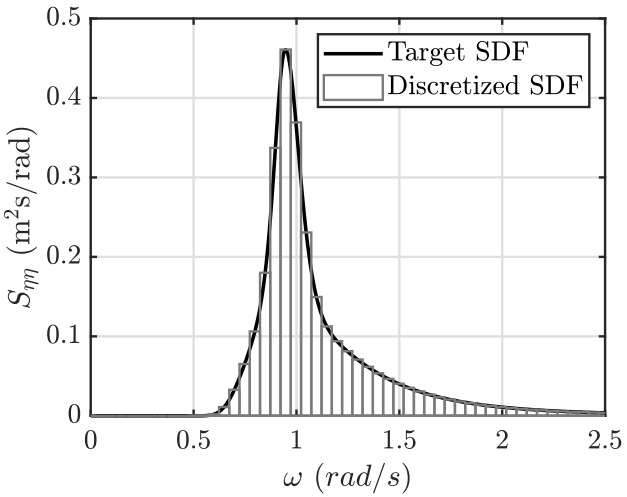

Figure 2.6: Example of a spectrum discretization for the HRA method.

2.2.5 Irregular wave force generation

The input $\mathbf{f}_E$ of the time domain system 2.42 is called wave excitation force that may be split into three parts [141]:

- Mean wave drift forces;
- Low frequency drift forces;
- First-order excitation forces.

In this work, mean and low-frequency drift forces are neglected for most of the dissertation since their importance become relevant when the station keeping of the floating moored structure is under study (out of the scope of this thesis). The drift forces are considered only in Chapter 6, where the mooring actions are included into the Kalman Filter observer and Neural Network model to estimate the wave excitation force as a part of a Model Predictive Control strategy. However, for the models comparison, described in Chapter 3 and in the design stage, subject of Chapter 4 and 5, it is possible to assume that during operational conditions the

mooring loads not have a relevant effect on the performance of the device [148]. The design of the mooring system requires the knowledge of the deployment site characteristics (e.g. the bathymetry) and the geometrical/inertial properties of the floater, therefore, it will be carried out in a later design stage.

Considering the single unidirectional ($\theta = 0$) wave profile realization $\tilde{\eta}(t)$ composed of M finite frequency components, the complex transfer function $\mathbf{H}_{\eta E}(\omega)$ is used to link the wave elevation and the wave excitation force for the single DoF d as follows:

$$\tilde{\mathrm{f}}_{Ed}(t) = \sum_{k=0}^{M} |H_{\eta Ed}(\omega_k)| \tilde{\eta}_{0k} \cos(\omega_k t + \phi_k + \angle H_{\eta Ed}(\omega_k)) \tag{2.72}$$

where $H_{\eta Ed}(\omega_k)$ is the Froude-Krylov and diffraction coefficient associated to the $d-th$ DOF and the $k-th$ wave frequency.

Drift forces are, in general, a function of the square of the wave amplitude. The information about the slowly-varying second-order forces are provided by the amplitudes envelope of the irregular wave. More precisely, the SDF of the wave provides information about the mean period and the magnitude of the low frequency wave forces. Usually a long wave record is required to obtain an accurate envelope spectrum [160], thus low frequency wave drift forces are derived used the Quadratic Transfer Function (QTF), output of the potential flow hydrodynamic analysis. However, the direct computation of the drift forces is time consuming and a more efficient approximation is required. Here, the time series of the drift forces are derived through the Newman approximation [179] for the $d-th$ DoF [30]:

$$\tilde{\mathrm{f}}_{Drd}(t) = 2 \left(\sum_{k=0}^{M} \tilde{\eta}_{0k} \sqrt{f_{dd}(\omega_k)} \cos(\omega_k t + \phi_k) \right)^2 \tag{2.73}$$

where $f_{dd}(\omega_k)$ is the drift force coefficient for each frequency component for the $d-th$ DoF. Newman's approximation is normally accepted for the hydrodynamic analysis of moored offshore structures in moderate and deep water depth in long crested waves [141].

2.2.6 Sea sites

Regarding the performance analysis and the design of a WEC system, it is important to consider several sea-sites with different level of wave resource in order to evaluate the influence this has on design process itself. In this study, wave data statistics from four locations along the European coasts are used. The occurrences diagrams of the four sites are given in Figure 2.7 as a function of the energetic period (T_e) and significant wave height (H_s). For a specific sea-site, the annual occurrences represents the annual probability associated to a single wave defined

by its spectral parameters (e.g. T_e and H_s). In this regards, different sea-sites have different mean annual power density content, that can be computed as follows:

$$\overline{P}_w = \sum_{n_w=1}^{n_W} P_{w,n_w} o_{n_w} \tag{2.74}$$

where n_W is the total number of waves, P_{w,n_w} is the specific power carried by the $n_w - th$ wave, computed with equation 2.52, and o_{n_w} the annual occurrence associated to the $nw - th$ wave. Two of the four sea-sites considered belong to the Mediterrean Sea (Alghero and Pantelleria) and the other two to the Atlantic Ocean (Balder and Capo Verde). The synthetic parameters associated to each sea-site are reported in Table 2.1.

Site	Bathymetry (m)	$\overline{P}_w$ (kW/m)	Most recurrent T_e (s)	Most recurrent H_s (m)	Most energetic T_e (s)	Most energetic H_s (m)
Alghero	85	12.9	3.75	0.25	10.25	4.75
Balder	125	34.8	5.5	1.5	7.5	3.5
Capo Verde	178	18.1	7	1.75	12.5	2.25
Pantelleria	35	6.8	5.5	0.3	8	3.2

Table 2.1: Basic sea-site info for each location of interest.

Starting with Alghero, the data available are obtained through measurements of the Rete Ondametrica Nazionale (RON) [180] with a wave detection system of the ISPRA (Istituto Superiore Per la Ricerca Ambientale) at the GPS Position 40.54N-8.11E. The bathymetry of the site is about 85 m and the distance from the coast 70 km. overall the Alghero sea-site has a medium energy content, with occurrences concentrated at relatively low energy periods (3.75s) and small significant wave height (0.25m). However, the occurrence distribution has a modest spread toward high energetic sea-states (see Figure 2.7a), resulting a most energetic wave with T_e=10.25s and H_s=4.75m. Balder is the most energetic site, having a mean power density $\overline{P}_w$ equal to 34.8 kW/m. The wave data are available from the Wam10 hindcast model operated by the Norwegian Meteorological Institute [181]. The data presented in Figure 2.7b refer to hindcast data from the period 1958 – 2014 (56 years) and with a sea state duration of 3 hours. Balder has a peaky occurrence distribution compared with the other sea-sites, leading a similar energy period between the most occurrent and most energetic wave, as reported in Table 2.1. This could represent an advantage since the ISWEC designed in respect to the Balder location should be optimal in all its sea-state conditions. On the other and, the high bathymetry, equal to 125 m, may lead high deployment costs. The other oceanic location is Capo Verde, which shows a double peak occurrences distribution [182]. Cape Verde is a volcanic archipelago formed by 10 volcanic islands off the north-west coast of Africa and it is influenced by the semi-permanent

Azores high-pressure system, prevailing north-easterly trade winds, and the Azores and Canary Currents. The wave data of Figure 2.7c are retrieved from ECMWF ERA5 [183] for the period 2000-2019 at location with coordinates 25.16W-17.20N. Concerning the Pantelleria sea-site, the analysis have been performed with wave spectral data by DHI and HyMOLab [184] with the reference location at 36.825N-11.92E. The dataset provided is the MWM (Mediterranean Wind Wave Model) and hourly data from 1979 to 2018 have been produced and analysed. In particular, from the directional wave spectra relative to 30 frequencies and 24 directions the wave parameters were calculated and the occurrences distribution reported in Figure 2.7d.

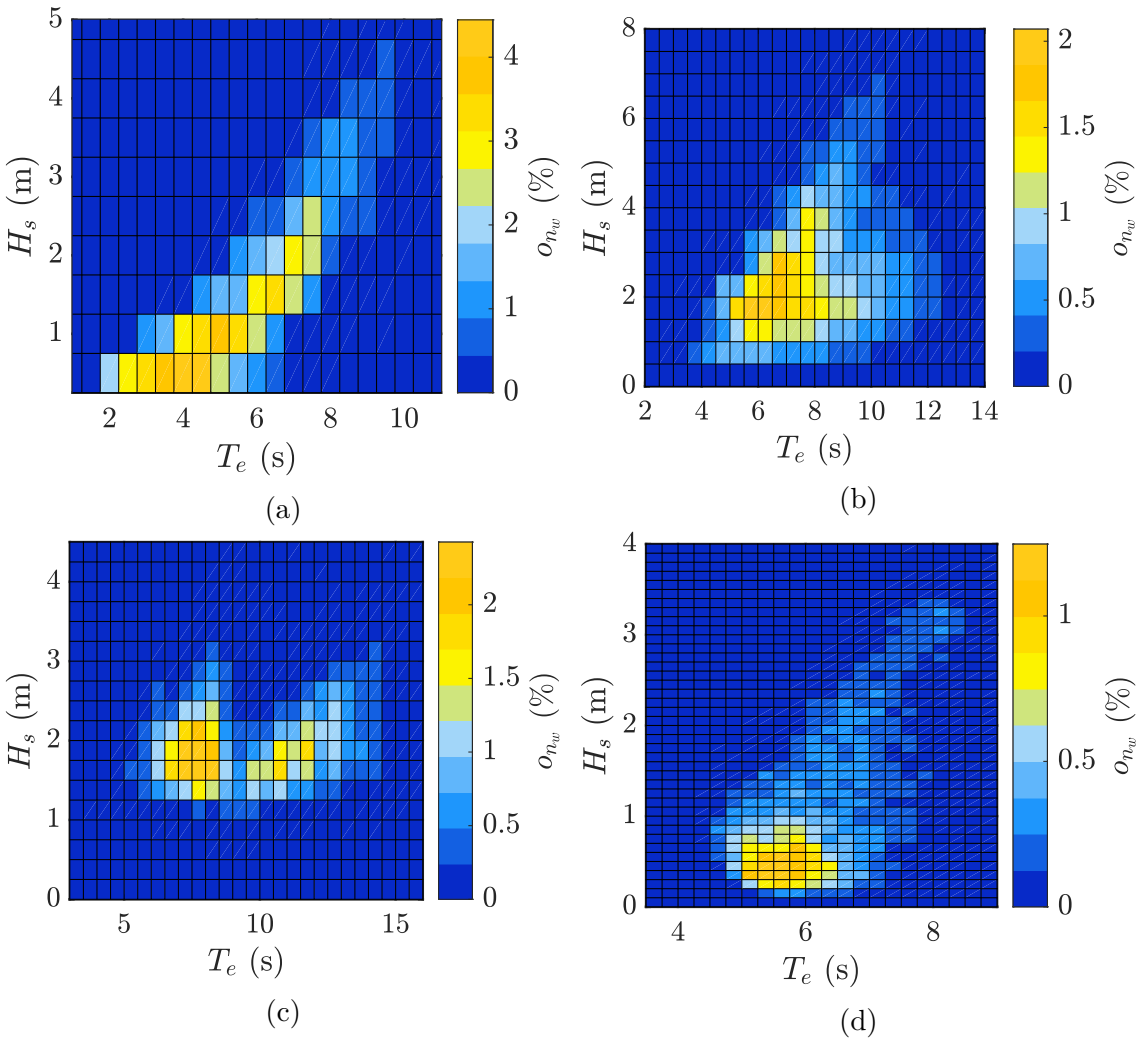

Figure 2.7: Sea-sites of interest and their occurrences distributions: (a) Alghero, (b) Balder, (c) Capo Verde and (d) Pantelleria.

Originally, the ISWEC device has been designed for the Mediterranean Sea or,

more in general, for low-medium energetic sea. One of the aims of this work is to explore the performances of the ISWEC device in high energetic seas toward an oceanic version of the device, called IOWEC (Inertial Ocean Wave Energy Converter). In the work of Sirigu [185], IOWEC has been studied and designed through a first version of the design process proposed in this thesis. As stated by the author [185], and described in Section 1.3, as the size of a WEC device increase, the advantages of the hydraulic technology compared to a mechanical one are dominant and the hydraulic transmission represents a valid PTO solution. In this regards, the ISWEC device will be designed for the Balder sea-site, being the most energetic site under study, and evaluated also in the other three locations.

2.3 Gyro-pendulum model

In this section, the simplified model equations of the gyro-pendulum are recalled, with the only purpose to define the gyroscope model coherent with the scope of this thesis and highlight its importance in the power conversion chain. ISWEC is a gyroscope based WEC using the gyroscopic reaction of a spinning flywheel to extract power from sea waves. The gyroscopic structure, depicted in Figure 2.8, is accommodated in a sealed floating body excited to oscillate at pitch motion by the incident waves.

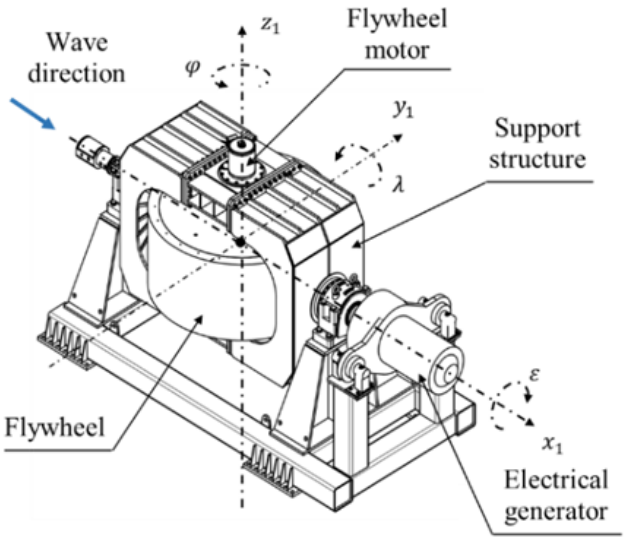

Figure 2.8: Detailed design of the gyorscope system and its reference frame

Thus, the flywheel reacts with a precession motion that is braked by a PTO system, converting its mechanical power into electricity. Moreover, an eccentric mass is fixed at the support frame of the gyroscope, acting as an elastic recall

to avoid the stabilization of the gyroscope. This mechanical solution is proposed to reduce the presence of reactive power delivered by the electrical generator and thus simplify the PTO control logic [186]. The complete derivation of the gyro-pendulum equation in a 6-DoF framework is treated in a simplified way in the following sections with the main scope to derive the simplified equation of such a mechanical system along the precession axis ε and to compute the rection torque acting on the floater pitch axis δ.

2.3.1 Reference frames definition

For fully describing the motion of the gyro-pendulum mechanism the reference frame has to be firstly defined. Figure 2.9 shows the reference frame of the gyroscopic system. The floater reference frame is coherent with the one defined in Figure 2.2. For the gyro-pendulum dynamic a new reference system (x_1, y_1, z_1), with the origin on the centre of gravity of the flywheel, is defined. (x_1, y_1, z_1) is the gimbal fixed reference frame rotating with respect the precession axis ε. Then, (x_2, y_2, z_2) is the flywheel fixed reference frame rotating with respect its rotation axis φ.

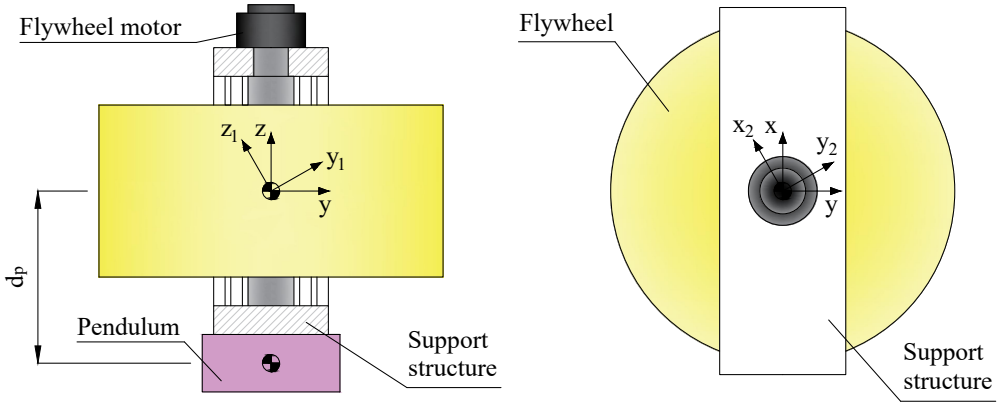

Figure 2.9: Front section and top view of the gyro-pendulum system with its reference frame.

The flywheel spins along its φ-axis with angular speed $\dot{\varphi}$ and the gyroscope system constitutes a 1-DoF system restrained to oscillate only around its precession axis ε. The inertia matrix of the flywheel is:

$$\mathbf{I}_{fw} = \begin{bmatrix} I_{fw_{xx}} & 0 & 0 \\ 0 & I_{fw_{yy}} & 0 \\ 0 & 0 & J \end{bmatrix} \tag{2.75}$$

the one of the support frame is:

$$\mathbf{I}_s = \begin{bmatrix} I_{s_{xx}} & 0 & 0 \\ 0 & I_{s_{yy}} & 0 \\ 0 & 0 & I_{s_{zz}} \end{bmatrix} \tag{2.76}$$

and the one of the pendulum is:

$$\mathbf{I}_p = \begin{bmatrix} I_{p_{xx}} + m_p d_p^2 & 0 & 0 \\ 0 & I_{p_{yy}} + m_p d_p^2 & 0 \\ 0 & 0 & I_{p_{zz}} \end{bmatrix} \tag{2.77}$$

where m_p is the pendulum mass and d_p the distance between the centre of mass of the pendulum and the ε-axis. All the kinematic variable has to be referred with respect the floater reference frame. Appropriate transformation are required in order to transform the inertial frame variable to the floater reference frame. In particular, the derivatives of the states variables have to be transformed into the floater angular velocities with respect to its inertial axes:

$$\omega_x = \dot{\alpha} - \dot{\psi}\sin(\delta) \tag{2.78a}$$
$$\omega_y = \dot{\delta}\cos(\alpha) + \dot{\psi}\sin(\alpha)\cos(\delta) \tag{2.78b}$$
$$\omega_z = \dot{\psi}\cos(\delta)\cos(\alpha) + \dot{\delta}\sin(\alpha) \tag{2.78c}$$

where ω_x, ω_y and ω_z are the angular velocity of the floater in respect to its inertial axis. The transformations 2.78 implies that the time-derivative of the floater angles α, δ and ψ differ from the angular velocities of the floater with respect its inertial axes.

2.3.2 Lagrange approach

For a 6-DoF ISWEC the development of a set of equation based on quasi-coordinates may be more convenient then the representation of the system through the generalized coordinates. The *Lagrange Equation* of motion for generalized coordinates can be written in the matrix form as follows:

$$\frac{d}{dt}\left(\frac{\partial \mathcal{L}}{\partial \dot{q}_i}\right) - \frac{\partial \mathcal{L}}{\partial q_i} = Q_i \tag{2.79}$$

where $\mathcal{L}$ is the Lagrangian of the system equal to the difference between its kinetic $\mathcal{T}$ and potential $\mathcal{U}$ energy, Q_k coincides with the non-conservative forces associated to the $i-th$ generalized coordinate q_k. For our concrete system, the interest is to derive the equation of the gyro-pendulum dynamic when the floater

is exited along the whole DoFs. To obtain the equation of motion about three orthogonal axes, the Lagrange equation shall be used in terms of quasi-coordinates[2].

The moment equation of motion about about (x_1, y_1, z_1) in the general matrix form follows:

$$\frac{d}{dt}\left(\frac{\partial \mathcal{T}}{\partial \boldsymbol{\omega}}\right) + \boldsymbol{\omega}\frac{\partial \mathcal{T}}{\partial \boldsymbol{\omega}} - \mathbf{u}\frac{\partial \mathcal{T}}{\partial \mathbf{u}} = \mathbf{T} \tag{2.80}$$

where $\mathbf{T} \in \mathbb{R}^3$ is the column matrix of torque components about axes x_1, y_1 and z_1, $\boldsymbol{\omega} \in \mathbb{R}^{3\times3}$ and $\mathbf{u} \in \mathbb{R}^{3\times3}$ are the angular and linear velocities in the gimbal reference frame (x_1, y_1, z_1), respectively. In particular, the matrix $\boldsymbol{\omega}$ is the skew-symmetric matrix of the angular velocity components of the inner gimbal axes (x_1, y_1, z_1):

$$\boldsymbol{\omega} = \begin{bmatrix} 0 & -\omega_{z_1} & \omega_{y_1} \\ \omega_{y_1} & 0 & -\omega_{x_1} \\ -\omega_{y_1} & \omega_{x_1} & 0 \end{bmatrix} \tag{2.81}$$

and $\mathbf{u}$ is the analogous matrix corresponding to the linear velocities:

$$\mathbf{u} = \begin{bmatrix} 0 & -u_{z_1} & u_{y_1} \\ u_{y_1} & 0 & -u_{x_1} \\ -u_{y_1} & u_{x_1} & 0 \end{bmatrix} \tag{2.82}$$

The total angular velocities in the gimbal reference frame (x_1, y_1, z_1) are given by the floater velocities projection and by the precession angular velocity $\dot{\varepsilon}$, defined as follows:

$$\omega_{x_1} = \omega_x + \dot{\varepsilon} \tag{2.83a}$$
$$\omega_{y_1} = \omega_y \cos(\varepsilon) + \omega_z \sin(\varepsilon) \tag{2.83b}$$
$$\omega_{z_1} = -\omega_y \sin(\varepsilon) + \omega_z \cos(\varepsilon) \tag{2.83c}$$

Then, the angular velocities of the flywheel with respect to the (x_1, y_1, z_1) reference frame read:

$$\omega_{x_2} = \omega_x + \dot{\varepsilon} \tag{2.84a}$$
$$\omega_{y_2} = \omega_y \cos(\varepsilon) + \omega_z \sin(\varepsilon) \tag{2.84b}$$
$$\omega_{z_2} = -\omega_y \sin(\varepsilon) + \omega_z \cos(\varepsilon) + \dot{\varphi} \tag{2.84c}$$

[2]For the true coordinates, if the velocity $\dot{q}_i$ is a known function of time, an integration with respect to time yields the coordinate q_i; the quasi-coordinates are defined as a linear combination of true system coordinates [187].

The gyro-pendulum numerical model is reduced to a single differential equation that describes the dynamics of the precession axis of the gyroscope which coincides with the electrical PTO axis:

$$\begin{aligned} I_g(\ddot{\varepsilon} + \dot{\omega}_x) = &-m_p d_p(\ddot{y}\cos(\varepsilon) + \ddot{z}\sin(\varepsilon)) + \\ &+ I_{g\varepsilon}(\omega_y\cos(\varepsilon) + \omega_z\sin(\varepsilon))(-\omega_y\sin(\varepsilon) + \omega_z\cos(\varepsilon)) - \\ &+ m_p d_p(-\omega_y\sin(\varepsilon) + \omega_z\cos(\varepsilon))(\dot{x} - d_p(\omega_y\cos(\varepsilon) + \omega_z\sin(\varepsilon))) - \\ &+ J(\omega_y\cos(\varepsilon) + \omega_z\sin(\varepsilon))(\dot{\varphi} - \omega_y\sin(\varepsilon) + \omega_z\cos(\varepsilon)) + \\ &+ m_p d_p(\dot{y}\sin(\varepsilon) + \dot{z}\cos(\varepsilon))\omega_x - \\ &+ m_p d_p g(\cos(\varepsilon)\cos(\delta)\sin(\alpha) + \sin(\varepsilon)\cos(\delta)\cos(\alpha)) - \\ &+ T_{PTO} \end{aligned} \tag{2.85}$$

where T_{PTO} is the PTO reaction. I_g and $I_{g\varepsilon}$ are defined as follows:

$$I_g = I_{s_{xx}} + I_{fw_{xx}} + I_{p_{xx}} + m_p d_p^2 \tag{2.86a}$$

$$I_{g\varepsilon} = I_{s_{xx}} + I_{fw_{xx}} + I_{p_{xx}} - I_{s_{zz}} - I_{p_{zz}} \tag{2.86b}$$

A consistent treatment of analytical dynamics and mathematical theory behind the derivation of equation 2.85 can be found in the books of Meirovitch [187] and Zipfel [188].

2.3.3 Simplification of the gyro-pendulum equations

As demonstrated in [35, 131], the gyroscopic unit is excited, with a acceptable approximation, by the pitch motion of the hull only. Thus, the single DoF model is considered in this section. For a detailed derivation of the dynamic model equations for the complete system the reader is referred to the works of Vissio [35] and Raffero [131]. The assumption behind the following simplifications are:

- Unidirectional wave aligned with the x-axis of the floater (null roll and yaw angles (α and ψ), null y motion);
- Flywheel angular rate $\dot{\varphi}$ one order of magnitude higher than $\dot{\delta}$;
- Small linear velocities $\dot{x}$ and $\dot{z}$, and accelerations $\ddot{x}$ and $\dot{z}$;

Under these assumptions, the equation 2.85 reduces to the following simplified dynamical equation governing the precession angle ε:

$$I_g\ddot{\varepsilon} + m_p d_p g\sin(\varepsilon) = T_\varepsilon - T_{PTO} \tag{2.87}$$

Consistently, the forcing and the reaction torques acting on the gyroscope axis ε and discharged on the δ-axis and the λ-axis are:

$$T_\varepsilon = J\dot{\varphi}\dot{\delta}\cos(\varepsilon) \tag{2.88a}$$

$$T_\delta = -J\dot{\varphi}\dot{\varepsilon}\cos(\varepsilon) \tag{2.88b}$$

$$T_\lambda = -J\dot{\varphi}\dot{\varepsilon} \tag{2.88c}$$

The flywheel angular momentum $L = J\dot{\varphi}$ determines the entity of the coupling torques T_ε and T_δ between the floater and the gyroscope. Therefore, the parameter L is fundamental during the design of the system, and it can be regulated in operational condition varying the flywheel speed $\dot{\varphi}$ to be optimal for various sea-states. However, the gyroscope effect can induce the roll motion of the floater and degrade the performance of the device. To overcome this problem, the gyroscopic units may be suited in the floater in even numbers with opposite flywheel speed direction to cancel the roll gyroscopic torque.

The non-linear gyroscopic model has been experimentally validated during the ISWEC full-scale testing (see the work of Vissio [35]), and the coupled floater-gyroscope non-linear model was validated with model-scale experimental tests in regular wave conditions [135] with good matching.

2.4 Power Take-Off models of the ISWEC

Originally, the PTO of the ISWEC device consists of a Permanent Magnet Synchronous Generator (PMSG) connected to the gyroscope shaft by means a single-stage gearbox. This technological solution is well suited for low-medium energetic sea-states (e.g. the Mediterranean Sea) since the electric generator favours, generally, high angular rates and low torque densities. Since commercial PMSGs show limitation in terms of nominal torque and single-stage commercial gearboxes have a maximal gear ratio of 30 (see, for example, Desch gearbox catalogue [189]), the electro-mechanical solution may limit the power extraction for high energetic sea states. Another PTO technology for the ISWEC device may be the electro-hydraulic transmission. Hydraulic components offer high torque densities at the commercial stage that matches the requirement of the wave energy industry. As far as PTO modelling is concerned, both the electro-mechanical and electro-hydraulic PTO models are presented in this section.

2.4.1 Mechanical power take-off

The electro-mechanical PTO or, simply, Mechanical PTO (MPTO), is composed of a single-stage gearbox to link the gyroscope shaft to the generator one. The

generator is a PMSG connected to a inverter in order to continuously control the torque exerted by the generator. The ISWEC PTO control logic [35] was based on the concept of impedance matching for the maximization of the power absorption, frequently used in wave energy applications [101]. The concept is to control the generator torque to constitute a spring-damping system:

$$T_{MPTO} = \begin{cases} k_g\varepsilon + c_g\dot{\varepsilon} & \text{if } -T_{sat} \leq k_g\varepsilon + c_g\dot{\varepsilon} \leq T_{sat} \\ T_{sat} & \text{if } k_g\varepsilon + c\dot{\varepsilon} > T_{sat} \\ -T_{sat} & \text{if } k_g\varepsilon + c_g\dot{\varepsilon} < -T_{sat} \end{cases} \tag{2.89}$$

where k_g and c_g are the control parameters named stiffness and damping coefficients and T_{sat} is the saturation torque, limited by the driver in order to avoid the generator overcome its torque limits. The torque acting on the gyroscope is exerted by the electric generator and acts on the ε-axis through a single-stage gearbox with transmission ratio τ_{gb}. In this regards, the electric generator torque, angular speed and angular position read:

$$T_{gm} = \frac{T_{MPTO}}{\tau_{gb}}\eta_{gm} \tag{2.90a}$$

$$\dot{\alpha}_{gm} = \dot{\varepsilon}\tau_{gb} \tag{2.90b}$$

$$\alpha_{gm} = \varepsilon \tag{2.90c}$$

where η_{gm} stands for the mechanical efficiency including the gearbox efficiency collected from the supplier catalogue (Desch gearbox [189]), and the mechanical efficiency of the generator. Then, the instantaneous mechanical power extracted from the generator follows:

$$P_{gm} = T_{gm}\dot{\alpha}_{gm} \tag{2.91}$$

Actually, the ISWEC device is controlled with a "slow-tuning" philosophy: the control parameters, say $\dot{\varphi}$, c_g and k_g, are tuned in respect to the spectral properties of the incoming sea-state (e.g. energy period T_e, significant wave height H_s, etc.) with the incoming sea-state, avoiding the the complexity of a wave-by-wave control logic (e.g. Model Predictive Control [190]). The slow-tuning control logic is schematic in the block diagram of Figure 2.10. First, the system is numerically simulated and optimized for each sea-state of interest with regards to the sea-site occurrences. Once the optimal performances are derived for each wave, the related optimal parameters are collected in a table as a function of the energetic period and significant wave height. In operating conditions, the controller is able to deduce the spectral properties of the actual sea-state through estimation techniques described in the work of Sirigu [191] and then choose the optimal control parameters

to guarantee, at least theoretically, the optimal power production. The appellation "slow-tuning" refers to the fact that the control parameters are changed when the spectral properties of the actual sea-state evolve and no importance is attached to the instantaneous wave profile. Moreover, the MPTO implements some safety algorithms to avoid the system failures in heavy sea-states and storm conditions. In presence of extreme waves, the gyroscope is turned to a horizontal position along its precession axis ($\varepsilon = 90°$) in order to provide a null the gyroscopic effect ($T_\varepsilon = 0$); if the extreme sea remain the flywheel is turned off. For a detailed description of both control and safety algorithms tested on the ISWEC device, the interested reader should refer to the work of Vissio [35].

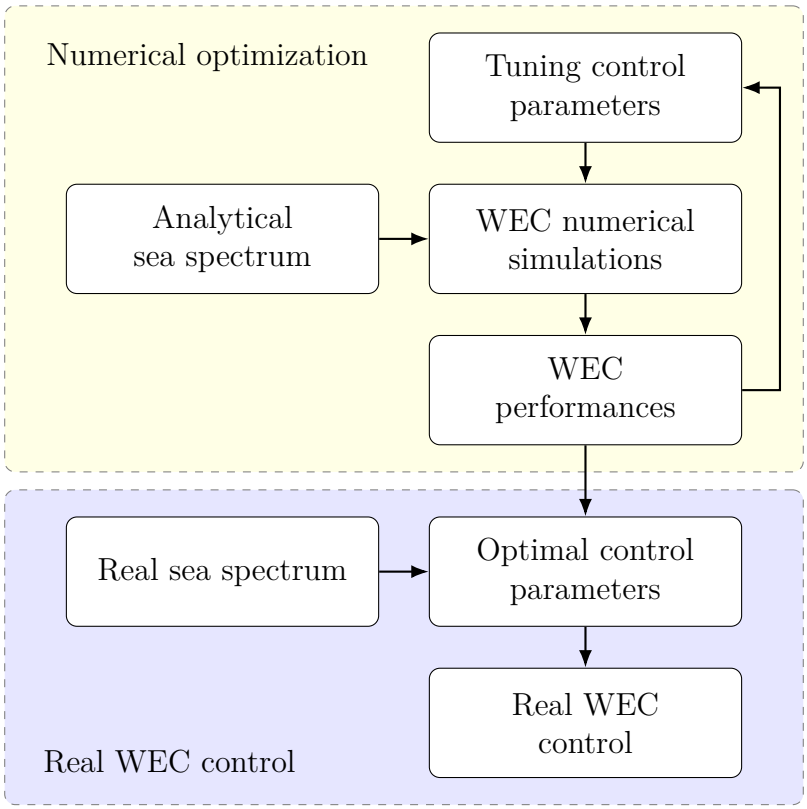

Figure 2.10: Optimal control parameters calculation procedure and application.

2.4.2 Hydraulic power take-off

The Hydraulic PTO (HPTO) includes all those components between the gyroscope shaft and the electrical generator that contribute to the energy conversion. Several solutions have been explored, coherently with the ones revised in Section 1.3. A balance must be found between designing a simple inefficient PTO that should

require minimal maintenance and a complex PTO but more efficient that could require more maintenance [192]. For our concrete system, the HPTO architecture is shown in Figure 2.11. The prime mover (the gyroscope) is coupled to a hydraulic a pump which is in closed-circuit connection with a hydraulic motor. The precession motion of the gyroscope drives the pump that pressurises a fluid inside a controlled manifold. At the other end of the transmission, the pressurised fluid is used to move a rotary hydraulic motor coupled with an electrical generator. Between the input and the output sources there are four different auxiliary components with different functions. First, a clutch-declutch valve is installed to perform the well-known declutch control [106], that is used to regulates in an on-off manner the pressure over the hydraulic pump. Downstream of the clutch-declutch valve a Graetz bridge composed of four check-valve is employed to rectify the bi-directional flow generated by the oscillating motion of the pump. In this regard, the flow directed toward the hydraulic motor forces it to spin always in the same direction. Two cylinder-type accumulators are used to smooth the flow fluctuations and provide a minimum charge pressure for the low pressure ram in order to avoid cavitation. Then, a relief valve is provided to avoid the pressure to overcome the peak pressure limit supported by the hydraulic components. A hydraulic transmission of this type works as a gearbox, reducing the output torque on the gyroscope, and at the same time allows rectifying the input motion and attenuating its fluctuations. The all-enclose architecture of the ISWEC represents a valid barrier against the oil leakage, a common problem of hydraulic systems. Mineral oil is used inside the closed circuit architecture. The closed-circuit avoids the overflow ram and, thus, overflow pumps and oil tanks, reducing the cost of the PTO. A drainage accumulator should be used to guarantee the minimum recommended charge pressure of both pumps and motors, reducing the risk of cavitation. In this way, the drained flow of pump and motor is collected in the drainage accumulator and re-inject in the circuit through the check valves. Moreover, this configuration is scalable to multi-gyroscope systems, where each gyroscope unit install a bi-directional hydraulic pump that drives the generated flow into a unique downstream generation stage.

Different modelling technique are proposed in literature with different level of accuracy. In [113] the Simcentre Amesim® software [193] is used to model a dual-stroke pendulum WEC integrating a water/oil transmission system. Amesim® offers a simple and intuitive modelling tool including different hydraulic components allowing a fast and detailed post processing of the simulation results. A modelling technique not too widespread in the wave energy field is the bond graph method. To the best of the author knowledge, the first appearance of the bond graph model for modelling WECs was in [194]. However, several works in literature that models the HPTO through the bond graph technique can be found, such [195, 196, 197, 198, 199]. In particular, Kurniawan [199] suggested to employ the bond graph method due to its multidisciplinary nature and the potential ability in assessing the system behaviour of various wave energy conversion concepts. For a general introduction

to bond graph, see [200]. In [116] and [124] the Simscape™ Fluids toolbox™ [201] implemented in Simulink® environment is used to model the hydraulic transmission. The Fluids toolbox™ allowing to model the compressibility of the fluid including the effect of its flow regime and its thermal properties combining mechanical, electrical, thermal, and other physical systems into the model.

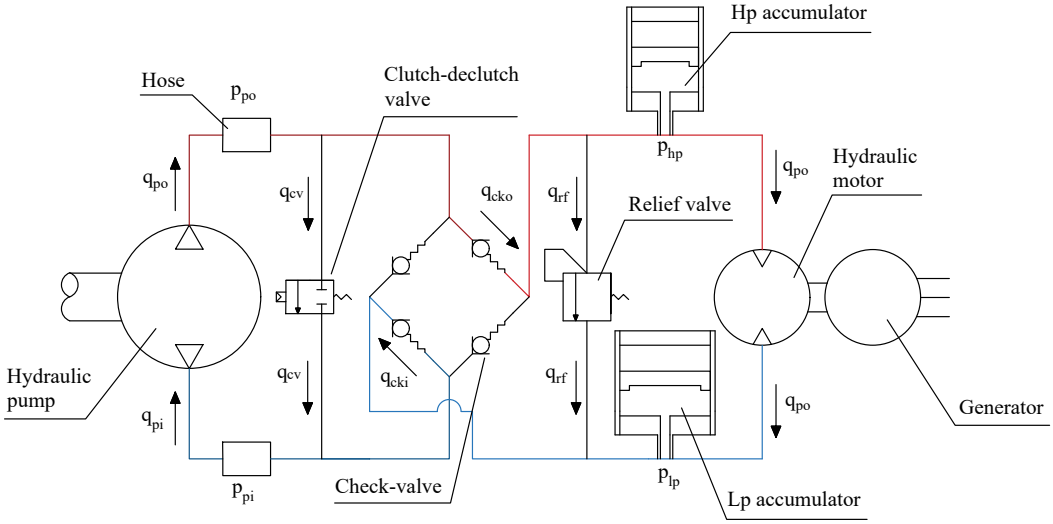

Figure 2.11: Hydraulic PTO components and variables. Letters q refer to the oil flow and letters p to the oil pressure.

In this work, a Simulink®-based model of the architecture depicted in Figure 2.11 is proposed. The model includes the pump efficiency maps, the clutch-declutch control logic, the effect of the oil compressibility, the valve pressure drops, the accumulator dynamics and both the motor and generator dynamics and efficiency.

Hydraulic pump model

First, the working principle of the ISWEC restricts the choice of the prime actuator to rotational hydraulic units (e.g. hydraulic pump) able to drive a bi-directional flow also for partial angular displacement of the gyroscope to avoid low efficiencies during low energetic seas. Moreover, in the ISWEC application the slow angular speed ($\dot{\varepsilon} \approx 20rpm$) in input of the HPTO requires a low-speed/high-torque pump type. A suitable option is the radial piston pump: this kind of hydraulic machines performs with high efficiency during low speed and low-pressure operations. The selected commercial component is the Hägglunds CB and CBp radial piston pump with constant displacement offered by Bosch Rexroth [202]. An illustrative example of the unit is reported in Figure 2.12. It has an even number of pistons that operate alternatively in a reciprocating motion. Its particular architecture

allows each piston to perform more than one pumping stroke for a single revolution permitting the machine to drive flow even with partial angular displacements, which suits perfectly with the irregular behaviour of the precession motion. The CBp series replicate the sizes of the CB ones in powerful torque and speed range. In particular, the CBp solution offers low weight and, according with the CBp data-sheet, the most powerful Hägglunds motor in term of power per weight unit.

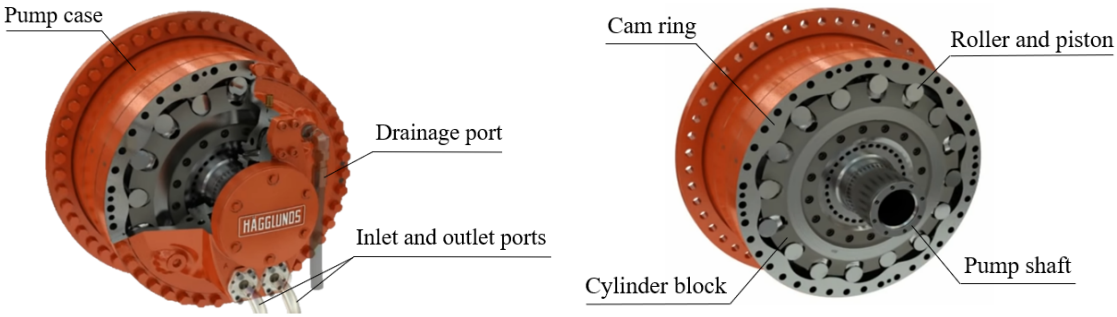

Figure 2.12: Rendering of the CB unit: (a) external and (b) internal architecture of the radial piston pump. Adapted from [202].

In addition, some tandem configurations are considered to widen the field of possible solutions [202]. A further degree of controllability is added to the system allowing to switch from one, two or three different displacements introducing a regulation in respect to the torque demanded by the system. An example of tandem configuration is reported in Figure 2.13.

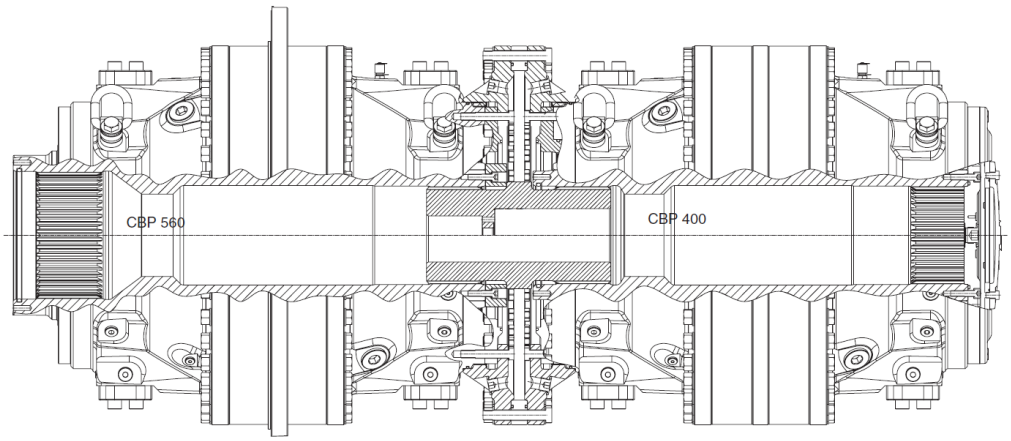

Figure 2.13: Technical design of the tandem CBp solution offered by Bosch Rexroth. A CBp-560 and a CBp-400 are connected with a Tandem kit TBP-40. Adapted from [202].

The hydraulic pump is rigidly connected to the gyroscope shaft and thus the inlet-outlet flow can be calculated proportional to its rotational speed and pump displacement as follows:

$$q_{pi} = D_p|\dot{\varepsilon}| \tag{2.92a}$$
$$q_{po} = D_p|\dot{\varepsilon}|\eta_{pv} \tag{2.92b}$$

where D_p is the pump displacement and η_{pv} the volumetric efficiency. The volumetric efficiency considers both the flow circulation inside the pump mechanical components, and thus not delivered outside, and the one drained out from the drainage port. Since the HPTO designed for the ISWEC is a closed-circuit, the drained flow is collected in a drainage accumulator with the purpose to maintain the low pressure ram over the recommended charge pressure required by the hydraulic pump (and motor). The pump reacts on the gyroscope shaft with a pure braking torque proportional to the pressure drop above its inlet and outlet ports. Then, the PTO torque T_{HPTO} reads:

$$T_{HPTO} = \text{sign}(\dot{\varepsilon})\frac{(p_{po} - p_{pi})D_p}{\eta_{pm}} \tag{2.93}$$

where p_{pi} and p_{po} are the pressures discharged on the pump inlet and outlet ports, and η_{pm} the mechanical efficiency of the pump. The mechanical power delivered by the gyroscope can be computed as follows:

$$P_{pm} = T_{HPTO}\dot{\varepsilon} \tag{2.94}$$

Then, the hydraulic power generated by the pump is defined as:

$$P_{ph} = (p_{po} - p_{pi})q_{po} \tag{2.95}$$

Combining equations 2.94 and 2.95 yields the pump overall efficiency:

$$\eta_p = \frac{P_{ph}}{P_{pm}} = \frac{(p_{po} - p_{pi})q_{po}}{T_{HPTO}\dot{\varepsilon}} = \frac{(p_{po} - p_{pi})D_p|\dot{\varepsilon}|\eta_{pv}\eta_{pm}}{\text{sign}(\varepsilon)(p_{po} - p_{pi})D_p\dot{\varepsilon}} = \\ = \eta_{pv}\eta_{pm} \tag{2.96}$$

Both the mechanical and volumetric efficiency are derived from the efficiency diagram indicated in the pump data-sheet. Gaspar, in [121, 203], proposed an Artificial Neural Network (ANN) in a feed-forward configuration to model the pump efficiency due to its capability of generalize non-linear relations among available data. The author argues that if the pump efficiency data is not indicated by the

manufacturer a ANN network with the available data might generalize pump efficiency to other pump displacements. The ANN input layer receives external information (e.g. pump torque, pressure and/or speed) while the output layer gives the efficiency estimation. The overall efficiency of the hydraulic pumps is modelled with data collected from two bent axis type pump efficiency plots. The comparison shows that modelling pump efficiency with an artificial neural network is more reliable than the approach presented in [87]. Another example of ANN application can be found in [80], where the hydraulic cylinder efficiency is carried out with the Adaptive Neuro Fuzzy Inference System (ANFIS). ANFIS techniques provide a method for the fuzzy modelling procedure to learn information about a data set implementing a hybrid learning algorithm to tune the parameters of a Sugeno-type Fuzzy Inference System (FIS) [204]. The algorithm applies a combination of the least-squares and back-propagation gradient descent methods to model an input/output map. However, as reported in Figure 2.14, both CB and CBp catalogues indicates the overall efficiency of the unit η_p and a simple look-up table is used in this work. It is noticeable that the pump performs with maximal efficiency ($\eta_p \approx 95\% \div 96\%$) around low rotational speed consonant with the ISWEC operating range. The numerical model computes the overall efficiency through a look-up table interpolating the diagram of Figure 2.14 in respect to the pump torque T_{HPTO} and speed $\dot{\varepsilon}$ magnitudes. Once η_p is obtained, it is equally split into η_{pv} and η_{pm}.

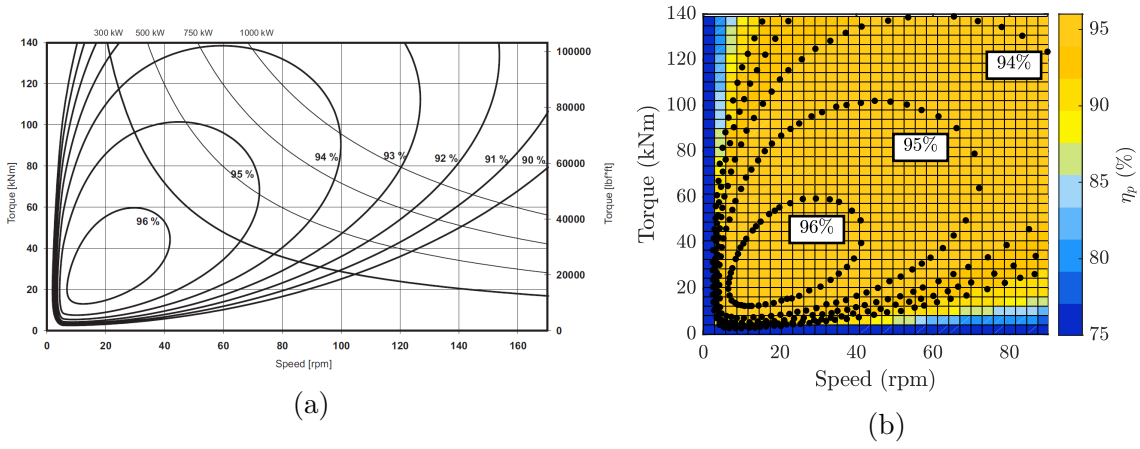

(a) (b)

Figure 2.14: Efficiency plots from data-sheet of a CBp unit, model CBp-400: (a) efficiency from CBp catalogue [202] and (b) efficiency diagram implemented in Simulink®.

Transmission line model

The flow absorbed/generated by the bi-directional motion of the pump is driven into the manifold exciting the transmission line dynamics. In other terms, the flow

within pipes/hoses and valves is compressed and faces friction resistance. Moreover, a transient time is needed to accelerate the mass of the fluid itself. In [123], the hoses friction is modelled through an empirical model based on the pipe dimensions, oil properties and Reynolds number. The model considers the transition between the laminar and turbulent regime with a hyperbolic tangent function for creating a continuous transition between linear and turbulent pressure drop with the aim to increase the robustness of the simulation. In another work of Hansen [87], the pipe-line model assumes the fluid within the line as a single mass column, which is accelerated by the pressure difference at the line inlet and outlet; then the dynamics of the line flow velocity is modelled using the momentum equation. However, since the fluid mass is limited and, as a first approximation, the pipes friction can be neglected, only the effect of the oil compressibility and valve resistances (induced by the check-valves) are considered. First, the compressibility of the oil is modelled with the flow continuity equation [205]. Hence, the pressure derivative is derived as (considering e.g. the volume of a hose constant and expressed by V_h):

$$\dot{p}_{pi} = \frac{\beta_{oil}}{V_h}(u_c q_{cki} - q_{pi} + (1-u_c)q_{cv}) \tag{2.97a}$$

$$\dot{p}_{po} = \frac{\beta_{oil}}{V_h}(q_{po} - u_c q_{cko} - (1-u_c)q_{cv}) \tag{2.97b}$$

where q_{cki} and q_{cko} are the flow passing through the check-valves, as defined later, q_{cv} the flow that passes through the clutch-declutch valve and β_{oil} the oil bulk modulus, considered constant and limited to 8000 *bar* [118]. u_c is the clutch-declutch control variable: if u_c is set equal to 1 the pump is fully operating, pumping oil into the high pressure accumulator; if u_c is equal to 0 the pump is by-passed, and no flow is delivered to the rectifier bridge. The pressures p_{pi} and p_{po} act on the inlet and outlet ports of the hydraulic pump. The reader may notice that, for the sake of simplicity, the inlet and outlet pressure port of the pump are considered always the same despite the bi-directional motion at which the pump operates. In fact, in equation 2.92 and 2.93 the pump generated and absorbed flows along with the HPTO torque contain the absolute value of $\dot{\varepsilon}$ and the sign(ε) function to "rectify" the kinematic and dynamic quantities of the pump, accounting for the, let say, "symmetry" induced by the rectifier bridge. Then, only two check-valves are modelled here. The flows q_{cki}, q_{cko} and q_{cv} are described by the orifice equation:

$$q_{cki} = C_{ck}A_{ck}\sqrt{\frac{2(p_{lp}-p_{pi})}{\rho_{oil}}} \tag{2.98a}$$

$$q_{cko} = C_{ck}A_{ck}\sqrt{\frac{2(p_{po}-p_{hp})}{\rho_{oil}}} \tag{2.98b}$$

$$q_{cv} = C_{cv}A_{cv}\sqrt{\frac{2(p_{po}-p_{pi})}{\rho_{oil}}} \tag{2.98c}$$

where C_{ck} and C_{cv} are the discharge coefficient, ρ_{oil} the fluid density, A_{ck} and A_{cv} the valve opening area, and p_{lp} and p_{hp} are the pressures on the low and high pressure accumulators. The values of C_{ck}, A_{ck}, C_{cv} and A_{cv} are collected from the data-sheet of the valve supplier. The Bosch Rexroth 2-way cartridge valves with directional function is considered as a valid solution for the ISWEC application. In particular, the cartridge element are able to discharge high flow rates (up to 25000 l/min according to the product data-sheet [206]) with limited pressure drop. Moreover, the cartridge element guarantees high Mean Time To Failure (MTTFd), equal to 150 years[3].

For what concern the declutching control, the clutch-declutch valve is used to digitally module the pressure drop across the hydraulic pump in order to regulate the T_{HPTO} torque. As described in [106, 208], the declutching control is essential to improve the HPTO performances and controllability. Contrary to the MPTO, the electrical generator is decoupled from the WEC prime mover due to the accumulators and no continuous torque control can be performed. In this regard, the by-pass valve (named clutch-declutch valve) is used to avoid the stall of the prime mover due to the pressure drop acting on it: as shown in Figure 2.15, the prime hydraulic unit (the hydraulic pump for our concrete system) is by-passed to cancel the pressure drop imposed by the accumulators for some part of the wave cycle. A sub-optimal declutching control is applied that consists in clutching the pump when its speed exceeds a "clutch" threshold value and declutching it when the pump speed diminishes under a "declutch" threshold. One can refer to Figure 2.15 to better understand the declutching control logic. This allows achieving more control over the torque delivered by the PTO on the gyroscope. For the parts of the cycle where the kinetic energy of the gyroscope is low, no torque is applied, excluding the pump from the hydraulic transmission. On the other hand, when the speed of the gyroscope exceeds the clutching speed value, the PTO acts on the gyroscope with a braking torque.

From here on, the HPTO considered in Chapters 3, 4 and 5 implements the declutching control following the logic shown in Figure 2.15. The optimal speed thresholds are chosen in respect to the current sea-state, according to the procedure outlined in Figure 2.10. Then, in Chapter 6 a Model Predictive Control is proposed following the optimal command theory to optimally switch the clutch-declutch valve in order to maximize the HPTO power production.

[3]For further details about the MTTFd see data sheet 08012 [207], concerning the reliability characteristics and functional safety according to EN ISO 13849.

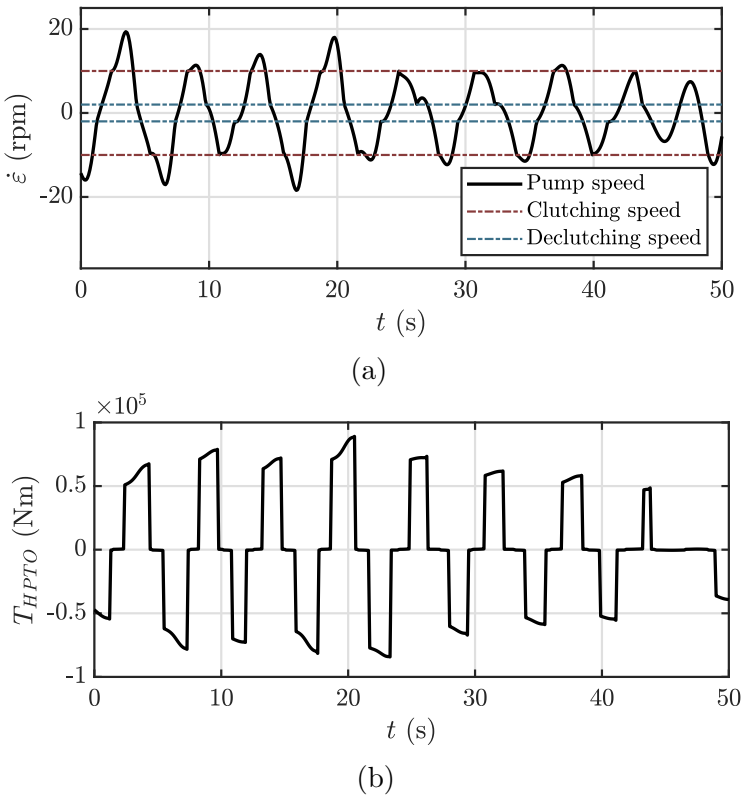

Figure 2.15: Example of angular velocity (a) and PTO torque (b) profiles of the HPTO system controlled with the clutch-declutch logic.

Gas accumulator model

The pump drives high pressure oil to a high pressure (hp) accumulator and get oil from a low pressure (lp) one, which are essential to prevent the large short term power peaks experienced in real seas and provide a minimum charge pressure to the lp ram in order to prevent cavitation. Several accumulator models are presented in literature with different physical phenomena involved. Hansen [87], along with other authors (e.g. Gaspar [209]), modelled the accumulator taking into account the temperature influence and the heat-exchange between the accumulator wall, the gas and the fluid inside it; in particular, the accumulator thermal time constant is determined with the equation presented by Pourmovahed [210]. In [211], a cylinder type accumulator has been modelled adding the effect of the pressure bounds in fully discharged mode, conditions in which the accumulator stops to work and the pressure is computed through the continuity equation applied to the hose below the accumulator, similar to equations 2.98. A bladder-type accumulator is considered by Do, where the gas pressure is expressed by the Beattie–Bridgman considering the nitrogen gas non-ideal and accounting for its thermal properties [212]. In this work, two cylinder-type gas accumulators are considered and described by means of a

simple adiabatic process [102] where volume of the gas contained in the accumulator changes in time as follows:

$$\dot{V}_{hp} = -u_c q_{cko} + q_{mi} + q_{rf} \tag{2.99a}$$

$$\dot{V}_{lp} = -q_{mo} + u_c q_{cki} - q_{rf} \tag{2.99b}$$

where q_{mi} and q_{mo} are the flow absorbed and drained by the hydraulic motor at the end of the transmission, respectively. The equations describing the pressure dynamic can be expressed as follows:

$$\dot{p}_{hp} = -\gamma_{gas} \frac{p_{hp}}{V_{hp}} \dot{V}_{hp} \tag{2.100a}$$

$$\dot{p}_{lp} = -\gamma_{gas} \frac{p_{lp}}{V_{lp}} \dot{V}_{lp} \tag{2.100b}$$

where γ_{gas} is the adiabatic coefficient associated to the nitrogen. A relief valve is included to limit the high pressure magnitude for safety purposes. In same way of the check-vales, the relief valve is modelled defining the discharged flow from the hp accumulator to the lp accumulator as follows:

$$q_{rf} = C_{rf} A_{rf} \sqrt{\frac{2(p_{hp} - p_{lp})}{\rho_{oil}}} \tag{2.101}$$

where C_{rf} is the discharge coefficient associated to the relief valve and A_{rf} is the relief valve opening area. The relief valve is supplied by Winner that offers a cheap and valid solution able to discharge high flow rates in case of emergency (up to 800 l/min according to the product data-sheet [213]). The opening and closing of the valve is described as a hyperbolic function, similar to the one proposed in [108]. The tanh function provides a smooth approximation to the step operation of the valve aiming to increase the simulation speed. The analytical function of A_{rf} reads:

$$A_{rf}(\Delta p_{rf}) = \frac{A_{rf,max}}{2} \left(1 + \tanh\left(\frac{k_{rf}}{p_{rf,max}} \left(\Delta p_{rf} - \frac{p_{rf,max} + p_{rf,c}}{2}\right)\right)\right) \tag{2.102}$$

where the pressure drop over the relief valve is the pressure difference imposed by the accumulators $\Delta p_{rf} = p_{hp} - p_{lp}$. Figure 2.16 illustrates the relief valve opening area.

The opening area depend on the valve cracking pressure $p_{rf,c}$, the max opening pressure $p_{rf,max}$ and the gain coefficient k_{rf} determining the steepness of the hyperbolic tangent function.

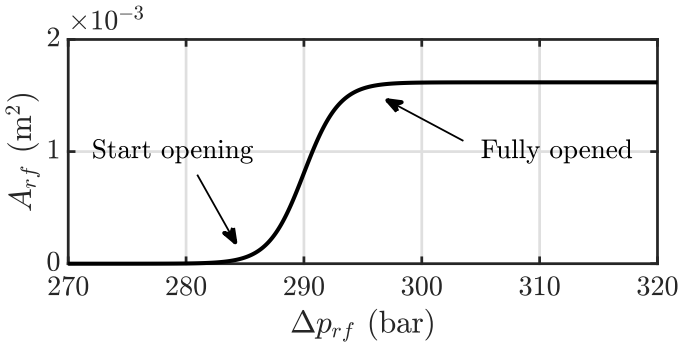

Figure 2.16: Relief valve opening area function.

Hydraulic motor and electrical generator model

Typical topology concerns the axial piston motors with fixed or adjustable displacement: as illustrated in Figure 2.17 the pistons (3) are located in a swash-plate (8) design, which is connected to the drive shaft (1); by applying pressure to the pistons on one side, the normal force acting on the pistons will generate a net torque on the swash-plate providing the piston rotation; as the pistons moves on the inclined plate, they make a reciprocating movement, thereby producing flow. By adjusting the angle of the swash-plate, torque and flow of the motor may be controlled.

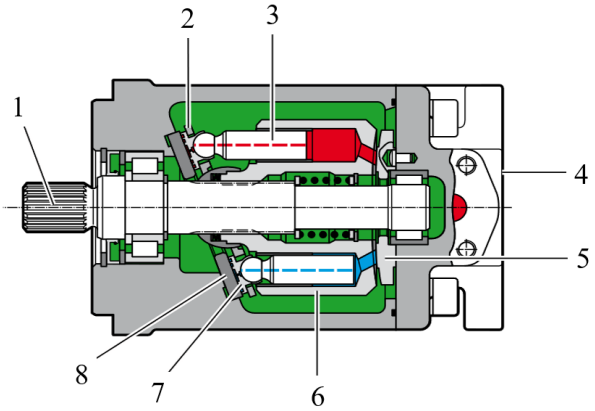

Figure 2.17: Axial piston motor scheme. (1) Drive shaft, (2) retaining plate, (3) piston, (4) port plate, (5), control plate, (6) cylinder, (7) slipper pad and (8) swash-plate. Adapted from [214].

In this work both axial and radial piston motor offered by Bosch Rexroth and Moog are considered and, for illustrative purpose, two examples are reported in Figure 2.18. The Bosch Rexroth units are A4FM Series 10 and 30 [215] and A10FM/A10FE models [215]. The Bosch Rexroth solution is coupled with PMSG

provided by SIEMENS, serie 1PH8, available at [216]. Moog supplies an interesting innovative Electro-hydrostatic Pump (EPU) unit [217] composed of a radial piston motor and an electric PMSG, rigidly connected to the motor shaft.

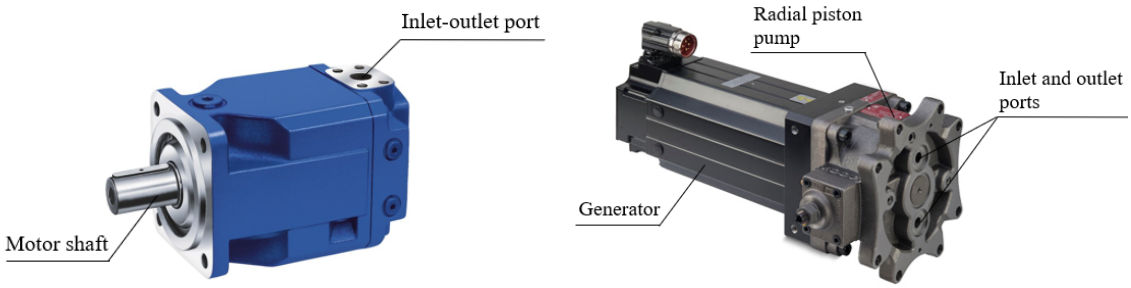

(a) (b)

Figure 2.18: Rendering of the hydraulic motor units: (a) axial piston motor, model A4FM [215] by Bosch Rexroth and (b) radial piston motor, model EPU [217] by Moog.

The axial piston motor efficiency can be modelled as proposed in [126], where the Wilson Model (WM) [218, 110], and Sholoesser formula (SF) [87, 219], have been improved as suggested by Hutala [220] considering an Improved Jeong Model (IJM) combining the Jeong's theory [221] and the starting torque model proposed in [222]. The experimental validation of the axial piston motor model is reported in [223]. Moreover, in [100] the HPTO numerical model includes the friction and leakage losses of the hydraulic motor and the generator-inverter efficiency models. However, for the purpose of this work, the hydraulic motor is modelled with a simple constant volumetric and mechanical efficiency and the electric generator as a simple linear damper with a fixed electric efficiency collected from the generator supplier. This assumption derives from the smoothing effect of the accumulator that allows the motor-generator to operate around their nominal conditions.

The pressure differential imposed by the hp and lp accumulators across the motor facilitates hydraulic fluid to flow through the inlet to outlet ports of the hydraulic unit. The dynamic equation of the motor-generator reads:

$$I_{mg}\ddot{\alpha}_{gh} = (p_{hp} - p_{lp})D_m\eta_{mm}\eta_{gh} - T_{gh} \tag{2.103}$$

where I_{mg} accounts for both motor and generator inertia, D_m is the hydraulic motor displacement, η_{mm} is the mechanical efficiency of the motor, η_{gh} is the mechanical efficiency of the generator and T_{gh} is the control torque of the electrical generator. In this work, the electrical generator is torque controlled as a linear damper in order to provide a breaking torque proportional to its angular velocity:

$$T_{gh} = \begin{cases} \beta_g \dot{\alpha}_{gh} & \text{if} \quad -T_{sat} \leq \beta_g \dot{\alpha}_{gh} \leq T_{sat} \\ T_{sat} & \text{if} \quad \beta_g \dot{\alpha}_{gh} > T_{sat} \\ -T_{sat} & \text{if} \quad \beta_g \dot{\alpha}_{gh} < -T_{sat} \end{cases} \tag{2.104}$$

where, similarly to the MPTO, β_g is the linear damping imposed by the control logic (chosen with the same scheme of Figure 2.10), $\dot{\alpha}_{gh}$ the angular velocity of the generator and T_{sat} the saturation torque. The inlet-outlet flow of the motor can be calculated proportional to the motor rotational speed and motor displacement as follows:

$$q_{mi} = \frac{D_m \dot{\alpha}_{gh}}{\eta_{mv}} \tag{2.105a}$$

$$q_{mo} = D_m \dot{\alpha}_{gh} \tag{2.105b}$$

where η_{mv} is the volumetric efficiency of the hydraulic motor. The hydraulic power discharged on the hydraulic motor is defined as:

$$P_{hm} = (p_{hp} - p_{lp}) q_{mi} \tag{2.106}$$

Likewise the MPTO, the instantaneous mechanical power extracted by the electric generator is:

$$P_{gh} = T_{gh} \dot{\alpha}_{gh} \tag{2.107}$$

Then, the motor-generator overall efficiency can be obtained combining the equations 2.103, 2.106 and 2.107 in stationary conditions ($\ddot{\alpha}_{gh} = 0$):

$$\begin{aligned} \eta_{mot,gen} &= \frac{P_{gh}}{P_{hm}} = \frac{T_{gh} \dot{\alpha}_{gh}}{(p_{hp} - p_{lp}) q_{mi}} = \frac{\beta_g \dot{\alpha}_{gh} \dot{\alpha}_{gh} \eta_{mv}}{(p_{hp} - p_{lp}) D_m \dot{\alpha}_{gh}} = \\ &= \frac{(p_{hp} - p_{lp}) D_m \dot{\alpha}_{gh} \eta_{mm} \eta_{gh} \eta_{mv}}{(p_{hp} - p_{lp}) D_m \dot{\alpha}_{gh}} = \\ &= \eta_{mv} \eta_{mm} \eta_{gh} \end{aligned} \tag{2.108}$$

2.5 Power loss models

For a reliable and accurate evaluation of the ISWEC performances, power losses play a crucial role. In fact, the settings of the control algorithm and, more in general, the choice of the WEC components, impact on the system efficiency. The mechanical power extracted from the electrical generator defined in equations 2.91

and 2.107 is used to compute the net power extracted from the WEC, regardless the PTO type:

$$P_n = P_g - P_l \tag{2.109}$$

where P_l are the power losses. From here on, the gross power will refer to the mechanical power extracted by the electricd generator. The computation of the ISWEC power losses is, in part, detailed in a previous work of the author in [224]. In [224] an exhaustive discussion about the principal power losses of the ISWEC system is presented and a method to up-scale the power losses is analytically derived. In order to describe such dissipations, it is necessary to consider a reference geometry. Figure 2.19 shows the architecture of the gyroscope unit.

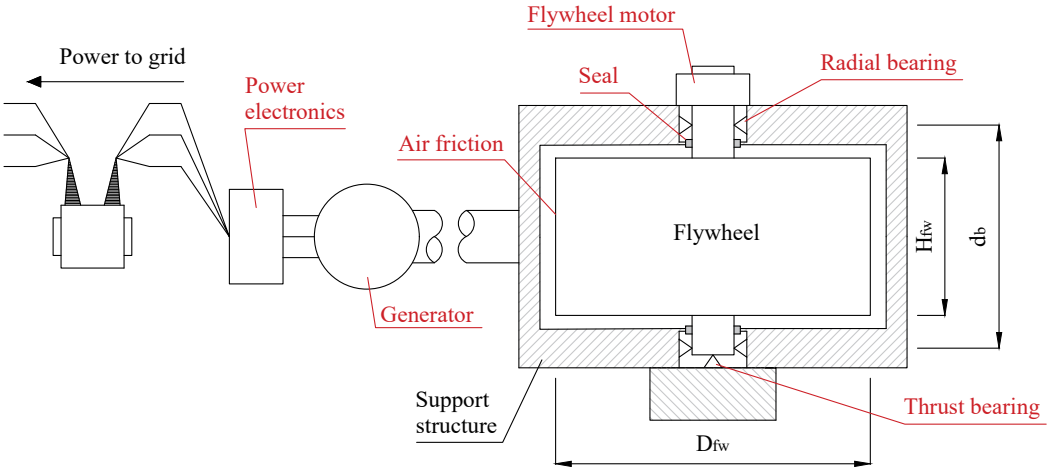

Figure 2.19: ISWEC gyroscope scheme, supports and main dimensions: D_{fw} is the flywheel diameter, H_{fw} the height of the flywheel and d_b the bearing distance. In red colour the source of losses considered in this section.

The flywheel is supported by two radial bearings and one thurst braring in order to sustain the flywheel mass allowing its rotation around the φ-axis. Bearings are cooled and lubricated by means of oil, which is properly recirculated and filtered in order to maintain the system at the optimal temperature. A couple of seals insulate the bearings housing avoiding the oil leakage. The insulation is guaranteed thanks to the contact between the seals and the flywheel shaft. Intuitively, bearings and seals provides power losses due to the friction. Moreover, the ISWEC system suffers from other three power losses: aerodynamic losses, electric losses and base load losses. The formulation of the total power losses follows:

$$P_l = P_{l,bearings} + P_{l,seals} + P_{l,aero} + P_{l,electric} + P_{l,base} \tag{2.110}$$

The discussion proposed is based on the architecture of the gyroscope represented in Figure 2.19. The different dissipations are identified and described, focusing on the contribution of each physical variable involved in the calculation. The reader has to consider the following power losses derived for a single gyroscopic unit.

2.5.1 Bearing losses

The gyroscope flywheel is supported by three spherical roller bearings that allow its rotation around the φ-axis. The two radial bearings support only the radial loads while the thrust bearing constraints the axial ones. In a first instance it is assumed that the loads due to the floater accelerations are negligible compared with gyroscopic loads and weight. Considering the gyroscopic torques given by equations 2.88a and 2.88a and the flywheel mass, it is possible to obtain the mathematical equations of the radial and axial loads:

$$F_{rad} = \sqrt{\left(\frac{J\dot{\varphi}\dot{\delta}\cos(\varepsilon)}{d_b}\right)^2 + \left(\frac{J\dot{\varphi}\dot{\varepsilon}}{d_b}\right)^2 + \left(\frac{1}{2}m_{fw}g\sin(\varepsilon)\right)^2} \tag{2.111a}$$

$$F_{ax} = |m_{fw}g\cos(\varepsilon)| \tag{2.111b}$$

where m_{fw} is the flywheel mass and d_b the bearing distance. Once the forces acting on bearings are calculated, the mathematical expressions of the power losses for both axial and radial loads can be determined according to the SKF friction formulation that consists in non-analytical functions of a set of bearing properties [225]:

$$P_{l,rad} = f_{rad}(F_{rad}, \{bp\}_{rad}) \tag{2.112a}$$

$$P_{l,ax} = f_{ax}(F_{rad}, \{bp\}_{ax}) \tag{2.112b}$$

$$P_{l,bearings} = P_{l,rad} + P_{l,ax} \tag{2.112c}$$

where f_{rad} and f_{ax} are non-analytical functions explained in detain in the manufacturer data-sheet and depending on the bearing typology (radial ball bearing, radial roller bearing, axial roller bearing, etc.) [225]. Both radial and axial loads and, thus, the bearing power losses, depends directly on $\dot{\varphi}$, and indirectly on the PTO torque, which acts on the precession angle ε. Therefore, the control strategy must not only maximize the net productivity, but also respect structural constraints and limit the bearing losses.

2.5.2 Seal losses

In order to prevent oil leakages from the bearings housing, a couple of seals are installed near the bearings. Moreover, the seals are in contact, with a certain force, with the flywheel shaft surfaces. According to the indications provided by the manufacturer, the seal dissipated power can be written as follows:

$$P_{l,seal} = F_{seal}\pi\frac{d_{seal}^2}{2}\dot{\varphi}n_{seal} \tag{2.113}$$

where F_{seal} is the friction force per unit of length acting on the contact area between the seal, d_{seal} the seal internal diameter and n_{seal} the number of seal mounted on the flywheel. The friction force F_{seal} depends on the pressure difference between the air inside and outside the chamber and on the seal material. However, contrary to the gyroscope architecture presented in [224], the vacuum chamber is not considered and the flywheel is directly in contact with the atmospheric pressure. In this regards, Pantecnica, the manufacturer of the bearing seals, gives the value of F_{seal} equal to 67 N [226].

2.5.3 Aerodynamic losses

The ventilation losses arise from the interaction between the flywheel surfaces and the surrounding air. These losses depend on both the fluid speed regime (laminar or turbulent) and the geometric features of the flywheel. A detailed analysis of the aerodynamic losses on the ISWEC can be found in [227], where two mathematical models of increasing complexity are considered and successfully validated against experimental data.

As depicted in Figure 2.19, the interaction between the air and the flywheel surfaces leads to two different dissipation components: the first is due to the flywheel crown, while the second is related to the horizontal surfaces:

$$P_{l,aero} = P_{l,disk} + P_{l,cylinder} \tag{2.114}$$

First, the Reynolds (Re) number can be computed and, according to Childs [228] (see p.84), it is equal for both disk and radial surface:

$$Re_{fw} = \frac{\dot{\varphi}R_{fw}^2}{\nu_{air}} \tag{2.115}$$

where R_{fw} is the flywheel radius and ν_{air} the dynamics viscosity of the air. Depending on Re number, the flow regime can be laminar or turbulent. According to Schlichting [229], the resulting power loss contribution for the disk surface reads:

$$P_{l,disk} = 2\left(\frac{1}{2}C_{m_{disk}}\rho_{air}\dot{\varphi}^3R_{fw}^5\right) \tag{2.116}$$

where $C_{m_{disk}}$ is the dimensionless torque coefficient for the disk contribution. The disk contribution is multiplied by two accounting for both top and bottom surfaces of the flywheel. Two flow regimes need to be distinguished to calculate $C_{m_{disk}}$ [229]:

$$C_{m_{disk}} = \begin{cases} \dfrac{1.935}{\sqrt{Re_{fw}}} & \text{if } Re_{fw} < 3 \cdot 10^5 \\ \dfrac{0.073}{Re_{fw}^{0.2}} & \text{if } Re_{fw} \geq 3 \cdot 10^5 \end{cases} \tag{2.117}$$

For what concern the radial contribution, the flywheel can be studied as a simple cylinder rotating around its axis and immersed in a fluid (air). The flow regime is influenced by both friction drag and centrifugal forces. Following the assumption of turbulent flow (see p. 102 of [228]), the friction torque coefficient can be calculated using the empirical correlation found by Theodorsen and Regier [230]:

$$\frac{1}{\sqrt{C_{m_{cylinder}}}} = \left(-0.8572 + 1.25 \ln\left(Re_{fw}\sqrt{C_{m_{cylinder}}}\right)\right)^2 \tag{2.118}$$

Equation 2.118 is solved iteratively, and convergence is found in five iterations [228]. Then, the resulting power loss contribution for the lateral surface can be derived [228]:

$$P_{l,cylinder} = \frac{1}{2} C_{m_{cylinder}} \rho_{air} \dot{\varphi}^3 R_{fw}^4 H_{fw} \tag{2.119}$$

where H_{fw} is the flywheel height.

2.5.4 Electric losses

As described in Section 1.4 of Chapter 1, in the ISWEC system both electrical generator and motor are used to extract the energy captured from the PTO and to drive the flywheel at the desired speed $\dot{\varphi}$. All the electric units installed on the system are PMSG equipped with a converter for the grid connection to enable variable speed control. The torque of the generator is controlled by an inverter. Both the generator and inverter losses can be modelled as an efficiency map in respect to the generator/motor angular speed and torque. However, as a first approximation, synthetic values of electric efficiency are used in this work. In particular, for the flywheel motor the electric efficiency η_{efw} is fixed to 0.97, and two different values of the generator efficiency η_{eg} are considered depending on the PTO type:

- η_{eg}=0.82 for the MPTO generator;
- η_{eg}=0.95 for the HPTO generator.

This choice is driven by the fact that in the MPTO the speed/torque regimes are strongly irregular, as shown in Figure 1.9. The conversion efficiency is not constant for different load regimes (e.g. see [40]) and this leads to consider a mean overall efficiency lower than the nominal one, generally near to 0.95 (e.g. according to the Siemens catalogue of PMSG [231]). The value of 0.82 is derived from the practical experience gained with the real full-scale ISWEC prototypes deployed in Pantelleria and Adriatic sea, from 2015 to 2020. On the other hand, the effect of the hydraulic accumulator allows to smooth the variability of the load exerted by the electric generator and the PMSG unit should work around its nominal efficiency, fixed to 0.95.

For the flywheel motor, the electric power dissipated accounts for the contributions of bearing frictions 2.112, seal frictions 2.113, and aero losses 2.116 and 2.119:

$$P_{l,fw} = \frac{1-\eta_{efw}}{\eta_{efw}} \left(P_{l,rad} + P_{l,ax} + P_{l,seal} + P_{l,disk} + P_{l,cylinder}\right) \tag{2.120}$$

For the generator stage, the electric losses reads:

$$P_{l,g} = (1-\eta_g)\, P_g \tag{2.121}$$

Then, the total electric losses are:

$$P_{l,electric} = P_{l,fw} + P_{l,g} \tag{2.122}$$

2.5.5 Base load losses

The ISWEC WEC is equipped with various auxiliary components to manage, for example, the cooling of both electrical and mechanical components (e.g. flywheel and gyroscope bearings), to control the electric units (e.g. motors and generators) and supply the power electronics and the data acquisition system [35]. The power loss due to the base loads are computed as the sum of all the auxiliary contributions:

$$P_{l,base} = \sum P_{l,aux} = \frac{5000 + 2500\left(\frac{n_{gyros}}{2} - 1\right)}{n_{gyros}} \tag{2.123}$$

where n_{gyros} is the number of gyroscopic units. The base loads accounts for 2000 W of the cooling system (including both water and oil circuits), 2500 W of the DC/DC and DC/AC converters to manage super-capacitors, batteries and Active Front End (AFE) units, and 500 W of the power electronics (nominal voltage 24 V). For more than one couple of gyroscopic units, part of the auxiliary components can be shared between different gyroscopes and, for instance, passing from 2 to 4 gyroscopes does not imply doubling the base losses. Similarly to the generator and flywheel motor losses, the base loads are based on previous experience on the

ISWEC full-scale prototypes deployed in real sea and on the state-of-the-art of their commercial components.

The control algorithm supervises the consumptions of the ISWEC system including the base loads and, when the net extracted power is negative, the system is shut down to avoid unnecessary losses. Contrary to the base loads, the other losses depends only on the system kinematics and dynamics and they can be reduced acting on the control parameters of the WEC. In first approximation, the base consumptions are constant and they determine the down-time of the ISWEC in low-energetic sea states, when the magnitude of the incoming energy becomes similar to the base losses.

Chapter 3

Numerical Experiments and Models Comparison

Designing a WEC device demands several numerical experiments in order to evaluate its performances related to the sea-site of interest. Both frequency- and time-domain simulations are usually considered in order to optimize the parameters of the converter, aiming to find the best compromise between cost, productivity and reliability of the WEC. Behind this multi-objective optimization, as will be presented in Chapter 4, millions of numerical simulations have to be performed to statistically predict the WEC performances. In particular, time-domain simulations are employed to solve non-linear state space equations, involving complex non-linearities to accurate predict WEC behaviours, requiring a considerable computational effort compared with frequency- or spectral-domain models [232]. On the other hand, for the initial draft of a WEC device, frequency- and spectral-domain models are suggested being able to provide a simple and fast simulation tool to compare various system architectures and solutions.

In this chapter a first draft of the ISWEC device designed for the Mediterranean sea, precisely for the Pantelleria island sea-climate (Italy), is presented and its numerical models defined and compared. The frequency- and time-domain model equations presented in Chapter **??** are combined to define three different ISWEC models:

- **Time-domain models**;
- **Frequency-domain models**;
- **Spectral-domain models**.

In this chapter, the ISWEC models are compared in term of performance accuracy and computational time required to reproduce the statistical sense of the ensemble averages between simulations (consistently with the considerations outlined in Section 2.2). The reader should note that there will be a little abuse of

notation in order to distinguish between the numerous model presented. Unless otherwise specified, the capital F in the subscripts stands for "Frequency domain", capital S for "Spectral domain", capital T for "Time domain", capital M for "Mechanical PTO" and capital H for "Hydraulic PTO".

3.1 Time-domain models

Despite the computational efficiency of frequency-domain models, usually employed for the first stages of WEC design [233], to prove the validity of a WEC architecture and design a control strategy a more realistic approach is often needed. In such cases, a Time-Domain Model (TDM) is generally advisable to provide the final steps toward cost and performance estimates [234]. Moreover, in time-domain, it is possible to test complex control algorithms such MPC and MPC-like techniques [190], not simulable in frequency-domain, along with moorings or structural components, that are generally highly non-linear. For a general overview about TDMs, the Chapter 3 [232] of the Folley book [134] offers a simple and straightforward description of the main time-domain modelling technique for WECs.

With the general notation of equation 2.1 and Figure 2.1, the time-domain system can be formulated combining the floater equation 2.42 with the radiation forces approximation 2.44 and the gyro-pendulum model 2.87 along with the gyroscopic effects 2.88a and 2.88b. The non-linear state-space equation reads:

$$\mathbf{M}_T\ddot{\mathbf{X}}_T + \mathbf{B}_T\dot{\mathbf{X}}_T + \mathbf{K}_T\mathbf{X}_T + \boldsymbol{\Theta}_T(\mathbf{X}_T, \dot{\mathbf{X}}_T, \ddot{\mathbf{X}}_T) = \mathbf{f}_T(t) \tag{3.1}$$

The system 3.1 includes the kinematic variable of interest $\mathbf{X}_T \in \mathbb{R}^{n_T}$, the mass matrix $\mathbf{M}_T \in \mathbb{R}^{n_T \times n_T}$, the damping matrix $\mathbf{B}_T \in \mathbb{R}^{n_T \times n_T}$, the stiffness matrix $\mathbf{K}_F \in \mathbb{R}^{n_F \times n_T}$, the non-linear function $\boldsymbol{\Theta}_T : \mathbb{R}^{n_T} \to \mathbb{R}^{n_T}$ and the external forces $\mathbf{f}_T(t) \in \mathbb{R}^{n_T}$. The non-linear term $\boldsymbol{\Theta}_T$ includes several non linearities, involving both the floater, the gyroscope and, depending on the ISWEC architecture, the PTO. n_T is the system dimension and it depends on the PTO considered.

3.1.1 Non-linear mechanical PTO model

Considering the MPTO, the following notation is used to re-write the system 3.1:

$$\mathbf{M}_{TM}\ddot{\mathbf{X}}_{TM} + \mathbf{B}_{TM}\dot{\mathbf{X}}_{TM} + \mathbf{K}_{TM}\mathbf{X}_{TM} + \boldsymbol{\Theta}_{TM}(\mathbf{X}_{TM}, \dot{\mathbf{X}}_{TM}, \ddot{\mathbf{X}}_{TM}) = \mathbf{f}_{TM}(t) \tag{3.2}$$

Here, the state vector $\mathbf{X}_{TM} \in \mathbb{R}^{n_{TM}}$ contains the floater DoFs $\mathbf{X}_f$, the radiation states $\boldsymbol{\zeta}$ and the gyroscope precession angle ε:

$$\mathbf{X}_{TM} = \begin{bmatrix} \mathbf{X}_f & \boldsymbol{\zeta} & \varepsilon \end{bmatrix}^T \tag{3.3}$$

The non-linear term $\boldsymbol{\Theta}_{TM} : \mathbb{R}^{n_{TM}} \rightarrow \mathbb{R}^{n_{TM}}$ includes the MPTO reaction along with the gyroscopic effects and the pendulum contribution:

$$\boldsymbol{\Theta}_{TM} = \begin{bmatrix} 0 \\ 0 \\ 0 \\ 0 \\ -J\dot{\varphi}\dot{\varepsilon}\cos(\varepsilon) \\ 0 \\ \mathbf{0} \\ J\dot{\varphi}\dot{\delta}\cos(\varepsilon) + m_g d_p g \sin(\varepsilon) + T_{MPTO} \end{bmatrix} \tag{3.4}$$

Concerning the PTO torque, the equation 2.89 holds. The linear terms, concerning the matrices $\mathbf{M}_{TM} \in \mathbb{R}^{n_{TM} \times n_{TM}}$, $\mathbf{B}_{TM} \in \mathbb{R}^{n_{TM} \times n_{TM}}$ and $\mathbf{K}_{TM} \in \mathbb{R}^{n_{TM} \times n_{TM}}$, are defined as follows:

- The mass matrix:

$$\mathbf{M}_{TM} = \begin{bmatrix} \mathbf{M}_f & \mathbf{0} & \mathbf{0} \\ \mathbf{0} & \mathbf{0} & \mathbf{0} \\ \mathbf{0} & \mathbf{0} & I_g \end{bmatrix} \tag{3.5}$$

- The damping matrix:

$$\mathbf{B}_{TM} = \begin{bmatrix} -\mathbf{D}_r & \mathbf{0} & \mathbf{0} \\ -\mathbf{B}_r & \mathbf{I} & \mathbf{0} \\ \mathbf{0} & \mathbf{0} & 0 \end{bmatrix} \tag{3.6}$$

- The stiffness matrix:

$$\mathbf{K}_{TM} = \begin{bmatrix} \mathbf{K}_f & -\mathbf{C}_r & \mathbf{0} \\ \mathbf{0} & -\mathbf{A}_r & \mathbf{0} \\ \mathbf{0} & \mathbf{0} & 0 \end{bmatrix} \tag{3.7}$$

For what regards the external force, $\mathbf{f}_{TM}(t) \in \mathbb{R}^{n_{TM}}$ reads:

$$\mathbf{f}_{TM}(t) = \begin{bmatrix} \mathbf{f}_E(t) & \mathbf{0} & 0 \end{bmatrix}^T \tag{3.8}$$

The terms $\mathbf{0}$ and $\mathbf{I}$ are zeros and identity matrices of appropriate dimensions. Relations from 3.3 to 3.8 have to be plugged into 3.1 to obtain the non-linear ISWEC model based on the MPTO.

3.1.2 Non-linear hydraulic PTO models

Considering the HPTO, the following equation holds:

$$\mathbf{M}_{TH}\ddot{\mathbf{X}}_{TH} + \mathbf{B}_{TH}\dot{\mathbf{X}}_{TH} + \mathbf{K}_{TH}\mathbf{X}_{TH} + \mathbf{\Theta}_{TH}(\mathbf{X}_{TH}, \dot{\mathbf{X}}_{TH}, \ddot{\mathbf{X}}_{TH}) = \mathbf{f}_{TH}(t) \tag{3.9}$$

Here, the state vector $\mathbf{X}_{TH} \in \mathbb{R}^{n_{TH}}$ contains the floater DoFs $\mathbf{X}_f$, the radiation states $\boldsymbol{\zeta}$, the gyroscope precession angle ε, the pipe pressures p_{pi} and p_{po}, the hp and lp accumulator gas volumes V_{hp} and V_{lp}, and pressures p_{hp} and p_{lp}, and the generator angular position α_{gh}:

$$\mathbf{X}_{TH} = \begin{bmatrix} \mathbf{X}_f & \boldsymbol{\zeta} & \varepsilon & p_{pi} & p_{po} & V_{hp} & p_{hp} & V_{lp} & p_{lp} & \alpha_{gh} \end{bmatrix}^T \tag{3.10}$$

The non-linear term $\mathbf{\Theta}_{TH} : \mathbb{R}^{n_{TH}} \to \mathbb{R}^{n_{TH}}$ includes the HPTO reaction on the gyroscope axis ε, the gyroscopic effects, the pendulum contribution, the hoses equations, the accumulators equations and the motor-generator controlled torque:

$$\mathbf{\Theta}_{TH} = \begin{bmatrix} 0 \\ 0 \\ 0 \\ 0 \\ -J\dot{\varphi}\dot{\varepsilon}\cos(\varepsilon) \\ 0 \\ \mathbf{0} \\ J\dot{\varphi}\dot{\delta}\cos(\varepsilon) + m_g d_p g \sin(\varepsilon) + \text{sign}(\dot{\varepsilon})\frac{(p_{po}-p_{pi})D_p}{\eta_{pm}} \\ -\frac{\beta_{oil}}{V_h}\left(u_c C_{ck} A_{ck}\sqrt{\frac{2(p_{lp}-p_{pi})}{\rho_{oil}}} - D_p|\dot{\varepsilon}| + (1-u_c)C_{cv}A_{cv}\sqrt{\frac{2(p_{po}-p_{pi})}{\rho_{oil}}}\right) \\ -\frac{\beta_{oil}}{V_h}\left(D_p|\dot{\varepsilon}|\eta_{pv} - u_c C_{ck} A_{ck}\sqrt{\frac{2(p_{po}-p_{hp})}{\rho_{oil}}} - (1-u_c)C_{cv}A_{cv}\sqrt{\frac{2(p_{po}-p_{pi})}{\rho_{oil}}}\right) \\ -u_c C_{ck} A_{ck}\sqrt{\frac{2(p_{po}-p_{hp})}{\rho_{oil}}} + \frac{D_m\dot{\alpha}_{gh}}{\eta_{mv}} + C_{rf}A_{rf}\sqrt{\frac{2(p_{hp}-p_{lp})}{\rho_{oil}}} \\ \gamma_{gas}\frac{p_{hp}}{V_{hp}}\left(-u_c C_{ck} A_{ck}\sqrt{\frac{2(p_{po}-p_{hp})}{\rho_{oil}}} + \frac{D_m\dot{\alpha}_{gh}}{\eta_{mv}} + C_{rf}A_{rf}\sqrt{\frac{2(p_{hp}-p_{lp})}{\rho_{oil}}}\right) \\ -D_m\dot{\alpha}_{gh} + u_c C_{ck} A_{ck}\sqrt{\frac{2(p_{lp}-p_{pi})}{\rho_{oil}}} - C_{rf}A_{rf}\sqrt{\frac{2(p_{hp}-p_{lp})}{\rho_{oil}}} \\ \gamma_{gas}\frac{p_{lp}}{V_{lp}}\left(-D_m\dot{\alpha}_{gh} + u_c C_{ck} A_{ck}\sqrt{\frac{2(p_{lp}-p_{pi})}{\rho_{oil}}} - C_{rf}A_{rf}\sqrt{\frac{2(p_{hp}-p_{lp})}{\rho_{oil}}}\right) \\ T_{gh} \end{bmatrix} \tag{3.11}$$

The analytical function of A_{rf} is defined in equation 2.102 and the generator torque T_{gh} in 2.104. The linear terms, concerning the matrices $\mathbf{M}_{TH} \in \mathbb{R}^{n_{TH}\times n_{TH}}$, $\mathbf{B}_{TH} \in \mathbb{R}^{n_{TH}\times n_{TH}}$ and $\mathbf{K}_{TH} \in \mathbb{R}^{n_{TH}\times n_{TH}}$, are defined as follows:

- The mass matrix:

$$\mathbf{M}_{TH} = \begin{bmatrix} \mathbf{M}_f & \mathbf{0} & \mathbf{0} & \mathbf{0} & \mathbf{0} & \mathbf{0} & \mathbf{0} & \mathbf{0} & \mathbf{0} & \mathbf{0} \\ \mathbf{0} & \mathbf{0} & \mathbf{0} & \mathbf{0} & \mathbf{0} & \mathbf{0} & \mathbf{0} & \mathbf{0} & \mathbf{0} & \mathbf{0} \\ \mathbf{0} & \mathbf{0} & I_g & 0 & 0 & 0 & 0 & 0 & 0 & 0 \\ \mathbf{0} & \mathbf{0} & 0 & 0 & 0 & 0 & 0 & 0 & 0 & 0 \\ \mathbf{0} & \mathbf{0} & 0 & 0 & 0 & 0 & 0 & 0 & 0 & 0 \\ \mathbf{0} & \mathbf{0} & 0 & 0 & 0 & 0 & 0 & 0 & 0 & 0 \\ \mathbf{0} & \mathbf{0} & 0 & 0 & 0 & 0 & 0 & 0 & 0 & 0 \\ \mathbf{0} & \mathbf{0} & 0 & 0 & 0 & 0 & 0 & 0 & 0 & 0 \\ \mathbf{0} & \mathbf{0} & 0 & 0 & 0 & 0 & 0 & 0 & 0 & 0 \\ \mathbf{0} & \mathbf{0} & 0 & 0 & 0 & 0 & 0 & 0 & 0 & I_{mg} \end{bmatrix} \tag{3.12}$$

- The damping matrix:

$$\mathbf{B}_{TH} = \begin{bmatrix} -\mathbf{D}_r & \mathbf{0} & \mathbf{0} & \mathbf{0} & \mathbf{0} & \mathbf{0} & \mathbf{0} & \mathbf{0} & \mathbf{0} & \mathbf{0} \\ -\mathbf{B}_r & \mathbf{I} & \mathbf{0} & \mathbf{0} & \mathbf{0} & \mathbf{0} & \mathbf{0} & \mathbf{0} & \mathbf{0} & \mathbf{0} \\ \mathbf{0} & \mathbf{0} & 0 & 0 & 0 & 0 & 0 & 0 & 0 & 0 \\ \mathbf{0} & \mathbf{0} & 0 & 1 & 0 & 0 & 0 & 0 & 0 & 0 \\ \mathbf{0} & \mathbf{0} & 0 & 0 & 1 & 0 & 0 & 0 & 0 & 0 \\ \mathbf{0} & \mathbf{0} & 0 & 0 & 0 & 1 & 0 & 0 & 0 & \frac{D_m}{\eta_{mv}} \\ \mathbf{0} & \mathbf{0} & 0 & 0 & 0 & 0 & 1 & 0 & 0 & 0 \\ \mathbf{0} & \mathbf{0} & 0 & 0 & 0 & 0 & 0 & 1 & 0 & -D_m \\ \mathbf{0} & \mathbf{0} & 0 & 0 & 0 & 0 & 0 & 0 & 1 & 0 \\ \mathbf{0} & \mathbf{0} & 0 & 0 & 0 & 0 & 0 & 0 & 0 & 0 \end{bmatrix} \tag{3.13}$$

- The stiffness matrix:

$$\mathbf{K}_{TH} = \begin{bmatrix} \mathbf{K}_f & -\mathbf{C}_r & \mathbf{0} & \mathbf{0} & \mathbf{0} & \mathbf{0} & \mathbf{0} & \mathbf{0} & \mathbf{0} & \mathbf{0} \\ \mathbf{0} & -\mathbf{A}_r & \mathbf{0} & \mathbf{0} & \mathbf{0} & \mathbf{0} & \mathbf{0} & \mathbf{0} & \mathbf{0} & \mathbf{0} \\ \mathbf{0} & \mathbf{0} & 0 & 0 & 0 & 0 & 0 & 0 & 0 & 0 \\ \mathbf{0} & \mathbf{0} & 0 & 0 & 0 & 0 & 0 & 0 & 0 & 0 \\ \mathbf{0} & \mathbf{0} & 0 & 0 & 0 & 0 & 0 & 0 & 0 & 0 \\ \mathbf{0} & \mathbf{0} & 0 & 0 & 0 & 0 & 0 & 0 & 0 & 0 \\ \mathbf{0} & \mathbf{0} & 0 & 0 & 0 & 0 & 0 & 0 & 0 & 0 \\ \mathbf{0} & \mathbf{0} & 0 & 0 & 0 & 0 & 0 & 0 & 0 & 0 \\ \mathbf{0} & \mathbf{0} & 0 & 0 & 0 & 0 & 0 & 0 & 0 & 0 \\ \mathbf{0} & \mathbf{0} & 0 & 0 & 0 & 0 & 0 & 0 & 0 & 0 \\ \mathbf{0} & \mathbf{0} & 0 & 0 & 0 & 0 & -D_m\eta_{mm}\eta_{gh} & 0 & D_m\eta_{mm}\eta_{gh} & 0 \end{bmatrix} \tag{3.14}$$

For what regards the external force, $\mathbf{f}_{TH}(t) \in \mathbb{R}^{n_{TH}}$ reads:

$$\mathbf{f}_{TH}(t) = \begin{bmatrix} \mathbf{f}_E(t) & \mathbf{0} & 0 & 0 & 0 & 0 & 0 & 0 & 0 & 0 \end{bmatrix}^T \tag{3.15}$$

Relations from 3.10 to 3.15 have to be plugged into 3.9 to obtain the non-linear ISWEC model based on the HPTO. n_{TH} stands for the system dimension.

In addition, another model of the HPTO is considered since it will be used for the derivation of its spectral-domain version in Section 3.3.3. A simplified model is defined to describe the HPTO torque T_{HPTO} acting on the gyroscope shaft, in which the hydraulic moment is modelled by a Coulomb-like torque depending on the sign($\dot{\varepsilon}$) and on the pressure drop across the pump. As proposed in [235, 236], under the assumption of large hp and lp accumulators, the downstream of the hydraulic transmission (e.g. the hydraulic motor and generator) is decoupled from the upstream part (e.g. hydraulic pump, clutch-declutch valve, rectifier bridge) and the pressure drop over the hydraulic pump and motor is considered as a constant. Thus, the magnitude of the T_{HPTO} depends only on such pressure drop Δp_p and the pump displacement D_p as follows:

$$T_{HPTOs} = u_c \,\mathrm{sign}(\dot{\varepsilon}) \Delta p_p D_p \tag{3.16}$$

This simplification is justified by the need of derive a spectral-domain framework for the HPTO, that is employed for design purposes to improve the computational efficiency of the ISWEC design tool. Under this simplification, the system is truncated to the ε variable since the hydraulic PTO states, such circuit pressures, accumulator volumes and motor-generator speed, are not considered. The equation 3.9 is simplified to obtain the following system:

$$\mathbf{M}_{THs}\ddot{\mathbf{X}}_{THs} + \mathbf{B}_{THs}\dot{\mathbf{X}}_{THs} + \mathbf{K}_{THs}\mathbf{X}_{THs} + \boldsymbol{\Theta}_{THs}(\mathbf{X}_{THs}, \dot{\mathbf{X}}_{THs}, \ddot{\mathbf{X}}_{THs}) = \mathbf{f}_{THs}(t) \tag{3.17}$$

where the state vector $\mathbf{X}_{THs} \in \mathbb{R}^{n_{THs}}$ contains the floater DoFs $\mathbf{X}_f$, the radiation states $\boldsymbol{\zeta}$ and the gyroscope precession angle ε:

$$\mathbf{X}_{THs} = \begin{bmatrix} \mathbf{X}_f & \boldsymbol{\zeta} & \varepsilon \end{bmatrix}^T \tag{3.18}$$

and the non-linear term $\boldsymbol{\Theta}_{THs} : \mathbb{R}^{n_{THs}} \to \mathbb{R}^{n_{THs}}$ is:

$$\boldsymbol{\Theta}_{THs} = \begin{bmatrix} 0 \\ 0 \\ 0 \\ 0 \\ -J\dot{\varphi}\dot{\varepsilon}\cos(\varepsilon) \\ 0 \\ \mathbf{0} \\ J\dot{\varphi}\dot{\delta}\cos(\varepsilon) + m_g d_p g \sin(\varepsilon) + u_c \,\mathrm{sign}(\dot{\varepsilon}) \Delta p_p D_p \end{bmatrix} \tag{3.19}$$

In this framework, the pressure drop Δp_p is considered as a control parameter, fixed constant during the simulation and chosen to maximize the extracted

power from the pump. The matrices $\mathbf{M}_{THs} \in \mathbb{R}^{n_{THs} \times n_{THs}}$, $\mathbf{B}_{THs} \in \mathbb{R}^{n_{THs} \times n_{THs}}$ and $\mathbf{K}_{THs} \in \mathbb{R}^{n_{THs} \times n_{THs}}$ are obtained from the expressions 3.12, 3.13 and 3.14 excluding the elements associated to the hoses pressures (p_{pi} and p_{po}), accumulator pressures (p_{hp} and p_{lp}), accumulator volumes (V_{hp} and V_{lp}) and motor-generator angular position (α_{gh}). The external forces $\mathbf{f}_{THs}(t)$ coincides with the one defined in equation 3.8. n_{THs} is the system dimension and the subscript s stands for simplified.

3.2 Frequency-domain model

In order to achieve the major requirement of fast computation, some simplifications of the TDM mathematical model are needed [237] during the first assessment and optimization of WECs. Moreover, a certain number of wave realisations is required in time-domain to guarantee the statistical properties of the kinematics, dynamics and power assessment of the device. Adopting a frequency-domain representation of the system 3.1 it is possible to reduce the computation effort and at the same time ensure the Gaussian properties of the system outputs as described in Section 2.2.2. Under these circumstances, the WEC dynamics is carried out in frequency-domain. Such linear system becomes a simple set of algebraic linear equations that may be solved merely with a single frequency-domain simulation or, being driven by the stochastic wave elevation process η, through a spectral domain representation [175].

With reference to the non-linear model previously discussed, the following assumptions and linearisation are considered to obtain a Frequecy-Domain Model (FDM):

- The hydrodynamic of the floater is defined in frequency domain and not in time domain;
- The drift forces are neglected since the mooring system is not considered here;
- linearisation of the gyroscopic torques and pendulum elastic recall (equations 2.87 and 2.88);
- The PTO system is assumed linear and ideal, hence excluding saturations from the model.

Such assumptions are reasonable if the precession angle is, on average, small. The linearisation is found as the linear approximation of $\sin(\varepsilon)$ and $\cos(\varepsilon)$ around ε=0 and neglecting the saturation limit of the MPTO. Unfortunately, unlike the MPTO, the HTPO system cannot be obtained in FDM due to its source of non-linearity. Let us define the kinematic variables of interest for the FDM framework as:

$$\mathbf{X}_{FM} = \begin{bmatrix} \mathbf{X}_f & \varepsilon \end{bmatrix}^T \tag{3.20}$$

The system model can be represented in a matrix form in respect to an harmonic input at the intended angular frequency ω:

$$\left[-\omega^2 \mathbf{M}_{FM}(\omega) + \mathrm{i}\omega \mathbf{B}_{FM}(\omega) + \mathbf{K}_{FM}\right] \hat{\mathbf{X}}_{FM} = \mathbf{H}_{\eta FM}(\omega)\hat{\eta}(\omega) \tag{3.21}$$

where the $\mathbf{M}_{FM} \in \mathbb{R}^{n_{FM} \times n_{FM}}$ is the frequency dependent mass matrix, $\mathbf{B}_{FM} \in \mathbb{R}^{n_{FM} \times n_{FM}}$ the frequency dependent damping matrix, $\mathbf{K}_{FM} \in \mathbb{R}^{n_{FM} \times n_{FM}}$ the stiffness matrix and $\mathbf{H}_F \in \mathbb{C}^{n_F}$ the complex transfer function between the wave profile and the resultant excitation forces. n_{FM} is the dimension of the MPTO frequency-domain system. For our concrete model with a MPTO, the mass matrix $\mathbf{M}_{FM}$ includes the floater mass matrix $\mathbf{M}_f$, the radiation contribution $\mathbf{A}_R(\omega)$ and the gyroscope inertia I_g:

$$\mathbf{M}_{FM} = \begin{bmatrix} \mathbf{M}_f + \mathbf{A}_R & \mathbf{0} \\ \mathbf{0} & I_g \end{bmatrix} \tag{3.22}$$

The damping matrix $\mathbf{B}_{FM}$ includes the radiation contribution $\mathbf{B}_R(\omega)$, the linearised gyroscopic torques $T_\delta = -J\dot{\varphi}\dot{\varepsilon}\cos(\varepsilon)$ and $T_\varepsilon = J\dot{\varphi}\dot{\delta}\cos(\varepsilon)$, and the MTPO damping coefficient c_g:

$$\mathbf{B}_{FM} = \begin{bmatrix} \mathbf{B}_R & -\mathbf{L}_g^T \\ \mathbf{L}_g & c_g \end{bmatrix} \tag{3.23}$$

where $\mathbf{L}_g = [0 \;\; 0 \;\; 0 \;\; 0 \;\; J\dot{\varphi} \;\; 0 \;\; 0]$. The stiffness matrix $\mathbf{K}_{FM}$ includes the stiffness matrix of the floater $\mathbf{K}_f$, the linearised pendulum elastic recall $m_p d_p g$ and the MTPO stiffness coefficient k_g:

$$\mathbf{K}_{FM} = \begin{bmatrix} \mathbf{K}_f & \mathbf{0} \\ \mathbf{0} & m_p d_p g + k_g \end{bmatrix} \tag{3.24}$$

The transfer function $\mathbf{H}_{\eta FM} \in \mathbb{C}^{n_{FM}}$ includes the transfer function defined in equation 2.31:

$$\mathbf{H}_{\eta FM} = \begin{bmatrix} \mathbf{H}_{\eta E} & 0 \end{bmatrix}^T \tag{3.25}$$

As stated by Folley [134], "*a probabilistic model uses a statistical representation of the waves, which when passed through an appropriate transformation function produces a probabilistic estimate of the WEC response*", it is well known from the stochastic process modelling that when a Gaussian stochastic input pass through a linear transfer function, also the output is a Gaussian process. The sea wave elevation can be described with a Gaussian pdf, and therefore also the displacements of the floater and gyroscope are described by a Gaussian pdf via the transfer function $\mathbf{H}_{\eta X_F}$:

$$\mathbf{H}_{\eta X_F}(\omega) = \frac{\mathbf{H}_{\eta F}}{-\omega^2 \mathbf{M}_F + \mathrm{i}\omega \mathbf{B}_F + \mathbf{K}_F} \tag{3.26}$$

In this context, the statistical properties of the sea state are fully described by its PSD and the following relations are valid to compute the statistical properties of ISWEC outputs in term of [164]:

- PSD of the output displacements:

$$\mathbf{S}_{X_F X_F}(\omega) = \mathbf{H}_{\eta X_F}(\omega) S_{\eta\eta}(\omega) \mathbf{H}^*_{\eta X_F}(\omega) \tag{3.27}$$

- Covariance matrix of the output variables:

$$\mathbf{V}_F = \begin{bmatrix} \sigma_x^2 & \sigma_{xy} & \sigma_{xz} & \sigma_{x\alpha} & \sigma_{x\delta} & \sigma_{x\psi} & \sigma_{x\varepsilon} \\ & \sigma_y^2 & \sigma_{yz} & \sigma_{y\alpha} & \sigma_{y\delta} & \sigma_{y\psi} & \sigma_{y\varepsilon} \\ & & \sigma_z^2 & \sigma_{z\alpha} & \sigma_{z\delta} & \sigma_{z\psi} & \sigma_{z\varepsilon} \\ & & & \sigma_\alpha^2 & \sigma_{\alpha\delta} & \sigma_{\alpha\psi} & \sigma_{\alpha\varepsilon} \\ & & & & \sigma_\delta^2 & \sigma_{\delta\psi} & \sigma_{\delta\varepsilon} \\ & & & & & \sigma_\psi^2 & \sigma_{\psi\varepsilon} \\ \mathrm{sym} & & & & & & \sigma_\varepsilon^2 \end{bmatrix} \tag{3.28}$$

where, for two generic system outputs X_1 and X_2 and their time-derivatives $\dot{X}_1$ and $\dot{X}_2$, the following relations hold [238]:

$$\begin{aligned} \sigma_{X_1}^2 &= \int_0^\infty S_{X_1 X_1}(\omega)\, d\omega \;, & \sigma_{X_1 X_2} &= \int_0^\infty S_{X_1 X_2}(\omega)\, d\omega \\ \sigma_{\dot{X}_1}^2 &= \int_0^\infty \omega^2 S_{X_1 X_1}(\omega)\, d\omega \;, & \sigma_{\dot{X}_1 \dot{X}_2} &= \int_0^\infty \omega^2 S_{X_1 X_2}(\omega)\, d\omega \\ \sigma_{X_1 \dot{X}_2} &= \mathrm{i} \int_0^\infty \omega S_{X_1 X_2}(\omega)\, d\omega \;, & \sigma_{X_1 \dot{X}_1} &= 0 \end{aligned} \tag{3.29}$$

3.3 Spectral domain models

A Spectral-Domain Model (SDM) is an extension of the frequency-domain representation that allows the inclusion of non-linear forces and thereby provides improved estimates of WEC performance, without the high computational cost of a time-domain framework. A SDM uses a probabilistic model of the system dynamics: basing on the assumption that each sea state may be represented as a stochastic ergodic process and the surface elevation as a stochastic input, when the wave spectrum is passed through an appropriate transfer function produces

a probabilistic estimate of the WEC response [239]. Similarly to the frequency-domain equation 3.27, the PSD of the input wave is used to compute the PSD of the WEC kinematics that provides a reasonable statistical representation of the WEC outputs:

$$\mathbf{S}_{X_S X_S}(\omega) = \mathbf{H}_{\eta X_S}(\omega) S_{\eta\eta}(\omega) \mathbf{H}^*_{\eta X_S}(\omega) \tag{3.30}$$

where $\mathbf{H}_{\eta X_S} \in \mathbb{C}^{n_S}$ is the SDM transfer function of the WEC. Here, n_S is the dimension of the spectral-domain system.

Probabilistic models can be also applied to non-linear systems, although the method of solution differs from the straightforward use of equation 3.27. Given the success of probabilistic methods in other research fields (e.g. response of buildings to wind loading and earthquakes [240]), it is surprising that these methods have only few recent applications to WECs. One of the first application of SDM can be found in the work of Gudmestad [241] that approached the resolution of the dynamics of a floating offshore structure with the *Morison Equation*, including the influence of currents. In the work of Folley [242], the same approaches as Gudmestad are employed to model the effects of the drag forces with wave torque decoupling on a flap-type WEC. Another work of Folley [235] concerns the spectral modelling of an array of heaving buoys with Coulomb friction damping. The most recent work of Folley [243] deals with the SDM of an OWC with vortex shedding and orifice damping. Also Professor P.D. Spanos, Honorary Member ASME and co-author with J.B. Roberts of the book [240] which gives an excellent and multidisciplinary vision of statistical linearisation methods, explored the spectral-domain modelling applied to WEC. In [244] a statistical linearisation technique for conducting random vibration analyses of single-point harvesters is proposed. Then, in [245], the reliability of a SDM of an OWC system is assessed versus relevant Monte Carlo data. Recently, Silva [246, 238] applied the spectral-domain technique to several WEC system with different source of non-linearities showing promising results in term of computational time and accuracy achieved against TDMs in predicting the average extracted power. In [246], the SDM is formulated for a heaving point absorber considering the non-linear hydrostatic restoring force, the PTO end-stop system, a snap-through mechanism, non-linear drag force and a HPTO. A more recent work of Silva [238] expanded the analyses carried out in [246]: here the efficacy of the statistical linearisation is demonstrated using three conceptually different WECs, a point absorber, an oscillating wave surge converter and an oscillating water column. The reliability of the SDM is demonstrated against non-linear time-domain simulations showing a good agreement between the two types of models for all WECs considered, while showing that SDM is approximately 3 to 4 orders of magnitude faster than the TDM. Generally, the drawback of a FDM is the neglection of all non-linearities and this simplification can affect the simulation accuracy. A SDM represents an intermediate solution between time- and frequency-domain

that exploits the statistical linearisation method to include non-linear effects inside the simulation. The main challenge lies in developing SDM of the ISWEC defining an appropriate transformation function $\mathbf{H}_{\eta X_S}$ for the two PTO architectures considered in this work. The aim of this section is to provide a generalized mathematical framework of a SDM for both mechanical and hydraulic PTO applied to the ISWEC. The model equations formulated from here on represents an advance in respect to the one described in published work on this topic along with the most recent researches.

3.3.1 Model equations and practical implementation

In order to obtain an approximate solution of the generic time-domain system 3.1 through a linear transfer function $\mathbf{H}_{\eta X_S}$ allowing the use of expression 3.30, it is useful to introduce an equivalent linear system as follows:

$$\mathbf{M}_S\ddot{\mathbf{X}}_S + \mathbf{B}_S\dot{\mathbf{X}}_S + \mathbf{K}_S\mathbf{X}_S = \mathbf{f}_S(t) \tag{3.31}$$

where the matrices $\mathbf{M}_S \in \mathbb{R}^{n_S \times n_S}$, $\mathbf{B}_S \in \mathbb{R}^{n_S \times n_S}$ and $\mathbf{K}_S \in \mathbb{R}^{n_S \times n_S}$ are the equivalent inertia, damping and stiffness matrices defined as:

$$\mathbf{M}_S = \mathbf{M}_{lin} + \mathbf{M}_{eq} \tag{3.32a}$$

$$\mathbf{B}_S = \mathbf{B}_{lin} + \mathbf{B}_{eq} \tag{3.32b}$$

$$\mathbf{K}_S = \mathbf{K}_{lin} + \mathbf{K}_{eq} \tag{3.32c}$$

The matrices in 3.32 are composed of a linear part, concerning the linear terms of the time-domain equations 3.2 and 3.9, and an equivalent part. The SDM procedure implies that the mathematical expectation of the difference between the non-linear system and the linearised equivalent system, indicated with ε_S, is minimized:

$$\varepsilon_S = \mathbf{\Theta}_S(\mathbf{X}_S, \dot{\mathbf{X}}_S, \ddot{\mathbf{X}}_S) - \mathbf{M}_{eq}\ddot{\mathbf{X}}_S - \mathbf{B}_{eq}\dot{\mathbf{X}}_S - \mathbf{K}_{eq}\mathbf{X}_S \tag{3.33}$$

Then, under the assumption of Gaussian distribution of the response $\mathbf{X}_S$, the elements of the equivalent linear system can be calculated as follows [240]:

$$\mathbf{M}_{eq} = \left\langle \nabla_{\ddot{\mathbf{X}}_S} \Theta_S \right\rangle \tag{3.34a}$$

$$\mathbf{B}_{eq} = \left\langle \nabla_{\dot{\mathbf{X}}_S} \Theta_S \right\rangle \tag{3.34b}$$

$$\mathbf{K}_{eq} = \langle \nabla_{\mathbf{X}_S} \Theta_S \rangle \tag{3.34c}$$

where the operator $\nabla_{\mathbf{X}}$ indicates the gradient in respect to the vector $\mathbf{X}$. Once obtained the linearised matrices to compute the terms 3.32, the response of the

SDM can be calculated through the equivalent linear transfer function expressed as:

$$\mathbf{H}_{\eta X_S}(\omega) = \frac{\mathbf{H}_{\eta S}}{-\omega^2 \mathbf{M}_S + \mathrm{i}\omega \mathbf{B}_S + \mathbf{K}_S} \tag{3.35}$$

Equation 3.35 underlines that the WEC displacements can be obtained as a linear transformation of the wave elevation η, which is assumed to be described by a Gaussian distribution. Therefore, despite the presence of non-linearities in the system dynamics, the assumption of a Gaussian distribution of the WEC response is considered valid when the non-linear forces are non-dominant [239]. However, strong non-linearities lead to a non-Gaussian response distributions [240] that could originate a spectral-domain results strongly different from the time-domain counterpart. Further, the formulation 3.35 remains valid for the analysis of stationary random vibration.

The main idea beyond the spectral-domain approach is to statistically linearise the non-linear terms through the equivalent linear matrices $\mathbf{M}_{eq}$, $\mathbf{B}_{eq}$ and $\mathbf{K}_{eq}$. No analytical solution exists to this problem and an iterative procedure is employed:

- Initialize the body response PSD $S_{X_S X_S}$ solving the linear system 3.30 with $\mathbf{M}_{eq}$, $\mathbf{B}_{eq}$ and $\mathbf{K}_{eq}$ equal to zero;
- Compute the variances of interest using equations 3.29;
- Calculate the equivalent linear matrices $\mathbf{M}_{eq}$, $\mathbf{B}_{eq}$ and $\mathbf{K}_{eq}$;
- Update the spectral-domain transfer function 3.35 and evaluate the spectral response of the ISWEC using equation 3.30;
- Check the convergence of the new values found in term of output variances. If convergence is not achieved return to the second step.

Generally, the stop criteria is verified comparing the relative error between the response used to estimate the equivalent coefficients with the response generated using these equivalent coefficients. As suggested by Silva, the results are considered converged when the error is less than 1% [238]. Typically, simple iterative algorithms with a relaxation method converge in $3 \div 10$ iterations depending on both the source and magnitude of non-linearities considered [239].

3.3.2 Mechanical PTO in spectral-domain

Concerning the MPTO, the transfer function 3.35 is re-written as follows:

$$\mathbf{H}_{\eta X_{SM}} = \frac{\mathbf{H}_{\eta SM}}{-\omega^2 \mathbf{M}_{SM} + \mathrm{i}\omega \mathbf{B}_{SM} + \mathbf{K}_{SM}} \tag{3.36}$$

and it is used to obtain the PSD of the system outputs as:

$$\mathbf{S}_{X_{SM}X_{SM}}(\omega) = \mathbf{H}_{\eta X_{SM}}(\omega) S_{\eta\eta}(\omega) \mathbf{H}^*_{\eta X_{SM}}(\omega) \tag{3.37}$$

Here, the output variables $\mathbf{X}_{SM} \in \mathbb{R}^{n_{SM}}$ and the wave force transfer function $\mathbf{H}_{\eta X_{SM}}(\omega) \in \mathbb{C}^{n_{SM}}$ are:

$$\mathbf{X}_{SM} = \begin{bmatrix} \mathbf{X}_f & \varepsilon \end{bmatrix}^T \tag{3.38}$$

$$\mathbf{H}_{\eta X_{SM}} = \begin{bmatrix} \mathbf{H}_{\eta E} & 0 \end{bmatrix}^T \tag{3.39}$$

The linear terms $\mathbf{M}_{M,lin} \in \mathbb{R}^{n_{SM} \times n_{SM}}$, $\mathbf{B}_{M,lin} \in \mathbb{R}^{n_{SM} \times n_{SM}}$ and $\mathbf{K}_{M,lin} \in \mathbb{R}^{n_{SM} \times n_{SM}}$ inside the mass, damping and stiffness matrices are:

$$\mathbf{M}_{M,lin} = \begin{bmatrix} \mathbf{M}_f + \mathbf{A}_R & \mathbf{0} \\ \mathbf{0} & I_g \end{bmatrix} \tag{3.40a}$$

$$\mathbf{B}_{M,lin} = \begin{bmatrix} \mathbf{B}_R & \mathbf{0} \\ \mathbf{0} & 0 \end{bmatrix} \tag{3.40b}$$

$$\mathbf{K}_{M,lin} = \begin{bmatrix} \mathbf{K}_f & \mathbf{0} \\ \mathbf{0} & 0 \end{bmatrix} \tag{3.40c}$$

The MPTO shows non-linearities in term of gyro-pendulum actions and in the piecewise defined PTO torque, as reported in equation 2.89. The equivalent matrices are obtained as follows:

$$\mathbf{M}_{M,eq} = \mathbf{0} \tag{3.41a}$$

$$\mathbf{B}_{M,eq} = \begin{bmatrix} 0 & 0 & 0 & 0 & 0 & 0 & 0 \\ 0 & 0 & 0 & 0 & 0 & 0 & 0 \\ 0 & 0 & 0 & 0 & 0 & 0 & 0 \\ 0 & 0 & 0 & 0 & 0 & 0 & 0 \\ 0 & 0 & 0 & 0 & 0 & 0 & -J\dot{\varphi}\langle\cos(\varepsilon)\rangle \\ 0 & 0 & 0 & 0 & 0 & 0 & 0 \\ 0 & 0 & 0 & 0 & J\dot{\varphi}\langle\cos(\varepsilon)\rangle & 0 & \langle\frac{\partial T_{MPTO}}{\partial \dot{\varepsilon}}\rangle \end{bmatrix} \tag{3.41b}$$

$$\mathbf{K}_{M,eq} = \begin{bmatrix} 0 & 0 & 0 & 0 & 0 & 0 & 0 \\ 0 & 0 & 0 & 0 & 0 & 0 & 0 \\ 0 & 0 & 0 & 0 & 0 & 0 & 0 \\ 0 & 0 & 0 & 0 & 0 & 0 & 0 \\ 0 & 0 & 0 & 0 & 0 & 0 & J\dot{\varphi}\langle\dot{\varepsilon}\sin(\varepsilon)\rangle \\ 0 & 0 & 0 & 0 & 0 & 0 & 0 \\ 0 & 0 & 0 & 0 & 0 & 0 & m_p g d_p \langle\cos(\varepsilon)\rangle - J\dot{\varphi}\langle\dot{\delta}\sin(\varepsilon)\rangle + \langle\frac{\partial T_{MPTO}}{\partial \varepsilon}\rangle \end{bmatrix} \tag{3.41c}$$

For what concern the stiffness matrix $\mathbf{K}_{M,eq} \in \mathbb{R}^{n_{SM} \times n_{SM}}$, the gyroscopic effect $J\dot{\varphi}\langle\dot{\varepsilon}\sin(\varepsilon)\rangle$ is tackled first. Since $\dot{\varepsilon}$ and ε are *uncorrelated*[1] with zero-mean and the $\sin(\cdot)$ function is odd, the following result holds:

$$K_{M,eq,\delta\varepsilon} = J\dot{\varphi}\langle\dot{\varepsilon}\sin(\varepsilon)\rangle = J\dot{\varphi}\langle\dot{\varepsilon}\rangle\langle\sin(\varepsilon)\rangle = 0 \tag{3.42}$$

Second, the pendulum contribution as well as the gyroscopic effect are linearised as follows (the T_{MPTO} contribution is derived after):

$$\begin{aligned} K_{M,eq,\varepsilon\varepsilon} &= m_p d_p g\langle\cos(\varepsilon)\rangle - J\dot{\varphi}\langle\dot{\delta}\sin(\varepsilon)\rangle + \left\langle\frac{\partial T_{MPTO}}{\partial\varepsilon}\right\rangle = \\ &= I_1 - I_2 + \left\langle\frac{\partial T_{MPTO}}{\partial\varepsilon}\right\rangle \end{aligned} \tag{3.43}$$

The two equivalent stiffness terms defined in equation 3.43 can be integrated separately. Starting with the pendulum contribution, the cosine term is tackled substituting $\cos(\varepsilon) = \mathrm{e}^{\mathrm{i}\varepsilon} + \mathrm{e}^{-\mathrm{i}\varepsilon}$, obtaining the following expression:

$$\begin{aligned} I_1 &= m_p d_p g \int_{-\infty}^{\infty} \cos(\varepsilon) f_\varepsilon(\varepsilon)\, d\varepsilon = \\ &= \frac{m_p d_p g}{2\sqrt{2\pi}\sigma_\varepsilon} \int_{-\infty}^{\infty} \left(\mathrm{e}^{\mathrm{i}\varepsilon} + \mathrm{e}^{-\mathrm{i}\varepsilon}\right) \mathrm{e}^{-\frac{\varepsilon^2}{2\sigma_\varepsilon^2}}\, d\varepsilon = \\ &= \frac{m_p d_p g}{2\sqrt{2\pi}\sigma_\varepsilon} \left(\int_{-\infty}^{\infty} \mathrm{e}^{-\left(\frac{\varepsilon}{\sqrt{2}\sigma_\varepsilon} - \frac{\mathrm{i}\sigma_\varepsilon}{\sqrt{2}}\right)^2 - \frac{\sigma_\varepsilon^2}{2}}\, d\varepsilon + \int_{-\infty}^{\infty} \mathrm{e}^{-\left(\frac{\varepsilon}{\sqrt{2}\sigma_\varepsilon} + \frac{\mathrm{i}\sigma_\varepsilon}{\sqrt{2}}\right)^2 - \frac{\sigma_\varepsilon^2}{2}}\, d\varepsilon \right) \end{aligned} \tag{3.44}$$

The integrals in equation 3.44 can be tackled through the following substitutions:

$$u_1 = \frac{\varepsilon - \mathrm{i}\sigma_\varepsilon^2}{\sqrt{2}\sigma_\varepsilon} \rightarrow du_1 = \frac{d\varepsilon}{\sqrt{2}\sigma_\varepsilon} \tag{3.45a}$$

$$u_2 = \frac{\varepsilon + \mathrm{i}\sigma_\varepsilon^2}{\sqrt{2}\sigma_\varepsilon} \rightarrow du_2 = \frac{d\varepsilon}{\sqrt{2}\sigma_\varepsilon} \tag{3.45b}$$

[1] Two jointly normally distributed random variables are *independent* if they are *uncorrelated* [247]. Since $\varepsilon(t)$ is a zero mean stationary Gaussian process, its derivative process is also zero mean stationary Gaussian with autocorrelation function $R_{\dot{\varepsilon}\dot{\varepsilon}}(\tau) = -R''_{\varepsilon\varepsilon}(\tau)$. Further, $\varepsilon(t)$ and $\dot{\varepsilon}(t)$ are jointly Gaussian stationary processes, and since $R_{\varepsilon\dot{\varepsilon}}(\tau) = -\frac{dR_\varepsilon(\tau)}{d\tau}$ we have $R_{\varepsilon\dot{\varepsilon}}(-\tau) = -R_{\varepsilon\dot{\varepsilon}}(\tau)$ which for $\tau = 0$ gives $R_{\varepsilon\dot{\varepsilon}}(\tau) = 0$, that implies $\langle\varepsilon\dot{\varepsilon}\rangle = \langle\varepsilon\rangle\langle\dot{\varepsilon}\rangle$ and, more in general, given two function $\alpha(\varepsilon)$ and $\beta(\dot{\varepsilon})$, $\langle\alpha(\varepsilon)\beta(\dot{\varepsilon})\rangle = \langle\alpha(\varepsilon)\rangle\langle\beta(\dot{\varepsilon})\rangle$.

Then, the relation 3.44 becomes:

$$\begin{aligned} I_1 &= \frac{m_p d_p g}{4} \mathrm{e}^{-\frac{\sigma_\varepsilon^2}{2}} \left(\int_{-\infty}^{\infty} \frac{2}{\sqrt{\pi}} \mathrm{e}^{-u_1^2}\, du_1 + \int_{-\infty}^{\infty} \frac{2}{\sqrt{\pi}} \mathrm{e}^{-u_2^2}\, du_2 \right) = \\ &= \frac{m_p d_p g}{4} \mathrm{e}^{-\frac{\sigma_\varepsilon^2}{2}} \left(\mathrm{erf}(u_1) \Big|_{-\infty}^{\infty} + \mathrm{erf}(u_2) \Big|_{-\infty}^{\infty} \right) = \\ &= \frac{m_p d_p g}{4} \mathrm{e}^{-\frac{\sigma_\varepsilon^2}{2}} \left(\mathrm{erf}\left(\frac{\varepsilon - \mathrm{i}\sigma_\varepsilon^2}{\sqrt{2}\sigma_\varepsilon} \right) \Big|_{-\infty}^{\infty} + \mathrm{erf}\left(\frac{\varepsilon + \mathrm{i}\sigma_\varepsilon^2}{\sqrt{2}\sigma_\varepsilon} \right) \Big|_{-\infty}^{\infty} \right) = \\ &= m_p d_p g \mathrm{e}^{-\frac{\sigma_\varepsilon^2}{2}} \end{aligned} \tag{3.46}$$

The integral I_2 has not a closed form since $\dot{\delta}$ and ε are *correlated*. It can be computed numerically:

$$\begin{aligned} I_2 &= J\dot{\varphi} \int_{-\infty}^{\infty} \int_{-\infty}^{\infty} \dot{\delta} \sin(\varepsilon) f_{\varepsilon\dot{\delta}}(\varepsilon, \dot{\delta})\, d\dot{\delta}\, d\varepsilon = \\ &= \frac{J\dot{\varphi}}{2\pi\sigma_{\dot{\delta}}\sigma_\varepsilon\sqrt{1-\rho_{\dot{\delta}\varepsilon}^2}} \int_{-\infty}^{\infty} \int_{-\infty}^{\infty} \dot{\delta} \sin(\varepsilon) e^{-\frac{1}{2\left(1-\rho_{\dot{\delta}\varepsilon}^2\right)} \left(\frac{\dot{\delta}^2}{\sigma_{\dot{\delta}}^2} - 2\rho_{\dot{\delta}\varepsilon} \frac{\dot{\delta}\varepsilon}{\sigma_{\dot{\delta}}\sigma_\varepsilon} + \frac{\varepsilon^2}{\sigma_\varepsilon^2} \right)} d\dot{\delta}\, d\varepsilon \end{aligned} \tag{3.47}$$

where $\rho_{\dot{\delta}\varepsilon} = \frac{\sigma_{\dot{\delta}\varepsilon}}{\sigma_{\dot{\delta}}\sigma_\varepsilon}$ is the correlation coefficient of $\dot{\delta}$ and ε. Note that the terms f refer to the pdf of the interested variables according with the definitions 2.53 and 2.55 of the univariate and multivariate Gaussian pdf.

Considering the equivalent damping matrix $\mathbf{B}_{M,eq} \in \mathbb{R}^{n_{SM} \times n_{SM}}$, the two gyroscopic contributions $J\dot{\varphi}\langle\cos(\varepsilon)\rangle$ are already solved since the expected value of the $\cos(\varepsilon)$ is derived in equation 3.46. Then, the equivalent damping terms $B_{SM,eq,\dot{\delta}\dot{\varepsilon}}$ and $B_{SM,eq,\dot{\varepsilon}\dot{\delta}}$ are:

$$B_{M,eq,\dot{\delta}\dot{\varepsilon}} = -J\dot{\varphi}\mathrm{e}^{-\frac{\sigma_\varepsilon^2}{2}} = -B_{M,eq,\varepsilon\delta} \tag{3.48}$$

The result obtained in equations 3.46 and 3.48 underlines an important aspect of the statistical linearisation. The gyroscopic torques depend on the magnitude of $\cos(\varepsilon)$; in fact, as the amplitude of ε oscillations increase, the gyroscopic effect decreases due to the $\cos(\varepsilon)$ term; typically, the $\cos(\cdot)$ function is linearised around the equilibrium position of the physical system ($\varepsilon = 0$ in our case) and $J\dot{\varphi}\dot{\delta}\cos(\varepsilon)$ and $J\dot{\varphi}\dot{\varepsilon}\cos(\varepsilon)$ become $J\dot{\varphi}\dot{\delta}$ and $J\dot{\varphi}\dot{\varepsilon}$ that are, precisely, linear in $\dot{\delta}$ and $\dot{\varepsilon}$. The spectral-domain includes the non-linear effects as an equivalent angular momentum $J\dot{\varphi}\mathrm{e}^{-\frac{\sigma_\varepsilon^2}{2}}$ depending on the variance σ_ε^2. The term $\mathrm{e}^{-\frac{\sigma_\varepsilon^2}{2}}$ acts as a correction coefficient

that diminish the linearised angular momentum $J\dot{\varphi}$ by a factor depending on the broadness of ε, in view of the expected value of $\cos(\varepsilon)$. In this regard, from the equations 3.46 and 3.48, the correction coefficient associated to the expected valued of $\cos(\varepsilon)$ and, thus, associated to the ε magnitude, is defined as:

$$T_{gc} = \mathrm{e}^{-\frac{\sigma_{\varepsilon}^2}{2}} \tag{3.49}$$

The last contribution to be derived is the controlled torque acted by the MPTO. In this case, the non-linearity refers to a saturation of the PTO torque when it overcomes the generator torque limits, named T_{sat} and $-T_{sat}$. The MPTO torque is a function of both ε and $\dot{\varepsilon}$ and it is piecewise continuous. Thus, both $\left\langle \frac{\partial T_{MPTO}}{\partial \varepsilon} \right\rangle$ and $\left\langle \frac{\partial T_{MPTO}}{\partial \dot{\varepsilon}} \right\rangle$ can be merely solved splitting the integration domain in two areas: the linear region and the saturated region. Figure 3.1 aims to clarify such integration process.

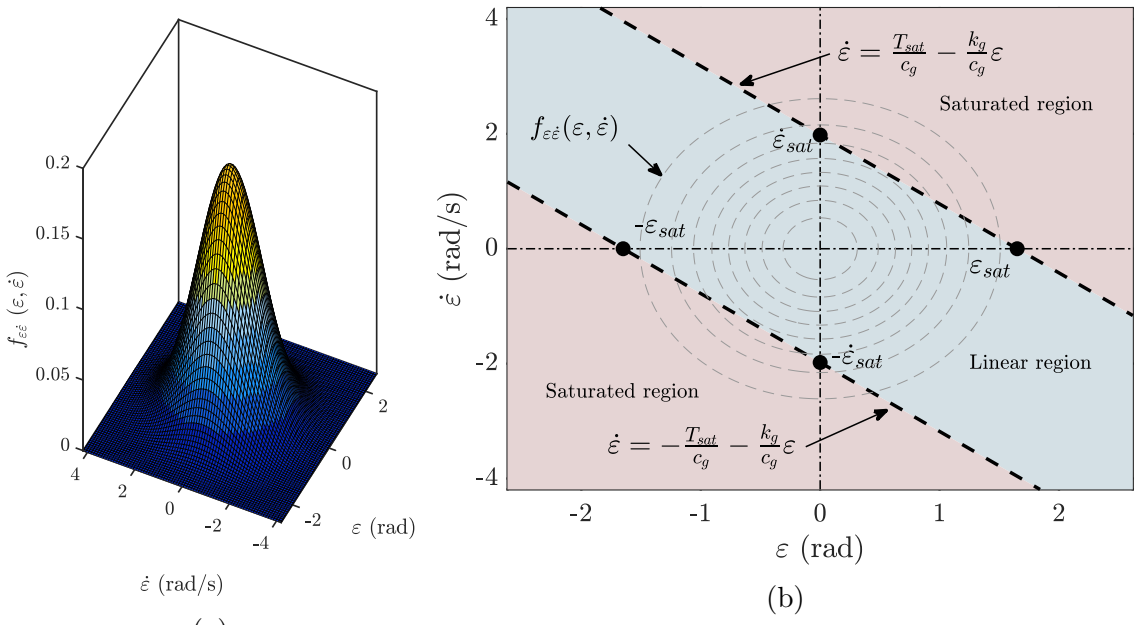

Figure 3.1: (a) ε and $\dot{\varepsilon}$ bi-variate pdf $f_{\varepsilon\dot{\varepsilon}}$. (b) Top view of ε and $\dot{\varepsilon}$ bi-variate pdf $f_{\varepsilon\dot{\varepsilon}}$ with saturation limits and integration regions. The grey dashed lines represent the $f_{\varepsilon\dot{\varepsilon}}$ levels. The black dashed straight lines are the upper and lower saturation limits.

First, the bi-variate distribution of ε and $\dot{\varepsilon}$ is represented in Figure 3.1a. The T_{MPTO} is dependent on both ε and $\dot{\varepsilon}$ and on the control parameters k_g and c_g. The integrals in 3.50 are solved integrating the derivative of the linear part multiplied by the pdf $f_{\varepsilon\dot{\varepsilon}}(\varepsilon,\dot{\varepsilon})$ in the linear region, as depicted in Figure 3.1b. Such a figure

shows a top view of $f_{\varepsilon\dot{\varepsilon}}(\varepsilon,\dot{\varepsilon})$ which levels are depicted with grey dashed lines and the integration limits with the two straight lines $\dot{\varepsilon} = -\frac{T_{sat}}{c_g} - \frac{k_g}{c_g}\varepsilon$ and $\dot{\varepsilon} = \frac{T_{sat}}{c_g} - \frac{k_g}{c_g}\varepsilon$. For both $\left\langle \frac{\partial T_{MPTO}}{\partial \varepsilon} \right\rangle$ and $\left\langle \frac{\partial T_{MPTO}}{\partial \dot{\varepsilon}} \right\rangle$ the following relations hold:

$$\left\langle \frac{\partial T_{MPTO}}{\partial \varepsilon} \right\rangle = k_g \int_{-\infty}^{\infty} \int_{-\frac{T_{sat}}{c} - \frac{k_g}{c}\varepsilon}^{\frac{T_{sat}}{c} - \frac{k_g}{c}\varepsilon} f_{\varepsilon\dot{\varepsilon}}(\varepsilon,\dot{\varepsilon})\, d\dot{\varepsilon}\, d\varepsilon + \left\langle \frac{\partial T_{sat}}{\partial \varepsilon} \right\rangle - \left\langle \frac{\partial T_{sat}}{\partial \varepsilon} \right\rangle \tag{3.50a}$$

$$\left\langle \frac{\partial T_{MPTO}}{\partial \dot{\varepsilon}} \right\rangle = c_g \int_{-\infty}^{\infty} \int_{-\frac{T_{sat}}{c} - \frac{k_g}{c}\varepsilon}^{\frac{T_{sat}}{c} - \frac{k_g}{c}\varepsilon} f_{\varepsilon\dot{\varepsilon}}(\varepsilon,\dot{\varepsilon})\, d\dot{\varepsilon}\, d\varepsilon + \left\langle \frac{\partial T_{sat}}{\partial \dot{\varepsilon}} \right\rangle - \left\langle \frac{\partial T_{sat}}{\partial \dot{\varepsilon}} \right\rangle \tag{3.50b}$$

The second and third terms in equations 3.50 are merely null since T_{sat} is a constant. First, the equation 3.50a can be solved integrating first the part dependent on $\dot{\varepsilon}$ and then the result dependent on ε, since ε and $\dot{\varepsilon}$ are uncorrelated:

$$\begin{aligned}
\left\langle \frac{\partial T_{MPTO}}{\partial \varepsilon} \right\rangle &= k_g \int_{-\infty}^{\infty} \int_{-\frac{T_{sat}}{c} - \frac{k_g}{c}\varepsilon}^{\frac{T_{sat}}{c} - \frac{k_g}{c}\varepsilon} f_{\varepsilon\dot{\varepsilon}}(\varepsilon,\dot{\varepsilon})\, d\dot{\varepsilon}\, d\varepsilon = \\
&= \frac{k_g}{2\pi\sigma_\varepsilon\sigma_{\dot{\varepsilon}}} \int_{-\infty}^{\infty} \mathrm{e}^{-\frac{\varepsilon^2}{2\sigma_\varepsilon^2}} \left(\int_{-\frac{T_{sat}}{c} - \frac{k_g}{c}\varepsilon}^{\frac{T_{sat}}{c} - \frac{k_g}{c}\varepsilon} \mathrm{e}^{-\frac{\dot{\varepsilon}^2}{2\sigma_{\dot{\varepsilon}}^2}}\, d\dot{\varepsilon} \right) d\varepsilon = \\
&= \frac{k_g}{2\pi\sigma_\varepsilon\sigma_{\dot{\varepsilon}}} \int_{-\infty}^{\infty} \frac{\sqrt{\pi}\sigma_{\dot{\varepsilon}} \operatorname{erf}\left(\frac{\dot{\varepsilon}}{\sqrt{2}\sigma_{\dot{\varepsilon}}}\right)}{\sqrt{2}} \Bigg|_{-\frac{T_{sat}}{c} - \frac{k_g}{c}\varepsilon}^{\frac{T_{sat}}{c} - \frac{k_g}{c}\varepsilon} \mathrm{e}^{-\frac{\varepsilon^2}{2\sigma_\varepsilon^2}}\, d\varepsilon = \\
&= \frac{k_g}{\sqrt{8\pi}\sigma_\varepsilon} \int_{-\infty}^{\infty} \left(\operatorname{erf}\left(\frac{k\varepsilon + T_{sat}}{\sqrt{2}c\sigma_{\dot{\varepsilon}}} \right) - \operatorname{erf}\left(\frac{k\varepsilon - T_{sat}}{\sqrt{2}c\sigma_{\dot{\varepsilon}}} \right) \right) \mathrm{e}^{-\frac{\varepsilon^2}{2\sigma_\varepsilon^2}}\, d\varepsilon = \\
&= k_g T_{MPTOc}
\end{aligned} \tag{3.51}$$

The same procedure is valid for the damping term 3.50b:

$$\begin{aligned}
B_{M,eq,\dot{\varepsilon}\dot{\varepsilon}} = \left\langle \frac{\partial T_{MPTO}}{\partial \dot{\varepsilon}} \right\rangle &= c_g \int_{-\infty}^{\infty} \int_{-\frac{T_{sat}}{c_g} - \frac{k_g}{c_g}\varepsilon}^{\frac{T_{sat}}{c} - \frac{k_g}{c_g}\varepsilon} f_{\varepsilon\dot{\varepsilon}}(\varepsilon,\dot{\varepsilon})\, d\dot{\varepsilon}\, d\varepsilon = \\
&= \frac{c_g}{\sqrt{8\pi}\sigma_\varepsilon} \int_{-\infty}^{\infty} \left(\operatorname{erf}\left(\frac{k\varepsilon + T_{sat}}{\sqrt{2}c\sigma_{\dot{\varepsilon}}} \right) - \operatorname{erf}\left(\frac{k\varepsilon - T_{sat}}{\sqrt{2}c\sigma_{\dot{\varepsilon}}} \right) \right) \mathrm{e}^{-\frac{\varepsilon^2}{2\sigma_\varepsilon^2}}\, d\varepsilon = \\
&= c_g T_{MPTOc}
\end{aligned} \tag{3.52}$$

Equations 3.51 and 3.52 can be interpreted similarly to equations 3.46 and 3.48. The MPTO torque is a linear function of k_g and c_g that saturates when it overcomes the generator limits. The integrals inside the relations 3.51 and 3.52 aim to diminish the stiffness and damping coefficients of the PTO due to the torque saturation. In fact, it is straightforward to demonstrate that the area underneath the pdf $f_{\varepsilon\dot{\varepsilon}}(\varepsilon, \dot{\varepsilon})$ over the linear region is strictly lower than one. Such integral acts as a correction coefficient that diminish the stiffness k_g and damping c_g by a factor depending on the broadness of ε, $\dot{\varepsilon}$ and T_{sat}. If T_{sat} grows to infinity, it is straightforward demonstrate that the equivalent stiffness and damping coincide with the original k_g and c_g:

$$\lim_{T_{sat}\to\infty} \left\langle \frac{\partial T_{MPTO}}{\partial \varepsilon} \right\rangle = \frac{k_g}{\sqrt{8\pi}\sigma_\varepsilon} \int_{-\infty}^{\infty} 2\mathrm{e}^{-\frac{\varepsilon^2}{2\sigma_\varepsilon^2}} d\varepsilon = \frac{k_g}{\sqrt{8\pi}\sigma_\varepsilon} \sqrt{8\pi}\sigma_\varepsilon = k_g \tag{3.53a}$$

$$\lim_{T_{sat}\to\infty} \left\langle \frac{\partial T_{MPTO}}{\partial \dot{\varepsilon}} \right\rangle = \frac{c_g}{\sqrt{8\pi}\sigma_\varepsilon} \int_{-\infty}^{\infty} 2\mathrm{e}^{-\frac{\varepsilon^2}{2\sigma_\varepsilon^2}} d\varepsilon = \frac{c_g}{\sqrt{8\pi}\sigma_\varepsilon} \sqrt{8\pi}\sigma_\varepsilon = c_g \tag{3.53b}$$

Similarly, if the standard deviation of both ε and $\dot{\varepsilon}$ are considerable lower than their saturation limits $\varepsilon_{sat} = T_{sat}/k_g$ and $\dot{\varepsilon}_{sat} = T_{sat}/c_g$, the PTO never saturates. In particular, the bi-variate Gaussian distribution $f_{\varepsilon\dot{\varepsilon}}$ tends to zero when ε and $\dot{\varepsilon}$ increase/decrease toward ∞ and $-\infty$; then, if $3\sigma_\varepsilon \ll \varepsilon_{sat}$ and $3\sigma_{\dot{\varepsilon}} \ll \dot{\varepsilon}_{sat}$ hold, the equivalent stiffness and damping coefficients can be approximated to:

$$\left\langle \frac{\partial T_{MPTO}}{\partial \varepsilon} \right\rangle \approx k_g \int_{-3\sigma_\varepsilon}^{3\sigma_\varepsilon} \int_{-3\sigma_{\dot{\varepsilon}}}^{3\sigma_{\dot{\varepsilon}}} f_{\varepsilon\dot{\varepsilon}}(\varepsilon, \dot{\varepsilon})\, d\dot{\varepsilon} d\varepsilon \approx k_g \tag{3.54a}$$

$$\left\langle \frac{\partial T_{MPTO}}{\partial \dot{\varepsilon}} \right\rangle \approx c_g \int_{-3\sigma_\varepsilon}^{3\sigma_\varepsilon} \int_{-3\sigma_{\dot{\varepsilon}}}^{3\sigma_{\dot{\varepsilon}}} f_{\varepsilon\dot{\varepsilon}}(\varepsilon, \dot{\varepsilon})\, d\dot{\varepsilon} d\varepsilon \approx c_g \tag{3.54b}$$

The approximation holds since integrating $f_{\varepsilon\dot{\varepsilon}}$ between $-3\sigma_\varepsilon$ and $3\sigma_\varepsilon$ approximately tends to 1 (exactly to 0.997).

3.3.3 Hydraulic PTO in spectral-domain

Concerning the HPTO, the transfer function 3.35 is re-written as follows:

$$\mathbf{H}_{\eta X_{SH}} = \frac{\mathbf{H}_{\eta SH}}{-\omega^2 \mathbf{M}_{SH} + \mathrm{i}\omega \mathbf{B}_{SH} + \mathbf{K}_{SH}} \tag{3.55}$$

and it is used to obtain the PSD of the system outputs as:

$$\mathbf{S}_{X_{SH}X_{SH}}(\omega) = \mathbf{H}_{\eta X_{SH}}(\omega) S_{\eta\eta}(\omega) \mathbf{H}^*_{\eta X_{SH}}(\omega) \tag{3.56}$$

Here, the output variables $\mathbf{X}_{SH} \in \mathbb{R}^{n_{SH}}$ and the wave force transfer function $\mathbf{H}_{\eta X_{SH}}(\omega) \in \mathbb{C}^{n_{SH}}$ are:

$$\mathbf{X}_{SH} = \begin{bmatrix} \mathbf{X}_f & \varepsilon \end{bmatrix}^T \tag{3.57}$$

$$\mathbf{H}_{\eta X_{SH}} = \begin{bmatrix} \mathbf{H}_{\eta E} & 0 \end{bmatrix}^T \tag{3.58}$$

Similarly to the MPTO, the linear terms $\mathbf{M}_{H,lin} \in \mathbb{R}^{n_{SH} \times n_{SH}}$, $\mathbf{B}_{H,lin} \in \mathbb{R}^{n_{SH} \times n_{SH}}$ and $\mathbf{K}_{H,lin} \in \mathbb{R}^{n_{SH} \times n_{SH}}$ inside the mass, damping and stiffness matrices are:

$$\mathbf{M}_{H,lin} = \begin{bmatrix} \mathbf{M}_f + \mathbf{A}_R & \mathbf{0} \\ \mathbf{0} & I_g \end{bmatrix} \tag{3.59a}$$

$$\mathbf{B}_{H,lin} = \begin{bmatrix} \mathbf{B}_R & \mathbf{0} \\ \mathbf{0} & 0 \end{bmatrix} \tag{3.59b}$$

$$\mathbf{K}_{H,lin} = \begin{bmatrix} \mathbf{K}_f & \mathbf{0} \\ \mathbf{0} & 0 \end{bmatrix} \tag{3.59c}$$

The HPTO shows the same gyro-pendulum non-linearities of the MPTO and a constant-amplitude coulomb-like PTO torque acting on the precession axis ε. The equivalent matrices of the HPTO are obtained as follows:

$$\mathbf{M}_{H,eq} = \mathbf{0} \tag{3.60a}$$

$$\mathbf{B}_{H,eq} = \begin{bmatrix} 0 & 0 & 0 & 0 & 0 & 0 & 0 \\ 0 & 0 & 0 & 0 & 0 & 0 & 0 \\ 0 & 0 & 0 & 0 & 0 & 0 & 0 \\ 0 & 0 & 0 & 0 & 0 & 0 & 0 \\ 0 & 0 & 0 & 0 & 0 & 0 & -J\dot{\varphi}\langle\cos(\varepsilon)\rangle \\ 0 & 0 & 0 & 0 & 0 & 0 & 0 \\ 0 & 0 & 0 & 0 & J\dot{\varphi}\langle\cos(\varepsilon)\rangle & 0 & \langle\frac{\partial T_{HPTO_s}}{\partial \dot{\varepsilon}}\rangle \end{bmatrix} \tag{3.60b}$$

$$\mathbf{K}_{H,eq} = \begin{bmatrix} 0 & 0 & 0 & 0 & 0 & 0 & 0 \\ 0 & 0 & 0 & 0 & 0 & 0 & 0 \\ 0 & 0 & 0 & 0 & 0 & 0 & 0 \\ 0 & 0 & 0 & 0 & 0 & 0 & 0 \\ 0 & 0 & 0 & 0 & 0 & 0 & J\dot{\varphi}\langle\dot{\varepsilon}\sin(\varepsilon)\rangle \\ 0 & 0 & 0 & 0 & 0 & 0 & 0 \\ 0 & 0 & 0 & 0 & 0 & 0 & m_p d_p g\langle\cos(\varepsilon)\rangle - J\dot{\varphi}\langle\dot{\delta}\sin(\varepsilon)\rangle \end{bmatrix} \tag{3.60c}$$

The HPTO torque can be interpreted as a Coulomb damping proportional to the pump displacement and the pressure drop over its inlet and outlet ports. Moreover, in case of a clutch-declutch control is applied, the HPTO torque can be defined as a piecewise constant function of the declutch and clutch speed limits $\dot{\varepsilon}_{dc}$ and $\dot{\varepsilon}_{cs}$ with the following formulation:

$$T_{HPTOs} = \begin{cases} 0 & \text{if} \quad -\dot{\varepsilon}_{dc} < \dot{\varepsilon} < \dot{\varepsilon}_{dc} \\ \dfrac{\Delta p_p D_p}{\dot{\varepsilon}_{cs} - \dot{\varepsilon}_{dc}}(\dot{\varepsilon} - \dot{\varepsilon}_{dc}) & \text{if} \quad \dot{\varepsilon}_{dc} \leq \dot{\varepsilon} < \dot{\varepsilon}_{cs} \\ \dfrac{\Delta p_p D_p}{\dot{\varepsilon}_{cs} - \dot{\varepsilon}_{dc}}(\dot{\varepsilon} + \dot{\varepsilon}_{dc}) & \text{if} \quad -\dot{\varepsilon}_{cs} < \dot{\varepsilon} \leq -\dot{\varepsilon}_{dc} \\ \Delta p_p D_p & \text{if} \quad \dot{\varepsilon} \geq \dot{\varepsilon}_{cs} \\ -\Delta p_p D_p & \text{if} \quad \dot{\varepsilon} \leq -\dot{\varepsilon}_{cs} \end{cases} \tag{3.61}$$

where Δp_p is the pressure drop across the pump unit considered as a constant. The relation 3.61 defines a ramp function in order to smooth the transition between the declutch and clutch conditions. In fact, in real applications, an hysteresis is used to avoid to continuously clutch-declutch the valve. Graphically, the hysteresis and the ramp formulations can be represented as Figure 3.2.

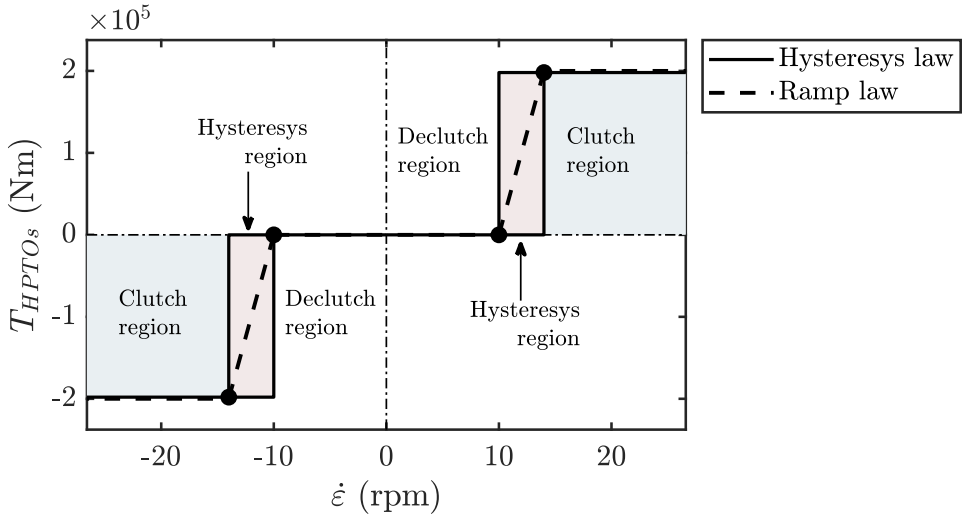

Figure 3.2: Graphical representation of the clutch-declutch logic. The continuous line refers to a hysteresis-type clutch-declutch in which the pump is clutched when its angular speed overcome the clutching speed and is bypassed when it goes below the declutching speed. The dashed lines represent a ramp-type clutch-declutch, where the passage between the declutch condition to the clutch condition is modelled as a ramp function.

The first, fourth and fifth integration intervals defined in equation 3.61 give an equivalent damping equal to zero since their derivative in respect to the gyroscope

angular speed $\dot{\varepsilon}$ are null. Then, the linear term can be tackled with the following integral:

$$
\begin{aligned}
B_{H,eq,\dot{\varepsilon}\dot{\varepsilon}} &= \left\langle \frac{\partial T_{HPTO}}{\partial \dot{\varepsilon}} \right\rangle = \frac{\Delta p_p D_p}{\dot{\varepsilon}_{cs} - \dot{\varepsilon}_{dc}} \left(\int_{-\dot{\varepsilon}_{cs}}^{-\dot{\varepsilon}_{dc}} f_{\dot{\varepsilon}\dot{\varepsilon}}(\varepsilon, \dot{\varepsilon})\, d\dot{\varepsilon} d\varepsilon + \int_{\dot{\varepsilon}_{dc}}^{\dot{\varepsilon}_{c}} f_{\dot{\varepsilon}\dot{\varepsilon}}(\varepsilon, \dot{\varepsilon})\, d\dot{\varepsilon} d\varepsilon \right) = \\
&= \frac{\Delta p_p D_p}{\sqrt{2\pi}\sigma_{\dot{\varepsilon}}(\dot{\varepsilon}_c - \dot{\varepsilon}_{dc})} \left(\int_{-\dot{\varepsilon}_{cs}}^{-\dot{\varepsilon}_{dc}} \mathrm{e}^{-\frac{1}{2}\frac{\dot{\varepsilon}^2}{\sigma_{\dot{\varepsilon}}^2}}\, d\dot{\varepsilon} + \int_{\dot{\varepsilon}_{dc}}^{\dot{\varepsilon}_{cs}} \mathrm{e}^{-\frac{1}{2}\frac{\dot{\varepsilon}^2}{\sigma_{\dot{\varepsilon}}^2}}\, d\dot{\varepsilon} \right) = \\
&= \frac{\Delta p_p D_p}{\sqrt{2\pi}\sigma_{\dot{\varepsilon}}(\dot{\varepsilon}_{cs} - \dot{\varepsilon}_{dc})} \left(\frac{\sqrt{\pi}\sigma_{\dot{\varepsilon}} \operatorname{erf}\left(\frac{\dot{\varepsilon}}{\sqrt{2}\sigma_{\dot{\varepsilon}}}\right)}{\sqrt{2}} \Bigg|_{-\dot{\varepsilon}_{cs}}^{-\dot{\varepsilon}_{dc}} + \frac{\sqrt{\pi}\sigma_{\dot{\varepsilon}} \operatorname{erf}\left(\frac{\dot{\varepsilon}}{\sqrt{2}\sigma_{\dot{\varepsilon}}}\right)}{\sqrt{2}} \Bigg|_{\dot{\varepsilon}_{dc}}^{\dot{\varepsilon}_{cs}} \right) = \\
&= \frac{\Delta p_p D_p}{\dot{\varepsilon}_{cs} - \dot{\varepsilon}_{dc}} \left(\operatorname{erf}\left(\frac{\dot{\varepsilon}_{cs}}{\sqrt{2}\sigma_{\dot{\varepsilon}}}\right) - \operatorname{erf}\left(\frac{\dot{\varepsilon}_{dc}}{\sqrt{2}\sigma_{\dot{\varepsilon}}}\right) \right)
\end{aligned}
\tag{3.62}
$$

The equation 3.62 gives a more general expression of the HPTO statistical linearisation compared to the one derived in [238] since the clutch-declutch control is considered and parametrized in respect to its thresholds $\dot{\varepsilon}_{dc}$ and $\dot{\varepsilon}_{cs}$. Note that the expression 3.62 can be evaluated for $\dot{\varepsilon}_{dc} \to 0$ and $\dot{\varepsilon}_{cs} \to 0$ if the clutch-declutch control is not applied leading the following result:

$$
\begin{aligned}
\lim_{\substack{\dot{\varepsilon}_{dc}\to 0 \\ \dot{\varepsilon}_{cs}\to 0}} B_{H,eq,\dot{\varepsilon}\dot{\varepsilon}} &= \lim_{\substack{\dot{\varepsilon}_{dc}\to 0 \\ \dot{\varepsilon}_{cs}\to 0}} \frac{\Delta p_p D_p}{\dot{\varepsilon}_{cs} - \dot{\varepsilon}_{dc}} \left(\operatorname{erf}\left(\frac{\dot{\varepsilon}_{cs}}{\sqrt{2}\sigma_{\dot{\varepsilon}}}\right) - \operatorname{erf}\left(\frac{\dot{\varepsilon}_{dc}}{\sqrt{2}\sigma_{\dot{\varepsilon}}}\right) \right) \approx \\
&\approx \lim_{\substack{\dot{\varepsilon}_{dc}\to 0 \\ \dot{\varepsilon}_{cs}\to 0}} \Delta p_p D_p \left(\sqrt{\frac{2}{\pi}} \frac{1}{\sigma_{\dot{\varepsilon}}} - \frac{\dot{\varepsilon}_{cs}^2}{3\sigma_{\dot{\varepsilon}}^2 \sqrt{2\pi}} + \mathcal{O}(\dot{\varepsilon}_{cs}^4) \right) = \\
&= \sqrt{\frac{2}{\pi}} \frac{\Delta p_p D_p}{\sigma_{\dot{\varepsilon}}}
\end{aligned}
\tag{3.63}
$$

The relation equals the expected value of a pure sign($\dot{\varepsilon}$) function coherently with the expression derived by Roberts [240] and with the results presented by Silva [238].

The derivation of the terms $B_{H,eq,\delta\varepsilon}$, $B_{H,eq,\varepsilon\delta}$, $K_{H,eq,\delta\varepsilon}$ and $K_{H,eq,\varepsilon\varepsilon}$, associated to the gyroscopic effects and the pendulum elastic recall, follow the same procedure used with the MPTO model.

3.4 Numerical models summary

One of the aims of this dissertation is to compare different ISWEC model with the two type of PTOs under study. Some of the main features and results of

the frequency-domain, spectral-domain and time-domain methods are illustrated in this section by means of a several numerical examples. The main aim is to analyse the SDMs applied to both mechanical and hydraulic PTO, showing their accuracy in terms of extracted power and annual productivity. The SDMs will be employed in the ISWEC design process due to the low computational time and their ability to ensure the statistical fairness of the output results [159]. In contrast, time-domain simulations require a proper number of wave realisations to perform exact evaluations in a statistical sense (mean values and standard deviation of the generated process). However, not all dynamic systems are suitable for a spectral-domain framework and, more important, time-domain simulations highlight the phase relationship between the WEC outputs.

Concerning the MPTO, three different models have been derived in this chapter: the FDM, SDM and the non-linear TDM. Table 3.1 summarizes the main features of such models and the associated system of equations. The FDM represents the most simple model framework for the MPTO, where the gyro-pendulum effects are linearised around $\varepsilon = 0$. Moreover, the electrical generator is considered with no torque limits, meaning that the saturation torque T_{sat} tends to infinity. The SDM version aims to handle the ISWEC non-linearities such the gyroscopic torques and the pendulum elastic recall, along with the PTO saturation. Such non-linearities are statistically linearised through an iterative process to obtain a statistical representation of the system outputs. In the end, the TDM is considered as the most detailed model under study, able to simulate the system dynamics in time-domain with the desired accuracy. The non-linear effects are fully considered as defined in equation 3.4.

	Mechanical PTO		
Label	Gyro-pendulum	Generator	Eq.
FDM	Linear	Linear	3.21
SDM	Stat. linearised	Stat. linearised	3.37
TDM	Non linear	Saturated	3.2

Table 3.1: ISWEC numerical models with MPTO. The label FDM stands for Frequency Domain Model, SDM for Spectral Domain Model and TDM for Time Domain Model. Stat. stands for statistically.

Concerning the HPTO, three models have been derived: the SDM, a simplified TDM and the fully non-linear TDM. Considering the summary in Table 3.2, the SDM considers the simplified version of the hydraulic transmission and the ISWEC non-linearities such the gyroscopic torques, the pendulum elastic recall and the simplified HPTO torque. The simplified TDM is considered as a direct benchmark for the SDM in order to assess the spectral-domain simulation performances in term of output accuracy and computational effort required. Moreover, the complete

TDM is considered to compare the results obtained with the SDM and the simplified TDM to evaluate the error introduced in the extracted power computation due to the simplification of the HPTO torque. In the TDM the non-linear effects are fully considered as defined in equation 3.11.

		Hydraulic PTO		
Label	Gyro-pendulum	Hydraulic circuit	Generator	Eq.
SDM	Stat. linearised	Const. pr. + Stat. linearised	n.m.	3.56
TDMs	Non linear	Const. pr.	n.m.	3.17
TDM	Non linear	Complete	Saturated	3.9

Table 3.2: ISWEC numerical models with HPTO. The label FDM stands for Frequency Domain Model, SDM for Spectral Domain Model and TDM for Time Domain Model. Stat. stands for statistically, const. for constant, pr. for pressure and n.m. for not modelled.

3.5 ISWEC device: a case study

The ISWEC device of reference is the newest designed prototype for the Pantelleria sea site, used as an illustrative example. This device, has been designed with the procedure presented in Chapter 4 choosing a good compromise between device mass, cost and the annual energy production. In particular, the low mass compared to other more productive solutions is chosen to reduce loads on the mooring and decrease the deployment costs of the device. No further details on the design procedure and optimality criteria are given here since an exhaustive analysis on the ISWEC design tool will be carried out in Chapter 5.

Figure 3.3 shows the device geometry, the subsystems layout and the hull profile construction. The case study implements two gyroscopic units which external dimensions are highlighted with continuous line red rectangles. The hull bow, keel and astern are filled with sand ballast in order to obtain the desired inertia along the pitch axis; the ballasts are indicated with dashed grey lines. Table 3.3 summarises the numerical values of the main physical parameters of the WEC. The wave to floater motion transfer functions computed along the wave direction θ=0 are reported in Figure 3.4. In the remainder of this chapter, and unless otherwise specified, a JONSWAP spectrum with H_s=1.5m, T_e=6s and γ=3.3 is retained to generate the single wave results based on the resonance condition of the ISWEC device considered (see Figure 3.4e).

Hull properties		
Label	Value	Unit
Hull length	15	m
Hull height	6.5	m
Hull width	20	m
Device draft	5	m
Hull mass	648000	kg
Pitch inertia	30675000	kgm^2
RAO peak period	6	s
Gyro-pendulum properties		
Label	Value	Unit
Flywheel diameter	2.5	m
Flywheel height	1.25	m
Flywheel mass	22000	kg
Bearings distance	1.75	m
Flywheel inertia (J)	26100	kgm^2
Pendulum mass	2800	kg
Pendulum distance	1.25	m
Mechanical PTO properties		
Label	Value	Unit
Generator rated torque	9900	Nm
Generator rated speed	250	rpm
Generator rated power	260	kW
Gearbox ratio	20	–
Hydraulic PTO properties		
Label	Value	Unit
Pump displacement	20100	cm^3/rev
Hp accumulator volume	250	l
Hp accumulator pre-charge pressure	30	bar
Motor displacement	140	cm^3/rev
Generator rated torque	585	Nm
Generator rated speed	1800	rpm
Generator rated power	110	kW
Max admissible pressure	350	bar

Table 3.3: ISWEC Pantelleria geometrical, inertial, hydrodynamic, gyroscope and PTO properties.

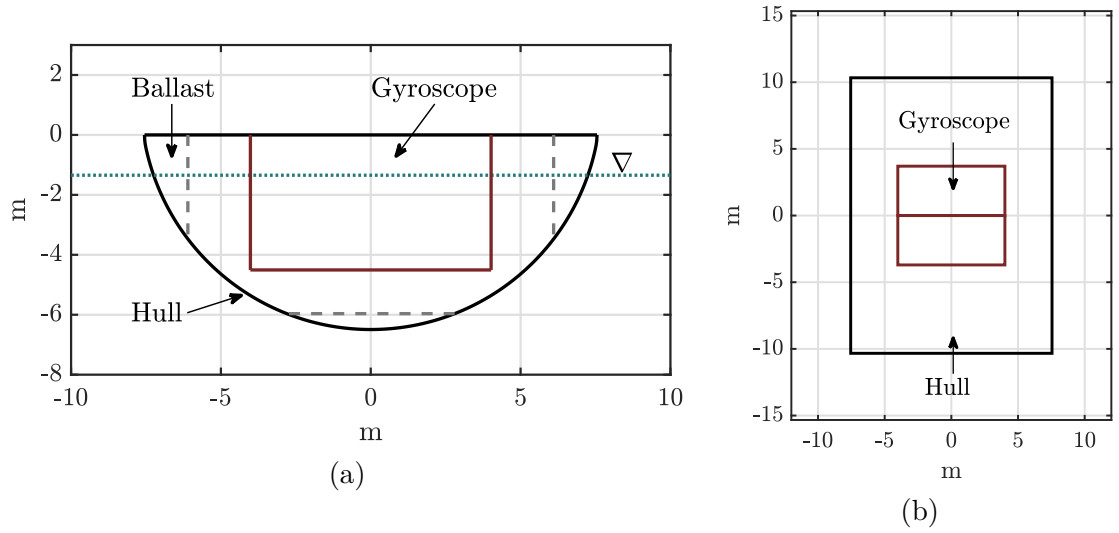

Figure 3.3: Schematic of the ISWEC Pantelleria: (a) lateral view and (b) top view.

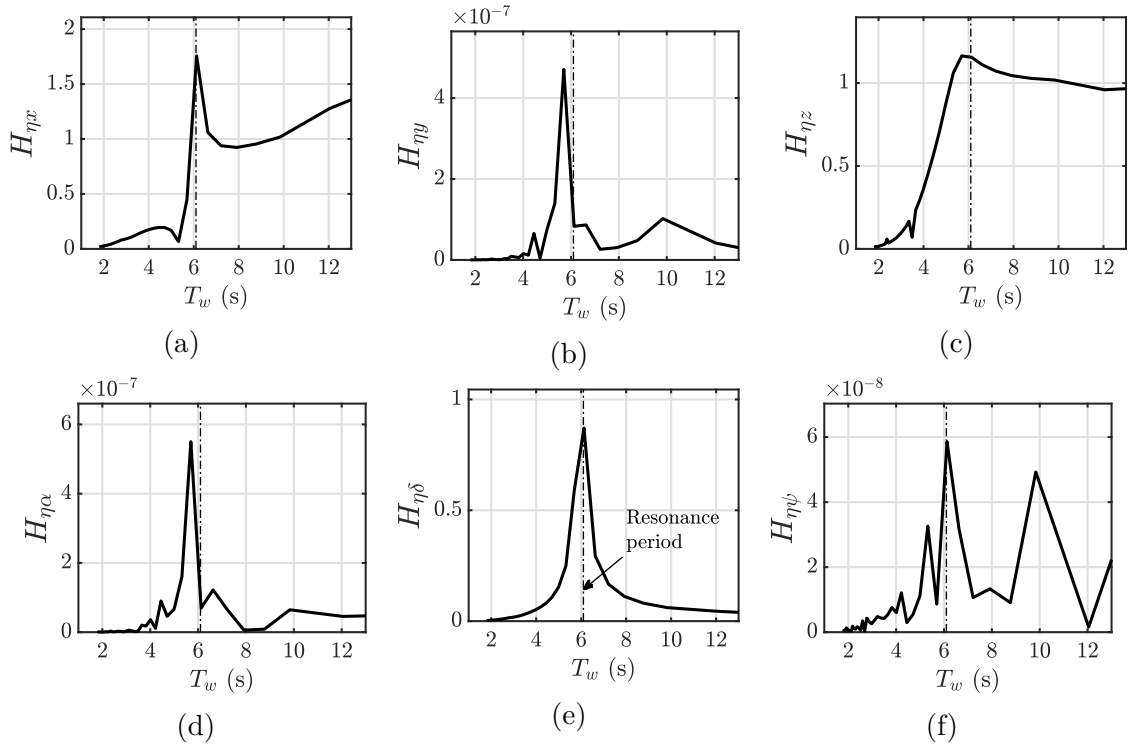

Figure 3.4: RAO of the ISWEC case-study: (a) surge DoF, (b) sway DoF, (c) heave DoF, (d) roll DoF, (e) pitch DoF and (f) yaw DoF. Wave directed along the x-axis.

3.6 Numerical models comparison

In this section the different models proposed are compared in term of gross and net extracted power, and annual productivity in the four sea-site of interest and computational time required.

3.6.1 Performance index of model comparison

Before proceeding further, the performance index employed to calculate the ISWEC performances must be defined. Since the mechanical and hydraulic PTO present evident dissimilarities in term of kinematic behaviour in time-domain, the internal dynamics of the PTO system is not compared here; therefore, only the extracted power and annual energy absorbed are used to measure the performances. In this context, two different parameters are used: average power production and annual productivity.

Average power production

The gross power consists in the mechanical power extracted downstream of the electrical generator. The net power is obtained from the gross power minus all the power losses, as defined in Section 2.5 of Chapter 2. However, only the time-average of the power matters in the productivity calculation. Different calculations are performed for time-domain and frequency/spectral-domain models:

- **Time-domain extracted power**: for the TDM, the mean gross power is obtained from the mean of all the mean gross power obtained for each wave realisation r underlying the same wave spectrum $S_{\eta\eta}$. The expression for the TDM reads:

$$\overline{P}_g = \frac{1}{R}\sum_{r=1}^{R}\langle P_{g,r}(t)\rangle = \frac{1}{R}\sum_{r=1}^{R}\tilde{P}_{g,r} \tag{3.64}$$

  where $\tilde{P}_{g,r}$ is the mean gross power associated to the $r-th$ wave realisation computed with equation 2.91 for the MPTO and equation 2.107 for the HPTO. Similarly, the expression of mean net power follows:

$$\overline{P}_n = \frac{1}{R}\sum_{r=1}^{R}\langle P_{n,r}(t)\rangle = \frac{1}{R}\sum_{r=1}^{R}\tilde{P}_{n,r} \tag{3.65}$$

  For the sake of simplicity, the subscript r will be removed from here on and $\tilde{P}_g$ and $\tilde{P}_g$ will refer to the $r-th$ mean gross and net power, respectively.

- **Frequency- and spectral-domain extracted power**: the generator power interested to the power extraction is equal to the active power obtained multiplying the damping torque exerted by the generator and its angular velocity. Then, from the hypotheses of Gaussian sea in input and Gaussian variables in output, the expected value $\overline{P}_g$ is computed as:

$$\begin{aligned}\overline{P}_g &= \langle c_{g,eq}\dot{\varepsilon}^2 \rangle = c_{g,eq} \int_{-\infty}^{\infty} \dot{\varepsilon}^2 f_{\dot{\varepsilon}}(\dot{\varepsilon})\, d\dot{\varepsilon} = \\ &= \frac{c_{g,eq}}{\sqrt{2\pi}\sigma_{\dot{\varepsilon}}} \int_{-\infty}^{\infty} \dot{\varepsilon}^2 \mathrm{e}^{-\frac{\dot{\varepsilon}^2}{2\sigma_{\dot{\varepsilon}}^2}}\, d\dot{\varepsilon} = \\ &= \frac{c_{g,eq}}{\sqrt{2\pi}\sigma_{\dot{\varepsilon}}} \left(\sigma_{\dot{\varepsilon}}^2 \dot{\varepsilon} \mathrm{e}^{-\frac{\omega_g^2}{2\sigma_{\dot{\varepsilon}}^2}} \Big|_{-\infty}^{\infty} + \int_{-\infty}^{\infty} \sigma_{\dot{\varepsilon}}^2 \mathrm{e}^{-\frac{\dot{\varepsilon}^2}{2\sigma_{\dot{\varepsilon}}^2}}\, d\dot{\varepsilon} \right)\end{aligned} \tag{3.66}$$

The first term inside the parenthesis is null in the integration limits and the second term is the well-known *Gaussian Integral*, solved as follows:

$$\begin{aligned}\overline{P}_g &= \frac{c_{g,eq}}{\sqrt{2\pi}\sigma_{\dot{\varepsilon}}} \left(\sqrt{\frac{\pi}{2}} \sigma_{\dot{\varepsilon}}^3 \operatorname{erf}\left(\frac{\dot{\varepsilon}}{\sqrt{2}\sigma_{\dot{\varepsilon}}} \right) \Big|_{-\infty}^{\infty} \right) = \\ &= c_{g,eq}\sigma_{\dot{\varepsilon}}^2\end{aligned} \tag{3.67}$$

which is coherent with the formula used in [238, 246]. For the sake of clarity, in the SDM the equivalent damping coefficient $c_{g,eq}$ is computed through the iterative process described in Section 3.3.1, with equation 3.52 for the MPTO and with equation 3.62 or 3.63 for the HPTO depending if the clutch-declutch logic is or it is not implemented. Whereas, for the FDM model, $c_{g,eq}$ it is equal to the original damping coefficient c_g chosen for the time-domain simulation.

Concerning the net power, the mean power losses $\overline{P}_l$ are approximated in spectral-domain considering formulae 2.112, 2.113, 2.114, 2.122 and 2.123, substituting the expected values of the required system outputs and variables. For what concern the seal, aerodynamic, electric and base losses, the formulae 2.113, 2.116, 2.119, 2.120, 2.121 and 2.123 are statistically valid in frequency- and spectral-domain: the expected value of $\dot{\varphi}$ is exactly itself since the flywheel speed is constant during the single wave simulation and both base and electric losses are assumed independent from the system variables. No other variables and system outputs concur in these losses calculations. However, in time-domain the bearing losses are computed through the time-average of the bearing reactions obtained with equations 2.111 as a function

of several system variables such as $\dot{\delta}$, ε and $\dot{\varepsilon}$. In frequency and spectral domain, the procedure is simplified. First the expected value of the radial bearing force component is obtained as follows:

$$\begin{aligned}\overline{F}_{rad} &= \left\langle \sqrt{\left(\frac{J\dot{\varphi}\dot{\delta}\cos(\varepsilon)}{d_b}\right)^2 + \left(\frac{J\dot{\varphi}\dot{\varepsilon}}{d_b}\right)^2 + \left(\frac{1}{2}m_{fw}g\sin(\varepsilon)\right)^2}\right\rangle \approx \\ &\approx \left\langle \sqrt{\left(\frac{J\dot{\varphi}\dot{\varepsilon}}{d_b}\right)^2 + \left(\frac{1}{2}m_{fw}g\sin(\varepsilon)\right)^2}\right\rangle\end{aligned} \tag{3.68}$$

Equation 3.68 can be computed numerically using the bi-variate distribution of ε and $\dot{\varepsilon}$. The simplifications applied on equation 3.68 is justified in Figure 3.5 where the magnitue of the three different contribution collected in equation 3.5 are compared, showing that the gyroscopic reaction and the flywheel weight are almost one order of magnitude larger than the gyroscopic torque contribution.

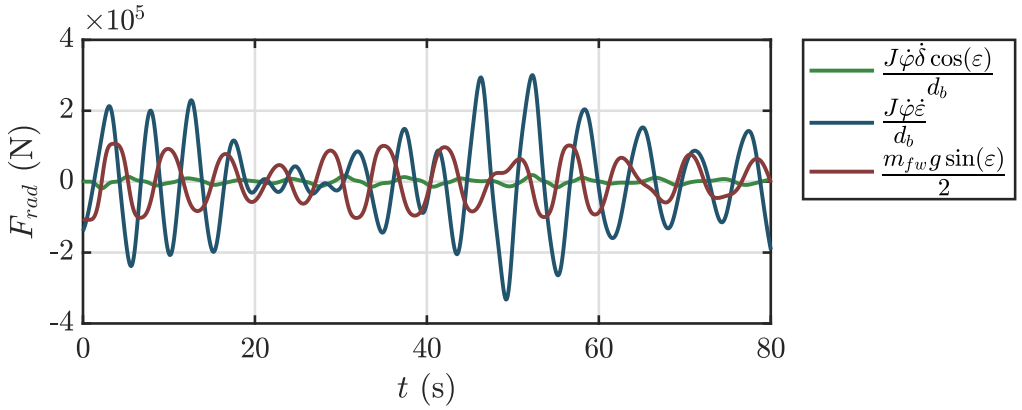

Figure 3.5: Example of radial load contributions discharged on one radial bearing. The ISWEC is simulated under irregular wave profile that matches the device resonance conditions.

For what concern the axial bearing reaction, the following relation holds:

$$\overline{F}_{ax} = m_{fw}g\langle|\cos(\varepsilon)|\rangle \tag{3.69}$$

Equation 3.69 can be computed numerically. Then, the expected values of total forces discharged on thrust and radial bearings are used in equations 2.112.

In addition, for the HPTO, the hydraulic circuit efficiency has to be considered for a correct evaluation of the net power extracted from the circuit. Here, the

gross power is computed with the Equation 3.67 considering the pump torque and speed, since the rest of the hydraulic transmission is not modelled. Then, through the expected values of the mean absolute pump torque and angular speed, the expected pump efficiency is computed via the lookup table shown in Figure 2.14b. In the end, the motor-generator efficiencies are considered constant, as specified in Section 2.4.2. In the SDM the valve pressure drops and the wasted power through the relief valve are not considered.

Annual productivity

The gross and net annual energy produced are calculated weighting the gross and net power matrices with the occurrences of the specific site in analysis with the following formulae:

$$E_g = \frac{8760}{10^6} \sum_{n_w=1}^{n_W} \overline{P}_{g,n_w} o_{n_w} \tag{3.70a}$$

$$E_n = \frac{8760}{10^6} \sum_{n_w=1}^{n_W} \overline{P}_{n,n_w} o_{n_w} \tag{3.70b}$$

where n_W is the total number of waves, $\overline{P}_{g,n_w}$ the average gross power extracted with the $n_w - th$ wave, $\overline{P}_{n,n_w}$ the average net power extracted with the $n_w - th$ wave and o_{n_w} the annual occurrence associated to the $n_w - th$ wave. The coefficient $\frac{8760}{10^6}$ converts the annual productivity in MWh/y.

3.6.2 Influence of finite-length wave realisations

Determining the output of a wave energy system under a specified wave spectrum in time-domain (in terms, for example, of power absorption, or any other physical variable of interest), requires the generation of finite-duration wave time series, or realisations, which accurately reflect the statistical properties of the underlying sea state. For a linear WEC model, the following two procedures are statistically equivalent [172]:

- Procedure 1 (P1): generate time series of the process η using the HRA method and obtain steady-state outputs of the WEC using a TDM; then, compute the outputs statistics to obtain the desired performance of the WEC (e.g. mean extracted power);
- Procedure 2 (P2): Using directly the $S_{\eta\eta}(\omega)$ instead of generate time series and obtain the SDF of the WEC outputs $\mathbf{S}_{XX}(\omega)$ through the system transfer function $\mathbf{H}_{\eta X}(\omega)$.

The procedure P2 is, generally, one/two order of magnitude faster than P1 since, with a linear system, only one frequency domain simulation is required to obtain the WEC output in term of mean values and standard deviations. However, if the system is non-linear, the procedure P2 cannot be applied directly and a linearisation (if possible) is required.

Understanding the statistical behaviour of $\overline{P}$ in finite-length simulations is crucial, for example, to determine how many simulations are necessary, or how long they should be, to obtain an accurate estimate of $\overline{P}$. Furthermore, one may not only want to know the average power output of the WEC, but also how the WEC performance over a finite duration fluctuates around its average value. In this section, the non-linear TDM model of ISWEC subject to simulated incident waves is considered to calibrate the parameters of procedure P1. The influence of the finite-length wave series is explored comparing the WEC performances for different number of realisation and simulation durations. For the sake of simplicity, only the single wave results are presented assuming representative of the behaviour of the ISWEC system in time-domain. Each simulation is run with the optimal control parameters that maximize the net extracted power ($\dot{\varphi}^*$ for the flywheel speed, k_g^* and c_g^* for the MPTO, and $\dot{\varepsilon}_{cs}^*$ and β_g^* for the HPTO).

WEC performance estimation

Concerning both the wave signal duration T and the number of HRA realisations R, it must be assessed that the numerical experiments produce accurate power estimates. First, for each device, TDM simulations are run in 50 different random wave inputs, over a range of T values. The results, in terms of gross and net average power absorption, are plotted in Figure 3.6 for what regards the MPTO and in Figure 3.7 for the HPTO one. Figure 3.6 indicates that, for the MPTO-based ISWEC, the average gross and net power fall within 5% of the reference value[2] at T=180s. Concerning the HPTO device, it is found that T=600s can be satisfying for the convergence of the device performances. However, to ensure that the average power production falls within the convergence interval also for ISWEC devices with slower dynamics (e.g. devices with larger flywheel units, bigger accumulators, etc.) and higher wave periods, the durations are slightly increased to T=250s and T=800s for the MPTO and HPTO, respectively. Figures 3.6 and 3.7 inherently show that, in order to obtain a fully developed steady-state response of the WEC, a time-series of one order of magnitude longer than the longer dominant period of the system has to be generated, allowing the system to reach steady-state conditions. For our case-study, the response time of the ISWEC system is analysed with a regular wave force exiting only the pitch DoF (δ-axis), in the form $\mathrm{f}_{E\delta}(t) = \mathrm{f}_{E\delta_0} \sin\left(\frac{2\pi}{T_w} t\right)$.

[2]The reference value is the gross or net power extracted with the higher simulation duration T_{max}.

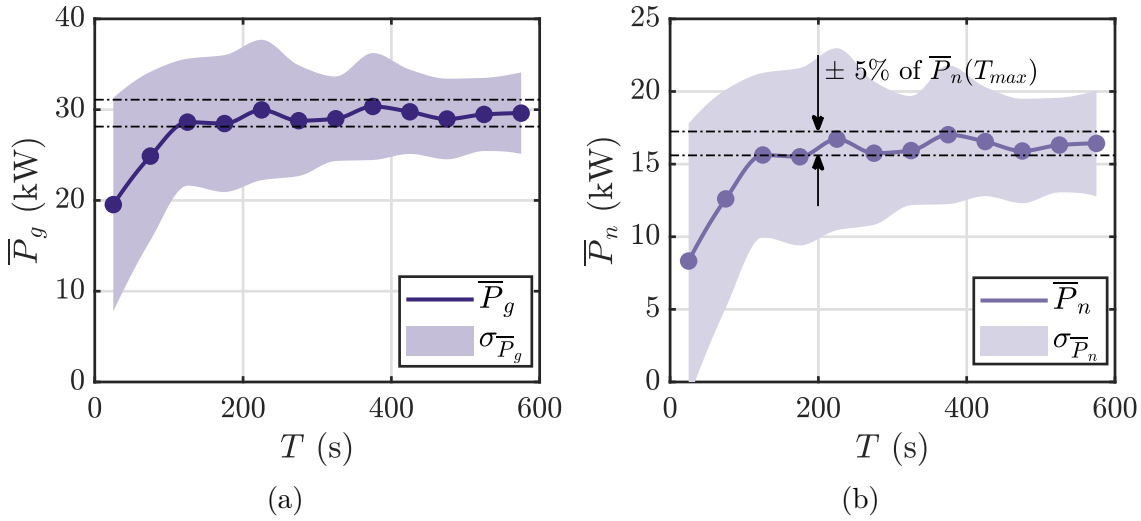

Figure 3.6: (a) Gross and (b) net average extracted power with the MPTO for different simulation durations T; the shaded area represents the standard deviation due to the random nature of the HRA realisations; dash-dot lines indicate the ±5% interval of the power obtained with the largest duration T_{max}.

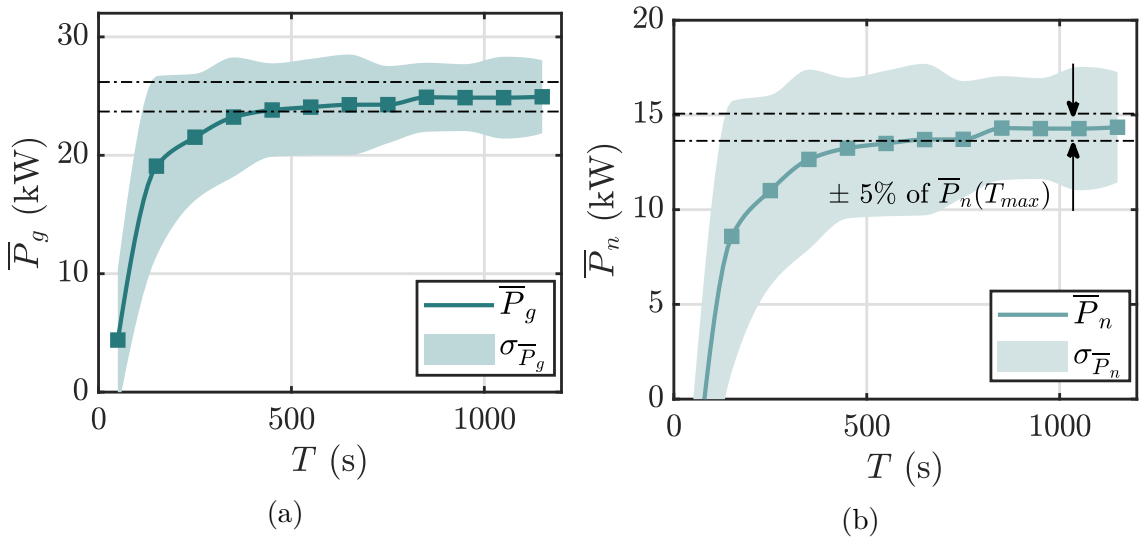

Figure 3.7: (a) Gross and (b) net average extracted power with the HPTO for different simulation durations T; the shaded area represents the standard deviation due to the random nature of the HRA realisations; dash-dot lines indicate the ±5% interval of the power obtained with the largest duration T_{max}.

From Figure 3.8 it is possible to demonstrate that the mechanical and hydraulic transmission reach a steady state in a different manner and, intuitively, the HPTO system is dominated by the accumulator dynamic response, which is at least one

order of magnitude slower than the wave periodicity.

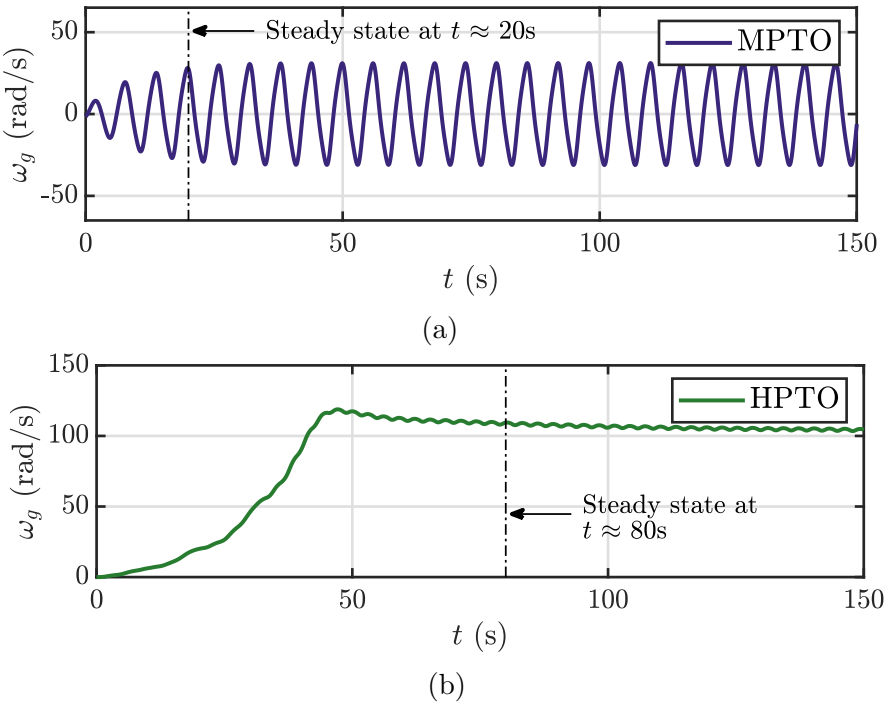

Figure 3.8: (a) MPTO and (b) HPTO generator angular speed time series for a regular wave simulation. The generated regular wave force is in the form $\mathrm{f}_{E\delta}(t) = \mathrm{f}_{E\delta_0} \sin\left(\frac{2\pi}{T_w}t\right)$, where $\mathrm{f}_{E\delta_0} = 10^6 Nm$ and $T_w = 6s$ and acts only on the pitch DoF.

Concerning the number of wave realisations, increasing number of wave profiles have been tested to obtain the minimum number of repetitions to guarantee the convergence of the system production. Figure 3.9 demonstrates that, for the MPTO, 30÷40 repetitions are enough to stabilize both gross and net extracted power and their standard deviation $\sigma_{\overline{P}}$. The same consideration is valid for the HPTO, which gross and net power results are depicted in Figure 3.10. Increasing the number of repetitions over R=40 does not lead to significant improvements on the average performances. In this regard, for both mechanical and hydraulic PTO, 40 wave realisations are performed in time-domain.

Computational time

In Chapter 4 the ISWEC design tool based on a evolutionary algorithm is presented and discussed. As will be described, thousands of different ISWEC configurations will be evaluated to design the optimal ISWEC device; moreover, each device will be numerically simulated R-times for each wave spectra of interest and its control parameters optimized with a simplex search method [248], resulting

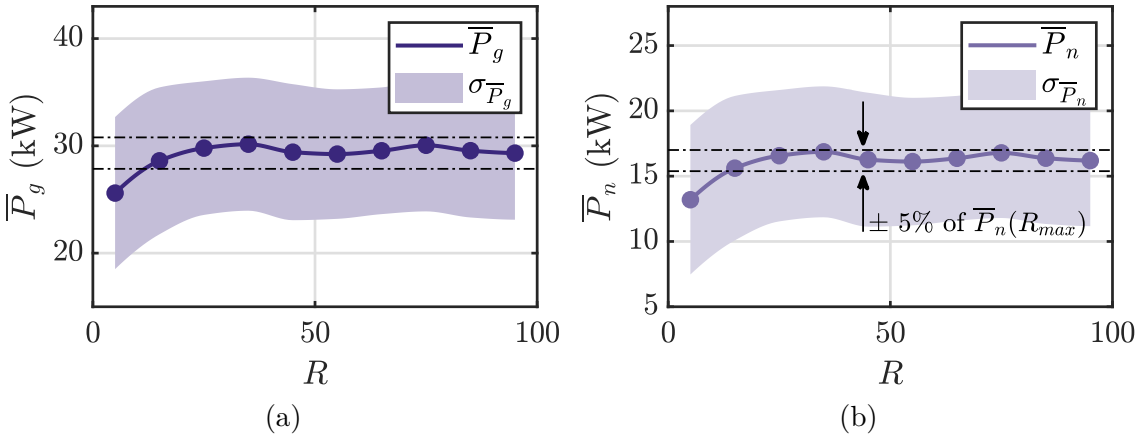

Figure 3.9: (a) Gross and (b) net average extracted power with the MPTO for different realisations R of the same wave spectrum; the shaded area represents the standard deviation due to the random nature of the HRA realisations; dash-dot lines indicate the ±5% interval of the power obtained with the highest number of realisations R_{max}.

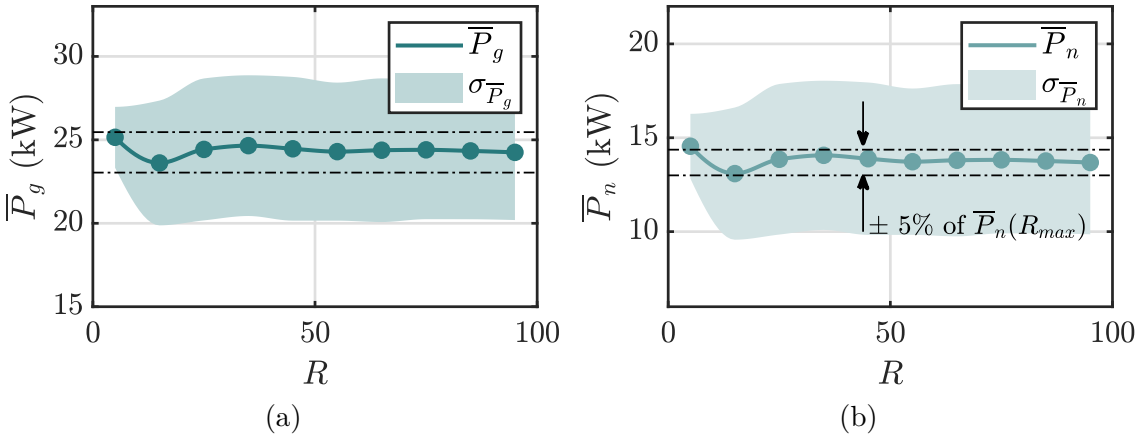

Figure 3.10: (a) Gross and (b) net average extracted power with the HPTO for different realisations R of the same wave spectrum; the shaded area represents the standard deviation due to the random nature of the HRA realisations; dash-dot lines indicate the ±5% interval of the power obtained with the highest number of realisations R_{max}.

in millions of time-domain simulations. Limit the computational burden becomes crucial to avoid weeks of simulations. Figure 3.11 aims to evaluate the mean computational time required for different simulation durations T. As expected, the MPTO performs quicker than the HPTO one since a more articulated numerical model is required. The slope of the linear interpolations (dash-dot lines of Figure 3.11) might be of interest since no relevant increase of $\bar{t}_{CPU}$ appears increasing

the simulation time T, specially for the MPTO. In fact, the offset near $T = 0$ is due to the Simulink routines and initializations, despite the "Fast restart" option has been used to avoid compiling the model for each wave realisation [249]. In this regard, if needed, the simulation time T could be increased with no relevant raise of $\bar{t}_{CPU}$.

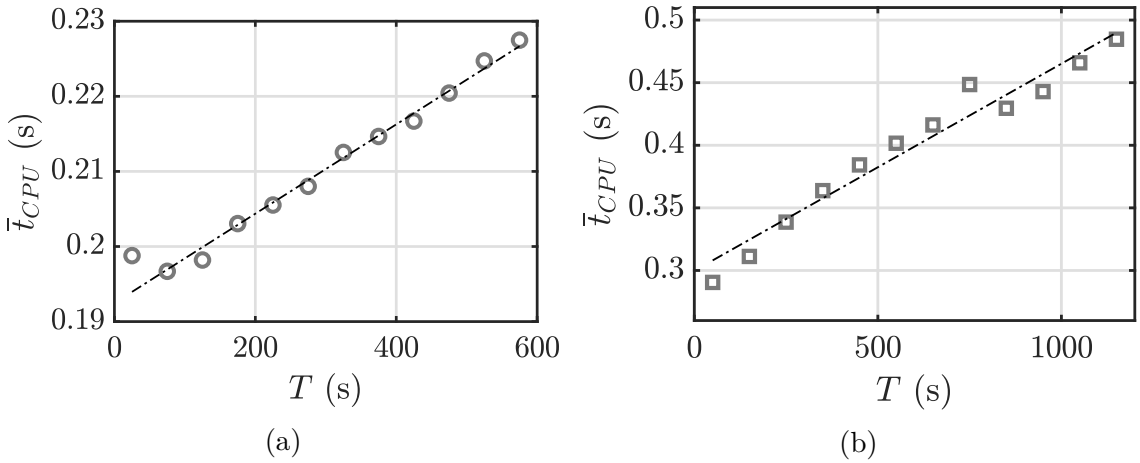

Figure 3.11: Average CPU time for different for different simulation durations T: (a) MPTO and (b) HPTO; dash-dot lines indicate the linear regression of the $\bar{t}_{CPU}$ points. All computation times are obtained from a Simulink® model run on a 2.8 GHz, 8-core Intel® processor.

3.6.3 Mechanical PTO model comparison

Starting with the MPTO, three models are compared in this section in term of average extracted power, annual productivity and computational time demanded for a single simulation. The TDM model is chosen as a point of comparison for the FDM and SDM. The comparison can be carried out by computing TDM results for several control parameters, such the generator damping c_g, and a set of the saturation limits T_{sat} to obtain different working conditions of the WEC. The aim is to stress the main non-linearities of the time-domain system defined in equation 3.2 and examining how the non-linear effects changes the frequency- and spectral-domain accuracy. Note that the FDM and SDM directly solves the system in one single frequency/spectral domain simulation. In contrast, to obtain a satisfactory characterisation of the WEC response in a given sea state in time-domain, 40 time series of the Gaussian wave input must be generated in a way which is statistically consistent with the Gaussian assumption. Therefore, for a relevant comparison, the performance of interest are evaluated as the average value of that performance

between all the realisations[3]. The relative percentage error encountered is computed as follows for a generic output X:

$$\Delta X = \left| \frac{X - X_{ref}}{X} \right| 100\% \tag{3.71}$$

where the reference value X_{ref} is the time-domain output. In this regard, it is possible to define an "acceptable zone" where the percentage error with the TDM remains below a given threshold, for example 10%. This value is considered acceptable since the main scope of the SDM is to design the ISWEC system (see Chapter 5) and a further evaluation of the designed solutions is performed in time-domain to precisely evaluate the their performances. Beside the results accuracy, the computational time has to be bounded to perform the ISWEC design within a reasonable time.

Influence of the generator damping

The methodology outlined above is applied to the ISWEC model, considering first the influence of the generator damping c_g. As reported in Figure 3.12, both the gross and net average power are compared for the three models under study varying the coefficient c_g. The extracted power computed with the FDM is higher than the SDM and TDM ones for all the simulation conditions. In particular, for small generator damping the error increases since the gyroscope shaft exhibits higher precession angle ε in amplitude due to a less restrained gyroscope motion. On the other hand, the SDM traces the output power of the TDM for most of the c_g values, showing an almost perfect overlap for $c_g > 2 \cdot 10^4$.

Figure 3.13a demonstrates the accuracy of the SDM against the FDM one. The gross power percentage error is lower than 10% for most the simulations, reaching a peak of 15% near the smallest c_g considered. The net power percentage error shows almost the same behaviour breaking the 10% limit for a $c_g < 1.5 \cdot 10^4$. The effect of the sine and cosine linearisation is highlighted in Figure 3.13b. The correction coefficient T_{gc}, defined in equation 3.49, represents the magnitude of the $\cos(\varepsilon)$ expected value that influences the gyroscopic torques and the pendulum recall. As expected, the accuracy of the SDM decrease when the expected value of $\cos(\varepsilon)$ diminishes, meaning that the precession angle ε grows. Overall, the net power error is higher than the one associated with the gross power. As described in Section 3.6.1, the radial loads associated to the flywheel radial bearings are approximated through the equation 3.68 and this affects the accuracy of the net power computation. However, the net power percentage error stands below the 10% threshold for T_{gc}

[3]For example, the average net power extracted $\overline{P}_n$ for a single wave spectrum $S_{\eta\eta}$ is computed averaging all the single mean net power $\tilde{P}_n$ as defined in equation 3.65.

values greater to 0.65, that is equivalent to a mean precession angle amplitude almost equal to 50°.

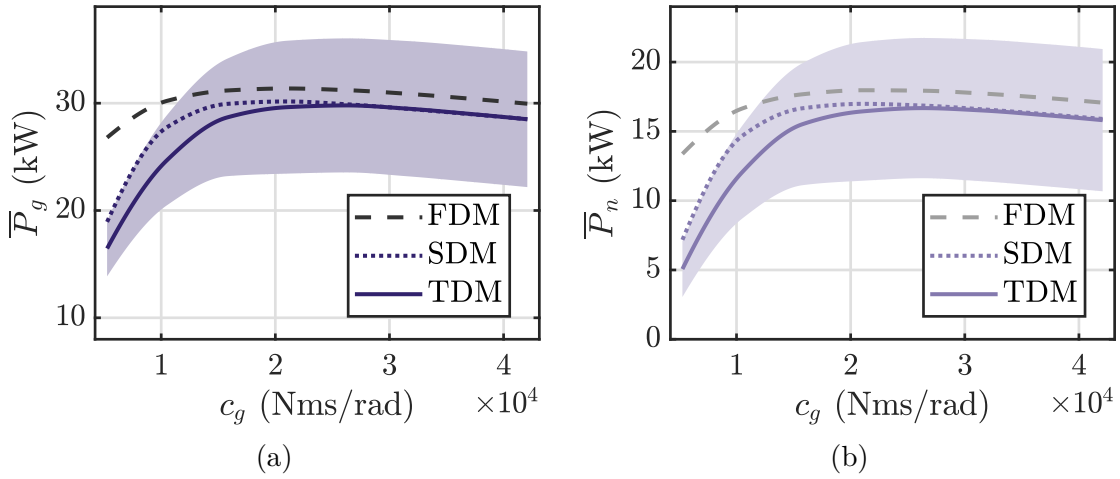

Figure 3.12: Extracted power comparison with MPTO in respect to the damping coefficient of the generator c_g: (a) gross power and (b) net power. The shaded area stands for the standard deviation of the time-domain results.

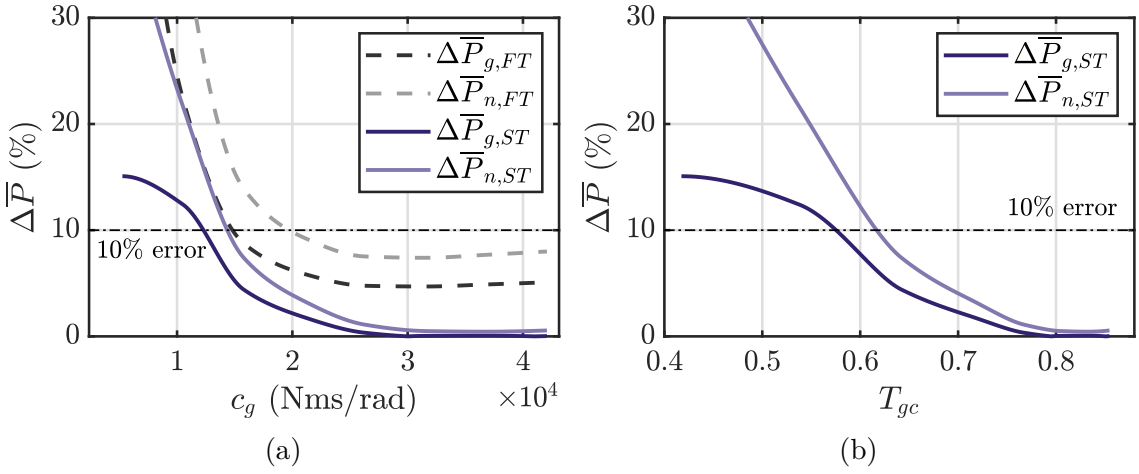

Figure 3.13: Percentage error on the extracted power: (a) percentage error on gross and net power in respect to the damping coefficient of the generator c_g; (b) percentage error on gross and net power in respect to the correction coefficient T_{gc}.

The effect of the so-called statistical linearisation is highlighted in Figure 3.14. Here, the equivalent angular momentum $L_{eq} = J\dot{\varphi}e^{\frac{\sigma_\varepsilon^2}{2}}$ and the equivalent pendulum elastic recall $k_{p,eq} = m_p d_p g e^{\frac{\sigma_\varepsilon^2}{2}}$ are reported as a function of the generator damping c_g. As the system deviates from its equilibrium position, where the approximations

$\cos(\varepsilon) \approx 1$ and $\sin(\varepsilon) \approx \varepsilon$ are valid, the statistical linearisation modulates the linearised equivalent term to account for the non-linear effects. In fact, as the damping coefficient decrease and the amplitudes of ε get larger, the gyroscopic effects are reduced to account for lower values of $\cos(\varepsilon)$. In the same way, the pendulum recall, that can be linearly approximated to $m_p d_p g \varepsilon$, is corrected with lower values of $k_{p,eq}$ to consider the effect of the $\sin(\varepsilon)$ that, for large values of ε, diverges from its approximation $\sin(\varepsilon) \approx \varepsilon$.

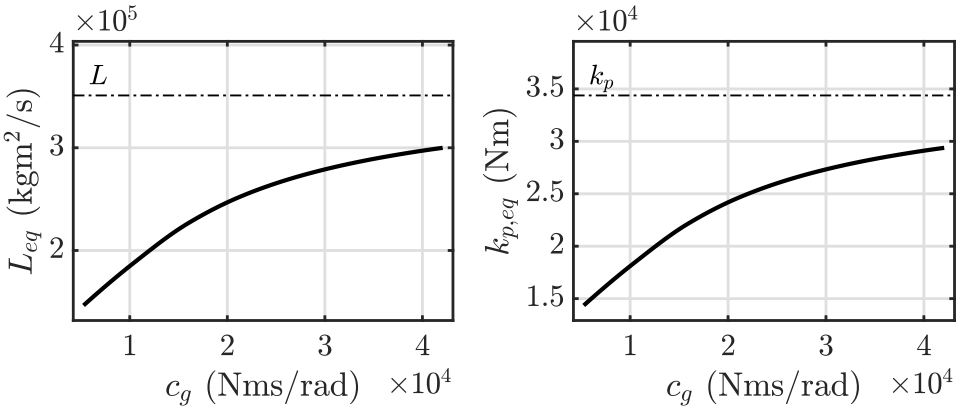

Figure 3.14: Effect of the generator damping c_g on ISWEC physical parameters $L = J\dot{\varphi}$ and $k_p = m_p d_p g$.

Figure 3.15 shows the precession angle probability functions for all the single wave realisations $\tilde{f}_\varepsilon$, their mean value $\overline{f}_\varepsilon$ and the pdf obtained with the SDM simulation f_ε.

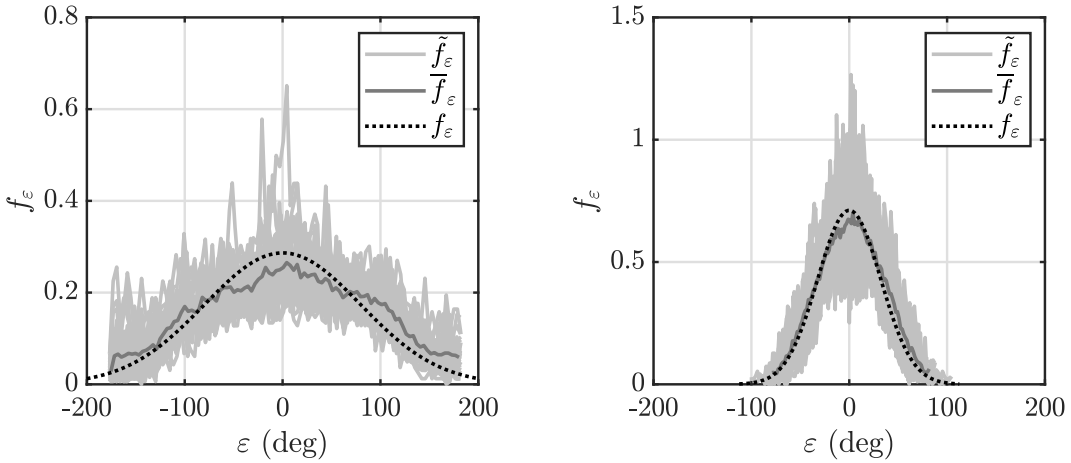

Figure 3.15: Precession angle ε distributions for two different generator damping: (a) $c_g = 3.5 \cdot 10^3 Nms/rad$ and (b) $c_g = 4.2 \cdot 10^4 Nms/rad$

Coherently with the outcomes above, for high values of the generator damping the spectral domain pdf traces accurately the mean pdf computed with the TDM. Figure 3.15b implies another important result: the time-domain outputs are calculated averaging all the outputs for each the single wave realisation $\tilde{\eta}$ underlying the same wave spectrum $S_{\eta\eta}$; since the mean TDM pdf and the SDM pdf are overlapped, the time-domain simulations are considered statistically correct in respect to a single spectral-domain simulation.

The considerations of this section are reasonably valid also for the influence of the generator elastic recall k_g, where large values of k_g should limit the excursion of ε reducing the magnitude of the non-linearities. The same argument can be applied to the flywheel speed $\dot{\varphi}$, determining the magnitude of the angular momentum of the system and influencing the magnitude of the gyroscopic torques.

Influence of the generator saturation

The same procedure is applied to assess the influence of the saturation limit T_{sat}. The electric generator torque T_g is limited to avoid to overcome the maximal admissible torque and save the machine integrity. An example of how T_{sat} affects the generator torque is depicted in Figure 3.16.

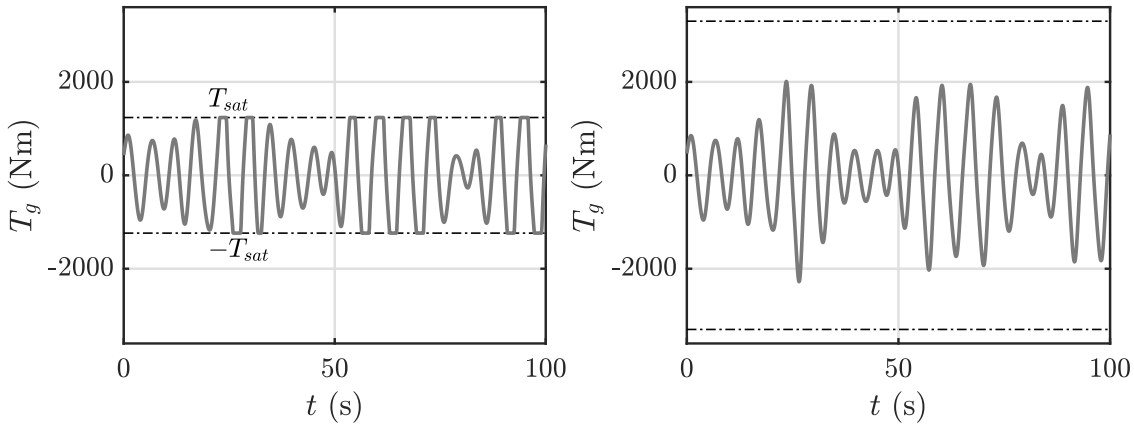

Figure 3.16: Generator torque time serie examples for two different values of T_{sat}.

Figure 3.17 compares the gross and net average extracted power for different values of T_{sat}. Such a figure points out that small saturation torques results in significant percentage error in terms of absorbed power of the FDM and, remarkably, that error is more significant close to the minimal value of T_{sat}. On the other hand, the SDM performs better in presence of PTO saturation compared to the FDM although a slight drop in extracted power appears decreasing the saturation limit. The saturation is a stronger non linearity in respect to the $\cos(\varepsilon)$ and $\sin(\varepsilon)$ ones and the SDM seems not completely able to handle this type of non-linear effect. In

fact, focusing on Figure 3.18a, the error on the extracted power overcome the 10% threshold for values of T_{sat} lower than 1600 Nm.

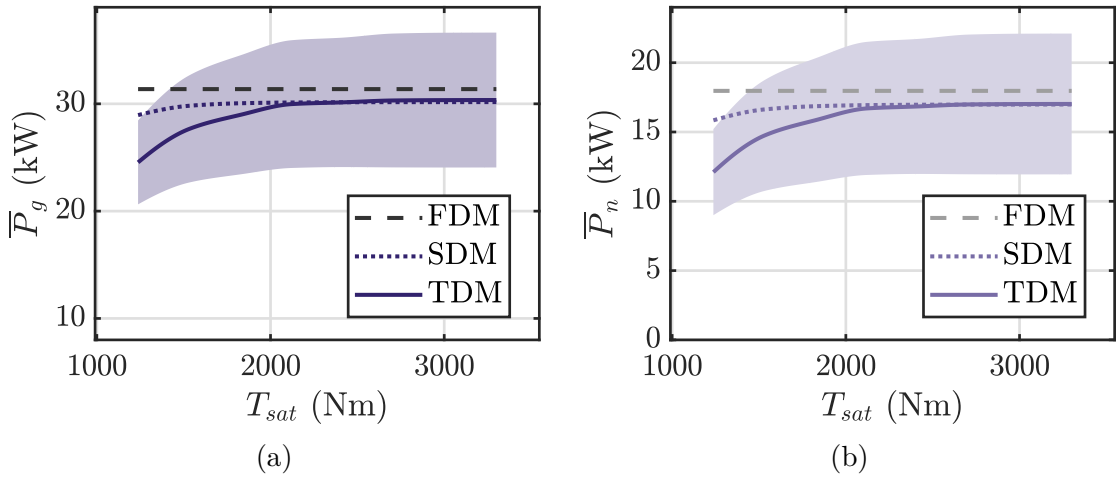

Figure 3.17: Extracted power comparison with MPTO in respect to the saturation torque of the generator T_{sat}: (a) gross power and (b) net power. The shaded area stands for the standard deviation of the time-domain results.

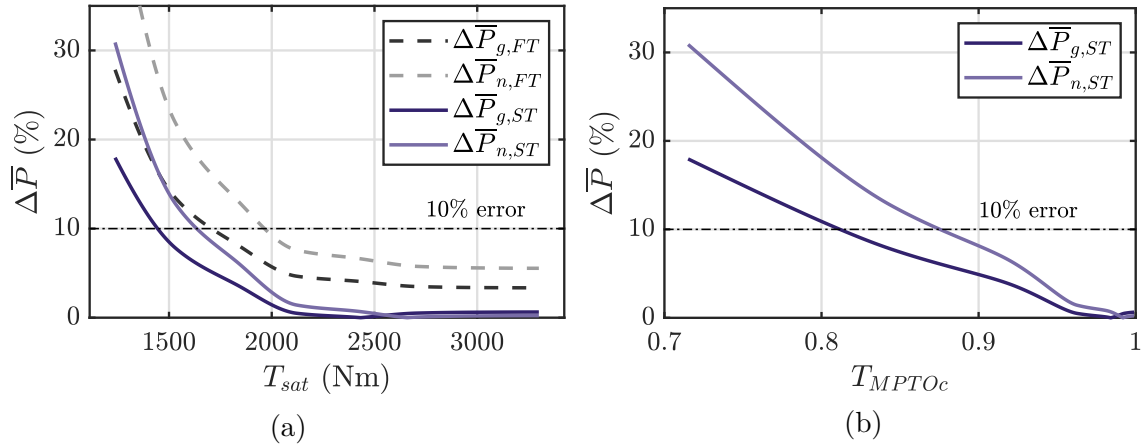

Figure 3.18: Percentage error on the extracted power: (a) percentage error on gross and net power in respect to the saturation torque of the generator T_{sat}; (b) percentage error on gross and net power in respect to the correction coefficient T_{MPTOc}.

The correction coefficient T_{MPTOc}, which influence is shown in Figure 3.18b, constitutes a measure of how much the electric generator is saturated. c_g and k_g are scaled down to account for the PTO saturation through the coefficient T_{MPTOc}. Reliable results are obtained for T_{MPTOc} higher than 0.9, when the PTO is not

heavily saturated. Similar to Figure 3.14, Figure 3.19 shows how the generator control parameters are corrected for increasing values of T_{sat}. As derived in Section 3.3.2, the saturation limit T_{sat} inflects both k_g and c_g reducing its magnitude in respect to the time-domain values.

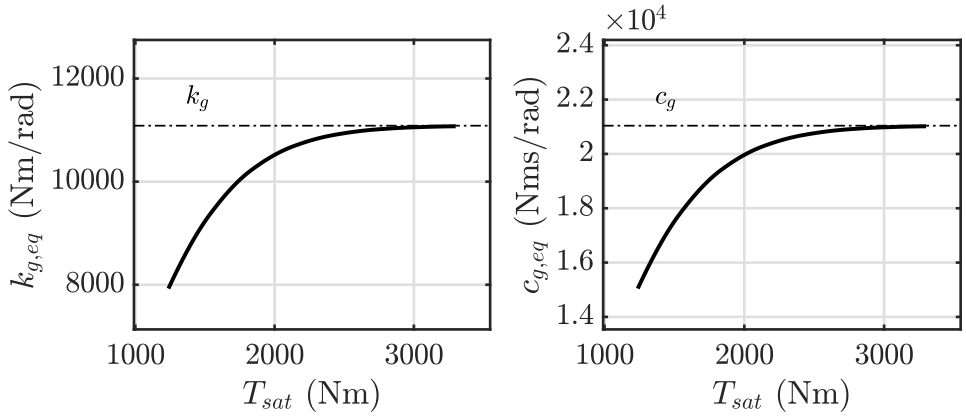

Figure 3.19: Effect of the saturation torque T_{sat} on the generator equivalent control parameters $k_{g,eq} = k_g T_{MPTOc}$ and $c_{g,eq} = c_g T_{MPTOc}$.

Annual productivity comparison

Despite the promising results reported in Figure 3.12 and 3.17, the single wave analysis is not enough to demonstrate the effectiveness of the spectral-domain simulation. The analysis is extended to the whole scatter diagram computing the annual productivity in frequency-, spectral- and time-domain for all the sea-sites of interest. Two different cases are considered: first, the PTO saturation limit is removed to avoid the saturation of the PTO torque and to analyse only the effect of the cos(ε) and sin(ε) linearisation; then, the T_{sat} is imposed to $1500Nm$ to focus on the influence of the PTO saturation.

The output of the productivity analysis is reported in Figure 3.20 for the system with no saturation imposed. Figure 3.20 compares the gross and net annual productivity for Alghero, Balder, Capo Verde and Pantelleria, showing that the FDM overestimates the system performances more than the SDM one. The percentage error on the annual productivity is shown in Figure 3.21. The effectiveness of the SDM is demonstrated since, on average, the percentage error on the annual gross and net productivity is lower than 7%, specially in Alghero and Balder. In particular, as presented in Figure 2.7, the Balder sea-site is more energetic than the other three locations, leading to larger WEC displacements that may enhance the system non linearities. However, the SDM performs with acceptable accuracy also in high energetic seas, maintaining an error on the net annual productivity lower

than 5% in the Balder. The FDM overestimates on average almost 12% the gross annual productivity and almost of 15% the net one.

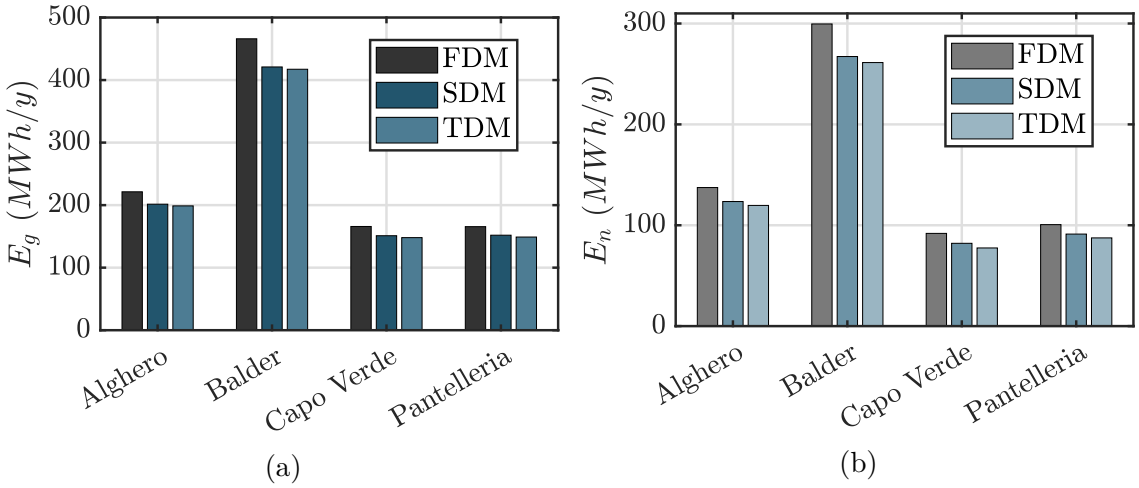

Figure 3.20: Annual productivity for different sea-site of interest with a MPTO: (a) gross productivity and (b) net productivity. The saturation is not considered here.

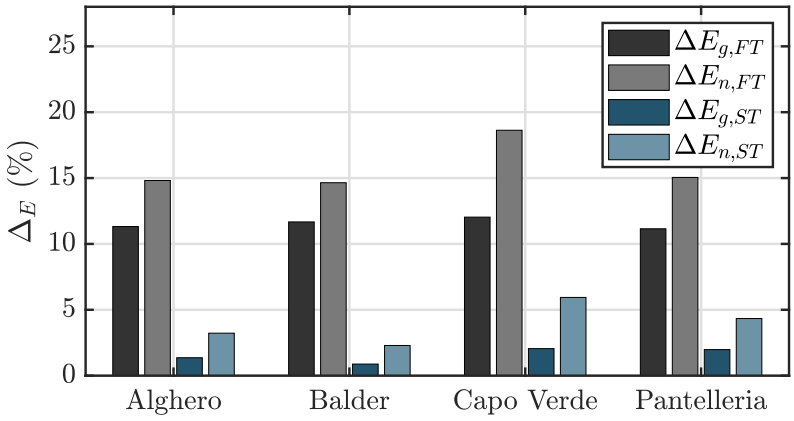

Figure 3.21: Percentage error on gross and net annual productivity with the MPTO. The grey bars compare the FDM with the TDM while the blue bar the SDM with the TDM. The saturation is not considered here.

Interesting results are obtained when the saturation is considered. Figure 3.22 remarks the ability of the SDM to handle the non-linearities of the ISWEC. When the saturation of the PTO is imposed, the FDM overestimates the gross annual productivity up to 24% and the net one up to 34%, as shown in Figure 3.23. The most striking result is that the SDM accuracy for the net productivity is always

below the 12% reaching its best value for the Balder site, at almost 6% of percentage error, despite the low saturation limit imposed on the PTO.

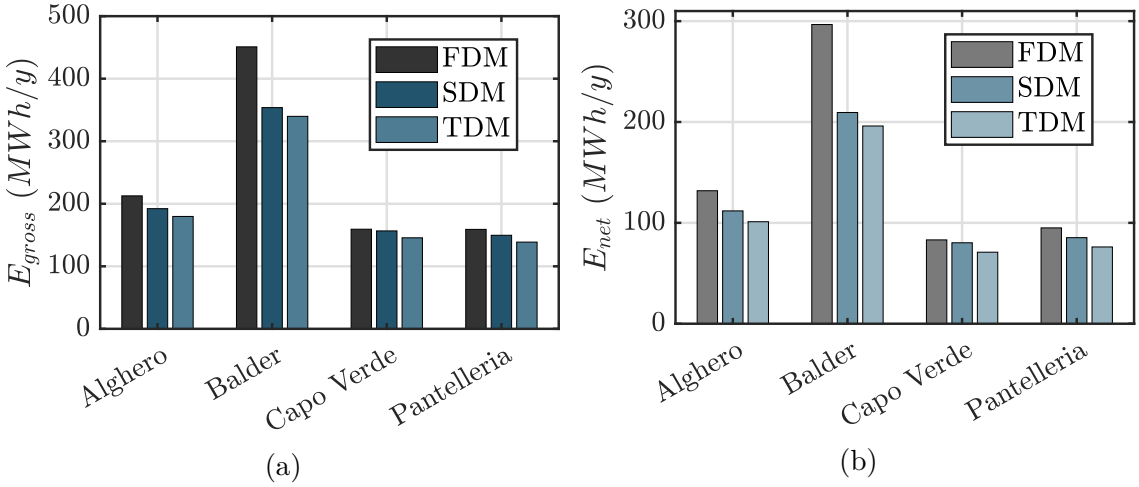

Figure 3.22: Annual productivity for different sea-site of interest with a MPTO: (a) gross productivity and (b) net productivity. The saturation is considered equal to T_{sat}=1500 Nm.

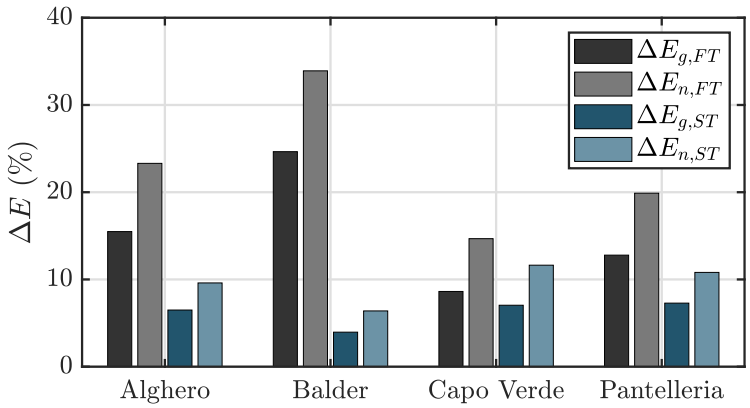

Figure 3.23: Percentage error on gross and net annual productivity with the MPTO. The grey bars compare the FDM with the TDM while the blue bar the SDM with the TDM. The saturation is considered equal to T_{sat}=1500 Nm.

3.6.4 Hydraulic PTO model comparison

Concerning the HPTO, three models are compared in term of average extracted power, annual productivity and computational time demanded for a single simulation. The TDM model is chosen as a point of comparison for the SDM and the

simple TDM (TDMs). In particular, the simple TDM is used as a benchmark to assess the validity of the statistical linearisation applied in the SDM. The same procedure followed for the MPTO is repeated with the HPTO models: the comparison is carried out by computing TDM results for several control parameters, such the generator damping β_g, and different clutching speed thresholds $\dot{\varepsilon}_{cs}$ to obtain different working conditions. Here, the non-linearities are represented by the sign($\dot{\varepsilon}$) function used to model the HPTO torque as a Coulomb-like action discharged on the primary pump and by the clutch-declutch logic, leading a piecewise-defined HPTO torque. Again, to obtain a satisfactory characterisation of the WEC response in a given sea state in time-domain, 40 time series of the wave input are generated coherently with the analysis carried out in Section 3.6.2. The relative percentage error encountered comparing the model results is computed with equation 3.71 and the same "acceptable limit" of 10% is considered. As pointed out in Section 3.2, the HPTO is practically non-linear and the application of FDM method is not possible. Therefore, the model comparison presented for this configuration is merely generated between SDM and TDM models.

Influence of the accumulator pressure

Considering first the influence of the accumulator pressure, the TDM is simulated and the root-mean-squared (rms) of the hp and lp accumulator gas pressure is computed. The β_g value cannot be used in the TDMs and SDM since they utilize a simplified model of the hydraulic transmission and a constant magnitude of the pressure drop over the pump has to be fixed. In this regard, the TDMs and SDM are simulated imposing a constant pressure drop equal to the rms value of the pump pressure drop obtained with the TDM simulation, indicated with $\Delta p_{p,rms}$. As reported in Figure 3.24, the gross average power obtained with the SDM is compared with the TDMs and TDM one for different values of $\Delta p_{p,rms}$. As expected, the extracted gross power computed with the SDM is slightly higher than the TMDs. However, despite the source of non-linearity that affects the hydraulic transmission model, the SDM fit almost perfectly the gross power extracted from its time-domain counterpart. On the other hand, the accuracy of the SDM simulation drops when it is compared with the complete TDM. Here, the hydraulic transmission is fully-modelled including a lot of components and dynamic effects not considered in the SDM (e.g. accumulators dynamic, hydraulic-motor generator, relief valve, etc.) and Figure 3.24b highlights a consistent difference between the two models. In particular, for high pressure drops $\Delta p_{p,rms}$, the error between the SDM and TDM increases due to the presence of the relief valve, not modelled in spectra-domain. However, no particular justification appears for a decrease in performance with low values of $\Delta p_{p,rms}$ since the hydraulic transmission is always practically non-linear regardless the pressure working conditions. The same considerations can be carried out looking at the net average power in Figure 3.25. Good performances are found

comparing the SDM and TDMs, demonstrating the effectiveness of the statistical linearisation also for computing the net power. Again, worst results are obtained comparing the SDM with the TDM one.

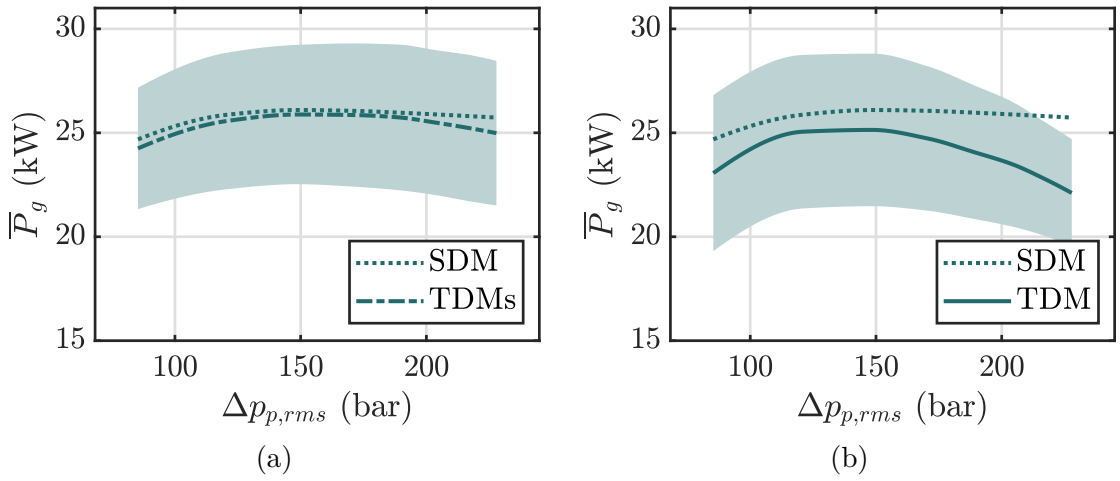

(a) (b)

Figure 3.24: Gross power comparison with HPTO in respect to the root-mean-squared value of the pump pressure drop $\Delta p_{p,rms}$: (a) SDM compared with the TDMs and (b) SDM compared with the TDM. The shaded area stands for the standard deviation of the time-domain results.

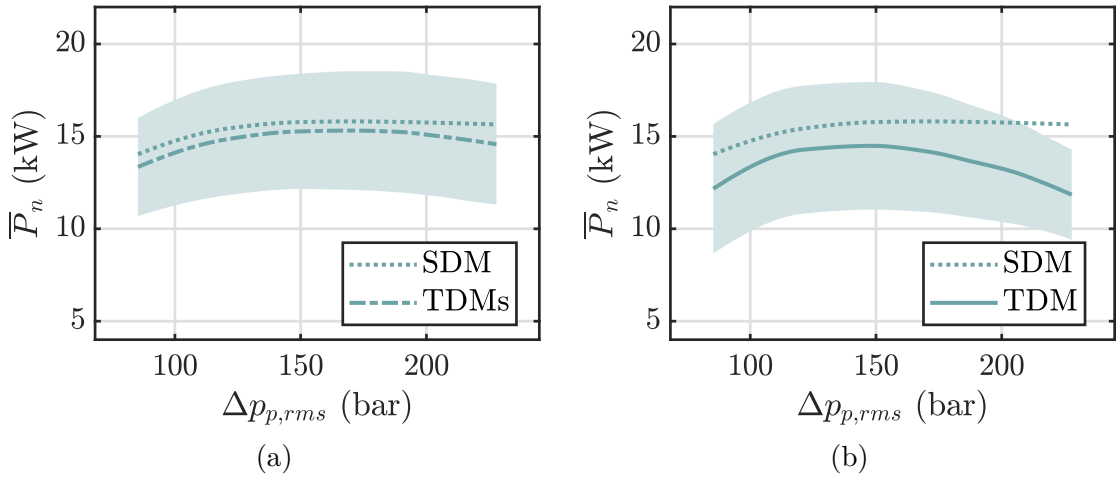

(a) (b)

Figure 3.25: Net power comparison with HPTO in respect to the root-mean-squared value of the pump pressure drop $\Delta p_{p,rms}$: (a) SDM compared with the TDMs and (b) SDM compared with the TDM. The shaded area stands for the standard deviation of the time-domain results.

Figure 3.26 demonstrates the accuracy of the SDM in respect to the TDMs and the limits against the TDM one. Figure 3.26a shows that the gross and net power

percentage error is lower than 10% for all the pressure drops conditions, reaching a minimum error of 0.5% and 3% for the gross and net power, respectively. If the SDM is compared with the TDM, Figure 3.26b indicates lower accuracy in term of expected power, especially for the net one, reaching a peak error higher than 20%. Overall, the net power error is higher than the one associated with the gross power.

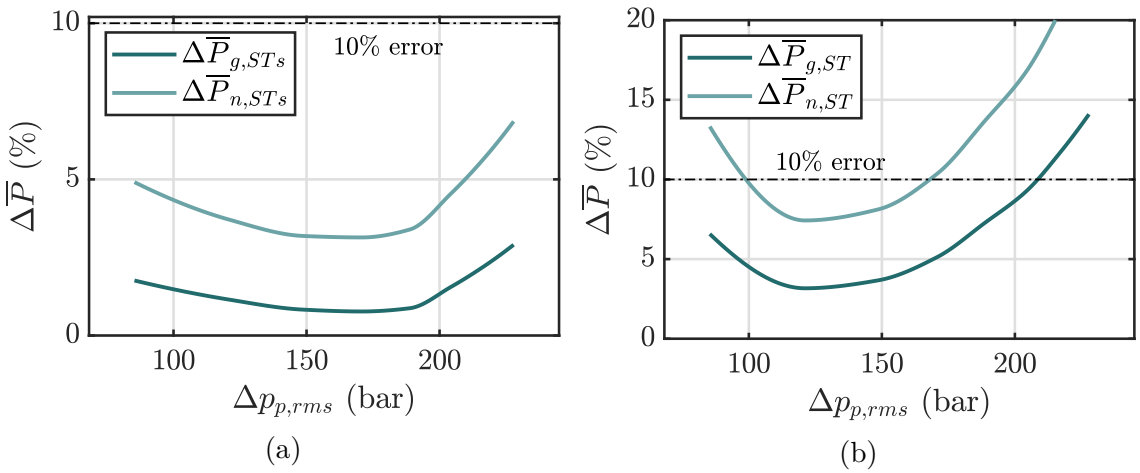

Figure 3.26: Percentage error on the extracted power in respect to the root-mean-squared value of the pump pressure drop $\Delta p_{p,rms}$: (a) SDM compared with the TDMs and (b) SDM compared with the TDM.

Influence of the clutching speed

The second HPTO control parameter is the clutch speed $\dot{\varepsilon}_{cs}$ that determines when the hydraulic pump is directly connected with the low and high pressure rams of the hydraulic circuit. The value of the $\dot{\varepsilon}_{cs}$ influences the behaviour of the HPTO torque in time determining, let say, "how much time the pump is bypassed or not" or, from another point of view, the rms value of the total torque acting on the gyroscope shaft. The procedure done for the circuit pressure influence is repeated for the clutch speed: different values of $\dot{\varepsilon}_{cs}$ are applied to the TDM computing the resultant rms value of the pump pressure drop; then, the $\Delta p_{p,rms}$ obtained from time-domain simulations is applied to the SDM and TDMs fixing the same $\dot{\varepsilon}_{cs}$ threshold used in the TDM. Figures 3.27 and 3.28 shows the extracted gross and net power for different set of $\dot{\varepsilon}_{cs}$. As reported in Figure 3.29, the percentage error obtained with the SDM is reported for different values of $\dot{\varepsilon}_{cs}$. Important errors appear varying the clutch speed value: decreasing the $\dot{\varepsilon}_{cs}$ leads to an increase of the percentage error since the T_{HPTOs} collapse to a pure Coulomb-damping torque, causing the stall of the gyroscope system for some part of the wave cycle; reasonably, increasing more the clutch threshold over 16 rpm will provide high percentage error due to the "high irregular behaviour" of the gyroscope shaft.

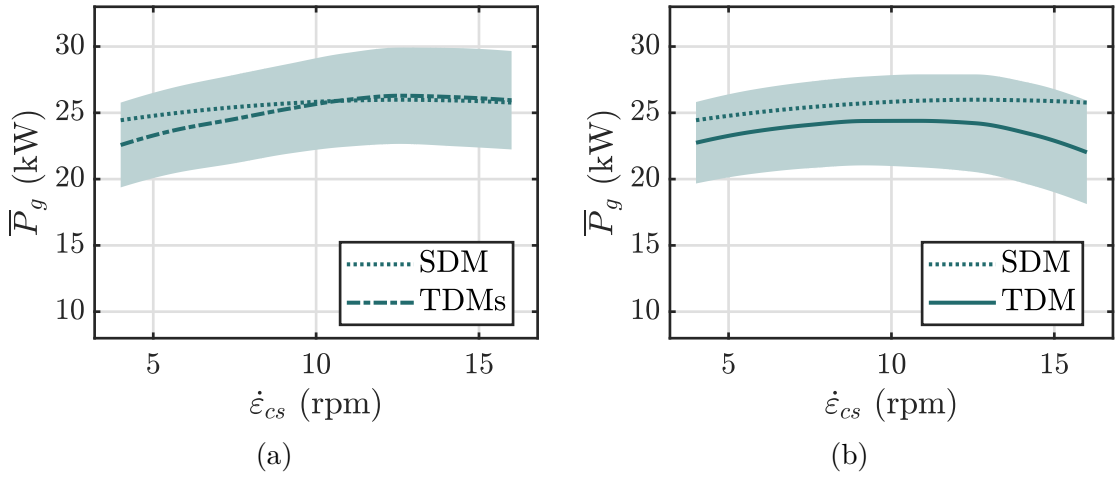

Figure 3.27: Gross power comparison with HPTO in respect to the clutch speed $\dot{\varepsilon}_{cs}$: (a) SDM compared with the TDMs and (b) SDM compared with the TDM. The shaded area stands for the standard deviation of the time-domain results.

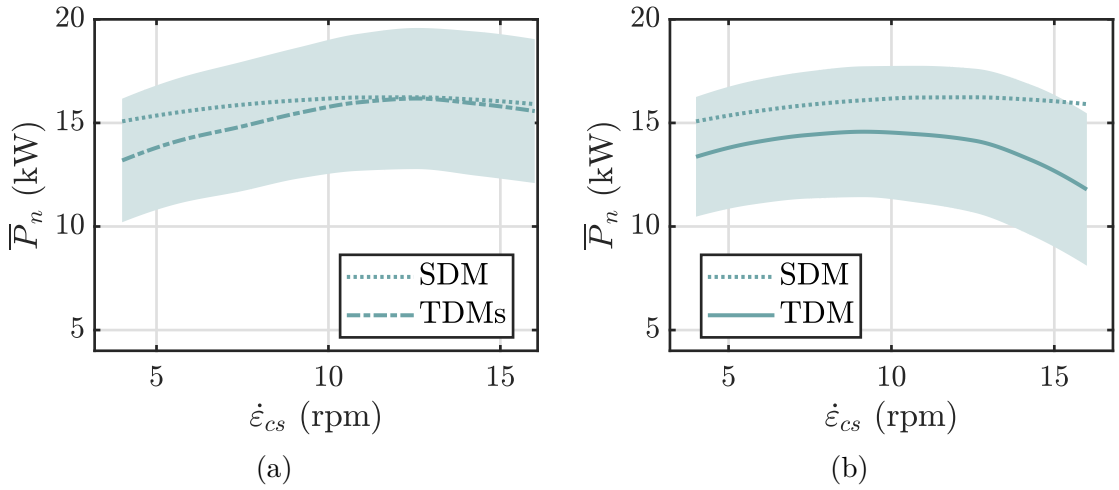

Figure 3.28: Net power comparison with HPTO in respect to the clutch speed $\dot{\varepsilon}_{cs}$: (a) SDM compared with the TDMs and (b) SDM compared with the TDM. The shaded area stands for the standard deviation of the time-domain results.

Figure 3.30 aims to clarify these conditions: first, in Figure 3.30a the effect of the gyroscope stall [125] is shown; Figure 3.30b highlights the irregular behaviour of the gyroscope that gets out from the linear conditions claimed in Section 3.6.3 for the validity of the spectral-domain approximations. Both simulations show strong irregular motions that are far from the harmonic profile like, for example, the one depicted in Figure 1.9 where a linear PTO torque is applied. This distortion in enhanced with low and high values of $\dot{\varepsilon}_{cs}$ leading bad performances of the SDM.

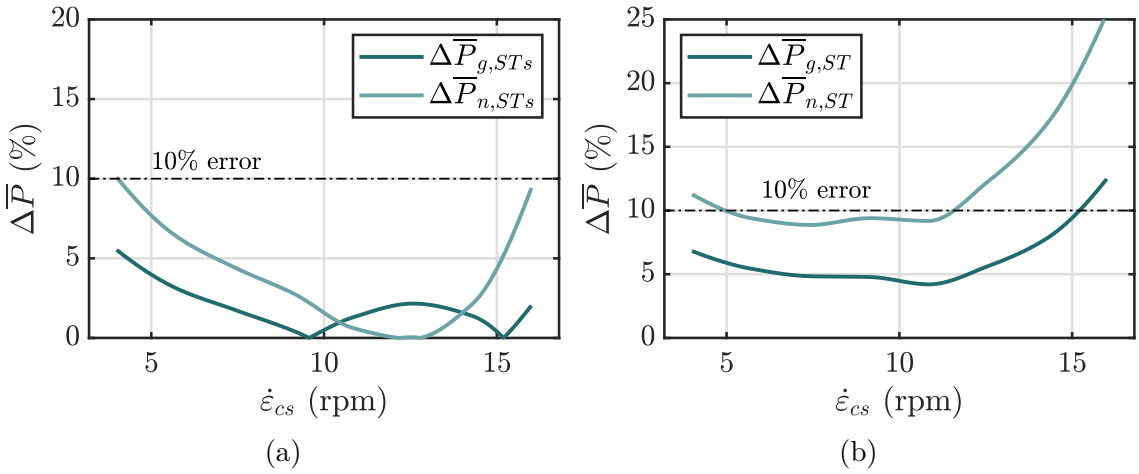

Figure 3.29: Percentage error on the extracted power in respect to the clutching speed threshold $\dot{\varepsilon}_{cs}$: (a) SDM compared with the TDMs and (b) SDM compared with the TDM.

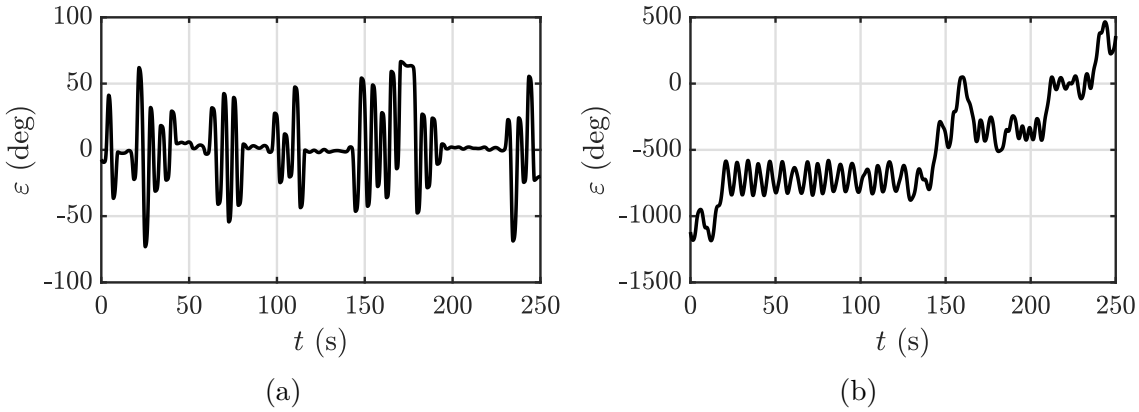

Figure 3.30: Example of irregular behaviour of the gyroscope motion: (a) stall behaviour due to the small clutching speed and (b) diverging behaviour due to the high clutching speed.

The effect of the clutching speed can be thorough with Figure 3.31. Different spectral-domain simulations has been carried out varying the clutching speed threshold $\dot{\varepsilon}_{cs}$ for different value of pressure drop $\Delta p_{p,rms}$. It is clear that the effect of the clutching speed is to decrease the equivalent pressure acting on the primary pump, that is computed as follows:

$$\Delta p_{p,eq} = \Delta p_{p,rms} \frac{\mathrm{erf}\left(\frac{\dot{\varepsilon}_{cs}}{\sqrt{2}\sigma_{\dot{\varepsilon}}}\right) - \mathrm{erf}\left(\frac{\dot{\varepsilon}_{dc}}{\sqrt{2}\sigma_{\dot{\varepsilon}}}\right)}{\dot{\varepsilon}_{cs} - \dot{\varepsilon}_{dc}} = \Delta p_{p,rms} T_{HPTOc} \tag{3.72}$$

The correction coefficient T_{HPTOc} reflects the magnitude of the clutching speed

that influences "how long the pump is short-circuited or not" and, thus, it modules the value of the pressure over the primary pump. As the clutching speed increases, the green lines in Figure 3.31 moves away from the linear bisector represented with a dash-dot line, diminishing the magnitude of the $\Delta p_{p,eq}$.

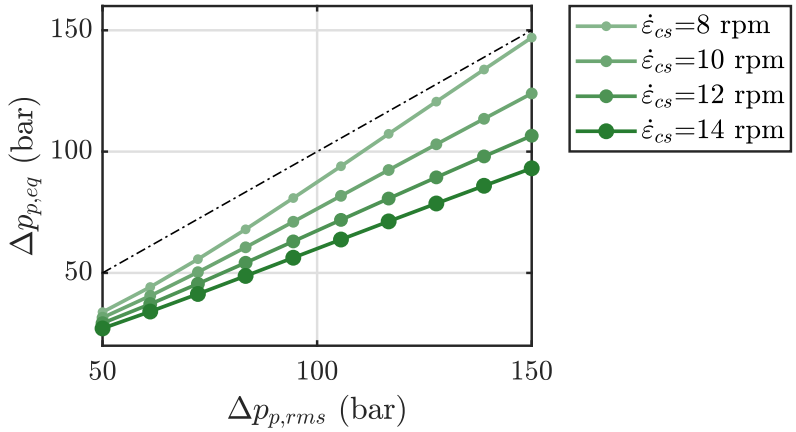

Figure 3.31: Effect of the clutching speed $\dot{\varepsilon}_{cs}$ with increasing values of $\Delta p_{p,rms}$. $\Delta p_{p,eq}$ is the equivalent pressure drop acting on the hydraulic pump computed with equation 3.72.

Annual productivity comparison

Concerning the HPTO, the single wave analysis is extended to the whole scatter diagram computing the annual productivity in spectral- and time-domain for all the sea-sites of interest. Here, the system is simulated optimizing both the clutch speed and generator damping for the TDM and the resultant $\Delta p_{p,rms}$ is applied to the TDMs and SDM computing the annual gross and net energy production.

The output of the productivity analysis is reported in Figure 3.32. The SDM slightly overestimates the system performances in respect to the simple TDM. On the other hand, the difference in productivity gets larger if SDM and the complete TDM are compared. The percentage error on the annual productivity is shown in Figure 3.33. Here, the effectiveness of the SDM is demonstrated against the simple hydraulic transmission model since, on average, the percentage error on the annual gross and net productivity is lower than 5%, despite the strong non-linearities that characterize the hydraulic model. No particular differences are shown between the different sea-site under analysis. Overall, the errors in respect to the TDM reach a maximum of 13% for the gross productivity and 17% for the net one, both computed for the Balder sea-site. However, the productivity predictions of the SDM are acceptable despite the percentage error over the acceptable limit (equal to 10%): as described in the next chapter, the ISWEC design tool concerns both the SDM and TDM of the HPTO; the first one will be used for a primary device design, aiming to

optimize all the main system parameters (hull properties, gyroscope properties and pump properties) allowing to perform fast simulations; then, the TDM is employed to optimized the HPTO parts (accumulator size, accumulator pre-charge pressure, motor and generator properties, etc.) choosing from the most promising devices obtained with the first optimization stage with the SDM. In short, the ISWEC design tool is composed of, let say, a first gross optimization to identify the most performing ISWEC configurations and a second refinement optimization to design the proper HPTO employing the high fidelity TDM.

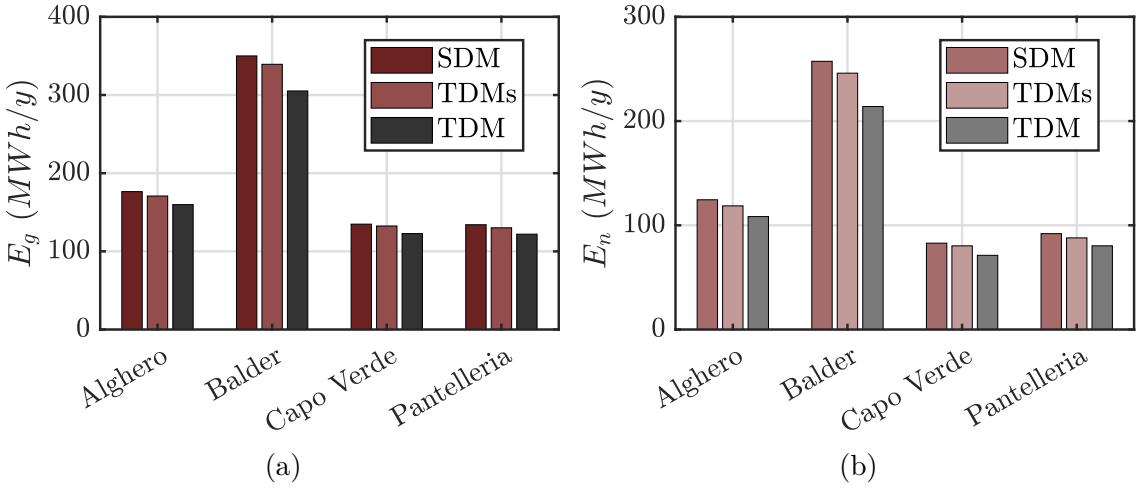

Figure 3.32: Annual productivity obtained with the spectral-, simplified time- and time-domain models for different sea-site of interest: (a) gross productivity and (b) net productivity.

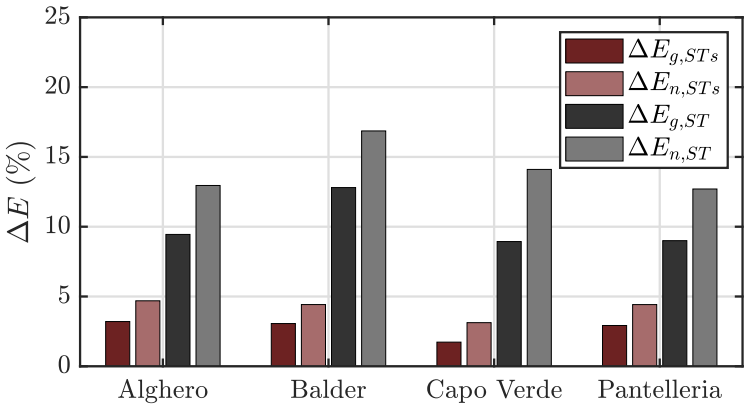

Figure 3.33: Percentage error on gross and net annual productivity with the HPTO. The grey bars compare the FDM with the TDM while the red bar the SDM with the TDMs.

3.6.5 Computational time evaluation

The computational burden play an important role for the design tool proposed in this thesis. Depending for the intended use, four models are employed to design the ISWEC device: the SDM and TDM for the MTPO, the SDM and TDM for the HPTO. The computational time required for all the models are compared in Figures 3.34d and 3.35d.

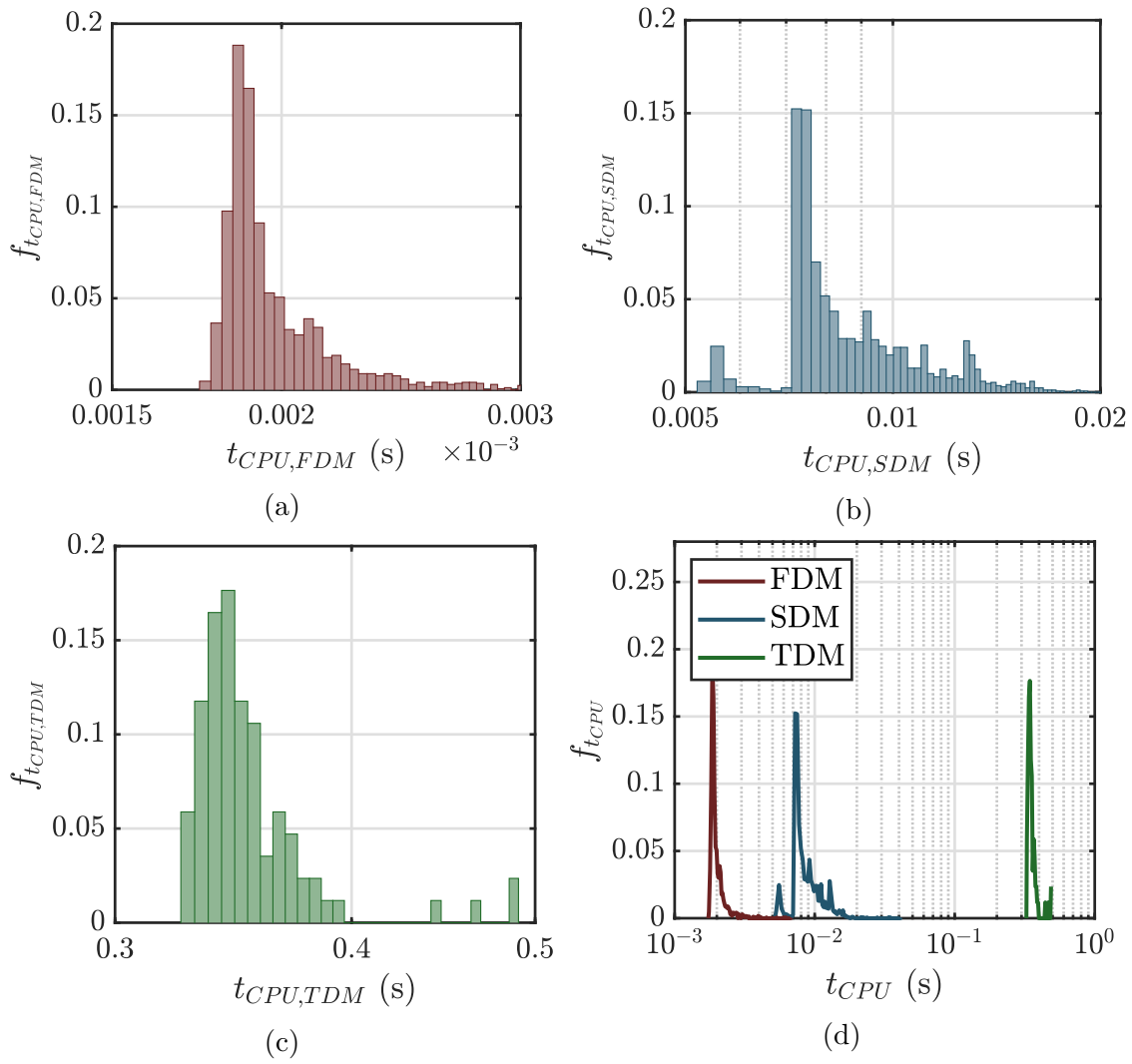

Figure 3.34: pdf of the CPU time required for the MPTO models. (a) FDM, (b) SDM, (c) TDM and (d) computational time comparison. All computational times are obtained on a 2.8 GHz, 8-core Intel® processor. Both the FDM and SDM are written in MATLAB while the TDM is built in Simulink environment.

As expected, the FDM of the MPTO is the faster, reaching a minimum simulation time near 0.0015 seconds. The computational time required by the SDM of

the MPTO is just over the FDM one, performing the simulations with a mean time almost equal to 0.009 seconds. Then, the TDM model require 0.3÷0.4 seconds to be solved, since its implementation in the Simulink environment heavily affects the computational time.

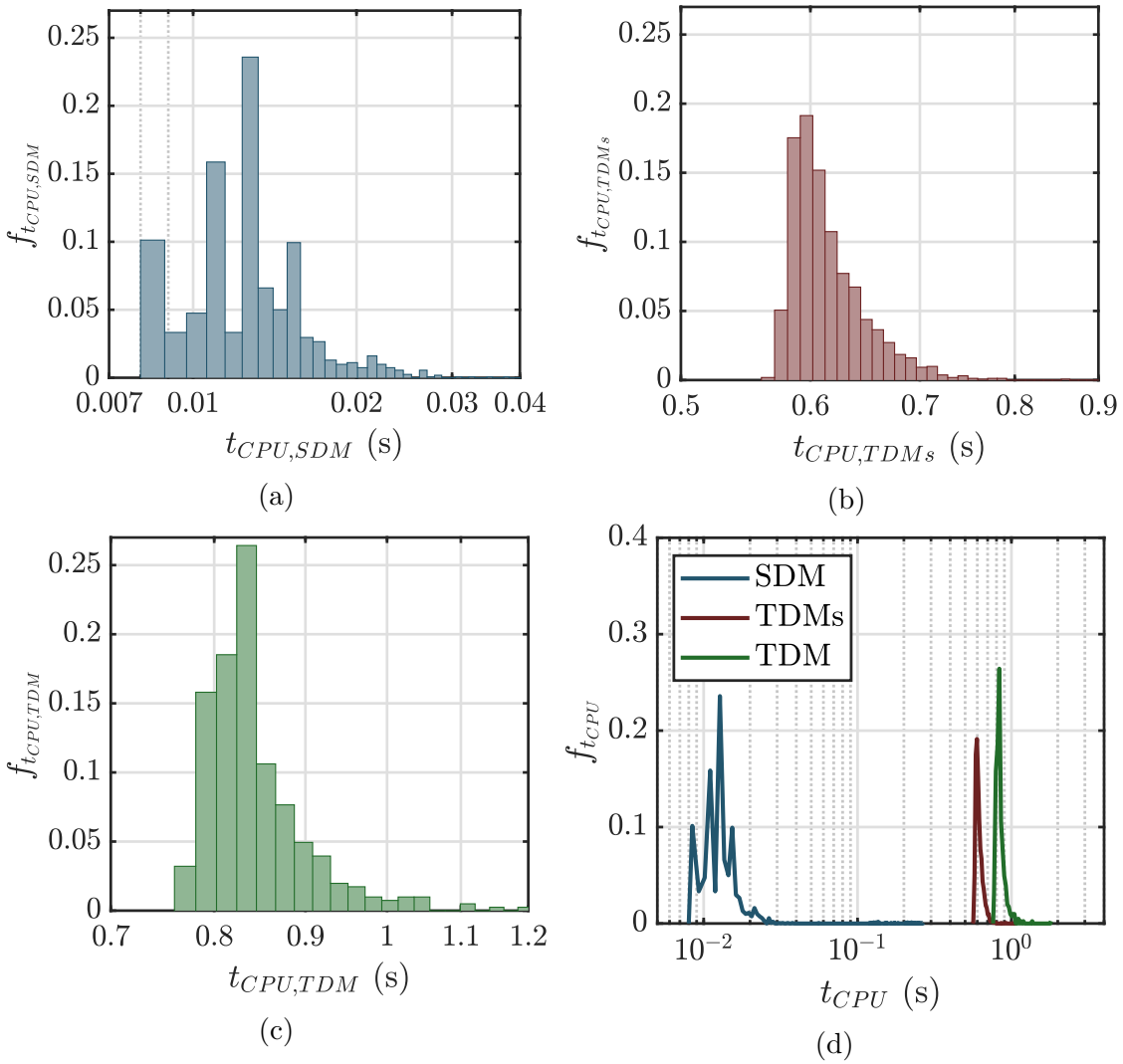

Figure 3.35: pdf of the CPU time required for the HPTO models. (a) SDM, (b) TDMs, (c) TDM and (d) computational time comparison. All computational times are obtained on a 2.8 GHz, 8-core Intel® processor. The SDM is written in MATLAB while the TDM is built in Simulink environment.

Concerning the HPTO, similar results are obtained. Overall, the computational time required by the SDM is comprised between 0.007÷0.03 seconds and it is one order of magnitude faster than the time-domain one, that is concentrated around 0.8÷1 seconds. Generally, the computation cost of the SDM solution is governed

by the number of iterations, which in turns depends on the relax coefficient, the starting point of the solution and the strength of the non-linear effects. In fact, Figures 3.34a and 3.35a shows that the spread of the $t_{CPU,SDM}$ is larger than the one associated to FDM, TDMs and TDM. In contrast, the computational time pdfs of the other models are more peaky and concentrated around their mean value.

3.7 Summary and remarks

Six ISWEC models, involving a variety of modelling techniques, number and nature of non-linear phenomena, and different PTO units, have been introduced in Sections 3.1, 3.2 and 3.3 in order to assess the practical value of their outputs and compare each other in term of performance prediction and computational time required. The model proposed in this chapter are: time-domain, frequency-domain and spectral-domain models of the ISWEC, modelling both the mechanical and hydraulic PTO. In particular, FDM, SDM and TDM are derived for the MPTO. The FDM is determined linearising the ISWEC non-linearities that arise from the gyroscope, the pendulum system and the PTO. However, the HPTO cannot modelled in frequency-domain due to its source of non-linearities (Coulomb-like PTO torque, Graetz bridge, relief valves, etc.). The HPTO is modelled in spectral- and time-domain, differentiating a simple TDM and a complete TDM: the former assumes a large size accumulators that give a constant pressure drop over the hydraulic pump; the latter includes all the main phenomena and components of the hydraulic transmission considered in this thesis (i.e. fluid compressibility, valves, accumulators, hydraulic motor and electrical generator). In Section 3.6.2 the time-domain models are tuned in term of minimal simulation duration and number of realisations of the Gaussian wave in input to obtain reliable output power estimations from a statistical point of view. The best compromise between the convergence of the results in term of average extracted power and computational time required is found as:

- MPTO simulations: 40 wave realisations, each 250 seconds long for a single wave spectra;
- HPTO simulations: 40 wave realisations, each 800 seconds long for a single wave spectra;

As expected, a longer simulation is required for the HPTO model since the presence of the accumulation stage introduces a slower dynamics compared with the wave frequency, requiring a higher simulation duration to obtain steady state conditions and, thus, a stable power output.

Concerning the results accuracy, the TDM model has been used as a benchmark to evaluate the reliability of the extracted power estimated with the frequency- and

Comparison	Error	Mechanical PTO Alghero	Balder	Capo Verde	Pantelleria
FDM vs TDM	$\Delta E_{g,FT}(\%)$	11.3	11.6	12.1	11.1
SDM vs TDM	$\Delta E_{g,ST}(\%)$	1.4	0.8	2.1	1.9
FDM vs TDM	$\Delta E_{n,FT}(\%)$	14.8	14.6	18.6	15.0
SDM vs TDM	$\Delta E_{n,ST}(\%)$	3.2	2.3	5.9	4.3
FDM vs TDM sat.	$\Delta E_{g,FT}(\%)$	15.4	24.6	8.6	12,7
SDM vs TDM sat.	$\Delta E_{g,ST}(\%)$	6.4	3.9	7.0	7.3
FDM vs TDM sat.	$\Delta E_{n,FT}(\%)$	23.3	33.9	14.7	19.8
SDM vs TDM sat.	$\Delta E_{n,ST}(\%)$	9.6	6.4	11.6	10.8
Comparison	Error	**Hydraulic PTO** Alghero	Balder	Capo Verde	Pantelleria
SDM vs TDMs	$\Delta E_{g,STs}(\%)$	3.5	3.4	1.9	3.3
SDM vs TDM	$\Delta E_{g,ST}(\%)$	9.3	13.1	8.9	9.1
SDM vs TDMs	$\Delta E_{n,STs}(\%)$	4.7	4.5	2.9	4.4
SDM vs TDM	$\Delta E_{n,ST}(\%)$	13.3	16.9	14.5	13.1

Table 3.4: Percentage error on the annual productivity for all the models under study. The top table refers to the MPTO results: the first part concerns the results without the generator saturation while the second one to a saturation limit imposed to $T_{sat} = 1500Nm$. The bottom table refers to the HPTO results.

spectral-domain models. Table 3.4 summarize the percentage error encountered with the FDM and SDM compared with the TDM.

For what concern the gross productivity, the SDM performs with acceptable accuracy giving a minimum percentage error equal to 0.8% for the MPTO without saturation simulated in Balder, a minimum of 3.9% for the MPTO with saturation simulated in Balder, a minimum of 1.9% for the HPTO simulated in Capo Verde against the simple TDM and a minimum of 8.9% for the HPTO simulated in Capo Verde against the complete TDM. The SDM presents higher errors in computing the net productivity, since the estimation of the power losses carried by the radial bearings have been simplified, as described in Section 3.6.1. In particular, the SDM of the MPTO shows percentage error up to 5.9% for the MPTO without saturation simulated in Capo Verde, up to 11.6% for the MPTO with saturation simulated in Capo Verde, up to 4.7% for the HPTO simulated in Alghero against the simple TDM and up to 16.9% for the HPTO simulated in Balder against the complete TDM. The most striking result is that the SDM remain true also for strong non-linearities, like saturations, sign(ε) function and clutch-declutch control. The SDM

overcome the accuracy of its frequency-domain counter part, showing a percentage error in estimating the annual productivity up to one order of magnitude lower than the SDM one. The FDM, tested only with the MPTO, has been excluded from here on since no acceptable accuracy is guaranteed in term of annual productivity. In particular, when strong non-linearities arise (e.g. low saturation limits) the accuracy of the FDM drops, showing estimation error up to 24.6% for the gross productivity and 33.9% for the net one, obtained against the saturated TDM of the MPTO. Despite the low accuracy of the SDM of the HPTO against the whole TDM of the hydraulic transmission, the spectral-domain framework is considered as a valid solution to be implemented in the first stage of the ISWEC design tool. Precisely, the mean percentage errors obtained with the SDM are almost equal to 10.1% and 14.4% for the gross and net productivity between the four sea-site. However, due to its computational efficiency, the SDM of the HPTO is employed to perform the first gross optimization of the ISWEC device, allowing to evaluate thousands of different ISWEC configurations in a reasonable time. Then, the TDM will be used for the second stage of the design tool, to perform a fine optimization of HPTO system concerning the most promising solutions obtained from the fist stage, evaluating hundreds of different PTO configurations.

Interesting results are obtained comparing the computational effort required by the models under study. Table 3.5 shows that the FDM is undoubtedly the fastest model considered, since only one simulation is required to obtain the system output. Also the SDM employ a single spectral-domain simulation to compute the output power of the WEC; however, an iterative process is required to complete the simulation, leading a computational time almost 5 time higher than the FDM one. Overall, the TDM is up to two order of magnitude slower than the FDM one and one order of magnitude than the SDM one.

PTO	Model	Mean CPU time (s)	CPU time std. dev. (s)
Mechanical	FDM	0.002	0.0003
Mechanical	SDM	0.009	0.002
Mechanical	TDM	0.355	0.030
Hydraulic	SDM	0.017	0.028
Hydraulic	TDMs	0.617	0.038
Hydraulic	TDM	0.851	0.080

Table 3.5: Mean computational time required and its standard deviation for all the models under study. The top table refers to the MPTO results and the bottom table refers to the HPTO results.

Chapter 4

Multi-Stage ISWEC Design Tool

WEC systems, that are less developed at present than other renewable-energy devices, does not have a consolidated design process and the existing models to estimate the costs are often oversimplified. The resulting scatter in the techno-economic assessments affects on the confidence of potential investors and constitutes an impediment to the development of wave energy technologies. In this context, wave energy conversion is far from being competitive with other renewable energy technologies, due to an excessive LCOE (Levelized Cost Of Energy) at the current stage of development. Generally, the nominal path should be enhance the Technology Performance Level (TPL) of the technology under development, focusing on small scale prototype testing (low economical impact), and therefore its Technology Readiness Level (TRL), gradually increasing the economical effort toward the commercialization [250, 251]. A major effort should be spent to perform an accurate estimation of the WEC performance at small scale and to adopt an all-embracing design tool that implements better design practices. However, the inherent limitations of small-scale devices and subsystems in predict their full-scale counterparts performances due to, for example, physical phenomena that are difficult to scale-up [224], leads to accelerate the WEC development toward high TRL levels. In order to reduce the errors behind the design of a WEC, techno-economic analyses should be taken into account adopting better design practices, since common approaches are inherently suboptimal. In practice, often, the design is performed in sequential fashion, considering different parts of the power conversion chain independently. Despite some WEC parts are difficult to design at the first stage (e.g. the mooring system for the ISWEC device) and predict their cost is not trivial (e.g. deployment costs, auxiliary components costs, maintenance costs, etc.), the common practice should suggest a holistic approach, based on representative wave-to-wire mathematical models, including the required control strategies, technological constraints and costs.

This Chapter proposes a comprehensive techno-economic optimisation of the ISWEC based on the framework proposed in another work of the author [252],

where a first version of such a design process is studied and applied to another device developed at the Politecnico di Torino, named PEWEC [30]. The design tool presented in [252] implements several novelties with respect to other design processes proposed in literature. First, similar only to [253], a high-detailed floater geometry is considered and, consequently, a wide design space with high dimensionality is investigated, counting up to 11 design variables such as: shape, dimensions and inertial properties of the floater, geometrical and inertial properties of the gyropendulum system and PTO components. Structural constraints and technological limits are included, based on subcomponents characteristics. The economic aspect is not neglected: a cost estimation is provided based on the cost of different material used for construction and commercial components of different PTOs from a catalogue. Moreover, the optimization is control-informed since a simple but realistic energy-maximising control strategy is implemented, including PTO constraints. The thesis of Sigiru [185] describes another version of the design tool applied to the ISWEC, originally proposed in a previous work by Sigiru himself [254]. The main improvements introduced in this thesis in respect to the work of Sirigu [185] concern the inclusion of the spectral-domain and time-domain numerical models that allow to simulate the dynamics of the device given the properties of the floater, gyroscope and PTO systems. The design tool presented in [252] implements a simple frequency-domain model with the linearised dynamic equations. In this context, also the inclusion of the HPTO and its optimization is a novelty introduced in this thesis, increasing the potential extracted power in oceanic sea-sites where the low speed and high torque profiles calls for the use of a hydraulic transmission in respect to the actual electro-mechanical solution. Overall, the main outcome will be providing a detailed practice of optimising a WEC during the early-stage development taking into account techno-economical aspects of different technological PTO solutions. Furthermore, the design tool is fully-developed in MATLAB/Simulink environments, making it completely customizable and easily-transferable to other users.

This Chapter is organised in four sections: Section 4.1 illustrates the architecture of the design tool and its optimization algorithm; Section 4.3 describes the parametrisation of the ISWEC subsystems; Section 4.4 focuses on the single device optimization explaining how a single solution of the ISWEC is evaluated on the sea-sites of interest; then, in Section 4.5 the key performance indicators considered are defined.

4.1 Design tool architecture

Often, a WEC design is performed in sequential fashion, considering different parts of the power conversion chain independently. A representative example is the optimisation of a device performances following an incremental approach: first,

the hydrodynamics performances are optimized regardless the control logic; second, an optimal controller is designed to enhance the system productivity; then, the technological constraints and the PTO efficiency are included to correct the expected power of the WEC; finally the costs are evaluated. Such an incremental approach leads to a suboptimal solution since all the elements that concur to a techno-economical evaluation of the WEC are optimized separately. This work proposes a multi-stage optimization, as represented in Figure 4.1, composed of two stages:

- **Stage 1 - Device optimization**;
- **Stage 2 - Performance evaluation**.

As indicated in Figure 4.1, if the MPTO is considered, the system is fully designed with one single stage, named Stage 1, since all the ISWEC parts are modelled in spectral-domain, including the whole PTO system (see Section 3.3.2). On the other hand, the hydraulic system has to be evaluated with two separated sub-stages. Initially, only the hydraulic pump and its control is considered in the Stage 1b. In this first sub-stage, the ISWEC device is designed and all its parameters optimized except for the HPTO system. A second sub-stage is required to optimize the rest of the HPTO since only a time-domain framework is suitable to simulate all the hydraulic components. In Stage 1b the most promising ISWEC solutions obtained from the Stage 1a are re-evaluated optimizing the HPTO configuration.

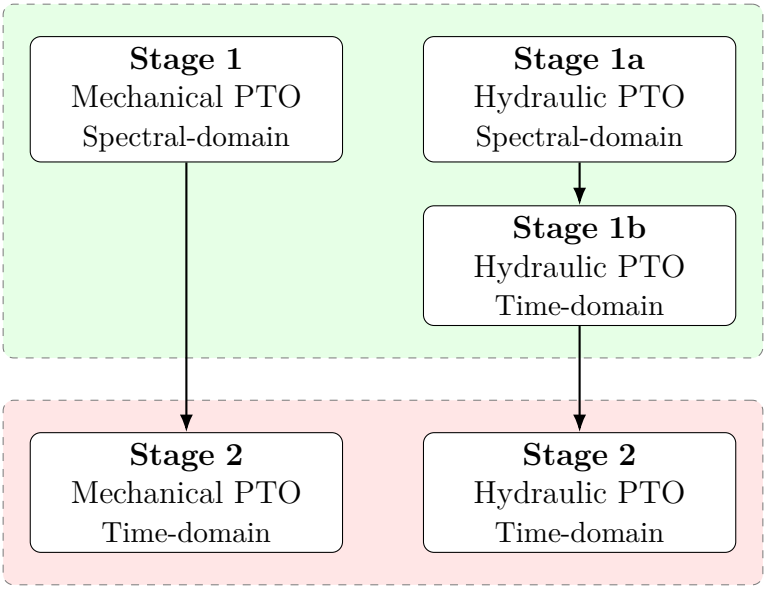

Figure 4.1: Multi-stage design tool workflow.

The two separated sub-stages are made mandatory due to the high computational effort required by the TDM that is impossible to be used to design the whole system in Stage 1a. In this regard, the system is first optimized with a simplified version of the HPTO (constant pressure assumption, see Section 3.1.2) in spectral-domain and the whole HPTO optimized subsequently in time-domain.

In short, in the first stage the device is designed optimizing its performances, costs and efficiency by identifying a certain amount of optimal solutions that reflects the optimization requirements. Numerous simulations are required and the SDM or TDM with only one single wave realisation are considered to break down the computational burden. The device is defined parametrically by 11 free parameters, if a MPTO is implemented, or 18 free parameters, if the HPTO is considered. Once the single ISWEC solution is parametrized, the algorithm compute its parameters (e.g. device inertia properties, hydrodynamic matrices and transfer functions, costs, etc.) and perform a single device optimization finding the optimal control set that maximize the net annual productivity; then, the key performances of the system are computed (e.g. cost of energy, device cost, system efficiency, etc.) and collected in order to find the best ISWEC solution. This process is schematically represented in Figure 4.2.

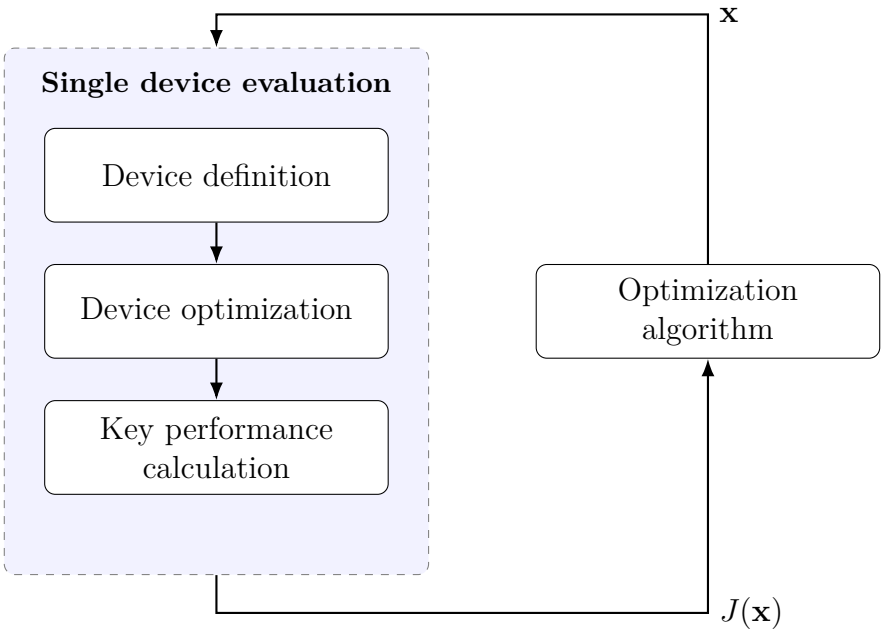

Figure 4.2: Architecture of the stage 1 optimization tool. $\mathbf{x}$ is the vector of free parameters that define a unique ISWEC device and $J(\mathbf{x})$ is the fitness function used as a performance indicator of the device $\mathbf{x}$.

Once the most promising technological solutions are obtained, a second optimization stage is employed to evaluate the performance of such ISWEC configurations with high-fidelity time-domain numerical models. Such models allow to complete the performance evaluation of the best solutions through a parametric analysis on the control parameters. In fact, the single device optimization of the first stage is performed on thousands of different devices and the high computational burden calls for a SDM or a TDM evaluated with a single wave realisation, that is far from being a reliable simulation as demonstrated in Chapter 3. In Stage 2, the TDM is simulated with multiple wave realisations to evaluate the performance of the system precisely in time-domain, also allowing the use of more complex model in respect to the first optimization stage. Moreover, some system parameters can be modified/refined accordingly to the output of this second stage, if needed.

Approximately, 5÷10 promising devices are produced by the Stage 1a of the HPTO and optimized again in Stage 1b to configure the proper the hydraulic transmission. Overall, 2÷3 optimal devices are produced by the Stage 1 for both the mechanical and hydraulic PTO and evaluated in Stage 2. The best individuals will be accurately compared in the next Chapter to pick the best ISWEC device for the intended key performance.

4.2 Optimization algorithm: a holistic approach

The optimization of a WEC system is treated in literature with different approaches, however, regarding for example the HPTO, Pedersen [118] assessed that *"in references where the HPTO system is mentioned, this is generally a simple non-optimized fluid power transmissions with very limited efficiency"* [107, 111, 76]. Generally, no unified guidelines or closed-form procedures are reported in literature that effectively provide a design process for a WEC system.

Regarding the design of the PTO system, its topology affects the two ends of the energy conversion chain: the hydrodynamics of wave energy absorption and the electrical equipment performance, including the rated power of the generator, power electronics and the quality of the produced electrical energy [107]. In order to address these questions that involve a relatively large number of variables, dimensionless quantities have been introduced in [107] and relationships established between them, that provide the wave energy converter designer with relatively simple rules and tools. However this procedure holds in linearised conditions and simple float geometry with linear hydrodynamic behaviour. In [100] a model based design of a multiple cylinder HPTO for the Wavestar WEC [23] is proposed. The design is based on a trial and error method based on the transmission requirements taking into account the efficiencies of the transmission components. In [125], that was an extension and a continuation of the research of [255], it was aimed to investigate how the magnitude of the HPTO force influences the power capture ability of

the two-raft-type WEC, and what are the relationships between the optimal power capture ability and the normalized optimal magnitude of the PTO force. According to Zheng, these would provide a valuable guidance for the optimal design of a HPTO unit by altering the parameters of the hydraulic components. Focusing again on the HPTO, in [127] a parametric evaluation of the hydraulic transmission parameters has been carried out to highlight the influence of each variable on the capture width ratio of the device.

Despite the references cited above regards the design of the HPTO system, that is the focus of this dissertation, the lack of a unified design approach affects all the system components since no particular global optimization algorithms is considered. The high-dimensionality of the problem and its multi-objective nature calls for a holistic approach. In this work, a tournament-based genetic algorithm is implemented as a stochastic optimisation logic, treating different variables as independent and random.

4.2.1 The genetic algorithm

Generally, the evaluation of a WEC performance and its optimization in respect to the system variables behave as grey or black boxes, as it required a try and error process to generate an optimal solution and no analytical closed form exists [252]. Due to the vast multi-dimensional search space and the multi-objective nature concerning the WEC design, genetic algorithms are one of the most common choice, since they can handle vast design spaces and complex cost functions and constraints, regardless the morphology of their mathematical structure [256]. Genetic algorithms are meta-heuristic optimisation codes based on the evolutionary theory, basing on the survival-of-the-fittest principle. Their stochastic approach favours the identification of a global optimum, reducing the risk of convergence to a local minimum. The Genetic Algorithm (GA) applied to WEC systems is studied in several works with different approaches. In [105] the GA is applied constrained optimization of the control parameters and the attach point of the cylinders to the absorber arms. The optimization has been conduced on eight different HPTO configurations to compare the performance when using the piston and rod size chambers attached to the hydrostatic transmission side and with or without rows of cylinders assembled in parallel. In [257] the HPTO system was optimised using a special GA optimisation tool in the Simcenter Amesim® software [193]. The simulation results showed that GA was effective to determine the optimal configuration parameters of HPTO system such as: diameter of piston, diameter of rod, accumulator capacity, accumulator pre-charge pressure, hydraulic motor displacement. The objective of the optimisation problem was to maximise the energy production of the system. In the work of Calvario [104] the GA is formulated as a constrained optimization problem with a penalty method, using a constant penalty to penalize

infeasible solutions [258]. The optimization aimed to maximize the average absorbed power (objective function). The decision variables are the distance of the mounting point of the cylinder and PTO control parameters. These variables are optimized with a heuristic approach based on evolutionary computation and commonly used for the optimization of an oscillating wave surge converter [259, 260]. However, to the best of the author's knowledge, no reports has been found so far using the GA to estimate the optimal configuration parameters for a wave energy conversion system including the floater, the internal mechanics and the PTO joint with their related costs. The interested reader should refer to [258, 261, 262, 263] for a detailed description of the evolutionary algorithms.

4.2.2 ISWEC multi-objective optimization

The multi-objective nature of the ISWEC design is call for a multi-objective GA. The ISWEC counts up to 18 design variables, comprising shape and dimensions of the floater, inertial properties, gyroscope dimensions and numerosity, PTO type and its components. Realistic geometrical and structural limitations are implemented, based on subcomponents encumbrances. Moreover, a simple energy-maximising control strategy is implemented, including explicit constraint on the physical variables of the system and its PTO, in order to perform a control-informed optimisation. Finally, a reliable preliminary cost estimation is based on the cost of different material used for construction and different commercial components considered. The architecture of the GA implemented in this work is described in the next two sections.

Problem formulation

The purpose of the optimization is to identify a set of devices optimal in all the strategic sea-sites of interest (Alghero, Balder Capo Verde and Pantelleria) to have one machine that performs well regardless of the location. Such optimization problem falls within the field of multi-objective optimization (known also as Pareto optimization), where more than one objectives concur in the design process. The objective to be minimized, or maximized, is also called fitness function or key performance indicator (see Section 4.5). In contrast with a simple single-objective optimization problem, the multi-objective optimization problem involves more than one objective function that must be minimized, and the superiority of a solution is given by its dominance and then by a set of optimal solutions [264]. For such a multi-objective problem, the *Pareto front* can be defined as the non-dominated solutions set: given a set of solutions, the non-dominated solution set is a set of all the solutions that are not dominated by any member of the solution set. The Pareto-optimal set is the frontier made from the union of the points of the Pareto-optimal front, as represented in Figure 4.3.

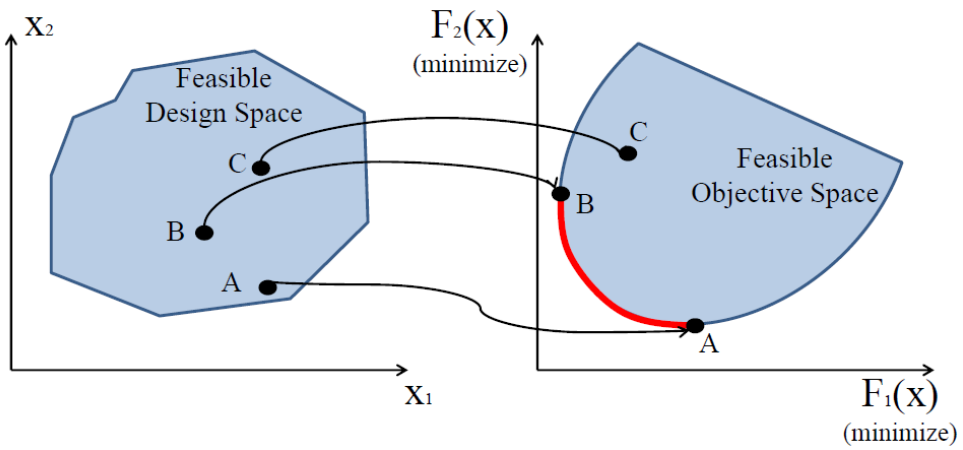

Figure 4.3: Graphical representation of the Pareto-optimal set concept. Solutions A and B are both optimal since they are non-dominated solutions. C is a suboptimal solution since A has a better fitness F_2 and B has a better fitness F_1.

In this context, Evolutionary Algorithms (EAs) present characteristics that fit naturally with multi-objective problems, and they constitute the state of the art in this field [264, 265]. EAs are a class of heuristic stochastic optimization methods that replicates the process of Darwinian evolution and natural selection. Their population-based nature that allows the generation in a single run of several solutions, evaluated in parallel to compute the required fitness function. Then, a selection procedure is performed to classify the best individual of a single generation to generate another pool of solutions until the convergence conditions are reached. The optimization process can be summarized in the following four steps:

- **Initial population definition**: the optimization process starts with a random set individuals, called population. Each individual is a solution of the problem obtained inside the design space and can be represented by a specific set of design parameters;
- **Fitness function calculation**: for each individual of the current population the objective function is evaluated and a penalty may be added to the function in case of constraint violation (e.g. unfeasible solution). The fitness function represents the score for a single individual giving a measure of how its design parameters are optimal or not regarding the objective of the optimization;
- **Elitism, crossover and mutation**: the individuals are ranked by their fitness values and the 5% fittest directly pass to the next generation. Then, pairs of individuals, called parents, are selected for the reproduction phase. The crossover operator simulates the natural reproduction, where the parameters of the parents are mixed and a new individual is generated. A crossover

point is chosen randomly inside the chromosome of both parents, then the offspring are created by exchanging the genes of parents until the crossover point. The aim is to produce the next generation made of genes of the fittest individuals of the previous generation. Another way to create part of the next generation individuals is the mutation: in order to maintain diversity within the population and avoid a premature convergence in a local minima or maxima, the mutation is performed changing the value of some genes of an offspring;

- **Reiteration or termination**: after the crossover and mutation stage, a new generation of solution is ready to be evaluated and the optimization process is repeated until achieving the maximum number of generations, or convergence conditions of the solutions are reached.

The optimization problem is formulated using the Optimization toolbox™ [266] and Global Optimization toolbox™ [267] implemented in MATLAB®. The function of reference is the native MATLAB function `ga` [268]. Then, the MI-LXPM algorithm has been chosen which structure is schematically shown in Figure 4.4:

- MI: mixed-integer [269];
- LX: Laplace crossover [270];
- PM: power mutation [271].

The detailed description of the tournament, Laplace crossover, power mutation and truncation steps implemented in the `ga` function can be found in the Appendix A of another work of the author [252].

Finally, the optimisation problem can be formuled as the minimisation of a generic scalar function $J(\mathbf{x}) : \mathbb{R}^{n_x} \to \mathbb{R}$ of a vector $\mathbf{x} \in \mathbb{R}^{n_x}$, subject to lower and upper bounds, $\mathbf{x}_L \in \mathbb{R}^{n_x}$ and $\mathbf{x}_U \in \mathbb{R}^{n_x}$. n_x is the dimension of the problem (11 for the MPTO, 11 for the stage 1a of the HPTO and 18 for the stage 1b of the HPTO). Note that all elements of $\mathbf{x}$ have discrete variations. The optimisation problem can be presented as follows:

$$\begin{aligned} &\min_{x} && J(\mathbf{x}) \\ &\text{subject to} && \mathbf{x}_L \leq \mathbf{x} \leq \mathbf{x}_U \end{aligned} \tag{4.1}$$

The tuning factors of the algorithm are summarized in Table 4.1. It is worth to specify that, although beyond of the scope of this thesis, a sensitivity analysis on the `ga` parameters can potentially improve the convergence rate of the algorithm.

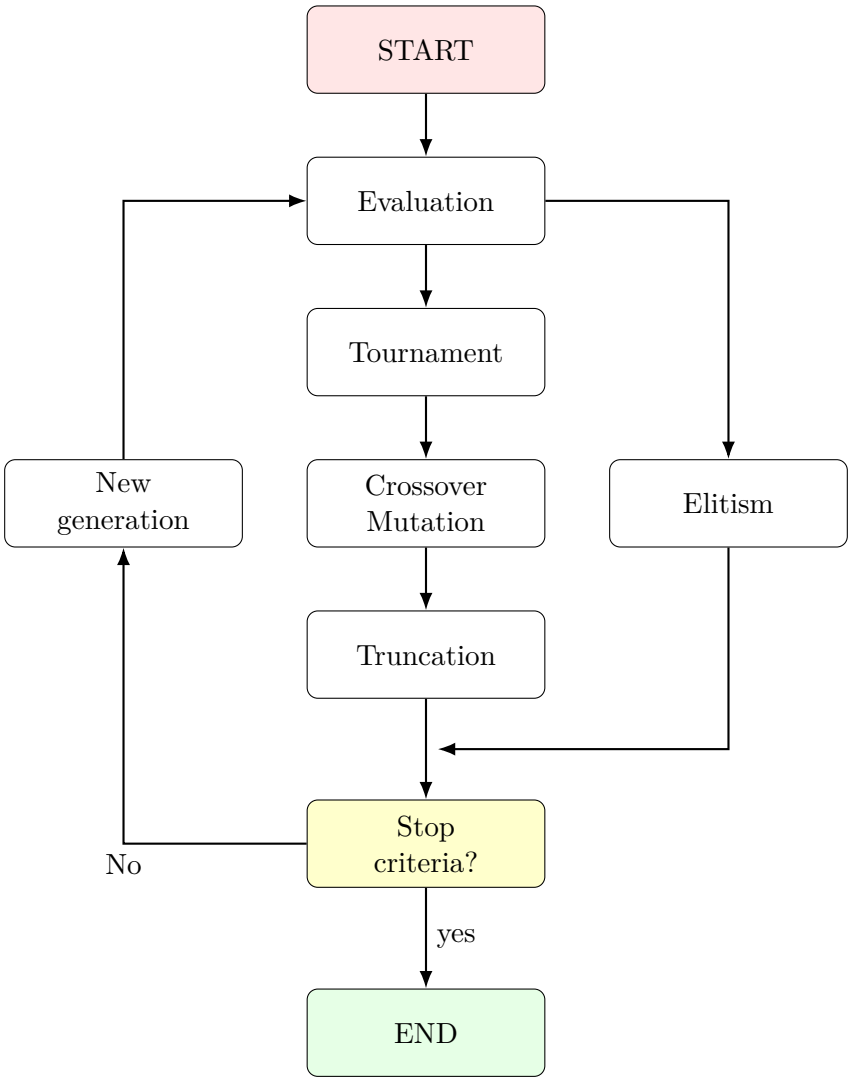

Figure 4.4: Flowchart of the MI-LXPM genetic algorithm. Adapted from [252].

Cost function and feasibility check

A common procedure to formulate a multi-objective problem is to define a series of single objective problems with the use of scalarization techniques [272]. The formulation of the single objective fitness function $J_f(\mathbf{x})$ is tackled by aggregating several objectives J_o of the original problem into a unique objective function that has to be optimized as follows:

$$J_f(\mathbf{x}) = \sum_{o}^{N_o} J_o(\mathbf{x}) w_o \tag{4.2}$$

Name	Symbol	Stage 1 / Stage 1a	Stage 1b
Population size	P_s	75	75
Maximum generations	G_m	150	50
Maximum stall generations	G_s	50	25
Convergence threshold	Δ	10^{-6}	10^{-6}
Elitism percentage	e_p	5%	5%
Tournament size	t_s	4	4

Table 4.1: Parameters of the genetic algorithm. Stage 1b (HPTO in time-domain) uses few generations than Stage 1 (MPTO in spectral-domain) and Stage 1a (HPTO in spectral-domain) due to the lower number of free parameters to be optimized and to limit the computational time.

where the $o-th$ objective $J_o(\mathbf{x})$ is weighted by the coefficient w_o. N_o is the total number of objectives, two in our concrete optimization problem. Through the choose of different weights that aggregate the objectives it is possible to build the Pareto-optimal set of the multi-objective problem. However, due to the high-dimensional search space, the risk of encounter unfeasible combinations may potentially hinder the success of the optimisation. The device can be uniquely defined by a set of design parameters but some combinations can lead to unfeasible solutions. In order to deal with unfeasible solutions, constraints are enforced by applying a parameter-free penalty function when a constraint violation appears. The usual way to handle constraints is via penalty functions, worsening the fitness value by a constant death penalty, increased by a measure of how much that constraint is violated [273, 274]. However, since there is no direct analytical formulation of the constraints based on the input variables, specific constraint handling based on the knowledge of the mathematical structure is not applicable. In this regards, considering the order of magnitude of the variable to be optimized, a constant penalty C equal to 10^4 is used to assign a penalty cost to the unfeasible devices. Moreover, an additive Δ_c cost is used to quantify the constraint violation, as reported schematic in Figure 4.5.

Therefore, the following fitness index is defined:

$$J(\mathbf{x}) = \begin{cases} J_f(\mathbf{x}) & \text{if feasible device} \\ C + \Delta_c & \text{if unfeasible device} \end{cases} \tag{4.3}$$

The most common reason of solution unfeasibility are the geometrical intersection of the subsystems and the hydrodynamic stability, for example: the gyroscope length, height and width are longer than respectively the hull length, height, width, there is not enough space for the desired quantity of ballast in the aft/fore or bottom compartment, geometrical collisions between ballast and the gyroscope units,

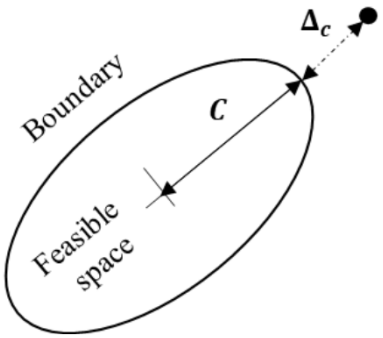

Figure 4.5: Schematic representation of the constraint violation handling.

roll or pitch instability[1], etc. The design tool is able to recognize any type of geometrical collision, and the solution is labelled as unfeasible, assigning a fitness function equal to the second term of equation 4.3.

4.3 Device definition and assumptions

The number of parameters that describes the ISWEC device can be numerous and not handy to manage, especially in a preliminary design phase. Therefore, some simplifications and assumptions are needed to relate some system parameters in order to reduce the design variables that defines uniquely the device. The goal is to have a set of limited but significant design variables that identify the remaining geometrical and inertial properties. In fact, the first phase of the optimization tool regards the device definition. The ISWEC device can be divided into three macro-subsystems: floater, gyro-pendulum and PTO.

Depending on the PTO architecture, up to 18 free parameters are chosen to describe the device, summarised in Table 4.2 and hereafter discussed in detail: six for the hull, four for the gyro-pendulum and one or seven for the MPTO or HPTO, respectively.

4.3.1 Floater geometry and parameters

The floater shape and its inertial properties play an important role in the dynamics and power absorption of the device. The shape of the hull is based on previous experience matured during the development of the first full-scale prototypes of ISWEC. For both technological effectiveness [275] and hydrodynamic performance

[1] A floater, to be stable at roll/pitch DoF, must have its metacentric height, defined as the distance between the device CoG and the transverse metacentre for roll and longitudinal metacentre for pitch, greater than a safety value that is set equal to 1 m [185].

Design parameter	Sym.	Unit	LB	UB	MPTO 1	HPTO 1a	HPTO 1b
Hull					**Stage**		
Hull length	L	m	10	45	•	•	○
Hull width factor	W_f	–	1	4	•	•	○
Bow/stern circ. ratio	h_f	–	0.5	1	•	•	○
Height ratio	k_f	–	0.5	1	•	•	○
Maximum pitch angle	δ_0	deg	10	20	•	•	○
Ballast filling ratio	BFR	–	0.35	1	•	•	○
Gyro-pendulum					**Stage**		
Design parameter	Sym.	Unit	LB	UB	MPTO 1	HPTO 1a	HPTO 1b
Flywheel inertia	J	kgm^2	10000	45000	•	•	○
Gyroscope units	n_{gyros}	–	2	4	•	•	○
Pendulum mass	m_p	kg	500	8000	•	•	○
Bearings id	ID_b	–	1	15	•	•	○
Mechanical PTO					**Stage**		
Design parameter	Sym.	Unit	LB	UB	MPTO 1	HPTO 1a	HPTO 1b
Mechanical PTO id	ID_{pto}	–	1	36	•		
Hydraulic PTO					**Stage**		
Design parameter	Sym.	Unit	LB	UB	MPTO 1	HPTO 1a	HPTO 1b
Pump id	ID_p	–	1	36		•	•
Hydraulic control id	ID_c	–	1	4		•	•
Hp volume	V_{hp0}	l	100	600			•
Hp pre-charge	p_{hp0}	bar	20	60			•
Motor-generator id	ID_{mg}	–	1	15			•
Added inertia	I_a	kgm^2	1	20			•
Number of circuts	n_c	–	1	2			•

Table 4.2: Design parameters used by the genetic algorithm to define a single ISWEC device. Discrete values with constant spacing are used, with lower (LB) and upper (UB) bounds to constraint the exploration domain. The bullet • means that the parameter is optimized in that stage; the circle ○ means that the parameter can be refined in that stage (optimized around the value found in the previous stage).

(minimal viscous damping along the pitch degree of motion [276]), the hull profile is assumed to be cradle shaped; then, it can be composed of a bottom circumference, tangential to two circumferences in the bow/stern sections, as shown in Figure 4.6, while the transversal section is extruded for all the hull width resulting in a floater symmetrical with respect to the $y-z$ and $x-z$ planes.

The hull profile is defined by the arcs of two circumferences tangent internally and parametrized as a function of some geometrical quantities:

- R: semi-length of the floater;

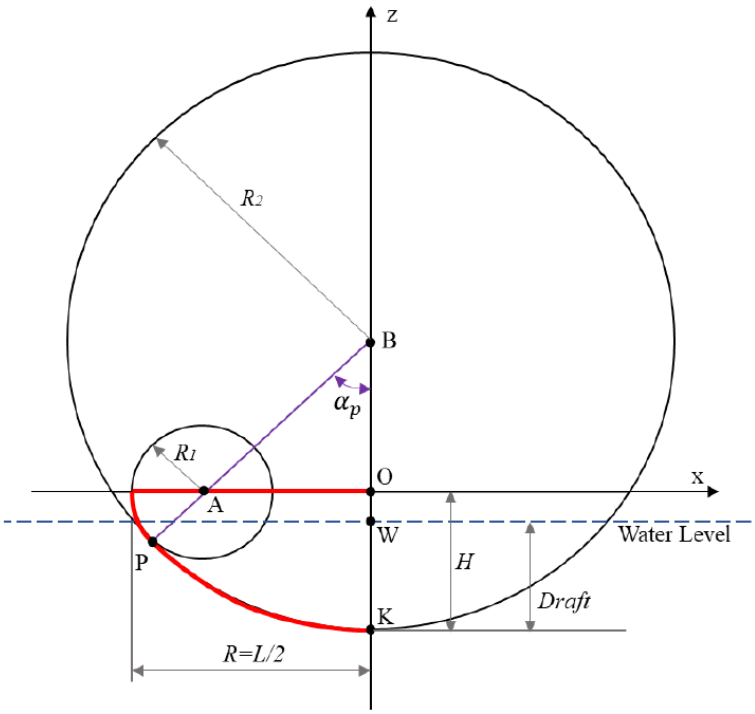

Figure 4.6: Parametric definition of the cross sectional of the floater. Adapted from [185].

- H: overall height of the hull, the distance between the keel and the deck;
- D: draft of the hull;
- R_1: radius of circumference C_1;
- (x_A, z_A): x- and z-coordinates of the centre of C_1, respectively, with z_A=0;
- R_2: radius of circumference C_2;
- (x_B, z_B): x- and z-coordinates of the centre of C_2, respectively, with x_B=0;
- $\alpha_p = \angle PBO$.

A subset of six independent geometrical and inertial parameters is defined, which are used in the genetic algorithm:

- L: length of the floater;
- $W_f = W/(W_g \times n_{gyros})$: hull width factor defines the width of the hull as a function of the gyroscope unit dimension;

- $h = x_A/R$: bow/stern circumference ratio;
- $k = D/H$: height ratio;
- $\delta_{\mathbf{0}} = \tan^{-1}\left(\frac{H-D}{R}\right)$: maximum pitching angle, defined as the maximum pitch rotation to avoid the deck to be submerged. It defines the hull draft D function of the floater semi-length R and the floater height H;
- BFR: ballast filling ratio, that is defined as the ratio of ballast located in aft/fore ballast tanks over the total ballast ($BFR = 1$: all the ballast is stored in aft/fore ballast tanks; $BFR = 0$: all the ballast is stored in bottom ballast tank).

Therefore, the floater profile can be expressed in uniquely as a function of these design parameters:

$$R_1 = R - x_A = R(1-h) \tag{4.4a}$$

$$z_B = R\frac{k^2 + 1 + 2kh - 2h - 2k}{2 - 2h} \tag{4.4b}$$

$$R_2 = z_B + H = z_B + kR \tag{4.4c}$$

$$\alpha_p = \sin^{-1}\left(\frac{z_B}{x_A}\right) \tag{4.4d}$$

where x_A is derived from h and R. Then, the floater profile function $z(x)$ can be defined as:

$$z(x) = \begin{cases} z_A - \sqrt{R_1^2 - (x - x_A)^2} & \text{if } \; -R < x < R_2\sin(\alpha_p) \\ z_B - \sqrt{R_2^2 - (x - x_B)^2} & \text{if } \; R_2\sin(\alpha_p) < x \leq 0 \end{cases} \tag{4.5}$$

Figure 4.7 explains how the geometrical ratios k and h influence the hull profile for a fixed hull length. For what concern the ballast filling ration BRF, filling the ballast compartments is assumed from the extremities inwards, providing higher inertia and being easier from a practical point of view. A schematic example of different filling ratio BFR is shown in Figure 4.8. The ballast mass and its spatial distribution are used to identify the best inertial configuration in order to maximize the energy harvesting for a specific site. The advantage is the possibility to tune, in a certain range, the hydrodynamic resonance period of the system for different installation sites avoiding the re-engineering of the device.

The hull material is considered to be concrete to reduce the device costs in respect to a steel-made hull. The density for the hull structure, considering also the structure steel reinforcements, is $\rho_h = 2400 kg/m^3$ and the density for the

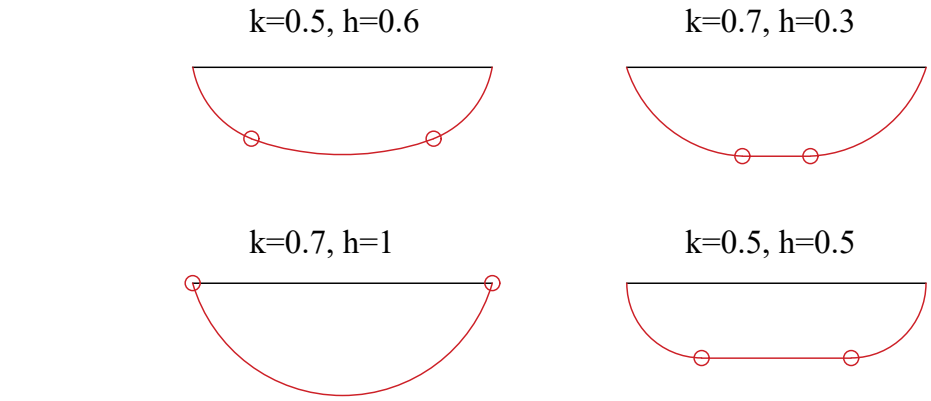

Figure 4.7: Examples of hull profiles for different values of k and h.

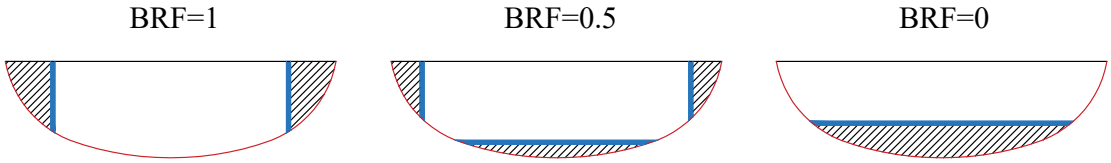

Figure 4.8: Examples of ballast mass distribution between the fore/aft and bottom compartments for a given hull geometry.

concrete ballast (no reinforcements) is $\rho_b = 2200kg/m^3$. The amount of ballast required (M_{bal}) is univocally defined by the mass of the displaced volume of water (M_{tot}), the mass of the hull structure (M_{hull}) and the mass of the gyro-pendumul units (M_{gyros}):

$$M_{bal} = M_{tot} - M_{hull} - M_{gyros} \tag{4.6}$$

Based on previous experience with prototyping of the ISWEC device, M_{hull} is assumed to be 90 times the total volume of the floater.

$$M_{hull} = 90 \times V_{hull} \tag{4.7}$$

This relation is derived from the mass and geometrical properties of full-scale ISWEC floater. Consequently, assuming the walls of the floater as thin plates, the equivalent structural thickness can be calculated from the lateral surface of the floater and M_{hull}, making the computation of inertial properties of the hull possible. As example, the x-coordinate of the COG and the moment inertia about the same

axis can be calculated as follows:

$$x_{G,sb} = \frac{\int x \, dA}{A} \tag{4.8a}$$

$$I_{x,sb} = \rho \int \left(y^2 + z^2\right) \, dV \tag{4.8b}$$

$$x_G = \frac{\sum_{sb} x_{G,sb} m_{sb}}{M_d} \tag{4.8c}$$

$$I_x = \sum_{sb} I_{x,sb} \tag{4.8d}$$

Once the center of gravity and moments of inertia of all subsystem sb are known, the inertial properties of the whole device can be calculated. m_{sb} is the mass associated to the $sb-th$ subcomponent and M_d is the displacement mass of the device. The same procedure is valid for the inertial properties related to the other DoFs y and z.

4.3.2 Gyro-pendulum parameters

The gyroscope represents the core of the ISWEC energy conversion process, and its geometrical optimization influences the maximization of power absorption, its costs and construction feasibility. Through the experience gained from the full-scale devices deployed in Pantelleria and Adriatic Seas, the technological solution shows in Figure 4.9 is considered in this work as the most effective one in terms of construction feasibility and costs.

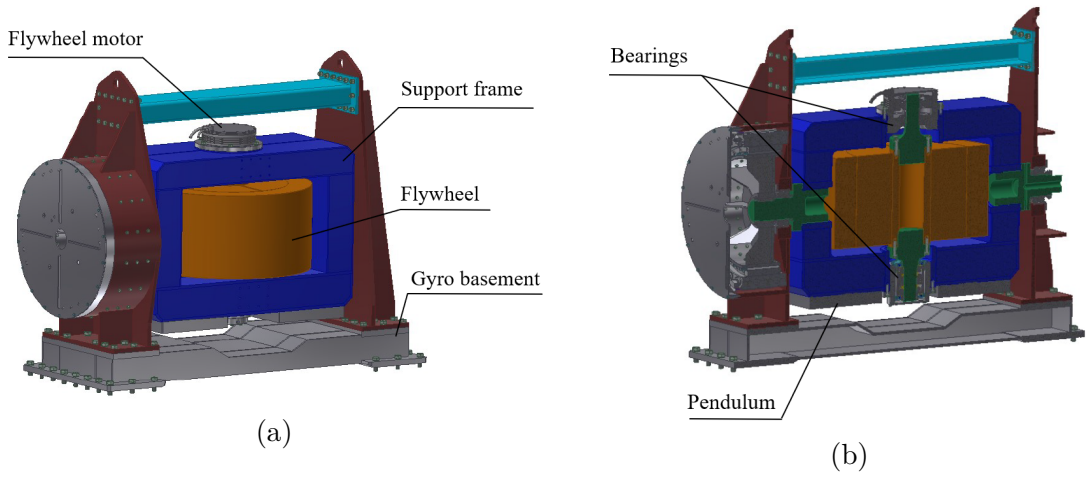

(a) (b)

Figure 4.9: (a) Gyroscope layout and (b) gyroscope section: (blue) Support frame in blue, flywheel in orange, shafts in green. Adapted from [185].

The flywheel can rotate about its symmetrical axis driven by an electrical motor controlled at a constant speed $\dot{\varphi}$. Two radial and one axial bearings constrain the flywheel on a support frame. Other two radial and one axial bearings constrain the support frame on the hull structure allowing its precession motion around the ε axis. The precession oscillation of the gyroscope is captured by the PTO system and converted into electrical energy. An eccentric pendulum is mounted on the bottom of the support frame to avoid the gyroscope to reach its equilibrium position at 90° providing a stiffness recall. The eccentric mass is implemented as a passive elastic recall and to modify the dynamic properties of the gyroscope about its precession axis ε and maximize the power extraction.

Gyroscope subsystem

Two design parameter are used for the gyroscopic system:

- J: the flywheel inertia about its vertical rotational axis. The term J determines the angular momentum $L = J\dot{\varphi}$ of the system and it is used to derive the dimensions of the whole gyroscope, on the basis of certain assumptions;
- n_{gyros}: the number of gyroscopic units inside the hull. The realization of one single gyroscope with a high inertia J can result in high loads and costs. Moreover, the device is not balanced one the roll axis since the precession motion of one single gyroscope affects the equilibrium around the α-axis of the floater. One solution is to distribute the inertia on multiple gyroscope units.

With reference to the Figure 4.10, the flywheel structure can be simplified as a hollow cylinder, which geometrical properties are defined by an external diameter, $D_{e_{fw}}$, an internal diameter $D_{i_{fw}}$ and a height H_{fw}.

The parametrization of the flywheel is related with geometrical ratios as follows:

- $k_{fw} = \frac{H_{fw}}{D_{e_{fw}}} = 0.5$: ratio between the flywheel height and the external diameter;
- $w_{fw} = \frac{D_{i_{fw}}}{D_{e_{fw}}} = 0.75$: ratio between the flywheel internal diameter and the external diameter.

Then, the principal moments of inertia for a hollow cylinder about the rotational

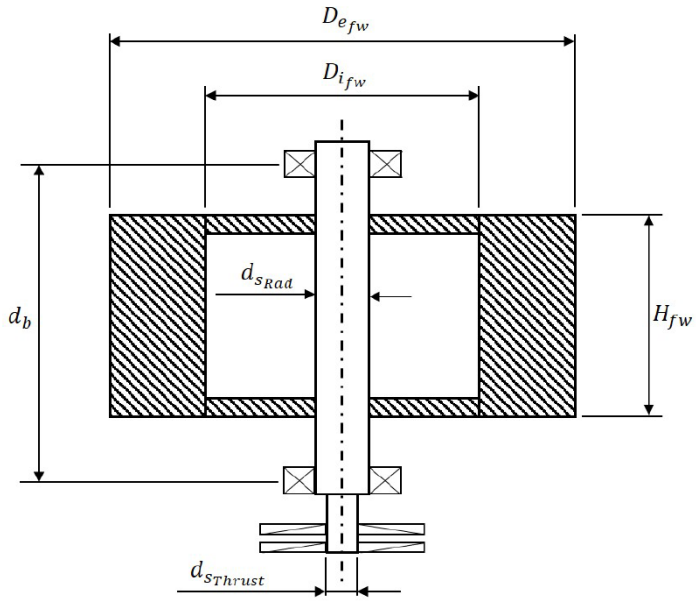

Figure 4.10: Scheme of the flywheel geometrical parametrization. Adapted from [185].

axis are:

$$m_{fw} = \rho_{fw} \pi H_{fw} \left(R_{e_{fw}}^2 + R_{i_{fw}}^2 \right) \tag{4.9a}$$

$$I_{fw_{xx}} = \frac{m_{fw}}{12} \left(3 \left(R_{e_{fw}}^2 + R_{i_{fw}}^2 \right) + H_{fw}^2 \right) \tag{4.9b}$$

$$I_{fw_{yy}} = \frac{m_{fw}}{12} \left(3 \left(R_{e_{fw}}^2 + R_{i_{fw}}^2 \right) + H_{fw}^2 \right) \tag{4.9c}$$

$$I_{fw_{zz}} = J = \frac{m_{fw}}{2} \left(R_{e_{fw}}^2 + R_{i_{fw}}^2 \right) \tag{4.9d}$$

where $I_{fw_{ii}}$ is the moment of inertial about the $i-th$ axis, m_{fw} the flywheel mass, $R_{e_{fw}}$ and $R_{i_{fw}}$ are the external and internal radius of the flywheel, ρ_{fw} is the density of the flywheel depending on the material used. Steel or cast-iron are two possible solutions with their related benefits and drawbacks in term of cost and mechanical performances. In this work the cast-iron has been considered due to its low cost compared with the steel. The flywheel geometry and moments of inertia about the horizontal axes x and y are uniquely defined given the parameters $R_{e_{fw}}$,

$R_{i_{fw}}$ and H_{fw} and the geometrical ratios:

$$R_{e_{fw}} = \sqrt[5]{\frac{J}{\rho_{fw}\pi k_{fw}\left(1 - w_{fw}\right)}} \tag{4.10a}$$

$$R_{i_{fw}} = R_{e_{fw}} w_{fw} \tag{4.10b}$$

$$H_{fw} = R_{e_{fw}} k_{fw} \tag{4.10c}$$

The moments of inertia $I_{s_{ii}}$ of the support frame about the $i-th$ axis are given as function of the flywheel moment inertia $I_{fw_{ii}}$. Similar to the flywheel, the inertial ratios are derived from the ISWEC full-scale device design experience:

$$hs_{xx} = \frac{I_{s_{xx}}}{I_{fw_{xx}}} = 0.75 \tag{4.11a}$$

$$hs_{yy} = \frac{I_{s_{yy}}}{I_{fw_{yy}}} = 1.80 \tag{4.11b}$$

$$hs_{zz} = \frac{I_{s_{zz}}}{I_{fw_{zz}}} = 0.855 \tag{4.11c}$$

$$hs_{m} = \frac{m_s}{m_{fw}} = 0.55 \tag{4.11d}$$

where I_s and m_s are respectively the moment of inertia and the mass of the support frame. It is assumed that the overall dimensions and moments of inertia of the gyroscope unit are a linear function respectively of the flywheel external diameter and its momenta of inertia (derived from the full-scale ISWEC device):

$$L_g = 2.3 D_{e_{fw}} + 3.2 \tag{4.12a}$$

$$W_g = D_{e_{fw}} + 1.2 \tag{4.12b}$$

$$H_g = 3.6 D_{e_{fw}} \tag{4.12c}$$

$$\mathbf{I}_g = \mathbf{I}_{fw} + \mathbf{I}_s + \mathbf{I}_p \tag{4.12d}$$

$$m_g = 3 m_{fw} \tag{4.12e}$$

where L_g is the length of the gyroscope unit, W_g is the width of the gyroscope unit, H_g is the width of the gyroscope unit, $\mathbf{I}_g$ is the inertial tensor of the whole gyroscopic unit and $\mathbf{I}_p$ the one of the pendulum, derived afterwards. For the sake of simplification, the centre of gravity of the gyroscopic unit is assumed to coincide with its geometrical centre. The calculation of the gyroscope unit overall dimensions are useful to verify the encumbrances inside the hull. As described in Section 4.2, a feasibility check and consequently the calculation of a penalty function is used to

avoid unfeasible devices. The verification of the internal encumbrances represents one of the feasibility check performed. The number of gyro units n_{gyros} influence this feasibility check. It is assumed that the gyroscopic units are in even number to avoid roll torques on the hull. The algorithm tries to locate the units along the y-axis of the floater and, if the total width of the gyroscope units exceed the hull width, it tries to arrange the units in two parallel and adjacent lines. The aim is to fit all the gyros into the floater in relation to their dimensions summarized in equations 4.12. Examples of two feasible and one unfeasible gyro arrangements are depicted in Figure 4.11

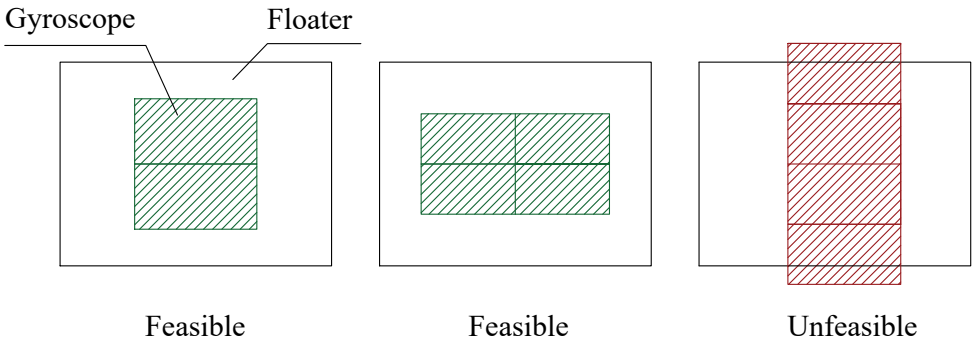

Figure 4.11: Different gyro arrangement solutions: two feasible and one unfeasible disposal.

Pendulum subsystem

The parameter used to define the pendulum subsystem is its mass m_p that, combined with the distance d_p, determines the magnitude of the elastic recall provided on the gyroscope around its precession axis ε. Figure 4.12 shows the scheme of the pendulum installed at the base of the flywheel support frame in the $x-z$ reference plane. It is assumed that the distance d_p between the ε-axis of the gyroscope and the centre of gravity of the eccentric mass is equal to the flywheel height:

$$d_p = H_{fw} \tag{4.13}$$

Then, given the mass and the distance of the eccentric mass, it is possible to compute the inertia tensor of the pendulum $\mathbf{I}_p$.

Flywheel bearings

The flywheel bearings affect both the power losses of the system and its lifespan, determining part of the power consumed by the flywheel motor and the maximum gyroscopic load tolerable. The mechanical design of the flywheel bearings involves

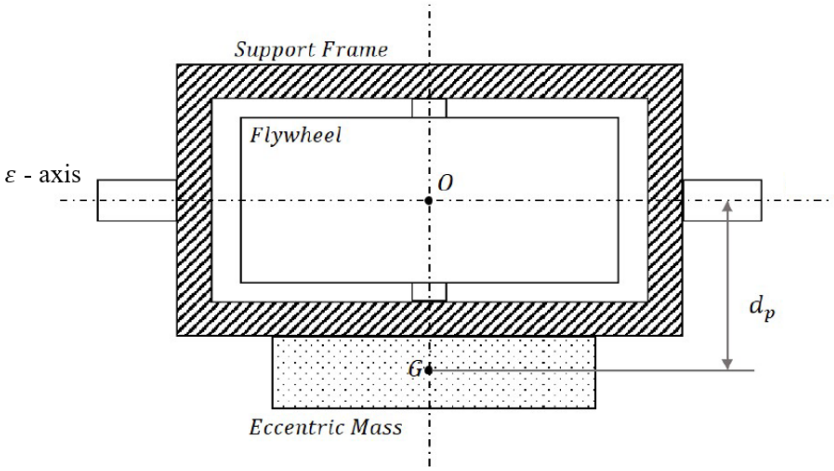

Figure 4.12: Scheme of the pendulum fixed at the base of the flywheel support frame. Adapted from [185].

a static and fatigue verification. The axial load are due mainly to the weight force. Instead, the radial bearings are subject to the radial forces, that are a combination of the weight force and the gyroscopic torques which are more relevant. The maximum static load is given in the bearings SKF catalogue [225] and named C_0 and, during the optimization of the system control parameters, a load verification is performed (see Section 4.4). 15 bearings couples are defined with the features shown in Figure 4.13 and the related optimization parameter is named ID_b. Such diagrams relate the inner diameter of the radial and axial bearings with their admissible static load. The optimization algorithm chooses from these bearings combinations to determines the optimal solution to fit the requirement of admissible loads (large bearings) and low power losses (small bearings). The reader may notice that 15 bearings are reported in Figure 4.13a while only 8 in Figure 4.13b: simply, there are thrust bearings repeated and coupled with different radial bearings, which are 15 different bearings instead.

The distance between the radial bearings d_b is supposed to be related with the flywheel height H_{fw} (derived from the full-scale ISWEC device):

$$d_b = 1.75 H_{fw} \tag{4.14}$$

Each bearing considered has been modelled according to the SKF catalogue [225] to carry out the power losses associated to it using the formulae 2.112.

4.3.3 Mechanical PTO parameters

The ISWEC MPTO is constituted by a PMSG, one for each gyroscope unit, combined with a planetary gearbox that is well suited for high torque and low

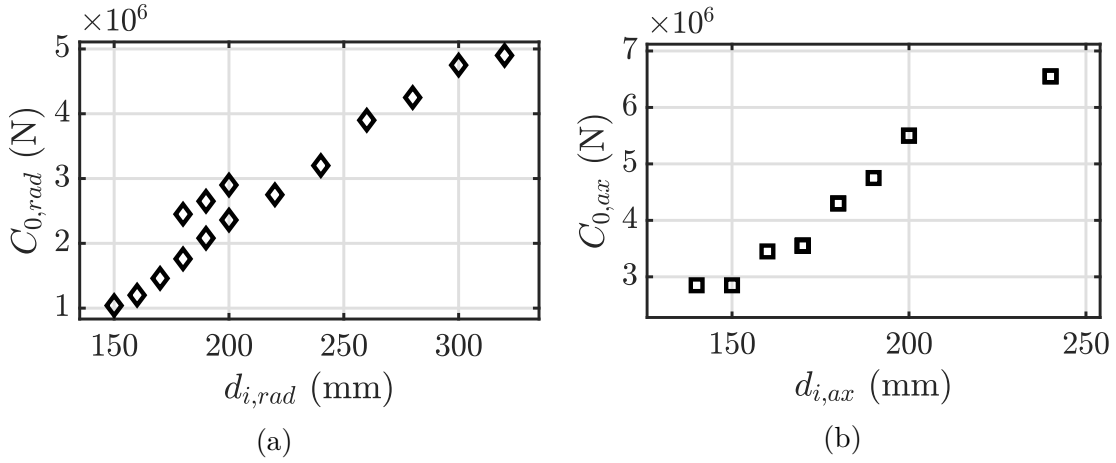

Figure 4.13: Set of selected radial bearings (a) and axial bearings with their inner diameter and the static load supported.

speed applications. SIEMENS [231] and Desch [189] collaborated to create a custom mechanical PTO catalogue with different combinations of electric generators and gearboxes. Therefore, the free parameters defining the MPTO are reduced to be the PTO id ID_{pto} that identifies one of the 36 combinations available. Figure 4.14 reports different combinations of nominal torque T_{pto} and rated power installed P_{pto} for different gearbox ratio τ_{gb} associated.

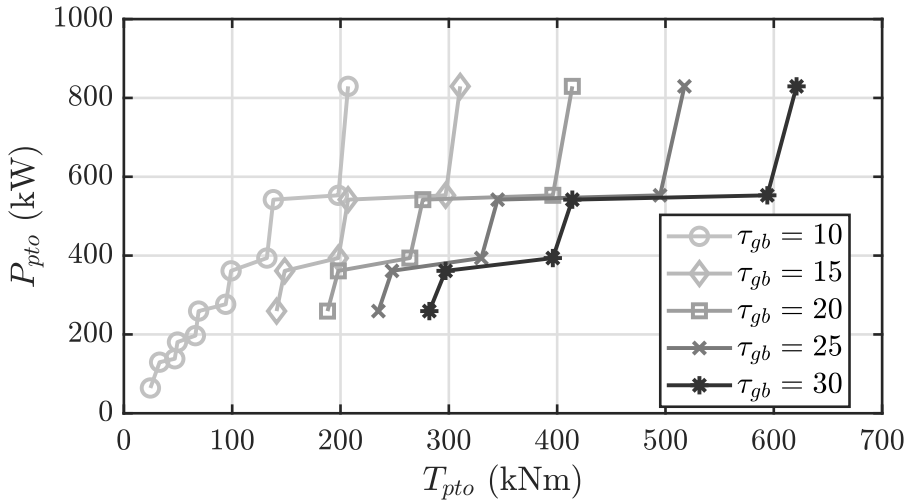

Figure 4.14: Rated power P_{pto} and nominal torque T_{pto} of each gearbox-generator combination considered in the optimization algorithm.

The combinations reported in Figure 4.14 allow to cover a wide range of nominal power and torque giving different solutions for the MPTO with different associated cost.

4.3.4 Hydraulic PTO parameters

As described in Section 4.1, the HTPO is optimized with two consecutive optimization stages: Stage 1a and Stage 1b. In the first stage, the free parameters considered are the pump unit ID_p and the hydraulic control type ID_c. Then, once the first optimization stage is finished, up to 10 promising individuals are optimized again in the stage 1b which performs the HPTO optimization, refining the hull and gyro-pendulum parameters (if needed) and optimizing the pump unit ID_p, the hydraulic control type ID_c, hp accumulator volume V_{hp0}, hp accumulator pre-charge pressure p_{hp0}, the motor-generator model ID_{mg} an added inertia on the electrical generator I_a and the number of hydraulic circuits n_c.

Hydraulic pump and control

The hydraulic pump is chosen from the Hägglunds CB and CBp radial piston pump catalogues offered by Bosch Rexroth. As described in Section 2.4.2, the CBp series replicate the sizes of the CB ones offering a powerful torque and speed range. Moreover, some tandem configurations are considered. The range of speed ω_{pump} and torque T_{pump} offered by the Hägglunds catalogue is reported in Figure 4.15, where 36 different solutions are considered.

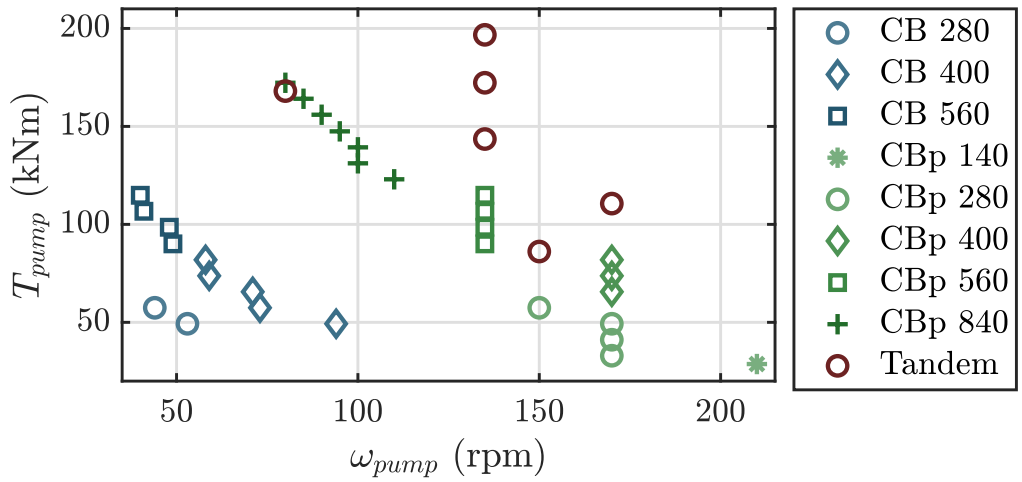

Figure 4.15: Hydraulic pump solutions offered by Bosch Rexroth in respect to their rated speed ω_{pump} and torque T_{pump}.

The pump model ID_p refers to one of the pump unit summarized in Figure 4.15. Each series, identified from the prefix CB or CBp, can offer more than one solution (e.g. the serie CBp 560 offers four different solutions: CBp 560-440, CBp 560-480, CBp 560-520 and CBp 560-560). The tandem configurations are composed by CBp units, for example CBp 280 + CBp 140. More details about the displacement, peak

torque, peak speed, rated power, efficiency and main dimensions of each unit can be found on the online catalogues [202].

The control mode of the primary pump ID_c is an optimization parameter since different control architectures can be considered with different benefits and drawbacks. First, it is possible to implement or not implement the declutching control logic. Since the hydraulic pumps have fixed displacement, the only way to regulate the torque acting on the gyroscope is to short-circuit the pump for some period of the wave cycle, as described in Section 2.4.2. This control could significantly improve the power production of the ISWEC system [277] in respect to a solution without the clutch-declutch valve. However, the clutch-declutch valve can be prone to failures due to the number open-close cycles demanded and thus can affect the reliability of the system increasing the down-times, which turn out to be costly in term of maintenance required. Then, the system is evaluated both with and without the declutching control logic. A further degree of controllability is added to the system if tandem units are used, allowing to switch from one, two or three different total displacements introducing a regulation in respect to the PTO torque. Also in this case, the optimization algorithm can choose from consider or not consider the switching of the pump units. The four control possibilities are summarized in Table 4.3.

ID_c	Declutching control	Pump switching*
1	no	no
2	yes	no
3	no	yes
4	yes	yes

Table 4.3: Pump control combinations considered by the optimization algorithm. $*$: the pump switching can be enabled only with tandem configurations; if a single pump is used, only the first two control logics are implementable.

Accumulators

The hp accumulator is optimized in respect to its:

- V_{hp0}: hp accumulator total volume, that influences the "filter effect" provided by the accumulator;
- p_{hp0}: hp pre-charge pressure that, similar to the hp accumulator total volume, influences the ability of the accumulator to smooth the flow peaks. Moreover, hp pre-charge pressure determines the minimum p_{hp} on the high-pressure ram and thus influences the minimum torque acting on pump and motor.

The effect of both V_{hp0} and p_{hp0} is shown in Figure 4.16. The hp accumulator should also be able to store energy as a compromise between the desire to be able to smoothen the output power, and the desire to keep the accumulators as small as possible, in order to keep the weight and costs as low as possible. The hp total volume is chosen from 100 and 600 litres while the pre-charge pressure from 20 to 60 bar. The lp accumulator volume is fixed to 600 l and its pre-charge pressure is chosen according to the minimum charge pressure required by the hydraulic components that is found on the supplier catalogues [202, 215, 214, 217] depending on the selected unit.

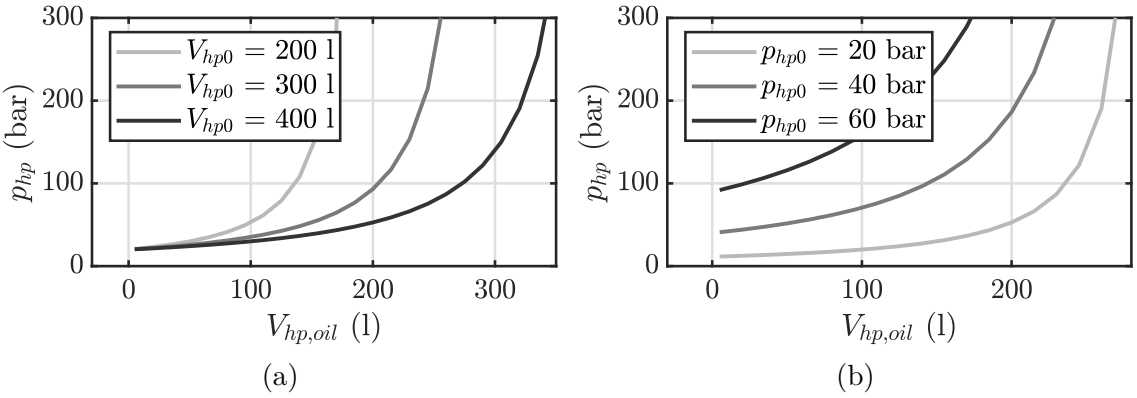

Figure 4.16: Effect of the accumulator total volume (a) and pre-charge pressure (b) on the accumulator adiabatic curve.

Motor-generator stage

The motor generator stage represents the last part of the HPTO. It undertook to transform the hydraulic energy given by the hp accumulator into a usable electric energy. Similarly to the hydraulic pump, the hydraulic motor and its coupled generator are chosen from a finite number of solutions provided by Moog, Bosch Rexroth and SIEMENS. For what concerns Moog, the solutions proposed by the American company are an all-in-one electro-hydraulic units with a radial-piston motor and a PMSG, as reported by the online catalogue [217]. On the other hand, Bosch Rexroth offers only the hydraulic motor part and SIEMENS is required to supply the electric generator. Axial piston motor with fixed displacement [215] and 1PH8 servomotors [216] are considered as the hydraulic and eletric unit, respectively. The range of speed ω_{motor} and torque T_{motor} of the hydraulic units is shown in Figure 4.17a. Then, in Figure 4.17b, the electric generator rated torque T_{gen} and power P_{gen} is reported. 15 different solutions are available, seven from Moog and eight from Bosch Rexroth and SIEMENS. Again, despite 7 solutions are provided by Moog, only 5 distinct hydraulic units are chosen from the EHA Moog catalogue [217] and 6 distinct generator units. These are combined to obtain the 7 solutions.

Similarly, despite 8 solutions are provided from the Bosch-SIEMENS collaboration, 7 distinct generator units are chosen from the SIEMENS catalogue [216] that are combined with 8 distinct hydraulic motor from Bosch Rexroth [215] to obtain 8 solutions. The motor-generator id ID_{mg} refers to one of the motor-generator combinations summarized in Figures 4.17a and 4.17b.

Furthermore, a flywheel is considered to improve the control characteristics of the electrical generator and avoid acceleration peaks as suggested by Gaspar in [119]. The value of this added inertia I_a is considered as a free parameter and chosen from 1 to 20 kgm^2.

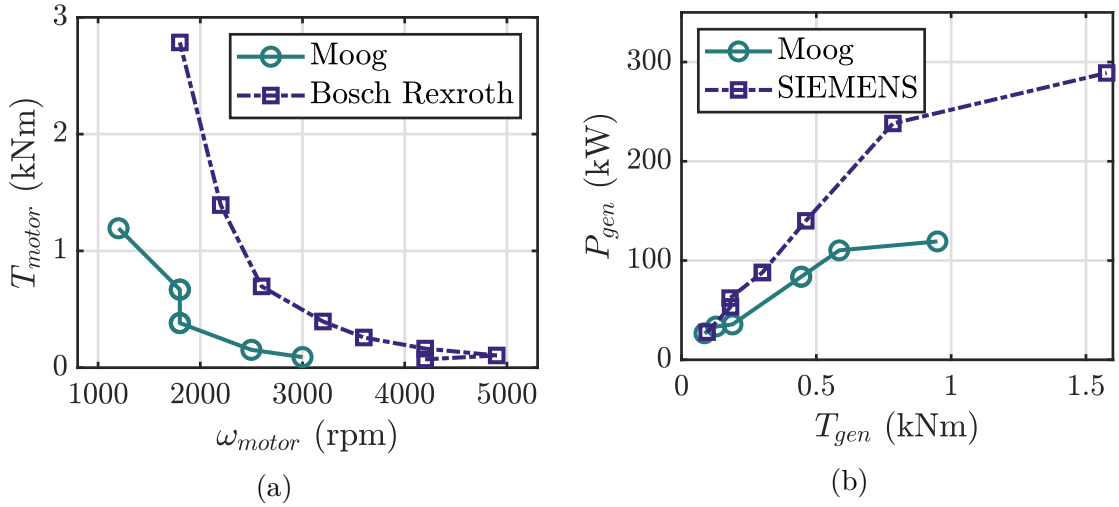

Figure 4.17: Hydraulic motors (a) and electric generators (b) rated speed, torque and power data.

Hydraulic circuit

With the aim to limit the system costs and to reduce the hydraulic components installed on the ISWEC, single or multiple hydraulic circuits can be considered. In this regard, the number of hydraulic circuits n_c is a free parameter to be optimized. Two examples of possible solutions are shown in Figure 4.18, where a single and multiple circuit architectures are compared. The first one reduces the number of hydraulic components installed as well as the electric components associated to the generator unit, reducing the overall costs and the risk of failure. However, in presence of multiple-circuits the ISWEC could continue to produce power also in case of a single motor-generator failure: the faulty unit can be turned off and the other circuits can continue to operate.

It is worth specify that the other auxiliary components, such as clutch-declutch valves and check-valves are chosen to provide the lowest power losses according to their catalogue [206]. The relief valves are chosen to guarantee the maximal pressure

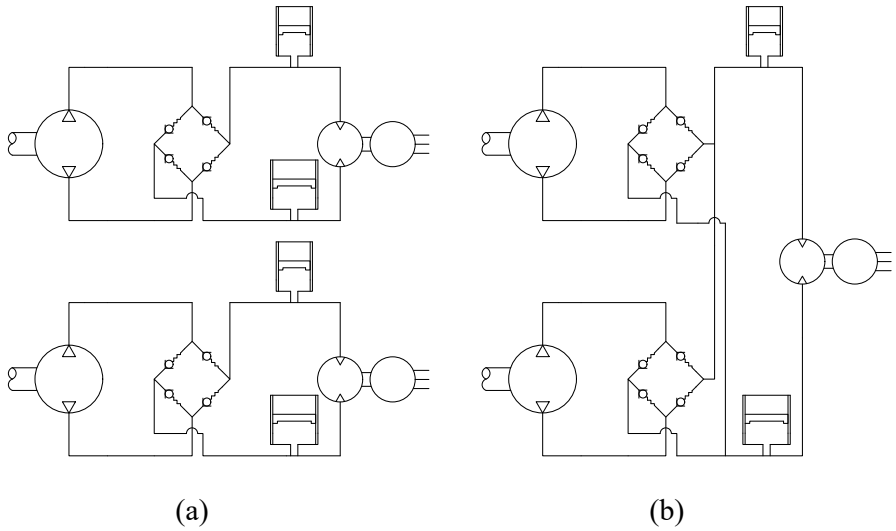

Figure 4.18: Multiple (a) and single (b) hydraulic circuit configurations.

limit under 300 bar to safeguard the hydraulic components of the circuits [213]. The hoses, junctions and sensors that composes the hydraulic manifold are not modelled and only the associated cost has been assigned to them (see Section 4.3.5).

4.3.5 Device cost estimation

The ISWEC optimization includes a preliminary evaluation of the total cost of the device in order to evaluate the investment behind a specific configuration and architecture. Three subsystems are considered into the cost evaluation: floater, gyro-pendulum unit and the PTO plus electronic/auxiliary systems. The overall cost of the device C_{tot} is given by the sum of the costs of each subsystem:

$$C_{TOT} = C_{HULL} + C_{GYRO} + C_{PTO} \tag{4.15}$$

Floater cost

The cost of the floater C_{hull} is proportional to its Overall volume V_h. In naval carpentry sector, the cost per unit of Overall volume can be reasonably assumed to be 275 €/m^3 if a the concrete is used as a construction material. Due to the experience derived from the full-scale systems, the following hull cost function holds:

$$C_{HULL} = 275 \times V_h \tag{4.16}$$

where V_h can be roughly computed considering the main dimensions of the hull (length, width and height):

$$V_h = L \times W \times H \tag{4.17}$$

Gyro-pendulum cost

The gyroscope cost function includes material and manufacturing costs of the flywheel, support frame structures, shafts and bearings. The cost of the gyroscope C_{gyro} can be set proportional to its structural mass m_g, computed via the last equation 4.12. In mechanical manufacturing, the cost per unit mass produced can be reasonably assumed to be 6000 €/ton. However, for small and high structural mass the cost is increased in respect to the linear function $6000 \times m_g$. The following gyro-pendulum cost function holds:

$$C_{gyro} = \begin{cases} 6000 \times m_g + \dfrac{8000 - 6000}{32} m_g(32 - m_g) & \text{if } \; m_g < 32ton \\ 6000 \times m_g & \text{if } \; 32ton \leq m_g \leq 50ton \\ 6000 \times m_g + \dfrac{7200 - 6000}{20} m_g(m_g - 50) & \text{if } \; m_g \geq 50ton \end{cases} \tag{4.18}$$

The cost C_{gyro} is related to a single gyro-pendulum unit and has to be multiplied by the total number of gyroscope units:

$$C_{GYRO} = C_{gyro} n_{gyros} \tag{4.19}$$

Mechanical PTO cost

The MPTO cost function includes the costs of: gearbox, generator, inverter, driver, super-capacitors, batteries, sensors, data acquisition system, software licenses, cables and other auxiliary systems related to the generation stage. In this work the power electronics associated to the PTO system is not modelled and the electric generator is considered a spring-damper system in the MPTO (see equation 2.89). However, the cost of the electrical auxiliary components have to be considered since it represent a large part of the PTO cost. The costs are referred to one gyroscope unit. SIEMENS and Desh collaborated to collect the cost of each combination of gearbox and electric generator along with their correlated power electronics and the result is depicted in Figure 4.19 in respect to the PTO nominal torque T_{pto}.

The C_{pto} has to be multiplied by the number of gyroscope units n_{gyros}:

$$C_{MPTO} = C_{pto} n_{gyros} \tag{4.20}$$

A complete description of the electrical system installed on the full-scale device can be found in [35].

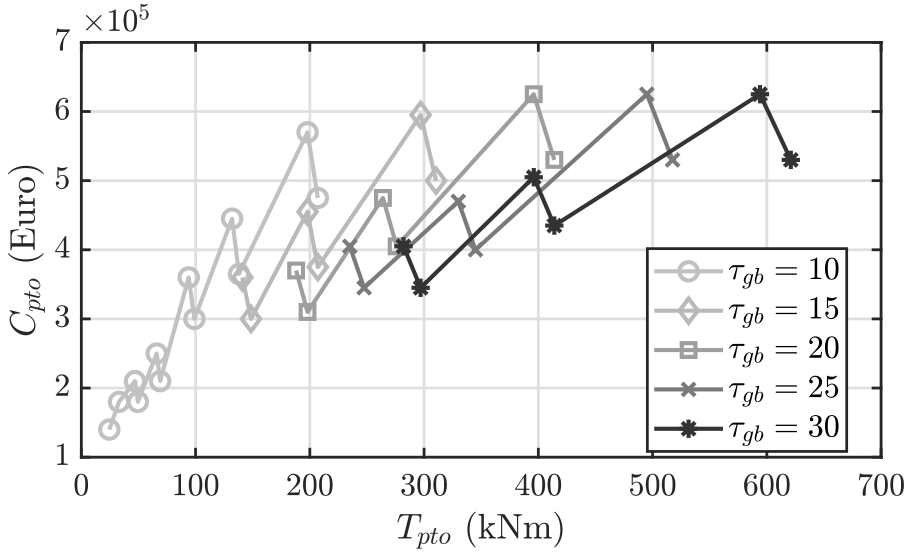

Figure 4.19: Cost of the mechanical PTO units in respect to the rated torque of the PTO and the gearbox installed.

Hydraulic PTO cost

Concerning the HPTO, different subsystems are quoted here according to each supplier involved in the market investigation. The cost of the hydraulic transmission can be split into several contributions: pump cost, accumulators cost, manifold cost, valves and auxiliary hydraulic components cost, motor-generator cost and the associated inverter, driver, super-capacitors, batteries, sensors, data acquisition system, software licenses, cables, etc.

$$C_{HPTO} = C_{PUMP} + C_{ACC} + C_{MAN} + C_{AUX} + C_{MOTGEN} \tag{4.21}$$

The costs of the hydraulic pumps are summarized in Figure 4.20 where the cost associated to each unit is reported in respect to their rated torque T_{pump}. As shown in Figure 4.20, the cost of the CB units are considerably lower than the CBp ones, since a lower specific hydraulic power is deliverable. On the other hand, the tandem units are the most expensive solutions since two hydraulic pumps are installed for each tandem unit. However, despite the higher investment required, the tandem solution allows to switch between each other giving three different values of the total displacement available: displacement of the unit 1 (D_{p1}), displacement of the unit 2 (D_{p2}) and the sum of the two displacements ($D_{p1} + D_{p2}$), improving the controllability of the system.

The overall cost is related to a single pump unit and it has to be multiplied by the number of gyroscope units n_{gyros}:

$$C_{PUMP} = C_{pump} n_{gyros} \tag{4.22}$$

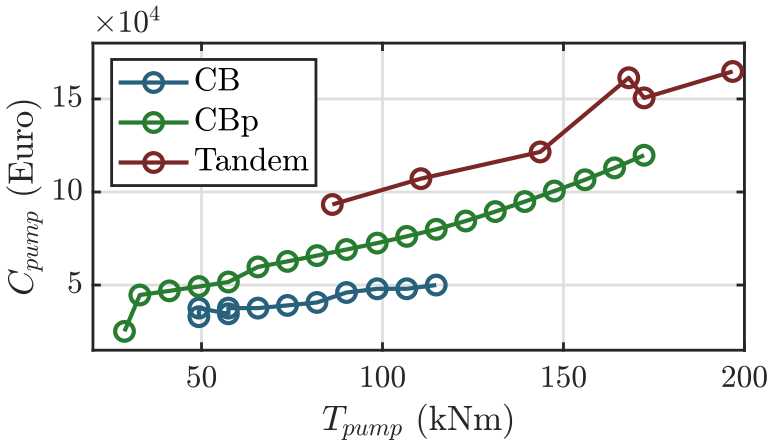

Figure 4.20: Cost of the pump units in respect to the rated torque of the pump and the pump type.

The cost of the accumulator can be expressed as a function of the accumulator volume V_{hp0}. An accurate market investigation allowed to determine the cost per litre equal to 22 €/l associated to the standard accumulator volume of 100 l. The hp accumulator volume span from 100 l to 600 l as indicated in Table 4.2, and the lp accumulator volume is fixed to 600 l. Then, the cost can be determined considering multiple 100 l modules plus the cost of junctions and tubes needed for the connection of the accumulators with the manifold, that are fixed to 250 € per accumulator unit. Under these assumptions, the following cost function holds:

$$C_{hp-acc} = V_{hp0} \times 22 + 250 \times n_{acc} \tag{4.23a}$$
$$C_{lp-acc} = 600 \times 22 + 250 \times 6 \tag{4.23b}$$
$$C_{ACC} = (C_{hp-acc} + C_{lp-acc}) n_c \tag{4.23c}$$

where n_{acc} is the number of hp accumulator units needed to obtain the required V_{hp0} and n_c the number of hydraulic circuits. Six accumulators are needed for the low-pressure ram.

Concerning the manifold, the cost has been fixed to 15000 € if one gyroscopic unit is connected to one manifold, 17500 € if two gyroscopic units are connected to one manifold and 20000 € if four gyroscopic units are connected to one manifold:

$$C_{MAN} = \begin{cases} 15000 \times n_c & \text{if } \dfrac{n_{gyros}}{n_c} = 1 \\ 17500 \times n_c & \text{if } \dfrac{n_{gyros}}{n_c} = 2 \\ 20000 \times n_c & \text{if } \dfrac{n_{gyros}}{n_c} = 4 \end{cases} \tag{4.24}$$

The costs per manifold have been determined according to a Italian manifold supplier. As the number of gyroscopes, and thus the number of the associated hydraulic pump units, connected to one single manifold increase, the dimensions as well as the auxiliary parts associated to one manifold unit grow, increasing the cost per manifold.

Concerning the auxiliary components, the cost associated to a single manifold unit is equal to 5000 €, accounting for the clutch-declutch valve, check-valves, relief valves and sensors. The oil cost is given equal to 4.5 €/l and the total volume of the oil can be calculated considering the lp accumulator volume[2] increased by a 30% to account for the oil inside the manifold hoses. The auxiliary costs follow:

$$C_{valves} = 5000€ \tag{4.25a}$$
$$C_{oil} = 4.5 \times V_{lp0} \times 1.3 \tag{4.25b}$$
$$C_{AUX} = (C_{valves} + C_{oil})n_c \tag{4.25c}$$

The costs of the motor-generator stage are summarized in Figure 4.21 where the cost associated to each combination motor-generator, with the related power electronics is reported in respect to the rated power of the electric generator P_{gen}.

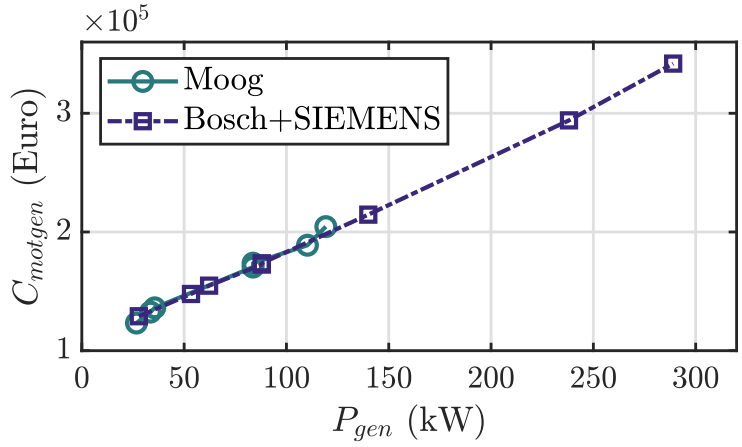

Figure 4.21: Cost of the motor-generator units, considering the associated power electronics cost and auxiliary components in respect to the rated power of the electric generator.

The solutions offered by Moog are completely comparable with the custom solutions obtained from the combination of the Bosch Rexroth hydraulic motors and the SIEMENS electric generators in term of cost per kW of installed power.

[2]It is assumed that when the ISWEC is at rest all the oil is stored in the lp accumulator completely full in order to provide enough oil for the hp accumulator during the operating conditions.

The cost of each generation unit have to be multiplied by the number of hydraulic circuits considered:

$$C_{MOTGEN} = C_{motgen} n_c \tag{4.26}$$

Here, the cost per kW associated to the power electronics has been diminished compared with the MPTO one. In fact, since the filter effect of the accumulators help to smooth the incoming power, the super-capacitors that have to be installed in a HPTO-based ISWEC device are reduced. This assumption has to be considered as preliminary and further analysis will be performed to accurately design the power electronics associated to a HPTO unit.

4.3.6 Hydrodynamic calculations

The hydrodynamic model coincides with the linear model defined in the frequency-domain equation 2.39 for what concern the SDM, and with the one reported in equations 3.2 and 3.9 for the TDM (the drift forces and the mooring actions are not considered here). Once all the geometrical and inertial quantities of each sub-system have been calculated, the centre of gravity and the moment of inertias of the device can be computed to perform the hydrodynamic calculations. The floater geometry is meshed with a MATLAB routine and the mesh panel dimension and number are parametrized as a function of the dimensions of the device. The hydrodynamic parameters (e.g., added mass, radiation damping, diffraction forces) are calculated using the open source BEM code Nemoh [144, 143]. The state-space representation of the radiation convolution term defined in equation 2.44 is identified using the open source toolbox FOAMM (Finite-Order Approximation by Moment Matching) [278]. Then, depending on the model domain considered (spectral- or time-domain), the calculation of the input of the numerical models can be performed in two ways:

- Spectral-domain input: only the JONSWAP spectra are formulated for each of the wave considered. The energy period T_e, the significant weve height H_s and the the peak enhancement factor γ are the input of the JONSWAP spectrum, computed with the open source MATLAB toolbox WAFO [279].
- Time-domain input: for the time-domain the JONSWAP spectra are defined for each of the wave considered. Then, the irregular wave forces are calculated using the equation 2.72 through the hydrodynamic transfer function obtained with NEMOH.

Hydrodynamic parameters

First, the longest and shortest wave length are chosen as a function of the overall length of the device L in order to have a flexible tool able to manage different

hull geometries: $\lambda_{min} = L/3$ and $\lambda_{max} = 10L$. Within this wave length range the hydrodynamics of the device is well described and 40 values of equidistant frequencies have been adopted based on a compromise between the accuracy of the hydrodynamic parameters calculation and the computational time required for solving the Boundary Value Problem (BVP). The NEMOH tool needs in input the mesh of the floater geometry that is created by a MATLAB in-house routine to have more control over the number and size of mesh panel. Figure 4.22 reports and example of the floater geometry mesh

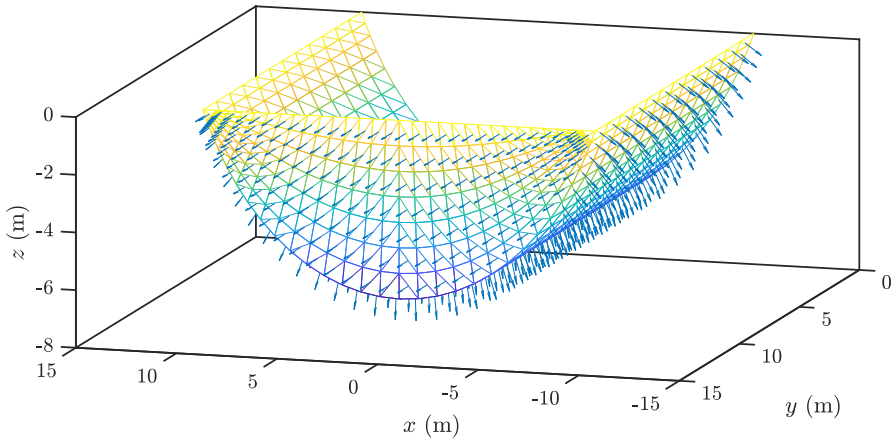

Figure 4.22: Example of the floater geometry mesh.

The influence of the mesh grid parameters and the convergence analysis on the calculation of the hydrodynamic matrices is studied in [185]. In [185], the Mean Relative Error (MRE) of the hydrodynamic parameters calculated with the various meshes with respect to a high-refined one are compared. The author found that a max panel size $\lambda_{min}/7 \div 1.9m$ gives the proper compromise between accuracy and computational time required for the hull dimensions bounds considered in Table 4.2. Figure 4.23 shows an example of the results of added mass and radiation damping computed with NEMOH.

Radiation state-space identification

As discussed in Section 2.1.4, the hydrodynamics of the floater in time-domain can be studied following the linear expression 2.42, known as the *Cummins' differential equation*. The hydrodynamic properties added mass at infinite frequency and the radiation impulse response can be calculated thanks to the *Ogilvie relations*. However, the radiation forces are represented by a convolution term, and it constitutes a drawback in terms of calculation time. It is convenient to approximate the convolution term with a state-space representation, as described in equation 2.44.

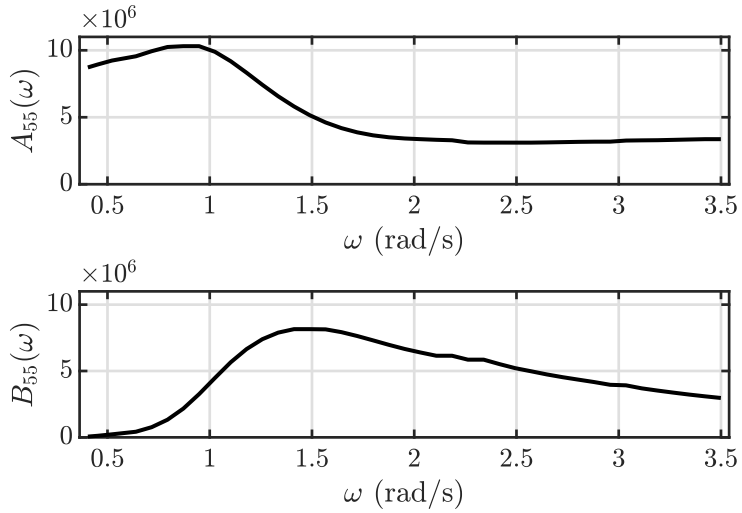

Figure 4.23: Example of added mass and radiation damping for the pitch DoF computed with NEMOH.

FOAMM is used to identify the state-space representation of the radiation convolution term [278]. The error is calculated between the estimated added mass and radiation damping and the added mass and radiation damping calculated originally trough NEMOH to verify the accuracy of the identification process. This routine is repeated for each DoF of the floater.

4.4 Single device optimization

The second step toward the evaluation of a single ISWEC individual consists in simulate and optimize the net annual productivity of the system. Once all the device parameters are defined and the hydrodynamic properties and forces are computed, spectral-domain or time-domain simulations are performed under some hypothesis and restrictions. The aim is to identify the optimal control parameters of the system in order to maximize the performance of such a configuration for all the sea-states considered.

4.4.1 Sea-states definition

The number of simulation waves is defined according to the scatter diagrams of Figure 2.7, concerning the annual occurrences carried by each wave for each sea-site of interest. Since the sea-sites are very different in term of occurrences and energy distributions, the proper number of waves as well as their synthetic parameters (T_e and H_s), have to be chosen. As shown in Figure 4.24, the waves considerd are highlighted with red dots and chosen to cover at least the 99% of the annual energy

of each sea-site, regardless the occurrences distribution. In this regards, all the 128 waves are simulated for a single device and, at the end of the simulation process, the key performances are computed indifferently for each sea-site of interest. The reader may notice that not all the waves described by the four scatter are signed by a red dot; however, once the performances of the devices are evaluated, an interpolation occurs to adapt the results obtained by the 128 sea-states for each scatter table.

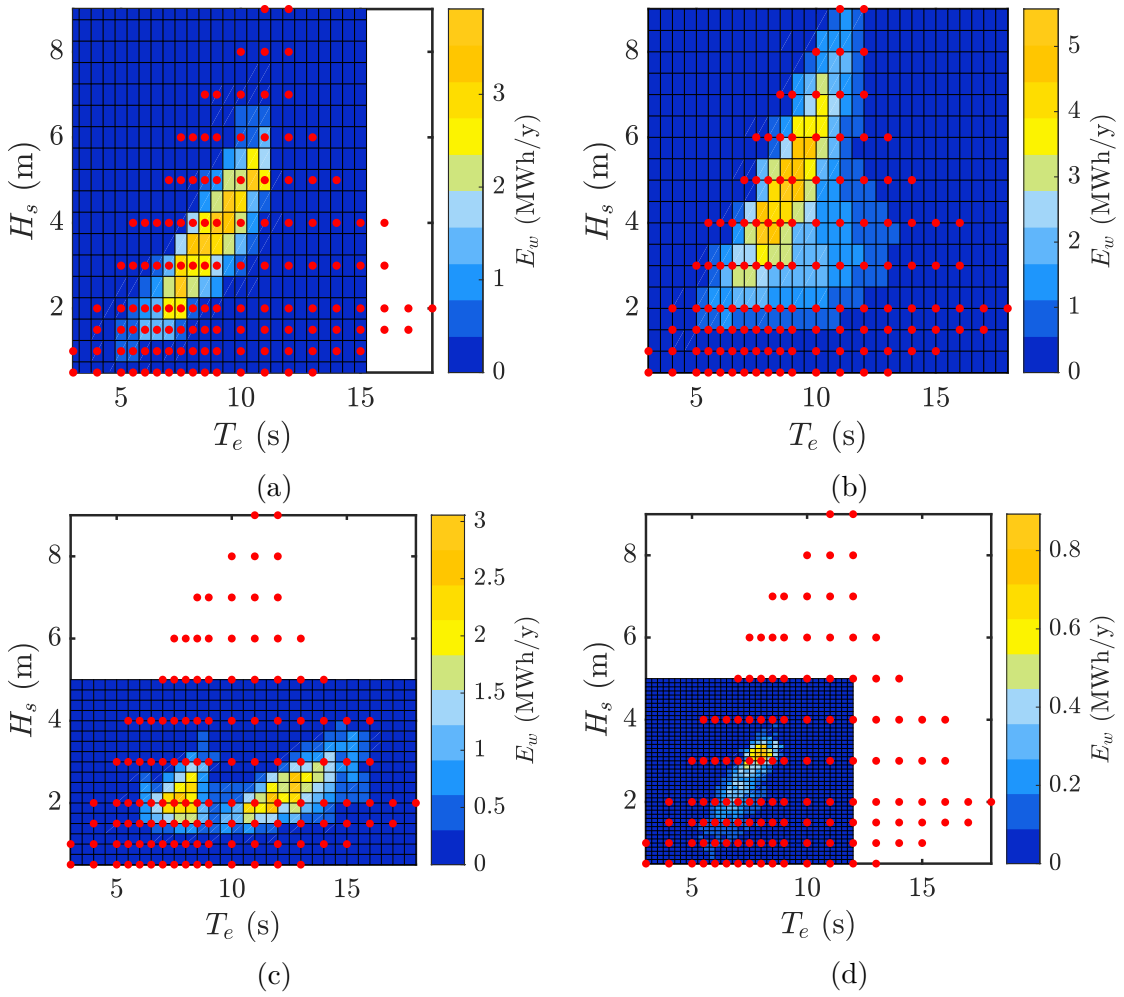

Figure 4.24: Simulation waves (red dots) superposed to the energy matrices of the four sea-sites of interest: (a) Alghero, (b) Balder, (c) Capo Verde and (d) Pantelleria.

4.4.2 Single wave optimization

The single individual is optimized varying its control parameters with the aim to maximize the net power extracted for each of the 128 waves considered. Note that at this stage it is essential to include an energy-maximising control strategy, since it has the ability to significantly increase power production performance over the operational sea. A control-informed optimization is mandatory since the control strategy has a great influence on the dynamic characteristic of the response of the device [280]. Control-informed means that the system is optimized not only in its physical parameters, handled by the genetic algorithm, but also the controller is optimized for each sea-state influencing the dynamic behaviour of the whole system [281, 282]. Moreover, the ability of the controller to optimise power absorption is highly dependent on force/displacement constraints. Such constraints depend on the electrical and mechanical subcomponents characteristics. In this regards, the single wave optimization is performed with a Nelder-mead simplex method [283], implemented in MATLAB with the native function `fminsearch`. The function aims to optimize the control parameters of the system (e.g. k_g, c_g, $\dot{\varphi}$, $\dot{\varepsilon}_{cs}$, etc.) for each sea-state (regardless the simulation domain) considering the following cost function J_{opt}:

$$J_{opt} = -\overline{P}_n + \sum_{c}^{I_c} p_c \tag{4.27}$$

The equation 4.27 includes two terms: $\overline{P}_n$ is mean net power extracted from the system for a single sea state and $\sum_c^{I_c} p_c$ are the sum of the "penalty costs" associated to the violation of the physical constraints I_c. As discussed in [254], when an optimization algorithm is applied to a dynamical model, there is the probability that some state variables overcome the limit conditions making the results not reliable or representative of the true system performances. Therefore, soft constraints are considered in the cost function adding a penalty term to the optimization problem defined as:

$$p_c = \frac{1 + \tanh(k_c(|x_c| - x_{c,lim}))}{2}|x_c| \tag{4.28}$$

The penalty term p_c associated to the system variable x_c that is constrained to the value $x_{c,lim}$ is computed with the function 4.28. k_c is the steepness coefficient to make the tanh function similar to a step function. Note that the mean net power $\overline{P}_n$ for the TDM is computed by averaging all the single $\tilde{P}_n$ according to the equation 3.65. The behaviour of the penalty expression is represented in Figure 4.25. When the variable x_c is below its limit $x_{c,lim}$, the value of the penalty function is equal to zero. On the other hand, as x_c excesses the limit $x_{c,lim}$, the penalty function increases affecting the value of the cost function J_{opt}.

Different variables contribute to compute the penalty function:

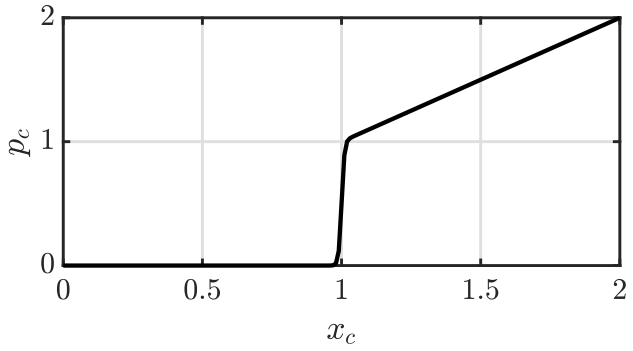

Figure 4.25: Example of a penalty function associated to the generic state variable x_c.

- Hull and gyroscope angular displacements: in order to obtain realistic results, the motion of both the hull and the gyroscope are constrained to be in a range considered replicable in real operating conditions. In particular, the root-mean-squared value of the pitching angle δ as well as the gyroscope precession angle ε are limited to 25° and 50°, respectively. The value of the pitching angle is limited both in spectral- and time-domain simulations while the gyroscope precession angle is limited only in spectral-domain to guarantee the accuracy of the SDM (see Figure 3.13). In time-domain no limits are imposed on the precession angle since no constraints on it exists in the real ISWEC device;

- PTO angular speed and torque: the rms value of the PTO torque and speed are constrained in the SDM through the penalty function. Both torque and speed limits are imposed depending on the electric generator characteristics derived from the catalogue supplier. In time-domain no penalty is assigned to these variables since the saturation and a safety control logic are implemented directly in the numerical model to avoid to overcome the electric generator limits;

- Bearing forces: the forces acting on both radial and axial bearings are verified considering the static limit C_0 and a safety factor equal to 4, giving the maximal tolerable force equal to $F_{max} = C_0/4$. This limit is applied both in spectral- and time-domain simulations.

Table 4.4 summarizes the control parameters to be optimized depending on the PTO considered, its control logic and the simulation domain.

Control parameter	Symbol	Mechanical PTO SDM	Mechanical PTO TDM	Hydraulic PTO SDM	Hydraulic PTO TDM
Flywheel speed	$\dot{\varphi}$	•	•	•	•
Stiffness coefficient	k_g	•	•		
Damping coefficient	c_g	•	•		
Pump switch*	s_p			•	•
Clutching speed*	$\dot{\varepsilon}_{cs}$			•	•
Pump pressure	Δp_p			•	
Generator damping	β_g				•

Table 4.4: Control parameters optimized for each single wave depending on the simulation domain and the PTO configuration. $*$: the number of activated pump and the clutching speed are optimized only if the control modes 3-4 and 2-4 are considered, respectively (see Table 4.3).

4.5 Key performance indicators

The GA aims to minimize an objective function defined through the equation 4.3. The choice of the proper fitness function is not arbitrary, and it relies heavily on the purpose of the optimization. For a WEC developer one objective could be maximize the annual productivity, limiting the associated system cost. A techno-economic optimization underlines a maximization of the economic efficiency of the system, giving different solution that have to be selected balancing the performance of the system and the investment required [284, 285]. Overall, the objective function is the ratio between the device cost and annual energy production. However, in order to highlight the impact of the performance index and to generate a Pareto front, two separated objectives are considered here:

- **AEP: Annual Energy Production** (MWh/y). With AEP we refer to the ISWEC net production, computed with relation 3.70b depending on the sea-site of interest;
- **CoE: Cost of Energy** (Euro/MWh). In this work the CoE is defined as the ration between the device cost and the AEP multiplied by the lifetime of the device, fixed to 25 years:

$$CoE = \frac{C_{TOT}}{25 \times AEP} \tag{4.29}$$

The definition of the fitness index beholds primary importance in the identification of an optimal device: the genetic algorithm iteratively tests several devices to find the one that minimises the objective function. A multi-objective problem is

formulated defining three different fitness functions that are evaluated in three independent optimisation cycles, in order to build the Pareto front [286], as reported in Table 4.5. The optimization of these two different metrics will produce different trends and design solutions. The two metrics will be optimized for the Balder sea-site and then the system performances will be evaluated on the other three sites of interest (Alghero, Capo Verde and Pantelleria) to investigate the influence of the occurrence distribution and power density of different deployment sites.

Set label	Description	AEP (w_1)	CoE (w_2)
1	AEP-driven	1	0
2	AEP-weighed-CoE-weighed	0.50	0.50
3	CoE-driven	0	1

Table 4.5: Multi objective weights w and performance metrices.

The objective of the genetic algorithm is now explicitly formulated: a multi-objective optimization regarding the AEP and the CoE of the system for each of the sea-sites of interest.

4.5.1 Secondary key performances

When it comes to select the best device following the resultant Pareto front of the multi-objective optimization, other drivers and considerations may influence the choice. For example, the device mass influences the mooring loads, the mooring costs, the manufacturability and installability of the device. Moreover, the gyroscope dimensions could affect the choice of the optimal device, influencing again the manufacturability of the ISWEC core. The number of PTO components, dedicated to harness the available wave power, could represent a critical parameter to be evaluated, affecting the reliability of the device, its down time and, thus, the maintenance cost of its lifespan. The quality and behaviour of the output power affects the choice of the PTO components and its electrical power stage (not modelled in this thesis). This work considers the electrical generator downstream to the PTO modelled as a linear spring-damper in the MPTO and a simple linear damper in the HPTO. The variability of the electrical power produced around its mean value determines the size of the electrical components (AC/DC converter, batteries, super-capacitors, etc.) and its efficiency in operating conditions. In this regard, the HPTO has an edge compared with the MPTO if the same annual productivity is guaranteed: the presence of hydraulic accumulators smooths the power peaks allowing the downsize of the electrical components at the end of the transmission. As specified in Sections 4.3.5 and 4.3.5, the algorithm assigns a lower cost per kW at the power electronics associated to the HPTO. However, the efficiency associated to these components is not modelled here and, reasonably, the efficiency

of the HPTO power electronics should be higher than the one of the MPTO since the electrical components should work around their nominal conditions with low variability.

Overall, the first economic investment can be an important driver compared to the annual energy production since more uncertainty is associated to the prediction of the system performances in respect to its cost. In the next Chapter all these factors will be considered for the choice of the optimal ISWEC configuration.

Chapter 5

ISWEC optimization

In this chapter, the optimization of the ISWEC device is discussed. The multi-stage design tool is employed to design two different ISWEC: one with the MPTO and one with the HPTO. First, Stage 1 is used to obtain four promising devices to be evaluated in Stage 2, two for the MPTO and two for the HPTO. In particular, attention is given to the annual energy production, the device cost, its manufacturability and feasibility along with the quality of the power produced by the system. Then, the optimal devices are evaluated in Stage 2 to compare the mechanical and hydraulic PTO solutions to evidence the pros and cons of each systems.

The first part of this Chapter focuses on the design of a HPTO-based ISWEC through the multistage 1a and 1b procedure described in Section 4.1. In Section 5.1, Stage 1a is employed to optimize the ISWEC system with a HPTO assuming a SDM of the device. The system parameters to be optimized concern the hull, gyro-pendulum, the pump unit and the hydraulic control, as specified in Table 4.2. The best two devices of this process go to the Stage 1b, where the HPTO is optimized considering the pump unit, the hydraulic control type, the volume and pre-charge pressure of the hp accumulator, the motor-generator unit and the added inertia, used to improve the controllability and the generator stage. The outcome of this second optimization will be two optimal devices to be evaluated in Stage 2. The same procedure is repeated for the MPTO, where the results are briefly discussed in Section 5.2: the optimization of a MPTO-based ISWEC has been treated in previous works [254, 185, 252] and only the main outcomes will be presented here. The last part, in Section 5.3, discusses the results of the optimization process with a comparison between the optimal solutions of the mechanical and hydraulic PTO. The system performances are obtained with the Stage 2 framework, employing the TDM of the ISWEC simulated with multiple random wave realisations, as discussed in Section 3.6.2.

The optimization is focused on the Balder sea-site, since the HPTO is expected to be favoured in high energetic sea-states compared with the MPTO. However, the purpose of the optimization is to identify a device (or a set of devices if needed)

as much site-agnostic as possible, e.g. to have one machine that performs well regardless of the deployment location. In fact, an extremely specialized device to an installation site it is likely to lead to poor performances in other sea-sites. On the contrary, a device capable to perform well in different locations would significantly reduce the production costs, exploiting economy of scales and enhance the industrialization process. In this regards, the performances of the ISWEC will be evaluated also in Alghero, Capo Verde and Pantelleria.

5.1 Hydraulic PTO optimization analysis

In this section the results of the multi-objective optimization of the ISWEC device concerning the HPTO are presented and discussed. First, the convergence of the GA is shown and commented, highlighting the results achieved on the Pareto front built with the single multi-objective optimizations reported in Table 4.5. Then, techno-economic considerations are made on the convergence of some design parameters and the impact they have on both the system productivity and cost, showing the techno-economic trends of the optimal solutions. At the end, two optimal solution are chosen from the devices belonging to the Pareto front with the lowest fittest value. The steps just outlined are applied to both Stage 1a and Stage 1b results concerning the HPTO.

5.1.1 Stage 1a results

The first step to design a ISWEC with a hydraulic transmission is to evaluate such architecture with the Stage 1a optimization. The Table 4.2 indicates that Stage 1a aims to optimize only the primary pump and its control along with the others floater and gyro-pendulum parameters. Then, through a cost-effectiveness analysis supported by techno-economic considerations, ten devices are analysed in this section in order to find the two best ISWEC individuals to be optimized again with the Stage 1b. Below are shown the results carried out with Stage 1a focusing on the algorithm convergence, techno-economic trends and the identified optimal solutions.

Convergence analysis

The free parameters defining a single unique individual of the ISWEC device cannot be combined at will and some unfeasible solutions appear during the optimization process. The so-called mortality rate, defined as the ratio between the number of unfeasible individuals and the total individuals, is shown through generations in Figure 5.1 for a AEP-driven optimization. The dashed line is the Moving Average (MA) of the mortality rate computed grouping 10 generations at once. The mortality drastically decrease in the first 20 generations and slighty increase

again between generation 80 and 100; then, it goes below 10% at the end of the optimization process. Overall, the method proposed in equation 4.3 to handle unfeasible devices is demonstrated to be effective since the mortality rate diminish as the generations progress. However, the mortality does not go to zero due to the exploratory nature of the GA that explores the solution domain in a stochastic way during the crossover and mutation operations.

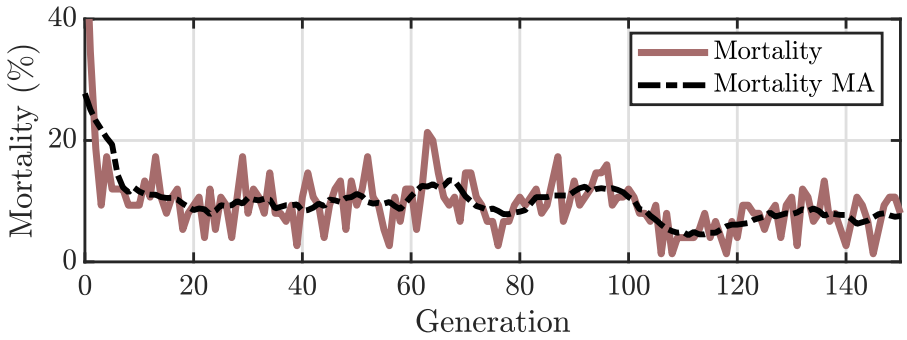

Figure 5.1: Mortality rate in respect to the generation number.

The overall development of the algorithm is shown in Figure 5.2 for the example of the AEP-driven optimisation. In Figure 5.2a, for each generation, individuals are sorted according to their AEP. Each point represents a single individual and unfeasible individuals are missing markers. The final generation count is 150 and, since the maximum stall generation criterion is 50 (see Table 4.1) and the associated function tolerance is 10^{-6}, the algorithm stops when the maximum number of generation is reached since the convergence criteria are not matched. Figure 5.2a has the purpose of showing the rate of fit individuals over the whole population changes as the generation number increase as expected and desired; however, the improvement is abrupt in early generations (until generation 25-50) and slows down afterwards (until generation 100). Although an extensive sensitivity analysis is an interesting topic for future investigation, it is believed that the current setup provides appropriate convergence and satisfactory results and the maximum number of generations allowed G_m could be reduced to 100÷120 to reduce te computational time. This results is confirmed in Figure 5.2b, where the AEP rate is reported in respect to the generation number. The AEP_{rate} is defined as follows:

$$AEP_{rate} = \left(1 - \frac{AEP_{max} - AEP_g}{AEP_g}\right) 100\% \tag{5.1}$$

where AEP_g is the AEP of the fittest value at generation g and AEP_{max} the best AEP value among all individuals. It is shown that at generation 100 the best individual performs 99% equal of the absolute best and for the subsequent 50 generations no relevant improvement of the fitness function are found.

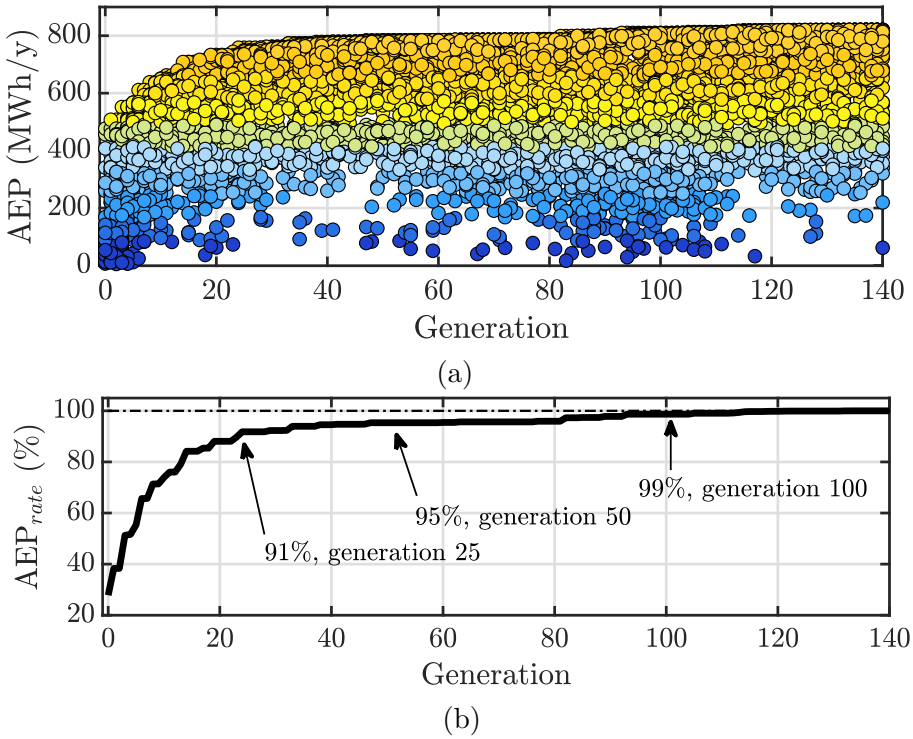

Figure 5.2: (a) AEP and (b) AEP rate of convergence in respect to the generation number. For each generation, individuals are sorted according to the objective function (AEP) to be maximized. The colour code corresponds to the AEP value.

Similarly, the convergence results of a CoE-driven optimization are showed in Figure 5.3. For each generation, individuals are sorted according to their CoE. Again, the algorithm stops when the maximum number of generation is reached since that the convergence criteria are not matched. Figure 5.3a reflects a better convergence speed than Figure 5.2a: the rate of fit individuals over the whole population converges over the 99 percentile at generation 50 and the number of devices at a high CoE rarely appear, suggesting that the algorithm is definitely converged. This results is confirmed in Figure 5.3b, where the CoE rate is reported in respect to the generation number. The CoE_{rate} is defined as follows:

$$CoE_{rate} = \left(1 + \frac{CoE_{min} - CoE_g}{CoE_g}\right) 100\% \tag{5.2}$$

where CoE_g is the CoE of the fittest value at generation g and CoE_{min} the minimal CoE value among all individuals.

Overall, the convergence speed of the GA based on a single-objective optimization have been demonstrated regarding an AEP-driven and a CoE-driven optimization. The GA is able to find the optimal solution near generation 100 evaluating

approximately 7500 individuals (75 individuals in 100 generations) despite the billions of feasible combinations. The considerations carried out above can be transferred without any loss of generality to the Stage 1 optimization concerning the MPTO system.

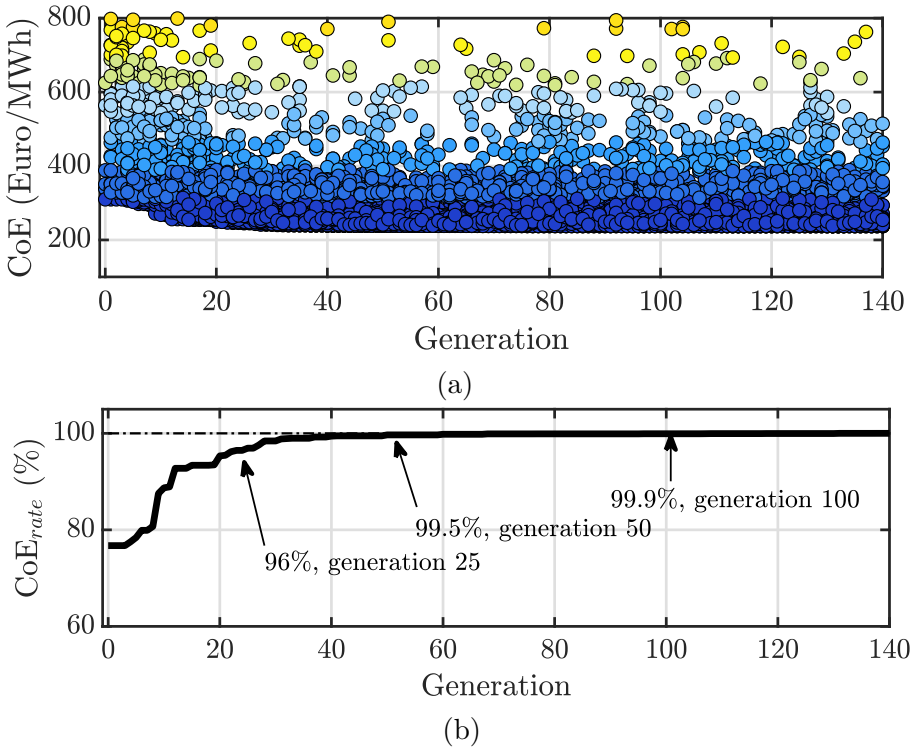

Figure 5.3: (a) CoE and (b) CoE rate of convergence in respect to the generation number. For each generation, individuals are sorted according to the objective function (CoE) to be minimized. The colour code corresponds to the CoE value.

AEP and CoE optimal solutions

The results presented in this chapter refers to a multi-objective optimization composed of multiple single-objective optimizations as summarized in Table 4.5. The optimal solutions carried out with a AEP-driven and a CoE-driven optimization are examined to understand the behaviour of the optimization process and which system parameters generate the fittest results. Figure 5.4a shows the ensemble of all the individuals generated from the two separate optimisations and Figure 5.4b the external contour generated from the points located at the limit of the solution clouds. Each point represents a feasible individual with its related AEP and CoE. Rectangular annotations on the graph indicate the most convenient region according to the respective metric (low CoE and high AEP). It is interesting

to analyse the direction that each optimisation tries to follow in order to improve the performance index. As expected, the optimal device with the best AEP differs from the one with lowest CoE. In fact, designing a system with high productivity leads to an increase of the system dimensions and costs; on the other hand, since there is not a linear relation between the system performances and its cost, the economic efficiency of the ISWEC has to be maximized with a CoE-driven optimization. The CoE-driven area is attracted towards the AEP-axis while the AEP-driven optimisation extends the furthest along the CoE-axis. In between, the multi-objective optimisation will reach a good compromises of the two metrics (see Section 5.1.1). The optimal devices stands in the south-west corner of the diagram, where the AEP is maximized and the CoE is minimized. The reader should note that the Y-axis is inverted.

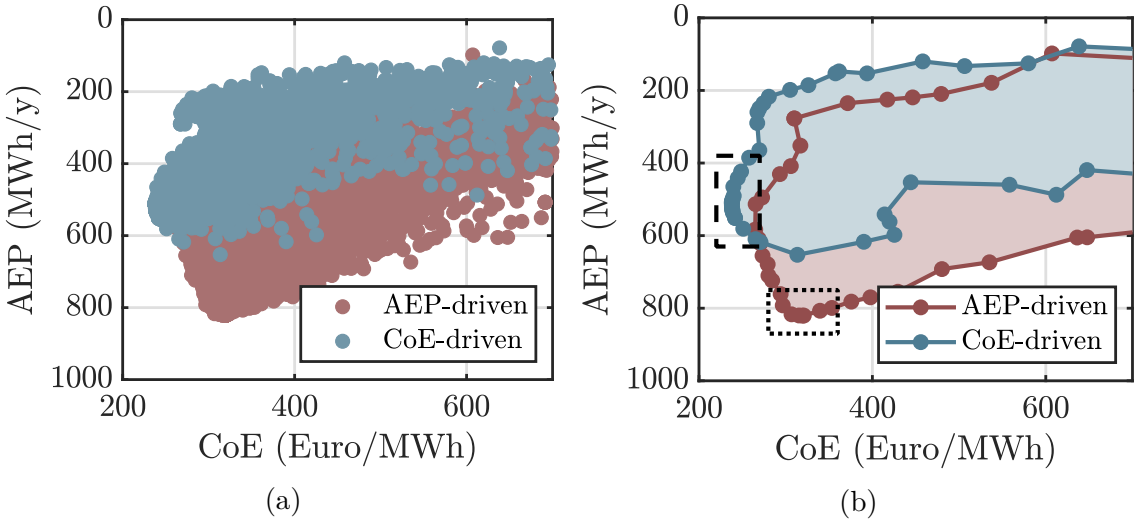

Figure 5.4: Optimization results of two different single-objective optimization with Stage 1a: AEP-driven optimization, with red dots, CoE-driven optimization, with blue dots. (a) All the evaluated individuals and (b) the external contour of the two single-objective optimizations. The rectangular annotations highlight the most convenient region according to the evaluation metric (low CoE and high AEP).

The AEP-driven optimization seeks to maximize the power captured by the ISWEC and thus points to maximize the hull width, the gyroscope dimensions and the hydraulic pump size. Figure 5.5 aims to highlight the convergence of the hull length L and the gyroscope moment of inertia J for the example of the AEP-driven optimisation. First, in Figure 5.5a the behaviour of the hull length L through generations shows that the hull length rapidly converge to the optimal value $L_{g,best}$ (represented with a black dashed line) that refers to the $g-th$ best individual of the generation g. An optimal value around 17 m is found for the most performing device; small and large hull length are not optimal. This results

is coherent with the hydrodynamic theory behind the WEC systems and, more in general, the hydrodynamic of floating body: short devices compared with the incident wavelength are expected to behave like a PA-WEC, inducing a predominant heave motion that in our concrete case does not contribute to the power generation; on the other hand, long devices acts like a low-pass filter due to the peak-to-trough distance of the wave crest that is not suitable to induce their oscillation. Concerning the gyroscope moment of inertia J, Figure 5.5b demonstrates that, as expected, for maximize the system productivity large gyroscopic units are required and thus the $J_{g,best}$ value converges to the upper bound imposed on J, equal to $45000 kgm^2$ (see Table 4.2).

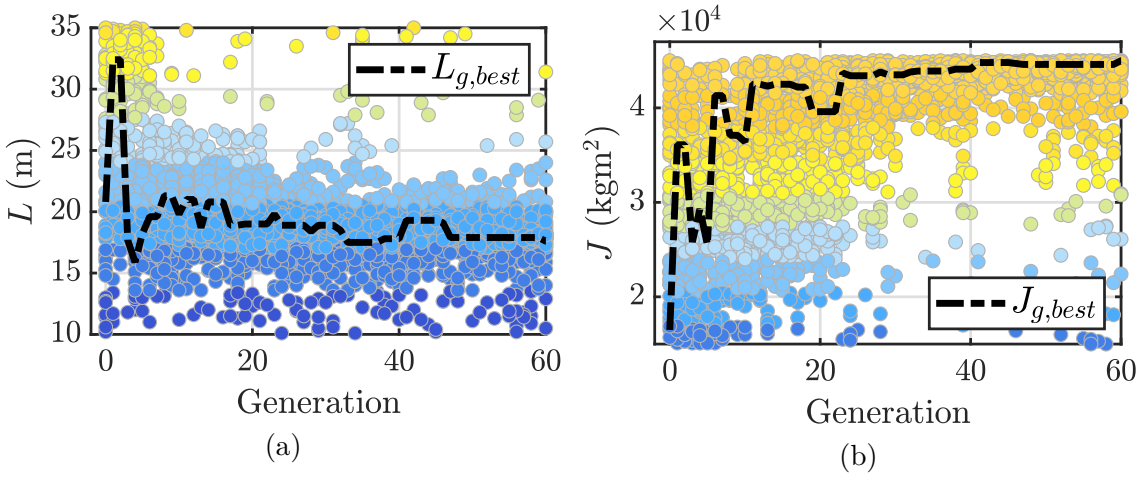

Figure 5.5: (a) Hull length L and (b) gyroscope moment of inertia J in respect to the generation number for a AEP-driven optimization. For each generation, individuals are sorted according to the magnitude of L and J represented by the colour code. The dashed line refers to the best individual of each generation.

Concerning the hydraulic parameters, the pump displacement D_p and the hydraulic control type ID_c are reported in Figure 5.6a and 5.6b, respectively. Again, intuitive results are carried out. The AEP is maximized through the larger pump unit available in the catalogue, that is able to exert the higher torque on the gyroscope unit and, thus, there are no theoretical limits exist in extracting the available power generated by the gyroscope motion. In this regards, the pump unit can be interpreted as an electrical generator: larger is the torque available by the electric generator, larger is its saturation limits and all the available power transferred to the gyroscope can be converted into electricity (at less than the PTO efficiency). Figure 5.6b determines that the most performing hydraulic control logic is the ID_c=4, regarding the tuning of the switching of the pump displacements and the clutching speed threshold (see Table 4.3). The control mode ID_c=4 is the most

versatile and ensure the best controllability of the hydraulic system: the clutch-declutch valve is able to regulate the pressure acting on the primary pump and, if a tandem configuration is installed, the possibility to switch between three different pump displacement allows a further degree of regulation of the PTO torque. Similarly to L and J, the algorithm find the best D_p and ID_c before the 50-th generation.

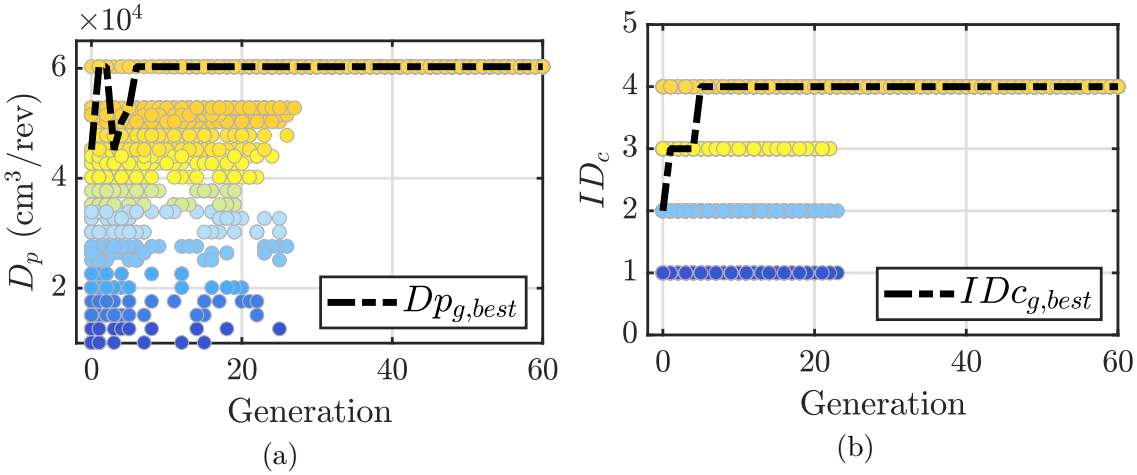

Figure 5.6: (a) Pump total displacement D_p and (b) hydraulic control mode ID_c in respect to the generation number for a AEP-driven optimization. For each generation, individuals are sorted according to the magnitude of D_p and the value of ID_c represented by the colour code. The dashed line refers to the best individual of each generation.

Despite the sea-site of interest for the ISWEC design is Balder, the performances of system are evaluated also in the other three sites under study. Figure 5.7 compares the AEP values of the ensemble of all the individuals evaluated in all the sea-site of interest. Each axis and the colour code report the annual productivity obtained with a specific individual evaluated in a specific location. It is shown that the performances of the individuals evaluated in Alghero, Balder and Pantelleria (see Figure 5.7a) have a modest spread suggesting that the optimal device designed for Balder will be (almost) optimal for Alghero and Pantelleria. In contrast, Figure 5.7b shows that the optimal devices for Capo Verde are not optimal for the other three locations. Figure 5.8 pursues to support this conclusion. The optimal devices for Alghero, Balder and Pantelleria performs almost likewise in other sea-sites. On the other hand, the optimal device of Capo Verde is not exactly optimal if evaluated in the other three locations. As depicted in Figure 2.7, the Capo Verde occurrences distribution significantly differs from the one of Alghero, Balder and Pantelleria leading to a different optimal device.

Table 5.1 quantifies the percentage difference between the AEP of a best device

evaluated in a certain sea-site (AEP_{site}) with the AEP of the best device of that sea-site (AEP_{best}). The difference in productivity is computed through the following relation:

$$\Delta_{AEP} = \frac{AEP_{site} - AEP_{best}}{AEP_{site}} 100\% \tag{5.3}$$

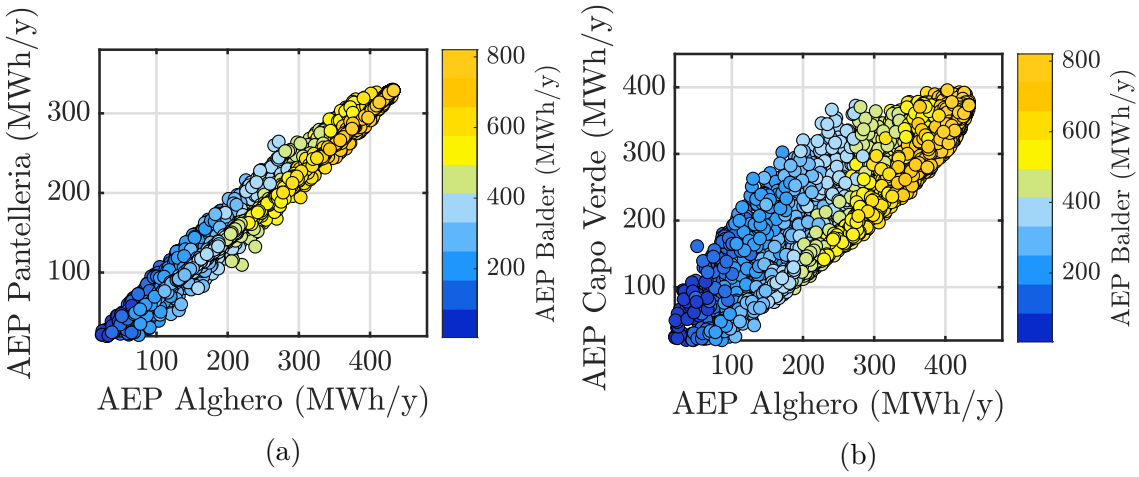

Figure 5.7: AEP results of a AEP-driven optimization for all the sea-sites of interest. (a) Alghero and Pantelleria compared with Balder; (b) Alghero and Capo Verde AEP compared with Balder; Balder AEP is reported with the colour code proportional to the AEP value.

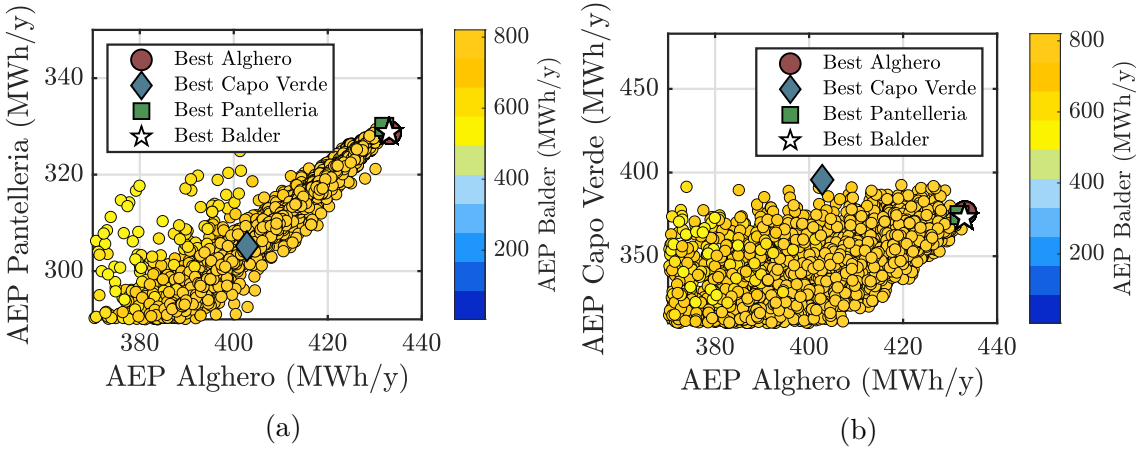

Figure 5.8: AEP results of a AEP-driven optimization for all the sea-sites of interest with a zoom on the optimal device region. Best devices for each site highlighted with markers.

For example, the best device of Capo Verde produces 402.8 MWh/y if evaluated in Alghero; then, its AEP is compared with the one of the best Alghero device, equal to 433.2 MWh/y, resulting in a Δ_{AEP} equal to -7.5%. Despite the apparent discrepancy in performance between the Capo Verde device and the others as reported in Figure 5.8, Table 5.1 highlights that the difference in productivity is always lower than 8%, leading to conclude that the best device for a particular sea-site could perform almost optimally in different locations. However, these results are obtained optimizing the AEP in Balder and the devices named as "best" for Alghero, Capo Verde and Pantelleria could not be the absolute best for these sea-site. Further analysis will be performed to assess the feasibility of designing a device that performs optimally at multiple locations.

	Alghero		**Balder**	
Device	AEP (MWh/y)	Δ_{AEP} (%)	AEP (MWh/y)	Δ_{AEP} (%)
Best Alghero	**433.2**	**0**	820.2	-0.01
Best Balder	433.1	-0.01	**820.3**	**0**
Best Capo Verde	402.8	-7.5	760.5	-7.9
Best Pantelleria	432.0	-0.3	818.2	-0.2
	Capo Verde		**Pantelleria**	
Device	AEP (MWh/y)	Δ_{AEP} (%)	AEP (MWh/y)	Δ_{AEP} (%)
Best Alghero	376.0	-5.2	328.7	-0.4
Best Balder	373.1	-6.1	328.8	-0.4
Best Capo Verde	**395.6**	**0**	305.2	-7.9
Best Pantelleria	374.5	-5.6	**329.9**	**0**

Table 5.1: AEP for each best device evaluated in other sea-site of interest. AEPs with bold font refer to the productivity of a best device evaluated in its sea-site of reference, then their Δ_{AEP} are equal to 0%.

In a CoE-driven optimization, the economic efficiency is the metrics of interest. From Figure 5.9a it is shown that the hull length converges to lower value compared to a AEP-driven optimization, almost equal to 14m. However, such a result confirms that the optimal hull longitudinal dimension stands in the same range regardless the optimization target in order to maximize the hydrodynamic performance of the system. Conversely, the gyroscope moment of inertia J is almost three times lower for a CoE-optimum device, standing around $16300 kgm^2$ (see Figure 5.9b). This represents the main difference emerging from the two optimizations: as shown in the next section, the gyroscope cost represents almost the 40÷45% of the total device cost and, in a CoE-driven design, the economic efficiency is favoured over the system performances, reducing the size of the gyroscopic units. The pump displacement optimal value, reported in Figure 5.10a, is slightly

lower than the AEP-optimum one, and it is referred to a single displacement unit. Despite the economical efficiency of the system is preferred to its annual productivity, the selected pump is again one of the larger units in the Bosch Rexroth catalogue. Balder is an high-energy sea site and the algorithm typically explore the most powerful PTO solution available to maximize the system productivity. Moreover, the hydraulic pump requires a low investment compared to the gyroscope unit (as demonstrated in the next section) and no relevant impact on the overall cost is obtained. As shown in Figure 5.10b, the most performing hydraulic control logic is the ID_c=2, concerning the clutch-declutch logic (see Table 4.3). The pump switch is not possible here because the optimal pump is a single displacement unit. Overall, the best value of L, J, D_p and ID_c are found the 50-th generation, demonstrating again the high rate of convergence of the GA.

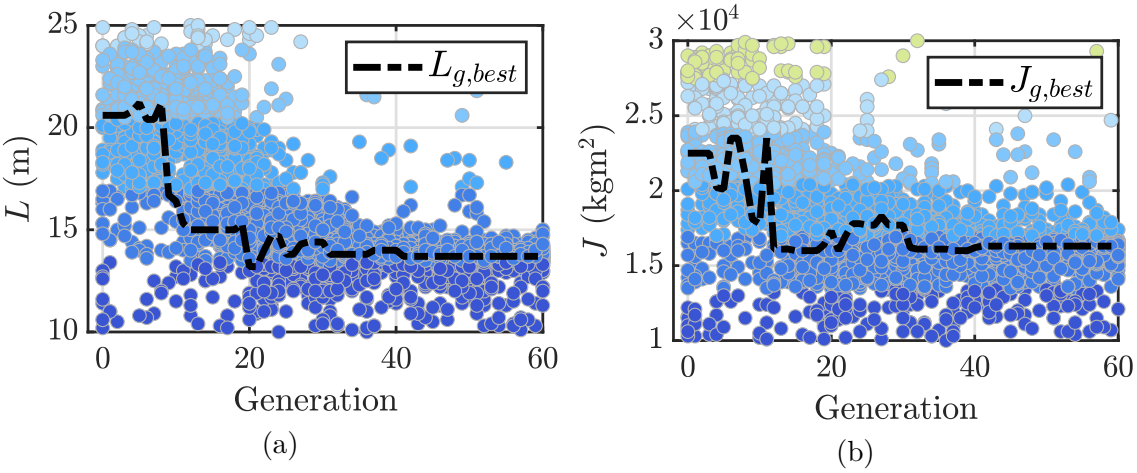

Figure 5.9: (a) Hull length L and (b) gyroscope moment of inertia J in respect to the generation number for a CoE-driven optimization. For each generation, individuals are sorted according to the magnitude of L and J represented by the colour code. The dashed line refers to the best individual of each generation.

Encouraging results are obtained evaluating the CoE of the best device for each sea-site in the other three locations under study. Similarly to Figure 5.7, Figure 5.11 compares the CoE values of the ensemble of all the individuals resulted from the CoE-driven optimization. Again, it is demonstrated that the performances of the individuals evaluated in Alghero, Balder and Pantelleria are similar to each other, concluding that the optimal device for Balder could be optimal also in Alghero and Pantelleria. As shown in Figure 5.12, the optimal individual for Capo Verde is not properly suited for the other three locations.

Coherently with Table 5.1, Table 5.2 reports the CoE percentage difference Δ_{CoE} between the CoE of a best device evaluated in a certain sea-site (CoE_{site}) with the CoE of the best device of that sea-site (CoE_{best}):

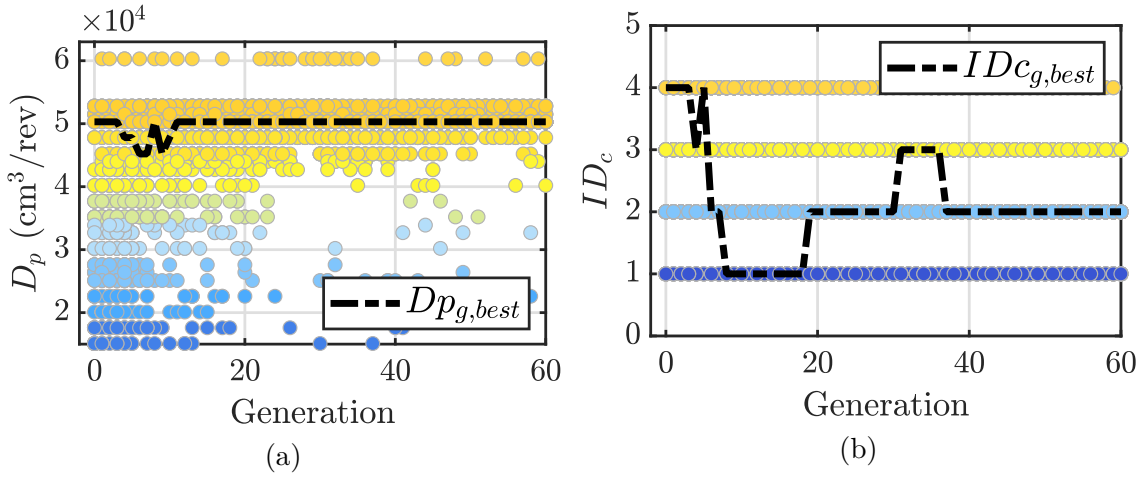

Figure 5.10: (a) Pump total displacement D_p and (b) hydraulic control mode ID_c in respect to the generation number for a CoE-driven optimization. For each generation, individuals are sorted according to the magnitude of D_p and the value of ID_c represented by the colour code. The dashed line refers to the best individual of each generation.

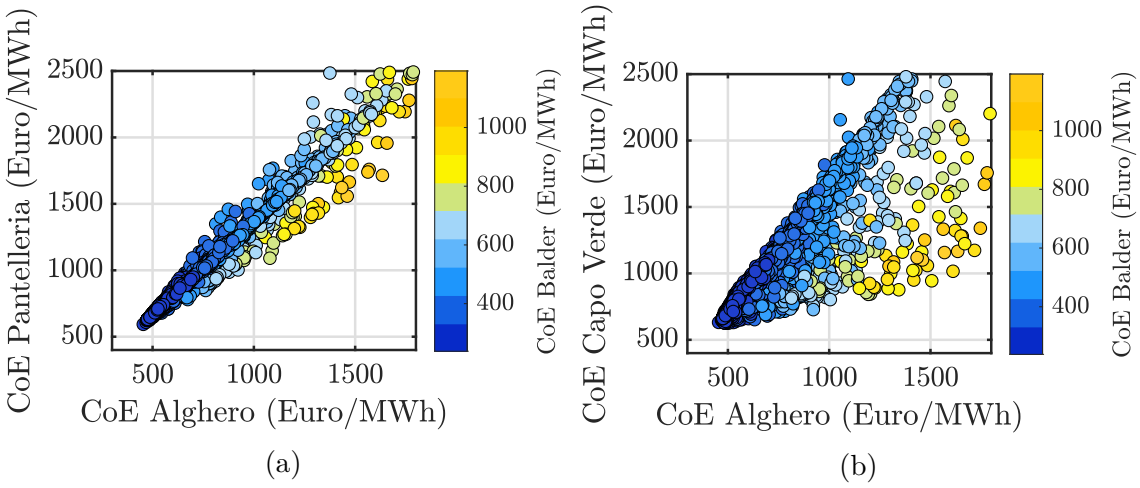

Figure 5.11: CoE results of a CoE-driven optimization for all the sea-sites of interest. (a) Alghero and Pantelleria compared with Balder; (b) Alghero and Capo Verde compared with Balder; Balder CoE is reported with the colour code proportional to the CoE value.

$$\Delta_{CoE} = \frac{CoE_{site} - CoE_{best}}{CoE_{site}} 100\% \tag{5.4}$$

Concerning the CoE, it is found that the best device for Alghero is exactly the best device for Pantelleria; moreover, the largest percentage difference is provided

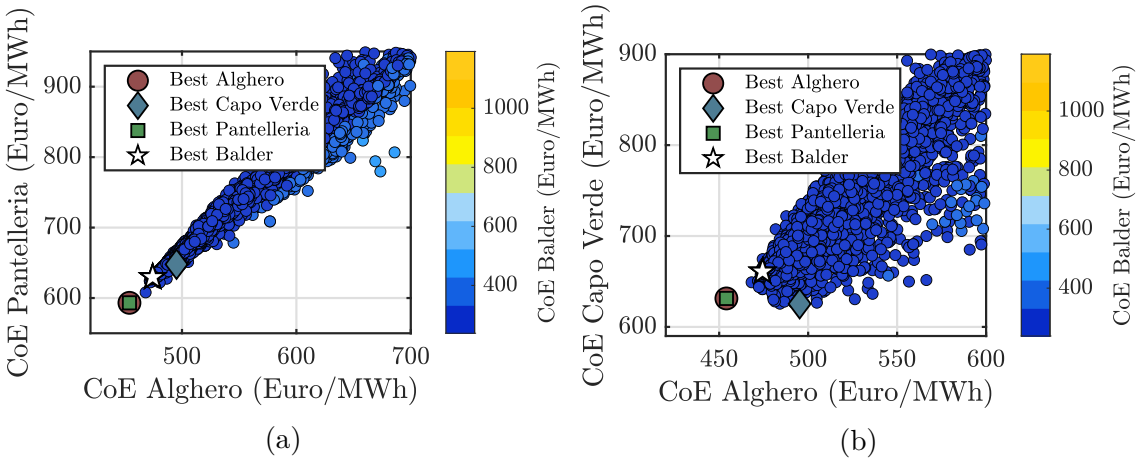

Figure 5.12: CoE results of a CoE-driven optimization for all the sea-sites of interest with a zoom on the optimal device region. Best devices for each site highlighted with markers.

comparing the individual CoE with the Capo Verde best device. The difference is always lower than 8.5% threshold, leading to conclude that the for the sea-sites of interest the design process concerning the CoE is, with a good approximation, site-agnostic as found for the AEP.

	Alghero		**Balder**	
Device	CoE (€/MWh)	Δ_{CoE} (%)	CoE (€/MWh)	Δ_{CoE} (%)
Best Alghero	**454.1**	**0**	239.6	0.75
Best Balder	474.3	4.21	**237.8**	**0**
Best Capo Verde	495.2	8.31	257.5	7.65
Best Pantelleria	454.1	0	239.6	0.75
	Capo Verde		**Pantelleria**	
Device	CoE (€/MWh)	Δ_{CoE} (%)	CoE (€/MWh)	Δ_{CoE} (%)
Best Alghero	631.3	0.95	593.1	0
Best Balder	660.8	5.37	629.5	5.78
Best Capo Verde	**625.3**	**0**	647.8	8.42
Best Pantelleria	631.3	0.95	**593.1**	**0**

Table 5.2: CoE for each best device evaluated in other sea-site of interest. CoEs with bold font refer to the cost of energy of a best device evaluated in its sea-site of reference, then their Δ_{CoE} are equal to 0%.

Finally, the characteristics of the two optimum devices for Balder according to different objective functions are hereafter discussed; namely, the AEP-driven

optimum and the CoE-driven optimum. Their parameters are summarized in Table 5.3 along with their AEP, CoE and total cost. The AEP-optimum is wider than the CoE-optimum, intercepting more wave-crest, hence enhancing the capture of incoming energy. The same rationale applies to the flywheel inertia, pump displacement and rated torque, that are driven to the upper limit available to extract as much energy as possible, regardless the device cost. Conversely, lower CoE requires a smaller floater and gyroscope units, along with a less powerful pump unit. The optimal control mode ID_c is, as expected, the one that gives the higher controllability to the system: ID_c=4, for the AEP-optimum, means that both the clutch-declutch logic and the switch of the tantem units is enabled; ID_c=2 consists in enabling clutch-declutch logic (here the pump switch is not possible since a single unit pump is considered). Overall, dimensions and mass of the AEP-driven optimum are higher compared with the CoE-driven one. This suggests that increasing the device size requires a higher increment in cost than the consequent increase in AEP, hence rising the resulting CoE.

Device parameter	Symbol	Unit	AEP-driven	CoE-driven
Hull length	L	m	17.1	13.6
Hull width	W	m	51.1	44.5
Hull height	H	m	8.4	5.6
Hull mass	M_{hull}	ton	2957	1366
Gyroscope unit mass	m_g	ton	88.2	47.9
Flywheel inertia	J	kgm^2	45000	16300
Gyroscope units	n_g	–	4	4
Pendulum mass	m_p	kg	5200	3250
Pump displacement*	D_p	cm^3/rev	35200+25100	45200
Pump rated torque	T_{pump}	kNm	197	147
Hydraulic control id	ID_c	–	4	2
Annual energy production	AEP	MWh	820.3	508.5
Cost of energy	CoE	€/MWh	319.4	237.8
Device cost	C_{TOT}	M€	6.5	3.1

Table 5.3: Device parameters of the AEP-driven optimum and the CoE-driven optimum devices designed for Balder and their key performance indicators. $*$: the AEP-optimum pump is a tandem unit then two displacement values are reported.

Techno-economic trends and Pareto front analysis

In the previous section, it was demonstrated that high overall cost consistently result in high AEP/high CoE, and vice versa, remarking that the economic ability

and the conversion efficiency can be contrasting objective [252]. However, a multi-objective optimization generates the so-called Pareto front, giving several optimal solution basing on the performance metrics of interest. It is important to remark that the devices of Table 5.3, although representative, are just the two external bounds of the Pareto Front. Figure 5.13 reports the ensemble of the best individuals obtained with the three single-objective optimizations specified in Table 4.5. The colour code is proportional to the device cost: ten cost intervals are used to identify the individuals, from 0 M€ to 10 M€ (millions of Euro). In particular, Figure 5.13b highlights the Pareto front (red line) concerning the best individuals according to the two evaluation metrics considered. Each individual on the Pareto front can be interpreted as a non-dominated solution of the solution set and here stands the optimal devices that can pass to the next optimization stage (Stage 1b). Note that, in order to improve readability, from here on some of the bulky figures are placed in Appendix A.

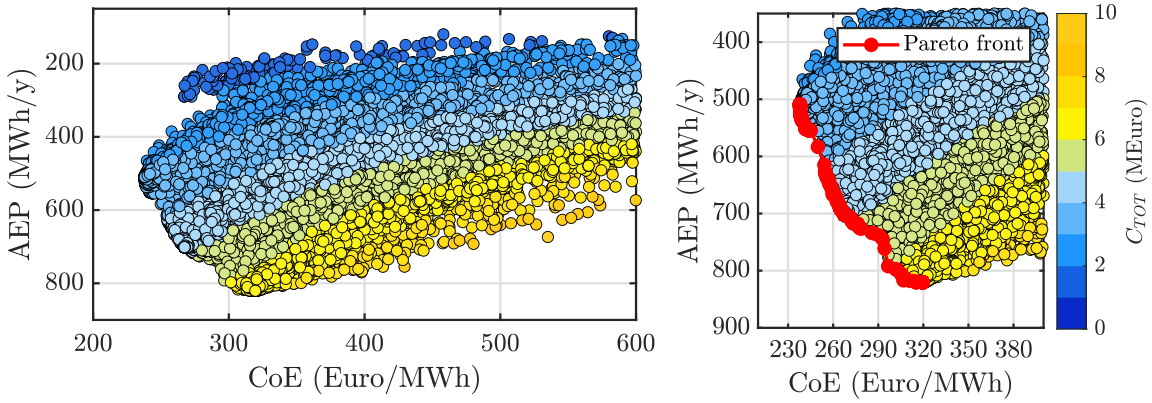

Figure 5.13: Productivity (AEP) versus cost of energy (CoE) of the ensemble of the three optimisations aggregated regarding the HPTO; each marker (individual) is coloured proportional to the device cost (C_{TOT}). (a) Feasible individuals with maximum CoE equal to 600 €/MWh and (b) a zoom on the Pareto front (red line) concerning the optimal individuals according to the evaluation metric (low CoE and high AEP).

As specified in Section 4.5.1, AEP and CoE are not the only parameters of interest. In order to investigate significant and more informative trends, Figure A.1 shows relevant results and design parameters for a selection of ten devices standing on the Pareto Front, chosen in order to be representative of the fittest individuals in the whole population. In practice, the range of CoE from 230 €/MWh to 320 €/MWh is equally divided into ten bins, and the individual with highest AEP of each bin is selected. In order to highlight the most convenient individual, according

to each metric, bars colour proportional to the device cost are used, so that cheapest devices are represented by sky-blue bars, while most expensive ones in orange. The highest AEP and the lowest CoE are achieved with significantly different individuals. In particular, it is evident that the increase in AEP is slower than the required increase in cost, so that the lowest CoE is found in the low cost region, in spite of a lower AEP. Contrary, achieving high AEP generally requires such an increase in device cost that the overall economical effort becomes unfavourable. In detail, Figure A.1b and A.1c explore variations in the hull length and mass, which are the main drivers of hydrodynamic performance and hull cost. While CoE consistently increases with the hull length, longer hulls generate high AEP, despite the hull longitudinal dimension remains bounded between 14 m and 17 m. The same behaviour is shown in the hull mass, that shows an upward trend as the AEP increases. Similarly, Figure A.1e and A.1d depict that a productive device calls for heavy and large gyroscope units. Despite the relevant increase of the gyroscope unit inertia, from $J = 16500 kgm^2$ to $J = 45000 kgm^2$, the gain in productivity does not follow the same rate of growth, confirming that the incremental investment required to produce more energy is not cost-effective. Concerning the pump unit, mainly as a consequence of the high AEP demand, the optimal pump displacement and rated torque grow from left to right resulting in more powerful hydraulic units installed (see Figure A.1f and A.1g). However, CoE and AEP are not particularly sensitive to the pump parameters since the most powerful pumps available are often selected. Such a trend suggests that, for the Balder sea-site, even more powerful pump units could improve the extracted energy of the ISWEC. Finally, as assessed at the end of the previous section, the optimal hydraulic control IDs require the use of the clutch-declutch logic and (if a tandem unit is installed) the pump switching.

The detailed device cost and the relative impact of different system parts is reported Figure 5.14. The costs are divided in hull, gyroscope unit and HPTO costs.

Figure 5.14a demonstrates that the absolute cost of each subcomponent tends to increase more rapidly than the resultant increase in AEP, leading higher CoE for high investments. On the one hand, the rates of increase seem to be different: the hull cost tends to become less relevant in favour of the gyroscope cost, although the mass of the hull increases (from 1400 tons to 3000 tons), as shown in Figure A.1c; therefore, the proportional increase of gyroscope unit size has a higher impact on the overall cost than the increase of hull dimensions and mass. In conclusion, a cost effective solution seeks for compact gyroscopic units rather than small hulls. Overall, hull and gyroscope split up almost equally the $80 \div 85\%$ of the device cost while the hydraulic transmission weighs just on the $15 \div 20\%$ of the investment.

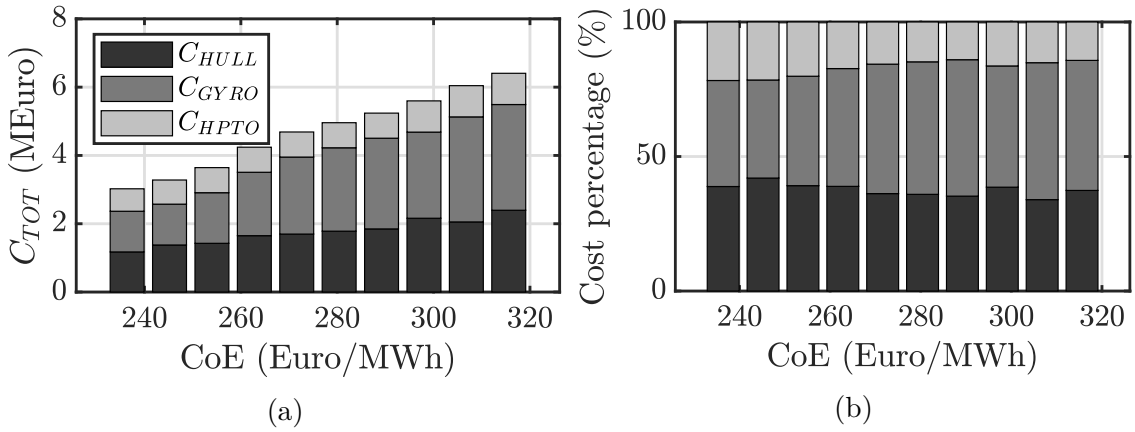

Figure 5.14: Ten individuals with HPTO on the pareto front with their CoE and the associated cost: hull, gyro-pendulum and HPTO (a) absolute cost and (b) percentage cost.

5.1.2 Stage 1b results

The range of optimal solutions identified due to the first optimization stage (Stage 1a) is considered as the starting point to complete the design of a HPTO-based ISWEC. Table 4.2 indicates that Stage 1b search for the best hydraulic transmission suited for a specific ISWEC device with a (almost) defined hull and gyroscopic unit. A restricted range of floater and gyroscope parameters is fixed to bound the search space, focusing mainly on the HPTO features. First, the initial investment is bounded 5 M€ to reduce the economical impact and promote low CoE solutions. Furthermore, the floater mass is limited to 2000 tons, to increase the manufacturability and reduce the resultant transport charges and deployment costs (not evaluated in this design process). Finally, the inertia of the gyroscope is chosen between 16000 kgm^2 and 32000 kgm^2, giving small and cost effective gyroscopic units coherently with the cost analysis showed in Figure 5.14. Considering the optimal solutions of Figure A.1 and the search bounds just outlined, two devices are chosen to be optimized in Stage 1b: Device-1 and Device-5. Figure 5.15 aims to clarify this decision.

Device-1 belongs to the first bar of the chart and it is the CoE-optimum device; Device-5 is the fifth bar and it represents the AEP-optimum according to the limits imposed. These two individuals are optimized again with two single-objective optimizations minimizing the CoE and maximizing the AEP, respectively.

Techno-economic trends

Figure 5.16 reports the ensemble of the best individuals obtained with the two single-objective optimizations, one AEP-driven for the Device-5 and one CoE-driven

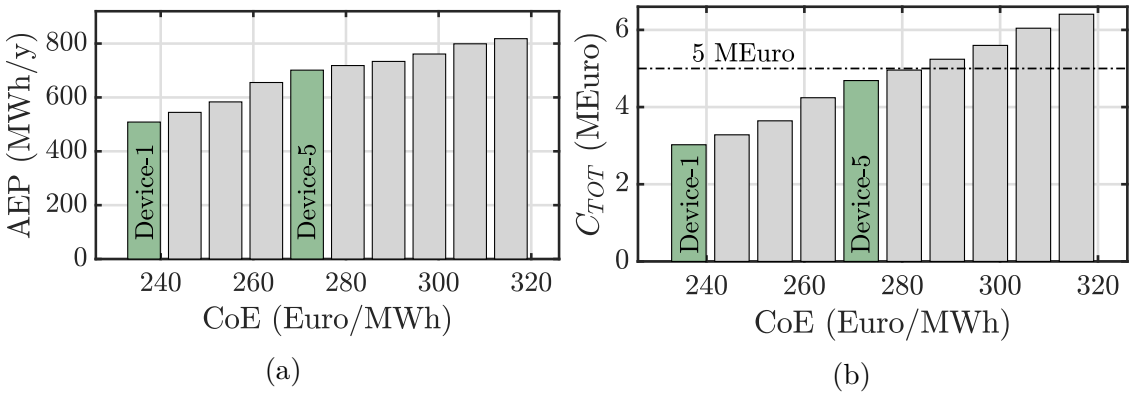

Figure 5.15: Optimal individuals for the HPTO-based device. Device-1 is the CoE-optimum and Device-5 is the AEP-optimum according to the limits imposed on the system size and cost. (a) AEP results and (b) total cost results.

for the Device-1. It is shown how, as expected, the two objectives attract the solutions toward the performance to be optimized: the red dots are attracted to the AEP-axis and the blue dots are drawn to the CoE-axis. The CoE-optimum device provides a CoE almost 18% lower than the AEP-optimum, which turns out to be 50% more productive than the CoE-optimum.

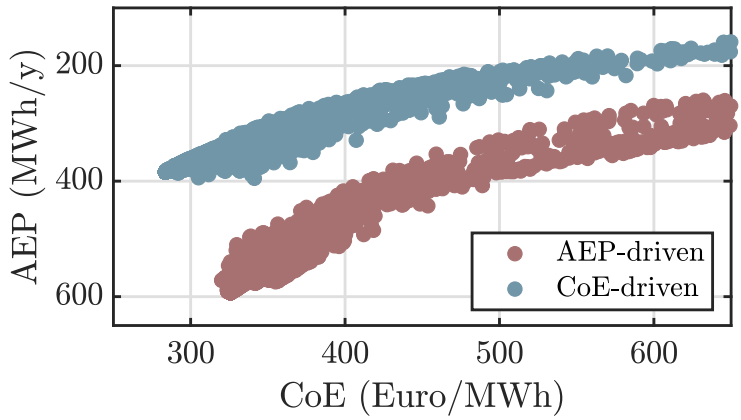

Figure 5.16: Optimization results of two different single-objective optimization with Stage 1b: AEP-driven optimization, with red dots, CoE-driven optimization, with blue dots.

Concerning the AEP-driven results, Figure 5.17 reports the ensemble of the best individuals with their PTO cost, classified in respect to the colour code. In the chart two region can be identified: the Low-Cost/High-AEP region and its dual, the High-Cost/Low-AEP region. These two limits are highlighted with the purpose to explain how the hydraulic transmission parameters affect the performance of the ISWEC device. In particular, high PTO costs does not necessarily mean high

productivity due to some optimization parameters, such as the hydraulic control logic ID_c, that not affect the cost of the transmission but heavily determines the system performances. Figure A.3 reports the performance achieved by the AEP-driven solutions related to the most important hydraulic parameters, classified in respect to the colour code. The pump unit converges to a single displacement pump with a rated torque equal to T_{pump}=172kNm (see Figure A.3a), that corresponds to the Hägglunds unit CBp 840-840 [202], the most powerful single displacement pump unit available. This results is coherent with the target of a AEP-driven optimization: maximize the system productivity. Intuitively, the Low-Cost region is populated by pump units with low rated torque. For what regard the hydraulic control logic, the optimal logic ID_c is the number 2, as shown in Figure A.3b, since the clutch-declutch logic allows to achieve a relevant improve in the system productivity in respect to not implementing it. In fact, the main difference between the Low-Cost/High-AEP and the High-Cost/Low-AEP region is determined by the control logic: in the first one the control logic 2 is used (sky-blue dots) while in the latter the control logic 1 and 3 dominates (dark-blue and yellow dots), resulting in a remarkable reduction of the system performances, regardless the size of the pump unit considered. The hp accumulators total volume, represented in Figures A.3c and determined by the sum of all the hp accumulators volumes[1] converges almost in the middle of its bounds. The optimal size of the accumulator is obtained as the minimal size to avoid wasted hydraulic power through the relief valve: a hp accumulator of 475 l is obtained, resulting in a total capacity of 950 l, since there are two hydraulic circuits. The hp accumulator pre-charge pressure does not influence the system productivity and no clear trend appers in Figure A.3d. On the other hand, the number of circuits represents a crucial parameter to maximize the system productivity. As depicted in Figure A.3e, two hydraulic circuits are needed to handle the high hydraulic power generated by the four hydraulic pumps, one for each gyroscope units. More hydraulic circuits determines expensive HPTO solutions given that they requires double accumulators and generation units (hydraulic motor and electric generator). Finally, the electric installed power is reported in Figure A.3f, computed summing the rated power of all the electric generator installed (one for each hydraulic circuit). As expected, the AEP is maximized through the elettro-hydraulic units with the large available power; however, in the High-Cost/Low-AEP region, the productivity of the system is low, despite powerful generation units are considered, due to the type of the hydraulic control logic, demonstrating again the utility of the clutch-declutch control. Overall, the most performing individuals require powerful pumps, powerful hydraulic motor and

[1]It is worth to remember that if more than one hydraulic circuit is used, as schematic in Figure 4.18, the hp accumulator has to be provided in each of the hydraulic circuits of the system. Thus, the total V_{HP0} is equal to $V_{hp0} \times n_c$.

electric generators, two hydraulic circuits and the clutch-declutch control logic.

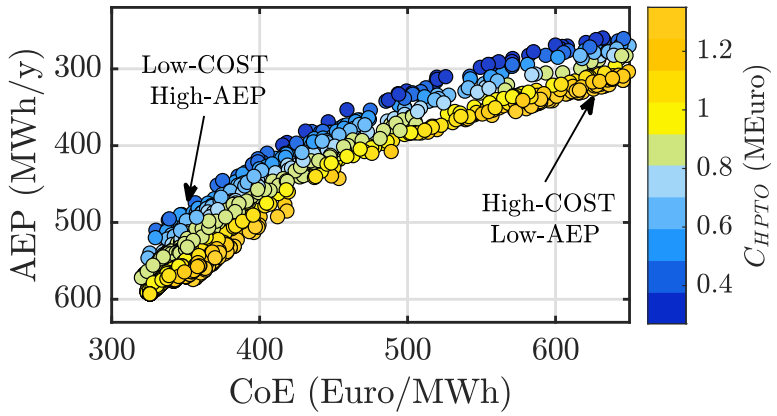

Figure 5.17: Optimization results of the AEP-driven optimization with Stage 1b. The colour code refers to the HPTO total cost. The arrows point to the Low-Cost/High-AEP region and to the High-Cost/Low-AEP region.

The CoE-driven optimization has been performed on Device-1 and the resultant optimal individuals are shown in Figure 5.18. Similarly to the AEP-optimization results, increasing the cost of the HPTO does not lead the same growth in AEP. Here the Low-Cost regions are highlighted, having almost the identical HPTO cost (0.4÷0.6 M€) but remarkable differences in AEP. Figure A.4 aims to clarify this outcome. First, Figure A.4a reports the optimal hydraulic pump units in respect to the rated torque available. In a CoE-driven optimization, the algorithm converge to a medium-size hydraulic pump, precisely the CB 400-360 [202] with rated torque equal to T_{pump}=73.7 kNm, almost 4 times lower than the AEP-optimum one. The control mode of the hydraulic pump again determines the performance of the entire PTO that are maximized if the control logic 2 is used (see Figure A.4b). A relevant degradation in performance appear moving toward the north-east part of the ID_c chart, where the control logics 1 and 3 appear. Since the flow generated by the hydraulic pump is lower compared to the one managed by the AEP-optimum, the total hp accumulator size required is considerable lower, and a total capacity equal to 425 l is shown to be the optimal value (see Figure A.4c). No clear trends are identified in the pre-charge pressure parameter (see Figure A.4d). A single hydraulic circuit is often selected in the CoE-driven optimization, reducing the auxiliary costs, the accumulators costs, the manifold cost, since only one transmission unit is required resulting in a more cost-effective solution. Another parameter that distinguish the Low-Cost/Low-AEP region in Figure 5.18 is the electric power installed on the system, reported in Figure A.4f. As expected, low performances are obtained with small-size generation units, with a rated power lower than 100 kW; contrary, the optimal solutions install a high-power solution, similar to the one obtained in the AEP-optimization, with the sole difference that only one motor-generator unit is

required here. For a CoE-optimum device, the most cost-effective individuals require medium-size pumps, high-size hydraulic motor and electric generators with only one hydraulic circuit and the clutch-declutch control logic.

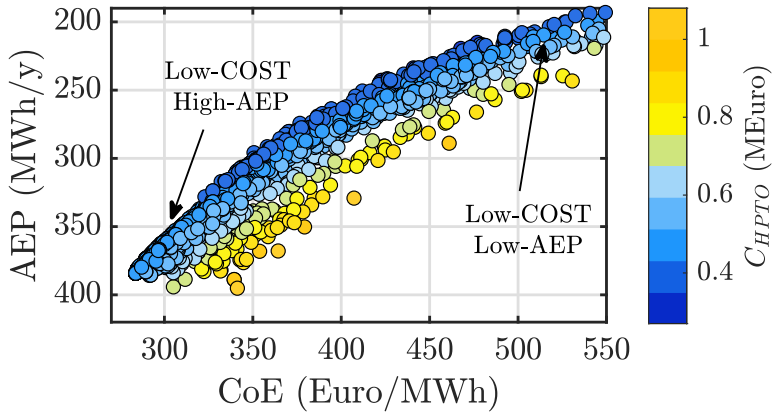

Figure 5.18: Optimization results of the CoE-driven optimization with Stage 1b. The colour code refers to the HPTO total cost. The arrows point to the Low-Cost/Low-AEP region and to the Low-Cost/High-AEP region.

Optimal solutions

Starting from the results presented above, the AEP- and CoE-optimum device from Stage 1b have to be chosen and compared with the AEP- and CoE-optimum for the MPTO architecture. Figure 5.19 collects the ten best AEP and CoE solutions. These best individuals perform at least 99% equal to the absolute best, that is the Device number 1. At least for the AEP and CoE point of view, the best ten devices are considered all optimal solutions. For what concern the pump unit, Figures 5.19a and 5.19b defines the best displacements and the associated rated torques; here, the Device-8 is chosen for the AEP performance and Device-4 for th CoE one. The aim is to pick the smaller unit to reduce the transmission cost. The Bosch Rexroth unit CBp 840-720 [202] is chosen for the AEP-optimum one, and the CB 280-280 [202] for the CoE-optimum one. Concerning the hp accumulator total volume, Figure 5.19c shows that the Device-8 for the AEP target and the Device-4 for the CoE target install the larger hp accumulators; since one of the goals of the HPTO is to filter the power peaks, large hp accumulators are suitable to filter out the flow irregularities generated by the hydraulic pumps. Finally, Figure 5.19d confirms that no logic trends are found with the p_{hp0} parameter. The other hydraulic parameters are not analysed since they are equals for all the best devices considered. In particular, all the ten AEP-optima require two hydraulic circuits and two hydraulic motor units with displacement equal to 250 cm^3/rev (model Bosch - A4FM NG 250 [214]) coupled with a electric generator with rated power equal to 238 kW (model Siemens

1PH8226 - 2L2 [216]). Concerning the CoE-optima, all the solutions require only one hydraulic circuit and one motor-generator unit equal to the AEP-optima. The device parameters of the chosen best AEP (Device-8) and best CoE (Device-4) are shown in Table 5.4 of Section 5.3.3, where the HPTO is compared with the MPTO.

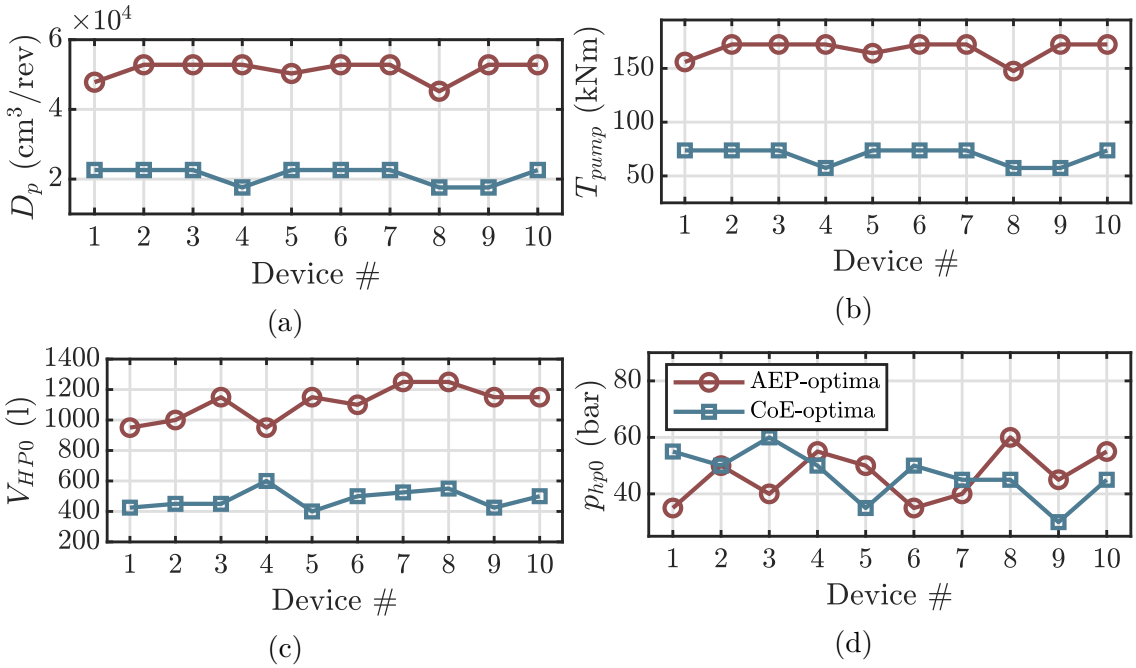

Figure 5.19: Pump and hp accumulator parameters for the best solutions of the AEP- and CoE-optimum devices (identified with red dots and blue squares, respectively), obtained with Stage 1b.

5.2 Mechanical PTO optimization analysis

The design process of the previous section is repeated for designing the ISWEC device with the MPTO. A multi-objective optimization is performed again considering the MPTO: the ensemble of the best individuals is reported in Figure 5.20a while the resultant Pareto front in Figure 5.20b. The colour code is proportional to the device cost: ten cost intervals are used to identify the individuals, from 1 M€ to 11 M€. For the sake of simplicity, only the Pareto front analysis and the MPTO optimal solutions are described here; no further discussions are reported on the convergence analysis. Similarly to Figure A.1, Figure A.2 shows the relevant design parameters for a selection of ten devices standing on the Pareto Front, chosen in order to be representative of the fittest individuals of the multi-objective optimization. Here, the range of CoE stands from 270 €/MWh to 350 €/MWh while the AEP ranges from 530 MWh/y to 860 MWh/y. The first difference from the HPTO

emerges here: the MPTO leads to reach an higher value in productivity due to a better efficiency compared with the HPTO; however, to ensure the high installed power demanded for maximize the annual productivity, the electro-mechanical solution is more expensive than the hydraulic one, increasing the CoE. Commercial hydraulic solutions give larger power densities compared with the mechanical ones at the same cost. Coherently to the HPTO, the highest AEP and the lowest CoE are achieved with significantly different individuals in terms of hull mass, gyroscope inertia, gyroscope mass and PTO installed power. In particular, the PTO installed power drops significantly if the optimization target is the minimization of the CoE. In fact, a relevant CoE reduction appears from the 10-th to the 7-th coloured bar of Figure A.2f, from 351 €/MWh to 320 €/MWh (almost 10%) due to a reduction of the PTO cost from 2 M€ to 1.4 € (almost 42%) resulting in a little drop in productivity from 860 MWh/y to 845 MWh/y (almost 1.7%). Despite the single PTO installed power decrease from 829 kW to 321 kW, no particular reduction on the system productivity appears: likely, the huge installed power in the AEP-optimum (10-th coloured bar) allows to harness the most energetic waves of the Balder site which, however, are linked to a low annual occurrence leading to a negligible increase in productivity.

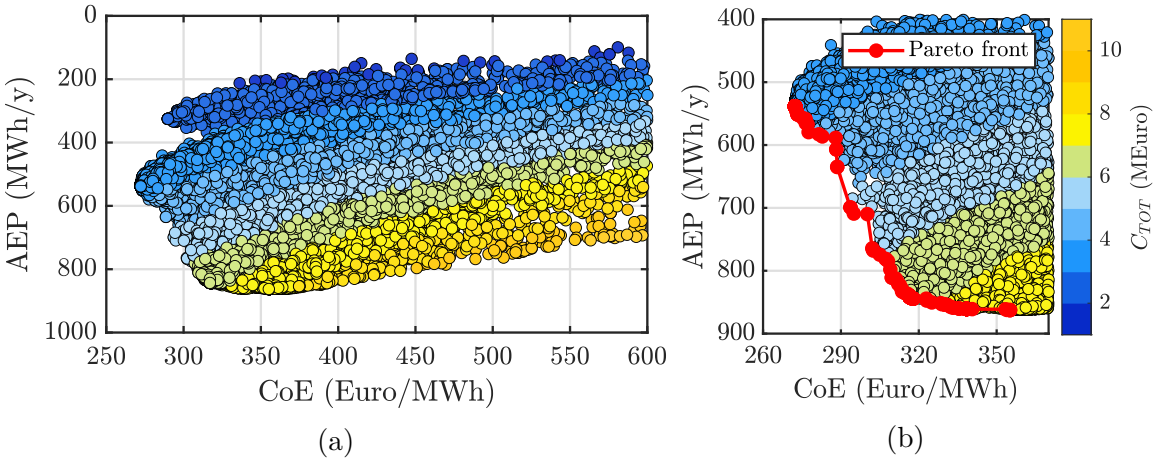

Figure 5.20: Productivity (AEP) versus cost of energy (CoE) of the ensemble of the three optimisations aggregated regarding the MPTO; each marker (individual) is coloured proportional to the device cost (C_{TOT}). (a) Feasible individuals with maximum CoE equal to 600 €/MWh and (b) a zoom on the pareto front (red line) concerning the optimal individuals according to the evaluation metric (low CoE and high AEP).

The device cost of a MPTO-based system, shown in Figure 5.21a, reflects the same behaviour of Figure 5.14a: the absolute cost of each subcomponent grows more rapidly than the associated increase in AEP. As depicted in Figure 5.21b, contrary to the HPTO, the MPTO cost impacts more on the total cost of the

device determining almost the 30÷35% of the total investment. Overall, the hull and gyroscope costs impact here on 65÷70% of the total investment.

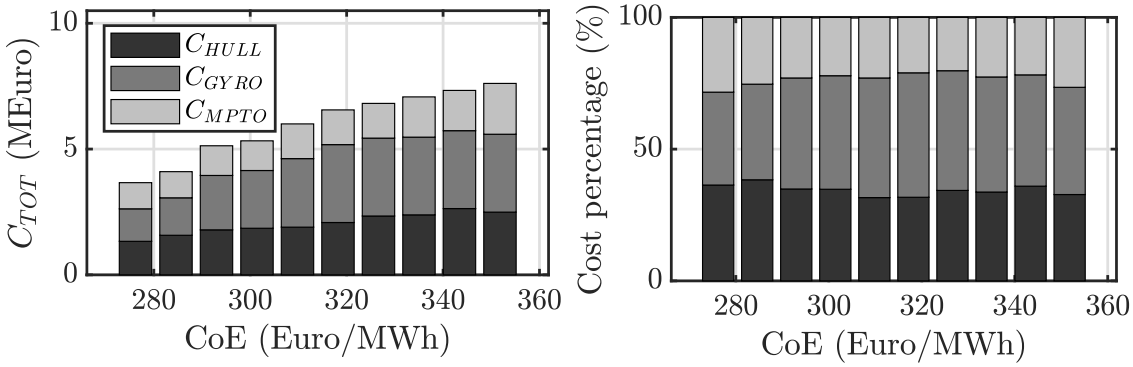

Figure 5.21: Ten individuals with MPTO on the pareto front with their CoE and the associated cost: hull, gyro-pendulum and MPTO (a) absolute cost and (b) percentage cost.

Designing an ISWEC based on the MPTO requires only one stage of optimization since the SDM of the MPTO allows to model all the power conversion chain. Here, the two best solution according to the performance metrics are chosen and they will be compared with the HPTO in the next section. The same limits listed at the begin of Section 5.1.2 are imposed to choose the optimal solutions concerning the MPTO: the initial investment is bounded to 5 M€, the floater mass to 2000 tons and, finally, the inertia of the gyroscope is chosen between 16000 kgm^2 and 32000 kgm^2. The aim is to make a fair comparison between the two PTO solutions. Considering the optimal solutions of Figure A.2 and the search bounds just outlined, two devices are chosen as the MPTO-optima: Device-1 and Device-3. Figure 5.22 highlights the two devices.

Device-1 belongs to the first bar of the chart and it is the CoE-optimum device; Device-3 is the third bar and it represents the AEP-optimum. Note that, despite the Device-3 slightly overcome the hull mass and total cost limits (see Figure A.2c and 5.21a), it has been chosen to avoid two similar devices with almost equal parameters and performances (Device-1 and Device-2). The values of the Device-1 and Device-3 parameters are shown in Table 5.4 of Section 5.3.3, where the final comparison between the MTPO and HPTO is carried out.

5.3 Mechanical and hydraulic PTO comparison

Mechanical and hydraulic PTO are compared to assess pros and cons of the two solutions. The optimal individuals obtained from the design tool stages (Stage 1

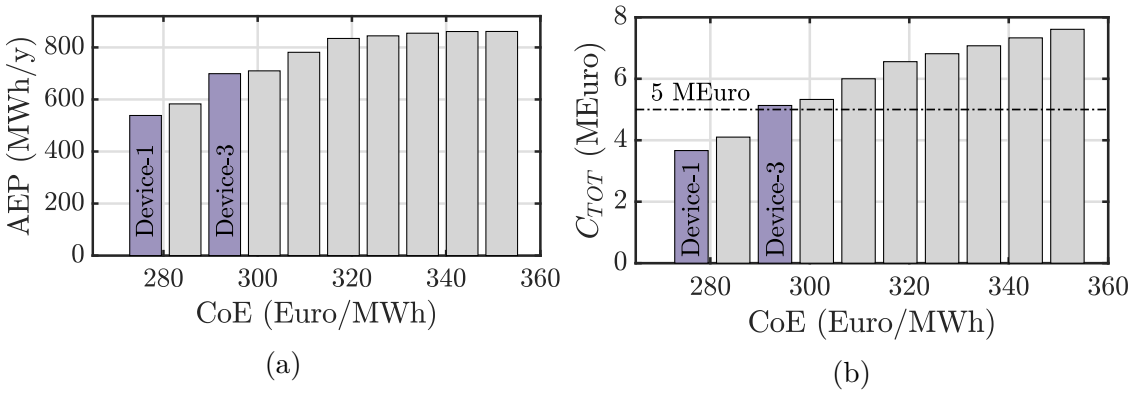

Figure 5.22: Optimal individuals for the MPTO-based device. Device-1 is the CoE-optimum and Device-3 is the AEP-optimum according to the limits imposed on the system size and cost. (a) AEP results and (b) total cost results.

and Stage 2) are analysed according to the primary and secondary key indicators described in Section 4.5. The study is extended to each of the sea locations to obtain a comprehensive comparison between the two PTOs.

5.3.1 Best devices recap

In the previous sections several individuals with different parameters and performances have been labeled as "optimal", "optimum" and/or "best". This introductory section aims to clarify which devices are chosen as optimal from the results of the design stages named as Stage 1a and 1b, for the HPTO, and Stage 1 for the MPTO. First, the hydraulic technology has been considered, concerning two consecutive design stages. From Stage 1a, a multi-objective optimization is carried out aiming to define the Pareto front (see Figure 5.13b) of the optimal HPTO-based solutions in respect to the two key performance indexes: AEP and CoE. Figure 5.15 proposed ten best devices in crescent order of CoE, AEP and cost: here, Device-1 (best CoE) and Device-5 (best AEP) have been chosen as optima coherently with the cost and weights limits imposed. These two individuals have been optimized again in Stage 1b in order to design the associated hydraulic transmission. Again, the ten best devices are reported in Figure 5.19 to evaluate the influence of the pump and hp accumulator parameters. Finally, Device-4/blue-line (best CoE) and Device-8/red-line (best AEP) are chosen due to the smallest pump unit (cost reduction) and the largest accumulator unit (high power smoothing capacity). Figure 5.23 summarizes the HPTO design process.

Concerning the MPTO design, Stage 1 produces the Pareto front showed in Figure 5.20b from which ten best devices are collected and reported in Figure 5.22 in respect to their CoE, AEP and cost performances. According to the limits imposed on the initial investment and on the hull and gyroscope size, Device-1

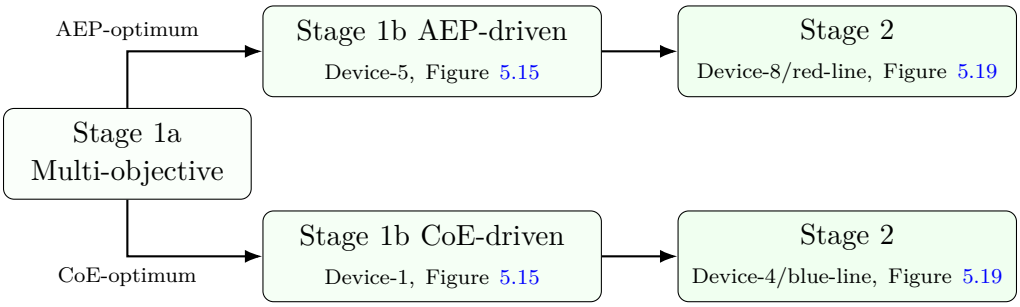

Figure 5.23: Design path and optimal devices for the HPTO technology.

(best CoE) and Device-3 (best AEP) have been chosen as optima for the MPTO. Figure 5.24 summarizes the MPTO design process.

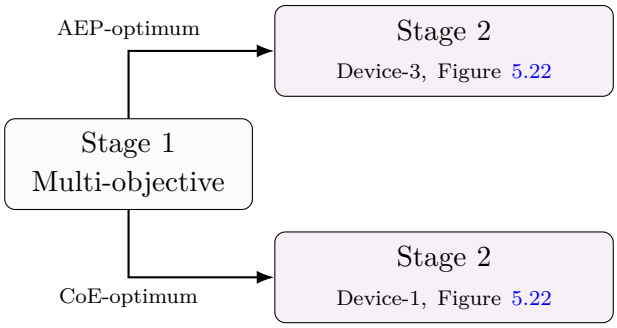

Figure 5.24: Design path and optimal devices for the MPTO technology.

5.3.2 Stage 1 results

Starting with Stage 1 results, the solution domain carried out with Stage 1 (MPTO) and Stage 1a (HPTO) are compared in Figure 5.25.

It is shown that the HPTO solutions are driven by a lower CoE compared to the MPTO ones. The implementation of a HPTO results in a optimum CoE of 237 €/MWh compared to a 273 €/MWh of the MPTO. On the other hand, the MPTO overcomes the annual extracted energy of the HPTO, due to its higher efficiency and the possibility to include a reactive control, that is not applicable for the hydraulic architecture considered in this thesis. The maximal AEP of the HPTO is equal to 820 MWh/y while the MPTO-optimum reaches 861 MWh/y. The improvement in CoE passing from an MPTO to a HPTO, almost equal to 15.1 %, is highlighted in Figure 5.26, where the ten optimal solutions of the two multi-objective optimizations are compared in term of AEP and CoE. Moreover, it is demonstrated that the HPTO AEP-optimum device produces almost 5% less than the MPTO AEP-optimum. Overall, the HPTO devices allows to reduce the CoE of the ISWEC, at least considering an optimization carried out with a SDM.

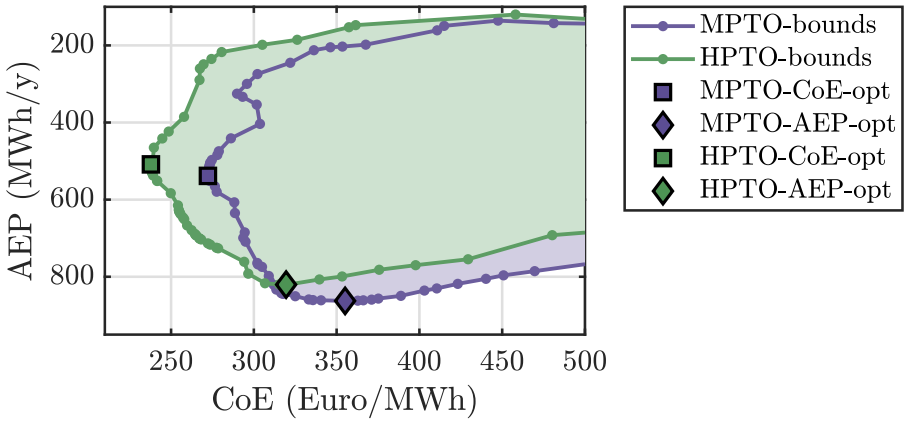

Figure 5.25: Stage 1 (MPTO) and Stage 1a (HPTO) solution domain comparison. Markers highlight the optimal solutions according to the evaluation metrics (CoE-optimum and AEP-optimum).

This could be an important advantage for the ISWEC device: despite the decrease of efficiency introduced by the hydraulic components and, practically, the expected reduction of the system reliability due to the large number of components, numerical simulations demonstrate the effectiveness of the HPTO in high-energetic sea sites as it offers a cost-effective/high-power-density solution.

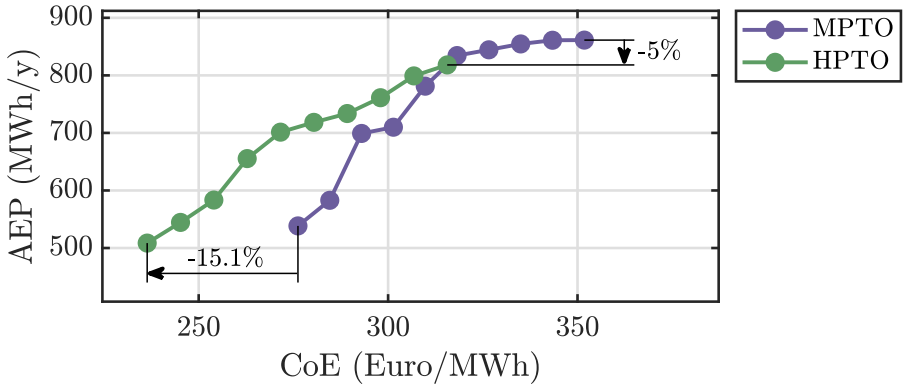

Figure 5.26: AEP and CoE comparison of the ten optimal solution found on the pareto front, for the MPTO and HPTO, respectively. Each dot corresponds to an optimal device.

Concerning the cost evaluation, Figure 5.27a compares the total device cost C_{TOT} of the two PTO configuration for the ten optimal solutions. The cost is reported for each optimal device. Mainly, the CoE reduction obtained with the HPTO is due to the low cost of the hydraulic architecture compared to the mechanical one, as depicted in Figure 5.27b. The cost reduction compensates the lower efficiency of the hydraulic transmission that results in a decrease of the system productivity.

Unfortunately, the outputs of Stage 1b (HPTO) and Stage 1 (MPTO) are not comparable since the numerical models employed are different (TDM for Stage 1b and SDM for Stage 1). For a final fair comparison, the results of Stage 2 have to be considered since the trend showed above are both associated to a SDM.

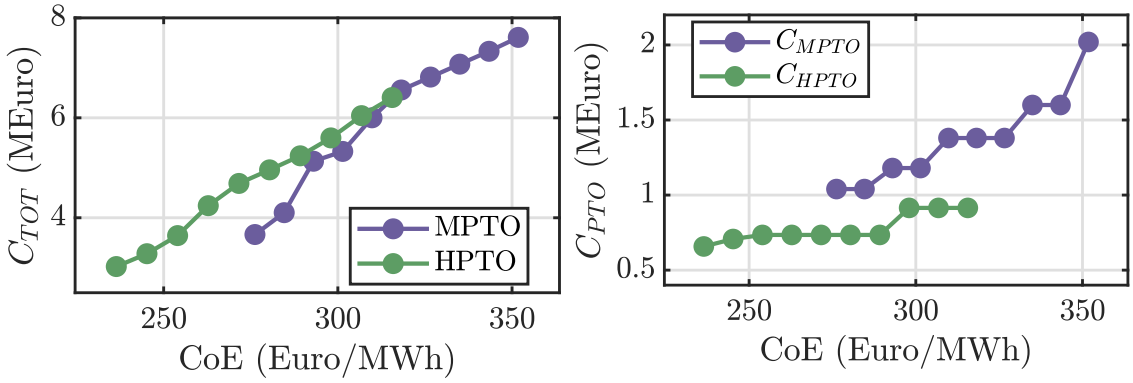

Figure 5.27: Cost comparison of the ten optimal solution found on the pareto front, for the MPTO and HPTO, respectively. (a) Total cost and (b) PTO cost.

5.3.3 Stage 2 results

The final comparison between the mechanical and hydraulic PTO technology is carried out considering the time-domain numerical models of the two systems evaluated over the whole scatter diagram of the sea-sites under study. The four optimal devices defined at the end of Sections 5.1.2 and 5.2 are compared in term of:

- Annual energy produced, AEP;
- Cost of energy, CoE;
- Device cost (total initial investment), C_{TOT};
- PTO cost, C_{MPTO} and C_{HPTO};
- Electric power installed, P_{GEN}: the total electric power is computed summing the rated electric power of each generator unit installed on the system. It is computed multiplying the number of gyroscope units n_{gyro} with the single generator power P_{gen}, for the MPTO, and multiplying the number of hydraulic circuits n_c with the single generator power P_{gen}, for the HPTO;

- Quality of the output power, $\overline{P}_q$: the quality of the output power is considered as an additional key performance indicator; it aims to quantify the spread of the mechanical power extracted from the electrical generator (computed via equations 2.91 and 2.107 for the MPTO and HPTO, respectively) in order to assess its impact on the generation stage.

The generation stage is mainly composed of DC/DC and DC/AC converters, super-capacitors, batteries, Active Front End (AFE) units and other power electronics components. These components manage the power extracted from the electric generator for charging the ISWEC batteries, to supply the flywheel motor and auxiliary components (e.g. cooling system), and to make it suitable of small grids, where the wave power irregularities have to be filtered out. In this context, the mean annual standard deviation of the generator power, named $\overline{P}_q$, is used to quantify the magnitude of "how much the generator power differs from its mean value", which is precisely the extracted power for each wave. An high standard deviation of the power leads the power electronics to work out from its nominal working condition, possibly reducing the efficiency of the final electric conversion. Moreover, the electrical parts have to be designed to handle all the generated power since the power peaks constitutes most of the overall production [37]. Then, $\overline{P}_q$ is computed as follows:

$$\overline{P}_q = \sum_{n_w=1}^{n_W} \sigma_{P_{g,n_w}} o_{n_w} \tag{5.5}$$

where $\sigma_{P_{g,n_w}}$ is the standard deviation of the instantaneous mechanical power extracted from the electric generator for the $n_w - th$ wave.

The main features of the optimal devices for the mechanical and hydraulic PTO are summarized in Table 5.4.

AEP and CoE comparison

The key performance indicators considered in this work relate the capability of the system to produce a certain amount of energy in a year and the resultant energy cost weighted on a lifespan of 25 years. These two metrics has been defined as AEP and CoE, respectively.

Figure 5.28a compares the AEP of the two AEP-optimum devices in all the sea-sites of interest and Figure 5.28b reports the percentage difference between the MPTO and HPTO performances. It is shown how, for the AEP-optimum, the HPTO slightly overcome the annual productivity of the MPTO in some sites, despite the lower efficiency and the absence of a reactive control (or phase control) that is crucial to maximize the extracted power [111]. However, in Balder and Capo Verde, the MPTO produces more than the HPTO although the difference is never lower than -4%. The most promising results comes from the CoE analysis.

Device parameter	Sym.	Unit	**AEP-optimum** MPTO	HPTO	**CoE-optimum** MPTO	HPTO
Hull length	L	m	15.8	15.9	14	13.6
Hull width	W	m	50.5	51.1	46.2	44.5
Hull height	H	m	6.87	6.36	6.16	5.6
Hull mass	M_{hull}	ton	2082	1971	1550	1366
Gyroscope unit mass	m_g	ton	70.7	71.9	50.76	47.9
Flywheel inertia	J	kgm^2	31100	32000	17900	16300
Gyroscope units	n_g	–	4	4	4	4
Pendulum mass	m_p	kg	4000	5200	1150	3250
Gearbox ratio	τ_{gb}	–	30	-	20	-
Pump displacement	D_p	cm^3/rev	-	45200	-	17600
Pump rated torque	T_{pump}	kNm	-	172.2	-	57.4
Hydraulic control id	ID_c	–	-	2	-	2
Hp volume	V_{hp0}	l	-	625	-	600
Hp pre-charge	p_{hp0}	bar	-	60	-	50
Added inertia	I_a	kgm^2	-	15	-	5
Number of circuts	n_c	–	-	2	-	1
Motor displacement	D_m	cm^3/rev	-	250	-	250
Motor rated torque	T_{motor}	kNm	-	1.39	-	1.39
Generator rated torque	T_{gen}	kNm	9.9	0.46	9.9	0.46
Generator rated power*	P_{gen}	kW	259	238	259	238

Table 5.4: Device parameters of the final AEP-optimum and the CoE-optimum devices designed for Balder for the two PTO technology under study. *: the rated power refers to the single generator unit; for the MPTO four generators are installed (one for each gyroscopic units) while the HPTO installs two and one generators for the AEP- and CoE-optimum, respectively.

Figure 5.29a shows the CoE of the two CoE-optimum devices in all the sea-sites and Figure 5.29b the percentage difference between the two PTO types. As desired, a relevant CoE reduction is achieved due to the HPTO implementation that leads to a CoE percentage reduction from -12% (Balder site) up to -22% (Pantelleria site). It is again demonstrated that the economic effectiveness of the hydraulic technology overcome the producitivity drop obtained due to its lower efficiency.

Cost comparison

The initial investment represent an important barrier for the development of a WEC and its reduction is one of the aim of the HPTO application. Figure 5.30a reports the total device cost C_{TOT} of each device evaluated in Stage 2 and Figure 5.30b

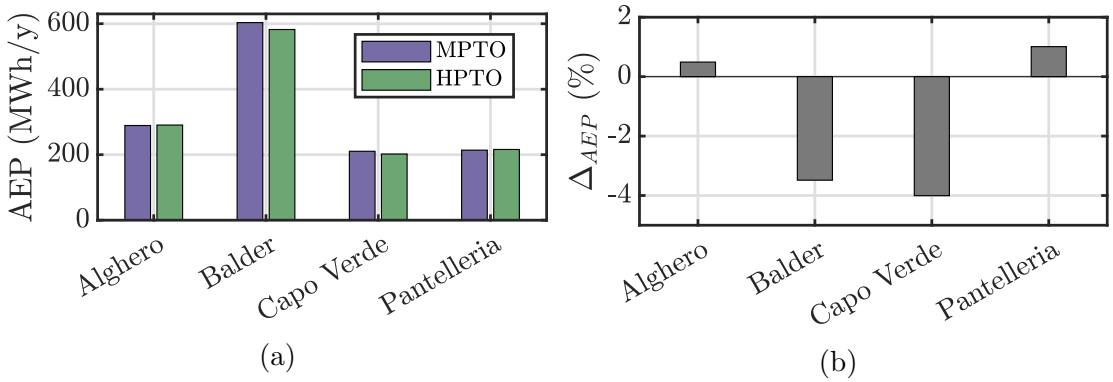

Figure 5.28: AEP results of the AEP-optimum devices evaluated in all the sea-sites under study. (a) total AEP and (b) the percentage difference between the MPTO and HPTO individuals.

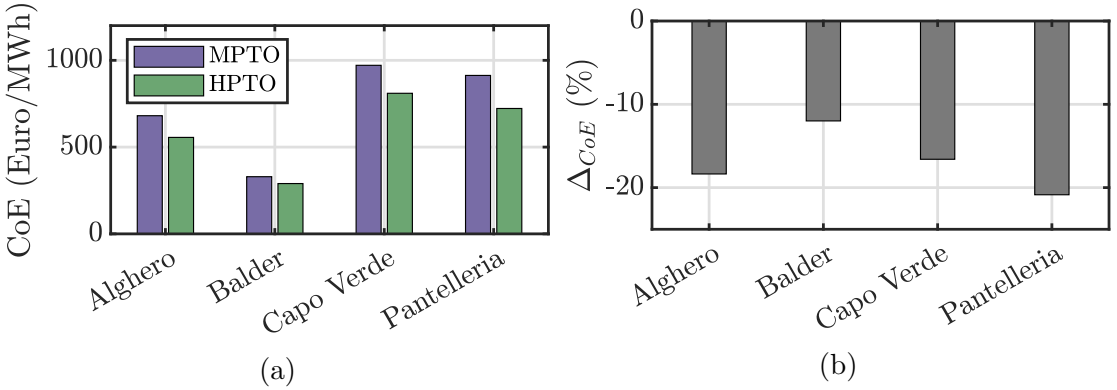

Figure 5.29: CoE results of the CoE-optimum devices evaluated in all the sea-sites under study. (a) Total CoE and (b) the percentage difference between the MPTO and HPTO individuals.

the percentage difference between the mechanical and hydraulic solutions. First, it is evident that the AEP-optimum devices are consistently more expensive than the CoE-optimum since the target of a AEP-optium individual relies on the maximization of the power production, regardless the prototype cost. The AEP-optimum devices have almost a similar cost (5.32 M€ for the MPTO and 5.01 M€ for the HPTO) while the two CoE-optimum presents a more concrete gap (3.66 M€ for the MPTO and 2.85 M€ for the HPTO). In particular, Figure 5.30a shows that for the CoE-optimum the HPTO cost is considerable lower than the MPTO one, leading to a potential cost reduction up to 53%, detectable in Figure 5.30b.

Focusing on the CoE-optimum devices, a deeper understanding of the PTO costs is reported to identify the reasons of such a cost reduction. The PTO cost is an

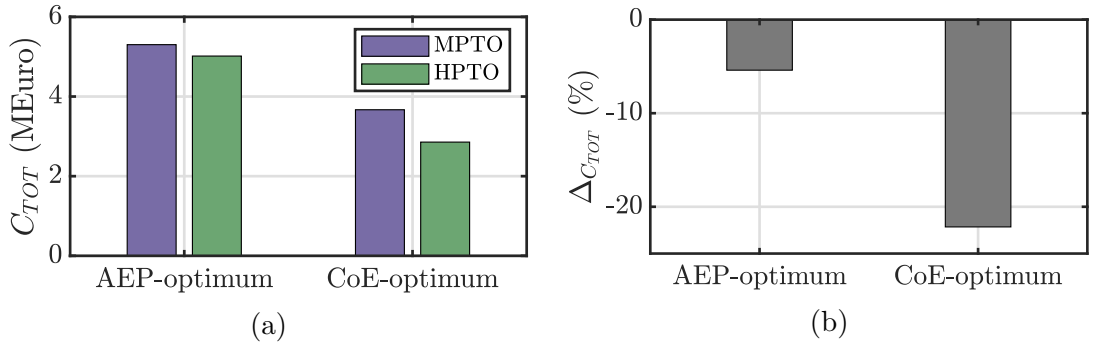

Figure 5.30: Total cost of both the AEP- and CoE-optimum devices. (a) Total cost C_{TOT} and (b) the percentage difference between the MPTO and HPTO individuals.

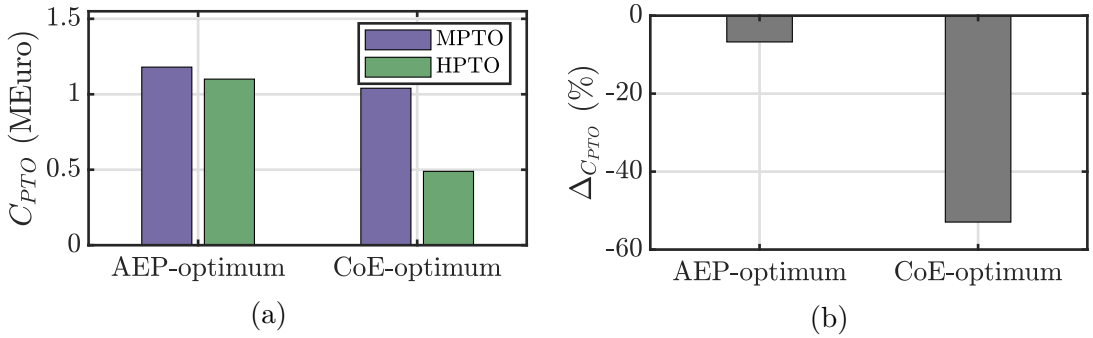

Figure 5.31: Total cost of both the AEP- and CoE-optimum devices. (a) PTO cost C_{PTO} and (b) the percentage difference between the MPTO and HPTO individuals.

aggregation of the single PTO parts cost obtained from an accurate market investigation. Figure 5.32 shows the split of the MPTO and HPTO costs. The MPTO cost is composed by the gearbox, the electric generator with its cables and driver, and the auxiliary electronics costs (super-capacitors, batteries, AFE and other auxiliary power electronics). The HPTO cost is constituted by the hydraulic pumps, accumulators, hydraulic auxiliary components (manifold valves and oil), hydraulic motor, electric generator with its cables and driver, and the auxiliary electronics costs. As reported in Figure 5.32, the power electronics and the electric auxiliary components determine most of the PTO cost, almost 48% in the MPTO and 52% for the HPTO. In this regards, in addition to the lower cost of the hydraulic parts compared to the mechanical ones, the downsize of the electrical auxiliary components due to the filter effect of the accumulators represents the most important driver for the PTO cost reduction. Precisely, for the CoE-optimum devices, the auxiliary costs are equal to 0.49 M€ for the MPTO and 0.25 M€ for the HPTO.

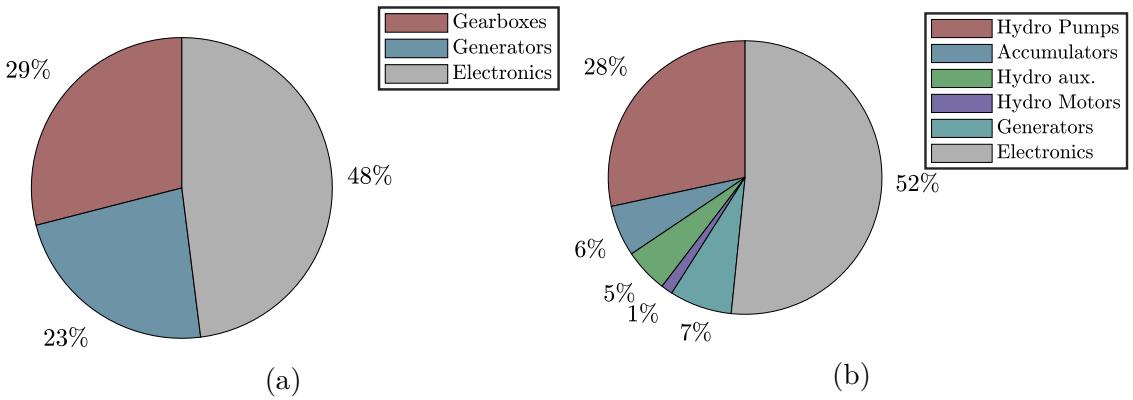

Figure 5.32: PTO cost percentage of each part for both the PTO technologies under study. The percentage refer to the PTO of the CoE-optimum devices. (a) MPTO costs and (b) HPTO costs.

Installed power and power quality comparison

A direct consequence of the accumulators and, more in general, the HPTO, is the possibility to downsize the electrical parts downstream of the transmission. In fact, one MPTO unit is installed on each gyroscope with a dedicated power electronics able to manage the power peaks generated from the incident wave. Conversely, the HPTO can harness all the extracted energy with only one electric generator in which converge all the power flux from each gyroscope unit; moreover, due to the accumulators, the installed power is lower in the HPTO and this result in a reduction of the generator costs and electrical components. Figure 5.33a aims to demonstrate that the installed power, computed by the sum of all the rated power of the electric generators, is considerable lower in the HPTO system, up to 77% lower in the CoE-optimum device (see Figure 5.33b).

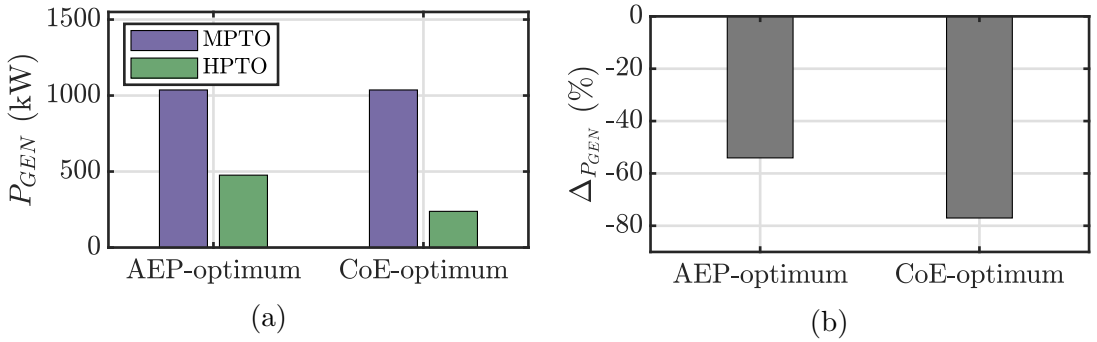

Figure 5.33: Total installed power of both the AEP- and CoE-optimum devices. (a) Installed power P_{GEN} and (b) the percentage difference between the MPTO and HPTO individuals.

Moreover, Figure 5.34 highlights another important key performance of the ISWEC: the mean power standard deviation. Such a parameter, computed through equation 5.5, measures the quality of the generator power, intended as "how far is the instantaneous power from its mean value". Overall, the power quality is better for the HPTO since the $\overline{P}_q$ value is smaller in all the sea-sites and devices under study, reaching a reduction between 66% and 74% (see Figures 5.34b and 5.34d).

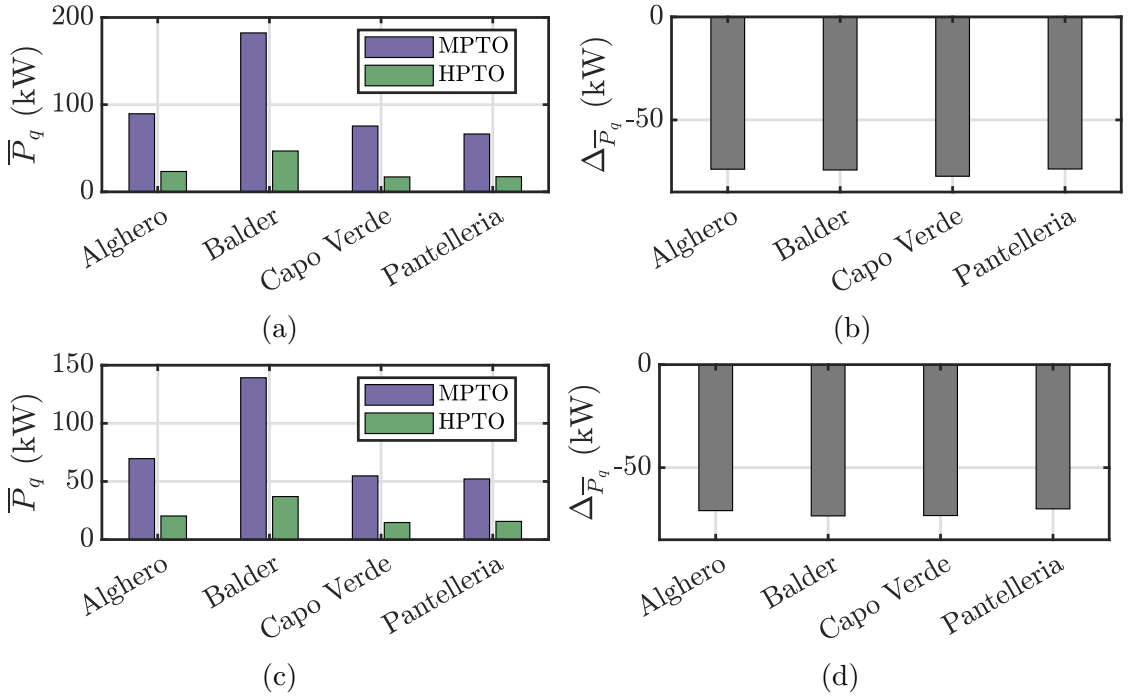

Figure 5.34: Total installed power of both the AEP- and CoE-optimum devices. (a) Installed power P_{GEN} and (b) the percentage difference between the MPTO and HPTO individuals.

A numerical example is reported in Figure 5.35 to compare the time-series of the generator power. One would prefer the HPTO power output in respect to the MPTO one to reduce the accumulation capacity needed to feed small grids environments, typical of small islands where WEC systems found their main application.

5.4 Summary and remarks

In this Chapter the results of the multi-stage design tool presented in Chapter 4 are discussed and an exhaustive comparison between the mechanical and the hydraulic PTO is reported. The main novelty of this new design tool concerns the introduction of the HPTO into the design stage of the ISWEC, limited until now only to the MPTO technology. Several aspects have to be considered during the

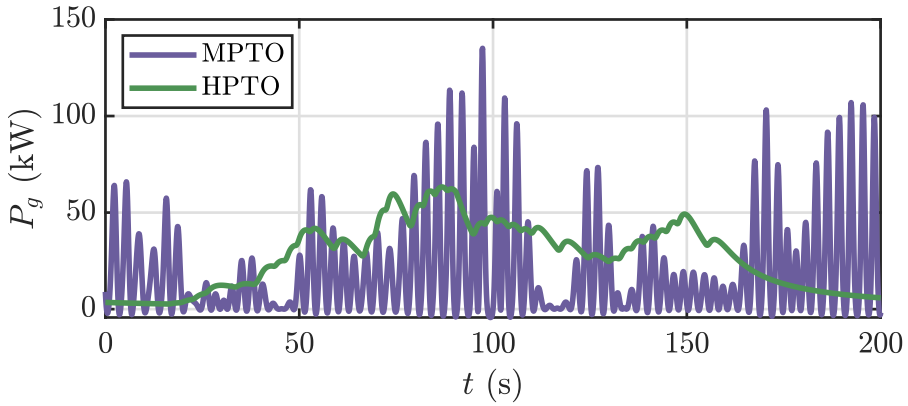

Figure 5.35: Time serie example of the instantaneous generator power obtained from the MPTO (violet line) and from the HPTO (green line). The results refer to the AEP-optimal devices simulated considering an irregular wave profile underlying a JONSWAP spectrum with H_s=1.5m, T_e=6s and γ=3.3.

design process: the power generation capacity, named here Annual Energy Production (AEP) and the economic efficiency, identified as the Cost of Energy (CoE). Also the initial investment play an important role in the decision process. Increasing the size of the ISWEC in order to deploy it in oceanic environments calls for a cost-effective and efficient PTO system able to address all the challenges of the wave energy technologies. Here, mechanical and hydraulic PTO are compared in order to find the best solution for an ISWEC device designed for high energetic seas.

First, the HPTO is designed following two consecutive stages: Stage 1a and Stage 1b. The first stage relies on the SDM and it is used to obtain two optimal ISWEC devices according to the performance metrics of interest. The two most performing devices, one designed to maximize the AEP and one to minimize the CoE, passes to the next stage, where the hydraulic transmission is designed. The process to design the MPTO is similar, although only one design stage is used to obtain the two optimal devices. At the end, the resultant optimal for the two PTO types are compared through the results obtained with Stage 2, that underlines several time-domain simulations generated according to the methodology defined in Sections 2.2 and 3.6.2. Overall, the outputs of the design tool are four different ISWEC devices based on the MPTO and HPTO technology optimized in respect the two metrics of interest: AEP and CoE.

The advantage of the HPTO relies in the capability of handle high power densities with low cost commercial components; moreover, the accumulators offer a cost-effective solution to filter the power peaks compared to the super-capacitors; another important aspect is the possibility to employ only one generation stage where all the power produced by the gyroscopic units of the ISWEC converges,

reducing the number of electrical components. The results suggest that the HPTO technology reduces the CoE of the ISWEC system up to 22% (if Pantelleria sea-site is considered) and, for a CoE-optimal device, the investment required for a full-scale prototype drops from 3.66 M€ to 2.85 M€ supported by a PTO cost reduction of almost 53%, making the ISWEC more attractive for investors. Also the power quality of the system is improved with the HPTO, reducing the mean annual standard deviation of the generator power up to 75%. On the other hand, the low efficiencies of the hydraulic transmission reduces the power extraction capabilities of the entire system. Moreover, due to the accumulators, the pump provides a Coulomb-like force load on the gyroscope, reducing the amount of absorbed energy. Contrary to expectations, if the aim of the ISWEC design is to maximize the annual productivity the MPTO constitutes the preferred solution despite the low power-densities provided. Overall, although the HPTO system introduces more power losses, its cost benefits could lead to a significantly lower CoE to close the gap toward commercial viability of the ISWEC.

The results discussed so far highlights the limitation of a single-objective design or, even worst, of a sequential design process, considering different parts of the power conversion chain independently. In particular, AEP and CoE are partially competing objectives, and two different optimal devices are generated in respect to the desired objective. The design tool presented aims to offer an all-encompassing optimization tool to cover both technical and economical aspects in order to help the design process of a WEC.

Chapter 6

Hydraulic PTO Towards an Optimal Control

The application of WEC systems to irregular wave sources requires a robust control logic capable of maximizing the extracted energy with acceptable efficiencies [80]. The control system is the heart of a WEC capable to enhance the performance of the device and, along with the a proper techno-economic design, is in charge of the maximization of the converter performances. According to Jusoh [74], a control strategy can be classified according to the direction of the PTO power flow (resistive [287, 106] or reactive [288]), the optimization event (offline [289] or online [290]) and the input data (causal or non-causal [291]). In particular, in the HPTO context, Jusoh [74] collected a comprehensive overview of the control strategies used in HPTOs.

This chapter focuses on a Model Predictive Control (MPC) strategy applied to the HPTO of the ISWEC with the aim to improve the system performances. The works of Faedo [190, 292] report a comprehensive review of the advances in optimal control, MPC and MPC-like techniques applied to the wave energy field along with an exhaustive comparison between optimisation- and non-optimisation-based energy-maximising control. The MPC logic generally underlines three different stages that have to be implemented to accomplish the optimal control:

- Measurements or estimation of the system states and input;
- Input and state prediction;
- Optimization of a cost function and calculation of the optimal control input.

In this work the first and the third stages are studied. Here, the prediction of the estimated input (wave excitation force) is not treated and a simple auto-regressive model is used. However, different approaches are proposed in literature [293, 294, 295] demonstrating the straightforwardness of such an operation. Further works

will include the effect of the prediction error on the performance on the proposed optimal control logic.

This chapter is organized as follows. First, in Section 6.1 the ISWEC model is simplified reducing the number of the hydrodynamic DoFs. In the sake of simplicity, the ISWEC model is treated in a 3-DoF version since the 3-DoF hydrodynamic model of the WEC has been experimentally validated by Pozzi [296] and the mooring of the ISWEC device favours the alignment of the floater toward the main wave direction [148]. However, the control framework proposed here can be applied to the 6-DoF version of the model without any loss of generality. Second, Section 6.2 presents a Kalman Filter and a Neural Network models to estimate the wave excitation force acting on ISWEC on the three hydrodynamic DoFs of interest (surge, heave and pitch). Once the wave excitation force estimation is performed, the most performing method is integrated in a MPC framework applied to the HPTO with the aim to enhance the extracted energy. Section 6.3 describes the optimal declutching control along with the results achieved. Strengths and weaknesses of each wave force estimation method are compared and numerical experiments are used to assess the optimal control performances in different wave conditions.

6.1 ISWEC 3-DoF mathematical model

The device considered in this Chapter is the optimal CoE device designed for the Balder sea-site. As described in Section 1.4 and pointed out in Section 2.3, the ISWEC device extracts energy from the sea exploiting only the motion around the pitch axis and the wave direction is fixed to θ=0. Moreover, the hull is symmetrical with respect to its longitudinal and transversal plane. Under these assumptions, a planar 3-DoF model of the ISWEC floater has been considered. In addition, the sensor and acquisition system model is presented here.

6.1.1 ISWEC planar model and sea-states

The reference plane of the 3-DoF model is identified by the vertical gravity axis z and the horizontal direction of the incoming wave x as shown in Figure 2.2. Moreover, the mooring forces are modelled through a quasi-static lookup table that relates the planar motion of the ISWEC to the mooring forces, as described in Section 2.1.4. Manipulating the equation 3.9, the 3-DoF HPTO model reads:

$$\mathbf{M}_p\ddot{\mathbf{X}}_p + \mathbf{B}_p\dot{\mathbf{X}}_p + \mathbf{K}_p\mathbf{X}_p + \boldsymbol{\Theta}(\mathbf{X}_p, \dot{\mathbf{X}}_p, \ddot{\mathbf{X}}_p) = \mathbf{f}_p(t) \tag{6.1}$$

Here, the state vector $\mathbf{X}_p \in \mathbb{R}^{n_p}$ contains the floater DoFs $\mathbf{X}_{fp}$, the radiation states $\boldsymbol{\zeta}_p$, the gyroscope precession angle ε, the pipe pressures p_{pi} and p_{po}, the hp and lp accumulator gas volume V_{hp}, V_{lp} and pressure p_{hp}, p_{lp}, and the generator angular position α_{gh}:

$$\mathbf{X}_p = \begin{bmatrix} \mathbf{X}_{fp} & \boldsymbol{\zeta}_p & \varepsilon & p_{pi} & p_{po} & V_{hp} & p_{hp} & V_{lp} & p_{lp} & \alpha_{gh} \end{bmatrix}^T \tag{6.2}$$

the vector $\mathbf{X}_{fp}$ contains the planar coordinates of the floater x, z and δ. The nonlinear term $\boldsymbol{\Theta}_p : \mathbb{R}^{n_p} \to \mathbb{R}^{n_p}$ includes the HPTO reaction on the gyroscope axis ε, the mooring forces, the gyroscopic effects, the pendulum contribution, the hoses equations, the hp and lp accumulator equations and the motor-generator controlled torque.

$$\boldsymbol{\Theta}_p = \begin{bmatrix} \mathrm{f}_{mx} \\ \mathrm{f}_{mz} \\ \mathrm{f}_{m\delta} - J\dot{\varphi}\dot{\varepsilon}\cos(\varepsilon) \\ \mathbf{0} \\ J\dot{\varphi}\dot{\delta}\cos(\varepsilon) + m_g d_p g \sin(\varepsilon) + \mathrm{sign}(\dot{\varepsilon})\frac{(p_{po}-p_{pi})D_p}{\eta_{pm}} \\ -\frac{\beta_{oil}}{V_h}\left(u_c C_{ck} A_{ck}\sqrt{\frac{2(p_{lp}-p_{pi})}{\rho_{oil}}} - D_p|\dot{\varepsilon}| + (1-u_c)C_{cv}A_{cv}\sqrt{\frac{2(p_{po}-p_{pi})}{\rho_{oil}}}\right) \\ -\frac{\beta_{oil}}{V_h}\left(D_p|\dot{\varepsilon}|\eta_{pv} - u_c C_{ck} A_{ck}\sqrt{\frac{2(p_{po}-p_{hp})}{\rho_{oil}}} - (1-u_c)C_{cv}A_{cv}\sqrt{\frac{2(p_{po}-p_{pi})}{\rho_{oil}}}\right) \\ u_c C_{ck} A_{ck}\sqrt{\frac{2(p_{po}-p_{hp})}{\rho_{oil}}} - C_{rf}A_{rf}\sqrt{\frac{2(p_{hp}-p_{lp})}{\rho_{oil}}} \\ \gamma_{gas}\frac{p_{hp}}{V_{hp}}\left(-u_c C_{ck} A_{ck}\sqrt{\frac{2(p_{po}-p_{hp})}{\rho_{oil}}} + \frac{D_m\dot{\alpha}_{gh}}{\eta_{mv}} + C_{rf}A_{rf}\sqrt{\frac{2(p_{hp}-p_{lp})}{\rho_{oil}}}\right) \\ -u_c C_{ck} A_{ck}\sqrt{\frac{2(p_{lp}-p_{pi})}{\rho_{oil}}} + C_{rf}A_{rf}\sqrt{\frac{2(p_{hp}-p_{lp})}{\rho_{oil}}} \\ \gamma_{gas}\frac{p_{lp}}{V_{lp}}\left(u_c C_{ck} A_{ck}\sqrt{\frac{2(p_{lp}-D_m\dot{\alpha}_{gh}-p_{pi})}{\rho_{oil}}} - C_{rf}A_{rf}\sqrt{\frac{2(p_{hp}-p_{lp})}{\rho_{oil}}}\right) \\ T_{gh} \end{bmatrix} \tag{6.3}$$

The analytical function of the generator torque is reported in equation 2.104. The linear matrices $\mathbf{M}_p \in \mathbb{R}^{n_p \times n_p}$, $\mathbf{B}_p \in \mathbb{R}^{n_p \times n_p}$ and $\mathbf{K}_p \in \mathbb{R}^{n_p \times n_p}$, are the same of equations 3.12, 3.13 and 3.14 except for the terms regarding the floater, that are reduced excluding the rows concerning the states y (sway), α (roll) and ψ (yaw). It is worth to anticipate that the optimal control aims to maximize the hydraulic power delivered to the accumulation stage controlling the position of the declutch valve, considering the accumulation system able to decouple the upstream components of the hydraulic transmission (pump, declutch valve, Greatz bridge, etc.) from the downstream ones (hydraulic motor, electric generator and relief valve). For what regards the external force, $\mathbf{f}_p(t) \in \mathbb{R}^{n_p}$ includes both the wave excitation forces and the drift forces:

$$\mathbf{f}_p(t) = \begin{bmatrix} \mathbf{f}_{Ep}(t) + \mathbf{f}_{Drp}(t) & \mathbf{0} & 0 & 0 & 0 & 0 & 0 & 0 & 0 & 0 \end{bmatrix}^T \tag{6.4}$$

Relations from 6.2 to 6.4 have to be plugged into 3.9 to obtain the non-linear ISWEC model based on the HPTO. n_p is the dimension of the problem. Overall,

the equation 6.1 is equal to the 6-DoF one, except for the floater states, the mooring forces and the drift forces.

Concerning the sea-states, the Balder sea-site is considered to evaluate the estimation performances as well as the optimal control results. However, only four sea-states are employed to tune the WEF observer and to tune the optimal control parameters according to the operating conditions of the ISWEC. The spectral parameters of the four sea-states are reported in Table 6.1, sorted in ascending order of wave power density P_w.

Wave Id	T_e (s)	H_s (m)	γ	P_w (K/m)
1	6.00	2.00	3.30	11.76
2	7.00	2.50	3.30	21.43
3	8.00	4.00	3.30	62.72
4	9.00	5.00	3.30	110.25

Table 6.1: Data of the four tuning waves.

Figure 6.1 gives a representation of annual occurrences and wave energy of the Balder sea-site: the squared white marker represents the four waves used for the tuning process of the WEF estimator and the MPC.

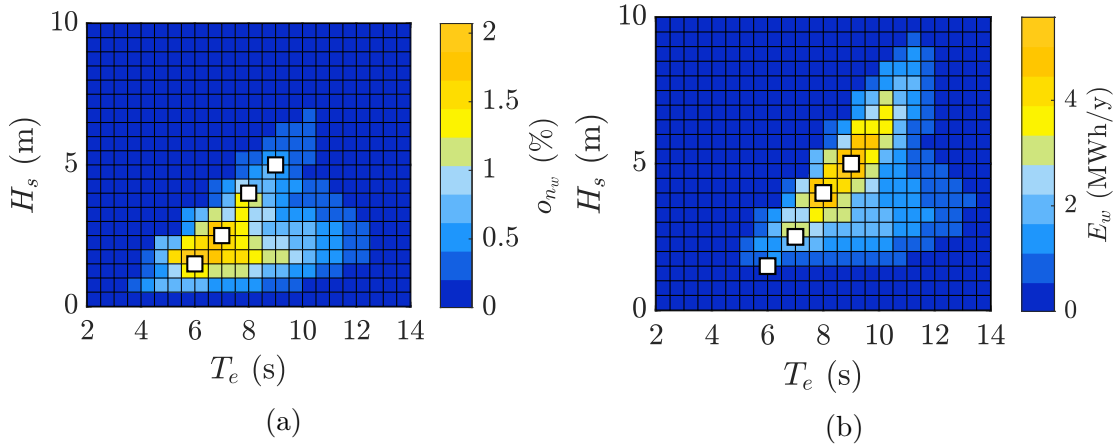

Figure 6.1: (a) Annual occurrences and (b) wave energy of the Balder site. The white squares indicates the tuning waves.

6.1.2 Sensor and acquisition system model

The full-scale ISWEC prototype is equipped with a Data AcQuisition (DAQ) system to record the WEC kinematics and the physical quantities of interest. Here,

only the measurements employed in the WEF estimation are presented. The acquisition of the hydraulic transmission quantities is not in the scope of this Chapter since they are not involved in the WEF estimation algorithms. The linear accelerations, angular orientations and angular rates of the floater are acquired by an Inertial Unit of Measurement (IMU), model MTi-30 AHRS provided by Xsens [297]. The sensor is fixed inside the ISWEC hull and appropriately oriented in respect to the reference system depicted in Figure 2.2. A data processor uses the velocity and orientation increments to give in output the orientations on the three rotational DoFs. The measurements collected from the IMU are: the linear accelerations ($\ddot{x}$ and $\ddot{z}$), the angular position and velocity of the floater (δ and $\dot{\delta}$). The precession motion of the gyroscope and the flywheel speed are measured with two digital encoders Heidenhain Ecn 413 [298]. The measurements available from the encoders are: the flywheel speed ($\dot{\varphi}$), the angular position and speed of the gyroscope (ε and $\dot{\varepsilon}$). The DAQ system is constituted of a National Instrument compactRIO NI cRIO-9030 [299] which is a dual core 1.33 GHz real time control unit.

The ISWEC device is a slack-moored WEC free to oscillate around its deployment location and no fixed x-y-z positions are guaranteed. Then, a precise measure of its absolute position is not trivial. In this context, a Differential GPS (DGPS) is considered to acquire the position x and elevation z of the ISWEC. The differential positioning technique allow to improve the GPS accuracy by comparing its data with those recorded in the same time interval by other multiple GPS receivers. The measurements given by the DGPS are: the absolute positions x and z. In order to increase the precision of the absolute displacements, IMU and DGPS can be combined to perform the sensor fusion technique [300, 301]. Motion Reference Units (MRU) represents a well-known instrument meant for measuring positions, velocities, accelerations, angular rates and orientations of a rigid body, generally employed in modern navigation systems and dynamic positioning applications. The MRU are more precise than IMU units and returns absolute positions and velocities relative to a specified equilibrium point. The measurements available from the MRU are: the positions (x and z), velocities ($\dot{x}$ and $\dot{z}$) and accelerations ($\ddot{x}$ and $\ddot{z}$) along the surge and heave directions, the angular position and velocity of the hull (δ and $\dot{\delta}$). Table 6.2 resumes all the frameworks considered in this work and their noise original deviations σ_m.

6.2 Wave excitation force estimation

In literature, various approaches have been proposed to address the problem of the Wave Excitation Force (WEF) estimation for control purposes. An exhaustive classification and comparison of several estimation techniques is presented in the work of [302] and some of them are reported in a previous work of the author [149]. Two methods are presented and studied here: a model-based approach, concerning

Measures	Unit	FM	MRU		IMU+DGPS		IMU	
		Data	Data	σ_m	Data	σ_m	Data	σ_m
x	m	•	○	0.05	○	0.5	–	–
$\dot{x}$	m/s	•	○	0.03	–	–	–	–
$\ddot{x}$	m/s^2	•	○	0.001	○	0.01	○	0.01
z	m	•	○	0.05	○	0.5	–	–
$\dot{z}$	m/s	•	○	0.03	–	–	–	–
$\ddot{z}$	m/s^2	•	○	0.001	○	0.01	○	0.01
δ	rad	•	○	$5 \cdot 10^{-4}$	○	0.01	○	0.01
$\dot{\delta}$	rad/s	•	○	10^{-4}	○	0.002	○	0.002
ε	rad	•	○	0.02	○	0.02	○	0.02
$\dot{\varepsilon}$	rad/s	•	○	0.001	○	0.001	○	0.001
$\dot{\varphi}$	rad/s	•	○	0.001	○	0.001	○	0.001

Table 6.2: Measurement frameworks available. Four cases are considered: Full Measurement (FM), Motion Reference Unit (MRU), Inertial Measurement Unit with Differential GPS (IMU+DGPS) and Inertial Measurement Unit (IMU) depending on the intended use and on the precision desired.

a Kalman Filter (KF) observer, and a model-free (or black box) approach, using a Neural Network (NN). Model-based techniques are widely used in literature. For example, in [294, 295], Ling and Garcia-Abril employed a KF observer on a linear PA-type converter. Both Ling and Garcia-Abril assumed that the WEF can be modelled as a linear superposition of fixed and finite harmonic components. In the work of [303] two approaches are presented: the first one is based on a KF coupled with a random-walk model of the WEF; the second performs a receding horizon – unknown input estimation. Other examples of model-based estimator can be found in [304, 305, 306]. Concerning the model-free approach, Li [307] studied a NN framework to estimate the wave forces on a PA-WEC. Similarly, Mohammed [308] tackled the estimation of the sea-wave elevation using the measurements from a nearby buoy joint with a Non-linear AutoRegressive with eXogenous input network (NARX). All the mentioned studies reports encouraging results in terms of estimation performances and robustness of the observer. However, most of the works refer to single DoF WECs (point absorber types) and few techniques are applied to non-linear multiple DoF systems.

In the ISWEC context, five different approaches have been applied in previous works. Genuardi [309], built an unknown state observer with a second order augmented state-space model for the estimation of the pitch excitation torque. The gain of the observer has been found with an LQR optimization. In [191] the PSD of the actual wave climate is derived by using the heave motion measurements and the results are compared with the wave data of a buoy measurement system. Then,

in two previous work of the author [310, 149], a KF and a feed-forward NN used to estimate the WEF acting on surge, heave and pitch DoFs are proposed and then compared. This section reports methods and results proposed and discussed in [149], where two approaches are applied to the non-linear 3-DoF model of the ISWEC to estimate the WEFs acting on surge, heave and pitch DoFs:

1. A model-based approach, with a KF observer [294, 295, 302];
2. A model-free approach with a feed-forward NN [310].

The main challenges and novelties proposed lie in considering a non-linear 3-DoF model and estimate the wave forces along three degrees of motion. The main outcomes of this investigation are compare the estimation performances with different measurement frameworks in presence of sensors noises and plant uncertainties. Another novelty is to perform an excitation force estimation decoupling the mooring forces or, more in general, undesired phenomena that will appear in real operating condition. Finally, the NN represents an almost unexplored framework for the WEF estimation problem. In fact, there are very few examples of NN application to a multi-DOF non-linear WEC systems. Overall, the main aim is to use the minimum amount of available measurements to model the unknown excitation forces in respect to the ISWEC kinematic. The floater model is considered to relates a set of measurements of the ISWEC kinematics to the unknown excitation forces through a KF observer and a NN model. The mooring forces are considered as a unknown disturb. The rest of the ISWEC model, concerning the HPTO, is not involved in the estimation process since its variables does not appear into the floater equation.

6.2.1 Wave excitation force estimation with Kalman Filter

The KF observer is ubiquitous in many engineering applications to estimate the current state of a linear (or non-linear if the Extended Kalman Filter is used) dynamic system from a set of measurements affected by uncorrelated Gaussian noise with known covariance. The KF estimator is optimal because it estimates the system states minimizing the covariance of the estimation error. The estimation framework is modelled following the approach proposed in [295], where the WEF is defined as the sum of finite harmonic components with fixed frequency and variable amplitudes. In order to obtain the KF formulation, the non-linear model is simplified considering the drift forces included into the wave excitation component term. Then, the state space model of the ISWEC is discretized in time-domain to derive the KF formulation. The mooring forces are treated as a undesired external disturbs and the filter is designed to decouple them from the signal to estimate.

Linear 3-DoF ISWEC model

The non-linear model 6.1 is re-written to obtain a linear state-space formulation of the floater equation, suitable for the KF implementation. The floater dynamics can be expressed by the following linear continuous-time state-space model, where the gyroscope reaction $\mathbf{f}_{gp}$ is considered a known input[1] of the system and the mooring forces $\mathbf{f}_{mp}$ as a unknown disturb:

$$\begin{aligned} \dot{\mathbf{X}} &= \mathbf{A}\mathbf{X} + \mathbf{B}\mathbf{f}_{gp} + \mathbf{B}\left(\mathbf{f}_p + \mathbf{f}_{mp}\right) \\ \mathbf{Y} &= \mathbf{C}\mathbf{X} + \mathbf{D}\mathbf{f}_{gp} + \mathbf{D}\left(\mathbf{f}_p + \mathbf{f}_{mp}\right) \end{aligned} \tag{6.5}$$

where $\mathbf{X} \in \mathbb{R}^{n_S}$ and $\mathbf{Y} \in \mathbb{R}^{m_S}$ are the states and measurements vectors defined as:

$$\begin{aligned} \mathbf{X} &= \begin{bmatrix} \mathbf{X}_{fp} & \dot{\mathbf{X}}_{fp} & \boldsymbol{\zeta}_p \end{bmatrix}^T \\ \mathbf{Y} &= \begin{bmatrix} \mathbf{X}_{fp} & \dot{\mathbf{X}}_{fp} & \ddot{\mathbf{X}}_{fp} \end{bmatrix}^T \end{aligned} \tag{6.6}$$

Note that the measurements available varies in respect to the measurement framework considered (see Table 6.2). $\mathbf{A} \in \mathbb{R}^{n_S \times n_S}$, $\mathbf{B} \in \mathbb{R}^{n_S \times n_D}$, $\mathbf{C} \in \mathbb{R}^{m_S \times n_S}$ and $\mathbf{D} \in \mathbb{R}^{m_S \times n_D}$ are given by:

$$\begin{aligned} \mathbf{A} &= \begin{bmatrix} \mathbf{0} & \mathbf{I} & \mathbf{0} \\ -\mathbf{K}_{fp}\mathbf{M}_{fp}^{-1} & -\mathbf{D}_{rp}\mathbf{M}_{fp}^{-1} & -\mathbf{C}_{rp}\mathbf{M}_{fp}^{-1} \\ 0 & \mathbf{B}_{rp} & \mathbf{A}_{rp} \end{bmatrix}, \quad \mathbf{D} = \begin{bmatrix} \mathbf{0} \\ \mathbf{M}_{fp}^{-1} \\ \mathbf{0} \end{bmatrix} \\ \mathbf{C} &= \begin{bmatrix} \mathbf{I} & \mathbf{0} & \mathbf{0} \\ \mathbf{0} & \mathbf{I} & \mathbf{0} \\ -\mathbf{K}_{fp}\mathbf{M}_{fp}^{-1} & \mathbf{0} & -\mathbf{C}_{rp}\mathbf{M}_{fp}^{-1} \end{bmatrix}, \quad \mathbf{D} = \begin{bmatrix} \mathbf{0} \\ \mathbf{0} \\ \mathbf{M}_{fp}^{-1} \end{bmatrix} \end{aligned} \tag{6.7}$$

The hydrodynamic matrices $\mathbf{K}_{fp}$, $\mathbf{M}_{fp}$, $\mathbf{A}_{rp}$, $\mathbf{B}_{rp}$, $\mathbf{C}_{rp}$ and $\mathbf{D}_{rp}$ have the same structure of the ones derived in Section 2.1.4 except for the number of DoF considered. The external known and unknown inputs are:

$$\begin{aligned} \mathbf{f}_{gp} &= \begin{bmatrix} 0 & 0 & T_\delta \end{bmatrix}^T \\ \mathbf{f}_p &= \begin{bmatrix} \mathrm{f}_x & \mathrm{f}_z & \mathrm{f}_\delta \end{bmatrix}^T \\ \mathbf{f}_{mp} &= \begin{bmatrix} \mathrm{f}_{mx} & \mathrm{f}_{mz} & \mathrm{f}_{m\delta} \end{bmatrix}^T \end{aligned} \tag{6.8}$$

Here, n_S is the number of states, n_D the number of inputs and m_S the number of outputs, $\mathbf{I}$ and $\mathbf{0}$ stands for identity and zero matrices according to the problem

[1] The gyroscope reaction on the floater, named T_δ, is derived from the flywheel and gyroscope measurements and computed through equation 2.88b.

dimensions. The system 6.5 represents the most general framework for a linear multi-DoF WEC model, where:

- The gyroscope reaction $\mathbf{f}_{gp}$ is the controlled input (e.g., the PTO action);
- The WEF $\mathbf{f}_p$ is the exogenous input to be estimated;
- The mooring forces $\mathbf{f}_{pm}$ are the unknown unmodelled phenomena to be decoupled from the $\mathbf{f}_p$ estimation.

Kalman Filter problem statement

Following the procedure proposed in [294, 295, 302], the WEF can be included into the state vector as an unknown state to be estimated and it can be split into N_W frequency components of variable amplitude. Then, the mooring forces are considered as a un-modelled phenomena to be decoupled from the estimation of $\mathbf{f}_p$ since, in real applications, it would be difficult to directly measure the action of the moorings. In normal working conditions, snatch loads do not appear, and the mooring forces have mainly the behaviour shown in Figure 6.2. $\mathbf{f}_{pm}$ is synthesised using the same method proposed for $\mathbf{f}_p$, using a harmonic model to describe its nature. For the sake of simplicity, the mooring forces are modelled with only one frequency for each component.

Lets define the state vector $\mathbf{X}_a$, including $\mathbf{X}$, the estimation of $\mathbf{f}_p$ and $\mathbf{f}_{mp}$. Consequently, the following augmented state-space holds:

$$\begin{aligned} \dot{\mathbf{X}}_a &= \mathbf{A}_a\mathbf{X}_a + \mathbf{B}_a\mathbf{f}_{gp} \\ \mathbf{Y} &= \mathbf{C}_a\mathbf{X}_a + \mathbf{D}_a\mathbf{f}_{gp} \end{aligned} \tag{6.9}$$

where $\mathbf{X}_a \in \mathbb{R}^{n_F}$ is the augmented state vector defined as:

$$\mathbf{X}_a = \begin{bmatrix} \mathbf{X} & \hat{\mathbf{f}}_p & \hat{\mathbf{f}}_p \end{bmatrix}^T \tag{6.10}$$

Here, $n_F = n_S + 2n_D(N_W + 1)$ is the augmented state vector dimension and $\hat{\mathbf{f}}_p \in \mathbb{R}^{n_D \times (N_W+1)}$ is the unknown wave force to be estimated. The single component of the estimated force, say for example $\hat{\mathbf{f}}_x$, is given by the single WEF harmonics and the mooring force as follows:

$$\hat{\mathbf{f}}_x = \begin{bmatrix} \hat{\mathrm{f}}_{x_1} & \hat{\mathrm{f}}_{x_2} & \dots & \hat{\mathrm{f}}_{x_{N_W}} & \hat{\mathrm{f}}_{mx} \end{bmatrix}^T \tag{6.11}$$

Therefore, the estimated $\hat{\mathrm{f}}_x$ is obtained by summing up all the harmonic contributions:

$$\hat{\mathrm{f}}_x = \sum_{i=1}^{N_W} \hat{\mathrm{f}}_{x_i} \tag{6.12}$$

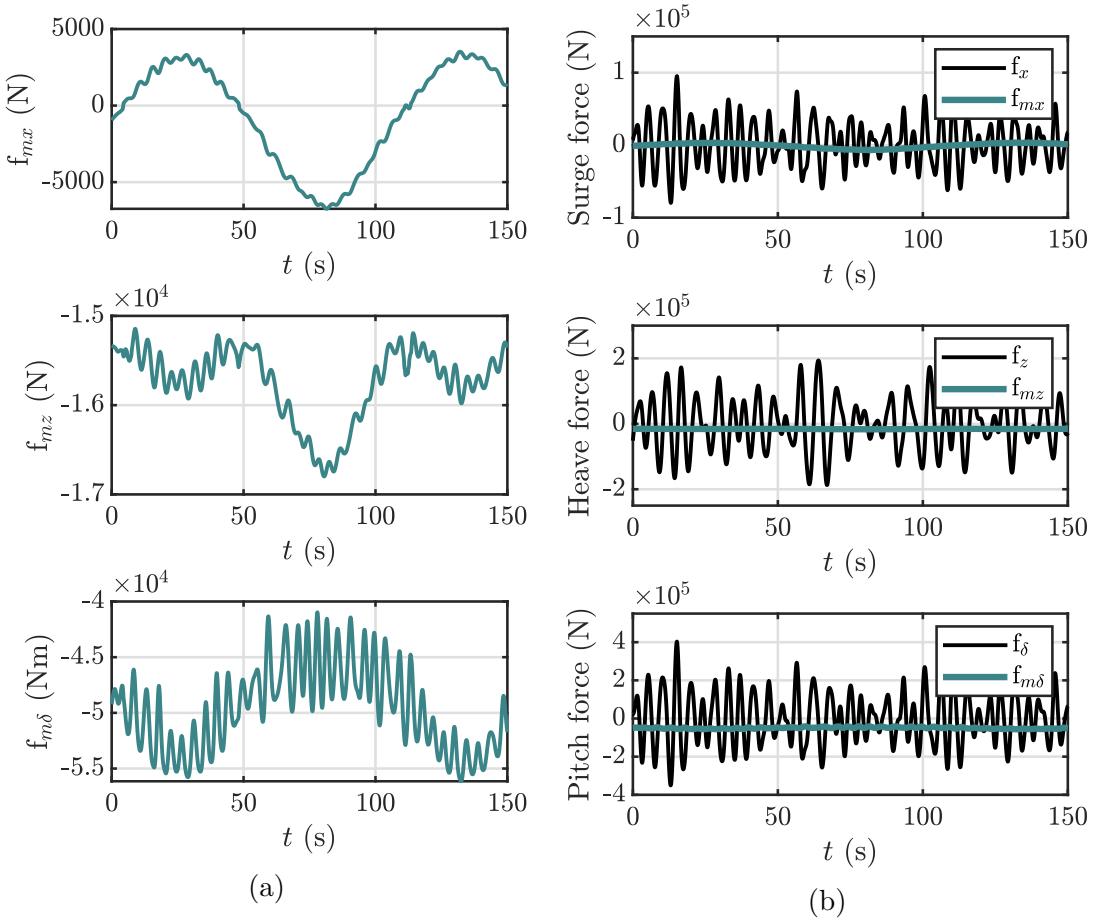

Figure 6.2: Mooring forces magnitude (a) and comparison with WEFs (b). The results have been obtained with Wave Id 2 of Table 6.1.

The augmented matrices $\mathbf{A}_a \in \mathbb{R}^{n_F \times n_F}$, $\mathbf{B}_a \in \mathbb{R}^{n_F \times n_D}$, $\mathbf{C}_a \in \mathbb{R}^{m_S \times n_F}$ and $\mathbf{D}_a \in \mathbb{R}^{m_S \times n_D}$ read:

$$\mathbf{A}_a = \begin{bmatrix} \mathbf{0} & \mathbf{I} & \mathbf{0} & \mathbf{0} & \mathbf{0} \\ -\mathbf{K}_{fp}\mathbf{M}_{fp}^{-1} & -\mathbf{D}_{rp}\mathbf{M}_{fp}^{-1} & -\mathbf{C}_{rp}\mathbf{M}_{fp}^{-1} & \mathbf{M}_{fp}^{-}1\mathbf{N} & \mathbf{0} \\ \mathbf{0} & \mathbf{B}_{rp} & \mathbf{A}_{rp} & \mathbf{0} & \mathbf{0} \\ \mathbf{0} & \mathbf{0} & \mathbf{0} & \mathbf{0} & \mathbf{I} \\ \mathbf{0} & \mathbf{0} & \mathbf{0} & -\mathbf{\Omega}^2 & \mathbf{0} \end{bmatrix}, \quad \mathbf{B}_a = \begin{bmatrix} \mathbf{0} \\ \mathbf{M}_{fp}^{-1} \\ \mathbf{0} \\ \mathbf{0} \\ \mathbf{0} \end{bmatrix} \tag{6.13}$$

$$\mathbf{C}_a = \begin{bmatrix} \mathbf{I} & \mathbf{0} & \mathbf{0} & \mathbf{0} & \mathbf{0} \\ \mathbf{0} & I & \mathbf{0} & \mathbf{0} & \mathbf{0} \\ -\mathbf{K}_{fp}\mathbf{M}_{fp}^{-1} & -\mathbf{D}_{rp}\mathbf{M}_{fp}^{-1} & -C_r\mathbf{M}_{fp}^{-1} & \mathbf{M}_{fp}^{-}1\mathbf{N} & \mathbf{0} \end{bmatrix}, \quad \mathbf{D}_a = \begin{bmatrix} \mathbf{0} \\ \mathbf{0} \\ \mathbf{M}_{fp}^{-1} \end{bmatrix}$$

$\mathbf{N} \in \mathbb{R}^{n_D \times (N_W+1)}$ is defined as:

$$N = \begin{bmatrix} \mathbf{I}_{1,N_W+1} & \mathbf{0} & \mathbf{0} \\ \mathbf{0} & \mathbf{I}_{1,N_W+1} & \mathbf{0} \\ \mathbf{0} & \mathbf{0} & \mathbf{I}_{1,N_W+1} \end{bmatrix} \tag{6.14}$$

where I_{1,N_W+1} is a $1 \times (N_W + 1)$ vector of ones. $\Omega \in \mathbb{R}^{3(N_W+1)\times 3(N_W+1)}$ is the diagonal matrix with the frequencies identified to approximate the unknown forces along the three DoFs:

$$\mathbf{\Omega} = \begin{bmatrix} \mathbf{\Omega}_x & \mathbf{0} & \mathbf{0} \\ \mathbf{0} & \mathbf{\Omega}_z & \mathbf{0} \\ \mathbf{0} & \mathbf{0} & \mathbf{\Omega}_\delta \end{bmatrix} \tag{6.15}$$

In equations 6.15, $\mathbf{\Omega}_x \in \mathbb{R}^{(N_W+1)\times(N_W+1)}$, $\mathbf{\Omega}_z \in \mathbb{R}^{(N_W+1)\times(N_W+1)}$ and $\mathbf{\Omega}_\delta \in \mathbb{R}^{(N_W+1)\times(N_W+1)}$ are diagonal matrices containing the frequencies of the unknown force components:

$$\mathbf{\Omega}_x = \begin{bmatrix} \text{diag}(\omega_{wx}) & 0 \\ 0 & \omega_{mx} \end{bmatrix} \tag{6.16}$$

where $\omega_{wx} \in \mathbb{R}^{N_W}$ stores the N_W harmonics to model the WEF. The number of frequencies in $\mathbf{\Omega}$ have to be chosen in order to have a compromise between the accuracy of the estimation and the computational effort. The matrices 6.16 include a term at low frequency to represent the contribution of the mooring forces.

Let us consider the following linear time-invariant stochastic discrete model representing the discrete-time version of the augmented System (6.9):

$$\begin{aligned} \hat{\mathbf{X}}_{ad}(k+1) &= \mathbf{A}_{ad}\hat{\mathbf{X}}_{ad}(k) + \mathbf{B}_{ad}\mathbf{f}_{gp}(k) + \mathbf{\Gamma}w(k) \\ \mathbf{Y}_d(k) &= \mathbf{C}_{ad}\hat{\mathbf{X}}_{ad}(k) + \mathbf{D}_{ad}\mathbf{f}_{gp}(k) + v(k) \\ w(k) &\sim \mathcal{N}(0, \mathbf{Q}) \\ v(k) &\sim \mathcal{N}(0, \mathbf{R}) \end{aligned} \tag{6.17}$$

where $\hat{\mathbf{X}}_{ad}(k)$ represents the system estimated states, $\mathbf{f}_{gp}(k)$ is the known input and $\mathbf{Y}_d(k)$ contains the measurements of the system dynamics. $w(k)$ and $v(k)$ are zero-mean white noise sequences with known covariance and uncorrelated with each other. $\mathbf{A}_{ad}$, $\mathbf{B}_{ad}$, $\mathbf{C}_{ad}$ and $\mathbf{D}_{ad}$ stand for the discretised versions of the matrices $\mathbf{A}_a$, $\mathbf{B}_a$, $\mathbf{C}_a$ and $\mathbf{D}_a$. $\mathbf{\Gamma}$ is the weighting matrix for the process disturbances. $\mathbf{Q}$ and $\mathbf{R}$ are the covariance matrices of the process and measurements noise. The KF algorithm estimates the process state at some time and then obtains feedback in the form of (noisy) measurements through the time-update equations and measurement-update equations [311]:

- Time Update:

$$\begin{aligned}\mathbf{P}^{-}(k) &= \mathbf{A}_{ad}\mathbf{P}(k-1)\mathbf{A}_{ad}^{T} + \mathbf{\Gamma}\mathbf{Q}\mathbf{\Gamma}^{T} \\ \hat{\mathbf{X}}_{a}^{-}(k) &= \mathbf{A}_{ad}\hat{\mathbf{X}}_{a}(k-1) + \mathbf{B}_{ad}\mathbf{f}_{gp}(k-1)\end{aligned} \tag{6.18}$$

- Measurement Update:

$$\begin{aligned}\mathbf{K}(k) &= \mathbf{P}_{k}^{-}C^{T}\left(\mathbf{C}_{ad}\mathbf{P}^{-}(k)\mathbf{C}_{ad}^{T} + \mathbf{R}\right)^{-1} \\ \mathbf{P}(k) &= \left(\mathbf{I} + \mathbf{K}(k)\mathbf{C}_{ad}\right)\mathbf{P}^{-}(k) \\ \hat{\mathbf{X}}_{ad}(k) &= \hat{\mathbf{X}}_{ad}^{-}(k) + \mathbf{K}(k)\left(\mathbf{Y}_{d}(k) - \mathbf{C}_{ad}\hat{\mathbf{X}}_{ad}^{-}(k) - \mathbf{D}_{ad}\mathbf{f}_{gp}(k)\right)\end{aligned} \tag{6.19}$$

In this framework, the KF algorithm can be implemented to estimate the unknown WEF vector $\hat{\mathbf{f}}_{p}(k)$ measuring the system dynamics $\mathbf{Y}_{d}(k)$ and the known input $\mathbf{f}_{gp}(k)$ at any instant k.

6.2.2 Wave excitation force estimation with neural network

The non-linear effects emerging in sever sea-states conditions and the reliability of the WEC model could negatively affect the estimation performances of the KF observer. In this context, when the system model is not reducible to a state-space equations or, even more, is based only on observed data, artificial NNs represent powerful tools to map the non-linear relations from sets of input-output data. Generally, NN models are trained to fit such input-output data, without any reference to the physical background and no information about the model equations. The WEF acting on the ISWEC at the instant k can be formulated as a non-linear function $f(\bullet)$ of the system inputs and floater/gyroscope measurements as follows [310]:

$$\hat{\mathbf{f}}_{p}(k) = f(\mathbf{f}_{gp}(k), ..., \mathbf{f}_{gp}(k - k_N + 1), \mathbf{Y}(k), ..., \mathbf{Y}(k - k_N + 1)) \tag{6.20}$$

where the system inputs $\mathbf{f}_{gp}$ and the avaiable measurements $\mathbf{Y}$ are collected from the discrete time $k-k_N+1$ to k, where k_N represents the delay steps of the available data. In a NN framework, it is key to assess both the ability to estimate data that are not considered in the training process and the accuracy in presence of model uncertainties. Here, the procedure studied in [149] is used: the NN is evaluated for all the sensor configurations reported in Table 6.2 and the sensitiveness and robustness analysis is extended to all the wave domain of the installation site. The NN architecture is schematic in Figure 6.3.

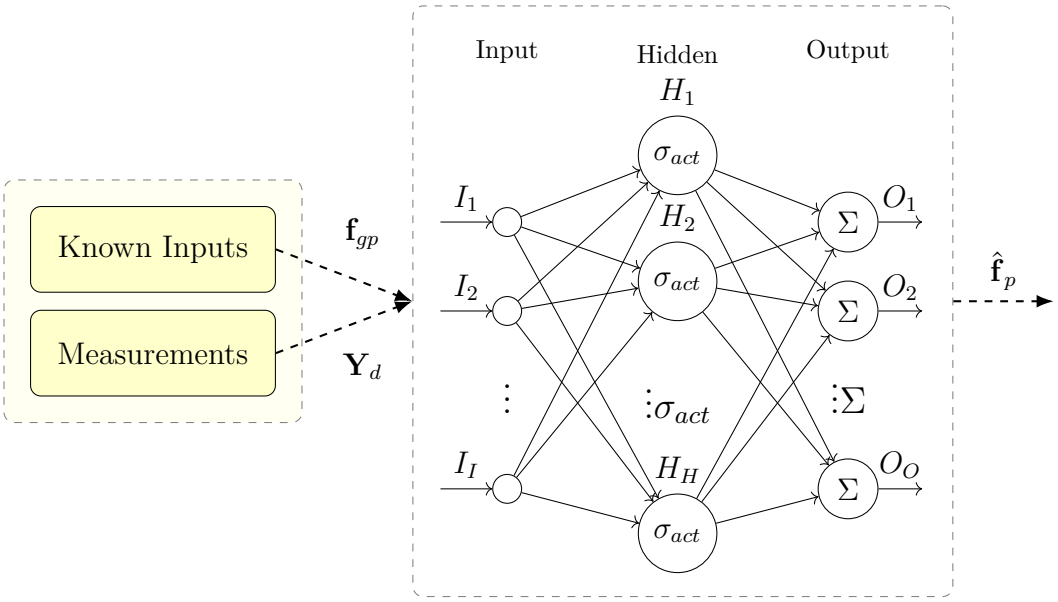

Figure 6.3: Neural Network architecture for ISWEC. Adapted from [149].

A feed-forward NN is composed of a series of neurons linked through three layers: the input layer, that collects a set of inputs I_I multiplying them by a set of weights, the hidden layer, that applies a non-linear activation function σ_{act} to the weighted sum of their inputs, and an output layer, where the outcomes of the hidden neurons are linearly combined by the output functions Σ to produce the network outputs O_O. The use of delays in the input variables enhance the reliability of the estimate allowing to model the dynamic behaviour of the ISWEC using static neurons [312], increasing the estimation accuracy and robustness to different wave conditions as demonstrated in [310, 149].

6.2.3 Kalman Filter and Neural Network tuning

In the KF context, tuning the matrices $\mathbf{\Omega}$, $\mathbf{Q}$ and $\mathbf{R}$ is crucial to achieve best performances in presence of measurement noise and un-modelled phenomena to distinguish them from the signal to be estimated. A sensitivity analysis has been performed to tune the diagonal terms of $\mathbf{\Omega}$, $\mathbf{Q}$ and $\mathbf{R}$ to maximize the estimation performances for each measurement framework considered. Similarly, the NN has been tuned to determine the delay steps k_N and neurons number n_N. Numerical experiments are conduced considering the four waves of Table 6.1.

The Goodness-of-Fit (GoF) proposed by [313], is considered to quantify the accuracy of the WEF estimation. For example, considering the x DoF, the GoF_x reads:

$$GoF_x = 1 - \frac{\sqrt{\sum_{k=1}^{T_s} \left(\mathrm{f}_x(k) - \hat{\mathrm{f}}_x(k)\right)^2}}{\sqrt{\sum_{k=1}^{T_s} \mathrm{f}_x(k)^2}} 100\% \tag{6.21}$$

where f_x and $\hat{\mathrm{f}}_x(k)$ are the true and estimated value of the wave force for the x DoF at the discrete time instant k. T_s is the total number of time samples.

Kalman Filter parameters

The frequency matrix $\mathbf{\Omega}$ has been tuned for 1, 3, 6 and 9 number of frequencies in order to find a compromise between the accuracy of the estimation and the KF complexity. The interval of the frequency (or period) values is chosen between period 5s and period 11s, linearly spaced. The mooring components are modelled with only one period: 100s for f_{mx} and 2000s for f_{mz} and $\mathrm{f}_{m\delta}$, considered as low frequency contributions (see Figure 2.3). In a practical setup, an accurate analysis the dominant periods is crucial to achieve the best performances from the KF. The frequency tuning has been performed with the FM framework.

Figure 6.4 summarizes the results obtained with respect to the number of frequencies N_W. In Figure 6.4a, the mean $\overline{GoF}$ obtained averaging the GoF obtained with each tuning wave of Table 6.1 is reported. Figure 6.4b highlights the percentage difference between each GoF from the GoF calculated with $N_W = 9$[2]. Negative values of Δ_{GoF} means that all the GoF are less accurate than the reference value at $N_W = 9$. A significant increase of accuracy is found from $N_W = 1$ to $N_W = 3$, while passing from $N_W = 3$ to $N_W = 6$ results in a slight increase of GoF_x and GoF_z, enhancing the quality of the estimation. Further enlarge of N_W does not provide any relevant upgrade in estimation accuracy. In particular, using only one frequency lead to a degradation in performance from 16% for the z DoF to 25%, to 27% for the δ DoF, both in respect to $N_W = 9$. Increasing from $N_W = 3$ to $N_W = 6$ lead to an average increase of almost 2% of accuracy. In this regard, $N_W = 6$ is considered a good trade-off between accuracy and complexity of the observer.

The covariance matrices, $\mathbf{Q}$ and $\mathbf{R}$, are chosen to guarantee an accurate estimation of the unknown states without amplifying the noise level and, thus, a different tuning for each measurement framework is needed. As reported in [149], the coefficients magnitude is inversely proportional to the noise intensity and they are tuned in respect to the energy content of the wave force components. In this way, the most relevant frequencies are amplified more than the others. Concerning the $\mathbf{R}$ coefficients, they are chosen to penalize the most inaccurate measurements giving

[2]Note that the percentage difference in $N_W = 9$ is equal to zero since it is calculated with itself.

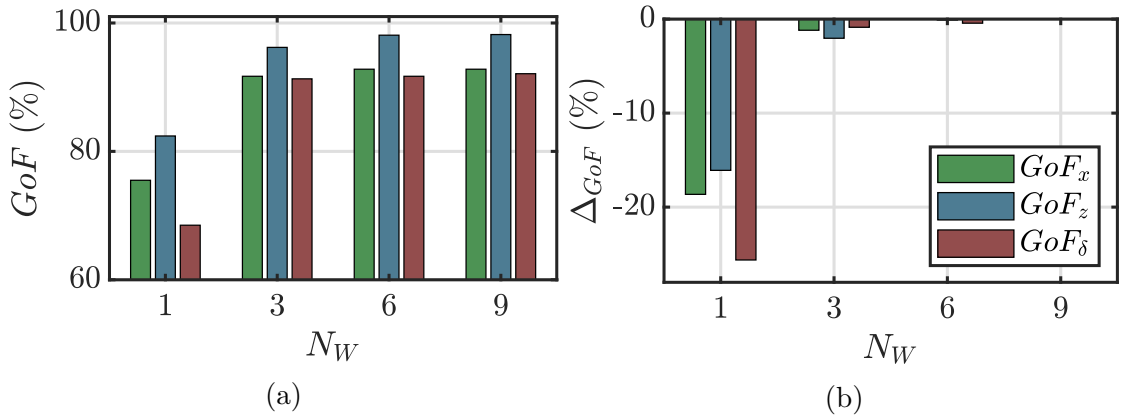

Figure 6.4: GoF and Δ_{GoF} percentage difference for different frequency components: (a) GoF values for each DoF and (b) percentage difference between the single GoF and the reference value at $N_W = 9$. The results are calculated averaging the GoF obtained from each of the four tuning wave of Table 6.1.

less importance to the related signals. Data reported in [149], indicate that the **R** coefficients grow as the noise magnitudes increase.

Neural Network parameters

The four wave profiles of Table 6.1 are employed to train the NN model for each measurement framework. The time domain model is simulated to generated the required NN input (floater and gyroscope states) and the resultant time-series are concatenated to generate a long training sets and normalized in the $[-1,1]$ to favor the training process. In order to avoid over-fitting the input data are randomly divided into three parts: 50% for training, 30% for validation and 20% for performance evaluation. The performance function is the Mean Squared Error (MSE) normalized between -1 and 1, ensuring that the output elements of different magnitude are treated as equally important. The delay steps are evaluated from 1 to 7 while the number of neurons from 5 to 20. The FM framework has been considered for tuning the network hyper-parameters while specific NN trainings are applied for each framework once the number of delay steps and neurons are found.

Similarly to Figure 6.5, Figure 6.5 shows the results of the delay step influence. Figure 6.5a reveals that it is worth to increase the number of delay steps from $k_N = 1$ to $k_N = 3$, especially for the pitch DoF since GoF_δ that passes from 88% to 0.97%. A similar behaviour is obtained for the GoF_x, where the mean estimation performance grows of 5.3 points. On the other hand, no relevant improvements are obtained for the heave DoF as well as for the other DoFs employing 5 and 7 delay steps (lower than 0.85% for all the DoF). Figure 6.5b demonstrates the increase of accuracy obtained passing from $k_N = 1$ to $k_N = 3$ and the negligible improvement

passing from $k_N = 5$ to $k_N = 7$. Then, 3 delays steps are chosen for the NN model.

Finally, Figure 6.6 reports the influence of the number of neurons on the estimation accuracy. 10 neurons seems to guarantee good estimation performances and, surprisingly, increasing the number of neurons over 10 leads to a slight degradation of performances, suggesting that during the learning process over-fitting happens with noisy data and the training algorithm is not able to converge properly. In fact, positive Δ_{GoF} values for $k_N = 10$ and $k_N = 15$ means that these number of neurons provide a better estimation accuracy than $k_N = 20$.

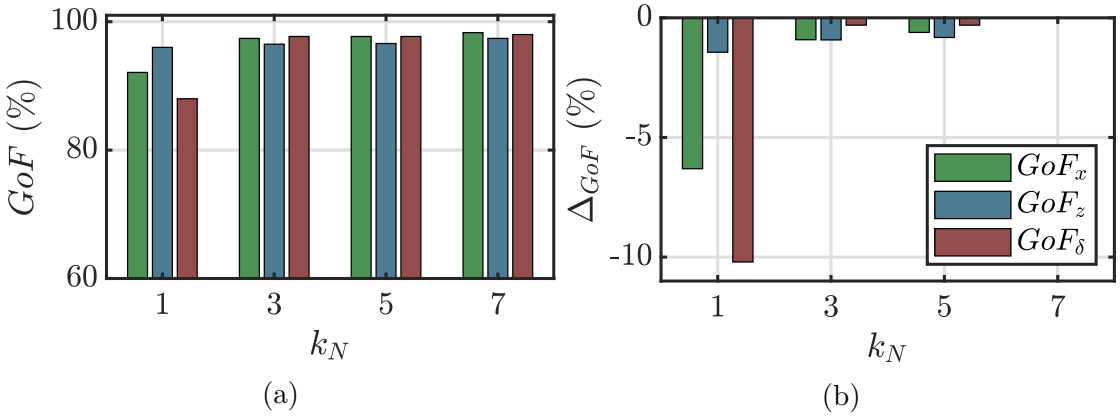

Figure 6.5: GoF and Δ_{GoF} percentage difference for different NN delay steps: (a) GoF values for each DoF and (b) percentage difference between the single GoF and the reference value at $k_N = 7$. The results are calculated averaging the GoF obtained from each of the four tuning wave of Table 6.1.

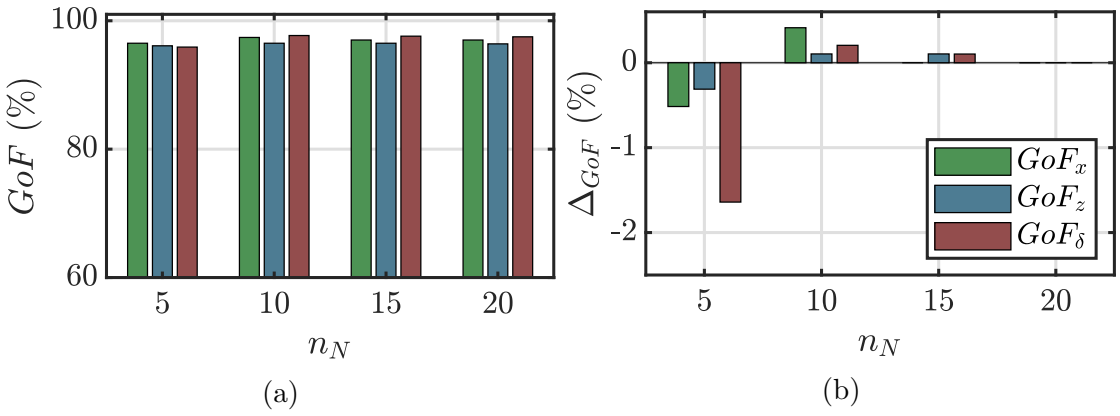

Figure 6.6: GoF and Δ_{GoF} percentage difference for different neuron numbers: (a) GoF values for each DoF and (b) percentage difference between each GoF with the reference value at $n_N = 20$. The results are calculated averaging the GoF obtained from each of the four tuning wave of Table 6.1.

6.2.4 Numerical results and discussions

An exhaustive evaluation of the KF and NN estimation performances in different wave conditions as well as a robustness analysis to different measurements and plant inaccuracies is provided in this section. The KF and NN are tested extending the wave domain to the whole Balder sea-site, represented in Figure 4.24. The GoF is weighted on the annual occurrences of the site under study as follows, for example for the x DoF:

$$\overline{GoF}_x = \sum_{n_w=1}^{n_W} GoF_{x,n_W} o_{n_W} \tag{6.22}$$

The same calculations are applied to the z and δ DoFs.

Influence of the measurement framework

The first analysis carried out concerns the influence of the available signals on the estimation performances. Three measurement configurations (MRU, IMU+DGPS and IMU) are compared considering noiseless data in order to highlight the impact of the missing measurements.

Focusing on the KF results, Figure 6.7 is quite revealing in several ways. The MRU provides the best estimation performances and it is considered as the measurements framework of reference. Figure 6.7a shows that the accuracy is almost the same for the force components in surge and pitch directions, regardless the framework employed. Despite the absence of the $\dot{x}$ and $\dot{z}$ signals, the IMU+DGPS solution is able to estimate the surge and heave wave force components with the same accuracy as the MRU one. Surprisingly, the accuracy of the IMU in estimating the surge and pitch components almost equals the MRU and IMU+DGPS one, although the IMU does not provide both x and $\dot{x}$. Since surge and pitch DoFs are coupled due to the device geometry, the surge force can be successfully estimated via the pitching motion (available in all the frameworks). In particular, as reported in Figure 6.7b, the percentage difference in $\overline{GoF}$ is lower than 1.8% if $\overline{GoF}_x$ and $\overline{GoF}_\delta$ are compared between MRU and IMU. For what concern the heave component, there is a remarkable difference between the $\overline{GoF}_z$ of the IMU and the other two equipments. The leak of both z and $\dot{z}$ decreases the IMU performances since, as illustrated in Figure 6.8, the KF is not able to estimate perfectly the floater vertical position z (since it is not provided by any sensor) resulting in a loss of estimation accuracy. In this case, the $\Delta_{\overline{GoF}_z}$ between the IMU and the MRU is almost -22% (see Figure 6.7b).

Considering the NN, Figure 6.9a shows that the NN performance is maximized with both a MRU and IMU+DGPS measurement framework. In agreement with the KF, if the absolute velocities $\dot{x}$ and $\dot{z}$ are not considered, a minimal decrease in estimation accuracy appears (≈0.1%). This finding is demonstrated in Figure 6.9b,

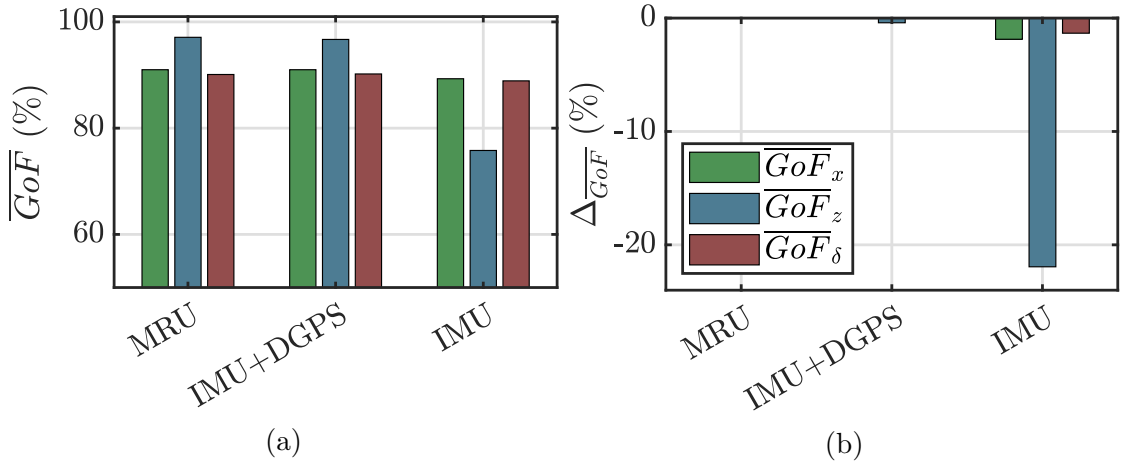

Figure 6.7: $\overline{GoF}$ and $\Delta_{\overline{GoF}}$ percentage difference obtained with the KF for different measurement frameworks: (a) $\overline{GoF}$ values for each DoF and (b) percentage difference between each $\overline{GoF}$ with the reference value provided by the MRU.

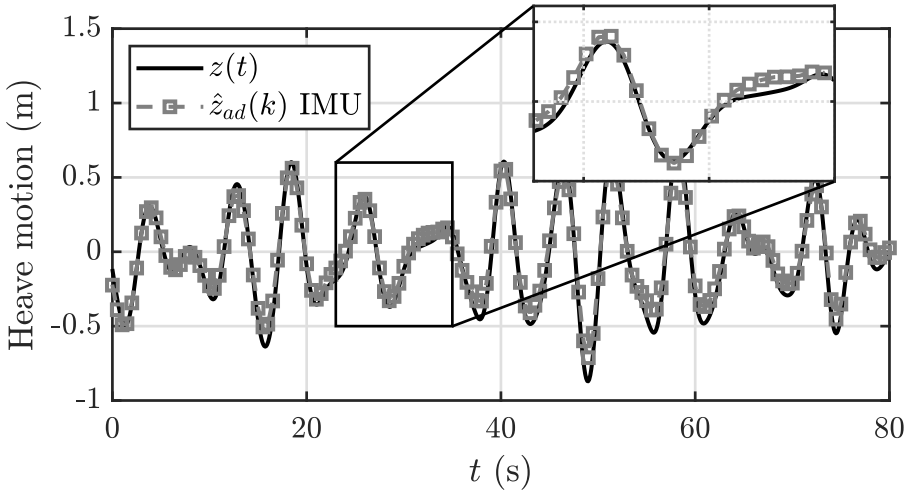

Figure 6.8: Heave motion $z(t)$ compared with its discrete time estimation $z_{ad}(k)$ obtained with the IMU framework (Wave Id 2).

where no $\Delta_{\overline{GoF}}$ are reported between MRU and IMU+DGPS. The lack of performance increase with the IMU architecture, specially for the heave DoF where the goodness of estimation significantly reduces for all the waves, suggesting that the NN does not provide an appropriate fit of the f_z if a full measurement framework is not provided. On the other hand, δ, $\dot{\delta}$ and $\ddot{x}$ are adequate to succesfully estimate the f_x and f_δ components, as demonstrated also for the KF observer. In detail, the worst result concerns the heave DoF, where a $\Delta_{\overline{GoF}_z}$ of -42.2% is found if MRU and IMU accuracy are compared. On the other hand, a $\Delta_{\overline{GoF}_x}$=-3.9% and $\Delta_{\overline{GoF}_\delta}$-2.1%

are found for the surge and pitch DoF respectively, if MRU and IMU accuracy are compared.

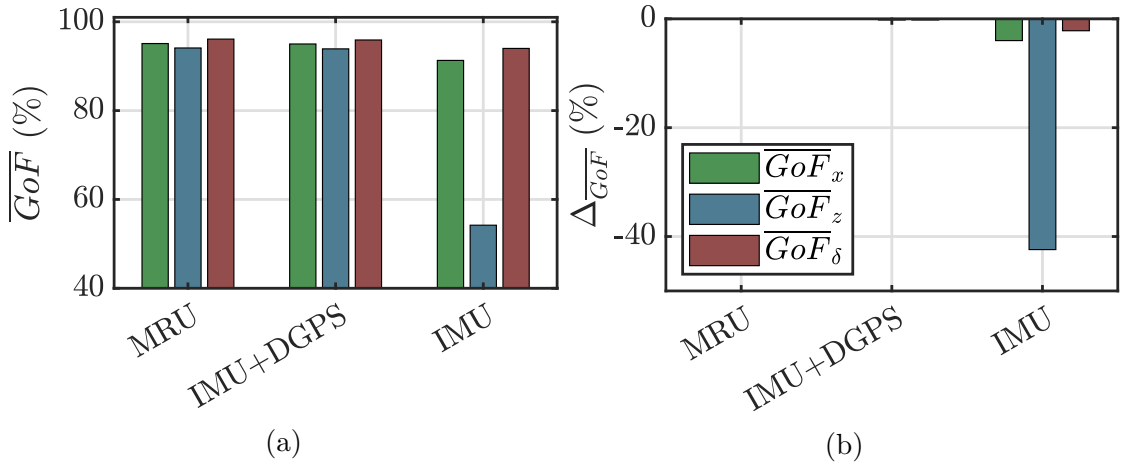

Figure 6.9: $\overline{GoF}$ and $\Delta_{\overline{GoF}}$ percentage difference obtained with the NN for different measurement frameworks: (a) $\overline{GoF}$ values for each DoF and (b) percentage difference between each $\overline{GoF}$ with the reference value provided by the MRU.

Overall, regardless the estimation technique, high $\overline{GoF}$ means than good performances are obtained in all the sea-states considered, suggesting a good versatility of both the KF and NN where the system is not tuned.

Sensor noise effect

In this section, realistic data are applied both to the KF and NN to assess the effect of the sensor disturbances. The impact of the measurement framework is the main focus of this section and study the influence of the sensor disturbance is mandatory to design the proper WEF estimator.

Starting with the KF observer, Figure 6.10a highlights that the MRU framework gives the best precision by far, especially for the heave and pitch excitation force components. MRU units are affected by minimal disturbances and offer accurate measures, included the absolute velocities and positions. On the other hand, the use of IMU+DGPS introduces higher estimation errors due to the increase of noise, in particular for what regard the surge and heave motion. These measures are the most polluted due to a noise RMS equal to 0.5 m as reported in Table 6.2 and as depicted in Figure 6.11. The reader should note that the errors introduced by the DGPS are the same order of magnitude of the heave motion, forcing to increase $\mathbf{R}$ coefficient associated to z to such an extent that its measurements are neglected by the KF reducing the accuracy of the f_z estimation. The performances provided by the IMU almost equalizes the IMU+DGPS ones. Similarly to the noiseless case, removing the DPGS noisy measurements of x and z does not decrease the

quality of the estimation. However, a good quality in δ, $\dot{\delta}$ and $\ddot{x}$ acquisitions allows to effectively estimate the wave forces of the coupled DoF (surge and pitch). As reported in Figure 6.10b, employing a IMU+DGPS or a simple IMU unit results in the same decrease of performance, almost equal to -2.6%, -14.7% and -8.4%, for f_x, f_z and f_δ respectively, if IMU+DGPS and IMU are compared with the MRU.

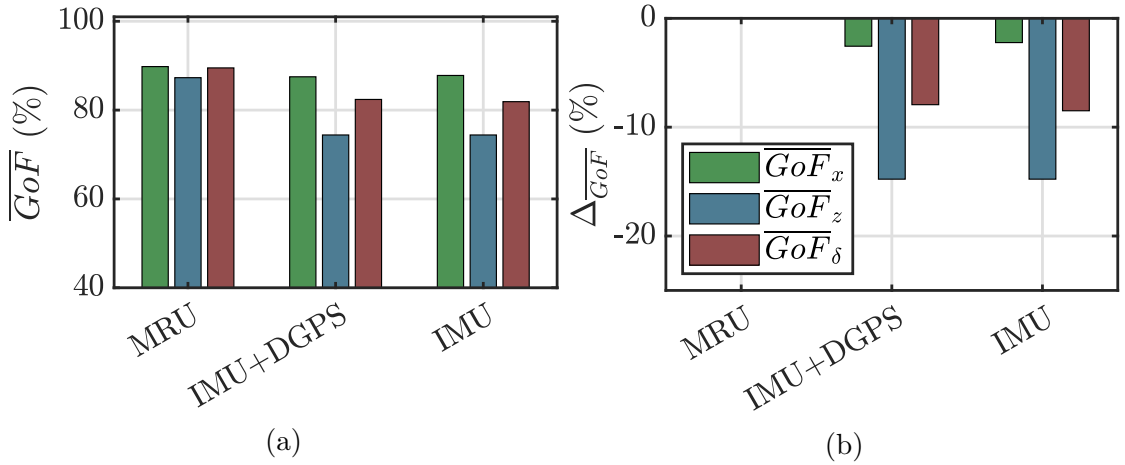

Figure 6.10: $\overline{GoF}$ and $\Delta_{\overline{GoF}}$ percentage difference obtained with the KF for different measurement frameworks with noise: (a) $\overline{GoF}$ values for each DoF and (b) percentage difference between each $\overline{GoF}$ with the reference value provided by the MRU.

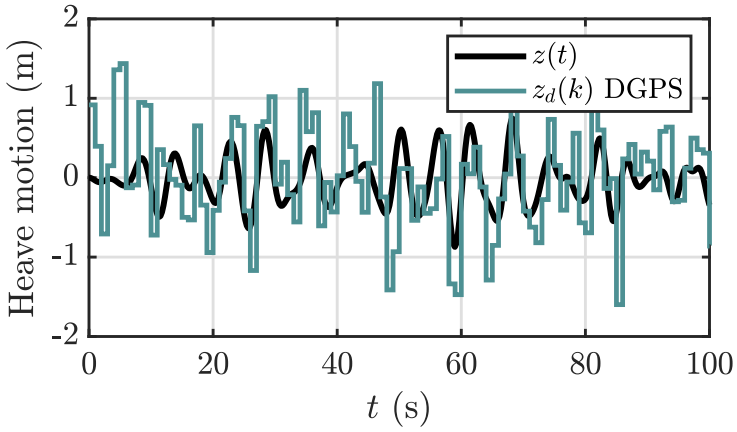

Figure 6.11: Heave motion compared with its DGPS acquired signal (Wave Id 2).

As shown in Figure 6.12a, the introduction of noisy measurements negatively affects the estimation accuracy of the NN more than the Kalman observer. A drastic degradation of performance is shown for the IMU+DGPS and IMU framework concerning the heave component. The high noise magnitude provided by the DGPS

makes the NN unable to estimate the heave force component with acceptable accuracy. Figure 6.12b highlights that the degradation of the $\overline{GoF}_z$ reaches almost a $\Delta_{\overline{GoF}_z}$=-60% if IMU+DGPS or IMU are considered. On the other hand, the degree of accuracy slightly diminish for the other two DoFs with the IMU+DGPS and IMU, up to -12% with the IMU if the f_δ components is estimated.

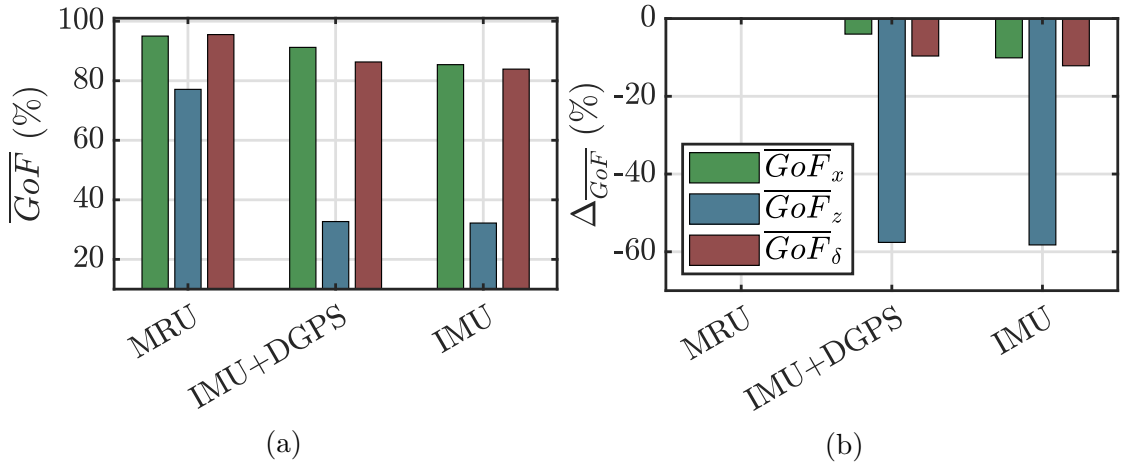

Figure 6.12: $\overline{GoF}$ and $\Delta_{\overline{GoF}}$ percentage difference obtained with the KNN for different measurement frameworks with noise: (a) $\overline{GoF}$ values for each DoF and (b) percentage difference between each $\overline{GoF}$ with the reference value provided by the MRU.

Sensitivity to plant variations

In practice, the physical properties of a WEC may differ from the ones used to tune and train the KF and NN estimators. In order to evaluate the effectiveness of both KF and NN, the mass matrix M_{fp} and stiffness matrix K_{fp} of the floater are modified to test the sensitivity of the estimation process to model errors. An iterative method is proposed varying both the mass and stiffness matrix in respect to the nominal value as follows:

$$\begin{aligned} M_c &= \overline{M} M_{fp} \\ K_c &= \overline{K} K_{fp} \end{aligned} \tag{6.23}$$

where $\overline{M}$ and $\overline{K}$ are the correction coefficients and M_c and K_c the corrected values. $\overline{M}$ and $\overline{K}$ span from 0.85 to 1.15.

The performances of the KF are shown in Figure 6.13. The variation of the mass matrix provides a slow decrease of performances for the surge component. The maximum variation of the mass matrix results in a decay of almost 10% of $\overline{GoF}_x$ for all the measurement frameworks. The stiffness matrix does not affect the

estimation of the surge component since the hydrostatic stiffness is null in the x direction and no variation of $\overline{GoF}_x$ is detected. Concerning the heave and pitch DoFs, the degradation of performance is quite sensitive to the mass and the stiffness variation. The mass matrix provides an high decrease in performance since pitch-surge modes are coupled and the estimation is influenced both by the diagonal and off-diagonal terms of M_{fp} [310]. In particular, a decrease up to 20% is obtained for the MRU framework for $\overline{M}$=1.15. A variation of K_{fp} results in a decay of almost 20÷30% in both $\overline{GoF}_z$ and $\overline{GoF}_\delta$ for all the measurement frameworks.

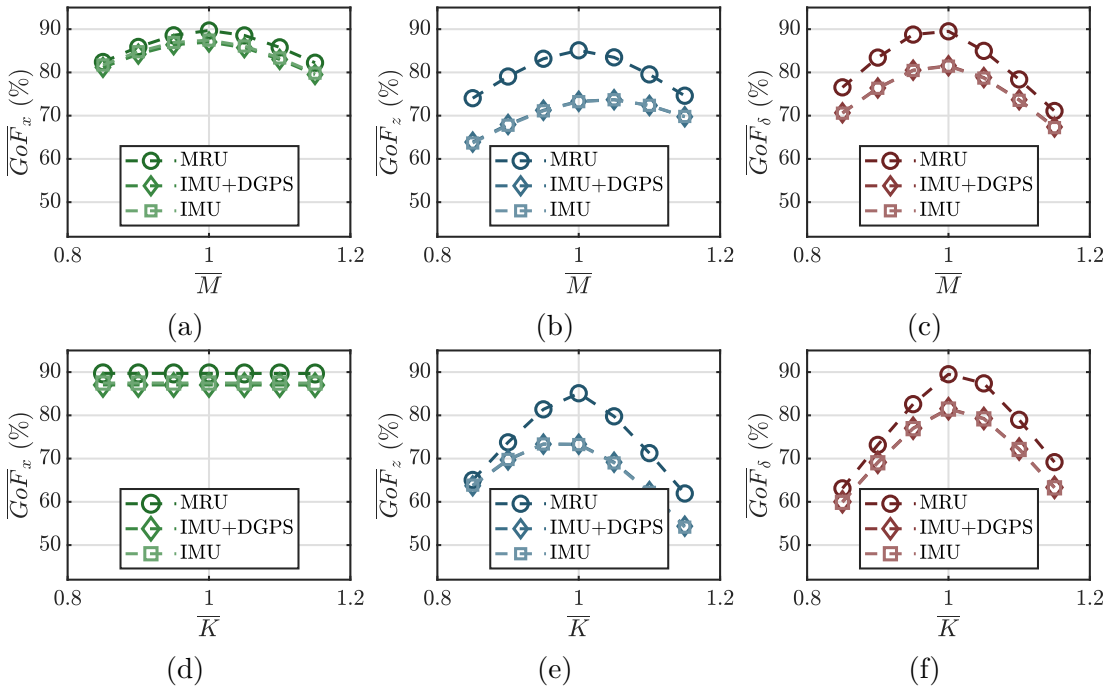

Figure 6.13: $\overline{GoF}$ results obtained with the KF varying $\overline{M}$ and $\overline{K}$. The first column refers to the x DoF, Figures (a) and (d), the second to the z DoF, Figures (b) and (e) and the third to the δ DoF, Figures (c) and (f)

Also the NN has been simulated with different values of $\overline{M}$ and $\overline{K}$, and the results are reported in Figure 6.14. Overall, since the NN is merely a non-linear function that relates a series of input-output arguments regardless of any physical background, a variation of the mass matrix influences all the measurements data provided to the network leading to a lower estimation accuracy. An average decrease of almost 10% is shown for all the measurement frameworks in presence of mass matrix variations, except for the δ, where a higher reduction appears with the MRU configuration. IMU+DGPS and IMU consider few measurements in respect to the MRU and they appear to be less sensitive to plant variations. The GoF_δ suffers of a decrease up to 30% for a $\overline{K}$ of 0.85 and almost 25% for a $\overline{K}$ equal to 1.15. Likewise, a stiffness matrix variation decreases the estimation accuracy of the surge

component despite its estimation is influenced (at least theoretically) only by δ, $\dot{\delta}$ and $\ddot{x}$ signals.

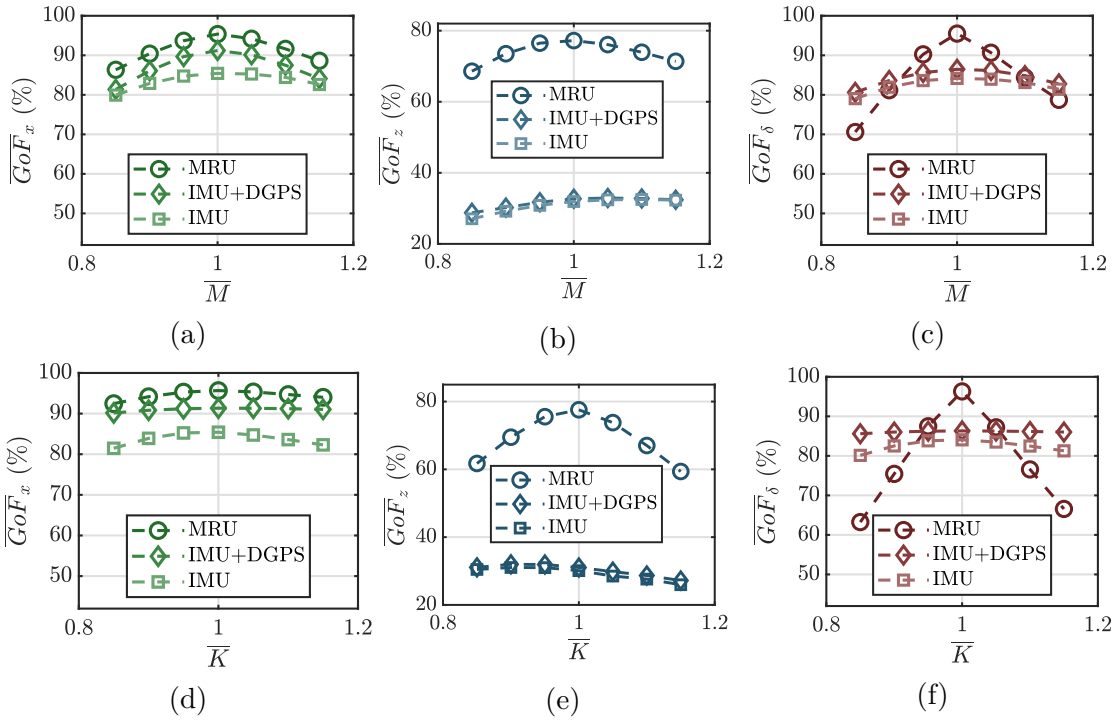

Figure 6.14: $\overline{GoF}$ results obtained with the NN varying $\overline{M}$ and $\overline{K}$. The first column refers to the x DoF, Figures (a) and (d), the second to the z DoF, Figures (b) and (e) and the third to the δ DoF, Figures (c) and (f)

Comparison between Kalman Filter and Neural Network

The KF and NN are compared in term of $\overline{GoF_x}$ and the results are summarized in Table 6.3. Starting from noiseless case, the $\overline{GoF}_x$ values demonstrate that the measurements of an IMU* unit are sufficient to estimate the surge and pitch components with acceptable accuracy. In particular, excluding the absolute displacements and velocity signals (x, $\dot{x}$, z and $\dot{z}$), the KF $\overline{GoF}_x$ slightly decreases from 91% to 89.3% and the $\overline{GoF}_\delta$ from 90.1% to 88.9%. The same behaviour is obtained for the NN, showing a drop between 2÷4% passing from MRU to IMU framework. On the other hand, the absence of z and $\dot{z}$ causes a remarkable drop in accuracy for the heave force estimation, especially passing from the IMU+DGPS* to IMU* framework where a decrease of 22% and 39% appear for the KF and NN, respectively. Contrary to expectations, the NN is able to handle noisy data better than the KF for both surge and pitch DoF, except for the IMU case. In particular, an accuracy of almost 95% is obtained for the f_x and f_δ components if the MRU is

used in the NN. The trend is confirmed with the IMU+DGPS framework, reaching a $\overline{GoF}_x$=91.2% and a $\overline{GoF}_\delta$=86.3% with the NN. However, the estimation of the WEF in heave direction is not reliable with the NN, providing an overall accuracy of almost 33.2% against a 74.4% obtained with the KF. Overall, the performance of the NN model overcomes the KF ones for surge and pitch DoFs, regardless the measurement framework.

Framework	**Kalman Filter**			**Neural Network**		
	$\overline{GoF_x}$ (%)	$\overline{GoF_z}$ (%)	$\overline{GoF_\delta}$ (%)	$\overline{GoF_x}$ (%)	$\overline{GoF_z}$ (%)	$\overline{GoF_\delta}$ (%)
MRU*	91.0	97.1	90.1	95.1	94.1	96.1
IMU+DGPS*	91.0	96.7	90.2	95.0	93.9	95.9
IMU*	89.3	75.8	88.9	91.3	54.2	94.0
MRU	89.8	87.3	89.5	95.0	77.1	95.5
IMU+DGPS	87.5	74.4	82.4	91.2	32.7	86.3
IMU	87.8	74.4	81.9	85.4	32.2	83.9

Table 6.3: $\overline{GoF}$ and $\Delta\overline{GoF}$ results of the KF observer and NN model for each measurement frameworks. The apex * means that no disturbances are considered.

The real ISWEC system is equipped with the MTi unit presented in Section 6.1.2. Unlike the MRU, the MTi unit provides only linear accelerations, angular displacements and angular rates, and the measurement noise are one order of magnitude higher. Although more information are available with the MRU, the IMU framework provide acceptable accuracy for both surge and pitch wave forces, directly involved in the power extraction. The worst case, when the noise is considered, the KF accuracy approaches 88% and 82% for $\overline{GoF}_x$ and $\overline{GoF}_\delta$, respectively; with the NN the accuracy reaches about 85% and 84% for $\overline{GoF}_x$ and $\overline{GoF}_\delta$, respectively. The MRU units are (usually) one order of magnitude more expensive than the IMU ones, and the precision provided does not justify the little increase of performances. Despite the low performances obtained for the WEF in heave direction (not directly involved in the power extraction), the NN and the IMU sensor is considered as a reliable combination for the estimation.

One unanticipated finding is that, in presence of plant inaccuracies, the sensitivity of the KF is higher compared to the NN. In particular, a relevant decrease in performance for the pitch force estimation estimation with a $\overline{M}$ and $\overline{K}$ variation appear when the KF is employed (IMU framework, see Figures 6.13c, 6.13f, 6.14c and 6.14f). In contrast, the NN guarantees a weighted $\overline{GoF}_\delta$ always greater than 77% suggesting low sensitivity with plant variations.

6.3 Optimal declutching control

In this work the clutch-declutch control is used to modulate in a on-off way the pressure over the prime mover. The details about this control strategy can be found in the work of Babarit [106]. Apart from this simple but effective control configuration, different categories of control strategies are identified concerning the HPTO, depending on the circuit configuration and its components [74]:

- **Hydraulic accumulator and active control valves**: labelled as the simplest and most used control strategy, this logic consists in adding extra control accumulators with an active control valve at the primary hydraulic unit (the pump in our concrete HPTO) in order to provide a phase control. The extra accumulator delivers energy to the primary unit in order to phase the motion of the WEC with the incoming wave. In [112] the simulation results demonstrates that this approach significantly improves the extracted power of the WEC. Another similar approach is proposed in [116], where a Maximum Power Point Tracking (MPPT) based on the current sea-state is implemented on CETO WEC coupled with a HPTO system: here the extra accumulator is used to control the damping force of the buoy, leading to an overall increase of the extracted power between 1÷6%. Other examples of control strategy based on a an active control valve with extra accumulators are presented in [87, 111, 314, 315];

- **Hydraulic cylinder and active control valves**: the combination of active valves leads the possibility to approximate a continuous force reference if applied to a constant pressure circuit. In [122], Hansen proposed a force control optimised at several stages, since the performance of wave conversion system depends on efficiencies of the WEC device that are related to the components of the HPTO system. First, a Wave Power Extraction Algorithm (WPEA) is created to calculate the maximum energy expected; then, in the second stage a Force Switching Algorithm (FSA) is formulated as a supervisory controller to provide an optimal reference signal to control the by-pass valves according to the force references generated by WPEA. The results from the simulation studies indicated that the overall efficiency can be achieved up to 80%. Other typical hydraulic PTO concept based on hydraulic cylinder and controlled with a series of switching valves can be found in [316, 117];

- **Hydraulic transformer with a digital control mechanism**: the concept of the hydraulic transformer, that is accurately described and studied in [80], allows to adjust the PTO force. For example, a hydraulic transformer control mechanism can be utilised to control the pressure and directly control the force of the hydraulic PTO within a desired reference computed, for example, by an MPC strategy. In [80] a Proportional–Integral–Derivative (PID)

controller is utilised to perform active or reactive control of the WEC device. The PID controller is used to compare the pressure of the high-pressure line to the desired pressure level in order to determine the optimal reference value for the digital displacement controller and thus control the PTO torque. Simulation results indicates that this approach is effective obtaining an average PTO efficiency of 71%. Furthermore, other similar approaches also have been proposed to control the speed of the hydraulic motor [119, 218].

Numerous application of MPC strategies have been explored in literature and applied to different concept of WECs. In the HPTO context, Hansen [316] studied a MPC to maximise the wave energy production by cleverly manipulating the PTO force. In [117], a comparison study of the different types of WPEA has been carried out: six different kinds of WPEA from previous literature, such as Singular Arc control (SA), Proportional-Derivative (PD) control, MPC, Pseudo-Spectral (PS) control, Proportional-Derivative Complex conjugate control (PDC3) and Shape-Based (SB) control has been compared. From the simulation results the MPC control strategy shows the greatest achievement among the six control strategies [117].

In order to improve the annual energy production of the ISWEC, an optimal command strategy based on the Pontryagin's principle has been used in this work to generate the references for the directional control valve. This control approach has an advantage in which it requires only a single active valve control mechanism compared to the other control method, which involves a more sophisticated control mechanism and components.

6.3.1 Optimal control problem formulation

The derivation of the MPC logic requires to rewrite the system 6.1. The mooring forces are not considered since none analytic form exists for the ISWEC device and their contribution can be neglected (see Figure 6.5). Then, equation 6.1 can be rewritten in a state-space form in respect to the following state vector:

$$\mathbf{X} = \begin{bmatrix} \mathbf{X}_{fp} & \dot{\mathbf{X}}_{fp} & \boldsymbol{\zeta}_p & \varepsilon & \dot{\varepsilon} & p_{pi} & p_{po} & V_{hp} & p_{hp} & V_{lp} & p_{lp} & \dot{\alpha}_{gh} \end{bmatrix}^T \tag{6.24}$$

Finally, the following non-linear state space system is defined:

$$\begin{aligned} \dot{\mathbf{X}} &= \boldsymbol{\Theta}(\mathbf{X}, \mathbf{f}_p, u_c) \\ \mathbf{X}(t_i) &= \mathbf{X}_0 \\ \mathbf{X}(t_f) &\text{ free} \end{aligned} \tag{6.25}$$

The explicit form of the system 6.25 is reported in Appendix B. $\boldsymbol{\Theta} : \mathbb{R}^n \to \mathbb{R}^n$ is the non-linear function describing the plant dynamics and n is the problem

dimension. It is assumed that $\mathbf{f}_p$ is estimated through the NN studied in the previous section and that u_c, that is the control variable linked to the clutch-declutch control logic, can be chosen with the constraint:

$$u_c \in [0,1] \tag{6.26}$$

In this context, let consider the objective of maximizing the extracted energy at the accumulator stage, computed by multiplying the flow discharger through the check-valves and the accumulator pressures, from an initial time t_i to a final time t_f:

$$\begin{aligned} E_h &= \int_{t_i}^{t_f} -P_h \, dt = \int_{t_i}^{t_f} -\left(u_c q_{cko} p_{hp} - u_c q_{cki} p_{lp}\right) \, dt = \\ &= \int_{t_i}^{t_f} -\left(u_c C_{ck} A_{ck} \sqrt{\frac{2(p_{po} - p_{hp})}{\rho_{oil}}} p_{hp} - u_c C_{ck} A_{ck} \sqrt{\frac{2(p_{lp} - p_{pi})}{\rho_{oil}}} p_{lp} \right) \, dt \end{aligned} \tag{6.27}$$

Figure 6.15 graphically represents the cost function E_h. The hydraulic power P_h at the accumulator stage accounts for the losses generated from the clutch-declutch valve and the check-valves; however, the wasted power due to the relief valve is not accounted.

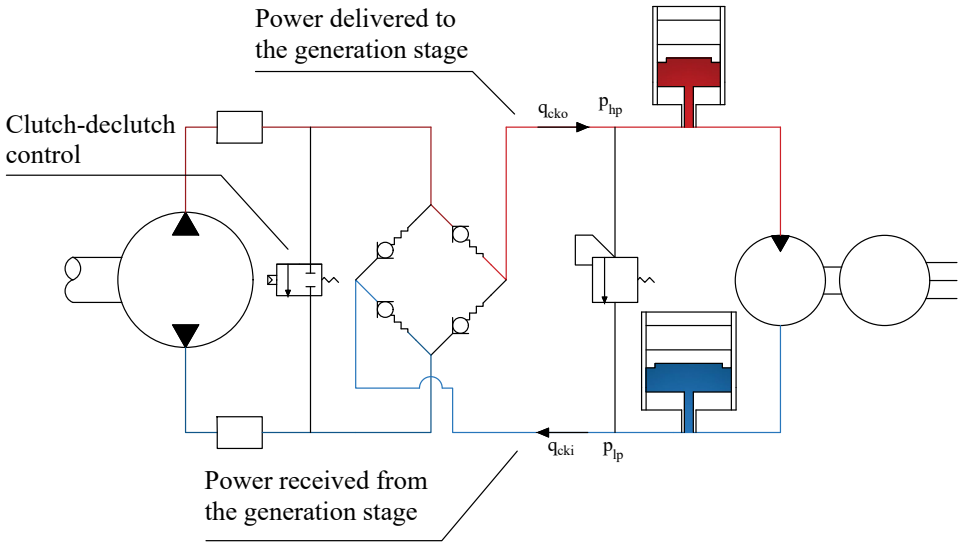

Figure 6.15: Hydraulic power to be maximized, calculated by the difference between the power delivered to the generation stage and the one received from the generation stage. The clutch-declutch valve represents the control variable.

Once the dynamic system is defined and the cost function formulated, the optimal command theory based on Pontryagin's maximum principle [317] can be applied to derive the the expression of the control variable u_c that maximize the objective function 6.27. To implement this theory with a good numerical efficiency, the declutching control is considered as a bang–bang strategy has to be formulated: when $u_c = 0$, no control is applied; when $u_c = 1$, the clutch-declutch valve is closed and the flow generated from the pump is driven toward the accumulators [287]. With a more general notation, the optimization problem can be formulated defining the Hamiltonian function of the optimization problem:

$$\mathcal{H} = -P_h + \mathbf{\Lambda}^T \mathbf{\Theta}(\mathbf{X}, \mathbf{f}_p, u_c) \tag{6.28}$$

where $\mathbf{\Lambda} \in \mathbb{R}^n$ are the co-states variables functions of time known as Lagrange multipliers. The co-states dynamic equation and the transversality conditions can be derived as follows:

$$\begin{aligned} \dot{\mathbf{\Lambda}} &= -\frac{\partial \mathcal{H}}{\partial \mathbf{X}} \\ \mathbf{\Lambda}(t_i) &\text{ free} \\ \mathbf{\Lambda}(t_f) &= \mathbf{0} \end{aligned} \tag{6.29}$$

The control problem, originally formulated as a constrained optimization problem with cost funtion 6.27, control constraints 6.26 and dynamic constraints 6.25 is know formulated as a unconstrained optimization problem with dimension $2 \times n$ that involves the Hamiltonian 6.28, the dynamics 6.25 and 6.29, and the control constraints 6.26. The goal is to find an optimal control policy function u_c that maximize (or negatively minimize) the Hamiltonian 6.28. The derivation of the Hamiltonian function as well as the co-states dynamic equation are reported in Appendix B. It can be noticed that the Hamiltonian can be reformulated grouping the terms depending on the control variable u_c and those who are not:

$$\mathcal{H} = u_c \Phi(\mathbf{X}, \mathbf{\Lambda}, \mathbf{f}_p) + \Psi(\mathbf{X}, \mathbf{\Lambda}, \mathbf{f}_p) \tag{6.30}$$

Here, the Hamiltonian is linear with respect to the control variable u_c. This simplify the optimization problem since the value of u_c is chosen with a bang-bang logic:

$$u_c = \begin{cases} 1 & \text{if } \Phi(\mathbf{X}, \mathbf{\Lambda}, \mathbf{f}_p) < 0 \\ u_{sing} & \text{if } \Phi(\mathbf{X}, \mathbf{\Lambda}, \mathbf{f}_p) = 0 \\ 0 & \text{if } \Phi(\mathbf{X}, \mathbf{\Lambda}, \mathbf{f}_p) > 0 \end{cases} \tag{6.31}$$

When the switching function $\Phi(\mathbf{X}, \mathbf{\Lambda}, \mathbf{f}_p)$ is lower than 0, the u_c is set to 1 to minimize the Hamiltonian while when the switching function $\Phi(\mathbf{X}, \mathbf{\Lambda}, \mathbf{f}_p)$ is greater than 0 u_c is set to 0. The case when $\Phi(\mathbf{X}, \mathbf{\Lambda}, \mathbf{f}_p)$=0 is called singular arc condition

[318]. The expression for u_c can be derived through multiple time derivation of $\mathcal{H}$ until the formulation of u_c appears explicitly; however, since the value of u_c is constrained to be 0 or 1, the derivation of the singular arc condition is not needed here. The equations for $\Phi(\mathbf{X}, \mathbf{\Lambda}, \mathbf{f}_p)$ and $\Psi(\mathbf{X}, \mathbf{\Lambda}, \mathbf{f}_p)$ are reported in Appendix B. In a practical implementation, the switching times for u_c can be found iteratively:

- **Step 1**: first, the system dynamics can be computed for the time interval $[t_i, t_f]$ via equation 6.25. At this stage the control u_c is assumed to be null;
- **Step 2**: Once the vector $\mathbf{X}$ is found, the adjoint trajectories $\mathbf{\Lambda}$ are calculated integrating backward the system 6.29, from t_f to t_i;
- **Step 3**: since both $\mathbf{X}$ and $\mathbf{\Lambda}$ are known the switching function $\Phi(\mathbf{X}, \mathbf{\Lambda}, \mathbf{f}_p)$ is used to compute the control u_c for the interval $[t_i, t_f]$ following the logic 6.31;
- **Step 4**: the new control u_c is substituted in 6.25 and the results are compared with the one obtained the previous iteration (Step 1): if the new results equals the previous one the process is converged; if not, the process is repeated with the new u_c.

For the simplest clutch-declutch control, the activation of the clutch-declutch valve happens when the speed of the gyroscope reaches and exceeded the threshold value represented by the clutch speed $\dot{\varepsilon}_{cs}$ that is fixed for the whole duration of the actual sea-state. Such a mean value corresponds to the condition that allows to achieve the best performance without actively adjust the switching time continuously. This logic does not require any knowledge of future wave. On the other hand, the aim of the optimal control is to compute the control sequence u_c in a optimal way to maximize the hydraulic power delivered to the hydraulic motor, regardless the speed of the hydraulic pump. In this regards, in addition to improve the extracted power, the control parameters to be tuned for each sea state are reduced to the flywheel speed $\dot{\varphi}$ and the generator damping β_g.

6.3.2 Numercal simulations and results

The MPC defined in the previous section concerns some free parameters to be tuned in order to balance the computational time required for each iteration and the extracted power. Once the MPC is tuned, the performances of the optimal CoE device for the Balder sea-site have been evaluated in irregular wave conditions and compared with the ones reported at the end of the previous Chapter (see Section 5.3). In this section, the clutch-declutch control with a constant clutching speed threshold is labelled as “simple”, “standard” or “original” clutch-declutch control to distinguish it from the MPC.

Tuning of the MPC parameters

Two parameters have relevant influence on the MPC performances: the number of maximum iterations allowed for the calculation of the optimal control sequence u_c and, even more, the prediction horizon $t_p = t_f - t_i$. The tuning is carried out on the four sea-states of Table 6.1 collecting the net power output produced by the system.

The iterative method, described at the end of Section 6.3.1, consist in calculate the control sequence u_c for the prediction horizon t_p computing the switching function Φ and following the switching logic reported in equation 6.31. The influence of the number of iterations is reported in Figure 6.16 for each of the four tuning wave. The normalized net power $\hat{P}_n$ has been computed for each iteration number by dividing the mean net power by its value obtained with the maximum number of iterations, equal to 38. As expected, the iterations required to compute the optimal control sequence are almost equal to 15/18, and no improvements are found increasing the iterations over 20. However, to ensure the convergence of the algorithm for all the simulation waves, the number of iterations is fixed to 25.

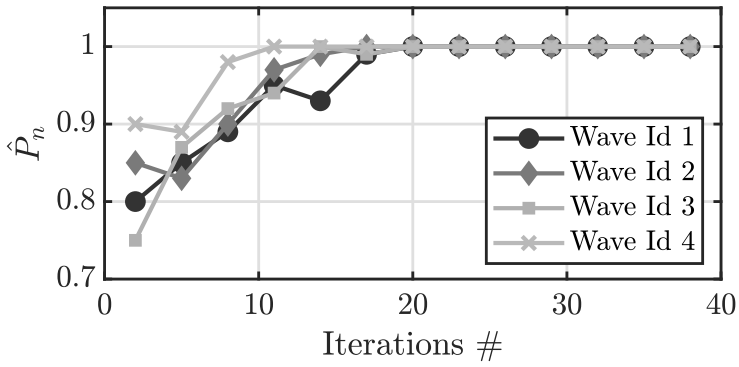

Figure 6.16: Convergence of the normalized net power $\hat{P}_n$ in respect to the number of iterations.

On the question of the prediction horizon, the productivity of the system has been extrapolated considering the variation of the prediction horizon t_p in the interval [1,4] seconds and the results are reported in Figure 6.17. Here, the normalized net power $\hat{P}_n$ is computed in respect to the maximum value achieved for the single t_p. The most relevant finding is that the normalized extracted power diminish on average if the prediction horizon is increased to 4 seconds. In practice, the accuracy of the wave force prediction diminish considerably after 5 seconds of prediction horizon [295], negatively affecting the performance of the MPC. Here, a simple autoregressive model is tuned to perform the wave force prediction and its prediction quality seems to affect the MPC optimization with long prediction horizon. In this regards, choosing 2.5 seconds as prediction horizon seems to guarantee the highest

extracted power and, at the same time, allows to contain the computational burden required.

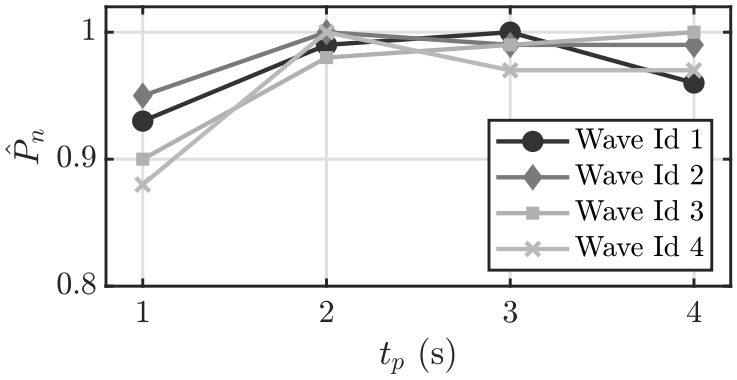

Figure 6.17: Convergence of the normalized net power $\hat{P}_n$ in respect to the prediction horizon t_p.

Productivity analysis

The performance evaluation is carried out on the same 128 waves considered in the previous section to evaluate the annual performances of the optimal CoE device. The simple clutch-declutch control has been optimized individually for each sea-state finding the best $\dot{\varphi}$, $\dot{\varepsilon}_{cs}$ and β_g combination to ensure the best extracted power. Therefore, the system controlled via MPC, has been evaluated with the same optimal values of $\dot{\varphi}$ and β_g while the switching of the clutch-decluth valve is performed through the algorithm defined in Section 6.3.1. Furthermore, a prediction horizon of 2.5 seconds and an iteration number of 25 has been fixed for all the simulations.

First, the power matrix obtained with the two controls are showed in Figure 6.18. The results refer to the waves for which the net power is greater than zero since, specially for low energetic waves, the basic loads overcomes the power produced and the ISWEC is switched off. Furthermore, when the wave is too energetic, the optimization algorithm discards the control parameters that leads to a surpass of the optimization constraints, as described in Section 4.4.2. Figure 6.19 quantify the percentage difference between the simple declutching control and the MPC-based declutching control: the chart shows a clear trend of increasing performance by passing from a classical control framework to an optimal one. It is apparent that the greatest increase is for the high energetic waves. On average, the increment is equal to 7.1%, up to 25% in some sea states. The most promising result concerns the ability of the MPC to always overcome the performances of the classic clutch-declutch control for all the waves, showing a minimum increase of 0.3%. It is worth to specify that the power produced with the MPC could be higher since

the other two control parameters ($\dot{\varphi}$ and β_g) have been optimized for the simple clutch-declutch control and replicated on the MPC.

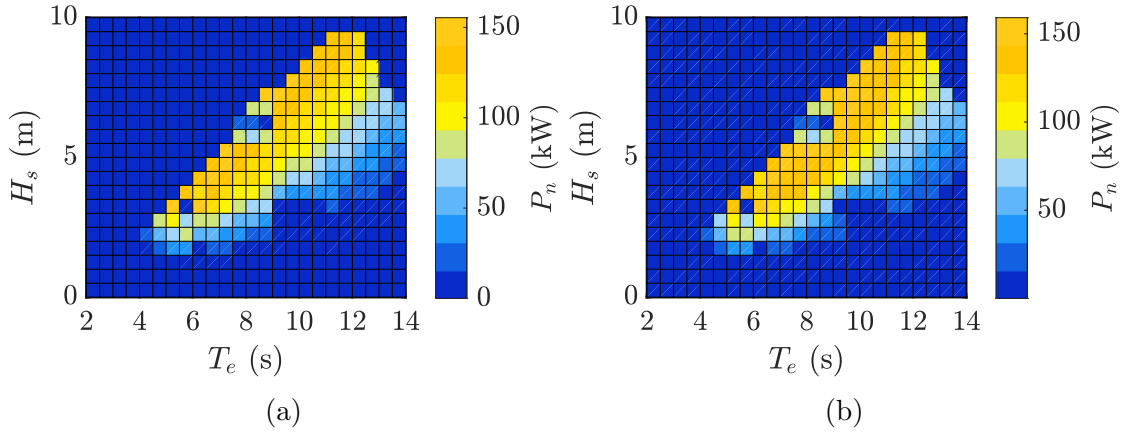

Figure 6.18: Power matrices obtained with the simple clutch-declutch control (a) and with the MPC (b).

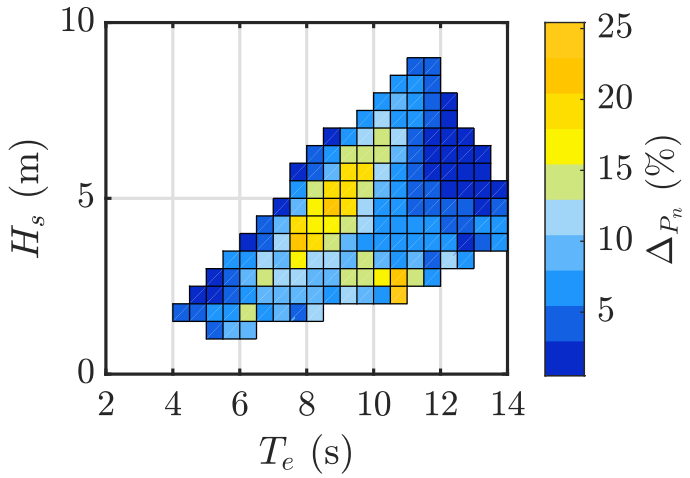

Figure 6.19: Percentage difference in net productivity between the simple clutch-declutch control and the MPC.

For a proper performance assessment, the annual net productivity, named also AEP, is calculated in all the four sea-sites under study. Figure 6.20 reports the annual productivity for the two control types and the percentage difference between the original control and the MPC. The chart of Figure 6.20b highlights that the MPC allows to extend the AEP up to 8% for the Balder sea-site. On the other hand, a minimal growth in productivity is obtained in Capo Verde, almost equal to 2%. This outcome is derived from the different sea-site energy distribution. Alghero, Balder, and Pantelleria show almost the same range of wave occurrence distribution

while Capo Verde reports a double peak occurrences distribution extended up to T_e=15s, far from the wave periods for which the WEF estimators have been tuned. In this regards, the effectiveness of the MPC is lower in this location.

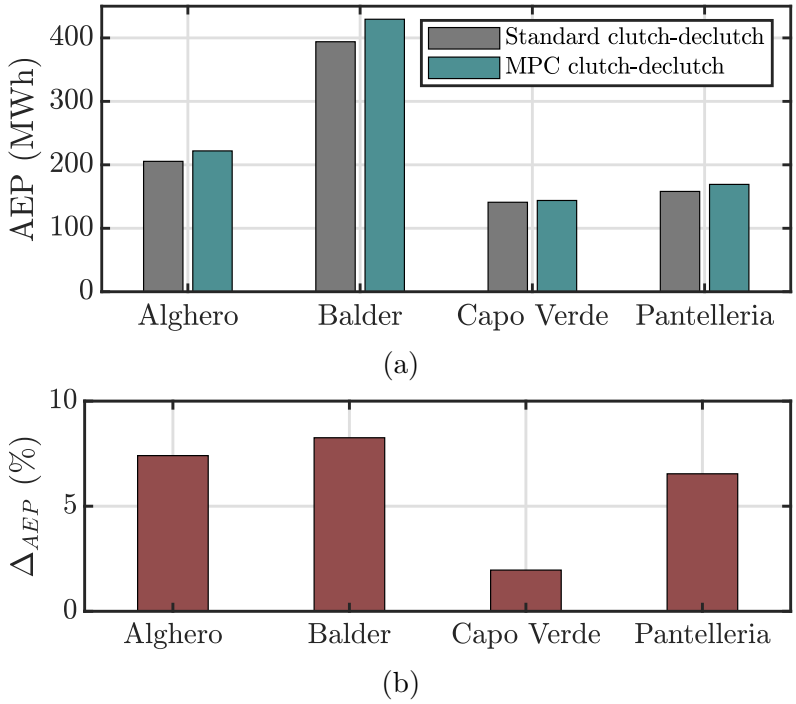

Figure 6.20: (a) AEP results for

6.4 Summary and remarks

The purpose of this chapter was the definition of an optimal control strategy applied to the clutch-declutch logic of the HPTO. Tha major aim was to evaluate two different wave force estimation strategies and apply the most effective one in a simple but effective MPC algorithm.

First, a model-based (KF observer) and a model-free (NN model) approach are compared in presence of three different sensor frameworks. The key of the KF is to approximate the expression of the WEFs as a linear superposition of finite harmonic components with a fixed frequencies tuned in respect to the sea-states of Balder. The effectiveness of this technique relies on the restrict bandwidth of the estimated disturbance as it can only handle the specified discrete frequencies. This makes it more robust to other external disturbances outside from the frequency range considered. The model free choice is based on a feed-forward NN that express the WEFs as a function of the system dynamics at current and past time instants taking into account the dynamic memory of the plant with no feedback data. Overall, it is

demonstrated that the KF performs well when applied to a non-linear WEC model. The KF shows best performances with the MRU and IMU+DGPS frameworks since more physical signals are available. The IMU framework gives the worst performances along the heave direction. The same argument applies for the NN, where an acceptable accuracy is obtained for $\overline{GoF}_x$ and $\overline{GoF}_\delta$. However, both the KF and NN are considered not reliable for the WEF estimation along the heave DoF if DGPS and IMU are employed. Contrary to expectations, the KF is affected by plant variations more than the NN. Further works are required to establish the underlying cause of this outcome, acting on the $\mathbf{Q}$ matrix to improve the mean performances of the KF observer.

Once the best wave force estimator has been chosen, an optimal control strategy based on the MPC logic is used to control the clutch-declutch valve. The objective of the optimization is the maximization of the hydraulic power delivered to the accumulation stage that coincides, except the part wasted through the relief valve, to the inlet power of the generation stage. After a tuning process, where the number of iterations and the prediction horizon of the MPC has been tuned, the performances of the optimal CoE device designed in the previous Chapter are assessed against the simple clutch-declutch logic. Overall, the MPC outperforms the original control of almost the $6 \div 7\%$, reducing the CoE by the same amount. On the other hand, the difficulties and uncertainties behind a real MPC implementation could be discouraging in the face of a relatively small increase in AEP. This is a preliminary optimal control strategy that is able to control only the clutch-declutch valve. Different optimal control logics are under study to include the flywheel speed and the generator damping into the control optimization and improve further the production capabilities of the ISWEC.

Chapter 7

Conclusions

The objective of this dissertation is to investigate the potential of a hydraulic transmission integrated into the ISWEC device with the major aim to reduce its cost of energy. ISWEC, an inertial WEC, exploit the energy coming from sea waves through a gyroscopic system installed in a sealed floater. This device, originally intended for a low-medium energetic seas, reached a technology development suitable to extend its operational domain to oceanic environments. In order to accomplish this technological leap, an extensive study on the Hydraulic PTO architecture is carried out with the aim to compare its performances with the Electro-Mechanical PTO, that represents the actual PTO system implemented on the ISWEC. In order to prove the Hydraulic PTO techno-economic effectiveness, the following steps have been completed:

- Development of the Mechanical and Hydraulic PTO numerical models of the ISWEC. Six different models are derived to simulate the dynamics of the whole system, constituted of three main parts: floater, gyroscope and PTO. Frequency-, spectral- and time-domain models are developed for the Mechanical PTO, while one spectral- and two time-domain models are defined for the Hydraulic one;

- Design of four optimal ISWEC devices for the Balder sea-site, two considering the Mechanical PTO and two considering the Hydraulic PTO. The optimization is carried out through a novel techno-economic multi-stage design tool implementing an in-house Genetic Algorithm to perform a multi-objective optimization. The optimal devices are compared in respect to the power production, the cost of energy, the resultant device cost, the installed power and the power quality;

- Implementation of a Model Predictive Control (MPC) on the Hydraulic PTO system. The optimal control problem is tackled designing two type of unknown input estimators: a model-based Kalman Filter observer and a model-free Neural Network. Then, the proposed control approach has been evaluated

on the CoE-optimum device designed for Balder in irregular ocean waves and the results compared to the original clutch-declutch control method.

Part I: Numerical Modelling

The work started with the definition of the ISWEC numerical models. Concerning the Mechanical PTO, a simple frequency-domain model and a novel spectral-domain are compared with the non-linear time-domain framework in term of results accuracy and computational time. As expected and desired, the spectral-domain model, that could be interpreted as a non-linear frequency-domain model, gives higher accuracy compared to the frequency-domain one, specially in presence of strong non-linearities (e.g. saturation of the electrical generator torque). In particular, the frequency-domain model gives an annual net productivity almost 25% higher than the time-domain one, while the spectral-domain overestimate the net performance only of 9.5% on average. Moreover, the spectral-domain simulation turned out to be one order of magnitude faster than the time-domain one. The same procedure is applied to the Hydraulic PTO model, that is formulated in spectral-domain and time-domain since the frequency-domain is not possible due to its source of non-linearity. Similarly, the accuracy of the spectral-domain model is demonstrated against a simple constant-pressure hydraulic PTO model. However, an higher gap is found if the spectral-domain model is compared with the complete time-domain one, which considers the whole hydraulic transmission dynamics. Despite its inaccuracies, the spectral-domain model of the Hydraulic PTO is used due to its computational efficiency in the first design stage of the ISWEC, where the floater, the gyroscope and the hydraulic pump are designed. Then, the high-fidelity time-domain model is employed to design the whole hydraulic transmission. The computational burden required by the spectral-domain model of the Hydraulic PTO is, at least, 10-15 times lower than the time-domain one; however, the spectral-domain model overestimates the annual net productivity of the system of 14% on average compared to its time-domain version. The frequency-domain model, originally implemented in the first stage of the ISWEC design tool, has been deprecated in favor of the spectral-domain one, both for the Mechanical and Hydraulic PTO.

Overall, the various models proposed could facilitate the development of the ISWEC technology, via efficient and accurate power assessment, and via the possibility of carrying out advanced design optimisation that goes beyond linear models.

Part II: ISWEC Design and PTO Comparison

In the second part of the work, the ISWEC system is designed for the Balder sea-site, representing the most energetic location under study. However, other three sites have been chosen for the assessment and proof the ISWEC solution: Alghero,

Capo Verde and Pantelleria. The design process consists in a multi-objective optimization aiming to maximize the Annual Energy Production (AEP) and, at the same time, minimize the Cost of Energy (CoE). First, the ISWEC is optimized taking into account the experienced and lessons learned during the full-scale tests in Pantelleria and Adriatic Sea. A series of free parameters uniquely defines the entire ISWEC device and the Genetic Algorithm operates to find the optimal combination to optimize the intended performance index. Concerning the Hydraulic PTO, Stage 1a is performed first, designing the ISWEC floater, the gyroscopic unit, the hydraulic pump and its control logic. Several optimal solutions are found and the best ten are compared in term of: AEP, CoE, hull mass, gyroscope mass and inertia, pump size and control logic. Intuitively, the AEP is maximized through massive hull and gyroscopes along with powerful pump units, while the minimum CoE is achieved with smaller and cost-effective parts. The multi-objective optimization demonstrates that the optimization of the power capabilities leads costly devices reducing the economic efficiency. Moreover, the optimal devices are evaluated in all the sea-sites under study showing a good adaptability of the system in different locations. In particular, the percentage difference in AEP and CoE of the optimal device for a specific site evaluated in other locations are lower than 9%, suggesting that the ISWEC is, with good approximation, site-agnostic. At this stage, two optimal individual are chosen to be optimized in Stage 1b: a AEP-optimum and a CoE-optimum. In order to limit the initial investment and improve the device manufacturability, the Overall cost is limited to 5 M€, the flywheel inertia is bounded to 32000 kgm^2 and the hull mass to 2000 ton. The second optimization stage, named Stage 1b, is performed to design the optimal hydraulic transmission for the two ISWEC solutions obtained with Stage 1a. Here, two separated AEP-driven and CoE-driven optimizations are carried out. Similarly to Stage 1a, the best ten devices of each optimization are compared in term of: hydraulic pump installed, pump control logic, high-pressure accumulator size and pre-charge, motor-generator unit and number of circuits. As expected, the AEP-driven optimization converged toward large pump and motor-generator units, high installed power and multiple hydraulic circuits; in contrast, the CoE-driven device installs a medium size hydraulic pump and only one motor-generator unit downstream the transmission, where all the power flux generated by the gyroscopes motion converges. All the optimal solutions implements the clutch-declutch control logic, able to maximize the extracted power and improve the controllability of the transmission. The output of the Stage 1b are the two optimal ISWEC devices implementing the Hydraulic PTO: one that maximize the AEP and one that minimize the CoE. The same procedure is applied to the Mechanical PTO, where only one single Stage is required to design the optimal AEP- and CoE-driven solutions. Once the four ISWEC devices are designed, an exhaustive comparison is provided. Concerning the AEP-optimum, it is found that the Hydraulic PTO performs slightly better than the Mechanical one in some sites, despite the lower efficiency. The most promising results comes

from the CoE analysis, showing that a remarkable CoE reduction is achieved due to the Hydraulic transmission implementation, from -12% if the system is evaluated in Balder, up to -22% if the deployment location is Pantelleria. Another important parameter is the device cost, representing the initial investments barrier for a full-scale device deployment. In fact, one should prefer, for equal performance, to reduce the initial investment as much as possible to limit the economic risk. The cost analysis reports a cost reduction up to 22% for the CoE-optimum device if the Hydraulic PTO is considered, due to a reduction of almost 53% of the PTO cost. The last comparison concerns the installed power and the power quality, defined as the mean annual standard deviation of the generator power. The Hydraulic PTO AEP-optimum installs a generator power 52% lower than the Mechanical solution while a further installed power reduction of 77% is obtained comparing the CoE optima. Moreover, it is demonstrated that the accumulators effectively filter out the flow peaks generated by the primary pump units, reducing the mean annual standard deviation of the generator power of 70% on average. These findings support the application of the hydraulic transmission for the ISWEC PTO, giving a breakthrough toward a acceptable CoE and remarkable device costs reduction. The hydraulic technology can significantly improve the commercial feasibility of the ISWEC representing a valid high-power and cost-effective PTO solution.

In short, the design tool proposed gives a generalised decision process in which the optimal solution of the ISWEC can be determined under certain assumption and for the desired target. Overall, such a design work flow could be extended to other WEC concepts with the main aim to accelerate the development of the wave energy industry.

Part III: Hydraulic PTO Optimal Control

The last part of this dissertation tackles the optimal control problem of the Hydraulic PTO. The aim is to improve the annual energy production of the ISWEC through a Model Predictive Control (MPC) logic. The device of reference is the optimal CoE device obtained at the end of Chapter 5. First, the Wave Excitation Force (WEF) estimation is addressed with two dual techniques: a Kalman Filter observer (model-based approach) and a Neural Network model (model-free approach). Both estimators are tuned with four sea-states representing the operating conditions of the ISWEC in Balder. Concerning the Kalman Filter, the WEF is modelled with fixed frequencies defining the principal harmonic components of the WEF; then, the number of frequencies and the covariance matrices are tuned to maximize the Kalman Filter accuracy with regard to the computational burden required. Similarly, the Neural Network is designed with respect to the number of neurons and the delay step of the signals in input. Once the estimators have been tuned, the estimation performances, defined as the Goodness of Fit are carried out for different measurement framework proposed: a MRU unit, a IMU+DGPS unit

and a IMU unit. As expected, the MRU unit gives the higher accuracy due to the number of measures provided and the associated accuracy. However, the IMU framework seems to perform slightly worse than the other two frameworks in estimating the surge and pitch force components and, since its cost is (generally) almost one order of magnitude lower than the MRU unit, it is considered as the sensor of reference in the MPC algorithm. However, the IMU performance in estimating the wave force along the heave DoF are not acceptable regardless the observer; on the other hand, since the heave motion does not contribute to the power generation in the ISWEC device, the IMU framework it is chosen anyway. Contrary to expectation, the Neural Network overcome the Kalman Filter performance in estimating the surge and pitch force components, except for the IMU framework in surge direction. Moreover, the sensitivity of the Neural Network due to plant variation is limited resulting in a reliable and robust estimator. The optimal control problem is derived through the Pontryagin's maximum principle in order to control the clutch-declutch valve in a optimal way. The formulation is reduced to a bang-bang type control that gives the optimal switching sequence. The AEP of the optimal CoE device with the Hydraulic PTO is computed with the MPC control and compared with the AEP obtained with the original clutch-declutch control logic. Promising results are obtained since an increase of 6.5% on average of the AEP. On the other hand, the MPC is difficult to implement in real-time due to its computational effort and the uncertainties associated to the WEF estimation, WEF force prediction and to the plant model.

Overall, the Neural Network is considered valid to address the WEF estimation or any other unknown input estimation for the ISWEC, leading for the DoF of interest an average accuracy always higher than 83%. Further analyses are required to improve the performance of the MPC logic proposed in this work, including also the flywheel and the electrical generator control in the optimization, which requires to be re-formulated to handle all the control parameters of a Hydraulic PTO-based ISWEC system.

Further works

The results of this work demonstrate the capability of the Hydraulic PTO to reduce the cost of energy of the ISWEC along with the whole investment, the installed power and improve the power quality. Further work will be done on the basis of these preliminary results:

- The spectral-domain model of the Hydraulic PTO will be expanded to account also for the dynamic behaviour of the accumulator and the hydraulic motor in order to improve its accuracy reducing the performance gap with the time-domain model. Moreover, other non-linear modelling techniques will be evaluated (e.g. the Harmonic balance method proposed in [159]) in order to

further reduce the computational time of the ISWEC numerical simulation and thus accelerate its design process. Full-scale tests of the hydraulic transmission may be conducted to validate the different Hydraulic PTO models.

- The design tool can be further improved introducing a multi-objective algorithm that is able to generate the Pareto front of the optimal solutions. The NSGA-2 algorithm [319] represents a valid solution to reduce the computational burden of the optimization since it is a native multi-objective algorithm able to generate the Pareto front autonomously, without the need of multiple single-objective optimizations. Moreover, the accuracy of the cost function of the hull and gyroscope will be improved together with a more detailed Hydraulic PTO cost calculations (e.g. detailed auxiliary costs).
- The MPC proposed can be improved employing a non-linear MPC logic to handle both the flywheel speed and the generator damping of the Hydraulic PTO. The average AEP increase should be enhanced further to justify the complexity required for a real-time implementation of such a control. However, the MPC logic should be developed also for the Mechanical PTO to accomplish a fair comparison between the two PTO technologies.

Appendix A

Chapter 5 Figures

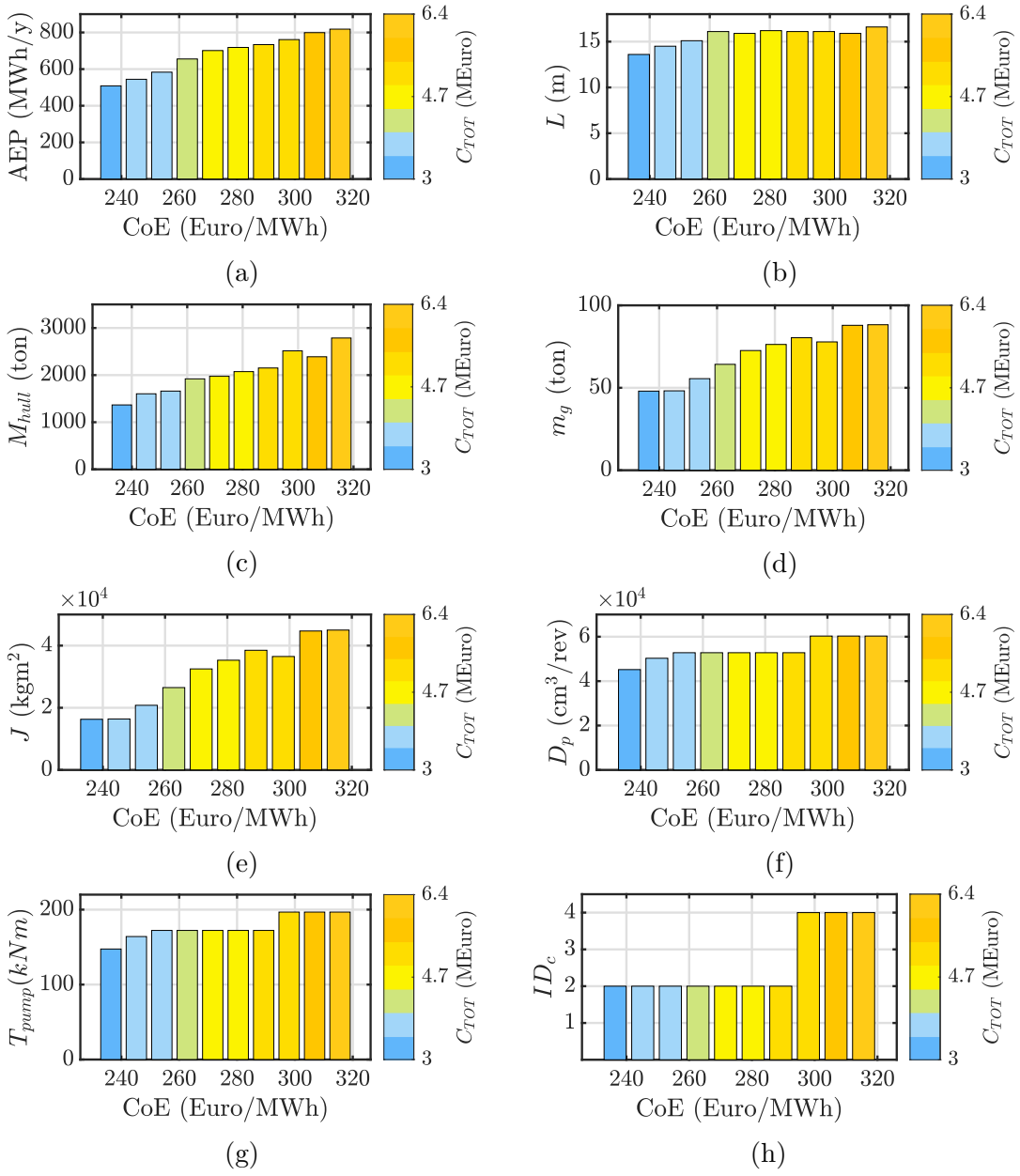

Figure A.1: 10 individuals with HPTO on the pareto front in respect to their CoE and the associated performance and system parameters. The results refer to a Stage 1a optimization. Bars coloured proportionally to the device cost C_{TOT}. (a) AEP, (b) hull length L, (c) hull mass M_{hull}, (d) gyroscope mass m_g, (e) gyroscope inertia J, (f) pump displacement D_p, (g) pump rated torque T_{pump} and (h) hydraulic control id ID_c.

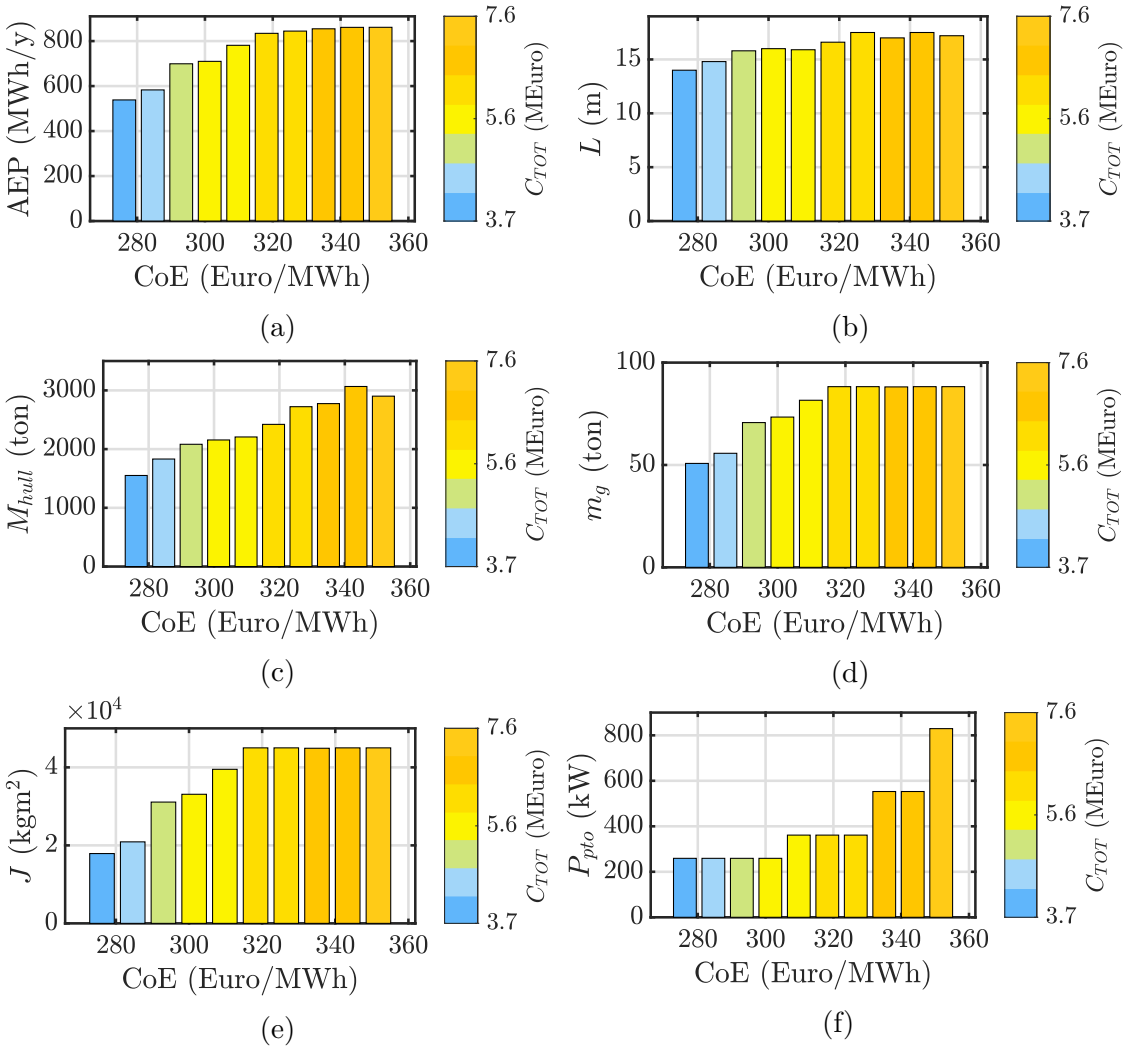

Figure A.2: 10 individuals with MPTO on the pareto front with their CoE and the associated system parameters. The results refer to a Stage 1 optimization. Bars coloured proportionally to the device cost C_{TOT}. (a) annual energy production AEP, (b) hull length L, (c) hull mass M_{hull}, (d) gyroscope unit mass m_g, (e) gyroscope inertia J and (f) PTO rated power P_{pto}.

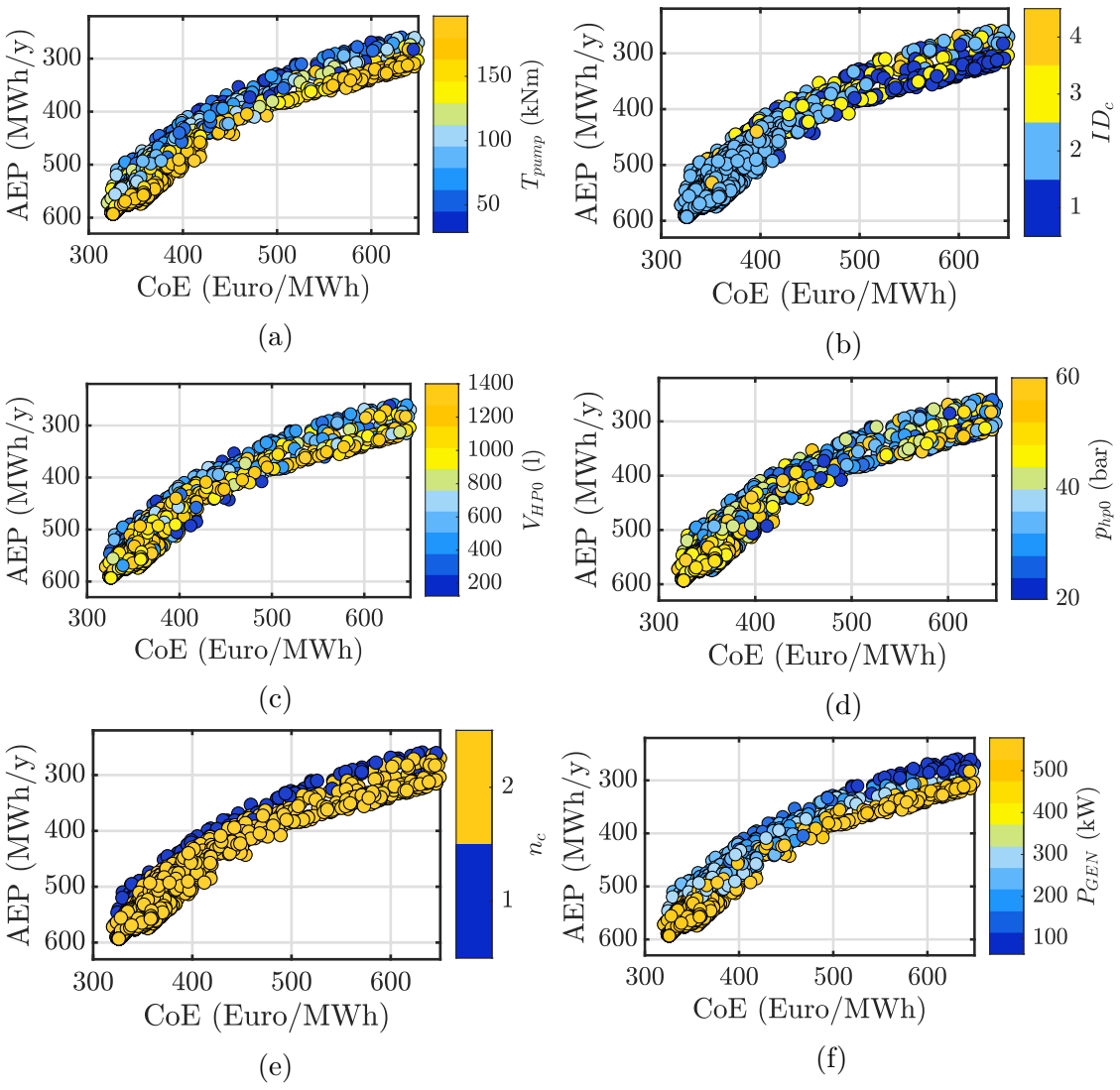

Figure A.3: Individuals obtained with the AEP-driven optimization with Stage 1b in respect to their associated parameters. (a) pump rated torque T_{pump}, (b) hydraulic control id ID_c, (c) hp accumulator total volume V_{HP0}, (d) hp pre-charge pressure p_{hp0}, (e) number of circuits n_c and (f) total generator rated power P_{GEN}.

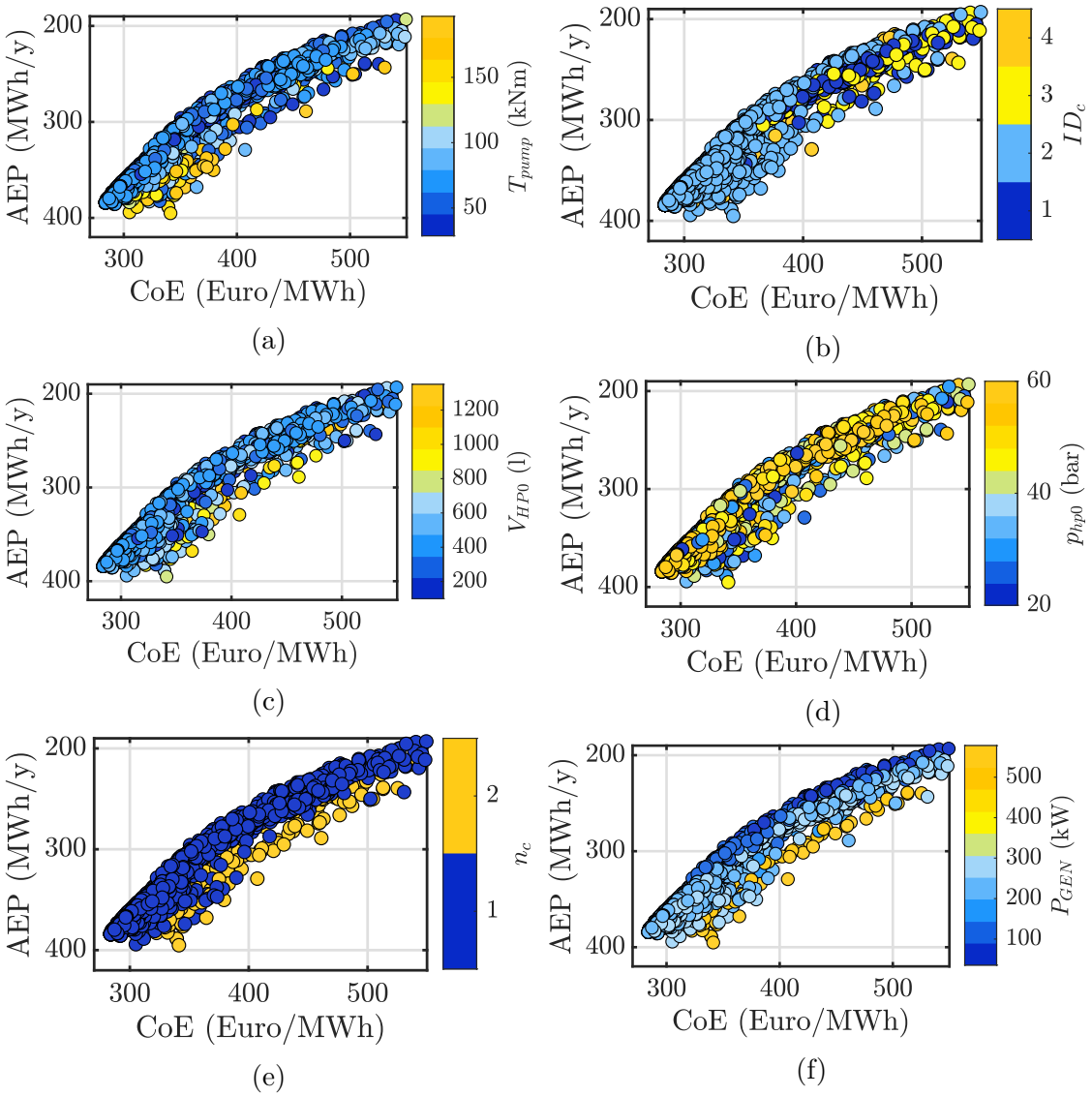

Figure A.4: Individuals obtained with the CoE-driven optimization with Stage 1b in respect to their associated parameters. (a) pump rated torque T_{pump}, (b) hydraulic control id ID_c, (c) hp accumulator total volume V_{HP0}, (d) hp pre-charge pressure p_{hp0}, (e) number of circuits n_c and (f) total generator rated power P_{GEN}.

Appendix B

Chapter 6 Equations

The planar model of the ISWEC expressed in equation 6.1 can be rewritten in a non-linear state-space formulation as follows:

$$
\begin{aligned}
\dot{\mathbf{X}}_1 &= \mathbf{X}_2 \\
\dot{\mathbf{X}}_2 &= \mathbf{M}_{fp}^{-1}\left(-\mathbf{K}_{fp}\mathbf{X}_1 - \mathbf{C}_{rp}\mathbf{X}_3 - \mathbf{D}_{rp}\mathbf{X}_2 - \mathbf{f}_{gp} + \mathbf{f}_p\right) \\
\dot{\mathbf{X}}_3 &= \mathbf{A}_{rp}\mathbf{X}_3 + \mathbf{B}_{rp}\mathbf{X}_2 \\
\dot{X}_4 &= X_5 \\
\dot{X}_5 &= \frac{1}{Ig}\left(-m_p g d_p \sin(X_4) - \frac{Dp}{\eta_{pm}}\operatorname{sign}(X_5)(X_7 - X_6) - J\dot{\varphi}\mathbf{\Pi}\mathbf{X}_2\cos(X_4)\right) \\
\dot{X}_6 &= \frac{\beta_{oil}}{V_h}\left(u_c C_{ck} A_{ck}\sqrt{\frac{2(X_{11} - X_6)}{\rho_{oil}}} - D_p|X_5| + (1-u_c)C_{cv}A_{cv}\sqrt{\frac{2(X_7 - X_6)}{\rho_{oil}}}\right) \\
\dot{X}_7 &= \frac{\beta_{oil}}{V_h}\left(D_p|X_5|\eta_{pv} - u_c C_{ck} A_{ck}\sqrt{\frac{2(X_7 - X_9)}{\rho_{oil}}} - (1-u_c)C_{cv}A_{cv}\sqrt{\frac{2(X_7 - X_6)}{\rho_{oil}}}\right) \\
\dot{X}_8 &= -u_c C_{ck} A_{ck}\sqrt{\frac{2(X_7 - X_9)}{\rho_{oil}}} + \frac{D_m}{\eta_{mv}}X_{12} + C_{rf}A_{rf}\sqrt{\frac{2(X_9 - X_{11})}{\rho_{oil}}} \\
\dot{X}_9 &= \gamma_{gas}\frac{X_9}{X_8}\left(-u_c C_{ck} A_{ck}\sqrt{\frac{2(X_7 - X_9)}{\rho_{oil}}} + \frac{D_m}{\eta_{mv}}X_{12} + C_{rf}A_{rf}\sqrt{\frac{2(X_9 - X_{11})}{\rho_{oil}}}\right) \\
\dot{X}_{10} &= u_c C_{ck} A_{ck}\sqrt{\frac{2(X_{11} - X_6)}{\rho_{oil}}} - D_m X_{12} - C_{rf}A_{rf}\sqrt{\frac{2(X_9 - X_{11})}{\rho_{oil}}} \\
\dot{X}_{11} &= \gamma_{gas}\frac{X_{11}}{X_{10}}\left(u_c C_{ck} A_{ck}\sqrt{\frac{2(X_{11} - X_6)}{\rho_{oil}}} - D_m X_{12} - C_{rf}A_{rf}\sqrt{\frac{2(X_9 - X_{11})}{\rho_{oil}}}\right) \\
\dot{X}_{12} &= \frac{1}{I_{gm}}\left(D_m\eta_{mm}\eta_{gh}(X_9 - X_{11}) - \beta_g X_{12}\right)
\end{aligned}
\tag{B.1}
$$

where the vector $\mathbf{\Pi} \in \mathbb{R}^{1\times 3}$ is a vector with two zero terms and one unitary term in the last position in order to pick only the $\dot{\delta}$ from the state variable $\mathbf{X}_2$:

$$\mathbf{\Pi} = \begin{bmatrix} 0 & 0 & 1 \end{bmatrix} \tag{B.2}$$

The state vector $\mathbf{X}$, composed of the state variables $\mathbf{X}_1$, $\mathbf{X}_2$, etc., is defined in equation 6.24:

$$\begin{aligned} \mathbf{X} &= \begin{bmatrix} \mathbf{X}_{fp} & \dot{\mathbf{X}}_{fp} & \boldsymbol{\zeta}_p & \varepsilon & \dot{\varepsilon} & p_{pi} & p_{po} & V_{hp} & p_{hp} & V_{lp} & p_{lp} & \dot{\alpha}_{gh} \end{bmatrix}^T = \\ &= \begin{bmatrix} \mathbf{X}_1 & \mathbf{X}_2 & \mathbf{X}_3 & X_4 & X_5 & X_6 & X_7 & X_8 & X_9 & X_{10} & X_{11} & X_{12} \end{bmatrix}^T \end{aligned} \tag{B.3}$$

The Hamiltonian, defined in equation 6.28, can be made explicit as follows:

$$\begin{aligned} \mathcal{H} = &- \left(u_c C_{ck} A_{ck} \sqrt{\frac{2(X_7 - X_9)}{\rho_{oil}}} X_9 - u_c C_{ck} A_{ck} \sqrt{\frac{2(X_{11} - X_6)}{\rho_{oil}}} X_{11} \right) + \\ &+ \mathbf{\Lambda}_1^T \mathbf{X}_2 + \mathbf{\Lambda}_2^T \mathbf{M}_{fp}^{-1} \left(-\mathbf{K}_{fp} \mathbf{X}_1 - \mathbf{C}_{rp} \mathbf{X}_3 - \mathbf{D}_{rp} \mathbf{X}_2 - \mathbf{f}_{gp} + \mathbf{f}_p \right) + \\ &+ \mathbf{\Lambda}_3^T \left(\mathbf{A}_{rp} \mathbf{X}_3 + \mathbf{B}_{rp} \mathbf{X}_2 \right) + \Lambda_4 X_5 + \\ &+ \frac{\Lambda_5}{Ig} \left(-m_p g d_p \sin(X_4) - \frac{Dp}{\eta_{pm}} \operatorname{sign}(X_5)(X_7 - X_6) - J \dot{\varphi} \mathbf{\Pi} \mathbf{X}_2 \cos(X_4) \right) + \\ &+ \Lambda_6 \frac{\beta_{oil}}{V_h} \left(u_c C_{ck} A_{ck} \sqrt{\frac{2(X_{11} - X_6)}{\rho_{oil}}} - D_p |X_5| + (1 - u_c) C_{cv} A_{cv} \sqrt{\frac{2(X_7 - X_6)}{\rho_{oil}}} \right) + \\ &+ \Lambda_7 \frac{\beta_{oil}}{V_h} \left(D_p |X_5| \eta_{pv} - u_c C_{ck} A_{ck} \sqrt{\frac{2(X_7 - X_9)}{\rho_{oil}}} - (1 - u_c) C_{cv} A_{cv} \sqrt{\frac{2(X_7 - X_6)}{\rho_{oil}}} \right) + \\ &+ \Lambda_8 \left(-u_c C_{ck} A_{ck} \sqrt{\frac{2(X_7 - X_9)}{\rho_{oil}}} + \frac{D_m}{\eta_{mv}} X_{12} + C_{rf} A_{rf} \sqrt{\frac{2(X_9 - X_{11})}{\rho_{oil}}} \right) + \\ &+ \Lambda_9 \gamma_{gas} \frac{X_9}{X_8} \left(-u_c C_{ck} A_{ck} \sqrt{\frac{2(X_7 - X_9)}{\rho_{oil}}} + \frac{D_m}{\eta_{mv}} X_{12} + C_{rf} A_{rf} \sqrt{\frac{2(X_9 - X_{11})}{\rho_{oil}}} \right) + \\ &+ \Lambda_{10} \left(u_c C_{ck} A_{ck} \sqrt{\frac{2(X_{11} - X_6)}{\rho_{oil}}} - D_m X_{12} - C_{rf} A_{rf} \sqrt{\frac{2(X_9 - X_{11})}{\rho_{oil}}} \right) + \\ &+ \Lambda_{11} \gamma_{gas} \frac{X_{11}}{X_{10}} \left(u_c C_{ck} A_{ck} \sqrt{\frac{2(X_{11} - X_6)}{\rho_{oil}}} - D_m X_{12} - C_{rf} A_{rf} \sqrt{\frac{2(X_9 - X_{11})}{\rho_{oil}}} \right) + \\ &+ \frac{\Lambda_{12}}{I_{gm}} \left(D_m \eta_{mm} \eta_{gh} (X_9 - X_{11}) - \beta_g X_{12} \right) \end{aligned} \tag{B.4}$$

Then, the Hamiltonian B.4 can be rewritten grouping the terms dependent on the control variable u_c:

$$
\begin{aligned}
\mathcal{H} = u_c \Bigg(& - C_{ck} A_{ck} \sqrt{\frac{2(X_7 - X_9)}{\rho_{oil}}} X_9 + C_{ck} A_{ck} \sqrt{\frac{2(X_{11} - X_6)}{\rho_{oil}}} X_{11} - \\
& - \Lambda_6 \frac{\beta_{oil}}{V_h} C_{ck} A_{ck} \sqrt{\frac{2(X_{11} - X_6)}{\rho_{oil}}} + \Lambda_6 \frac{\beta_{oil}}{V_h} C_{cv} A_{cv} \sqrt{\frac{2(X_7 - X_6)}{\rho_{oil}}} \\
& + \Lambda_7 \frac{\beta_{oil}}{V_h} C_{ck} A_{ck} \sqrt{\frac{2(X_7 - X_9)}{\rho_{oil}}} - \Lambda_7 \frac{\beta_{oil}}{V_h} C_{cv} A_{cv} \sqrt{\frac{2(X_7 - X_6)}{\rho_{oil}}} + \\
& + \Lambda_8 C_{ck} A_{ck} \sqrt{\frac{2(X_7 - X_9)}{\rho_{oil}}} + \Lambda_9 \gamma_{gas} \frac{X_9}{X_8} C_{ck} A_{ck} \sqrt{\frac{2(X_7 - X_9)}{\rho_{oil}}} \\
& - \Lambda_{10} C_{ck} A_{ck} \sqrt{\frac{2(X_{11} - X_6)}{\rho_{oil}}} - \Lambda_{11} \gamma_{gas} \frac{X_{11}}{X_{10}} C_{ck} A_{ck} \sqrt{\frac{2(X_{11} - X_6)}{\rho_{oil}}} \Bigg) + \\
& + \mathbf{\Lambda}_1^T \mathbf{X}_2 + \mathbf{\Lambda}_2^T \mathbf{M}_{fp}^{-1} \left(-\mathbf{K}_{fp} \mathbf{X}_1 - \mathbf{C}_{rp} \mathbf{X}_3 - \mathbf{D}_{rp} \mathbf{X}_2 - \mathbf{f}_{gp} + \mathbf{f}_p \right) + \\
& + \mathbf{\Lambda}_3^T \left(\mathbf{A}_{rp} \mathbf{X}_3 + \mathbf{B}_{rp} \mathbf{X}_2 \right) + \Lambda_4 X_5 + \\
& + \frac{\Lambda_5}{Ig} \left(-m_p g d_p \sin(X_4) - \frac{Dp}{\eta_{pm}} \operatorname{sign}(X_5)(X_7 - X_6) - J \dot{\varphi} \mathbf{\Pi} \mathbf{X}_2 \cos(X_4) \right) + \\
& + \Lambda_6 \frac{\beta_{oil}}{V_h} \left(-D_p |X_5| + C_{cv} A_{cv} \sqrt{\frac{2(X_7 - X_6)}{\rho_{oil}}} \right) + \\
& + \Lambda_7 \frac{\beta_{oil}}{V_h} \left(D_p |X_5| \eta_{pv} - C_{cv} A_{cv} \sqrt{\frac{2(X_7 - X_6)}{\rho_{oil}}} \right) + \\
& + \Lambda_8 \left(\frac{D_m}{\eta_{mv}} X_{12} + C_{rf} A_{rf} \sqrt{\frac{2(X_9 - X_{11})}{\rho_{oil}}} \right) + \\
& + \Lambda_9 \gamma_{gas} \frac{X_9}{X_8} \left(\frac{D_m}{\eta_{mv}} X_{12} + C_{rf} A_{rf} \sqrt{\frac{2(X_9 - X_{11})}{\rho_{oil}}} \right) + \\
& + \Lambda_{10} \left(-D_m X_{12} - C_{rf} A_{rf} \sqrt{\frac{2(X_9 - X_{11})}{\rho_{oil}}} \right) + \\
& + \Lambda_{11} \gamma_{gas} \frac{X_{11}}{X_{10}} \left(-D_m X_{12} - C_{rf} A_{rf} \sqrt{\frac{2(X_9 - X_{11})}{\rho_{oil}}} \right) + \\
& + \frac{\Lambda_{12}}{I_{gm}} \left(D_m \eta_{mm} \eta_{gh} (X_9 - X_{11}) - \beta_g X_{12} \right) = \\
& = u_c \Phi(\mathbf{X}, \mathbf{\Lambda}, \mathbf{f}_p) + \Psi(\mathbf{X}, \mathbf{\Lambda}, \mathbf{f}_p)
\end{aligned}
\tag{B.5}
$$

where $\Phi(\mathbf{X}, \mathbf{\Lambda}, \mathbf{f}_p)$ is the switching function.

The costates dynamics is computed via equation 6.29 and reads:

$$\dot{\mathbf{\Lambda}}_1 = \left(\mathbf{M}_{fp}^{-1}\mathbf{K}_{fp}\right)^T \mathbf{\Lambda}_2$$

$$\dot{\mathbf{\Lambda}}_2 = -\mathbf{\Lambda}_1 + \left(\mathbf{M}_{fp}^{-1}\mathbf{D}_{rp}\right)^T \mathbf{\Lambda}_2 - \mathbf{B}_{rp}^T\mathbf{\Lambda}_3 + \frac{\Lambda_5 J\dot{\varphi}}{I_g}\mathbf{\Pi}^T\cos(X_4)$$

$$\dot{\mathbf{\Lambda}}_3 = \left(\mathbf{M}_{fp}^{-1}\mathbf{C}_{rp}\right)^T \mathbf{\Lambda}_2 - \mathbf{A}_{rp}^T\mathbf{\Lambda}_3$$

$$\dot{\Lambda}_4 = -\frac{\Lambda_5}{Ig}\left(-m_p g d_p\cos(X_4) + J\dot{\varphi}\mathbf{\Pi}\mathbf{X}_2\sin(X_4)\right) +$$
$$+ \left(\mathbf{M}_{fp}^{-1}\begin{bmatrix}0 & 0 & -J\dot{\varphi}X_5\sin(X_4)\end{bmatrix}^T\right)^T \mathbf{\Lambda}_2$$

$$\dot{\Lambda}_5 = -\Lambda_4 + \Lambda_6\frac{\beta_{oil}}{V_h}D_p\,\mathrm{sign}(X_5) - \Lambda_7\frac{\beta_{oil}}{V_h}D_p\eta_{pv}\,\mathrm{sign}(X_5) +$$
$$+ \left(\mathbf{M}_{fp}^{-1}\begin{bmatrix}0 & 0 & J\dot{\varphi}\cos(X_4)\end{bmatrix}^T\right)^T \mathbf{\Lambda}_2$$

$$\dot{\Lambda}_6 = \Lambda_6\frac{\beta_{oil}}{V_h}\frac{u_c C_{ck}A_{ck}}{\sqrt{2\rho_{oil}(X_{11}-X_6)}} - \Lambda_6\frac{\beta_{oil}}{V_h}\frac{(u_c-1)C_{cv}A_{cv}}{\sqrt{2\rho_{oil}(X_7-X_6)}} + \Lambda_7\frac{\beta_{oil}}{V_h}\frac{(u_c-1)C_{cv}A_{cv}}{\sqrt{2\rho_{oil}(X_7-X_6)}} +$$
$$+ \Lambda_{10}\frac{u_c C_{ck}A_{ck}}{\sqrt{2\rho_{oil}(X_{11}-X_6)}} + \Lambda_{11}\gamma_{gas}\frac{X_{11}}{X_{10}}\frac{u_c C_{ck}A_{ck}}{\sqrt{2\rho_{oil}(X_{11}-X_6)}}$$

$$\dot{\Lambda}_7 = \Lambda_6\frac{\beta_{oil}}{V_h}\frac{(u_c-1)C_{cv}A_{cv}}{\sqrt{2\rho_{oil}(X_7-X_6)}} + \Lambda_7\frac{\beta_{oil}}{V_h}\frac{u_c C_{ck}A_{ck}}{\sqrt{2\rho_{oil}(X_7-X_9)}} - \Lambda_7\frac{\beta_{oil}}{V_h}\frac{(u_c-1)C_{cv}A_{cv}}{\sqrt{2\rho_{oil}(X_7-X_6)}} +$$
$$+ \Lambda_8\frac{u_c C_{ck}A_{ck}}{\sqrt{2\rho_{oil}(X_7-X_9)}} + \Lambda_9\gamma_{gas}\frac{X_9}{X_8}\frac{u_c C_{ck}A_{ck}}{\sqrt{2\rho_{oil}(X_7-X_9)}}$$

$$\dot{\Lambda}_8 = \Lambda_9\gamma_{gas}\frac{X_9}{X_8^2}\left(-u_c C_{ck}A_{ck}\sqrt{\frac{2(X_7-X_9)}{\rho_{oil}}} + \frac{D_m}{\eta_{mv}}X_{12} + C_{rf}A_{rf}\sqrt{\frac{2(X_9-X_{11})}{\rho_{oil}}}\right)$$

$$\dot{\Lambda}_9 = -\Lambda_7\frac{\beta_{oil}}{V_h}\frac{u_c C_{ck}A_{ck}}{\sqrt{2\rho_{oil}(X_7-X_9)}} - \Lambda_8\frac{u_c C_{ck}A_{ck}}{\sqrt{2\rho_{oil}(X_7-X_9)}} - \Lambda_8\frac{C_{rf}A_{rf}}{\sqrt{2\rho_{oil}(X_9-X_{11})}} -$$
$$- \frac{\Lambda_9\gamma_{gas}}{X_8}\frac{u_c C_{ck}A_{ck}\,(3X_9-2X_7)}{\sqrt{2\rho_{oil}(X_7-X_9)}} - \frac{\Lambda_9\gamma_{gas}}{X_8}\frac{C_{rf}A_{rf}\,(3X_9-2X_{11})}{\sqrt{2\rho_{oil}(X_9-X_{11})}} +$$
$$+ \Lambda_{10}\frac{C_{rf}A_{rf}}{\sqrt{2\rho_{oil}(X_9-X_{11})}} + \Lambda_{11}\gamma_{gas}\frac{X_{11}}{X_{10}}\frac{C_{rf}A_{rf}}{\sqrt{2\rho_{oil}(X_9-X_{11})}}$$

$$\dot{\Lambda}_{10} = \gamma_{gas}\frac{X_{11}}{X_{10}^2}\left(u_c C_{ck}A_{ck}\sqrt{\frac{2(X_{11}-X_6)}{\rho_{oil}}} - D_m X_{12} - C_{rf}A_{rf}\sqrt{\frac{2(X_9-X_{11})}{\rho_{oil}}}\right)$$

$$\dot{\Lambda}_{11} = -\Lambda_6\frac{\beta_{oil}}{V_h}\frac{u_c C_{ck}A_{ck}}{\sqrt{2\rho_{oil}(X_{11}-X_6)}} + \Lambda_8\frac{C_{rf}A_{rf}}{\sqrt{2\rho_{oil}(X_9-X_{11})}} +$$

$$
\begin{aligned}
&+\Lambda_9\gamma_{gas}\frac{X_9}{X_8}\frac{C_{rf}A_{rf}}{\sqrt{2\rho_{oil}(X_9-X_{11})}}-\Lambda_{10}\frac{u_cC_{ck}A_{ck}}{\sqrt{2\rho_{oil}(X_{11}-X_6)}}-\Lambda_{10}\frac{C_{rf}A_{rf}}{\sqrt{2\rho_{oil}(X_9-X_{11})}}-\\
&-\frac{\Lambda_{11}\gamma_{gas}}{X_{10}}\frac{u_cC_{ck}A_{ck}\left(3X_{11}-2X_9\right)}{\sqrt{2\rho_{oil}(X_{11}-X_6)}}-\frac{\Lambda_{11}\gamma_{gas}}{X_{10}}\frac{C_{rf}A_{rf}\left(3X_9-2X_{11}\right)}{\sqrt{2\rho_{oil}(X_9-X_{11})}}\\
&\dot{\Lambda}_{12}=-\Lambda_8\frac{D_m}{\eta_{mv}}-\Lambda_9\gamma_{gas}\frac{X_9}{X_8}\frac{D_m}{\eta_{mv}}+\Lambda_{10}D_m+\Lambda_{11}\gamma_{gas}\frac{X_{11}}{X_{10}}D_m+\frac{\Lambda_{12}}{I_{gm}}\beta_g\\
&+\Lambda_9\gamma_{gas}\frac{X_9}{X_8}\frac{C_{rf}A_{rf}}{\sqrt{2\rho_{oil}(X_9-X_{11})}}-\Lambda_{10}\frac{u_cC_{ck}A_{ck}}{\sqrt{2\rho_{oil}(X_{11}-X_6)}}-\Lambda_{10}\frac{C_{rf}A_{rf}}{\sqrt{2\rho_{oil}(X_9-X_{11})}}-\\
&-\frac{\Lambda_{11}\gamma_{gas}}{X_{10}}\frac{u_cC_{ck}A_{ck}\left(3X_{11}-2X_9\right)}{\sqrt{2\rho_{oil}(X_{11}-X_6)}}-\frac{\Lambda_{11}\gamma_{gas}}{X_{10}}\frac{C_{rf}A_{rf}\left(3X_9-2X_{11}\right)}{\sqrt{2\rho_{oil}(X_9-X_{11})}}\\
&\dot{\Lambda}_{12}=-\Lambda_8\frac{D_m}{\eta_{mv}}-\Lambda_9\gamma_{gas}\frac{X_9}{X_8}\frac{D_m}{\eta_{mv}}+\Lambda_{10}D_m+\Lambda_{11}\gamma_{gas}\frac{X_{11}}{X_{10}}D_m+\frac{\Lambda_{12}}{I_{gm}}\beta_g
\end{aligned}
\tag{B.6}
$$

Bibliography

[1] D Connolly, H Lund, and B V Mathiesen. "Smart Energy Europe: The technical and economic impact of one potential 100% renewable energy scenario for the European Union". In: *Renewable and Sustainable Energy Reviews* 60 (2016), pp. 1634–1653. ISSN: 1364-0321. DOI: https://doi.org/10.1016/j.rser.2016.02.025. URL: http://www.sciencedirect.com/science/article/pii/S1364032116002331.

[2] European Commission. *Clean energy for all Europeans package*. URL: https://ec.europa.eu/energy/topics/energy-strategy/clean-energy-all-europeans%7B%5C_%7Den (visited on 11/16/2020).

[3] European Commission. *DIRECTIVE (EU) 2018/2001 OF THE EUROPEAN PARLIAMENT AND OF THE COUNCIL of 11 December 2018 on the promotion of the use of energy from renewable sources*. 2018. URL: https://eur-lex.europa.eu/legal-content/EN/TXT/?uri=uriserv:OJ.L%7B%5C_%7D.2018.328.01.0082.01.ENG%7B%5C&%7Dtoc=OJ:L:2018:328:TOC (visited on 11/16/2020).

[4] John Twidell and Tony Weir. *Renewable Energy Resources*. 3rd Editio. London, 2015, pp. 1–816. ISBN: 9781315766416. DOI: 10.4324/9781315766416.

[5] IEA. *Global Energy Review 2020*. 2020, pp. 1–56. DOI: https://doi.org/https://doi.org/10.1787/a60abbf2-en. URL: https://www.oecd-ilibrary.org/content/publication/a60abbf2-en.

[6] Francisco Taveira-Pinto et al. "Preface to Special Topic: Marine Renewable Energy". In: *Journal of Renewable and Sustainable Energy* 7.6 (2015). ISSN: 19417012. DOI: 10.1063/1.4939086. URL: http://dx.doi.org/10.1063/1.4939086.

[7] Kester Gunn and Clym Stock-Williams. "Quantifying the global wave power resource". In: *Renewable Energy* 44 (2012), pp. 296–304. ISSN: 09601481. DOI: 10.1016/j.renene.2012.01.101.

[8] Mehmet Melikoglu. "Current status and future of ocean energy sources: A global review". In: *Ocean Engineering* 148.November 2017 (2018), pp. 563–573. ISSN: 00298018. DOI: 10.1016/j.oceaneng.2017.11.045. URL: https://doi.org/10.1016/j.oceaneng.2017.11.045.

[9] Liliana Rusu and Florin Onea. "The performance of some state-of-the-art wave energy converters in locations with the worldwide highest wave power". In: *Renewable and Sustainable Energy Reviews* 75.August 2015 (2017), pp. 1348–1362. ISSN: 18790690. DOI: 10.1016/j.rser.2016.11.123. URL: http://dx.doi.org/10.1016/j.rser.2016.11.123.

[10] Andreas Uihlein and Davide Magagna. "Wave and tidal current energy – A review of the current state of research beyond technology". In: *Renewable and Sustainable Energy Reviews* 58 (2016), pp. 1070–1081. ISSN: 1364-0321. DOI: https://doi.org/10.1016/j.rser.2015.12.284. URL: http://www.sciencedirect.com/science/article/pii/S1364032115016676.

[11] D. Clemente, P. Rosa-Santos, and F. Taveira-Pinto. "On the potential synergies and applications of wave energy converters: A review". In: *Renewable and Sustainable Energy Reviews* 135.January 2020 (2021), p. 110162. ISSN: 18790690. DOI: 10.1016/j.rser.2020.110162. URL: https://doi.org/10.1016/j.rser.2020.110162.

[12] Stephen H Salter. "Wave Power". In: *Nature* 249.720-724 (1974), pp. 720–724. ISSN: 0028-0836. DOI: 10.1038/249720a0. URL: http://www.nature.com/articles/249720a0.

[13] C. Guedes Soares et al. "Review and classification of wave energy converters". In: *Maritime Engineering and Technology - Proceedings of 1st International Conference on Maritime Technology and Engineering, MARTECH 2011* November (2012), pp. 585–594. DOI: 10.1201/b12726-82.

[14] António F.de O. Falcão. "Wave energy utilization: A review of the technologies". In: *Renewable and Sustainable Energy Reviews* 14.3 (2010), pp. 899–918. ISSN: 13640321. DOI: 10.1016/j.rser.2009.11.003.

[15] B Drew, A R Plummer, and M N Sahinkaya. "A Review of Wave Energy Converter Technology". In: *Journal of Power and Energy* 223.8 (2009), pp. 887–902. ISSN: 09576509. DOI: 10.1243/09576509JPE782. arXiv: 1106.1595.

[16] *Ocean Energy Systems*. 2020. URL: http://www.ocean-energy-systems.org/ocean%7B%5C_%7Denergy/waves/ (visited on 11/17/2020).

[17] Eugen Rusu and Florin Onea. "A review of the technologies for wave energy extraction". In: *Clean Energy* 2.1 (2018), pp. 10–19. ISSN: 2515396X. DOI: 10.1093/ce/zky003.

[18] *OPT Ocean Power Technologies*. 2020. URL: https://oceanpowertechnologies.com/new-homepage-alt/ (visited on 11/17/2020).

[19] *Carnegie Clean Energy*. 2020. URL: https://www.carnegiece.com/ (visited on 11/17/2020).

[20] Maria Angeliki Chatzigiannakou, Irina Dolguntseva, and Mats Leijon. "Offshore deployments of wave energy converters by seabased industry AB". In: *Journal of Marine Science and Engineering* 5.2 (2017), pp. 1–11. ISSN: 20771312. DOI: 10.3390/jmse5020015.

[21] *WaveBob Company Profile*. 2020. URL: https://ita.calameo.com/books/000674314aec3c0329ef5 (visited on 11/17/2020).

[22] R.W. Yemm, R.M. Henderson, and C.A.E. Taylor. "The OPD Pelamis WEC: Current status and onward programme". In: *International Journal of Ambient Energy* 24.1 (2003), pp. 21–28. ISSN: 21628246. DOI: 10.1080/01430750.2003.9674899.

[23] Wave Star. *Unlimited Clean Energy with The Wavestar machine*. URL: http://wavestarenergy.com/.

[24] Emiliano Renzi et al. "How does Oyster work? The simple interpretation of Oyster mathematics". In: *European Journal of Mechanics-B/Fluids* 47.June 2012 (2014), pp. 124–131. DOI: 10.1016/j.euromechflu.2014.03.007. URL: http://dx.doi.org/10.1016/j.euromechflu.2014.03.007.

[25] *Wave Dragon*. 2020. URL: http://www.wavedragon.net/ (visited on 11/17/2020).

[26] S De Chowdhury et al. *A review of hydrodynamic investigations into arrays of ocean wave energy converters*. 2015. arXiv: 1508.00866 [physics.flu-dyn].

[27] Morten Kramer, Laurent Marquis, and Peter Frigaard. "Performance evaluation of the wavestar prototype". In: *Proceedings of the 9th European Wave and Tidal Energy Conference*. Sout, 2011.

[28] *Oyster Wave Power*. URL: http://www.reuk.co.uk/wordpress/wave/oyster-wave-power/ (visited on 11/29/2020).

[29] A. P. McCabe et al. "Developments in the design of the PS Frog Mk 5 wave energy converter". In: *Renewable Energy* 31.2 (2006), pp. 141–151. ISSN: 09601481. DOI: 10.1016/j.renene.2005.08.013.

[30] Nicola Pozzi et al. "PeWEC: Experimental validation of wave to PTO numerical model". In: *Ocean Engineering* 167 (2018), pp. 114–129. ISSN: 0029-8018. DOI: https://doi.org/10.1016/j.oceaneng.2018.08.028.

[31] C. Josset, A. Babarit, and A. H. Clément. "A wave-to-wire model of the SEAREV wave energy converter". In: *Proceedings of the Institution of Mechanical Engineers Part M: Journal of Engineering for the Maritime Environment* 221.2 (2015), pp. 81–93. ISSN: 20413084. DOI: 10.1243/14750902JEME48.

[32] Wello. *WELLO - THE POWER OF WAVES*. URL: https://invest.invesdor.com/en/pitches/888 (visited on 11/29/2020).

[33] S Crowley et al. "Modelling of the WITT wave energy converter". In: *Renewable Energy* 115 (2018), pp. 159–174. ISSN: 0960-1481. DOI: https://doi.org/10.1016/j.renene.2017.08.004. URL: http://www.sciencedirect.com/science/article/pii/S0960148117307565.

[34] F Salcedo et al. "OCEANTEC: Sea Trials of a Quarter Scale Prototype". In: *Proceed8th European Wave and Tidal Energy Conference (EWTEC)* June 2014 (2009), pp. 460–465.

[35] Giacomo Vissio. "ISWEC toward the sea-Development, Optimization and Testing of the Device Control Architecture". PhD Thesis. Politecnico di Torino, 2018. DOI: 10.6092/polito/porto/2697259. URL: http://porto.polito.it/2697259/.

[36] Amélie Têtu. "Power Take-Off Systems for WECs". In: *Handbook of Ocean Wave Energy*. Ed. by Arthur Pecher and Jens Peter Kofoed. Cham: Springer International Publishing, 2017, pp. 203–220. ISBN: 978-3-319-39889-1. DOI: 10.1007/978-3-319-39889-1_8. URL: https://doi.org/10.1007/978-3-319-39889-1%7B%5C_%7D8.

[37] S. H. Salter, J. R.M. Taylor, and N. J. Caldwell. "Power conversion mechanisms for wave energy". In: *Proceedings of the Institution of Mechanical Engineers, Part M: Journal of Engineering for the Maritime Environment* 216.1 (2002), pp. 1–27. ISSN: 20413084. DOI: 10.1243/147509002320382103.

[38] Johannes Falnes. "Optimum control of oscillation of wave-energy converters". In: *International Journal of Offshore and Polar Engineering* 12.2 (2002), pp. 147–155. ISSN: 10535381.

[39] Joao Cruz. *Ocean Wave Energy*. Springer-Verlag Berlin Heidelberg, 2008. ISBN: 978-3-540-74894-6. DOI: 10.1007/978-3-540-74895-3.

[40] Rico Hjerm Hansen. "Design and control of the powertake-off system for a wave energy converter with multiple absorbers". PhD thesis. Aalborg Universitet, 2013. URL: https://core.ac.uk/download/pdf/60558659.pdf.

[41] Raju Ahamed, Kristoffer McKee, and Ian Howard. "Advancements of wave energy converters based on power take off (PTO) systems: A review". In: *Ocean Engineering* 204.August 2019 (2020), p. 107248. ISSN: 00298018. DOI: 10.1016/j.oceaneng.2020.107248. URL: https://doi.org/10.1016/j.oceaneng.2020.107248.

[42] M Takao and T Setoguchi. "Air Turbines for Wave Energy Conversion". In: *International Journal of Rotating Machinery* 2012 (2012), p. 10.

[43] Toshiaki Setoguchi and Manabu Takao. "Current status of self rectifying air turbines for wave energy conversion". In: *Energy Conversion and Management* 47.15 (2006), pp. 2382–2396. ISSN: 0196-8904. DOI: https://doi.org/10.1016/j.enconman.2005.11.013. URL: https://www.sciencedirect.com/science/article/pii/S0196890405003158.

[44] *PICO OWC*. 2020. URL: http://www.pico-owc.net/en/ (visited on 11/17/2020).

[45] Cuan B. Boake et al. "Overview and Initial Operational Experience of the LIMPET Wave Energy Plant". In: *Proceedings of the International Offshore and Polar Engineering Conference* 12.January (2002), pp. 586–594.

[46] J P Kofoed and P Frigaard. "Hydraulic evaluation of the LEANCON wave energy converter". In: Tech. Rep. no. 45 (2008).

[47] A F O Falcão and J C C Henriques. "Oscillating-water-column wave energy converters and air turbines: A review". In: *Renewable Energy* 85 (2016), pp. 1391–1424. ISSN: 18790682. DOI: 10.1016/j.renene.2015.07.086.

[48] A Weinstein et al. "AquaBuOY - the offshore wave energy converter numerical modeling and optimization". In: *Oceans '04 MTS/IEEE Techno-Ocean '04 (IEEE Cat. No.04CH37600)*. Vol. 4. 2004, 1854–1859 Vol.4. DOI: 10.1109/OCEANS.2004.1406425.

[49] *Tapered Channel Wave Energy*. URL: https://taperedchannelwaveenergy.weebly.com/ (visited on 11/17/2020).

[50] Resen Waves. *Wave energy made simple*. URL: http://www.resenwaves.com/ (visited on 02/09/2021).

[51] Mario López et al. "The Wave Energy Converter CECO: Current Status and Future Perspectives". In: *Proceedings* 2.23 (2018). ISSN: 2504-3900. DOI: 10.3390/proceedings2231423. URL: https://www.mdpi.com/2504-3900/2/23/1423.

[52] Markel Penalba and John V. Ringwood. "A review of wave-to-wire models for wave energy converters". In: *Energies* 9.7 (2016). ISSN: 19961073. DOI: 10.3390/en9070506.

[53] Tom Smith. "Personal communication with S". In: *Nadel. February* (2006).

[54] R. Waters et al. "Experimental results from sea trials of an offshore wave energy system". In: *Applied Physics Letters* 90.3 (Jan. 2007), p. 034105. ISSN: 0003-6951. DOI: 10.1063/1.2432168. URL: http://aip.scitation.org/doi/10.1063/1.2432168.

[55] A LiVecchi et al. "Powering the blue economy; exploring opportunities for marine renewable energy in maritime markets". In: *US Department of Energy, Office of Energy Efficiency and Renewable Energy. Washington, DC* (2019), p. 207.

[56] *L10*. 2020. URL: https://www.smithsonianmag.com/science-nature/catching-a-wave-powering-an-electrical-grid-30145572/ (visited on 11/17/2020).

[57] Yue Hong et al. "Status update of the wave energy research at Uppsala University". In: *10th European Wave and Tidal Conference (EWTEC)*. 2013.

[58] O Danielsson et al. *A Direct Drive Wave Energy Converter: Simulations and Experiments*. June 2005. DOI: 10.1115/OMAE2005-67391. URL: https://doi.org/10.1115/OMAE2005-67391.

[59] Mats Leijon et al. "Wave Energy from the North Sea: Experiences from the Lysekil Research Site". In: *Surveys in Geophysics* 29.3 (2008), pp. 221–240. ISSN: 1573-0956. DOI: 10.1007/s10712-008-9047-x. URL: https://doi.org/10.1007/s10712-008-9047-x.

[60] K. Budal and J. Falnes. *Preliminary design and model test of a wave-power converter: Budal's 1978 design type E*. Tech. rep. Trondheim, Norway: University of Trondheim, 1978. URL: http://folk.ntnu.no/falnes/w%7B%5C_%7De/rpts%7B%5C_%7Dscnnd/RptPublFree/P357%7B%5C_%7D1992Budal%7B%5C_%7DTypeE1978design.pdf.

[61] J Falnes. *Principles for capture of energy from ocean waves. Phase control and optimum oscillation*. Tech. rep. Trondheim, Norway.: Department of Physics, NTNU, 1997. URL: http://folk.ntnu.no/falnes/web%7B%5C_%7Darkiv/InstFysikk/phcontrl.pdf.

[62] Stephen H Salter. "Power conversion systems for ducks". In: *Proceedings of International Conference on Future Energy Concepts, London, Institution of Electrical Engineers*. Vol. 171. 1979, pp. 100–108.

[63] R. Clare, D.V. Evans, and T.L. Shaw. "Harnessing sea wave energy by a submerged chylinder device". In: *Proceedings of the Institution of Civil Engineers* 73.3 (1982), pp. 565–585. DOI: 10.1680/iicep.1982.1677. URL: https://doi.org/10.1680/iicep.1982.1677.

[64] V. Ferdinande and M. Vantorre. "The Concept of a Bipartite Point Absorber BT - Hydrodynamics of Ocean Wave-Energy Utilization". In: *Hydrodynamics of Ocean Wave-Energy Utilization*. Ed. by David V Evans and António F O de Falcão. Berlin, Heidelberg: Springer Berlin Heidelberg, 1986, pp. 217–226. ISBN: 978-3-642-82666-5.

[65] Kim Nielsen. "On the Experimental Investigation of a Wave Power Converter". In: *Hydrodynamics of Ocean Wave-Energy Utilization*. Ed. by David V Evans and António F O de Falcão. Berlin, Heidelberg: Springer Berlin Heidelberg, 1986, pp. 93–101. ISBN: 978-3-642-82666-5.

[66] D C Hicks and C M Pleass. "Physical and Mathematical Modelling of a Point Absorber Wave Energy Conversion System with Nonlinear Damping". In: *Hydrodynamics of Ocean Wave-Energy Utilization*. Ed. by David V Evans and António F O de Falcão. Berlin, Heidelberg: Springer Berlin Heidelberg, 1986, pp. 113–124. ISBN: 978-3-642-82666-5.

[67] S.H. Salter and W.H.S. Rampen. "The wedding cake multi-eccentric radial piston hydraulic machine with direct computer control of displacement". In: *Proc. 10th International Conference on Fluid Power* (1993).

[68] S.H. Salter and C. Lin. "The sloped IPS wave energy converter". In: *Proc. Second European Wave Energy Conference*. Lisbon, Portugal.

[69] Grégory S. Payne et al. "Numerical modelling of the sloped IPS buoy wave energy converter". In: *Proceedings of the International Offshore and Polar Engineering Conference* January (2006). ISSN: 10986189.

[70] H. Eidsmoen. "Tight-moored amplitude-limited heaving-buoy wave-energy converter with phase control". In: *Applied Ocean Research* 20.3 (1996), pp. 157–161. ISSN: 0141-1187. DOI: https://doi.org/10.1016/S0141-1187(98)00013-3. URL: http://www.sciencedirect.com/science/article/pii/S0141118798000133.

[71] H. Eidsmoen. *Simulation of a Slack-Moored Heaving-Buoy Wave-Energy Converter*. Tech. rep. May. Trondheim, Norway: Norwegian University of Science and Technology, 1996, pp. 1–37. URL: http://folk.ntnu.no/falnes/web%7B%5C_%7Darkiv/InstFysikk/simwec.pdf.

[72] T.E. Blake and R.V. Chaplin. "The P.S.FROG: latest developments and model testing." In: *Proceedings of the 3rd European wave energy conference* (1998). URL: https://eprints.lancs.ac.uk/id/eprint/20363/.

[73] Rob Bracewell. "Frog And PS Frog: A Study Of Two Reactionless Ocean Wave Energy Converters". PhD thesis. University of Lancaster, 1990. DOI: 10.1.1.22.7243&rep=rep1&type=pdf. URL: http://citeseerx.ist.psu.edu/viewdoc/download;jsessionid=025E5A3B36F190AF22262D9A9C22AD5E?.

[74] Mohd Afifi Jusoh et al. "Hydraulic power take-off concepts for wave energy conversion system: a review". In: *Energies* 12.23 (2019), pp. 1–23. ISSN: 19961073. DOI: 10.3390/en12234510.

[75] Yonggang Lin et al. "Review of hydraulic transmission technologies for wave power generation". In: *Renewable and Sustainable Energy Reviews* 50 (2015), pp. 194–203. ISSN: 18790690. DOI: 10.1016/j.rser.2015.04.141.

[76] Ross Henderson. "Design, simulation, and testing of a novel hydraulic power take-off system for the Pelamis wave energy converter". In: *Renewable energy* 31.2 (2006), pp. 271–283.

[77] AWS Ocean Energy Ltd. *Sub-sea wave power*. URL: http://www.awsocean.com/ (visited on 01/24/2021).

[78] AW-Energy. *https://aw-energy.com/waveroller/*. 2020. URL: https://aw-energy.com/waveroller/.

[79] Dahai Zhang et al. "An overview of hydraulic systems in wave energy application in China". In: *Renewable and Sustainable Energy Reviews* 16.7 (2012), pp. 4522–4526. ISSN: 13640321. DOI: 10.1016/j.rser.2012.04.005. URL: http://dx.doi.org/10.1016/j.rser.2012.04.005.

[80] José F. Gaspar et al. "Power take-off concept for wave energy converters based on oil-hydraulic transformer units". In: *Renewable Energy* 86 (2016), pp. 1232–1246. ISSN: 18790682. DOI: 10.1016/j.renene.2015.09.035.

[81] P. Beirão. "Modelling and Control of a Wave Energy Converter: Archimedes Wave Swing". PhD thesis. UNIVERSIDADE TÉCNICA DE LISBOA, 2007. URL: https://www.researchgate.net/profile/Pedro%7B%5C_%7DBeirao/publication/247160804%7B%5C_%7DModelling%7B%5C_%7Dand%7B%5C_%7DControl%7B%5C_%7Dof%7B%5C_%7Da%7B%5C_%7DWave%7B%5C_%7DEnergy%7B%5C_%7DConverter%7B%5C_%7DArchimedes%7B%5C_%7DWave%7B%5C_%7DSwing/links/5731f71108ae9ace8404753b.pdf.

[82] Simon Lindroth and Mats Leijon. "Offshore wave power measurements - A review". In: *Renewable and Sustainable Energy Reviews* 15.9 (2011), pp. 4274–4285. ISSN: 13640321. DOI: 10.1016/j.rser.2011.07.123. URL: http://dx.doi.org/10.1016/j.rser.2011.07.123.

[83] Jackson Giles and Boxx Randy. "Persistence and survival in entrepreneurship: The case of the wave energy conversion corporation of America". In: *New England Journal of Entrepreneurship* 15.1 (2012), pp. 19–27. ISSN: 2574-8904. DOI: 10.1108/NEJE-15-01-2012-B002. URL: https://doi.org/10.1108/NEJE-15-01-2012-B002.

[84] The Engineering Business Ltd. *EB Frond Wave Energy Converter - Phase 2*. Tech. rep. 2005. URL: http://ukerc.rl.ac.uk/pdf/DTI%7B%5C_%7DV06002040000%7B%5C_%7DEB%7B%5C_%7DFrond%7B%5C_%7DPhase%7B%5C_%7D2r.pdf.

[85] H.D. Shi, F.F. Cao, and N. Qu. "The latest progress in wave energy conversions in China and the analysis of a heaving buoy considering pto damping". In: *Journal of Marine Science and Technology (Taiwan)* 23.6 (2015), pp. 888–892. DOI: 10.6119/JMST-015-0610-6. URL: https://www.scopus.com/inward/record.uri?eid=2-s2.0-84961383004%7B%5C&%7Ddoi=10.

6119%7B%5C%%7D2FJMST-015-0610-6%7B%5C&%7DpartnerID=40%7B%5C&%7Dmd5=e19070b86ad86837f7367461e2f668da.

[86] A. Leirbukt and P. Tubaa. *A wave of renewable energy: There's no such thing as bad weather*. 2006. URL: https://library.e.abb.com/public/1e2fadd298a58d14c12571d900412482/29-31%203M646%7B%5C_%7DENG72dpi.pdf (visited on 11/20/2020).

[87] Rico H. Hansen, Morten M. Kramer, and Enrique Vidal. "Discrete displacement hydraulic power take-off system for the wavestar wave energy converter". In: *Energies* 6.8 (2013), pp. 4001–4044. ISSN: 19961073. DOI: 10.3390/en6084001.

[88] A Poullikkas. "Technology prospects of wave power systems". In: *Electron. J. Energy Environ.* 2.1 (2014), pp. 47–69.

[89] Arthur Pecher et al. "Results of an experimental study of the langlee wave energy converter". In: *The Twentieth International Offshore and Polar Engineering Conference*. International Society of Offshore and Polar Engineers. 2010.

[90] P.E. Ventures. *Task-2.1.1-EPRI-Wave-Energy-Tech-Assessment-2009*. Tech. rep. December. 2009. URL: https://ir.library.oregonstate.edu/concern/technical%7B%5C_%7Dreports/2n49t635h.

[91] Albatern Ltd. *WaveNet Series 12 - WES Novel Wave Energy Converter Stage 1 Project - Public Report*. Tech. rep. 2017. URL: https://library.waveenergyscotland.co.uk/development-programmes/novel-wave-energy-converter/stage-1/nw11%7B%5C_%7Dalb/nw11%7B%5C_%7Dalb%7B%5C_%7Dwes-public-report/.

[92] J R Joubert et al. "Wave energy converters (WECs)". In: *CRSES: Matieland, South Africa* (2013).

[93] Nathan P. Sell, Andrew R. Plummer, and Andrew J. Hillis. "A Self-zeroing position controller for oscillating surge wave energy converters with strong asymmetry". In: *Journal of Ocean Engineering and Marine Energy* 4.2 (2018), pp. 137–151. ISSN: 21986452. DOI: 10.1007/s40722-018-0113-2. URL: https://doi.org/10.1007/s40722-018-0113-2.

[94] Songwei Sheng et al. "Model research and open sea tests of 100 kW wave energy convertor Sharp Eagle Wanshan". In: *Renewable Energy* 113 (2017), pp. 587–595. ISSN: 18790682. DOI: 10.1016/j.renene.2017.06.019. URL: http://dx.doi.org/10.1016/j.renene.2017.06.019.

[95] *BioPower Systems Pty Ltd*. URL: https://bps.energy/ (visited on 11/20/2020).

[96] *Triton WEC*. URL: https://www.oscillapower.com/tritonwec (visited on 11/20/2020).

[97] *Introducing Chinese Sharp Eagle WEC*. URL: https://www.offshore-energy.biz/introducing-chinese-sharp-eagle-wec/ (visited on 11/20/2020).

[98] Azura. *Azura*. URL: https://azurawave.com/ (visited on 11/20/2020).

[99] Piero Ruol et al. "NEAR-SHORE FLOATING WAVE ENERGY CONVERTERS: APPLICATIONS FOR COASTAL PROTECTION". In: *Coastal Engineering Proceedings* 1.32 (2011), structures.61. DOI: 10.9753/icce.v32.structures.61. URL: https://icce-ojs-tamu.tdl.org/icce/index.php/icce/article/view/1419.

[100] Rico Hjerm Hansen, Torben O. Andersen, and Henrik C. Pedersen. "Model Based Design of Efficient Power Take-Off Systems for Wave Energy Converters". In: *Proceedings of the 12th Scandinavian International Conference on Fluis Power* January (2011), pp. 1–15.

[101] J V Ringwood, G Bacelli, and F Fusco. "Energy-Maximizing Control of Wave-Energy Converters: The Development of Control System Technology to Optimize Their Operation". In: *IEEE Control Systems Magazine* 34.5 (2014), pp. 30–55. ISSN: 1941-000X. DOI: 10.1109/MCS.2014.2333253.

[102] Markel Penalba et al. "Validating a wave-to-wire model for a wave energy converter-part I: The hydraulic transmission system". In: *Energies* 10.7 (2017), pp. 1–22. ISSN: 19961073. DOI: 10.3390/en10070977.

[103] Markel Penalba et al. "A high-fidelity wave-to-wire simulation platform for wave energy converters: Coupled numerical wave tank and power take-off models". In: *Applied Energy* 226.June (2018), pp. 655–669. ISSN: 03062619. DOI: 10.1016/j.apenergy.2018.06.008. URL: https://doi.org/10.1016/j.apenergy.2018.06.008.

[104] M. Calvário et al. "Oil-hydraulic power take-off concept for an oscillating wave surge converter". In: *Renewable Energy* 159 (2020). ISSN: 18790682. DOI: 10.1016/j.renene.2020.06.002.

[105] José F. Gaspar et al. "Design tradeoffs of an oil-hydraulic power take-off for wave energy converters". In: *Renewable Energy* 129 (2018), pp. 245–259. ISSN: 18790682. DOI: 10.1016/j.renene.2018.05.092.

[106] Aurélien Babarit, Michel Guglielmi, and Alain H. Clément. "Declutching control of a wave energy converter". In: *Ocean Engineering* 36.12-13 (2009), pp. 1015–1024. ISSN: 00298018. DOI: 10.1016/j.oceaneng.2009.05.006.

[107] Antonio F de O Falcao. "Modelling and control of oscillating-body wave energy converters with hydraulic power take-off and gas accumulator". In: *Ocean Engineering* 34.14-15 (2007), pp. 2021–2032. ISSN: 00298018. DOI: 10.1016/j.oceaneng.2007.02.006.

[108] Ratanak So et al. "Development of PTO-Sim: A Power Performance Module for the Open-Source Wave Energy Converter Code WEC-Sim". In: *Proceedings of the ASME 2015 34th International Conference on Ocean, Offshore and Arctic Engineering*. St. John's, Newfoundland, Canada: Ocean Renewable Energy, 2015. DOI: 10.1115/OMAE2015-42074.

[109] Pedro Beirão and Cândida Malça. "Hydraulic Power Take-off and Buoy Geometries Charac-terisation for a Wave Energy Converter". In: *Energy and Power Engineering* 05.04 (2013), pp. 72–77. ISSN: 1949-243X. DOI: 10.4236/epe.2013.54b014.

[110] C. J. Cargo, A. J. Hillis, and A. R. Plummer. "Strategies for active tuning of Wave Energy Converter hydraulic power take-off mechanisms". In: *Renewable Energy* 94 (2016), pp. 32–47. ISSN: 18790682. DOI: 10.1016/j.renene.2016.03.007. URL: http://dx.doi.org/10.1016/j.renene.2016.03.007.

[111] António F.de O. Falcão. "Phase control through load control of oscillating-body wave energy converters with hydraulic PTO system". In: *Ocean Engineering* 35.3-4 (2008), pp. 358–366. ISSN: 00298018. DOI: 10.1016/j.oceaneng.2007.10.005.

[112] Pierpaolo Ricci et al. "Control strategies for a wave energy converter connected to a hydraulic power take-off". In: *Renewable Power Generation, IET* 5.3 (2011), pp. 234–244. ISSN: 1752-1416. DOI: 10.1049/iet-rpg.2009.0197.

[113] Y. G. Lin et al. "A study on dual-stroke pendulum wave energy conversion technology based on a water/oil integrated transmission system". In: *Ocean Engineering* 67 (2013), pp. 27–34. ISSN: 00298018. DOI: 10.1016/j.oceaneng.2013.04.014.

[114] Dominic Dießel et al. "Wavepod a transmission for wave energy converters - Set-up and testing". In: *International Journal of Fluid Power* 16.2 (2015), pp. 75–82. ISSN: 14399776. DOI: 10.1080/14399776.2015.1055990.

[115] Nguyen Minh Tri et al. "A novel control method to maximize the energy-harvesting capability of an adjustable slope angle wave energy converter". In: *Renewable Energy* 97 (2016), pp. 518–531. ISSN: 18790682. DOI: 10.1016/j.renene.2016.05.092. URL: http://dx.doi.org/10.1016/j.renene.2016.05.092.

[116] Boyin Ding et al. "Sea-state based maximum power point tracking damping control of a fully submerged oscillating buoy". In: *Ocean Engineering* 126.September (2016), pp. 299–312. ISSN: 00298018. DOI: 10.1016/j.oceaneng.2016.09.020. URL: http://dx.doi.org/10.1016/j.oceaneng.2016.09.020.

[117] Shangyan Zou and Ossama Abdelkhalik. "Control of wave energy converters with discrete displacement hydraulic power take-off units". In: *Journal of Marine Science and Engineering* 6.2 (2018), pp. 1–24. ISSN: 20771312. DOI: 10.3390/jmse6020031.

[118] H. C. Pedersen et al. "Design of full scale wave simulator for testing Power Take off systems for wave energy converters". In: *International Journal of Marine Energy* 13 (2016), pp. 130–156. ISSN: 22141669. DOI: 10.1016/j.ijome.2016.01.005. URL: http://dx.doi.org/10.1016/j.ijome.2016.01.005.

[119] José F. Gaspar et al. "Speed control of oil-hydraulic power take-off system for oscillating body type wave energy converters". In: *Renewable Energy* 97 (2016), pp. 769–783. ISSN: 18790682. DOI: 10.1016/j.renene.2016.06.015.

[120] José F. Gaspar et al. "Analysis of electrical drive speed control limitations of a power take-off system for wave energy converters". In: *Renewable Energy* 113 (2017), pp. 335–346. ISSN: 18790682. DOI: 10.1016/j.renene.2017.05.085.

[121] J. F. Gaspar and C. Guedes Soares. "Modelling pump efficiency in a generic hydraulic power take-off for wave energy point absorbers". In: *Maritime Technology and Engineering - Proceedings of MARTECH 2014: 2nd International Conference on Maritime Technology and Engineering* (2015), pp. 1233–1241. DOI: 10.1201/b17494-167.

[122] R H Hansen, T O Andersen, and H C Perdersen. "Analysis of discrete pressure level systems for Wave Energy Converters". In: *Proceedings of 2011 International Conference on Fluid Power and Mechatronics*. 2011, pp. 552–558. DOI: 10.1109/FPM.2011.6045825.

[123] Anders Hedegaard Hansen, Henrik C Pedersen, and Rico Hjerm Hansen. "Validation of Simulation Model for Full Scale Wave Simulator and Discrete Fuild Power PTO System". In: *Proceedings of the 9th JFPS International Symposium on Fluid Power*. Japan Fluid Power System Society, 2014. URL: https://jfps.or.jp/souko/Proceedings2014/proceedings/pdf/1D2-4.pdf.

[124] Celalettin Doğukan Engin and Aydin Yeşildirek. "Designing and modeling of a point absorber wave energy converter with hydraulic power take-off unit". In: *2015 4th International Conference on Electric Power and Energy Conversion Systems, EPECS 2015* (2015). DOI: 10.1109/EPECS.2015.7368507.

[125] Chang Hai Liu, Qing Jun Yang, and Gang Bao. "Performance investigation of a two-raft-type wave energy converter with hydraulic power take-off unit". In: *Applied Ocean Research* 62 (2017), pp. 139–155. ISSN: 01411187. DOI: 10.1016/j.apor.2016.12.002. URL: http://dx.doi.org/10.1016/j.apor.2016.12.002.

[126] Yue Xuhui et al. "A novel nonlinear state space model for the hydraulic power take-off of a wave energy converter". In: *Energy* 180 (2019), pp. 465–479. ISSN: 03605442. DOI: 10.1016/j.energy.2019.05.095. URL: https://doi.org/10.1016/j.energy.2019.05.095.

[127] Changhai Liu, Qingjun Yang, and Gang Bao. "Influence of hydraulic power take-off unit parameters on power capture ability of a two-raft-type wave energy converter". In: *Ocean Engineering* 150.November 2017 (2018), pp. 69–80. ISSN: 00298018. DOI: 10.1016/j.oceaneng.2017.12.063. URL: https://doi.org/10.1016/j.oceaneng.2017.12.063.

[128] Andrew F. Colombo, Pedro Lee, and Bryan W. Karney. "A selective literature review of transient-based leak detection methods". In: *Journal of Hydro-Environment Research* 2.4 (2009), pp. 212–227. ISSN: 15706443. DOI: 10.1016/j.jher.2009.02.003. URL: http://dx.doi.org/10.1016/j.jher.2009.02.003.

[129] G H Lim, P S K Chua, and Y B He. "Modern water hydraulics—the new energy-transmission technology in fluid power". In: *Applied Energy* 76.1 (2003), pp. 239–246. ISSN: 0306-2619. DOI: https://doi.org/10.1016/S0306-2619(03)00064-3. URL: http://www.sciencedirect.com/science/article/pii/S0306261903000643.

[130] G Bracco et al. "Performance assessment of the full scale ISWEC system". In: *2015 IEEE International Conference on Industrial Technology (ICIT)*. 2015, pp. 2499–2505.

[131] Mattia Raffero. "Design of a Wave Energy Converter A case of application: ISWEC". Phd thesis. Politecnico di Torino, 2014.

[132] Fabian Wendt et al. "Ocean Energy Systems wave energy modeling task : modeling , verification , and validation of wave energy converters". In: *Journal of Marine Science and Engineering* 7.379 (2019), pp. 1–22. DOI: 10.3390/jmse7110379.

[133] Edward Ransley et al. "A blind comparative study of focused wave interactions with floating structures (CCP-WSI blind test series 3)". In: *International Journal of Offshore and Polar Engineering* 30.1 (2020), pp. 1–10. ISSN: 10535381. DOI: 10.17736/ijope.2020.jc774.

[134] Matt Folley. *Numerical modelling of wave energy converters - State of the art techniques for single devices and arrays*. Ed. by Matt Folley. Elsevier, 2016. ISBN: 9780128032107. DOI: 10.1016/c2014-0-04006-3.

[135] Giovanni Bracco et al. "Experimental validation of the ISWEC wave to PTO model". In: *Ocean Engineering* 120 (2016), pp. 40–51. DOI: 10.1016/j.oceaneng.2016.05.006.

[136] Andrea Cagninei et al. "Productivity analysis of the full scale inertial sea wave energy converter prototype: A test case in Pantelleria Island". In: *Journal of Renewable and Sustainable Energy* 7 (2015), p. 61703. DOI: 10.1063/1.4936343.

[137] Mattia Raffero et al. "Stochastic control of inertial sea wave energy converter". In: *Scientific World Journal* 2015.2014 (2015). ISSN: 1537744X. DOI: 10.1155/2015/980613.

[138] Johannes Falnes. *Ocean Waves and Oscillating Systems: Linear Interactions Including Wave-Energy Extraction*. Cambridge University Press, 2002. DOI: 10.1017/CBO9780511754630.

[139] S Chakrabarti and Bala Murali. *Hydrodynamics of offshore structures*. WIT Press, 1994. ISBN: 9780905451664.

[140] George Biddell Airy. *Tides and Waves*. Ed. by B. Fellowes. 1845.

[141] O M Faltinsen. *Sea Loads on Ships and Offshore Structures*. Cambridge University Press, 1993.

[142] Aurélien Babarit and Gerard Delhommeau. "Theoretical and numerical aspects of the open source BEM solver NEMOH". In: *Proceedings of the 11th European Wave and Tidal Energy Conference*. September 2015 (2015), pp. 1–12. DOI: hal-01198800. URL: http://130.66.47.2/redmine/attachments/download/235/EWTEC2015%20Babarit.

[143] Markel Penalba, Thomas Eoin Kelly, and John V Ringwood. "Using NEMOH for Modelling Wave Energy Converters : A Comparative Study with WAMIT". In: *Proceedings of the 12th European Wave and Tidal Energy Conference* (2017).

[144] LHEEA. *NEMOH-Presentation*. URL: https://lheea.ec-nantes.fr/valorisation/logiciels-et-brevets/nemoh-presentation (visited on 12/17/2020).

[145] W E Cummins. "The impulse response function and ship motions". In: *Technical Report 1661* (1962), Department of the Navy, David Taylor model basin.

[146] Tristan Perez and Thor I. Fossen. "Joint identification of infinite-frequency added mass and fluid-memory models of marine structures". In: *Modeling, Identification and Control* 29.3 (2008), pp. 93–102. ISSN: 03327353. DOI: 10.4173/mic.2008.3.2.

[147] Tristan Pérez and Thor I. Fossen. "Time-vs. frequency-domain Identification of parametric radiation force models for marine structures at zero speed". In: *Modeling, Identification and Control* 29.1 (2008), pp. 1–19. ISSN: 03327353. DOI: 10.4173/mic.2008.1.1.

[148] Sergej Antonello Sirigu et al. "Experimental Investigation of Mooring System on a Wave Energy Converter in Operating and Extreme Wave Conditions". In: *Journal of Marine Science and Engineering* 8.180 (2020), pp. 1–31. DOI: 10.3390/jmse8030180.

[149] Mauro Bonfanti et al. "Real-Time Wave Excitation Forces Estimation: An Application on the ISWEC Device". In: *Journal of Marine Science and Engineering 2020, Vol. 8, Page 825* 8.10 (Oct. 2020), p. 825. DOI: 10.3390/JMSE8100825. URL: https://www.mdpi.com/864586.

[150] Willard J Pierson. "Wind Generated Gravity Waves". In: ed. by H E Landsberg. Vol. 2. Advances in Geophysics. Elsevier, 1955, pp. 93–178. DOI: https://doi.org/10.1016/S0065-2687(08)60312-X. URL: http://www.sciencedirect.com/science/article/pii/S006526870860312X.

[151] G B Whitham. *Linear and Nonlinear Waves*. Pure and Applied Mathematics: A Wiley Series of Texts, Monographs and Tracts. Wiley, 2011. ISBN: 9781118031209. URL: https://books.google.it/books?id=84Pulkf-Oa8C.

[152] Michel K Ochi. *Ocean Waves: the stochastic approach*. Vol. 6. Cambridge University Press, 2005.

[153] Stanislaw R Massel. *Ocean surface waves: their physics and prediction*. World Scientific Singapore, 1996, xvi, 491 p. ISBN: 9810216866 9810221096.

[154] M St Denis. "WJ Pierson. Motions of ships in confused seas". In: *Annual Meeting of the Society of Naval Architects and Marine Engineers*. Vol. 61. 1953, pp. 280–357.

[155] Norbert Wiener. *Extrapolation, Interpolation, and Smoothing of Stationary Time Series*. The MIT Press, 1964. ISBN: 0262730057.

[156] Willard J Pierson. *A unified mathematical theory for the analysis, propagation, and refraction of storm generated ocean surface waves*. Vol. pt.1 (1952. [New York] :New York University, College of Engineering, Dept. of Meteorology, 1952, p. 80. URL: https://www.biodiversitylibrary.org/item/86957.

[157] Willard J Pierson. *A unified mathematical theory for the analysis, propagation, and refraction of storm generated ocean surface waves*. Vol. pt.2 (1952. [New York] :New York University, College of Engineering, Dept. of Meteorology, 1952, p. 316. URL: https://www.biodiversitylibrary.org/item/86672.

[158] A. M. Yaglom. *Correlation Theory of Stationary and Related Random Functions*. New York: Springer-Verlag New York, 1987. ISBN: 9781461290865.

[159] Alexis Merigaud. "A harmonic balance framework for the numerical simulation of non-linear wave energy converter models in random seas". PhD Thesis. National University of Ireland Maynooth, 2018. URL: http://mural.maynoothuniversity.ie/10861/.

[160] J.M.J. Journée and W.W. Massie. *Offshore Hydromechanics*. First. Delft University of Technology, 2001, pp. 1–570. URL: https://ocw.tudelft.nl/wp-content/uploads/OffshoreHydromechanics%7B%5C_%7DJournee%7B%5C_%7DMassie.pdf.

[161] Klaus Hasselmann et al. "Measurements of wind-wave growth and swell decay during the Joint North Sea Wave Project (JONSWAP)". In: *Deut. Hydrogr. Z.* 8 (1973), pp. 1–95.

[162] IAHR Working Group on Wave Generation and Analysis. "List of sea-state parameters". In: *Journal of Waterway, Port, Coastal, and Ocean Engineering* 115.6 (1989), pp. 793–808.

[163] Peter Frigaard et al. "IAHR List of Sea Parameters: an update for multidirectional waves". In: *Proceedings of the 27th IAHR Congress, San Francisco, 10-15 August 1997*. Ed. by Mansard Etienne (ed.) Canada: Canadian Government Publishing, 1997. ISBN: 0660170930.

[164] A Papoulis and Unnikrishna Pillai. *Probability, random variables and stochastic processes*. 4th. McGraw-Hill, 2001.

[165] C. Vignat. "A generalized Isserlis theorem for location mixtures of Gaussian random vectors". In: *Statistics and Probability Letters* 82.1 (2012), pp. 67–71. ISSN: 01677152. DOI: 10.1016/j.spl.2011.09.008. arXiv: 1107.2309. URL: https://arxiv.org/pdf/1107.2309.pdf.

[166] Yoshimi Goda. *Numerical Experiments on Statistical Variability of Ocean Waves*. Tech. rep. Port and Airport Research Institute, 1977. URL: https://www.pari.go.jp/en/report%7B%5C_%7Dsearch/detail.php?id=1977060160201.

[167] S O Rice. "Mathematical analysis of random noise". In: *The Bell System Technical Journal* 23.3 (1944), pp. 282–332. ISSN: 0005-8580. DOI: 10.1002/j.1538-7305.1944.tb00874.x.

[168] M Tucker, P Challenor, and D Carter. "Numerical simulation of a random sea: a common error and its effect upon wave group statistics". In: *Applied Ocean Research* 6 (1984), pp. 118–122.

[169] Donald B. Percival. "Simulating Gaussian Random Processes with Specified Spectra". In: *Computing Science and Statistics* 24 (1992), pp. 534–538.

[170] E Funke and E Mansard. *A Rationale for the Use of the Deterministic Approach to Laboratory Wave Generation*. 1987.

[171] DNV. *DNVGL-RP-N103 Modelling and analysis of marine operations*. Tech. rep. DNV, 2011. URL: https://oilgas.standards.dnvgl.com/download/dnvgl-rp-n103-modelling-and-analysis-of-marine-operations.

[172] Alexis Merigaud and John V. Ringwood. "Free-Surface Time-Series Generation for Wave Energy Applications". In: *IEEE Journal of Oceanic Engineering* 43.1 (2018), pp. 19–35. ISSN: 03649059. DOI: 10.1109/JOE.2017.2691199.

[173] Josep R Medina and Carlos R Sanchez-Carratala. "Comparisons of numerical random wave simulators". In: *Coastal Engineering Proceedings* 1.21 (1988), p. 70. DOI: 10.9753/icce.v21.70. URL: https://journals.tdl.org/icce/index.php/icce/article/view/4277.

[174] L Borgman. "Ocean wave simulation for engineering design". In: *Journal of the Waterways and Harbors Division* 95 (1967), pp. 557–586.

[175] Masanobu Shinozuka and George Deodatis. "Simulation of Stochastic Processes by Spectral Representation". In: *Applied Mechanics Reviews* 44.4 (Apr. 1991), pp. 191–204. ISSN: 0003-6900. DOI: 10.1115/1.3119501. URL: https://doi.org/10.1115/1.3119501.

[176] V. Belenky. "Risk evaluation at extreme seas". In: *Proc. of 7th International Ship Stability Workshop*. Shanghai, Cina, 2004.

[177] P.D. Spanos and M.P. Mignolet. *Arma Monte Carlo Simulation in Probabilistic Structural Analysis*. 1989. DOI: 10.1177/058310248902101103.

[178] P D Spanos and B A Zeldin. "Monte Carlo Treatment of Random Fields: A Broad Perspective". In: *Applied Mechanics Reviews* 51.3 (Mar. 1998), pp. 219–237. ISSN: 0003-6900. DOI: 10.1115/1.3098999. URL: https://doi.org/10.1115/1.3098999.

[179] J. N. Newman. "Second order, slowly-variying forces on vessel in irregular waves". In: *International Symposium on the Dynamics of Marine Vehicles and Structures in Waves, London IME Vehicles and Structures in Waves*. 1, pp. 182–186.

[180] RON. *Rete Ondametrica Nazionale*. URL: http://dati.isprambiente.it/dataset/ron-rete-ondametrica-nazionale/ (visited on 03/09/2021).

[181] DNV GL. *Metocean Criteria for Jotun, Balder and Ringhorne. Balder FPU Life Extension 2018*. Tech. rep. 2018.

[182] M K Ochi and E N Hubble. "Six-parameter wave spectra". In: *Coastal Engineering* (1976), pp. 301–328.

[183] European Centre for Medium-Range Weather Forecasts. *ERA5*. 2021. URL: https://www.ecmwf.int/en/forecasts/datasets/reanalysis-datasets/era5 (visited on 03/09/2021).

[184] University of Trieste. *HyMOLab*. URL: http://hymolab.units.it/ (visited on 03/09/2021).

[185] Sergej Antonello Sirigu. "Development of a resonance-tunable Wave Energy Converter". PhD thesis. Politecnico di Torino, 2019.

[186] M Bonfanti et al. "A passive control strategy applied to the iswec device: Numerical modelling and experimental tests". In: *International Journal of Mechanics and Control* 21.2 (2020), pp. 143–154.

[187] Leonard Meirovitch. *Methods of Analytical Dynamics*. New York, United States: Dover Publications Inc., 2010, p. 544. ISBN: 0486432394.

[188] Zipfel PH , Author and Schiehlen W , Reviewer. "Modeling and Simulation of Aerospace Vehicle Dynamics". In: *Applied Mechanics Reviews* 54.6 (Nov. 2001), B101–B102. ISSN: 0003-6900. DOI: 10.1115/1.1421113. URL: https://doi.org/10.1115/1.1421113.

[189] Desch. *DESCH - Smart drive solutions*. 2020. URL: https://www.desch.com/en/products.html.

[190] Nicolás Faedo, Sébastien Olaya, and John V. Ringwood. "Optimal control, MPC and MPC-like algorithms for wave energy systems: An overview". In: *IFAC Journal of Systems and Control* 1 (2017), pp. 37–56. ISSN: 24686018. DOI: 10.1016/j.ifacsc.2017.07.001.

[191] S.A. Sirigu et al. "On-board sea state estimation method validation based on measured floater motion". In: *IFAC-PapersOnLine* 51.29 (2018). ISSN: 24058963. DOI: 10.1016/j.ifacol.2018.09.471.

[192] Christopher Cargo. "Design and control of hydraulic power take-offs for wave energy converters". PhD thesis. University of Bath, 2012. URL: https://researchportal.bath.ac.uk/en/studentTheses/design-and-control-of-hydraulic-power-take-offs-for-wave-energy-c.

[193] SIEMENS. *Simcenter Amesim*. 2020. URL: https://www.plm.automation.siemens.com/media/global/cz/Siemens-PLM-Simcenter-Amesim-eb-72523-A20-2%7B%5C_%7Dtcm84-55207.pdf (visited on 11/05/2020).

[194] E.R. Jefferys. "Simulation of wave power devices". In: *Applied Ocean Research* 6.1 (1984), pp. 31–39. ISSN: 0141-1187. DOI: https://doi.org/10.1016/0141-1187(84)90026-9. URL: http://www.sciencedirect.com/science/article/pii/0141118784900269.

[195] Gary Nolan and John Ringwood. "Design and control considerations for a wave energy converter". In: *Proc. Irish Signals and Systems Conf.* 2004, pp. 1–6.

[196] H. Engia and J. Hals. "Modelling and simulation of sea wave power conversion systems". In: *Proceedings of the 7th European Wave and Tidal Energy Conference*. Porto, Portugal, 2007, pp. 1–7.

[197] Giorgio Bacelli, Jean-Christophe Gilloteaux, and John Ringwood. "State space model of a hydraulic power take off unit for wave energy conversion employing bondgraphs". In: *10th World Renewable Energy Congress - WRECX*. Ed. by Ali Sayigh. Brighton: WREC, 2008, pp. 1–4. URL: http://mural.maynoothuniversity.ie/4419/.

[198] L. Yang, J. Todalshaug, and T. Moan. "A wear model for assessing the reliability of wave energy converter in heave with hydraulic power take-off". In: *8th European Wave and Tidal Energy Conference*. Uppsala, Sweden, 2009, pp. 874–881.

[199] Adi Kurniawan, Eilif Pedersen, and Torgeir Moan. "Bond graph modelling of a wave energy conversion system with hydraulic power take-off". In: *Renewable Energy* 38.1 (2012), pp. 234–244. ISSN: 09601481. DOI: 10.1016/j.renene.2011.07.027. URL: http://dx.doi.org/10.1016/j.renene.2011.07.027.

[200] Peter C. Breedveld. "Port-based modeling of mechatronic systems". In: *Mathematics and Computers in Simulation* 66.2-3 (2004), pp. 99–128. ISSN: 03784754. DOI: 10.1016/j.matcom.2003.11.002.

[201] The MathWorks Inc. *Simscape User's Guide*. 2020. URL: https://it.mathworks.com/help/pdf%7B%5C_%7Ddoc/physmod/simscape/simscape%7B%5C_%7Dug.pdf (visited on 11/05/2020).

[202] Bosch Rexroth. *Hägglunds Drive Systems and Solutions*. 2020. URL: https://dc-us.resource.bosch.com/media/us/products%7B%5C_%7D13/product%7B%5C_%7Dgroups%7B%5C_%7D1/industrial%7B%5C_%7Dhydraulics%7B%5C_%7D5/pdfs%7B%5C_%7D4/R999000124A%7B%5C_%7D2016-5.pdf (visited on 01/22/2021).

[203] José F. Gaspar et al. "Power take-off concept for wave energy converters based on oil-hydraulic transformer units". In: *Renewable Energy* 86 (2016), pp. 1232–1246. ISSN: 18790682. DOI: 10.1016/j.renene.2015.09.035.

[204] J.S.R. Jang. "ANFIS: Adaptive-Network-Based Fuzzy Inference System". In: *IEEE Transactions on Systems, Man and Cybernetics* 23.3 (1993), pp. 665–685. DOI: 10.1109/21.256541.

[205] Herbert E. Merritt. *Hydraulic Control Systems*. Ed. by Inc. John Wiley & Sons. 1991, pp. 1–368. ISBN: 978-0-471-59617-2.

[206] Bosch Rexroth. *2-way cartridge valves, directional functions*. 2020. URL: https://dc-us.resource.bosch.com/media/us/products%7B%5C_%7D13/product%7B%5C_%7Dgroups%7B%5C_%7D1/industrial%7B%5C_%7Dhydraulics%7B%5C_%7D5/pdfs%7B%5C_%7D4/re21010.pdf (visited on 01/22/2021).

[207] Bosch Rexroth. *Reliability characteristics MTTFD regarding the functional safety according to EN ISO 13849*. 2020. URL: https://dc-us.resource.bosch.com/media/us/products%7B%5C_%7D13/product%7B%5C_%7Dgroups%7B%5C_%7D1/industrial%7B%5C_%7Dhydraulics%7B%5C_%7D5/pdfs%7B%5C_%7D4/re08012.pdf (visited on 01/22/2021).

[208] Jinming Wu et al. "Latching and declutching control of the solo duck wave-energy converter with different load types". In: *Energies* 10.12 (2017). ISSN: 19961073. DOI: 10.3390/en10122070.

[209] J. Gaspar, M. Calvário, and C. Guedes Soares. "Pump and gas accumulator based phase control of wave energy converters". In: *Renewable Energies Offshore - 1st International Conference on Renewable Energies Offshore, RENEW 2014* Falcão 2007 (2015), pp. 295–303. DOI: 10.1201/b18973-43.

[210] A. Pourmovahed and D.R. Otis. "An Experimental Thermal Time-Constant Correlation for Hydraulic Accumulators". In: *Journal of Dynamic Systems, Measurement, and Control* 112.1 (1990), pp. 116–121. ISSN: 0022-0434. DOI: 10.1115/1.2894128. URL: https://doi.org/10.1115/1.2894128.

[211] C Qijuan et al. "Dynamic performance of key components for hydraulic power take-off of the wave energy converter". In: *IET Renewable Power Generation* 13.15 (2019), pp. 2929–2938. ISSN: 1752-1424. DOI: 10.1049/iet-rpg.2018.6097.

[212] Hoang Thinh Do, Tri Dung Dang, and Kyoung Kwan Ahn. "A multi-point-absorber wave-energy converter for the stabilization of output power". In: *Ocean Engineering* 161.March (2018), pp. 337–349. ISSN: 00298018. DOI: 10.1016/j.oceaneng.2018.03.093. URL: https://doi.org/10.1016/j.oceaneng.2018.03.093.

[213] Winner. *Relief 2 Ports*. 2020. URL: https://www.winnerhydraulics.com/category-37.htm (visited on 02/13/2021).

[214] Bosch Rexroth. *Axial Piston Fixed Motor A4FM*. 2020. URL: https://site.hypneumat.com.br/wp-content/uploads/2019/07/Axial-Piston-Fixed-Motor-A4FM.pdf (visited on 02/05/2021).

[215] Bosch Rexroth. *Fixed Motor*. 2020. URL: https://www.boschrexroth.com/it/xc/products/product-groups/industrial-hydraulics/motors/axial-piston-motors/fixed-motors (visited on 02/05/2021).

[216] SIEMENS. *1PH8 servomotors (synchronous)*. URL: https://mall.industry.siemens.com/mall/it/it/Catalog/Products/10045151%7B%5C#%7D (visited on 02/05/2021).

[217] Moog. *Electrohydrostatic Actuation Systems*. 2020. URL: https://www.moog.com/content/sites/global/en/products/actuation-systems/industrial.html (visited on 02/05/2021).

[218] C. J. Cargo, A. J. Hillis, and A. R. Plummer. "Optimisation and control of a hydraulic power take-off unit for a wave energy converter in irregular waves". In: *Proceedings of the Institution of Mechanical Engineers, Part A: Journal of Power and Energy* 228.4 (2014), pp. 462–479. ISSN: 20412967. DOI: 10.1177/0957650913519619.

[219] Markel Penalba and John V Ringwood. "A high-fidelity wave-to-wire model for wave energy converters". In: *Renewable Energy* 134 (2019), pp. 367–378. ISSN: 18790682. DOI: 10.1016/j.renene.2018.11.040.

[220] K. Huhtala and M. Vilenius. "Comparison of steady state models of hydraulic pump". In: *Proc. 5th Scand. Int. Conf. Fluid Power*. Linkoping, Sweden., 1997.

[221] Heon-Sul Jeong. "A novel performance model given by the physical dimensions of hydraulic axial piston motors: Model derivation". In: *Journal of Mechanical Science and Technology* 21.1 (2007), pp. 83–97. ISSN: 1738-494X. DOI: 10.1007/BF03161714. URL: https://doi.org/10.1007/BF03161714.

[222] Akira Hibi and Tsuneo Ichikawa. "Mathematical Model of the Torque Characteristics for Hydraulic Motors". In: *Bulletin of JSME* 20.143 (1977), pp. 616–621. DOI: 10.1299/jsme1958.20.616. URL: https://www.jstage.jst.go.jp/article/jsme1958/20/143/20%7B%5C_%7D143%7B%5C_%7D616/%7B%5C_%7Darticle.

[223] Heon-Sul Jeong and Hyoung-Eui Kim. "A novel performance model given by the physical dimensions of hydraulic axial piston motors: Experimental analysis". In: *Journal of Mechanical Science and Technology* 21.4 (2007), p. 630. ISSN: 1738-494X. DOI: 10.1007/BF03026968. URL: https://doi.org/10.1007/BF03026968.

[224] Nicola Pozzi, Mauro Bonfanti, and Giuliana Mattiazzo. "Mathematical Modeling and Scaling of the Friction Losses of a Mechanical Gyroscope". In: *International Journal of Applied Mechanics* 10.3 (2018). ISSN: 1758826X. DOI: 10.1142/S1758825118500242.

[225] SKF. *Cuscinetti Super-precision*. 2015. URL: https://www.skf.com/binaries/pub44/Images/0901d196803e9f7d-13383%7B%5C_%7D1-IT%7B%5C_%7Dtcm%7B%5C_%7D44-129877.pdf (visited on 01/26/2020).

[226] Pantecnica. *Sistemi di Tenuta Radiale DOMSEL*. 2017. URL: https://www.pantecnica.it/engineered-sealing-systems/rotanti/ (visited on 01/25/2021).

[227] Antonello Sergej Sirigu et al. "Numerical and Experimental Identification of the Aerodynamic Power Losses of the ISWEC". In: *Journal of Marine Science and Engineering* 8.49 (2020), pp. 1–25. DOI: 10.3390/jmse8010049.

[228] Peter R.N. Childs. *Rotating Flow*. Ed. by Peter R N Childs. Oxford: Butterworth-Heinemann, 2011. ISBN: 978-0-12-382098-3. DOI: 10.1016/C2009-0-30534-6.

[229] Hermann Schlichting and Klaus Gersten. *Boundary-Layer Theory*. Springer Berlin Heidelberg, 2017. DOI: 10.1007/978-3-662-52919-5.

[230] T Theodorsen and Arthur A Regier. *Experiments on Drag of Revolving Disks, Cylinders, and Streamline Rods at High Speeds*. Tech. rep. NACA, 1944.

[231] SIEMENS. *SIMOTICS T-1FW3 complete torque motors for SINAMICS S120*. 2020. URL: https://mall.industry.siemens.com/mall/en/it/Catalog/Products/10034485 (visited on 02/04/2021).

[232] P Ricci. "Chapter 3 - Time-Domain Models". In: *Numerical Modelling of Wave Energy Converters*. Ed. by Matt Folley. Academic Press, 2016, pp. 31–66. ISBN: 978-0-12-803210-7. DOI: https://doi.org/10.1016/B978-0-12-803210-7.00003-7. URL: http://www.sciencedirect.com/science/article/pii/B9780128032107000037.

[233] B Bosma et al. "Wave energy converter modeling in the frequency domain: A design guide". In: *2012 IEEE Energy Conversion Congress and Exposition (ECCE)*. 2012, pp. 2099–2106. DOI: 10.1109/ECCE.2012.6342553.

[234] Pierpaolo Ricci et al. "Time-domain models and wave energy converters performance assessment". In: *Proceedings of the International Conference on Offshore Mechanics and Arctic Engineering - OMAE*. Vol. 6. May 2015. 2008, pp. 699–708. ISBN: 9780791848234. DOI: 10.1115/OMAE2008-57642.

[235] Matt Folley and Trevor Whittaker. "Preliminary cross-validation of wave energy converter array interactions". In: *ASME 2013 32nd International Conference on Ocean, Offshore and Arctic Engineering*. American Society of Mechanical Engineers Digital Collection. 2013.

[236] Aurelien Babarit et al. *The NumWEC Project: Numerical Esitmation of Energy Delivery from a Selection of Wave Energy Converters*. Tech. rep. December. 2011, pp. 1–317. DOI: 10.13140/RG.2.1.3807.8885.

[237] M Alves. "Chapter 2 - Frequency-Domain Models". In: *Numerical Modelling of Wave Energy Converters*. Ed. by Matt Folley. Academic Press, 2016, pp. 11–30. ISBN: 978-0-12-803210-7. DOI: https://doi.org/10.1016/B978-0-12-803210-7.00002-5. URL: http://www.sciencedirect.com/science/article/pii/B9780128032107000025.

[238] L. S.P. Silva et al. "Stochastic analysis of nonlinear wave energy converters via statistical linearization". In: *Applied Ocean Research* (2020). ISSN: 01411187. DOI: 10.1016/j.apor.2019.102023.

[239] M Folley. "Chapter 4 - Spectral-Domain Models". In: *Numerical Modelling of Wave Energy Converters*. Ed. by Matt Folley. Academic Press, 2016, pp. 67–80. ISBN: 978-0-12-803210-7. DOI: https://doi.org/10.1016/B978-0-12-803210-7.00004-9. URL: http://www.sciencedirect.com/science/article/pii/B9780128032107000049.

[240] J.B. Roberts and P.D. Spanos. *Random vibration and statistical linearization*. Courier Corporation, 2003. ISBN: 9780486432403.

[241] Ove T Gudmestad and Jerome J Connor. "Linearization methods and the influence of current on the nonlinear hydrodynamic drag force". In: *Applied Ocean Research* 5.4 (1983), pp. 184–194. ISSN: 0141-1187. DOI: https://doi.org/10.1016/0141-1187(83)90032-9. URL: http://www.sciencedirect.com/science/article/pii/0141118783900329.

[242] M Folley and T Whittaker. "Spectral modelling of wave energy converters". In: *Coastal Engineering* 57.10 (2010), pp. 892–897. ISSN: 0378-3839. DOI: https://doi.org/10.1016/j.coastaleng.2010.05.007. URL: http://www.sciencedirect.com/science/article/pii/S0378383910000700.

[243] Matt Folley and Trevor Whittaker. "Validating a spectral-domain model of an OWC using physical model data". In: *International Journal of Marine Energy* 2 (2013), pp. 1–11. ISSN: 2214-1669. DOI: https://doi.org/10.1016/j.ijome.2013.05.003. URL: http://www.sciencedirect.com/science/article/pii/S2214166913000040.

[244] Pol D. Spanos et al. "Efficient dynamic analysis of a nonlinear wave energy harvester model". In: *Journal of Offshore Mechanics and Arctic Engineering* 138.4 (2016), pp. 1–8. ISSN: 1528896X. DOI: 10.1115/1.4032898.

[245] Pol D Spanos et al. *Stochastic Dynamic Analysis of U-OWC Wave Energy Converters*. June 2017. DOI: 10.1115/OMAE2017-61522. URL: https://doi.org/10.1115/OMAE2017-61522.

[246] Leandro S.P. Da Silva et al. "Nonlinear analysis of a heaving point absorber in frequency domain via statistical linearization". In: *Proceedings of the International Conference on Offshore Mechanics and Arctic Engineering - OMAE* 9.June (2019). DOI: 10.1115/OMAE2019-95785.

[247] L J Bain and M Engelhardt. *Introduction to Probability and Mathematical Statistics*. Classic Series. Brooks/Cole Cengage Learning, 1992. ISBN: 9780534380205. URL: https://books.google.it/books?id=MkFRIAAACAAJ.

[248] C Lagarias, Jeffrey et al. "Convergence properties of the nelder–mead simplex method in low dimensions". In: *SIAM Journal on Optimization* 9.1 (1998), pp. 112–147. URL: http://citeseerx.ist.psu.edu/viewdoc/download?doi=10.1.1.120.6062%7B%5C&%7Drep=rep1%7B%5C&%7Dtype=pdf.

[249] The MathWorks Inc. *Get Started with Fast Restart*. 2020. URL: https://www.mathworks.com/help/simulink/ug/fast-restart-workflow.html (visited on 01/29/2021).

[250] J Weber. "WEC Technology Readiness and Performance Matrix – finding the best research technology development trajectory". In: *International Conference on Ocean Energy, ICOE*. 2012, pp. 1–10.

[251] Jochem Weber et al. "Cost, time and risk assessment of different wave energy converter technology development trajectories". In: *Proceedings of the 12th European Wave and Tidal Energy Conference. Cork, Ireland*. 2017, pp. 1–8. URL: https://www.researchgate.net/publication/326986133%7B%5C_%7DCost%7B%5C_%7Dtime%7B%5C_%7Dand%7B%5C_%7Drisk%7B%5C_%7Dassessment%7B%5C_%7Dof%7B%5C_%7Ddifferent%7B%5C_%7Dwave%7B%5C_%7Denergy%7B%5C_%7Dconverter%7B%5C_%7Dtechnology%7B%5C_%7Ddevelopment%7B%5C_%7Dtrajectories.

[252] Sergej Antonello Sirigu et al. "Techno-Economic optimisation for a wave energy converter via genetic algorithm". In: *Journal of Marine Science and Engineering* 8.8 (2020). ISSN: 20771312. DOI: 10.3390/JMSE8070482.

[253] J Cordonnier et al. "SEAREV: Case study of the development of a wave energy converter". In: *Renewable Energy* 80 (2015), pp. 40–52. ISSN: 18790682. DOI: 10.1016/j.renene.2015.01.061.

[254] Sergej A. Sirigu et al. "ISWEC design tool". In: *International Journal of Marine Energy* 15 (2016), pp. 201–213. ISSN: 22141669. DOI: 10.1016/j.ijome.2016.04.011. URL: http://dx.doi.org/10.1016/j.ijome.2016.04.011.

[255] Si-Ming Zheng et al. "Numerical study on the dynamics of a two-raft wave energy conversion device". In: *Journal of Fluids and Structures* 58 (2015), pp. 271–290. ISSN: 0889-9746. DOI: https://doi.org/10.1016/j.jfluidstructs.2015.07.008. URL: http://www.sciencedirect.com/science/article/pii/S0889974615001942.

[256] Kalyanmoy Deb. "An efficient constraint handling method for genetic algorithms". In: *Computer Methods in Applied Mechanics and Engineering* 186.2-4 (2000), pp. 311–338. ISSN: 00457825. DOI: 10.1016/S0045-7825(99)00389-8.

[257] M. A. Jusoh et al. "Parameters estimation of hydraulic power take-off system for wave energy conversion system using genetic algorithm". In: *IOP Conference Series: Earth and Environmental Science* 463.1 (2020). ISSN: 17551315. DOI: 10.1088/1755-1315/463/1/012129.

[258] T. Baeck, D.B. Fogel, and Z. Michalewicz. *Handbook of Evolutionary Computation*. Taylor & Francis, 1997. ISBN: 9780750308953. URL: https://books.google.it/books?id=n5nuiIZvmpAC.

[259] Dripta Sarkar, Kenneth Doherty, and Frederic Dias. "The modular concept of the Oscillating Wave Surge Converter". In: *Renewable Energy* 85 (2016), pp. 484–497. ISSN: 18790682. DOI: 10.1016/j.renene.2015.06.012. URL: http://dx.doi.org/10.1016/j.renene.2015.06.012.

[260] Dripta Sarkar et al. "Prediction and optimization of wave energy converter arrays using a machine learning approach". In: *Renewable Energy* 97 (2016), pp. 504–517. ISSN: 18790682. DOI: 10.1016/j.renene.2016.05.083. URL: http://dx.doi.org/10.1016/j.renene.2016.05.083.

[261] S. N. Sivanandam and S. N. Deepa. *Introduction to genetic algorithms*. Springer-Verlag Berlin Heidelberg, 2008, pp. 1–442. ISBN: 9783540731894. DOI: 10.1007/978-3-540-73190-0.

[262] Panos Pardalos and H. Edwin Romeijn. *Handbook of Global Optimization. Volume 2*. Springer US, 2002. ISBN: 978-1-4020-0632-6. DOI: 10.1007/978-1-4757-5362-2. URL: https://www.springer.com/gp/book/9781402006326.

[263] Jasbir Arora. *Introduction to Optimum Design*. Academic Press, 2012. ISBN: 9780123813756. DOI: 10.1016/C2009-0-61700-1. URL: http://mu.menofia.edu.eg/PrtlFiles/Staff/1045/Portal/Files/Introduction%20to%20Optimum%20Design,%203nd%20Ed(3).pdf.

[264] Kalyanmoy Deb. *Multi-Objective Optimization Using Evolutionary Algorithms: An Introduction*. Tech. rep. Kanpur Kanpur, India: Department of Mechanical Engineering Indian Institute of Technology, 2011. DOI: 10.1001/jama.1943.02840160014004.

[265] Carlos Coello Coello, Gary B. Lamont, and David A. van Veldhuizen. *Evolutionary Algorithms for Solving Multi-Objective Problems*. Springer US, 2007, p. 800. ISBN: 978-0-387-33254-3. DOI: 10.1007/978-0-387-36797-2.

[266] The MathWorks Inc. *Optimization Toolbox User's Guide*. 2020. URL: https://www.mathworks.com/help/pdf%7B%5C_%7Ddoc/optim/optim.pdf (visited on 11/05/2020).

[267] The MathWorks Inc. *Global Optimization Toolbox User's Guide*. 2020. URL: https://www.mathworks.com/help/pdf%7B%5C_%7Ddoc/gads/gads.pdf (visited on 11/05/2020).

[268] The MathWorks Inc. *Find minimum of function using genetic algorithm*. 2021. URL: https://www.mathworks.com/help/gads/ga.html (visited on 03/05/2021).

[269] Kusum Deep et al. "A real coded genetic algorithm for solving integer and mixed integer optimization problems". In: *Applied Mathematics and Computation* 212.2 (2009), pp. 505–518. ISSN: 00963003. DOI: 10.1016/j.amc.2009.02.044.

[270] Kusum Deep and Manoj Thakur. "A new mutation operator for real coded genetic algorithms". In: *Applied Mathematics and Computation* 193.1 (2007), pp. 211–230. ISSN: 00963003. DOI: 10.1016/j.amc.2007.03.046.

[271] Kusum Deep and Manoj Thakur. "A new crossover operator for real coded genetic algorithms". In: *Applied Mathematics and Computation* 188.1 (2007), pp. 895–911. ISSN: 00963003. DOI: 10.1016/j.amc.2006.10.047.

[272] Miettinen Kaisa. *Nonlinear Multiobjective Optimization*. Vol. 12. International Series in Operations Research & Management Science. Boston, USA: Kluwer Academic Publishers, 1999.

[273] Jeffrey A Joines and Christopher R Houck. "On the use of non-stationary penalty functions to solve nonlinear constrained optimization problems with GA's". In: *IEEE Conference on Evolutionary Computation - Proceedings*. 2/-. IEEE, 1994, pp. 579–584. DOI: 10.1109/icec.1994.349995.

[274] Abdollah Homaifar, Charlene X Qi, and Steven H Lai. "Constrained Optimization Via Genetic Algorithms". In: *SIMULATION* 62.4 (Apr. 1994), pp. 242–253. ISSN: 0037-5497. DOI: 10.1177/003754979406200405. URL: http://journals.sagepub.com/doi/10.1177/003754979406200405.

[275] Anna Garcia-Teruel, David I M Forehand, and Henry Jeffrey. "Wave Energy Converter hull design for manufacturability and reduced LCOE". In: *Proc. of the 7th International Conference on Ocean Energy (ICOE)* (2018), pp. 1–9. URL: https://www.icoe-conference.com/publication/wave-energy-converter-hull-design-for-manufacturability-and-reduced-lcoe/.

[276] Markel Penalba, Giussepe Giorgi, and John V. Ringwood. *Mathematical modelling of wave energy converters: A review of nonlinear approaches*. 2017. DOI: 10.1016/j.rser.2016.11.137.

[277] Daniele Chiccoli et al. "Numerical Analysis of Two Different Hydraulic Power Take-Off Configurations for Renewable Energy Applications". In: *In Proceedings of the 4th Asian Wave and Tidal Energy Conference (AWTEC)*. Taipei (Taiwan), 2018.

[278] Yerai Peña-Sanchez et al. "Finite-Order hydrodynamic Approximation by Moment-Matching (FOAMM) toolbox for wave energy applications". In: *13th European Wave and Tidal Energy Conference* (2019).

[279] P A Brodtkorb, D Myrhaug, and H Rue. "Joint distribution of wave height and wave crest velocity from reconstructed data". In: *Proceedings of the 1999 Ninth International Offshore and Polar Engineering Conference (Volume 3), Brest, France, 30 May - 4 June 1999*. Ed. by J S Chung et al. International Society of Offshore and Polar Engineers, 1999, pp. 66–73. ISBN: 1880653427.

[280] Giuseppe Giorgi and John V Ringwood. "Parametric motion detection for an oscillating water column spar buoy." In: *Proceedings of the 3rd International Conference on Renewable Energies Offshore RENEW*. Lisbon, 2018.

[281] Jean-christophe Gilloteaux and John V Ringwood. "Control-informed geometric optimisation of wave energy converters". In: *IFAC Proceedings Volumes (IFAC-PapersOnline)* 1 (2010), pp. 366–371. ISSN: 14746670. DOI: 10.3182/20100915-3-DE-3008.00072.

[282] Paula Garcia-Rosa, Giorgio Bacelli, and John Ringwood. "Control-Informed Geometric Optimization of Wave Energy Converters: The Impact of Device Motion and Force Constraints". In: *Energies* 8.12 (2015), pp. 13672–13687. ISSN: 1996-1073. DOI: 10.3390/en81212386. URL: http://www.mdpi.com/1996-1073/8/12/12386.

[283] Jeffre C Lagarias et al. "Convergence properties of the nelder–mead simplex method in low dimensions". In: *SIAM Journal on Optimization* 9.1 (1998), pp. 112–147. URL: http://citeseerx.ist.psu.edu/viewdoc/download?doi=10.1.1.120.6062%7B%5C&%7Drep=rep1%7B%5C&%7Dtype=pdf.

[284] Adrian de Andres et al. "Techno-economic related metrics for a wave energy converters feasibility assessment". In: *Sustainability (Switzerland)* 8.11 (2016). ISSN: 20711050. DOI: 10.3390/su8111109.

[285] Driscoll Frederick R, Weber Jochem W, and Jenne Dale S. *Methodology to Calculate the ACE and HPQ Metrics Used in the Wave Energy Prize*. English. Tech. rep. United States, 2018. DOI: 10.2172/1426063. URL: https://www.osti.gov/biblio/1426063%20https://www.osti.gov/servlets/purl/1426063.

[286] Michael T M Emmerich and André H Deutz. "A tutorial on multiobjective optimization: fundamentals and evolutionary methods". In: *Natural Computing* 17.3 (2018), pp. 585–609. ISSN: 15729796. DOI: 10.1007/s11047-018-9685-y.

[287] A. Babarit and A. H. Clément. *Optimal latching control of a wave energy device in regular and irregular waves*. 2006. DOI: 10.1016/j.apor.2006.05.002.

[288] Liguo Wang, Jan Isberg, and Elisabetta Tedeschi. "Review of control strategies for wave energy conversion systems and their validation: the wave-to-wire approach". In: *Renewable and Sustainable Energy Reviews* 81 (2018), pp. 366–379. ISSN: 1364-0321. DOI: https://doi.org/10.1016/j.rser.2017.06.074. URL: https://www.sciencedirect.com/science/article/pii/S136403211731016X.

[289] E Anderlini et al. "Control of a Realistic Wave Energy Converter Model Using Least-Squares Policy Iteration". In: *IEEE Transactions on Sustainable Energy* 8.4 (2017), pp. 1618–1628. ISSN: 1949-3037. DOI: 10.1109/TSTE.2017.2696060.

[290] E Anderlini et al. "Reactive control of a two-body point absorber using reinforcement learning". In: *Ocean Engineering* 148 (2018), pp. 650–658. ISSN: 0029-8018. DOI: https://doi.org/10.1016/j.oceaneng.2017.08.017. URL: https://www.sciencedirect.com/science/article/pii/S0029801817304699.

[291] J V Ringwood. "Chapter 12 - Control Optimisation and Parametric Design". In: *Numerical Modelling of Wave Energy Converters*. Ed. by Matt Folley. Academic Press, 2016, pp. 229–251. ISBN: 978-0-12-803210-7. DOI: https://doi.org/10.1016/B978-0-12-803210-7.00012-8. URL: http://www.sciencedirect.com/science/article/pii/B9780128032107000128.

[292] Nicolas Faedo et al. "Optimisation- vs. non-optimisation-based energy-maximising control for wave energy converters: A case study". In: *European Control Conference 2020, ECC 2020* May (2020), pp. 843–848.

[293] F. Fusco, J.C. Gilloteaux, and J. V. Ringwood. "A study on Prediction Requirements in time-domain Control of Wave Energy Converters". In: *IFAC Proceedings Volumes*. Vol. 43. 20. IFAC, 2010, pp. 372–377. ISBN: 9783902661883. DOI: 10.3182/20100915-3-DE-3008.00075. URL: http://dx.doi.org/10.3182/20100915-3-DE-3008.00075.

[294] Bradley A Ling and Belinda A Batten. "Real Time Estimation and Prediction of Wave Excitation Forces on a Heaving Body". In: *Volume 9: Ocean Renewable Energy*. Vol. Volume 9: International Conference on Offshore Mechanics and Arctic Engineering. American Society of Mechanical Engineers, May 2015. ISBN: 978-0-7918-5657-4. DOI: 10.1115/OMAE2015-41087.

URL: https://asmedigitalcollection.asme.org/OMAE/proceedings/OMAE2015/56574/St.%20John's,%20Newfoundland,%20Canada/280023.

[295] M. Garcia-Abril, F. Paparella, and J. V. Ringwood. "Excitation force estimation and forecasting for wave energy applications". In: *IFAC-PapersOnLine* 50.1 (2017), pp. 14692–14697. ISSN: 24058963. DOI: 10.1016/j.ifacol.2017.08.2499.

[296] Nicola Pozzi et al. "Experimental evaluation of different hydrodynamic modelling techniques applied to the ISWEC". In: (2017), pp. 1–10.

[297] *MTi User Manual*. 2020. URL: https://www.xsens.com/hubfs/Downloads/usermanual/MTi%7B%5C_%7Dusermanual.pdf.

[298] *ECN 413, ECN 425, ERN 487, Product Information ECN*. 2017. URL: https://www.heidenhain.com/fileadmin/pdb/media/img/587717%7B%5C_%7D07%7B%5C_%7DA%7B%5C_%7D02%7B%5C_%7DExN%7B%5C_%7D4xx%7B%5C_%7DAufzugtechnik%7B%5C_%7Den.pdf.

[299] *NI cRIO-9030 user manual*. 2020. URL: http://www.ni.com/pdf/manuals/376260a%7B%5C_%7D02.pdf.

[300] Bahador Khaleghi et al. "Multisensor data fusion: A review of the state-of-the-art". In: *Information Fusion* 14.1 (2013), pp. 28–44. ISSN: 15662535. DOI: 10.1016/j.inffus.2011.08.001. URL: http://dx.doi.org/10.1016/j.inffus.2011.08.001.

[301] Man Lok Fung, Michael Z.Q. Chen, and Yong Hua Chen. "Sensor fusion: A review of methods and applications". In: *Proceedings of the 29th Chinese Control and Decision Conference, CCDC 2017* (2017), pp. 3853–3860. DOI: 10.1109/CCDC.2017.7979175.

[302] Yerai Pena-Sanchez et al. "A Critical Comparison of Excitation Force Estimators for Wave-Energy Devices". In: *IEEE Transactions on Control Systems Technology* October (2019), pp. 1–13. ISSN: 1063-6536. DOI: 10.1109/tcst.2019.2939092.

[303] H.-N. Nguyen and Paolino Tona. "Wave Excitation Force Estimation for Wave Energy Converters of the Point-Absorber Type". In: *IEEE Transactions on Control Systems Technology* 26 (2018), pp. 2173–2181.

[304] M Abdelrahman et al. "Estimation of wave excitation force for wave energy converters". In: *2016 3rd Conference on Control and Fault-Tolerant Systems (SysTol)*. 2016, pp. 654–659. DOI: 10.1109/SYSTOL.2016.7739823.

[305] Yerai Pena-Sanchez et al. "Estimation and Forecasting of Excitation Force for Arrays of Wave Energy Devices". In: *IEEE Transactions on Sustainable Energy* 9.4 (2018), pp. 1672–1680. ISSN: 19493029. DOI: 10.1109/TSTE.2018.2807880.

[306] A. J. Hillis, A. Brask, and C. Whitlam. "Real-time wave excitation force estimation for an experimental multi-DOF WEC". In: *Ocean Engineering* 213.June (2020), p. 107788. ISSN: 00298018. DOI: 10.1016/j.oceaneng.2020.107788. URL: https://doi.org/10.1016/j.oceaneng.2020.107788.

[307] Liang Li, Zhen Gao, and Zhi Ming Yuan. "On the sensitivity and uncertainty of wave energy conversion with an artificial neural-network-based controller". In: *Ocean Engineering* (2019). ISSN: 00298018. DOI: 10.1016/j.oceaneng.2019.05.003.

[308] Mohammed A A Desouky and Ossama Abdelkhalik. "Wave prediction using wave rider position measurements and NARX network in wave energy conversion". In: *Applied Ocean Research* 82 (2019), pp. 10–21. ISSN: 0141-1187. DOI: https://doi.org/10.1016/j.apor.2018.10.016.

[309] L. Genuardi et al. *An application of model predictive control logic to inertial sea wave energy converter*. Vol. 73. 2019. DOI: 10.1007/978-3-030-20131-9_351.

[310] Mauro Bonfanti et al. "Excitation Forces Estimation for Non-linear Wave Energy Converters : A Neural Network Approach". In: *IFAC-PapersOnLine* (2020).

[311] John L Crassidis and John L Junkins. *Optimal Estimation of Dynamic Systems*. 2nd. Chapman; Hall/CRC, 2011. ISBN: 1439839859.

[312] S Ablameyko et al. *Neural Networks for Instrumentation, Measurement and Related Industrial Applications*. Vol. 185 of NAT. Amsterdam, The Netherlands: IOS Press, 2003. ISBN: 978-1-58603-303-3.

[313] Q Laurent. "Estimation and prediction of wave input and system states based on local hydropressure and machinery response measurements". PhD thesis. 2016.

[314] Ruiyin Song, Yong Ming Dai, and Xiaohua Qian. "Intermittent wave energy generation system with hydraulic energy storage and pressure control for stable power output". In: *Journal of Marine Science and Technology (Japan)* 23.4 (2018), pp. 802–813. ISSN: 09484280. DOI: 10.1007/s00773-017-0512-4. URL: http://dx.doi.org/10.1007/s00773-017-0512-4.

[315] Zhen Liu et al. "Study on energy conversion and storage system for a prototype buoys-array wave energy converter". In: *Energy for Sustainable Development* 34 (2016), pp. 100–110. ISSN: 23524669. DOI: 10.1016/j.esd.2016.07.004.

[316] Anders Hedegaard Hansen, Magnus F. Asmussen, and Michael M. Bech. "Model predictive control of awave energy converter with discrete fluid power power take-off system". In: *Energies* 11.3 (2018). ISSN: 19961073. DOI: 10.3390/en11030635.

[317] Richard B Vinter. "Optimal Control and Pontryagin's Maximum Principle". In: *Encyclopedia of Systems and Control*. Ed. by John Baillieul and Tariq Samad. London: Springer London, 2013, pp. 1–9. ISBN: 978-1-4471-5102-9. DOI: 10.1007/978-1-4471-5102-9_200-1. URL: https://doi.org/10.1007/978-1-4471-5102-9%7B%5C_%7D200-1.

[318] R W M Hendrikx et al. "Optimal control of a wave energy converter". In: *2017 IEEE Conference on Control Technology and Applications (CCTA)*. 2017, pp. 779–786. DOI: 10.1109/CCTA.2017.8062556.

[319] K Deb et al. "A fast and elitist multiobjective genetic algorithm: NSGA-II". In: *IEEE Transactions on Evolutionary Computation* 6.2 (2002), pp. 182–197. DOI: 10.1109/4235.996017.

This Ph.D. thesis has been typeset by means of the TEX-system facilities. The typesetting engine was pdfLATEX. The document class was `toptesi`, by Claudio Beccari, with option `tipotesi=scudo`. This class is available in every up-to-date and complete TEX-system installation.